frontiers | Research Topics

Engineered biomimetic micro/nano-materials for tissue regeneration

Edited by
Juan Wang, Tonghe Zhu, Yawei Du,
Liang Chen and Régis Laurent

Published in
Frontiers in Bioengineering and Biotechnology

ISSN 1664-8714
ISBN 978-2-8325-4749-6
DOI 10.3389/978-2-8325-4749-6

About Frontiers

Frontiers is more than just an open access publisher of scholarly articles: it is a pioneering approach to the world of academia, radically improving the way scholarly research is managed. The grand vision of Frontiers is a world where all people have an equal opportunity to seek, share and generate knowledge. Frontiers provides immediate and permanent online open access to all its publications, but this alone is not enough to realize our grand goals.

Frontiers journal series

The Frontiers journal series is a multi-tier and interdisciplinary set of open-access, online journals, promising a paradigm shift from the current review, selection and dissemination processes in academic publishing. All Frontiers journals are driven by researchers for researchers; therefore, they constitute a service to the scholarly community. At the same time, the *Frontiers journal series* operates on a revolutionary invention, the tiered publishing system, initially addressing specific communities of scholars, and gradually climbing up to broader public understanding, thus serving the interests of the lay society, too.

Dedication to quality

Each Frontiers article is a landmark of the highest quality, thanks to genuinely collaborative interactions between authors and review editors, who include some of the world's best academicians. Research must be certified by peers before entering a stream of knowledge that may eventually reach the public - and shape society; therefore, Frontiers only applies the most rigorous and unbiased reviews. Frontiers revolutionizes research publishing by freely delivering the most outstanding research, evaluated with no bias from both the academic and social point of view. By applying the most advanced information technologies, Frontiers is catapulting scholarly publishing into a new generation.

What are Frontiers Research Topics?

Frontiers Research Topics are very popular trademarks of the *Frontiers journals series*: they are collections of at least ten articles, all centered on a particular subject. With their unique mix of varied contributions from Original Research to Review Articles, Frontiers Research Topics unify the most influential researchers, the latest key findings and historical advances in a hot research area.

Find out more on how to host your own Frontiers Research Topic or contribute to one as an author by contacting the Frontiers editorial office: frontiersin.org/about/contact

Engineered biomimetic micro/nano-materials for tissue regeneration

Topic editors

Juan Wang – Shanghai Jiao Tong University, China
Tonghe Zhu – Shanghai University of Engineering Sciences, China
Yawei Du – Shanghai Jiao Tong University, China
Liang Chen – Shanghai Jiao Tong University, China
Régis Laurent – UPR8241 Laboratoire de Chimie de Coordination (LCC), France

Citation

Wang, J., Zhu, T., Du, Y., Chen, L., Laurent, R., eds. (2024). *Engineered biomimetic micro/nano-materials for tissue regeneration*. Lausanne: Frontiers Media SA.
doi: 10.3389/978-2-8325-4749-6

Table of contents

frontiers | Frontiers in Bioengineering and Biotechnology

TYPE Original Research
PUBLISHED 19 December 2022
DOI 10.3389/fbioe.2022.1058355

OPEN ACCESS

EDITED BY
Yawei Du,
Shanghai Jiao Tong University, China

REVIEWED BY
Yiwei Li,
North Carolina State University, United States
Wei Xiong,
Beijing Tongren Hospital, Capital Medical University, China
Tuo Yang,
University of California, San Diego, United States

*CORRESPONDENCE
Luis García-Fernández,
luis.garcia@csic.es

SPECIALTY SECTION
This article was submitted to Biomaterials, a section of the journal Frontiers in Bioengineering and Biotechnology

RECEIVED 30 September 2022
ACCEPTED 07 December 2022
PUBLISHED 19 December 2022

CITATION
Escalante S, Rico G, Becerra J, San Román J, Vázquez-Lasa B, Aguilar MR, Durán I and García-Fernández L (2022), Chemically crosslinked hyaluronic acid-chitosan hydrogel for application on cartilage regeneration.
Front. Bioeng. Biotechnol. 10:1058355.
doi: 10.3389/fbioe.2022.1058355

Chemically crosslinked hyaluronic acid-chitosan hydrogel for application on cartilage regeneration

Sandra Escalante[1,2], Gustavo Rico[1,2], José Becerra[1,2], Julio San Román[2,3], Blanca Vázquez-Lasa[2,3], Maria Rosa Aguilar[2,3], Iván Durán[1,2] and Luis García-Fernández[2,3]*

[1]Department of Cell Biology, Genetics and Physiology, Faculty of Science, University of Malaga, Malaga, Spain, [2]Centro de Investigación Biomédica en Red de Bioingeniería, Biomateriales y Nanomedicina (CIBER-BBN), Instituto de Salud Carlos III, Madrid, Spain, [3]Grupo de Biomateriales, Departamento de Nanomateriales Poliméricos y Biomateriales, Instituto de Ciencia y Tecnología de Polímeros (ICTP), CSIC, Madrid, Spain

Articular cartilage is an avascular tissue that lines the ends of bones in diarthrodial joints, serves as support, acts as a shock absorber, and facilitates joint's motion. It is formed by chondrocytes immersed in a dense extracellular matrix (principally composed of aggrecan linked to hyaluronic acid long chains). Damage to this tissue is usually associated with traumatic injuries or age-associated processes that often lead to discomfort, pain and disability in our aging society. Currently, there are few surgical alternatives to treat cartilage damage: the most commonly used is the microfracture procedure, but others include limited grafting or alternative chondrocyte implantation techniques, however, none of them completely restore a fully functional cartilage. Here we present the development of hydrogels based on hyaluronic acid and chitosan loaded with chondroitin sulfate by a new strategy of synthesis using biodegradable di-isocyanates to obtain an interpenetrated network of chitosan and hyaluronic acid for cartilage repair. These scaffolds act as delivery systems for the chondroitin sulfate and present mucoadhesive properties, which stabilizes the clot of microfracture procedures and promotes superficial chondrocyte differentiation favoring a true articular cellular colonization of the cartilage. This double feature potentially improves the microfracture technique and it will allow the development of next-generation therapies against articular cartilage damage.

KEYWORDS

hydrogel, cartilage regeneration, microfracture, hyaluronic acid, chitosan, chondroitin sulfate, diisocyanate

1 Introduction

Articular cartilage (AC) is an avascular connective tissue located in the diarthrodial joints covering the surface of bones, their main function is to provide a low friction surface for transmitting the mechanical load between bones (Adams et al., 2009).

AC is formed by chondrocytes distributed within an extracellular matrix (ECM). This ECM is composed of collagen, mainly of type II, glycosaminoglycans (GAGs) and proteoglycans (Mow et al., 1992). The main characteristics of this tissue, in addition to its peculiar structure and topography (Becerra et al., 2010), are its low metabolism and the absence of blood vessels, nerves and lymphatic systems. These features could be the reasons for its limited capability of repair and regeneration, especially for large defects (>3 mm^2) (Doherty, 1992; Armiento et al., 2018).

Cartilage damage, one of the major skeletal morbidities in our society, is usually produced by repeating loads, sudden impact, foreign bodies or damage in other connective tissue, but also because of the natural degeneration due to the decrease of biological and biomechanical properties through aging. In both cases, the progressive degeneration of AC is the most common form of joint disease and represents one of the main causes of osteoarthritis (OA) (Lawrence et al., 2008).

Currently there are several options for the treatment of cartilage defects, but most of the current treatments are focused on symptom relief (Mollon et al., 2013):

- Non-surgical treatment: Oral analgesia, physiotherapy, intraarticular injection of GAGs, platelet rich plasma (PRP) and/or anti-inflammatory drugs (Pontes-Quero et al., 2019; García-Fernández et al., 2020).
- Arthroscopic chondroplasty: The damaged cartilage, loose bodies, and chondral fragments are removed (mechanical saver devices, radiofrequency ablation...) to produce a smooth chondral surface and decrease the mechanical joint irritation (Liptak and Theodoulou, 2017).
- Pridie Drilling or Microfracture (MF): Minimally invasive procedure that drills the subchondral bone at the defected site with the objective of releasing osteoprogenitor cells into the defect (Dehghani and Fathi, 2017).
- Autologous or allogenic osteochondral grafting: This technique uses allogenic or autologous osteochondral tissue to fill the defect (Dehghani and Fathi, 2017). Autologous Chrondrocytes Implant (ACI): Implantation of chondrocytes coming from an enzymatically treated biopsy from patient cartilage (Mistry et al., 2017).
- Matrix Autologous Chondrocytes Implant (MACI): Similar to ACI, but the cells are growing in a matrix, and this matrix is implanted to the patient (Mistry et al., 2017).

A typical lesion of professional athletes and sport players exposed to great efforts consists on articular damage with an average size of around 2–3 mm^2 without affection of the subchondral bone. In this situation, the most used procedure is the microfracture (Sledge, 2001). Microfracture is an inexpensive technique, it presents a quick recovery time and reports positive result in pain relief and joint functionality (Mollon et al., 2013). This technique consists of the micro-perforation of the subchondral bone, allowing bleeding. The blood coming from the subchondral bone fills the damage and forms a clot with high levels of stem cells and growth factors (Frehner and Benthien, 2018). This clot acts as a scaffold for the development of the new cartilage. However, this technique often results in the formation of fibrocartilage with lower biomechanical properties than those of hyaline cartilage. Other problems with this procedure are the instability of the clot (resulting in a deficient integration with the surrounding tissue) and the fast rate of degradation (not allowing the complete regeneration of the cartilage) (Chung and Burdick, 2008).

Recent advances in cartilage repair focus on the use of scaffolds enhancing the biochemical and biomechanical properties of the cartilage regeneration process. In these studies, different biomaterials have been proposed as scaffolds for cartilage regeneration like gellan gum, polyglucosamine/glucosamine carbonate hydrogel or fibrin-hyaluronan matrix among others (Nehrer et al., 2008; Oliveira, 2010; Vilela et al., 2018; Pipino et al., 2019).

In this article, we present the development of an adhesive polymer scaffold based on hyaluronic acid (HA) and chitosan (Ch) to fit into a cartilage defect after a microfracture procedure with the capacity to stabilize the blood clot in the cartilage. HA is non-immunogenic natural polymer with a unique viscoelastic nature and one of the main components of the hyaline cartilage. (Chartrain et al., 2022). It is commonly used in intra-articular injections to stimulate and repair damaged cartilage because it promotes cell adhesion and proliferation and presents anti-inflammatory properties as well as non-immunogenicity (Shiroud Heidari et al., 2023). However, hydrogels made of HA present quick degradation rates, for this reason it is necessary to modify them to enhance their degradation properties. Ch is a cationic polysaccharide easy to obtain from crustacean shells. It is widely used as biomaterial due to its low toxicity and good biocompatibility and degradability (Shigemasa and Minami, 1996). Ch also present good adhesive properties to tissue and hemostasis, these properties allow a normal clot formation and impeding clot retraction (Shive et al., 2006; Chen, 2018; Pereira et al., 2018). Different studies demonstrate the efficacy of the marrow-derived mesenchymal stem cells (MSC) to migrate into the defect, proliferate, fill cavities and differentiate creating new cartilage (Shapiro et al., 1993; Anraku, 2009). Chondroitin sulfate (CS) is one of the principal GAGs presents in the cartilage ECM. CS present anti-inflammatory activity promotes cell differentiation and protect cartilage from ECM degradation due to regulation of the

metabolism of cartilage tissue (Lafuente-Merchan, 2022). This together with the fact that blood drained from subchondral bone contains MSC constitutes the hypothesis to study differentiation processes in our novel biomaterial, testing it on this stem cell population. Our results demonstrate that our biomaterial composed of HA, Ch and Chondroitin Sulfate (HAChCS) not only favors MSC settlement but also induces their differentiation into cartilage tissue highly resembling the articular cartilage in its surface.

2 Materials and methods

2.1 Materials and reagents

High molecular weight (800–100 kDa) sodium hyaluronate (HA, pharmaceutical grade) and sodium chondroitin sulfate from bovine (injectable grade) were kindly supplied by Bioiberica (Barcelona, Spain). Medical grade Ch of low molecular weight (260 kDa) and 90.5% of deacetylation degree was purchased from Altakitin (Lisbon, Portugal). L-lysine diisocyanate (97%) was purchased from BOC Sciences (NY, United States), acetic acid and Pluronic F-127 was purchased from Sigma-Aldrich (St. Louise, United States).

All products were used as received without further purification.

2.2 Preparation of hydrogel scaffolds

Hyaluronic acid-Chitosan scaffolds (HACh) were prepared by crosslinking with L-lysine diisocyanate (LDI). HA was dissolved in an aqueous solution of Pluronic F-127 (1% w/v) and acetic acid (1% v/v) at a concentration of 20 mg/ml. Pluronic F-127 was added as a surfactant to preserve the porosity until the hydrogel is formed. Ch was added in a 1:1 relationship and stirred at 37°C until complete dissolution. In the case of hydrogels containing chondroitin sulfate 4 mg/ml of CS were added at this point. The final solution was mixed with LDI in a NH_2/LDI relationship of 1:5, dispersed with an UltraTurrax at 15,000 rpm for a minute and placed on a Teflon mold. The dispersion was allowed to crosslink at 37°C in a humidified chamber for 1 h. The final scaffold was washed with distilled water and freeze-dried to obtain the final scaffold.

2.3 Physicochemical characterization

2.3.1 Scanning electron microscopy and energy dispersive spectroscopy analysis

The morphology of the scaffolds was analyzed by analytic scanning electron microscopy (SEM) using a JEOL JSM-6010LV (Tokyo, Japan). Prior analysis all samples were sputter-coated with gold using a Leica EM ACE600 coater (Leica Microsystems, Wien, Austria). Elemental composition was performed by energy dispersive spectroscopy (EDS, Bruker XFlash model with detector 5030) installed in the SEM. Three independent areas were selected in the scaffolds.

2.3.2 Fourier transform infrared attenuated total reflectance (ATR-FTIR)

ATR-FTIR spectroscopy was performed in a Perkin Elmer Spectrum One FTIR spectrometer using 32 scans, and a resolution of 4 cm^{-1}.

2.3.3 Dynamic mechanical analysis

Rheology measurements were carried out in a stress-controlled oscillatory rheometer ARG2 (TA Instruments) using parallel plate geometry, using a 20 mm diameter steel plate. Oscillatory frequency sweeping test of scaffolds was conducted with a frequency scanning from 0.01 to 20 Hz at 0.1% strain and 25°C. Five replicates of each sample swollen in phosphate buffer were evaluated.

2.4 Swelling-degradation profile and chondroitin sulfate release

The gravimetric swelling ratio is defined as the fractional increase in the weight of the hydrogel due to water absorption. The gravimetric swelling capacity was measured in rounded scaffolds (d = 11 mm). The dried scaffolds were weighed (m_0) and then incubated in PBS at 37°C for 1 day. At regular intervals, the scaffolds were removed from the PBS solution, the excess of water was eliminated with filter paper and the samples were weighed (m_t). The gravimetrically swelling percentage was calculated as:

$$Gravimetric\ Swelling\ (\%) = 100 \times (m_t - m_0)/m_0 \quad (1)$$

The volumetric swelling ratio is defined as the volume increase of the hydrogel due to water absorption. The volumetric swelling capacity was measured in rounded scaffolds (d = 11 mm). The dimensions were measured (V_0) prior to incubation in PBS at 37°C for 1 day. At regular intervals, the scaffolds were removed from the PBS solution and the samples were measured (V_t). The volumetric swelling percentage was calculated as:

$$Volumetric\ Swelling\ (\%) = 100 \times (V_t - V_0)/V_0 \quad (2)$$

The stability of HACh and HAChCS scaffolds was carried out by immersing the membranes in 5 ml of PBS solutions and incubating at 37°C. After different periods of time the samples were removed from de PBS, washed with distilled water to eliminate the remaining salts and freeze-dried to obtain the

weight of the sample at time t. The weight loss of the sample can be determined as:

$$Weight\ loss\ (\%) = 100 \times (m_i - m_t)/m_i \quad (3)$$

where m_i is the initial weight of the sample and m_t is the weight of the degraded sample at each time point.

For release experiments, scaffolds containing CS were incubated in PBS at 37°C. At regular intervals, the supernatant liquid was collected and analyzed by UV (Nanodrop One, Thermofisher). The absorbance value at 222 nm where compare with a calibration curve previously calculated to obtain the concentration of CS on the supernatant liquid.

2.5 Adhesion strength test

The bioadhesion properties of the scaffolds to bone tissue were tested using a modification of the ASTM F2258-05 method. Chicken keel bone were cut into homogeneous samples of 12 mm × 12 mm × 3 mm (length, width, thickness). To simulate the microfracture procedure five holes (d = 0.1 mm) were made on the surface of the bone. The corresponding scaffold were swollen in different conditions: PBS, fibrin glue (FG) or with chicken blood, and put in contact for 1 min with the bone. This time allow the coagulation of the fibrin glue or the formation of the clot. Adhesion strength was tested in a Universal Testing Machine (UTM, Instron model 3366) comparing drilled and non-drilled bones. The data were collected using a 100 N load cell and a loading rate of 5 mm/min.

2.6 *In vitro* toxicity and cell adhesion experiments

2.6.1 Cell cultures

Primary human osteoblast from femoral bone tissue (hOBs), and human articular chondrocytes from knee articular cartilage (hACs) (Innoprot, Derio, Spain) were used in this study. hOBs were grown in DMEM/F12 medium (Dulbecco's modified Eagle's medium/F12; Gibco®, Life Technologies, Carlsbad, United States) supplemented with 10% (v/v) fetal bovine serum (FBS; Life Technologies, Carlsbad, CA, United States) and 1% (v/v) penicillin/streptomycin solution (final concentration of penicillin 100 units/ml and streptomycin 100 mg/ml, Life Technologies, Carlsbad, CA, United States). Both cell lines were cultured until 90% of confluence at 37°C and 5% CO_2, changing the culture medium every 2–3 days to be ready for the different assays.

2.6.2 Cytotoxicity assay

An MTT test ((3-(4,5-dimethylthiazol-2-yl)-2,5-diphenyltetrazolium bromide)) was used to indirectly analyze the cytotoxicity of the different scaffolds. Rounded scaffold (d = 11 mm) were immersed in 5 ml of FBS-free culture medium and incubated at 37°C. Thermanox® (TMX) discs (Nunc®, Thermofisher) were used as negative control. Aliquots of the supernatant medium were taken at 1, 2, 7, 14 and 21 days under sterile conditions and replaced with fresh medium. The samples were kept frozen until use. hObs and hACs were seeded separately in a 96-well plate at 9×10^4 cells/ml of density and incubated for 24 h in complete medium. Then, the medium was substituted by the extracts and incubated at 37°C. After 24 h the medium was replaced by a solution of MTT (0.5 mg/ml) in warm FBS-free medium and the cells were incubated at 37°C for 3–4 h. Mediua containing MTT were removed and DMSO was added to dissolve the formazan crystals formed in the cells. The absorbance of the medium was measured with a Biotek Synergy HT detector at 570 nm and a reference wavelength of 630 nm. Cell viability was calculated as:

$$Cell\ Viability\ (\%) = 100 \times (OD_S - OD_B)/(OD_C - OD_B) \quad (4)$$

where OD_S, OD_B and OD_C are the optical density (OD) of formazan production for the sample, blank and control, respectively.

2.6.3 Cell adhesion and proliferation assay

Cell adhesion and proliferation on the scaffolds were tested by the Alamar Blue assay following the manufacturer's instructions. Cells were seeded at 4×10^5 cell/ml on the previously swollen scaffolds and incubated at 37°C in a humidified atmosphere with 5% CO_2. Cell proliferation was measured at determinate times (1, 4, 7, 14 and 21 days) by replacing the culture medium with a 10% solution of AB in phenol red free DMEM medium. After 4 h the solution was transferred into a 96-well plate and the fluorescence was measured in a microplate reader (Synergy HT, BioTek, Instruments, United States). The excitation wavelength was 530 nm and the emission was recorded at 590 nm.

2.7 *In vitro* evaluation of cartilage formation on HACh scaffolds

2.7.1 Cell culture

C3H10T1/2 cell line (mouse: ATTC, CCL-226) was cultured in 75-cm^2 polystyrene culture flask in Dulbecco's Modified Eagle's Medium—low glucose (Sigma, D5546-1X500ML) supplemented with 10% fetal bovine serum (GIBSO, F7524-500ml), 1% Penicillin-Streptomycin (Sigma, P4333-100ML) and 1% Glutamax (GIBCO, 35050-038) in a humidified incubator at 37°C with 5% CO_2. Passages were performed at 80% confluence with Trypsin-EDTA 0.05% (Thermofihser, 25300096) and cells were always used in the 15th passage.

2.7.2 Scaffold seeding

Ch , HACh and HAChCS disks were rinsed in 70% ethanol for 20 min in agitation and punched into cylinders of 3 mm diameter. The pieces were sterilized in 70% ethanol for 2 h, rinsed in PBS for 30 min three times and maintained in culture medium at 4°C until use.

For the scaffold seeding, the cylinders obtained from each material were left at room temperature for 1 h, partially dried with a cell strainer (DICSA) and placed on a non-treated culture petri dish. C3H10 cells were trypsinized, resuspended in culture media and 1×10^5 cells were seeded in each 3 mm cylinders of biomaterial. The scaffolds were incubated at 37°C and 5% CO2 for 2 h to allow adhesion, adding 3 µl of culture media every 30 min. Then, the cylinders were placed in the center of a well in a standard 48-well plate (Jet BioFil) and incubated in culture media in a humidified incubator at 37°C with 5% CO_2 for 1 and 2 weeks. Culture media were replaced every 2–3 days the first week and 3–4 days the second week. Micromass of C3H10 cells was also obtained as controls by centrifugation of 1×10^5 cells at 1.800 rpm at 5 min, removing the supernatant and adding 250 µl of culture media. Micromass was kept under the same conditions as Ch scaffolds. To stimulate differentiation, the biomaterials were incubated in culture media containing 100 ng/ml BMP-2 (R&D Systems, 355-BM-050) at 37°C in a humidified incubator with 5% CO_2 for 1 and 3 weeks. Culture media were replaced every 2–3 days the first week and 3–4 days the second week.

2.7.3 Histology

After the differentiation assays, the scaffolds were rinsed with PBS and fixed with 4% paraformaldehyde at 4°C overnight. Then, they were washed in PBS, dehydrated with a graded series of ethanol, embedded in paraffin and sectioned at 15 µm thick. For histological analysis, sections were rehydrated and stained with Alcian Blue and Safranin-O.

2.7.4 Immunohistochemistry

For immunohistochemistry, sections were treated with citrate buffer for antigen retrieval and quenched by peroxidase solution. After blocking with goat serum, Aggrecan antibody (13880 Proteintech) was incubated overnight 1:100. Sections were developed with histostain plus kit with DAB as a chromogen (Invitrogen). Negative controls for primary antibody were included. Briefly, control slides were exposed to antigen retrieval and maximum DAB development to confirm no unspecific signal development (Supplementary Figure S3).

2.7.5 Real-time polymerase chain reaction (qPCR)

Total RNA from the cultured scaffolds was extracted using the Trizol reagent (ThermoFisher, 15596018) and RNA concentrations were determined using Nanodrop 2000 spectrophotometer (Thermo Fisher Scientific). Complementary DNA (cDNA) was amplified with the PrimeScript™ RT Master Mix (Takara, RR036A) and used for qPCR, which was performed in triplicates by using the TB Green® Premix Ex Taq™ (Takara, RR420L) on the Bio-Rad C1000 Thermal Cycler (Bio-Rad). The housekeeping gene, β-actin, was used for gene expression normalization and the fold change expression was calculated using the $2^{-\Delta\Delta CT}$ method. Primer sequences were purchased from Invitrogen and listed in Table 1.

2.8 Statistical analysis

Results are given as mean and standard deviation (minimum n = 4). Data from the different groups were compared in pairs with ANOVA test. All the statistical analyses were performed using the Origin 9 (Origin Lab corporation, Northampton,United States). The significance level was set at $^*p < 0.05$, $^{**}p < 0.01$ and $^{***}p<0.001$.

3 Results and discussion

3.1 Scaffold synthesis and characterization

The use of lysine diisocyanates as crosslinker allows different reactions between Ch and HA as is shown in Figure 1A.

The presence of the different reactions could be elucidated by ATR-FTIR spectra of HA, Ch and HACh scaffolds (Figure 1B). HA spectrum showed the most characteristics bands: the broad band around 3330 cm^{-1} is associated with the intra- and intermolecular stretching vibration of –OH group. The signal at 2,875 cm^{-1} correspond to the stretching of $-CH_2$ group; the bands from 1,610 and 1,405 cm^{-1} are correlated with symmetric and asymmetric vibration of COO^- group. Finally, the peak from 1,033 cm^{-1} is related with the C–O–C from the saccharide units (Vasi, 2014).

Ch spectrum showed also their typical bands: The strong bands at 3369 and 3295 cm^{-1} correspond to N-H and O-H stretching. The bands at 2,921 and 2,867 cm^{-1} correspond to C-H stretching (symmetric and asymmetric). At 1,654 cm^{-1} correspond to C=O stretching of amide I and at 1,589 cm^{-1} correspond to the N-H bending of the primary amine. The absorption band at 1,153 cm^{-1} can be attributed to asymmetric stretching of the C-O-C bridge.

Analyzing the HACh spectrum, the signal of HA at 1,610 and 1,405 cm^{-1} (stretching of carboxylate group) was vanished, indicating that the conjugate was formed through the COO^{-1} group. In the case of the Ch, the signal corresponding to the primary amine (1,589 cm^{-1}) also disappears in the HACh spectrum, indicating the formation of the crosslinking between the amine and isocyanate group. In the HACh spectrum, new signals appear at 1,550 and 1725 cm^{-1}, which

TABLE 1 Sequences of qRT-PCR primers.

Gene	Forward	Reverse
β-actin	5′-GGAGATTACTGCCCTGGCTCCTA-3′	5′-GACTCATCGTACTCCTGCTTGCTG-3′
Sox9	5′-GAGGCCACGGAACAGACTCA-3′	5′-CAGCGCCTTGAAGATAGCATT-3′
Acan1	5′-GGTCACTGTTACCGCCACTT-3′	5′-CCCCTTCGATAGTCCTGTCA-3′

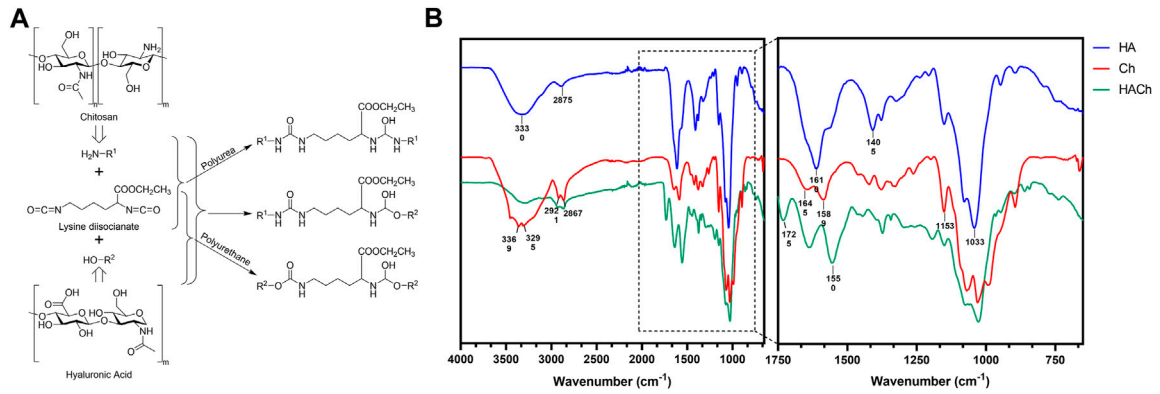

FIGURE 1
(A) Proposed scheme reaction for HACh scaffolds. **(B)** ATR-FTIR spectra of HA, Ch and HACh scaffolds.

are in the range of the secondary amine bands and C=O stretching in polyurethanes and polyureas. These results demonstrate the formation of a stable scaffold.

The use of the UltraTurrax in the synthesis process produced scaffolds with a high porosity due to the introduction of microbubbles in the system (Figure 2).

In HACh scaffolds (Figures 2A1, A2), we can observe the presence of two different kinds of microstructures: a macroporosity (≈200 μm) and a microporosity (≈10 μm). The microporosity is partially occulted on CS loaded scaffolds (Figures 2B1, B2). In this case, CS is deposited on the microstructure partially covering it. The presence of CS on the surface was corroborated using EDS (Supplementary Table S1) that detected the presence of sulfur coming from the CS. This porosity pattern will allow the colonization of the scaffold by the cells contributing to the full regeneration of the damage.

Mechanical properties of HACh and HAChCS swollen scaffolds were analyzed by rheology (Supplementary Figure S1A). Storage and loss moduli exhibited a visco-elastic solid behavior close to a gel-like. HAChCS scaffolds showed lower storage moduli values in comparison with not loaded scaffolds.

Previous studies define the behavior of articular cartilage using the complex modulus (G*) and define different ranges: immature cartilage: G* < 1 MPa and mature cartilage 5 < G*< 16 MPa at low frequencies (Perni and Prokopovich, 2020). The values obtained for our scaffold (Supplementary Figure S1B) are in the range of an immature cartilage (0.5–0.8 MPa) (Perni and Prokopovich, 2020) being adequate for the regeneration of new tissue when it is applied in articular defects currently treated with microfracture procedure.

3.2 Swelling, degradation and CS release

Liquid adsorption capacity is an essential feature and determine the ability of the scaffold to interact with the blood coming from the microfracture process. This adsorption needs to be fast to stabilize the blood clot and adsorb the growth factors and stem cells coming from the blood. Figure 3A shows the swelling capacity of the HACh and HAChCS scaffolds. The maximum water-uptake equilibrium is reached after 4–6 h, reaching values of 225% for HACh and 200% for HAChCS. High initial swelling degrees are necessary for ensuring an appropriate source of nutrients to the whole scaffold, but too high swelling degrees can compromise scaffold integrity (Mora-Boza, 2020).

Volumetric swelling is an important scaffold characteristic to determine the ability of the gel to remain inside the microfracture holes. High volume changes could affect the stability of the gels once they are implanted in the defect. In our case (Figure 3B), the

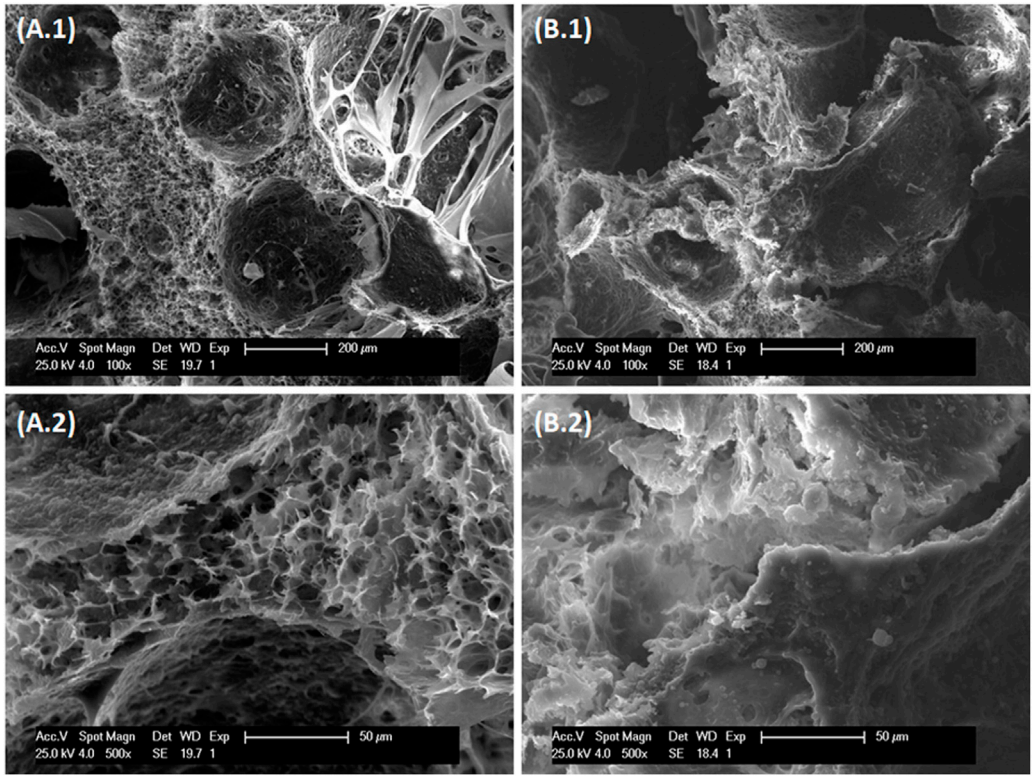

FIGURE 2
SEM images of **(A)** HACh and **(B)** HAChCS at different magnifications: **(A1,B1)** ×100 and **(A2,B2)** ×500.

volume increase values are only 27% for HACh scaffolds and 17% for HAChCS scaffolds, being the maximum variation in the diameter of the scaffold of 0.55 ± 0.08 mm which ensures the permanence of our hydrogels in the defect.

Figure 3C shows the degradation profile of the scaffolds submerged in PBS at 37°C. Both scaffolds showed an initial weight loss due to the release of not integrated polymer chains and then they were stable for more than 2 months. The HAChCS presented a more sustained degradation may due to polyelectrolyte interactions between chondroitin sulfate and Ch (Rodrigues et al., 2016). Figure 3D shows the release of chondroitin sulfate from the HAChCS scaffold. The release profile shows an initial fast release of CS (10%) that was progressively increasing with the time until reaching a value of 40% after 40 days. This behavior is typical for systems that are capable of swelling and whose release profile fit the Korsmeyer-Peppas model Eq. 5:

$$\frac{M_t}{M_\infty} = k \cdot t^n \tag{5}$$

were $\frac{M_t}{M_\infty}$ is the fraction of CS released at time t, k is the release rate constant and n is the diffusional exponent which is indicative of the transport mechanism (Ritger and Peppas, 1987). Assuming our scaffold as a thin film we fit our data to Eq. 5 obtaining a value of n = 0.4982. Table 2 shows model values for n of the Peppas equation and that of the HAChCS sample.

Then, our system fit to thin film were the CS is released by Fickian diffusion from the swollen matrix. The CS that is homogeneously distributed in the polymer matrix is released by diffusion through the pores of the matrix.

3.3 Adhesion strength test

Ch is a natural mucoadhesive and could be a good option to stabilize the scaffold in the microfracture procedure. There are several options to stabilize the scaffold as can it be the use of fibrin glue o surgical adhesives (Frehner and Benthien, 2018; Orth et al., 2020). To measure the mucoadhesive properties of our scaffolds we put in contact the scaffold with bone tissue in different conditions. Figure 4 displays the values of adhesion strength of the scaffolds to bone:

The adhesion of the scaffolds to the bone in absence of microfracture was practically negligible even when fibrin glue was applied. After the application of the microfracture to the bone, the adhesion strength noticeably increased by the

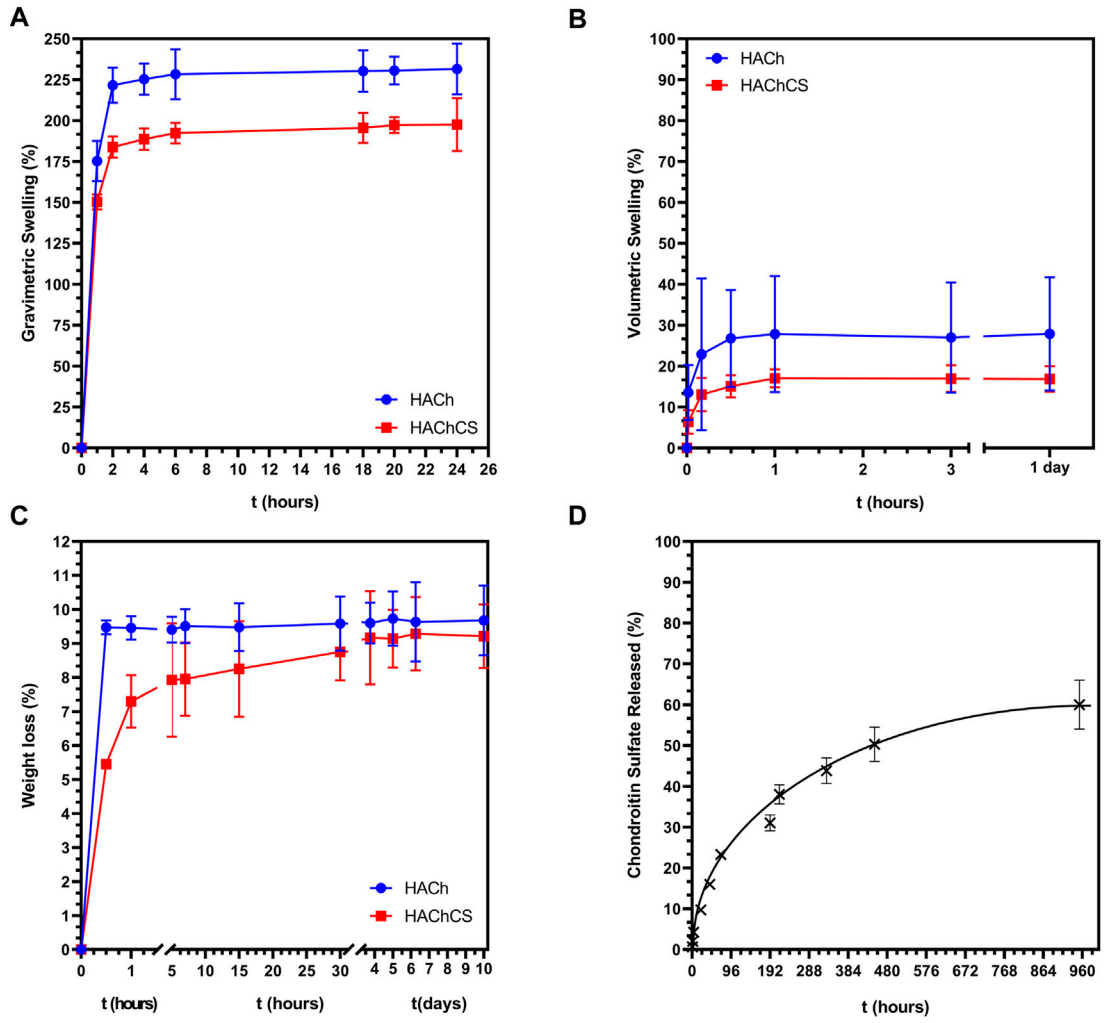

FIGURE 3
(A,B) Swelling behavior of HACh and HAChCS scaffolds in PBS at 37°C. **(C)** Degradation of HACh and HAChCS scaffolds in PBS at 37°C. **(D)** Chondroitin sulfate released from HAChCS scaffolds in PBS at 37°C.

TABLE 2 Experimental and theoretical exponent n of the Peppas equation for drug release mechanism.

HAChCS	Thin film	Cylinder	Sphere	Drug release mechanism
Exponent, *n*				
0.4982	0.5	0.45	0.43	Fickian diffusion
	$0.5 < n < 1.0$	$0.45 < n < 0.85$	$0.43 < n < 1.45$	Anomalous transport
	1.0	0.89	0.85	Case-II transport

augmentation of the contact surface due to the bone holes. In addition, there was also observed an important difference between the use of fibrin glue or blood to seal the scaffold. The adhesion strength was significantly higher in the presence of blood. Moreover, the presence of Ch could accelerate blood coagulations, platelet adhesion and thrombin generation

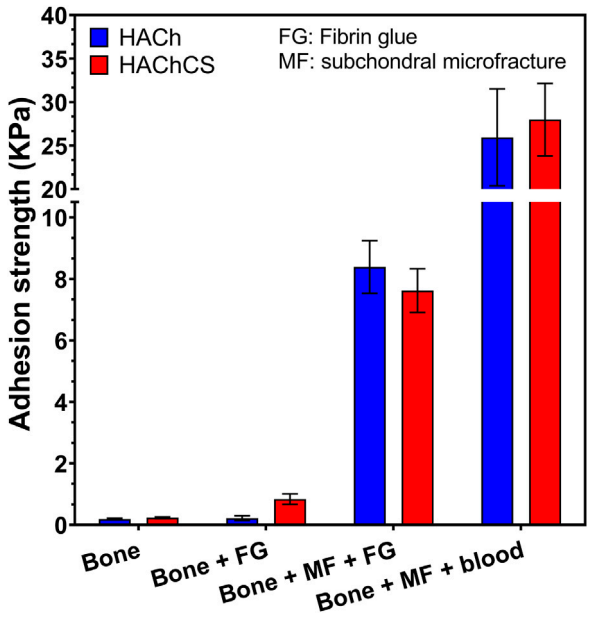

FIGURE 4
Adhesion strength of the scaffolds to a bone in different conditions. FG: the scaffold was swollen with fibrin glue. MF: A microfracture procedure was applied to the bone. Blood: The scaffold was swollen with blood.

resulting in an increase of the adhesion strength (Hu, 2018). This improvement of the adhesion strength makes this kind of systems good candidates to stabilize the clot coming from the microfracture process in the treatment of cartilage injures.

3.4 *In vitro* toxicity and cell adhesion studies

The toxicity of lixiviates coming from the different scaffolds was evaluated on hACs and hOBs (Figures 5A, B). Cell viability of studied samples with hACs (Figure 5A) was not affected on the first 2 days in comparison with the control. After 7 days, significant differences in the viability were observed but in general, the cell viability in presence of any extract was higher than 90%. In the case of hOBs (Figure 5B) cell viability increased in contact with scaffold lixiviates. Ho (2014) observed that the presence of low molecular weight chains of Ch and/or HA in the culture medium improved the cell growth.

Cell adhesion and proliferation on the different scaffolds was evaluated by Alamar Blue assay (Figures 5C, D, Supplementary Figure S2). Cell proliferation increased over time for all the systems but was lower on the scaffolds that on the control. This difference can be ascribed to the surface of the scaffolds, the cells needs more time to adhered on an irregular surface, but

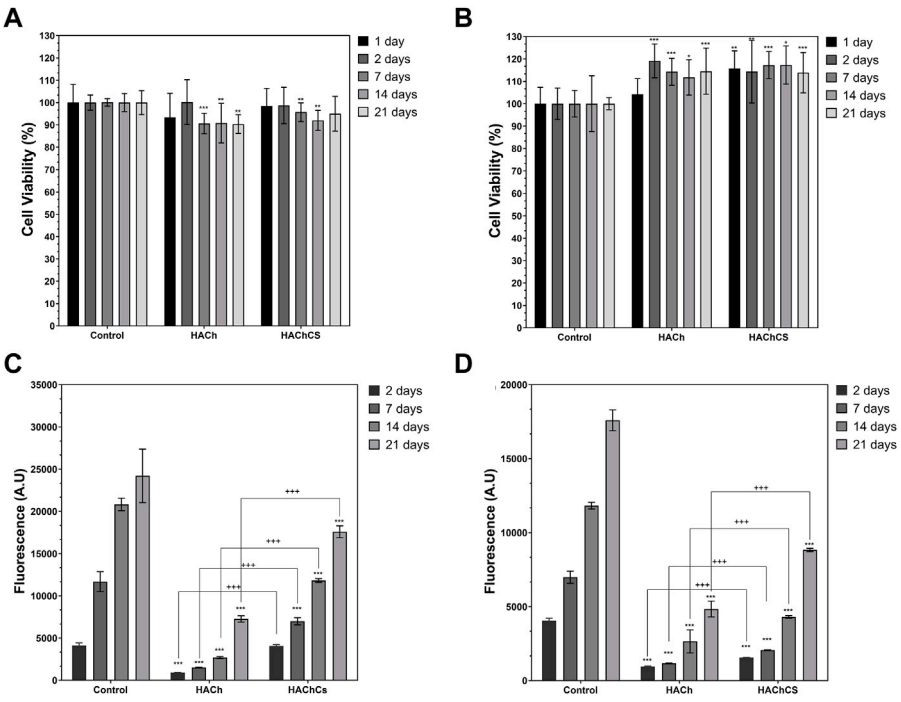

FIGURE 5
(A,B) Cell viability of hACs **(A)** and hOBs **(B)** cultures with HACh and HAChCS scaffolds lixiviates. Significant differences with the control at each time are marked with * (*$p < 0.05$, **$p < 0.01$, ***$p < 0.001$) **(C,D)** Cell proliferation values of hACs **(C)** and hOBs **(D)** seeded on HACh and HAChCS scaffolds. Significant differences with the control (Thermanox® discs) at each time are marked with * (*$p < 0.05$, **$p < 0.01$, ***$p < 0.001$) and between scaffolds are marked with + ($^{+}p < 0.05$, $^{++}p < 0.01$, $^{+++}p < 0.001$).

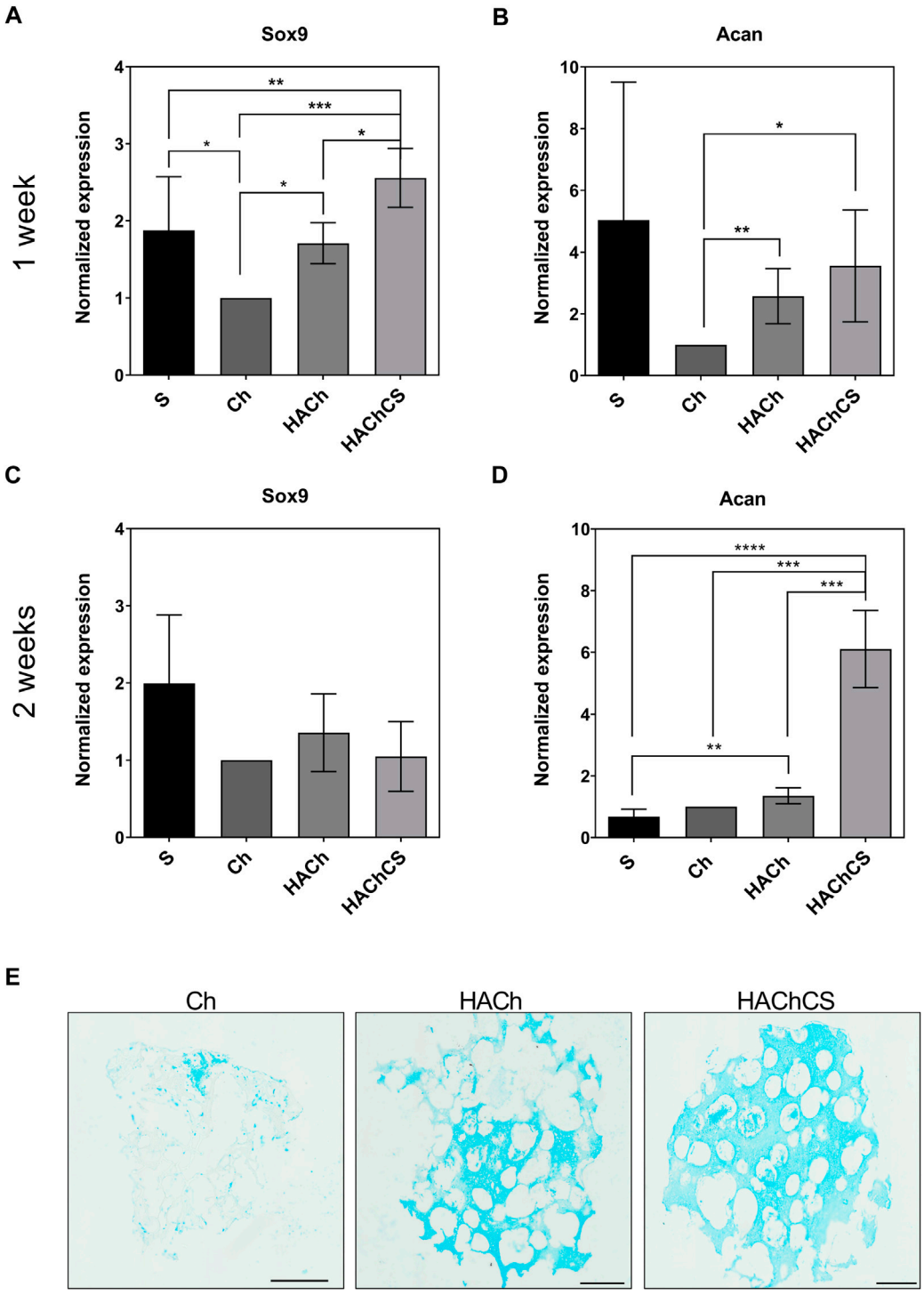

FIGURE 6
Expression level of Sox9 **(A,C)** and Acan **(B,D)** genes in MSC seeded as spheroids micromass (S) or on scaffolds: Ch, HACh and HAChCS during1 week **(A,B)** or 2 weeks **(C,D)**. Results are expressed as mean ± standard deviation (*$p < 0.05$, **$p < 0.01$, ***$p < 0.001$). **(E)**: Alcian Blue stained sections of Ch, HACh and HAChCS scaffolds seeded with MSC during 1 week. Bars represent 500 µm.

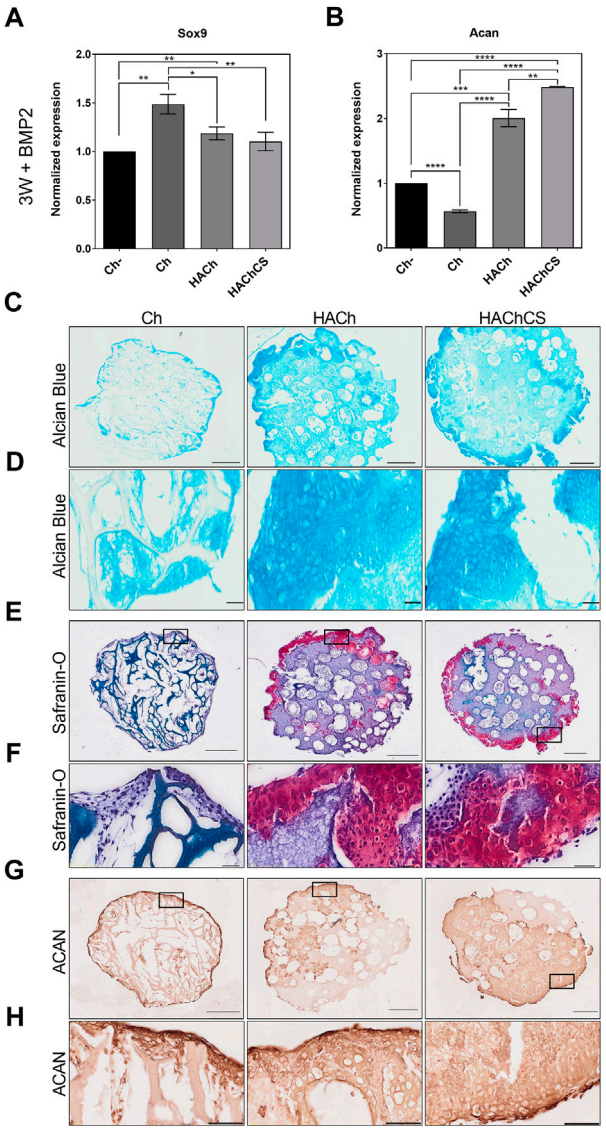

FIGURE 7
(A,B): Expression level of Sox9 and Acan genes in MSC seeded on Ch without BMP-2 stimulation (Ch-) and Ch, HACh and HAChCS scaffolds after 3 weeks of differentiation with BMP-2 stimulation. Results are expressed as mean ± standard deviation (*$p < 0.05$, **$p < 0.01$, ***$p < 0.001$). **(C)**: Alcian Blue stained sections of Ch, HACh and HAChCS scaffolds with MSC and BMP-2 stimulation for 3 weeks. Bars represent 500 μm **(D)**: High magnification showing well differentiated chondrocytes on the Ch, HACh and HAChCS scaffolds Bars represent 50 μm. **(E)**: Safranin-O stained sections of Ch, HACh and HAChCS scaffolds with MSC and BMP-2 stimulation. Bars represent 500 μm **(F)**: High magnification showing safranin-O staining on the Ch, HACh and HAChCS scaffolds. Bars represent 50 μm. **(G)** ACAN (Aggrecan) immunohistochemical analysis of paraffin-embedded sections of Ch, HACh and HAChCS scaffolds seeded with MSC and BMP-2 stimulation. Bars represent 500 μm **(H)** High magnification showing ACAN (Aggrecan) immunohistochemical analysis on the Ch, HACh and HAChCS scaffolds. Bars represent 50 μm.

after the first 7 days the cell growing on the scaffold surface significantly increase with the time. In SEM pictures (Supplementary Figure S2) we can observe some groups of cells on the surface of the scaffold after 2 days, but after 21 days, the scaffold is completely cover by both tupes of cells. Also in both kinds of cells, the presence of CS on the scaffold improve cell proliferation because CS is one of the main components in ECM and is involved on cell differentiation and proliferation processes (Izumikawa et al., 2014).

3.5 Cartilage differentiation on HA based scaffolds

To determine the true potential of our new scaffold in cartilage repair we performed different *in vitro* articular cartilage differentiation assays. The two most common articular cartilage repair interventions (drilling or microfracture surgical procedures), infuse the damaged zone with MSC. We decided to test the differentiation capabilities of our novel biomaterial using a MSC line with and without BMP2 stimulation. This is a reliable way to induce chondrocyte differentiation from MSC lineages (Shea, 2003). We determined the cartilage formation capacity on the three biomaterial combinations (Ch, HACh and HAChCS) and compared to that of a scaffold-free control generating MSC spheroids, a standard protocol for cartilage differentiation (Denker et al., 1995). Then, we measured two aspects of chondrogenesis by quantitative gene expression: 1) predifferentiation towards chondrogenesis measuring Sox9 expression; 2) actual cartilage ECM production measuring aggrecan (Acan) transcription, one of the major components of the cartilage ECM.

First, we tested the MSC reaction to the different scaffolds to determine if the biomaterials could be pro-chondrogenic activity by themselves without external differentiation factors. Short-term experiments for 1 week of differentiation showed that HAChCS had the best performance giving the highest expression of Sox9, the gene marker for early stages of chondrogenic differentiation, compared even to the standard spheroid method of cartilage differentiation (Figure 6A). Regarding cartilage ECM production, HAChCS also showed higher Acan expression levels than Ch or HACh, with similar performance to standard spheroids (Figure 6B). Mid-term culture of MSC on tested scaffolds during 2 weeks showed similar levels for chondrogenesis marker Sox9 for all biomaterials (Figure 6C). However, at 2 weeks cartilaginous ECM expression significantly increased in HAChCS scaffold (Figure 6D). Histological analysis by Alcian Blue revealed more production of proteoglycans, a major component of

cartilage extracellular matrix, and presence of more cells on HAChCS compared to Ch scaffold (Figure 6E). This was confirmed by histological analysis with Alcian Blue, a high affinity staining to cartilaginous proteoglycans, which preferentially binds to cartilaginous ECM (Figure 6E). These results suggest that HA based scaffolds, and more specifically, HAChCS biomaterial inherently induces chondrogenesis in MSC. These results could be due to the release of CS from the scaffolds. CS has shown capacity to activate MSC chondrogenesis and neocartilage deposition (Wang and Yang, 2017).

Even if scaffolds are prochondrogenic, to produce fully differentiated chondrocytes, cell 3D culture systems need differentiation factors such as BMP-2. To reproduce the microfracture procedure and the articular cartilage environment in the biomaterial, we stimulated MSC with BMP-2 (one of the factors provided by the blood coming from the microfracture of the subchondral bone) allowing cartilage differentiation during 3 weeks (Figure 7). Under these conditions, Sox9 chondrogenic marker showed stabilized levels similar to unstimulated culture after 2 weeks (Figures 6C, 7A), as expected for an early differentiation factor. On the other hand, Acan expression showed higher levels on HA based materials; especially the HAChCS scaffold (Figure 7B. Histological analysis by Alcian Blue (Figures 7C, D) and Safranin-O (Figures 7E, F) showed a production of proteoglycans own of mature articular cartilage (Figure 7C) correlated with well-differentiated chondrocytes with a preferential location on the scaffold surface (Figure 7). Immunostaining of aggrecan, a chondrocyte specific component of cartilaginous extracellular matrix, showed a tissue specific deposition of cells in contact with the HACh and the HAChCS biomaterials, mainly in the surface region of the engineered tissue, confirming its similarities to articular cartilage (Figures 7G, H).

These results suggest that HACh and HAChCS biomaterials promoted *in vitro* chondrogenic differentiation process, as shown by chondrogenic expression markers and cartilage-like tissue formation, and it is expected that they do it in the case of their use in a microfracture procedure.

4 Conclusion

Microfracture procedure is a common technique used in cartilage diseases but present several limitations. The use of HAChCS scaffolds on this process could improve the regeneration of articular cartilage. HAChCS presents physico-chemical properties similar to immature cartilage that could allow the regeneration and formation of articular cartilage. Also, the mucoadhesive properties could stabilize the clot coming from the microfracture process and improve the integration with the surrounding tissues. HAChCS did not present toxicity and allowed the adhesion and proliferation of articular cartilage and mesenchymal stem cells. The capacity to release CS activated chondrogenesis process on MSC and the production of proteoglycans without the necessity of any other supplements. Finally, we simulated the environment of a microfracture procedure by addition of BMP-2, one of the common compounds present on the subchondral blood. In these conditions, both HACh and HAChCS scaffolds promoted the chondrogenic differentiation process and cartilage-like tissue formation doing these systems good candidates for their use in the microfracture procedure as well as a scaffold for stem cell and chondro-lineages in next-generation therapies.

Data availability statement

The raw data supporting the conclusion of this article will be made available by the authors, without undue reservation.

Author contributions

SE: Data curation. Formal analysis. Investigation. Methodology. GR: Data curation. Formal analysis. Investigation. Methodology. Writing—review and editing. JB: Funding acquisition. Resources, Supervision, Writing—review and editing. JSR: Conceptualization, Funding acquisition. Resources, Supervision, Writing—review and editing. BV-L: Funding acquisition. Resources, Supervision, Writing—review and editing. MRA: Funding acquisition. Resources, Supervision, Writing—review and editing. ID: Conceptualization, Formal analysis, Investigation, Methodology, Supervision, Validation, Visualization, Writing—original draft. LG-F: Conceptualization, Data Curation, Formal analysis, Funding acquisition, Investigation, Methodology, Project administration, Supervision, Validation, Visualization, Writing—original draft.

Funding

This work was supported by the Ministry of Science, Innovation and Universities (Spain) (PID 2020-114086RB-I00 and PID 2020-117255RB-I00-VASCUBONE) and by the Biomedical Research Networking Center in Bioengineering, Biomaterials and Nanomedicine (CIBER-BBN, project name: HYDROCARTREG). This research work was performed in the framework of the Nanomedicine CSIC HUB (ref202180E048) and BV-L, LG-F and MRA are members of the SusPlast + platform from the CSIC.

Conflict of interest

The authors declare that the research was conducted in the absence of any commercial or financial relationships that could be construed as a potential conflict of interest.

Publisher's note

All claims expressed in this article are solely those of the authors and do not necessarily represent those of their affiliated organizations, or those of the publisher, the editors and the reviewers. Any product that may be evaluated in this article, or claim that may be made by its manufacturer, is not guaranteed or endorsed by the publisher.

Supplementary material

The Supplementary Material for this article can be found online at: https://www.frontiersin.org/articles/10.3389/fbioe.2022.1058355/full#supplementary-material

References

Adams, M. A., Dolan, P., and McNally, D. S. (2009). The internal mechanical functioning of intervertebral discs and articular cartilage, and its relevance to matrix biology. *Matrix Biol.* 28 (7), 384–389. doi:10.1016/j.matbio.2009.06.004

Anraku, Y. (2009). Analyses of early events during chondrogenic repair in rat full-thickness articular cartilage defects. *J. Bone Mineral Metabolism* 27 (3), 272–286. doi:10.1007/s00774-009-0038-x

Armiento, A. R., Stoddart, M., Alini, M., and Eglin, D. (2018). Biomaterials for articular cartilage tissue engineering: Learning from biology. *Acta Biomater.* 65, 1–20. doi:10.1016/j.actbio.2017.11.021

Becerra, J., Andrades, J. A., Guerado, E., Zamora-Navas, P., Lopez-Puertas, J. M., and Reddi, A. H. (2010). Articular cartilage: Structure and regeneration', *Tissue engineering. Part B, reviews. Tissue Eng. Part B Rev.* 16 (6), 617–627. doi:10.1089/TEN.TEB.2010.0191

Chartrain, N. A., Gilchrist, K. H., Ho, V. B., and Klarmann, G. J. (2022). 3D bioprinting for the repair of articular cartilage and osteochondral tissue. *Bioprinting* 28, e00239. doi:10.1016/j.bprint.2022.e00239

Chen, H. (2018). An injectable self-healing hydrogel with adhesive and antibacterial properties effectively promotes wound healing. *Carbohydr. Polym.* 201, 522–531. doi:10.1016/j.carbpol.2018.08.090

Chung, C., and Burdick, J. A. (2008). Engineering cartilage tissue. *Adv. Drug Deliv. Rev.* 60 (2), 243–262. doi:10.1016/j.addr.2007.08.027

Dehghani, F., and Fathi, A. (2017). Challenges for cartilage regeneration. *Tissue Eng. Part B Rev.* 18, 389–466. doi:10.1007/978-3-662-53574-5_14

Denker, A. E., Nicoll, S. B., and Tuan, R. S. (1995). Formation of cartilage-like spheroids by micromass cultures of murine C3H10T1/2 cells upon treatment with transforming growth factor-β1', *Differentiation. Differentiation* 59 (1), 25–34. doi:10.1046/J.1432-0436.1995.5910025.X

Doherty, M. (1992). Articular cartilage and osteoarthritis. *Ann. Rheumatic Dis.* 51 (9), 1028. doi:10.1136/ard.51.9.1028-a

Frehner, F., and Benthien, J. P. (2018). Microfracture: State of the art in cartilage surgery?', *cartilage. SAGE Publ. Inc.* 9 (4), 339–345. doi:10.1177/1947603517700956

García-Fernández, L., Olmeda-Lozano, M., Benito-Garzon, L., Perez-Caballer, A., San Roman, J., and Vazquez-Lasa, B. (2020). Injectable hydrogel-based drug delivery system for cartilage regeneration. *Mater. Sci. Eng. C* 110, 110702. doi:10.1016/j.msec.2020.110702

Ho, M. H. (2014). Improving effects of chitosan nanofiber scaffolds on osteoblast proliferation and maturation. *Int. J. Nanomedicine* 9, 4293. doi:10.2147/IJN.S68012

Hu, Z. (2018). Chitosan-based composite materials for prospective hemostatic applications. *Mar. Drugs* 16 (8), 273273. doi:10.3390/MD16080273

Izumikawa, T., Sato, B., and Kitagawa, H. (2014). Chondroitin sulfate is indispensable for pluripotency and differentiation of mouse embryonic stem cells. *Sci. Rep.Nature Publ. Group* 4 (1), 37011–37012. doi:10.1038/srep03701

Lafuente-Merchan, M. (2022). Chondroitin and dermatan sulfate bioinks for 3D bioprinting and cartilage regeneration. *Macromol. Biosci.* 22 (3), 2100435. doi:10.1002/MABI.202100435

Lawrence, R. C., Felson, D. T., Helmick, C. G., Arnold, L. M., Choi, H., Deyo, R. A., et al. (2008). Estimates of the prevalence of arthritis and other rheumatic conditions in the United States: Part II. *Arthritis Rheum.* 58 (1), 26–35. doi:10.1002/art.23176

Liptak, M. G., and Theodoulou, A. (2017). Arthroscopic chondral debridement using radiofrequency ablation for patellofemoral compartment pathology. *Arthrosc. Tech.* 6 (5), e1879–e1883. doi:10.1016/j.eats.2017.07.004

Mistry, H., Connock, M., Pink, J., Shyangdan, D., Clar, C., Royle, P., et al. (2017). Autologous chondrocyte implantation in the knee: Systematic review and economic evaluation', *Health technology assessment (winchester, england). Health Technol. Assess.* 21 (6), 1–294. doi:10.3310/HTA21060

Mollon, B., Kandel, R., Chahal, J., and Theodoropoulos, J. (2013). The clinical status of cartilage tissue regeneration in humans. *Osteoarthr. Cartil.* 21 (12), 1824–1833. doi:10.1016/j.joca.2013.08.024

Mora-Boza, A. (2020). Glycerylphytate crosslinker as a potential osteoinductor of chitosan-based systems for guided bone regeneration. *Carbohydr. Polym.* 241, 116269. doi:10.1016/j.carbpol.2020.116269

Mow, V. C., Ratcliffe, A., and Robin Poole, A. (1992). Cartilage and diarthrodial joints as paradigms for hierarchical materials and structures. *Biomaterials* 13 (2), 67–97. doi:10.1016/0142-9612(92)90001-5

Nehrer, S., Chiari, C., Domayer, S., Barkay, H., and Yayon, A. (2008). Results of chondrocyte implantation with a fibrin-hyaluronan matrix: A preliminary study. *Clin. Orthop. Relat. Res.* 466 (8), 1849–1855. doi:10.1007/s11999-008-0322-4

Oliveira, J. T. (2010). Injectable gellan gum hydrogels with autologous cells for the treatment of rabbit articular cartilage defects. *J. Orthop. Res.* 28 (9), 1193–1199. doi:10.1002/jor.21114

Orth, P., Gao, L., and Madry, H. (2020). Microfracture for cartilage repair in the knee: A systematic review of the contemporary literature', *Knee surgery, sports traumatology, arthroscopy : Official journal of the ESSKA. Knee Surg. Sports Traumatol. Arthrosc.* 28 (3), 670–706. doi:10.1007/S00167-019-05359-9

Pereira, D. R., Reis, R. L., and Oliveira, J. M. (2018). Layered scaffolds for osteochondral tissue engineering. *Adv. Exp. Med. Biol.* 1058, 193–218. doi:10.1007/978-3-319-76711-6_9

Perni, S., and Prokopovich, P. (2020). Rheometer enabled study of cartilage frequency-dependent properties. *Sci. Rep.Nature Publ. Group* 10 (1), 20696. doi:10.1038/s41598-020-77758-9

Pipino, G., Risitano, S., Alviano, F., Wu, E. J., Bonsi, L., Vaccarisi, D. C., et al. (2019). Microfractures and hydrogel scaffolds in the treatment of osteochondral knee defects: A clinical and histological evaluation. *J. Clin. Orthop. Trauma* 10 (1), 67–75. doi:10.1016/j.jcot.2018.03.001

Pontes-Quero, G. M., García-Fernández, L., and RosaAguilar, M. (2019). 'Active viscosupplements for osteoarthritis treatment'. *Seminars Arthritis Rheumatism* 49, 171–183. doi:10.1016/j.semarthrit.2019.02.008

Ritger, P. L., and Peppas, N. A. (1987). A simple equation for description of solute release I. Fickian and non-fickian release from non-swellable devices in the form of slabs, spheres, cylinders or discs. *J. Control. Release* 5 (1), 23–36. doi:10.1016/0168-3659(87)90034-4

Rodrigues, M. N., Oliveira, M. B., Costa, R. R., and Mano, J. F. (2016). Chitosan/chondroitin sulfate membranes produced by polyelectrolyte complexation for cartilage engineering. *Biomacromolecules* 17 (6), 2178–2188. doi:10.1021/acs.biomac.6b00399

Shapiro, F., Koide, S., and Glimcher, M. J. (1993). Cell origin and differentiation in the repair of full-thickness defects of articular cartilage. *J. Bone & Jt. Surg.* 75 (4), 532–553. doi:10.2106/00004623-199304000-00009

Shea, C. M. (2003). BMP treatment of C3H10T1/2 mesenchymal stem cells induces both chondrogenesis and osteogenesis. *J. Cell. Biochem.* 90 (6), 1112–1127. doi:10.1002/JCB.10734

Shigemasa, Y., and Minami, S. (1996). Applications of chitin and chitosan for biomaterials. *Biotechnol. Genet. Eng. Rev.* 13 (1), 383–420. doi:10.1080/02648725.1996.10647935

Shiroud Heidari, B., Ruan, R., Vahabli, E., Chen, P., De-Juan-Pardo, E. M., Zheng, M., et al. (2023). Natural, synthetic and commercially-available biopolymers used to regenerate tendons and ligaments. *Bioact. Mater.* 19, 179–197. doi:10.1016/j.bioactmat.2022.04.003

Shive, M. S., Hoemann, C. D., Restrepo, A., Hurtig, M. B., Duval, N., Ranger, P., et al. (2006). BST-CarGel: *In situ* ChondroInduction for cartilage repair. *Operative Tech. Orthop.* 16 (4), 271–278. doi:10.1053/j.oto.2006.08.001

Sledge, S. L. (2001). Microfracture techniques in the treatment of osteochondral injuries. *Clin. Sports Med.* 20 (2), 365–378. doi:10.1016/s0278-5919(05)70311-2

Vasi, A. M. (2014). Chemical functionalization of hyaluronic acid for drug delivery applications. *Mater. Sci. Eng. C* 38 (1), 177–185. doi:10.1016/J.MSEC.2014.01.052

Vilela, C. A., Correia, C., da Silva Morais, A., Santos, T. C., Gertrudes, A. C., Moreira, E. S., et al. (2018). *In vitro* and *in vivo* performance of methacrylated gellan gum hydrogel formulations for cartilage repair. *J. Biomed. Mat. Res. A* 106 (7), 1987–1996. doi:10.1002/jbm.a.36406

Wang, T., and Yang, F. (2017). A comparative study of chondroitin sulfate and heparan sulfate for directing three-dimensional chondrogenesis of mesenchymal stem cells. *Stem Cell. Res. Ther.* 8 (1), 284. doi:10.1186/s13287-017-0728-6

frontiers | Frontiers in Bioengineering and Biotechnology

TYPE Original Research
PUBLISHED 06 January 2023
DOI 10.3389/fbioe.2022.1062646

OPEN ACCESS

EDITED BY
Yawei Du,
Shanghai Jiao Tong University, China

REVIEWED BY
Jinglei Wu,
Donghua University, China
Lichen Wang,
Stevens Institute of Technology, United States

*CORRESPONDENCE
Lihua Luo,
luolihua81@126.com
Yan He,
helen-1101@hotmail.com
Qingsong Ye,
qingsongye@whu.edu.cn

†These authors have contributed equally to this work

SPECIALTY SECTION
This article was submitted to Biomaterials, a section of the journal Frontiers in Bioengineering and Biotechnology

RECEIVED 06 October 2022
ACCEPTED 19 December 2022
PUBLISHED 06 January 2023

CITATION
Luo L, Zhu Q, Li Y, Hu F, Yu J, Liao X, Xing Z, He Y and Ye Q (2023), Application of thermosensitive-hydrogel combined with dental pulp stem cells on the injured fallopian tube mucosa in an animal model. *Front. Bioeng. Biotechnol.* 10:1062646. doi: 10.3389/fbioe.2022.1062646

Application of thermosensitive-hydrogel combined with dental pulp stem cells on the injured fallopian tube mucosa in an animal model

Lihua Luo[1*†], Qunyan Zhu[1†], Yejian Li[1†], Fengting Hu[1], Jiangtao Yu[2], Xiangyan Liao[1], Zhenjie Xing[1], Yan He[3*] and Qingsong Ye[1,4*]

[1]School and Hospital of Stomatology, Wenzhou Medical University, Wenzhou, Zhejiang, China, [2]The First Affiliated Hospital of Wenzhou Medical University, Wenzhou, Zhejiang, China, [3]Tianyou Hospital, Wuhan University of Science and Technology, Wuhan, China, [4]Center of Regenerative Medicine, Renmin Hospital of Wuhan University, Wuhan, China

Objectives: Fallopian tube (FT) injury is an important factor that can lead to tubal infertility. Stem-cell-based therapy shows great potential for the treatment of injured fallopian tube. However, little research has shown that mesenchymal stem cells (MSCs) can be used to treat fallopian tube damage by *in situ* injection. In this study, we *in situ* transplanted PF127 hydrogel encapsulating dental pulp stem cells (DPSCs) into the injured sites to promote the repair and regeneration of fallopian tube injury.

Materials and methods: The properties of dental pulp stem cells were evaluated by flow cytometry, immunofluorescence analysis, and multi-differentiation detection. The immunomodulatory and angiogenic characteristics of dental pulp stem cells were analyzed on the basis of the detection of inflammatory factor expression and the formation of capillary-like structures, respectively. The biocompatibility of PF127 hydrogel was evaluated by using Live/Dead and CCK-8 assays. The effects of PF127 hydrogel containing dental pulp stem cells on the repair and regeneration of fallopian tube injury were evaluated by histological analysis [e.g., hematoxylin and eosin (H&E) and Masson's trichrome staining, TUNEL staining, immunofluorescence staining, and immunohistochemistry], Enzyme-linked immunosorbent assay (ELISA), and RT-PCR detections.

Results: Dental pulp stem cells had MSC-like characteristics and great immunomodulatory and angiogenic properties. PF127 hydrogel had a thermosensitive feature and great cytocompatibility with dental pulp stem cells. In addition, our results indicated that PF127 hydrogel containing dental pulp stem cells could promote the repair and regeneration of fallopian tube damage by inhibiting cell apoptosis, stimulating the secretion of angiogenic factors, promoting cell proliferation, modulating the secretion of inflammatory factors, and restoring the secretion of epithelial cells.

Conclusion: In this study, our results reported that *in situ* injection of PF127 hydrogel encapsulating dental pulp stem cells into the injured sites could provide an attractive strategy for the future treatment of fallopian tube injury in clinical settings.

KEYWORDS

dental pulp stem cells, fallopian tube injury, hydrogel, immunoregulation, repair

1 Introduction

The World Health Organization has reported that the infertility rate is more than 15% among women of reproductive age worldwide, and infertility should be regarded as a public health problem (Adegbola and Akindele 2013). Tubal infertility is a common cause of female infertility, accounting for 30%–35% (Zou et al., 2014). Many influencing factors, including infection, fallopian tube (FT) surgery, ectopic pregnancy, and endometriosis, may cause salpingitis or pelvic inflammation with FT mucosa damage and structural collapse, which are important indicators of tubal infertility (Li et al., 2017). At present, tubal infertility shows a yearly rising trend because of the popularity of sexually transmitted diseases and the repetitive infection of FT (Luo et al., 2015; Almasry et al., 2018).

Recently, the principal curing methods for tubal infertility include laparoscopic surgery and antibiotic therapy in clinical settings. However, the repetitive attachment of FT after surgery and the occurrence of antibiotic-resistant strains of the long-term use of antibiotics can lead to failure treatment of tubal infertility (Liao et al., 2019). Therefore, new therapeutic strategies have been required to repair the injury of FT and restore the reproduction function of FT, thereby reducing the incidence of tubal infertility.

Mesenchymal stem cells (MSCs) have pluripotent characteristics, and they can be induced to differentiate into many types of cells, which could provide tissue-reconstructing cells in the damaged sites. In addition, MSCs have shown strong paracrine effects by secreting several growth factors and providing immunosuppressive and anti-inflammatory actions in stem-cell-based therapies (Liao et al., 2019). Thus, MSC-based therapy can provide a novel strategy for the repair and regeneration of injured FT.

Dental pulp stem cells (DPSCs), as a kind of MSCs, can be readily cultured from the dental pulps which are isolated from impacted third molars, exfoliated deciduous teeth, permanent and primary teeth, and supernumerary teeth, without extra harm and invasive surgical procedures (Luo et al., 2018; Luo et al., 2021). DPSCs possess all MSCs-like properties, e.g. multi-differentiation potential and immunomodulatory properties, and high proliferative and self-renewal capacities (Luo et al., 2018). In addition, the capacity of DPSCs to secrete growth factors is higher than other tissue-derived MSCs such as bone-marrow-derived mesenchymal stem cells (BM-MSCs). Meanwhile, DPSCs have a higher proliferation rate and greater immunomodulatory properties than BM-MSCs (Lan et al., 2019). Therefore, DPSCs have become an attractive seeded cell in stem-cell-based therapies. Moreover, we have confirmed an angiogenic characteristics of DPSCs' in our previous work (Luo et al., 2018), where DPSCs participated in the formation of new blood vessels and enhanced the blood supply around injured sites. Angiogenesis is an important influencing factor for the treatment of FT injury.

Although DPSCs have outstanding MSC-like properties, using DPSCs alone can hardly receive ideal restoration of reproduction function after FT injury because of their poor cellular density and survival rate in damaged sites. As shown in previous studies, hydrogels have a 3D network structure and great porosity, which can be used to accommodate cells and provide a suitable microenvironment for cell survival and growth (Zhu and Marchant 2011). Our previous studies indicated that the thermosensitive Pluronic F-127 (PF127, also known as poloxamer 407) hydrogel, which has a solution state at 4°C and a hydrogel state at human body temperature, had a porous structure and great cytocompatibility, and it could be a great cell carrier in tissue engineering and regenerative medicine (Albashari et al., 2020). Furthermore, the controllable degradability of PF127 hydrogel could provide an appropriate microenvironment for cellular adhesion, growth and proliferation (Supplementary Figure S5). Thus, in this work, we used PF127 as the scaffold and transplanted PF127 hydrogel containing DPSCs into the damaged site to evaluate its effects on the repair and regeneration of FT injury.

2 Materials and methods

2.1 Ethics and animals

Twenty-four female New Zealand white rabbits (weighing 2,000 ± 250 g) were provided by the Animal Experimental Center of Wenzhou Medical University and housed with sufficient water and food in animal cages for 14 days before surgery. All experimental procedures were performed under the regulations of the committee of the Institutional Animal Care and the Ethics Committee of Wenzhou Medical University (wydw 2019-0949).

2.2 Isolation, culture, and identification of DPSCs

The isolation and culture procedures of DPSCs were performed as previously described (Luo et al., 2021). In brief, dental pulp tissues, which were collected from the tooth, were cut into small pieces and digested using the mixture of collagenase type I (Gibco, United States) and dispase (Sigma, Germany) for 30 min at 37°C in a 5% CO_2 cell incubator. Then, the pulp tissue was suspended and cultured using α-modified Eagle's medium (α-MEM, Gibco, United States) supplemented with 20% fetal bovine serum (FBS, Gibco, United States), 100 μg/ml of streptomycin, and 100 U/mL of penicillin (Gibco, United States) at 37°C in a 5% CO_2 cell incubator. The culture medium was replaced every 3 days. MSC-like characteristics of DPSCs were identified by flow cytometry, immunofluorescence analysis, and multi-differentiation detection. Flow cytometry was executed using human primary antibodies, including CD19, CD166, CD73, CD90 (BD Pharmingen™, United States), CD34, and HLA-DR (BioLegend, United States), and the data were evaluated using a CytoFLEX flow cytometer (Beckman Coulter, California, United States). The immunophenotype of DPSCs was analyzed using primary antibodies against CD44 (1:400, Abcam, Cambridge, United Kingdom), and the immunofluorescence of DPSCs was observed using a fluorescence microscope (Eclipse 80i, Nikon, Japan). Based on the procedures described in our previous work (Albashari et al., 2020; Luo et al., 2021), the multipotent property of DPSCs was analyzed by osteogenic, adipogenic, and chondrogenic differentiation with alizarin red S staining, Oil Red O staining, and Alcian blue staining, respectively. Images were observed using a light microscope (TS100, Nikon).

2.3 Effects of DPSCs on murine macrophage RAW264.7 cells

The effects of DPSCs on murine macrophage RAW264.7 cells were evaluated by performing a macrophage-DPSCs coculture experiment as previously described (Németh et al., 2009; Chen et al., 2019). First, the mouse monocyte-macrophage cells (RAW 264.7, ATCC, United States) were cultured in 24-well plates at a concentration of 2×10^5 cells/well. After incubation for 24 h, the supernatants were removed, and the cells were treated with lipopolysaccharide (LPS, Sigma; 1 μg/ml) for 24 h. Then, DPSCs (2×10^4 cells/well), which were cultured in insert membranes of the transwell system (.4 μm pore size, Corning), were transferred to the wells. After incubation for another 24 h, the supernatants were collected and stored at −20°C for further use. The expression of tumor necrosis factor-alpha (TNF-α) and interleukin-10 (IL-10) of challenged cells and supernatants was assessed by immunofluorescence staining and Enzyme-linked immunosorbent assay (ELISA) (R&D Systems), respectively.

2.4 Evaluation of angiogenic characteristics of DPSCs

To evaluate the angiogenic characteristics of DPSCs, following *in vitro* experiment was performed to assess the formation of capillary-like structures. 96-well plates were pre-coated with gelatin methacryloyl (GelMA) hydrogel as previously described (Chen et al., 2012). In brief, DPSCs and human umbilical vein endothelial cells (HUVECs, ATCC, United States) were plated onto hydrogel-treated 96-well plates and cultured with an endothelial cell growth medium-2™ (EGM-2™, Lonza Bioscience, Switzerland) supplemented with 2% FBS, .4% hFGF-B, .1% VEGF, .1% hEGF, .1% R3-IGF-1, .1% Heparin, .1% ascorbic acid, .1% gentamicin/amphotericin-B, and .04% hydrocortisone. The cultured medium was changed every 2 days. After differentiation for 7 days, the cells were fixed with 4% PFA and treated with Phalloidin-TRITC (1:200, Solarbio, China), and the nuclei were stained by 4′6-Diamidino-2-phenylindole-dihydrochloride (DAPI, Beyotime Institute of Biotechnology, Shanghai, China). The images were taken using a fluorescence microscope (Eclipse 80i, Nikon, Japan), and the vascular tube length and number were calculated using NIS-Elements AR 3.1 (Nikon).

2.5 Preparation of PF127 hydrogel

PF127 powder was slowly added to the complete α-MEM (containing 20% FBS, 100 μg/ml of penicillin, and 100 μg/ml of streptomycin) to prepare a 20% (w/v) solution. The solution was placed on a shaking table at 4°C for 24 h to ensure that the powder was fully dissolved. Then, the PF127 solution was filtered by using a .22 μm pore size bottle-top filter and stored at 4°C for future use. Our previous study confirmed that the PF127 solution could preserve a solution state at 4°C and transform a hydrogel state at body temperature (Albashari et al., 2020).

2.6 Cytocompatibility of PF127 hydrogel

The biocompatibility of PF127 hydrogel was evaluated using a Live/Dead Viability/Cytotoxicity Kit (Invitrogen, CA, United States) and Cell Counting Kit-8 (CCK-8, Dojindo Molecular Technologies) assay. In brief, the cultured DPSCs were trypsinized and resuspended in PF127 solution on ice. Then, 200 μl of cell-PF127 mixture solution containing 5×10^4 cells/ml was added to a 48-well plate. After seeding, the

plate was kept at 37°C in 5% CO_2 for 5 min to induce gel formation. The fresh medium was then added to each well, and the plate was transferred to a cell incubator. After being incubated for 1, 3, and 5 days, the Calcein-AM/pyridine iodide reagent mixture solution was added to the plates and incubated in the dark at 37°C for 10 min and observed using a fluorescence microscope (Eclipse 80i, Nikon, Japan). 10% CCK-8 solution was added to each well and transferred to a cell incubator for another 2 h to quantitatively analyze the cell proliferation activity. Absorbance at 450 nm was measured using an absorbance microplate reader (Varioskan LUX, Thermo Fisher Scientific).

2.7 Animal model establishment

All experiments were performed under sterile conditions. Female rabbits were anesthetized by a mixture of 2% isoflurane in 70% nitrous oxide and 30% oxygen and maintained with 1% isoflurane *via* a face mask. Then the skin was prepared, and a 4–5 cm incision was made to expose the FT and ovaries. The junction between the FT and the uterus was clamped with an arterial clip. .1 ml of absolute ethanol was injected into the FT using a 1 ml syringe. After 2 min, the arterial clip was loosened, and the FT was wiped around using a moist gauze and sutured. After 4 h, the HE results indicated that the FT had evident damage, and the structure of mucosa folds collapsed (Supplementary Figure S1), indicating that the animal model of FT injury was successfully constructed.

2.8 Experimental animals and grouping

Twenty four female white rabbits were randomly assigned to four groups: 1) sham group without any treatment; 2) FT injury (FTI) group that directly injected saline into the FT after the effect of anhydrous alcohol for 4 h; 3) DPSCs group that received an intravenous injection of DPSCs at the ear margin after the effect of anhydrous alcohol for 4 h; 4) PF127-encapsulated DPSCs (DPSCs-PF127) group that injected the mixture of DPSCs and PF127 into the FT after the effect of anhydrous alcohol for 4 h. After treatment for 4 weeks, the rabbits were euthanized by intraperitoneal injection of 3% pentobarbital sodium and the samples were collected and used for future analysis.

2.9 Histopathologic evaluation

The FT specimens were fixed in 4% formaldehyde, embedded in paraffin, sectioned into slides, stained with hematoxylin and eosin (H&E) and Masson's trichrome, and recorded using an optical microscope (ECLIPSE 80i, Nikon, Tokyo, Japan).

2.10 TdT-mediated dUTP nick-end labeling (TUNEL) staining

The TUNEL apoptosis assay kit (Beyotime, Nantong, Jiangsu, China) assay was performed as previously described (Zhu et al., 2020). In brief, the sections were dewaxed in xylene and rehydrated with gradient ethanol. Then, the sections were treated with TUNEL-FITC (1:200), and the nuclei were stained with DAPI for 10 min. Images were taken using a fluorescence microscope (Eclipse 80i, Nikon, Japan).

2.11 Immunofluorescence and immunohistochemistry

Immunofluorescence was performed to assess the primary antibody of VEGF-A and KI67 according to the manufacturer's procedures. The sections were treated with primary antibodies, namely, VEGF-A (1:200, Abcam, Cambridge, United Kingdom) and KI67 (1:200, Abcam, Cambridge, United Kingdom), overnight. Then, the sections were incubated with fluorogenic secondary antibodies for 1 h at 37°C. Finally, the sections were washed with PBS and incubated with DAPI for 10 min. For immunohistochemistry, the sections were treated with a primary antibody, namely, Vimentin (VIM; 1:200, Abcam, Cambridge, United Kingdom), overnight at 4°C and then incubated with horseradish-peroxidase-conjugated secondary antibody for another 2 h at 37°C. Then, the sections were developed using 3,3′-diaminobenzidine. All sections were observed using a fluorescence microscope (Eclipse 80i, Nikon, Japan).

2.12 ELISA

The concentrations of TNF-α and IL-10 in serum were measured using TNF-α (CSB-E06998Rb, CUSABIO Biotech Co., Ltd., Wuhan, China) and IL-10 (CSB-E06897Rb, CUSABIO Biotech Co., Ltd., Wuhan, China) ELISA kits. The blood of rabbits was collected; the serum was obtained after centrifugation, and the serum level of inflammatory cytokines was detected in accordance with the manufacturer's protocols. All of the samples were repeated.

2.13 Gene expression analysis

After 4 weeks, the FT was collected. Total RNA was extracted from 50 mg of FT using a TRIzol reagent (Invitrogen, CA, United States). One microgram of RNA was reverse transcribed into cDNA using a PrimeScript™ RT reagent kit gDNA Eraser (RR047A, TaKaRa BIO Inc., Kusatsu, Shiga, Japan). Real-time PCR was performed using the SYBR Premix EX TaqTM II. cDNA was amplified using the primer sequences

TABLE 1 Forward and reverse primer sequences.

Genes	Primer sequence (5′–3′)	
	Forward	Reverse
18S	GAATTCCCAGTAAGTGCGGGTCATA	CGAGGGCCTCACTAAACCATC
OVGP	GGATGTCTGAAGCACCCAGAGGT	AGGTCATCGTCATCTTGCCAGGG
IL10	GCCAAGCCTTGTCGGAGATGATC	CTGCTCCACTGCCTTGCTCTTG
KI67	ATGTTCCATTTCATCAGCCA	TTTAAATCGCTCCTCCATCC
Caspase-3	TGTAAATGCAGCAAACCTCG	GACTCCTTCATCACCGTGGC

shown in Table 1. The PCR cycling parameters used were as follows: 95°C for 10 s, annealed at 95°C for 5 s and extended at 60°C for 30 s for 40 cycles, followed by thermal denaturation. The mRNA expression was evaluated on the basis of SYBR green fluorescence for 18 s as the endogenous control.

2.14 Statistical analysis

Graph pad 7.0 statistics was used to process the data, and the results were presented as means ± standard errors. Statistical differences were obtained by Student's *t*-test and one-way analysis of variance, followed by Tukey's test or Dunnett *post hoc* test. $p < .05$ was considered as significant differences.

3 Results

3.1 DPSCs expressed MSC-like markers and possessed multipotency

The dental pulp is a soft connective tissue containing mesenchymal tissues, which is located in the medullary cavity of the tooth. DPSCs were extracted from the dental pulp, and the procedure for obtaining dental pulp tissues is shown in Supplementary Figure S2A. DPSCs had great cell proliferation capacity, and they can complete the whole primary culture for about 20 days (Supplementary Figure S2B). DPSCs possessed MSC-like properties and positively expressed MSC-like surface markers, including CD166, CD73, CD90, and CD44 (Supplementary Figures S3A, B), but they negatively expressed hematopoietic lineage markers, including CD19, CD34, and HLA-DR (Supplementary Figure S3A). Moreover, DPSCs had an excellent capacity for multilineage differentiation, and they could form mineralized nodules by positive staining of alizarin red S in the induced differentiation of osteoblasts. DPSCs were also induced to differentiate into adipogenesis with the formation of lipid droplets, which were stained with oil red O. In addition, DPSCs could differentiate into chondrocytes and show the evident staining of Alcian Blue (Supplementary Figure S3C).

3.2 DPSCs inhibited the expression of a pro-inflammatory factor (TNF-α) and enhanced the expression of an anti-inflammatory cytokine (IL-10)

The effects of DPSCs on the secretion of inflammatory factors in LPS-induced RAW264.7 cells were evaluated by immunofluorescence staining and ELISA. The results indicated that the expression of TNF-α and IL-10 was upregulated in macrophages by LPS stimulation for 24 h. The expression level of TNF-α was reduced in the presence of DPSCs (Figures 1A, B), whereas the expression of IL-10 was significantly increased (Figures 2A, B). As shown in Figures 1C, 2C, the results indicated that the level of TNF-α and IL-10 in supernatants was also increased after LPS induction for 24 h. In addition, DPSCs could downregulate the expression of TNF-α and upregulate the expression of IL-10, and they showed a significant difference compared with the LPS-induced one.

3.3 DPSCs promoted the formation of capillary-like structures

The angiogenic characteristics of DPSCs were evaluated by tubular network formation. The directly induced DPSCs (d-DPSCs), which were 3D cultured with GelMA hydrogel in the completed EGM-2™ medium, could form capillary-like networks. In addition, the number and diameter of closed networks were higher in d-DPSCs than in DPSCs cultured with α-MEM medium, and the difference was statistically significant (Figures 3A, B). Moreover, our results indicated that DPSCs could enhance the capillary-like structure formation of HUVECs using the indirectly cocultured system. Meanwhile, the number and length of capillary-like structures were higher in HUVECs cocultured with DPSCs than in HUVECs cultured alone (Figures 3C, D).

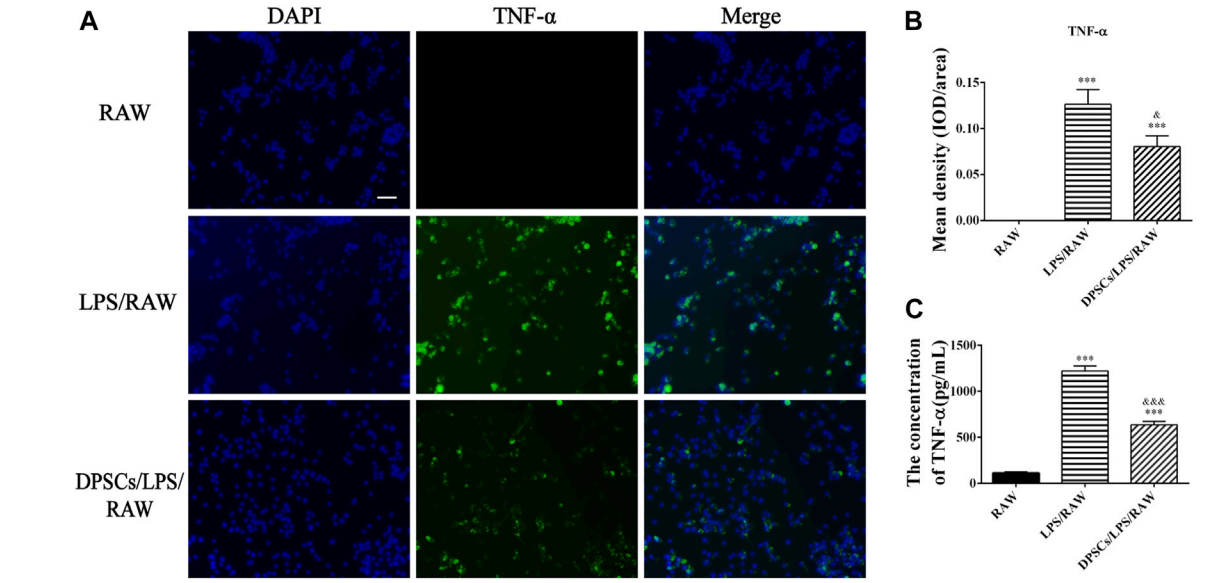

FIGURE 1
The expression of TNF-α in DPSCs co-cultured with RAW264.7 cells *in vitro*. **(A)** Immunofluorescence staining of TNF-α. Scale bar: 50 μm. **(B)** Quantification of the fluorescence intensity of TNF-α. ***$p < .001$ versus the RAW group. $^{\delta}p < .05$ versus the LPS/RAW group. **(C)** Comparison of the supernatants TNF-α concentration among groups. ***$p < .001$ versus the RAW group. $^{\delta\delta\delta}p < .001$ versus the LPS/RAW group.

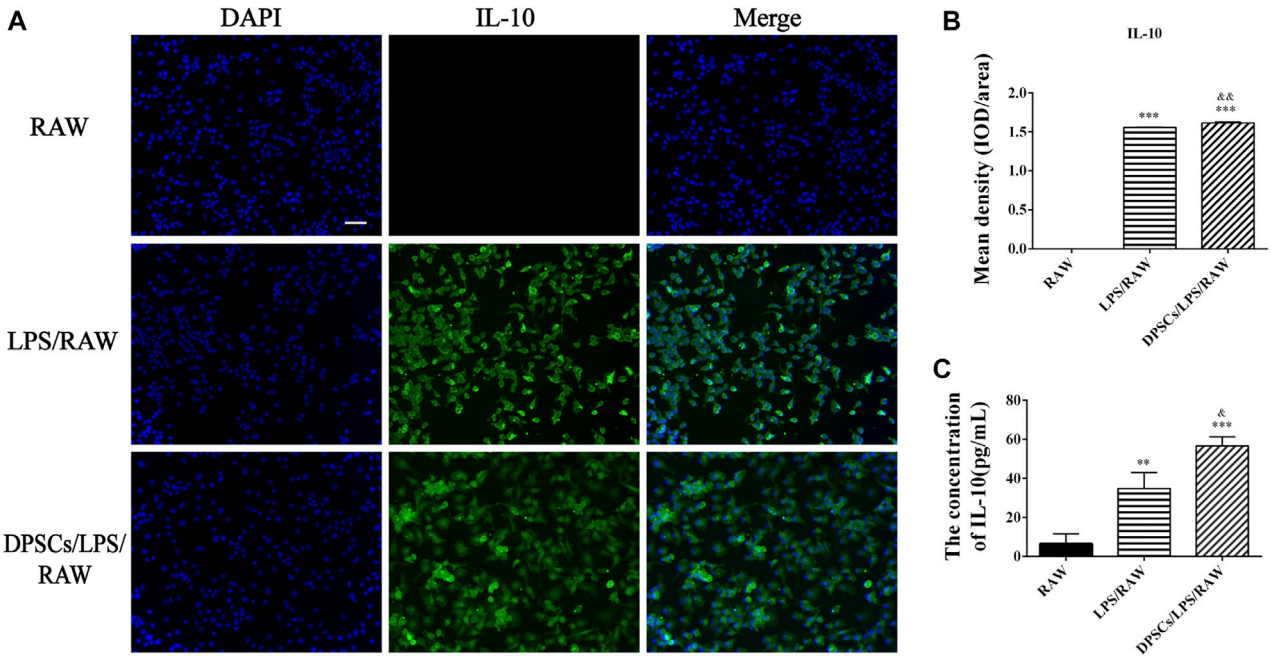

FIGURE 2
The expression of IL-10 in DPSCs co-cultured with RAW264.7 cells *in vitro*. **(A)** Immunofluorescence staining of IL-10. Scale bar: 50 μm. **(B)** Quantification of the fluorescence intensity of IL-10. ***$p < .001$ versus the RAW group. $^{\delta\delta}p < .01$ versus the LPS/RAW group. **(C)** Comparison of the supernatants IL-10 concentration among the groups. **$p < .01$, ***$p < .001$ versus the RAW group. $^{\delta}p < .05$ versus the LPS/RAW group.

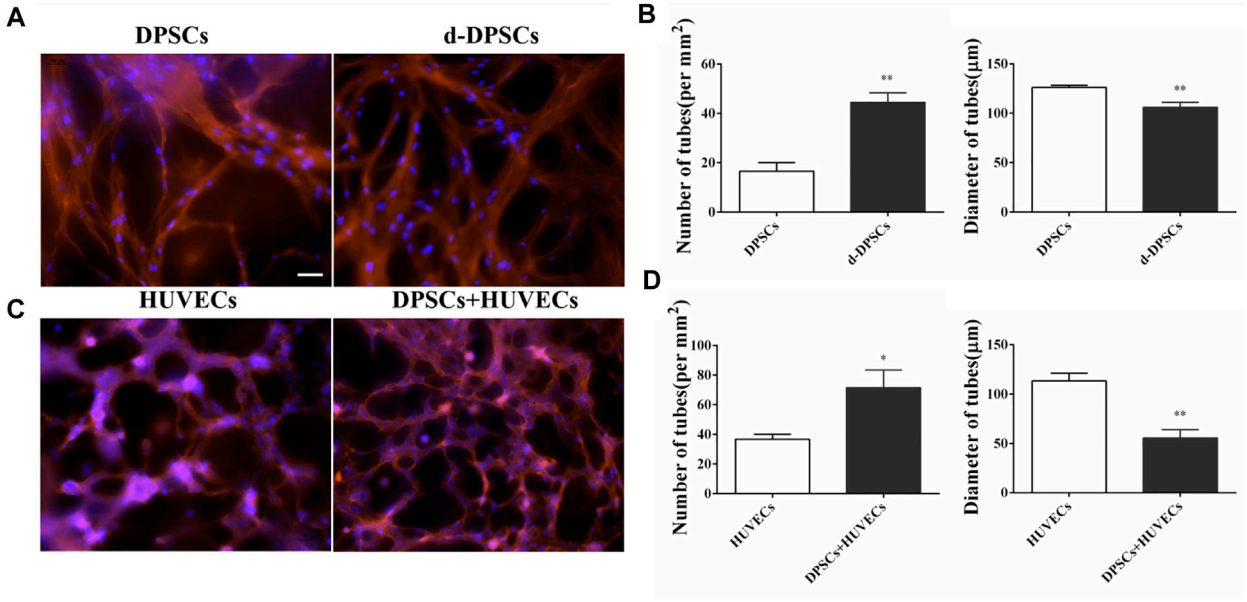

FIGURE 3
The effects of DPSCs on the formation of vessel-like structures. **(A)** The angiogenic potential of DPSCs by directly induced by EGM-2 TM complete culture medium. **(B)** The number and diameter of the formed tubes between the DPSCs group and the differentiated DPSCs (d-DPSCs). $^{**}p < .01$ versus the DPSCs group. **(C)** The effects of DPSCs on the tube formation of HUVECs by the cocultured system. **(D)** The number and diameter of the formed tubes between the HUVECs group and the HUVECs cocultured with DPSCs group (DPSCs+HUVECs).$^{*}p < .05$, $^{**}p < .01$ versus the HUVECs group. Scale bar: 50 μm.

3.4 PF127 hydrogel had a thermosensitive property and great biocompatibility

As shown in Figure 4A, PF127 hydrogel demonstrated a thermosensitive characteristic. It was clear and liquid solution when it was cold and transited to a homogeneous semi-solid hydrogel status at 37°C. Its gelation time was 80 ± 5 s. The biocompatibility of PF127 hydrogel containing DPSCs was evaluated using Live/Dead and CCK-8 assays. As for the Live/Dead assay, the results indicated that PF127 hydrogel had great cytocompatibility. After being cocultured with DPSCs, most of the cells were alive and stained with green from day 1 to day 5. In addition, the ratio of live cells had no difference between day 3 and day 5, but all of them were higher than that of day 1 (Figures 4B, C). The proliferation of encapsulated DPSCs in PF-127 hydrogel was detected for 5 days by CCK-8 assay. The results showed that DPSCs could continue to proliferate in PF127 hydrogel from day 1 to day 5, and the difference was statistically significant (Figure 4D).

3.5 DPSCs ameliorated the morphological features of the FT tissue

Four weeks after surgery, upon macroscopic view, injured part of the FT tissue in the FTI and DPSCs groups shrunk greatly (red arrow). In contrast, injured FT tissue in the DPSCs-PF127 group appeared normal and was similar to that of in the sham group (Supplementary Figure S4). Meanwhile, the cross-section of the middle site of the FT tissue was stained with H&E and Masson's trichrome among the experimental groups. As shown in Figure 5A, the H&E-staining results showed that the normal FT tissue had large mucosa-fold-filled lumen and loosely thick muscularis wall in the sham group. Moreover, the mucosal fold was composed of a single columnar epithelium and a branched core of vascular tissues. In the FTI group, the mucosal fold disappeared, and several infiltrated inflammatory cells and densely thin muscle layers could be observed in the damaged tube tissue. After treatment with DPSCs alone or DPSCs-PF127 *in situ* injection, the FT gradually returned to its normal structure, and mucosal folds with multi-branching recovered, but inflammatory infiltration also occurred in the lumen and muscle wall in the DPSCs group. In the DPSCs-PF127 group, the structure of mucosal folds and muscle walls was almost similar to that of the sham control group. As for Masson's trichrome staining in each group (Figure 5B), the results showed thin and sparse collagen fibers, which were stained with blue dispersed in the submucosal and muscle wall in the sham group. However, massive collagen fiber infiltration occurred, which was stained with deep blue in the muscle wall and lumen in the FTI group. After treatment with DPSCs alone, a moderate amount of collagen fibers (blue) scattered in the muscle

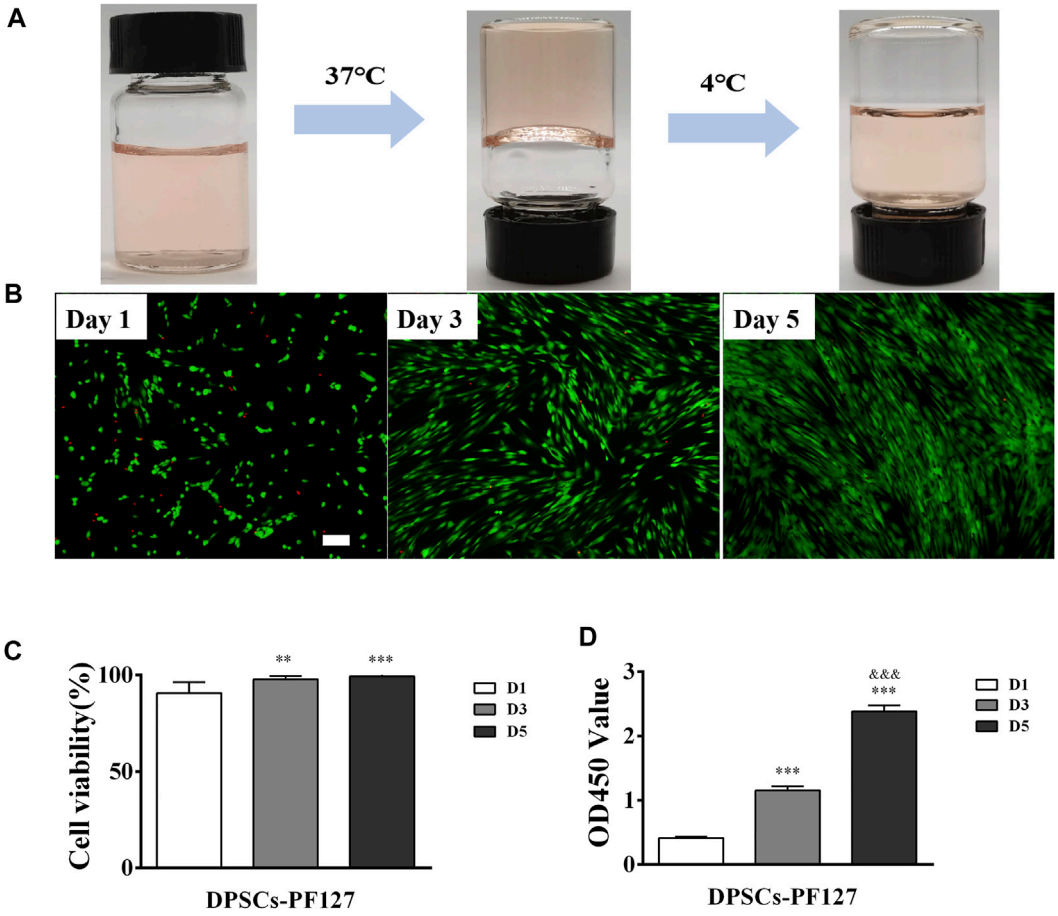

FIGURE 4
The biocompatibility of PF127 hydrogel. **(A)** The thermosensitive property of PF127. **(B)** The images of Dead/Live assay of DPSCs encapsulated into the PF127 hydrogel after 1, 3 and 5 days, Scale bar: 200 μm. **(C)** Statistical analysis of the cell viability. The ratio of green to green plus red cells provided the percentage of cell viability. $^{**}p < .01$, $^{***}p < .001$ versus the Day 1. **(D)** The proliferation activity of DPSCs encapsulated into the PF127 hydrogel after 1, 3 and 5 days were measured using Cell Counting Kit-8. $^{***}p < .001$ versus the Day 1, $^{\&\&\&}p < .001$ versus the Day 3.

wall, some of which were infiltrated in the lumen. In the DPSCs-PF127 group, the FT preserved its normal structure, and the muscle wall and mucosal fold were filled with a small number of collagen fibers, which had been shown in blue.

3.6 Evaluation of TUMEL, immunofluorescence staining, and immunohistochemistry

The effect of DPSCs on FT cell apoptosis was analyzed by TUNEL staining. As shown in Figure 6A, TUNEL staining showed evident green fluorescence in the FTI group, indicating that FT cells underwent significant apoptosis. However, a small amount of TUNEL staining cells were found in the sham group. After treatment of DPSCs, TUNEL staining with green fluorescence gradually reduced, but the expression of TUNEL in the DPSCs group was stronger than that in the DPSCs-PF127 group. The number of TUNEL staining cells was highest in the FTI group and lowest in the DPSCs-PF127 group (Figure 6B). The number of TUNEL staining cells had no significant difference between the sham group and DPSCs-PF127 group ($p > .05$).

For immunofluorescence staining and immunohistochemistry analysis, the expression of a cell proliferation marker (KI67) and endothelial cell markers (VEGF-A and VIM) was investigated to evaluate the effect of DPSCs on FT cell proliferation and vascularization *in vivo*. The fluorescence expression of KI67 and VEGF-1 in the DPSCs and DPSCs-PF127 groups was stronger than that in the FTI group. All of the markers were highly expressed in the DPSCs-PF127 group and moderately expressed in the DPSCs and sham groups but weakly expressed in the FTI group (Figures 7A, 8A). In the three experimental groups, the

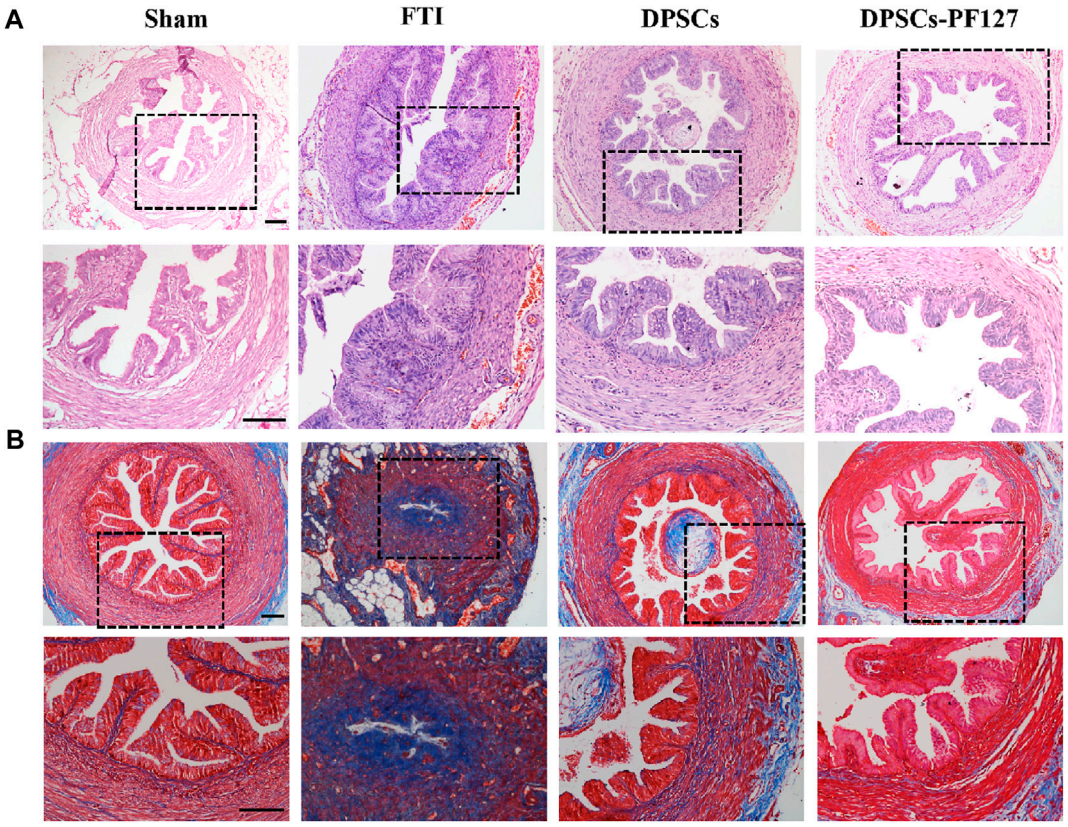

FIGURE 5
The H&E **(A)** and Masson trichrome **(B)** staining of FT after 4 weeks surgery among the groups. Scale bar: 100 μm.

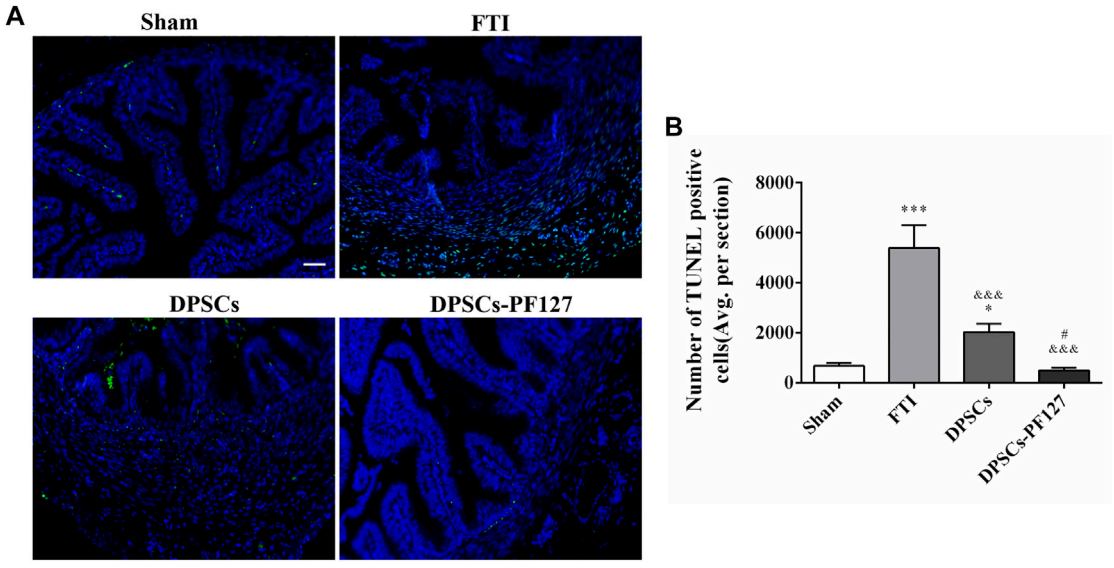

FIGURE 6
DPSCs-PF127 reduces cell apoptosis of the FT at 4 weeks after injury. **(A)** Immunofluorescence staining for TUNEL (green) of sections from the FT in each group. Scale bar: 50 μm. **(B)** Quantitative estimation of apoptotic and TUNEL cells from three independent sections. All data represent Mean values ±SEM. *$p < .05$, ***$p < .001$ versus the Sham group. $^{\&\&\&}p < .001$ versus the FTI group. $^{\#}p < .05$ versus the DPSCs group.

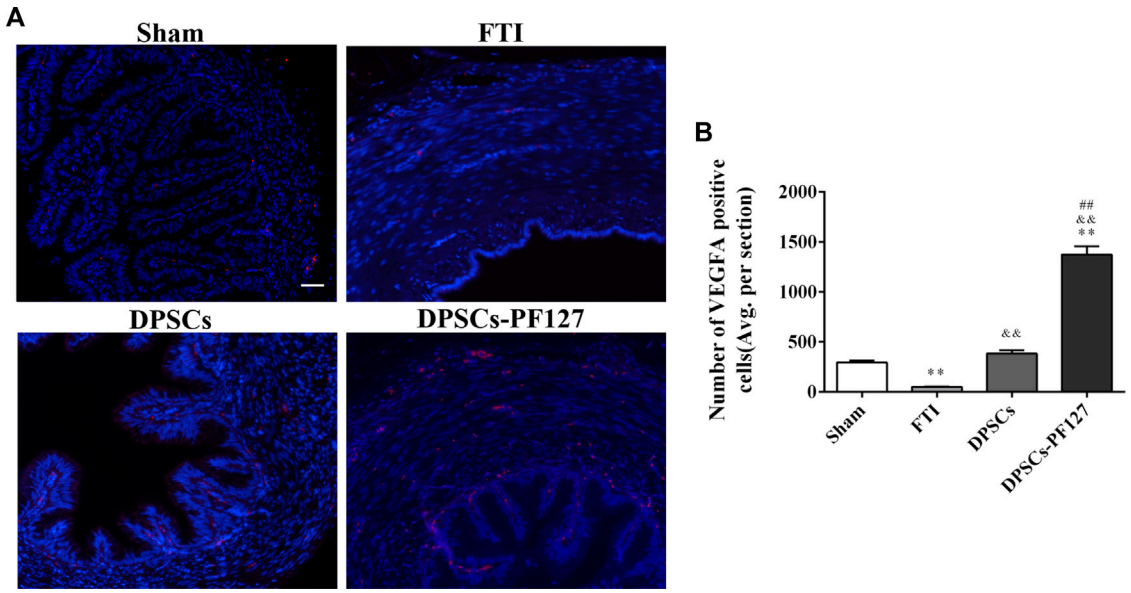

FIGURE 7
DPSCs-PF127 promotes angiogenesis of the FT at 4 weeks after injury. **(A)** Immunofluorescence staining for VEGF-A (red) of sections from the FT in each group. Scale bar: 50 μm. **(B)** Quantitative estimation of VEGF-A-positive cells from three independent sections. All data represent Mean values ±SEM. $^{**}p < .01$ versus the Sham group. $^{\&\&}p < .01$ versus the FTI group. $^{\#\#}p < .01$ versus the DPSCs group.

intensity of KI67 and VEGF-A-positive regions was presented in the following order: DPSCs-PF127 > DPSCs > FTI. Meanwhile, a statistically significant difference was found between the DPSCs-PF127 group and the sham group ($p < .01$, Figures 7B, 8B). For immunohistochemistry (Figure 9), the results showed that VIM was highly expressed in the DPSCs-PF127 group and moderately expressed in the sham group but weakly expressed in the DPSCs and the FTI groups (Figure 9A). The intensity of VIM-positive regions was highest in the DPSCs-PF127 group compared with that of the other groups, but no statistically significant difference was found between the DPSCs group and FTI group ($p > .05$, Figure 9B).

3.7 Detection of serum TNF-α and IL-10 expression levels and real-time PCR analysis

ELISA was used to evaluate the serum levels of TNF-α and IL-10 in each group. The results showed that the serum TNF-α levels in the FTI and DPSCs groups were significantly higher than those in the sham and DPSCs-PF127 groups ($p < .001$). Meanwhile, no statistically significant difference was observed between the DPSCs-PF127 and sham groups ($p > .05$). However, the serum IL-10 levels in the FTI group were lower than those in the other groups ($p < .01$), and no statistically significant difference was observed among these groups except for the FTI group ($p > .05$, Figure 10A). For real-time PCR (RT-PCR) analysis (Figure 10B), the results indicated that OVGP, IL-10, and KI67 mRNA were highly expressed in the DPSCs-PF127 group and moderately expressed in the DPSCs and sham groups but weakly expressed in the FTI group. However, no significant difference was observed between the sham and DPSCs groups ($p > .05$). In addition, caspase 3 mRNA was weakly expressed in the DPSCs-PF127 group and highly expressed in the TFI group. Moreover, the expression level of caspase 3 showed a significant difference between the TFI group and other groups ($p < .05$).

4 Discussion

The FT is important for egg transportation, sperm activation, and early embryonic development in the reproductive process. Therefore, FT, which preserves the normal structure, secretion property, and peristalsis, plays an important role in reproductive functions of women (Lyons et al., 2006; Duran et al., 2014). In addition, the integrity of mucosal fold and the great secretion of epithelial cells in the FT directly affect the surface area of cell reception and cell activation (Hunter 2005). In our previous study, the H&E results confirmed that the structure of FT, particularly the mucosal fold and muscle wall, was destroyed by anhydrous ethanol for 4 h (Supplementary Figure S1C). After 4 weeks, the mucosal fold disappeared, and inflammatory macrophage

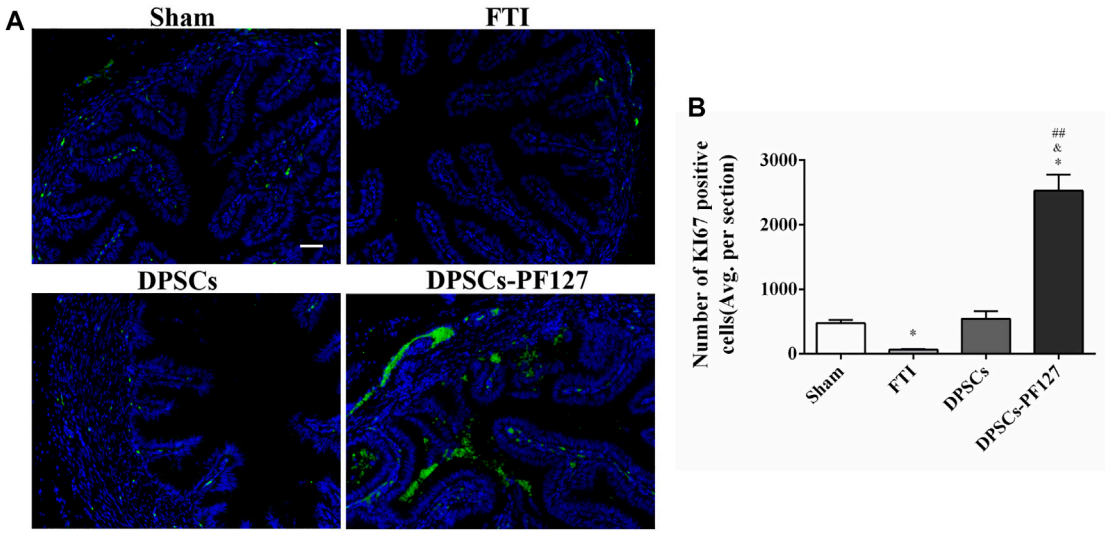

FIGURE 8
DPSCs-PF127 enhances cell proliferation of the FT at 4 weeks after injury. **(A)** Immunofluorescence staining for KI67 (green) of sections from the FT in each group. Scale bar: 50 μm. **(B)** Quantitative estimation of KI67-positive cells from three independent sections. All data represent Mean values ±SEM. $^{*}p < .05$ versus the Sham group. $^{\&}p < .05$ versus the FTI group. $^{\#\#}p < .01$ versus the DPSCs group.

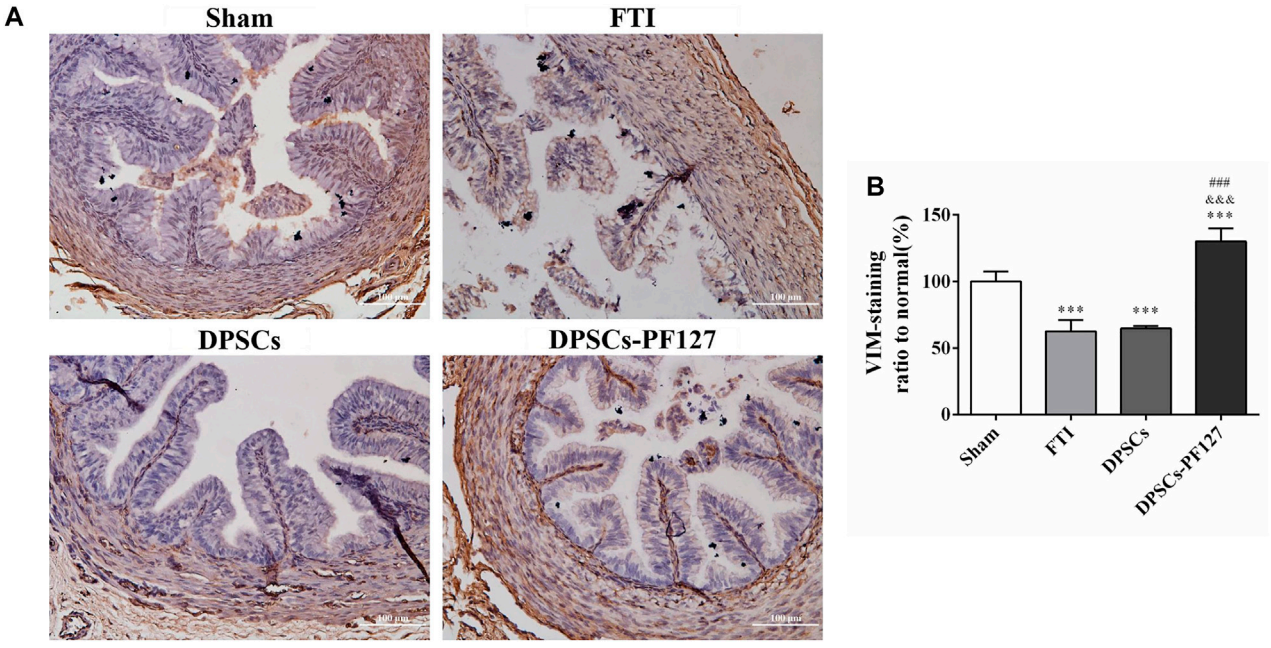

FIGURE 9
The immunohistochemisty assay of the FT at 4 weeks after injury. **(A)** Representative images of VIM from immunohistochemisty. Scale bar: 100 μm. **(B)** Quantification of the VIM positive staining ratio to normal in FT. The quantification results obtained by ImageJ. All data represent Mean values ±SEM. $^{***}p < .001$ versus the Sham group. $^{\&\&\&}p < .001$ versus the FTI group. $^{\#\#\#}p < .001$ versus the DPSCs group.

infiltration, muscle wall fibrosis, and lumen stenosis were observed in the FTI group, which had not received any treatment (Figure 5). Moreover, such structural and functional destructions in the FT would increase the tubal infertility rate. Therefore, the repair and regeneration of the damaged FT played important roles in reducing tubal infertility.

MSCs have shown a strong immunomodulatory property, which could be used as an immunosuppressive agent to modulate

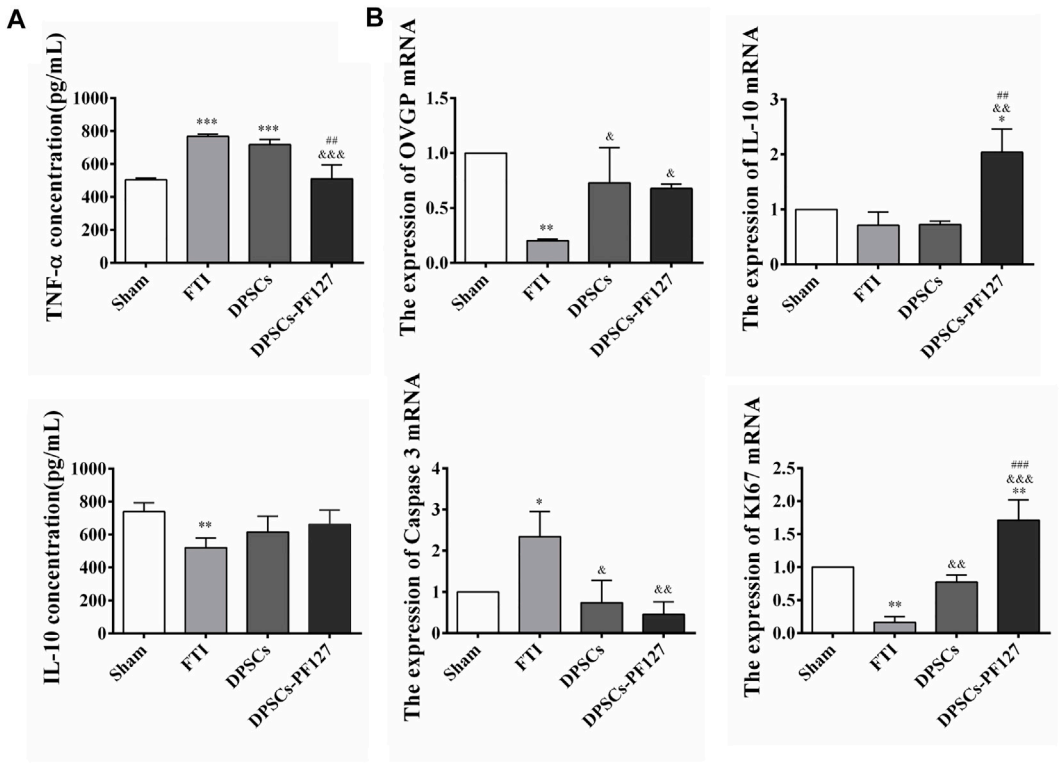

FIGURE 10
Concentration of inflammatory factors in serum and mRNA detection of the FT at 4 weeks after surgery. **(A)** Comparison of the serum TNF-α and IL-10 concentration among the groups. $^{**}p < .01$, $^{***}p < .001$ versus the Sham group. $^{\&\&\&}p < .001$ versus the FTI group. $^{\#\#}p < .01$ versus the DPSCs group. **(B)** The expression of OVGP, IL-10, Caspase 3, KI67 mRNA of the FT tissues among the groups. $^{*}p < .05$,$^{**}p < .01$ versus the Sham group. $^{\&}p < .05$, $^{\&\&}p < .01$, $^{\&\&\&}p < .001$ versus the FTI group. $^{\#\#}p < .01$, $^{\#\#\#}p < .001$ versus the DPSCs group.

the immune response in inflammatory or autoimmune diseases (Liu et al., 2020; Wu et al., 2020; Zhou et al., 2020). In addition, MSCs had a great angiogenic property, and they could promote vessel-like formation by secreting various growth factors or directly differentiating into endothelial cells (Takeuchi et al., 2019; Merckx et al., 2020; Santos et al., 2020). Thus, MSC-based cell therapy, such as Wharton's jelly-derived mesenchymal stem cells, BM-MSCs, and human umbilical cord mesenchymal stem cells, served as a suitable strategy for the treatment of FT injury. In these studies, most MSCs were used by intraperitoneal or intravenous injection, which had systemic effects on the repair and regeneration of FT injury (Luo et al., 2015; Li et al., 2017; Almasry et al., 2018; Liao et al., 2019). However, no study had reported that the therapeutic method of MSCs in the treatment of FT damage was currently used by *in situ* injection.

In this study, we used DPSCs, which were obtained from dental pulp without harm or invasive surgery, as seeded cells for the treatment of FT injury by PF127 hydrogel *in situ* transplantation. As previously described, PF-127 hydrogel had a thermosensitive property and great cytocompatibility with DPSCs, which was an ideal scaffold for cell survival and proliferation (Albashari et al., 2020). In *in vitro* cell culture experiments, our results indicated that DPSCs, which were dispersed in PF-127 hydrogel, could proliferate from day 1 to day 5 (Figures 4B–D). Moreover, DPSCs showed great immunomodulatory and angiogenic characteristics, and they could promote the expression and secretion of anti-inflammatory cytokines such as IL-10, but they could inhibit the expression and secretion of pro-inflammatory factors such as TNF-α (Figures 1, 2) and enhance the formation of vessel-like structures (Figure 3). Therefore, PF127 hydrogel containing DPSCs could provide an effective treatment for FT injury by *in situ* injection.

For histological analysis, the H&E and Masson's trichrome staining results indicated that FT structural damage was improved after treatment with DPSCs, but the repair effects in the DPSCs-PF127 group were better than those in the DPSCs group (Figure 5). Previous studies revealed that 3D-network hydrogel could be used as a cell carrier, which could not only ensure the number of active cells in the injured site but also provide a suitable microenvironment for cell growth and proliferation (Long et al., 2020; Villiou et al., 2020). In this study, the results indicated that PF127 hydrogel encapsulating DPSCs by *in*

situ injection could be used to promote the repair and regeneration of FT injury.

In our study, TUNEL assay was performed to detect FT apoptotic cells in the injured site because of massive DNA fragmentation in the nuclei of apoptotic cells, which could be labeled with green FITC fluorescence (Zhu et al., 2020; He et al., 2021). Caspase-3, as an important marker of programmed cell death, was responsible for the cleavage of many proteins during apoptosis (Elmore 2007). Our results showed that the positive region of TUNEL staining in the DPSCs-PF127 group was lowest among the groups; meanwhile, caspase-3 mRNA expression was significantly lower in the DPSCs-PF127 group than in the FTI group. These results supported *in situ* transplantation of PF127 hydrogel containing DPSCs into the injured FT, which likely promoted the repair and regeneration of the injured FT by inhibiting cell apoptosis.

KI67, which is a representative proliferation marker, was widely used to evaluate cell proliferation (Willenbacher et al., 2020; Murata et al., 2021). VEGF-A and VIM, which served as vascular endothelial-associated markers contributing to angiogenesis, were commonly used to assess the angiogenic property (Almasry et al., 2018; Chen et al., 2021). In our research, the results revealed that the expression level of KI67, VEGF-A, and VIM was higher in the DPSCs-PF127 group than in the sham control group. Meanwhile, the difference in KI67 and VEGF-A showed no statistically significant difference between the DPSCs and sham control groups, whereas VIM expression showed a contrary result. These results indicated that PF127 hydrogel containing DPSCs could enhance the damage repair and the tissue regeneration of FT, by stimulating the secretion of angiogenic factors and promoting cell proliferation at the injury site.

Tumor necrosis factor-alpha (TNF-α) and interleukin-10 (IL-10) are two representative cytokines produced by the immune cells. Both play key roles in maintaining immune homeostasis and modulate the inflammatory reaction (Wang et al., 2022). And IL-10 can inhibit the production of TNF-α (Kuwata et al., 2003; Passoja et al., 2010). Thus, in this study, TNF-α and IL-10 were used to evaluate the immunomodulatory function of DPSCs in the repair of injured FT. TNF-α, which is a pro-inflammatory factor produced by mononuclear macrophages, was closely associated with the reproductive immunization of the female genital system (Morales et al., 2006; Oróstica et al., 2013). IL-10, which served as a cytokine exerting anti-inflammatory effects, was produced by activated macrophages. A previous study indicated that DPSCs could upregulate the secretion of IL-10 by coculturing with T cells (Demircan et al., 2011). Our results showed that the expression of IL-10 in serum had no significant difference between the DPSCs-PF127 and sham control groups. Moreover, the mRNA expression of IL-10 in the DPSCs-PF127 group was higher than that in the sham control group. However, the level of TNF-α showed a lower expression in the DPSCs-PF127 group than in other groups. These results indicated that PF127 hydrogel containing DPSCs promoted the repair and regeneration of FT damage, thereby stimulating the secretion of IL-10 and inhibiting the secretion of TNF-α.

Oviductal glycoprotein (OVGP), which is a multi-protein complex produced by the secretion of FT epithelium, could be used to evaluate the function of epithelial cells (Luo et al., 2015; Li et al., 2017). Our results indicated that OVGP was highly expressed in the DPSCs and DPSCs-PF127 groups, which had no significant difference compared with the sham control group. In addition, OVGP was weakly expressed in the FTI group, indicating a serious damage in the mucosal fold. These results indicated that DPSCs could promote the repair and regeneration of mucosal fold and restore its secretion functions.

5 Conclusion

In the present study, the effects of PF127 hydrogel containing DPSCs on the repair and regeneration of FT injury were evaluated by histological analysis (e.g., H&E and Masson's trichrome staining, TUNEL staining, immunofluorescence staining, and immunohistochemistry), ELISA, and RT-PCR detections. Our results indicated that PF127 hydrogel containing DPSCs promoted the repair and regeneration of FT damage, thereby inhibiting cell apoptosis, stimulating the secretion of angiogenic factors, promoting cell proliferation, modulating the secretion of inflammatory factors, and restoring the secretion of epithelial cells. Therefore, this study was the first to report that *in situ* injection of PF127 hydrogel encapsulating DPSCs could be used to treat FT injury in clinical settings.

Data availability statement

The original contributions presented in the study are included in the article/Supplementary Material, further inquiries can be directed to the corresponding authors.

Ethics statement

The animal study was reviewed and approved by the Animal Experimental Center of Wenzhou Medical University. Written informed consent was obtained from the owners for the participation of their animals in this study.

Author contributions

QY, LL, and YL performed the majority of experiments and analyzed the data; QZ collected the data and performed statistical analysis; JY cultured DPSCs; ZX, XL, and FH performed multi-differentiation of DPSCs; LL, QY, and YH designed and coordinated the research; LL and QZ wrote the paper.

Funding

This research was partially supported by the National Natural Science Funding of China under Grant No. 81871503, the Wenzhou Major Scientific and Technological Innovation Key Medical and Health Project under Grant No. ZY2019010, and Zhejiang Provincial Natural Science Foundation of China under Grant No. LGF21H140007, and Zhejiang Province Program of the Medical and Health Science and Technology under Grant No. 2022KY218.

Conflict of interest

The authors declare that the research was conducted in the absence of any commercial or financial relationships that could be construed as a potential conflict of interest.

Publisher's note

Supplementary material

The Supplementary Material for this article can be found online at: https://www.frontiersin.org/articles/10.3389/fbioe.2022.1062646/full#supplementary-material

References

Adegbola, O., and Akindele, M. O. (2013). The pattern and challenges of infertility management in Lagos, Nigeria. *Afr. Health Sci.* 13 (4), 1126–1129. doi:10.4314/ahs.v13i4.37

Albashari, A., He, Y., Zhang, Y., Ali, J., Lin, F., Zheng, Z., et al. (2020). Thermosensitive bFGF-modified hydrogel with dental pulp stem cells on neuroinflammation of spinal cord injury. *ACS Omega* 5 (26), 16064–16075. doi:10.1021/acsomega.0c01379

Almasry, S. M., Elfayomy, A. K., and El-Sherbiny, M. H. (2018). Regeneration of the fallopian tube mucosa using bone marrow mesenchymal stem cell transplantation after induced chemical injury in a rat model. *Reprod. Sci.* 25 (5), 773–781. doi:10.1177/1933719117725824

Chen, H., Sun, J., Liu, J., Gou, Y., Zhang, X., Wu, X., et al. (2019). Structural characterization and anti-inflammatory activity of alkali-soluble polysaccharides from purple sweet potato. *Int. J. Biol. Macromol.* 131, 484–494. doi:10.1016/j.ijbiomac.2019.03.126

Chen, Y. C., Lin, R. Z., Qi, H., Yang, Y., Bae, H., Melero-Martin, J. M., et al. (2012). Functional human vascular network generated in photocrosslinkable gelatin methacrylate hydrogels. *Adv. Funct. Mater* 22 (10), 2027–2039. doi:10.1002/adfm.201101662

Chen, Z., Fang, Z., and Ma, J. (2021). Regulatory mechanisms and clinical significance of vimentin in breast cancer. *Biomed. Pharmacother.* 133, 111068. doi:10.1016/j.biopha.2020.111068

Demircan, P. C., Sariboyaci, A. E., Unal, Z. S., Gacar, G., Subasi, C., and Karaoz, E. (2011). Immunoregulatory effects of human dental pulp-derived stem cells on T cells: comparison of transwell co-culture and mixed lymphocyte reaction systems. *Cytotherapy* 13 (10), 1205–1220. doi:10.3109/14653249.2011.605351

Duran, M., Ustunyurt, E., Kosus, A., Kosus, N., Turhan, N., Hızlı, D., et al. (2014). Does vitamin E prevent tubal damage caused by smoking? A light microscopy and animal study. *Eur. J. Obstet. Gynecol. Reprod. Biol.* 175, 149–151. doi:10.1016/j.ejogrb.2014.01.020

Elmore, S. (2007). Apoptosis: a review of programmed cell death. *Toxicol. Pathol.* 35 (4), 495–516. doi:10.1080/01926230701320337

He, N., Zheng, X., He, T., Shen, G., Wang, K., Hu, J., et al. (2021). MCC950 reduces neuronal apoptosis in spinal cord injury in mice. *CNS Neurol. Disord. Drug Targets* 20 (3), 298–308. doi:10.2174/1871527319666201005170659

Hunter, R. H. (2005). The fallopian tubes in domestic mammals: How vital is their physiological activity? *Reprod. Nutr. Dev.* 45 (3), 281–290. doi:10.1051/rnd:2005020

Kuwata, H., Watanabe, Y., Miyoshi, H., Yamamoto, M., Kaisho, T., Takeda, K., et al. (2003). IL-10-inducible Bcl-3 negatively regulates LPS-induced TNF-α production in macrophages. *Blood* 102 (12), 4123–4129. doi:10.1182/blood-2003-04-1228

Lan, X., Sun, Z., Chu, C., Boltze, J., and Li, S. (2019). Dental pulp stem cells: An attractive alternative for cell therapy in ischemic stroke. *Front. Neurol.* 10, 824. doi:10.3389/fneur.2019.00824

Li, Z., Zhang, Z., Ming, W. K., Chen, X., and Xiao, X. M. (2017). Tracing GFP-labeled WJMSCs *in vivo* using a chronic salpingitis model: an animal experiment. *Stem Cell Res. Ther.* 8 (1), 272. doi:10.1186/s13287-017-0714-z

Liao, W., Tang, X., Li, X., and Li, T. (2019). Therapeutic effect of human umbilical cord mesenchymal stem cells on tubal factor infertility using a chronic salpingitis murine model. *Arch. Gynecol. Obstet.* 300 (2), 421–429. doi:10.1007/s00404-019-05209-6

Liu, H., Li, R., Liu, T., Yang, L., Yin, G., and Xie, Q. (2020). Immunomodulatory effects of mesenchymal stem cells and mesenchymal stem cell-derived extracellular vesicles in rheumatoid arthritis. *Front. Immunol.* 11, 1912. doi:10.3389/fimmu.2020.01912

Long, Y., Yan, L., Dai, H., Yang, D., Wu, X., Dong, X., et al. (2020). Enhanced proliferation and differentiation of neural stem cells by peptide-containing temperature-sensitive hydrogel scaffold. *Mater Sci. Eng. C Mater Biol. Appl.* 116, 111258. doi:10.1016/j.msec.2020.111258

Luo, H. J., Xiao, X. M., Zhou, J., and Wei, W. (2015). Therapeutic influence of intraperitoneal injection of Wharton's jelly-derived mesenchymal stem cells on oviduct function and fertility in rats with acute and chronic salpingitis. *Genet. Mol. Res.* 14 (2), 3606–3617. doi:10.4238/2015.april.17.10

Luo, L., He, Y., Jin, L., Zhang, Y., Guastaldi, F. P., Albashari, A. A., et al. (2021). Application of bioactive hydrogels combined with dental pulp stem cells for the repair of large gap peripheral nerve injuries. *Bioact. Mater* 6 (3), 638–654. doi:10.1016/j.bioactmat.2020.08.028

Luo, L., He, Y., Wang, X., Key, B., Lee, B. H., Li, H., et al. (2018). Potential roles of dental pulp stem cells in neural regeneration and repair. *Stem Cells Int.* 2018, 1–15. doi:10.1155/2018/1731289

Lyons, R. A., Saridogan, E., and Djahanbakhch, O. (2006). The reproductive significance of human Fallopian tube cilia. *Hum. Reprod. Update* 12 (4), 363–372. doi:10.1093/humupd/dml012

Merckx, G., Hosseinkhani, B., Kuypers, S., Deville, S., Irobi, J., Nelissen, I., et al. (2020). Angiogenic effects of human dental pulp and bone marrow-derived mesenchymal stromal cells and their extracellular vesicles. *Cells* 9 (2), 312. doi:10.3390/cells9020312

Morales, P., Reyes, P., Vargas, M., Rios, M., Imarai, M., Cardenas, H., et al. (2006). Infection of human fallopian tube epithelial cells with Neisseria gonorrhoeae protects cells from tumor necrosis factor alpha-induced apoptosis. *Infect. Immun.* 74 (6), 3643–3650. doi:10.1128/iai.00012-06

Murata, Y., Jo, J. I., and Tabata, Y. (2021). Molecular beacon imaging to visualize Ki67 mRNA for cell proliferation ability. *Tissue Eng. Part A* 27 (9-10), 526–535. doi:10.1089/ten.TEA.2020.0127

Németh, K., Leelahavanichkul, A., Yuen, P. S., Mayer, B., Parmelee, A., Doi, K., et al. (2009). Bone marrow stromal cells attenuate sepsis via prostaglandin E(2)-dependent reprogramming of host macrophages to increase their interleukin-10 production. *Nat. Med.* 15 (1), 42–49. doi:10.1038/nm.1905

Oróstica, M. L., Zuñiga, L. M., Utz, D., Parada-Bustamante, A., Velásquez, L. A., Cardenas, H., et al. (2013). Tumour necrosis factor-α is the signal induced by mating to shutdown a 2-methoxyestradiol nongenomic action necessary to

accelerate oviductal egg transport in the rat. *Reproduction* 145 (2), 109–117. doi:10.1530/rep-12-0389

Passoja, A., Puijola, I., Knuuttila, M., Niemelä, O., Karttunen, R., Raunio, T., et al. (2010). Serum levels of interleukin-10 and tumour necrosis factor-α in chronic periodontitis. *J. Clin. Periodontol.* 37 (10), 881–887. doi:10.1111/j.1600-051x.2010.01602.x

Santos, R. A., Asensi, K. D., de Barros, J. H. O., de Menezes, R. C. S., Cordeiro, I. R., Neto, J. M. B., et al. (2020). Intrinsic angiogenic potential and migration capacity of human mesenchymal stromal cells derived from menstrual blood and bone marrow. *Int. J. Mol. Sci.* 21 (24), 9563. doi:10.3390/ijms21249563

Takeuchi, R., Katagiri, W., Endo, S., and Kobayashi, T. (2019). Exosomes from conditioned media of bone marrow-derived mesenchymal stem cells promote bone regeneration by enhancing angiogenesis. *PLoS One* 14 (11), e0225472. doi:10.1371/journal.pone.0225472

Villiou, M., Paez, J. I., and Del Campo, A. (2020). Photodegradable hydrogels for cell encapsulation and tissue adhesion. *ACS Appl. Mater Interfaces* 12 (34), 37862–37872. doi:10.1021/acsami.0c08568

Wang, R., Zhang, X., and Wang, S. (2022). Differential genotypes of TNF-α and IL-10 for immunological diagnosis in discoid lupus erythematosus and oral lichen planus: A narrative review. *Front. Immunol.* 13, 967281. doi:10.3389/fimmu.2022.967281

Willenbacher, E., Brunner, A., Willenbacher, W., Zelger, B., Wolf, D., Rogge, D., et al. (2020). Visible and near-infrared hyperspectral imaging techniques allow the reliable quantification of prognostic markers in lymphomas: A pilot study using the Ki67 proliferation index as an example. *Exp. Hematol.* 91, 55–64. doi:10.1016/j.exphem.2020.09.191

Wu, X., Jiang, J., Gu, Z., Zhang, J., Chen, Y., and Liu, X. (2020). Mesenchymal stromal cell therapies: immunomodulatory properties and clinical progress. *Stem Cell Res. Ther.* 11 (1), 345. doi:10.1186/s13287-020-01855-9

Zhou, T., Li, H. Y., Liao, C., Lin, W., and Lin, S. (2020). Clinical efficacy and safety of mesenchymal stem cells for systemic lupus erythematosus. *Stem Cells Int.* 2020, 1–11. doi:10.1155/2020/6518508

Zhu, G., Shen, Q., Jiang, H., Ji, O., Zhu, L., and Zhang, L. (2020). Curcumin inhibited the growth and invasion of human monocytic leukaemia SHI-1 cells *in vivo* by altering MAPK and MMP signalling. *Pharm. Biol.* 58 (1), 25–34. doi:10.1080/13880209.2019.1701042

Zhu, J., and Marchant, R. E. (2011). Design properties of hydrogel tissue-engineering scaffolds. *Expert Rev. Med. Devices* 8 (5), 607–626. doi:10.1586/erd.11.27

Zou, S. E., Jin, Y., Ko, Y. L., and Zhu, J. (2014). A new classification system for pregnancy prognosis of tubal factor infertility. *Int. J. Clin. Exp. Med.* 7 (5), 1410–1416.

frontiers | Frontiers in Bioengineering and Biotechnology

TYPE Original Research
PUBLISHED 10 January 2023
DOI 10.3389/fbioe.2022.1067139

OPEN ACCESS

EDITED BY
Hengchong Shi,
Changchun Institute of Applied Chemistry (CAS), China

REVIEWED BY
Kai Wang,
Nankai University, China
Wei Nie,
Wake Forest Baptist Medical Center, United States

*CORRESPONDENCE
Ruilan Wang,
wangyusun@hotmail.com

SPECIALTY SECTION
This article was submitted to Biomaterials, a section of the journal Frontiers in Bioengineering and Biotechnology

RECEIVED 11 October 2022
ACCEPTED 19 December 2022
PUBLISHED 10 January 2023

CITATION
Zhang W, Du J, Zhu T and Wang R (2023), SiO_2 nanosphere coated tough catheter with superhydrophobic surface for improving the antibacteria and hemocompatibility.
Front. Bioeng. Biotechnol. 10:1067139.
doi: 10.3389/fbioe.2022.1067139

SiO_2 nanosphere coated tough catheter with superhydrophobic surface for improving the antibacteria and hemocompatibility

Weixing Zhang[1], Juan Du[2], Tonghe Zhu[2] and Ruilan Wang[1]*

[1]Department of Critical Care Medicine, School of Medicine, Shanghai General Hospital, Shanghai Jiao Tong University, Shanghai, China, [2]School of Chemistry and Chemical Engineering, Shanghai Engineering Research Center of Pharmaceutical Intelligent Equipment, Shanghai Frontiers Science Research Center for Druggability of Cardiovascular Non-coding RNA, Institute for Frontier Medical Technology, Shanghai University of Engineering Science, Shanghai, China

Catheter infection is the most common complication after vascular catheter placement, which seriously threatens the survival of critically ill patients. Although catheters with antibacterial drug coatings have been used, catheter infections have not been effectively resolved. In this research, a SiO_2 nanosphere-coated PTFE catheter (PTFE-SiO_2) with enhanced antibacterial and excellent mechanical properties was prepared *via* dopamine as a graft bridge. The microscopic morphology results show that the nanospheres are uniformly dispersed on the surface of the catheter. The physicochemical characterization confirmed that PTFE-SiO_2 had reliable bending resistance properties, superhydrophobicity, and cytocompatibility and could inhibit thrombosis. Antibacterial results revealed that PTFE-SiO_2 could hinder the reproduction of *E. coli* and *S. aureus*. This research demonstrates the hydroxyl-rich materials obtained by hydroboration oxidation have the advantages of better dispersion of functional coatings, indicating their potential for helpful modification of catheters.

KEYWORDS

superhydrophobic, SiO_2 nanosphere, catheter, antibacterial, blood compatibility

1 Introduction

Long-term intravenous fluid rehydration, central venous pressure and arterial monitoring, hemodialysis, and ECMO are important treatment methods in the critical care department through the placement of central venous catheters, hemodialysis catheters, and radial artery catheters (Gilbert et al., 2013; Shimizu et al., 2020; Schalk et al., 2022). However, catheter-related infection is a common and severe complication after implantation, which often requires removal of the catheter, performing catheter end and blood culture to determine the source of infection and bacterial species (Ferreira et al., 2020; Brescia et al., 2021). Finally, antibiotics are administered, and the catheter is reinserted at another site. The infectious bacteria associated with the catheter is MASA. Due to the poor antibacterial effect of most antibiotics, the emergence of super bacteria has caused great harm to human health. This causes pain for the patient, increases the cost of treatment, and increases the risk of other complications (Akhrass et al., 2011; Jana et al., 2018).

Previous studies have shown that bacteria's rapid, nonspecific adhesion to the hydrophilic and lipophilic groups on the catheter surface is the initial cause of catheter infection (Liu et al.,

2017; Alvarenga et al., 2020; Li et al., 2020). The effect of bacterial adhesion depends on the microscopic topography and chemical properties of the catheter surface, as well as the characteristics of the bacteria (Monzillo et al., 2012; Liu et al., 2017; Yu et al., 2017; Faustino et al., 2020; Yu et al., 2021). How to reduce the colonization of bacteria in the catheter and avoid the formation of biofilm, thereby reducing the occurrence of catheter infection and the difficulty of treatment, has increasingly become a fundamental problem in clinical medicine, and more and more studies are constantly proposing new methods to solve this problem (Goncalves et al., 2014; Radu Mihu et al., 2017; Zhang et al., 2019; Gunaratnam et al., 2020). The current research on catheter-related infection globally mainly focuses on the antibacterial treatment after catheter infection. Once infected, high-grade antibiotics are required for treatment. In terms of prevention, the primary method is to coat the catheter with antibiotics. There are currently dialysis catheters that use coatings such as bismuth, which reduce bacterial colonization and thus film formation (Schindler et al., 2010; Balikci et al., 2021; Pant et al., 2022).

In addition to coating antibacterial drugs on catheters, finding the best material for antibacterial is also one of the directions we need to work on. Inspired by the origin of bacterial adhesion, we expect to develop a new type of coated vascular catheter that can effectively isolate bacterial adhesion factors. Therefore, we plan to design a novel anti-infective superhydrophobic nanocomposite-coated vascular catheter. The catheter coating and base material will not use antibacterial drugs, and the anti-infection purpose is mainly achieved by the superhydrophobicity of the surfaces of material.

2 Materials and methods

2.1 Materials

Commercial venous catheters were purchased from Arrow International, Inc. (Cleveland, United States). Both PTFE membranes (FP301350, with 0.25 mm thickness) and PTFE catheters (with 0.6 mm wall thickness and 1.0 mm inner diamater) were purchased from Goodfellow Tading Co., Ltd. (Shanghai, China). SiO_2 nanosphere powder (average particle size is 20 nm) were purchased from Suzhou Vmicronano New Materials Co., Ltd. (Suzhou, China). Benzoin (purity ≥ 99.5%), potassium tert-butoxide (purity ≥ 99.9%), and borane tetrahydrofuran (purity ≥ 99.99%) were purchased from Adamas Reagent Co., Ltd. (Shanghai, China). Dimethyl sulfoxide (DMSO), tetrahydrofuran (THF), anhydrous ethanol (EtOH, purity ≥ 99.99%) were obtained from Sinopharm Chemical Reagent Co., Ltd. (Shanghai, China). Other reagents and materials are not treated before use unless otherwise specified.

2.2 Surface modification of PTFE membrane and catheter

2.2.1 Preparation of PTFE-OH membrane and catheter

The circular PEFE membranes with a diameter of 14 mm and PTFE catheters with 0.6 mm thickness and 1.0 mm inner diamater (uniformly named PTFE) were ultrasonically cleaned in 75% medical alcohol for 30 min, and then freeze-dried in vacuum for subsequent experiments, respectively.

Firstly, 1.5 g of benzoin and 5.1 g of potassium tert-butoxide were dissolved in 10 and 50 ml of dimethyl sulfoxide, respectively. Then, the above two harvested solutions were mixed until present clear and homogeneous (Costello and McCarthy, 1984). Secondly, The cleaned PTFE was added to the mixed solution, and the reaction was continued for 36 h at 54°C in a constant temperature water bath. After the reaction was over, the modified PTFE were washed twice with tetrahydrofuran reagent, following washed with deionized water for 5 times. Finally, the modified PTFE were freeze-dried for 48 h, namely PTFE-M.

Finally, hydroxyl groups were introduced on the surface of PTFE according to the hydroboration oxidation reaction (Meng et al., 2015; Dan et al., 2020): PTFE-M was added to 10 ml borane tetrahydrofuran solution in three-necked flask. Then the three-necked flask was sealed, and the reaction was carried out at room temperature for 12 h. The borane tetrahydrofuran solution was then transferred out, and then 10 ml of deionized water, 10 ml of 3 mol/L NaOH solution and 10 ml of 30% H_2O_2 were added in sequence. Finally, place the three-necked flask into the prepared ice-water mixture and ice-bath for 3 h under a magnetic stirrer. After the reaction is completed, the modified PTFE is washed with dilute hydrochloric acid solution, alkene sodium hydroxide solution and deionized water in sequence. Finally, the hydroxylated PTFE were vacuumed in a desiccator for 48 h to remove redisual solvent and namely PTFE-OH.

2.2.2 Preparation of PTFE-SiO_2 membrane and catheter

First, 200 mg of dopamine and 2 g of nanospheres were added to a Tris (pH = 8.5) solution, which were prepared using 200 ml deionized water. Then PTFE-OH was added to the above solution which was mixed well and soaked for 4 h. Finally, the modified PTFE were washed thoroughly with deionized water, following freeze-dried in a vacuum freeze dryer for 48 h to remove redisual solvent and namely PTFE-SiO_2.

2.3 Characterization and tests of prepared membrane or catheter

The morphology and surface structure of modified PTFE were carried out using a scanning electron microscope (SEM, Phenom XL, Netherlands) operating with sputter gold plating for 35 s at 5 mA at an accelerating voltage of 10 kV. FTIR spectra of modified PTFE were analyzed on a Nicolet 6700 spectrometer (Thermo Fisher, United States) in the spectrum range of 500 and 4000 cm^{-1} with a resolution of 1 cm^{-1}, setting 30 scans for a single analysis. A contact angle measuring device (JC 2000D 2A, Shanghai Zhongchen Digital Technology Equipment Co., Ltd., China) was used to testing the wettability of modified PTFE. In this testing, 0.02 ml deionized water was added to the sample, and three groups of parallel samples were taken from each group of PTFE to test the water contact angle and calculate the average value.

High-precision mechanical property testing machine (HY-025CS, Shanghai Hengyu Instrument Co., Ltd., China) with a transducer with a load range of 0–1000 N was employed to testing the compressive performance of prepared catheter in dry conditions at room temperature. Catheter with a size of 2 mm inner diameter, 50 mm

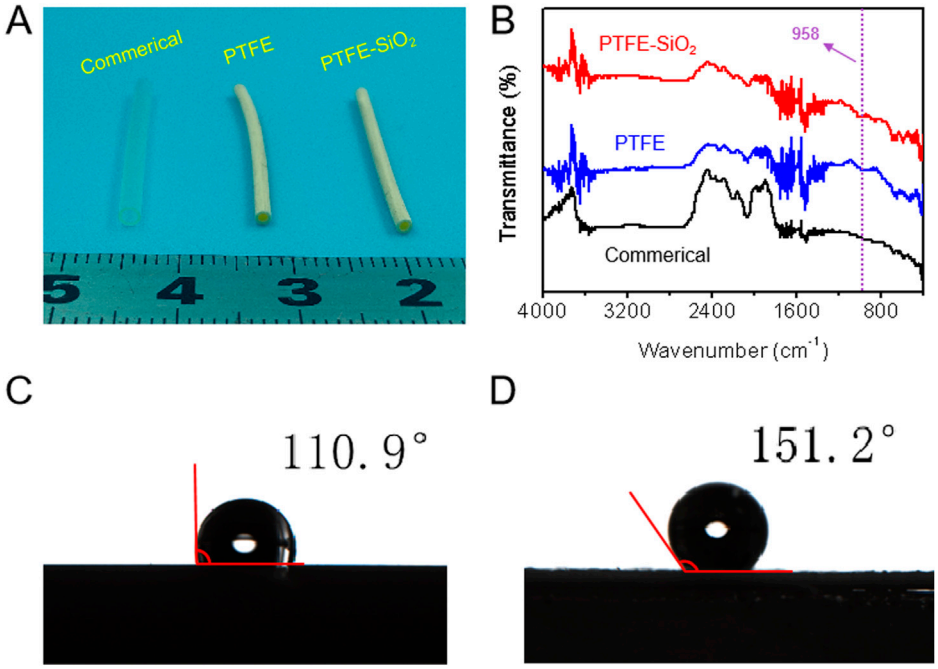

FIGURE 1
(A) The digital photos of commerical catheter, PTFE catheter, and PTFE-SiO_2 catheter, respectively; **(B)** FTIR spectra of commerical catheter, PTFE catheter, and PTFE-SiO_2 catheter, respectively; **(C)** and **(D)** Water contact angle of the lumen surface of the inner surfaces of PTFE catheter, and PTFE-SiO_2 catheter at the 5 s time point, respectively.

length, and approximately 0.5 mm in wall thickness were used for radial compression testing. The cyclic compression tests at 50% of the outer diameter of catheters were repeatedly performed 1000 times at a fixed rate of 0.2 mm/min. Each test was repeated five times during mechanical analysis.

2.4 Cell culture and cytocompatibility evaluation

Mice fibroblast cells (L929) were cultured with growth medium consisting of dulbecco's modified eagle medium (DMEM), 10% fetal bovine serum and 1% penicillin/streptomycin. Before cell seeding, the commercial membranes, PTFE, and PTFE-SiO_2 membranes were cut into discs with a diameter of 14 mm, then placed into 24-well plates one by one, following covered with sterilized stainless rings, respectively. Each sample was sterilized in 75% ethanol for 12 h and then washed with PBS three times, finally irradiated with ultraviolet for 2 h and socked in growth medium for incubation overnight. HUVECs were seeded at a density of 1.5×10^4 cells/well, and the culture medium was maintained to be replaced every 2 days.

The cell viability of L929 was tested by using the Cell Counting Kit-8 (CCK-8). The cells were cultured in commercial membranes, PTFE, and PTFE-SiO_2 membranes for 1 day, 3 days, and 5 days, respectively. When the set culture time point, the well plate was taken from the CO_2 incubator, and then a series of operations as removal medium, wash samples in well with PBS, adding 360 μL DMEM medium and 40 μL CCK-8 solution into the lucifugal well plate in sequence. After 1 h incubation in CO_2 incubator, The optical density (OD) value was measured with a microplate reader at a wavelength of 450 nm.

Before the cells SEM images test, the cultured L929 were fixed with 4% paraformaldehyde and dehydrated by gradient ethanol (30%, 50%, 70%, 80%, 90%, 95%, and 100%) on the 3rd day and the morphology carried out using a scanning electron microscope (SEM, Phenom XL, Netherlands) operating with sputter gold plating for 35 s at 5 mA at an accelerating voltage of 10 kV, respectively.

Additionally, the live cells (green) and dead cells (red) were stained with Calcein-AM/PI after 3 days' culture, respectively. The dyed samples were observed immediately under the TS100 fluorescence microscope (Nikon, Japan).

2.5 Blood compatibility test *in vitro*

Fresh blood, which was drawn from the marginal vein, and 3.2% sodium citrate solution in a volume ratio of 9:1 (v/v) were collected using a plastic vacuum blood collection tube (2.7 ml, Becton Dickinson, United States), containing 3.2% sodium citrate solution. All animal experimental protocols are in accordance with the policy of the Institutional Review Board for Human Investigations at School of Medicine of Shanghai Jiao Tong University. Detailed procedures are available in the Supplementary Material.

2.6 Testing of antibacterial activity *in vitro*

Staphylococcus aureus (*S. aureus*, BCRC 10451) and *Escherichia coli* (*E. coli*, BCRC 11634) were used to assess the antibacterial ability

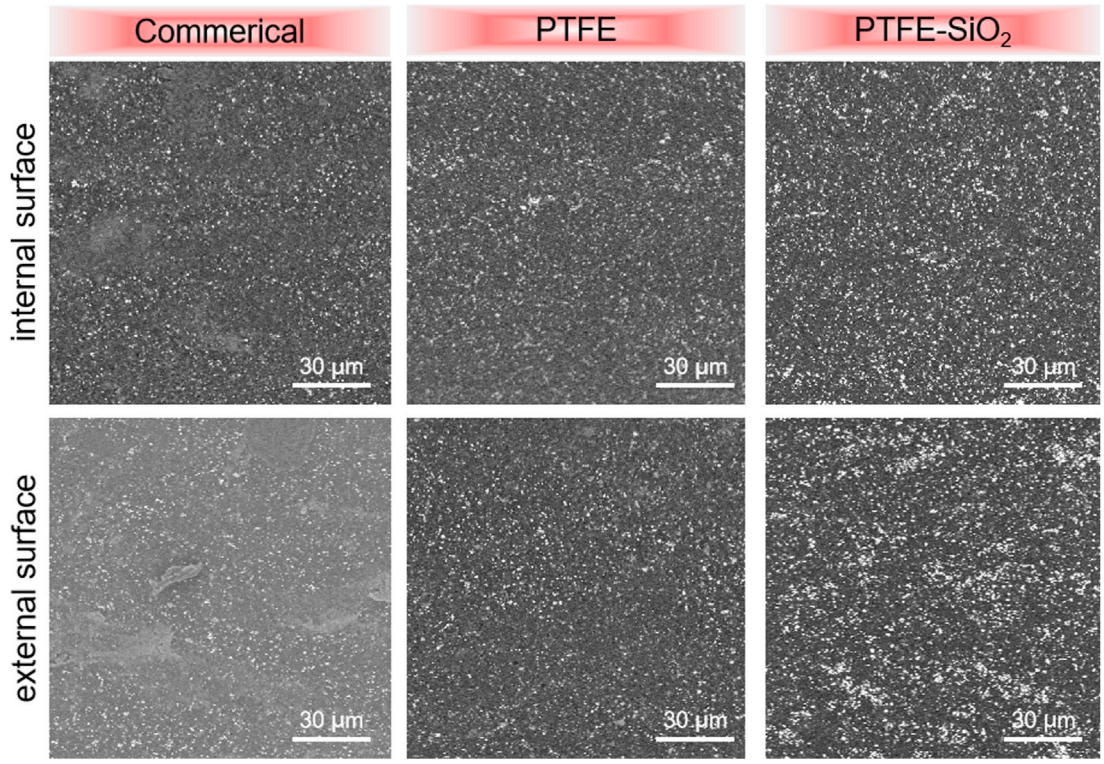

FIGURE 2
The suefaces SEM images of commerical catheter, PTFE catheter, and PTFE-SiO_2 catheter, respectively.

of commercial membranes, PTFE, and PTFE-SiO_2 membranes. Antibacterial activities were investigated by agar disc diffusion assay as described previously.

Firstly, commercial membranes, PTFE, and PTFE-SiO_2 membranes were pruned into rounded membranes with a diameter of 14 mm. Then, circular membranes were irradiated under an ultraviolet lamp for 12 h, following fumigated with ethanol overnight for thorough sterilization and stored in the bechtop for further testing or evaluation. For non-quantitative synthesis, the bacterial inhibition ring of the *E. coli* and *S. aureus* cultured on the LB agar plates was assessed. In short, *E. coli* and *S. aureus* infection fluid (200 μL) was the first diffusion into the agar plates and the experiment mats (commercial, PTFE, and PTFE-SiO_2 circular membranes) with a diameter of 14 mm and a thickness of about 300 μm were attached to the agar plate. After incubation at 37°C for 24 h, the bacterial inhibition ring of each specimen on the plate was visually measured. The inner and outer diameters and calculated diameter distinction were analyzed for evaluating the antimicrobial activity of prepared circular nanofibrous mats.

2.7 Biofilm experiment of catheter *in vitro*

First, all the catheter (commerical catheter, PTFE catheter, and PTFE-SiO_2 catheter) were cut into multiple segments with 5 mm length, following ultrasonic washed with distilled water and ethanol for 5 min, respectively. Then, all the samples were immersed into 200 μL of selected medium (BHI for VRE and TSB supplemented with 1% glucose for *S. aureus*) in a 96-well plate after vacuum freeze drying for 48 h. 1.0×10^6 CFU/ml bacteria suspension was made by diluting in 10 mM PBS with pH = 7.4 from overnight culture. 8 μL of the above prepared diluted bacteria suspension was added to each well, following the plate was incubated at 37°C for 24 h (Zhou et al., 2017). All the above samples were then removed and washed gently thrice with PBS to remove unattached bacteria. Then, all the samples were fixed with 4% paraformaldehyde and dehydrated by gradient ethanol (10%, 30%, 50%, 60%, 75%, 80%, 90%, and 100%) and the morphology carried out using a scanning electron microscope (SEM, Phenom XL, Netherlands) operating with sputter gold plating for 35 s at 5 mA at an accelerating voltage of 10 kV, respectively.

2.8 Statistical analysis

Origin 9.0 statistical software (Origin Lab Inc., United States), one-way ANOVA and Tukey's test were applied to statistical analysis of the data. All data are expressed as mean ± standard deviation (Mean ± SD). p-values < 0.05 (*) were deemed to be statistically significant. * indicates $p < 0.05$, ** indicates $p < 0.01$, *** indicates $p < 0.001$.

3 Results and discussion

3.1 Microstructure and surface phychemical properties of catheter

As a conduit material, PTFE has advantages in mechanical properties. However, PTFE is an inert material, which limits its

10.3389/fbioe.2022.1067139

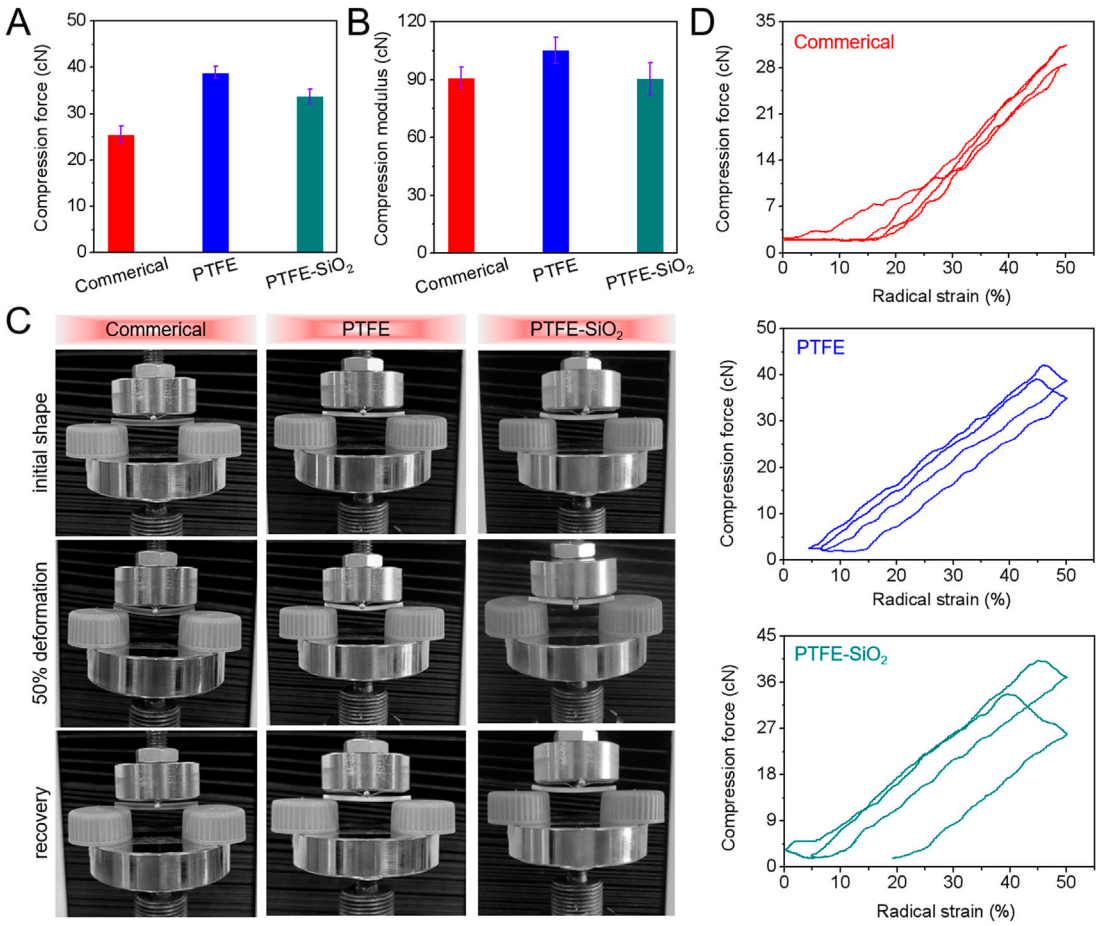

FIGURE 3
(A) Maximum compressive force and **(B)** compressive modulus after 1000 cycle compressive fatigue tests; **(C)** Images of three-point bending tests; **(D)** Typical the first and one thousandth loading-unloading compression cycle curves of commerical catheter, PTFE catheter, and PTFE-SiO_2 catheter.

application in medical catheters. In order to change the chemical inertness of the surface of PTFE catheter and improve the biocompatibility of PTFE, a very active unsaturated carbon chain layer was formed on the surface of PTFE by treating the mixed solution of benzoin and potassium tert butoxide. Then, a large number of hydroxyl groups were reactive grafted on the surface of PTFE membrane by borohydride oxidation reaction, following grafted SiO_2 nanosphere on the surface of PTFE matrix through dopamine bridging, which presented strong adhesion between the hydroxyl groups of polydopamine and the SiO_2 nanosphere surface. Macroscopically, the catheter could maintain its tubular shape after being treatment with organic solution (Figure 1A). We obtained catheters with a length of 25 mm and an inner diameter of 1.5 mm (Figure 1A). The presence of as coated SiO_2 nanosphere was verified *via* FTIR spectra, by which we demonstrated that PTFE-SiO_2 catheter received more characteristic peak of stretching vibration of Si-O bond at 958 cm^{-1} after coating (Figure 1B).

With the increasing attention of superhydrophobic surfaces, the reduction of bacterial adhesion by superhydrophobic surfaces has also been considered as an effective antibacterial method (Ozkan et al., 2021; Li et al., 2022). The superhydrophobic surface interface of PTFE catheter play an important role in the adsorption and the adhesion of bacteria. As shown in Figures 1C, D, the water contact angle values of the lumen surface of the inner surfaces of PTFE catheter and PTFE-SiO_2 catheter were 110.9° ± 1.8° and 151.2° ± 1.5° at 5 s, respectively. The SiO_2 nanosphere-coated PTFE catheter exhibits stronger hydrophobicity. The antibacterial mechanism of superhydrophobic surfaces is that bacteria are more likely to adhere to surfaces with high surface energy, while superhydrophobic surfaces have lower surface energy, which is not conducive to the adhesion of bacteria (Boinovich et al., 2018; Huang et al., 2018; Zhan et al., 2021). Moreover, the air layer trapped by the micro-nanostructure will isolate the bacteria from the SiO_2 coating. When the superhydrophobic catheter is in contact with bacteria, the contact area between the coating and the colony will reducing due to the effect of the air layer, which can avoid the formation of biofilm on the surface of the catheter, and finally achieve the effect of bacteriostasis.

The dispersion of the SiO_2 coating is also one of the main factors affecting the antibacterial effect of the catheter surface. The scanning electron microscope images in Figure 2 showed that the coating consists of many micro- and nano-scale protrusions and pits. These micro-nano structures are mainly formed by the accumulation of nano-SiO_2 particles. The nano-SiO_2 is tightly fixed

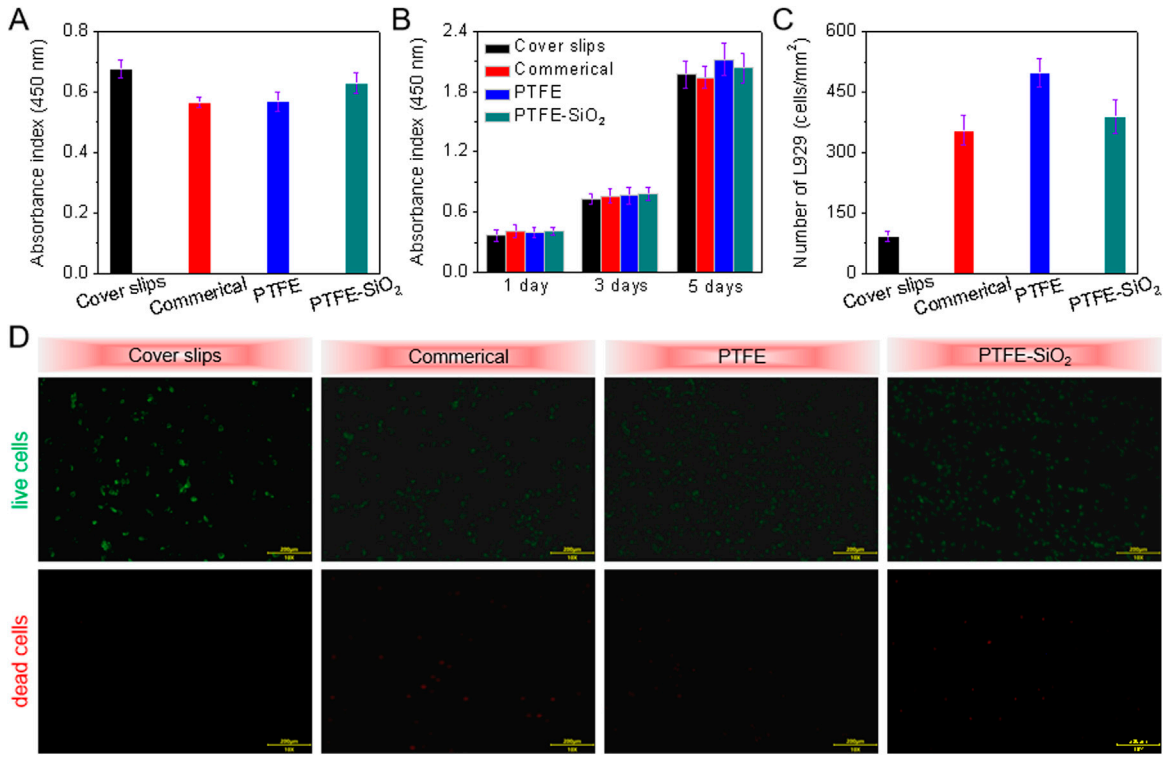

FIGURE 4
CCK-8 assay of **(A)** the adhesion viability after 24 h culture and **(B)** proliferation viability after 1, 3, and 5 days culture of HUVECs onto cover slips, commerical catheter, PTFE catheter, and PTFE-SiO_2 catheter, respectively; **(C)** Quantitative number measurements of L929 cells on the inner surfaces of cover slips, commerical catheter, PTFE catheter, and PTFE-SiO_2 catheter after culturing for 3 days; **(D)** Live/dead staining viability assay of L929 cells cultured on the inner surfaces of cover slips, commerical catheter, PTFE catheter, and PTFE-SiO_2 catheter after culturing for 3 days.

on the surface of the PTFE substrate by the dopamine matrix, which improves the mechanical stability of the surface of the superhydrophobic coating. Comparing the commerical group and the PTFE group, it is not difficult to find that the immobilized SiO_2 using dopamine after hydroxylation treatment not only shows a higher graft density, but also disperses more uniformly on the PTFE surface.

3.2 Mechanical properties

In order to clarify whether the original mechanical properties of PTFE catheters were changed after the grafting of SiO_2 nanospheres, mechanical properties experiments were carried out. The results of radial cyclic compression at 50% of the outer diameter of catheters after 1000 cycle compressive fatigue tests are shown in Figure 3. As shown in Figures 3A,B, the compressive and compressive modulus after 1000 cycle compressive fatigue tests of PTFE-SiO_2 catheter were significantly lower than those of PTFE group, but consistently superior to the commerical group. According to the standard guidelines of three-point bending test of ASTM F2606-09 as present in Figures 3C, D, all the samples were bendable and returned to their original shape without any visible damage and permanent deformation. Therefore, the modified catheter still maintains reliable bending resistance, which will be sufficient to support the catheter against any possible external force during surgical operation.

3.3 Cytocompatibility and hemocompatibility *in vitro*

To test the biocompatibility of the samples before and after modification, the same amount of L929 was inoculated on each sample. As shown in Figures 4A,B, the adhesion ability of the PTFE-SiO_2 group to L929 was higher than that of the commercial group and the PTFE group but still lower than that of the cover slips group. Figures 4C,D show that by day 3, the number of viable cells in the cover slips group and the commerical group was less than that in the other two groups. The PTFE-SiO_2 group had the smallest viable cells, mainly due to the hydrophobic surface and chemical inertness caused by the fluorocarbon structure. The SiO_2 nanocluster structure is unsuitable for cell adhesion and proliferation.

After vascular puncture, the catheter stays in the body for a long time, which can easily lead to nonspecific protein adsorption, microbial infection, and blood coagulation (Hitz et al., 2012; Erathodiyil et al., 2020). These phenomena eventually lead to deep vein thrombosis (PICC-DVT), pulmonary embolism (PE) due to thrombus shedding, and catheter-related bloodstream infections (CRBSIs) due to microbial infections. Currently, drugs such as heparin and antibiotics are injected into patients to reduce catheter-related complications. However, neither heparin nor antibiotics maintain long-term efficacy in the body. Repeated injections of chemicals will not only reduce the patient's immunity and cause suffering from drug side effects. Therefore, optimizing and modifying existing materials is an effective measure to reduce

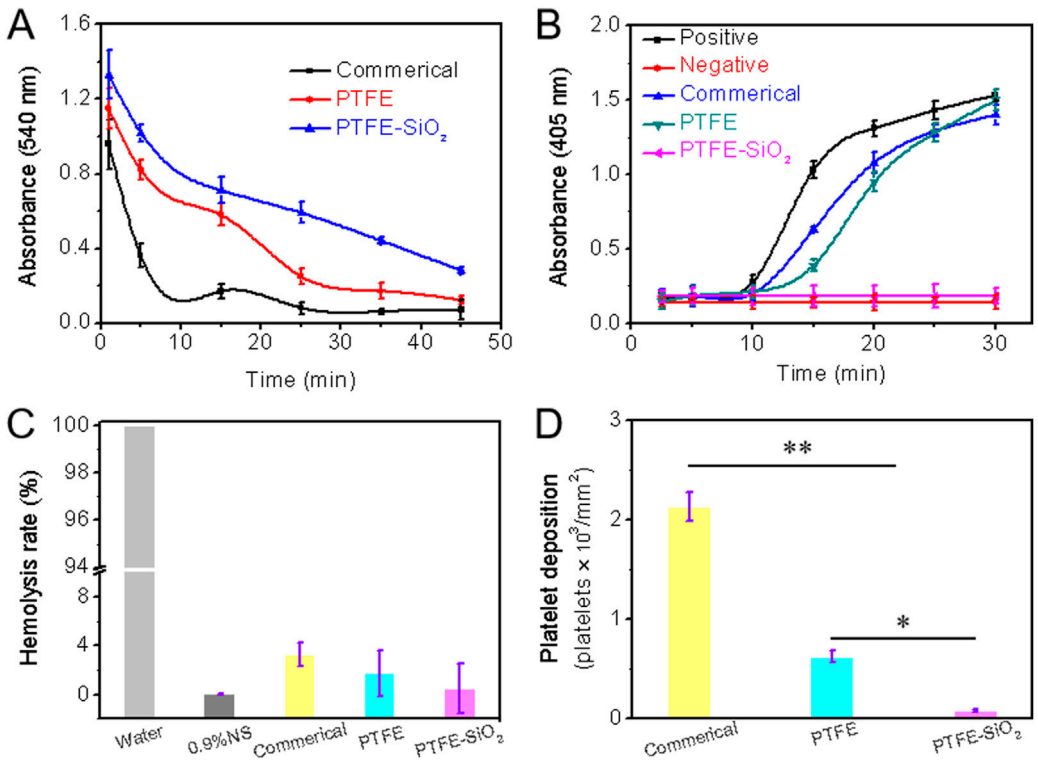

FIGURE 5
(A) Whole blood clotting time **(B)** Plasma recalcification time; **(C)** Quantification of relative hemolysis rate; **(D)** Platelet deposition determined by lactate dehydrogenase assay. (For plasma recalcification time test, TCPs exposed to PPP with and without $CaCl_2$ were used as positive control and negative control, respectively; For hemolysis test, water and 0.9% normal saline (NS) serve as positive and negative groups, respectively; *n = 5, *p < 0.05, **p < 0.01*).

catheter-related complications and improve the anticoagulant and antibacterial properties of catheters.

The anticoagulant property of all samples could be evaluated directly by whole blood clotting time, plasma recalcification time, quantification of relative hemolysis rate, and quantification of lactate dehydrogenase activity. We assessed the whole blood clotting of catheter by the whole blood clotting time test. After the whole blood incubation, the absorbance of the supernatant was measured at 540 nm, as shown in Figure 5A. Compared with the other two groups, the PTFE catheter coated with SiO_2 nanospheres had the maximum absorbance at any time point. The higher the absorbance, the higher the hemoglobin content in the supernatant, which means that there are more blood cells in the free state, less blood cells that produce coagulation, and the slower the coagulation speed. All in all, under the same experimental conditions, the clotting time of the control group was significantly shorter, indicating that the coated-modified PTFE catheter has highly hydrophobic properties and can resist the adhesion of proteins to the material surface. Therefore, PTFE-SiO_2 catheter can reduce the adhesion of blood cells and has outstanding anticoagulant properties.

As we all know, the essence of blood coagulation is the process of fibrinogen in plasma from soluble to insoluble, and blood coagulation is divided into two types: intrinsic coagulation and extrinsic coagulation. All coagulation factors involved in intrinsic coagulation are provided by plasma. When the plasma comes into contact with the material, the electrical charge on the surface activates the coagulation factors in the plasma. The plasma recalcification curve is a method used to characterize the endogenous coagulation system. The recalcification time is the time it takes for the plasma to coagulate after removing the calcium source and then adding Ca^{2+}. The kinetics of plasma recalcification can be seen in Figure 5B for the three water conduits, the positive control group and the negative control group. The positive control has the fastest clot formation time at 15 min, while the clot formation time of the commerical and PTFE group were 20 and 24 min, respectively. Notably, the PTFE-SiO_2 group consistently kept a low absorbance and closed to the negative control without emerging the inflection point. The above results indicate that the PTFE-SiO_2 group has a superhydrophobic surface interface effect, so the activation of endogenous coagulation is less, and the anticoagulation performance of the catheter is improved.

The hemolysis rate of a material refers to the degree to which hemoglobin is lysed by erythrocytes after the material is in contact with erythrocytes. According to international standards, the hemolysis rate of biological materials should be less than 5% (Zhu et al., 2021). Figure 5C is the hemolysis rate of PTFE catheters before and after coating. As shown in the figure, the hemolysis rate of the uncoated PTFE catheter was 1.756%, while after the SiO_2 nanosphere coating, the anti-hemolysis ability was significantly reduced. In conclusion, PTFE-SiO_2 had the best blood compatibility among all samples, and the hemolysis rate was only 0.521%, which was almost close to that of the negative control group.

10.3389/fbioe.2022.1067139

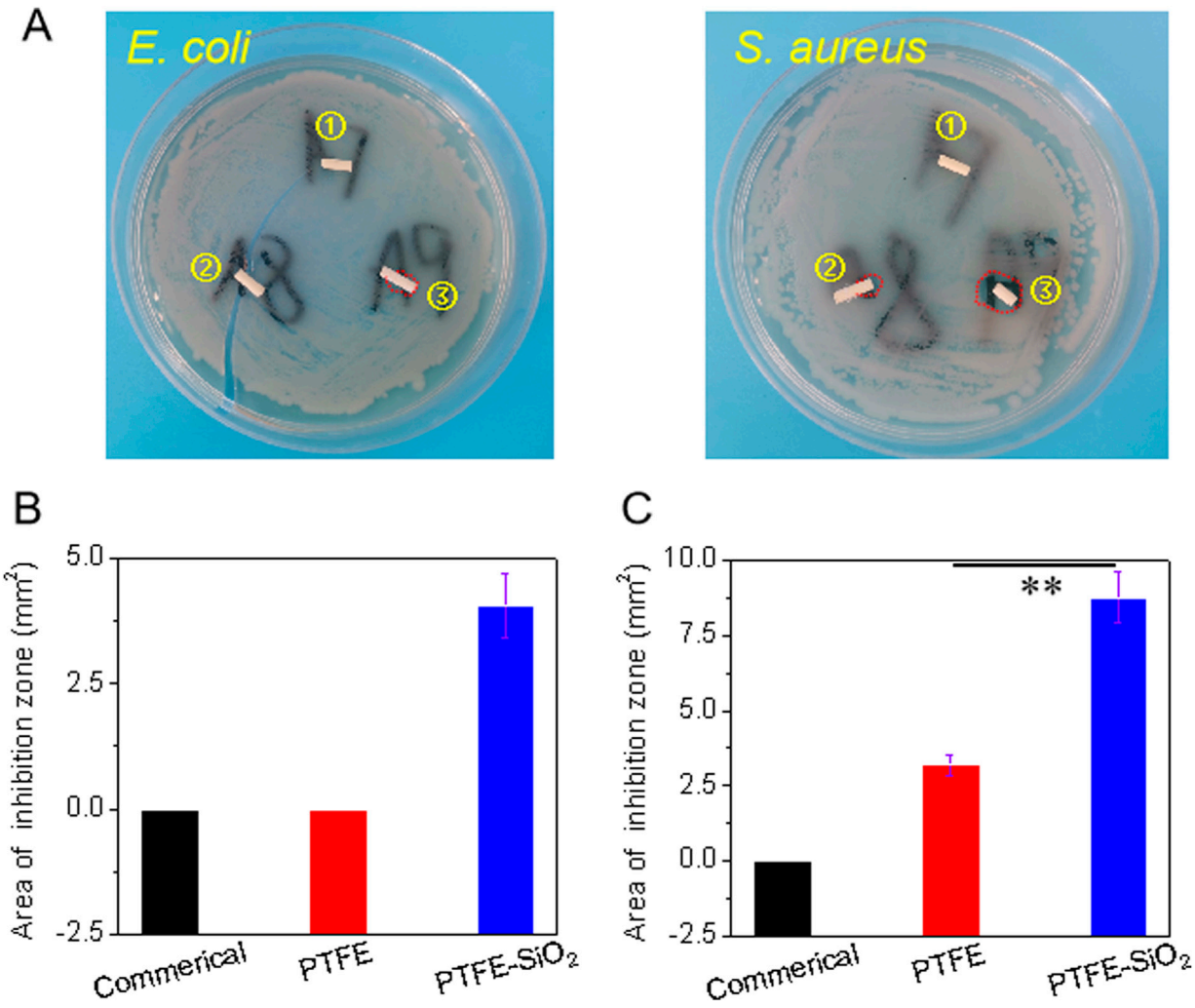

FIGURE 6
(A) Visual images of the antibacterial zone of catheter to *Escherichia coli* (*E. coli*) and *Staphylococcus aureus* (*S. aureus*) after incubation for 6 h. Spot ①, ②, and ③ represents commerical catheter, PTFE catheter, and PTFE-SiO_2 catheter, respectively; of commerical catheter, PTFE catheter, and PTFE-SiO_2 catheter, respectively; **(B)** and **(C)** Quantified antibacterial zone of commerical catheter, PTFE catheter, and PTFE-SiO_2 catheter after 6 h incubation with *E. coli* and *S. aureus*, respectively. (*n = 5, **p < 0.01*)

The lactate dehydrogenase (LDH) activity of platelet adhesion on the inner surface of catheter after 2 h incubation with rabbit platelet-rich plasma are shown in Figure 5D. The deposition of adhered platelets on the inner surface of PTFE-SiO_2 catheter was 85 platelets/mm^2, which was significantly reduced to 622 platelets/mm^2 for the PTFE catheter and to 2136 platelets/mm^2 for the commerical catheter. SiO_2 nanosphere coated-modified PTFE catheter adsorbed fewer platelets compared with the PTFE catheter, indicating that coated SiO_2 nanosphere not only significantly reduced platelet deposition but also efficiently suppressed the activation and transmutation of platelets.

3.4 Antibacterial effect *in vitro*

After the catheter enters the blood vessel, some nonspecific proteins (polyglycan matrix, *etc.*) will form a thin film on the surface of the catheter. Bacteria will then stick to the film and increase, following a biofilm formed. Because the resulting biofilm is not recognized by tissues and the bacteria are not killed by the immune system, it can eventually lead to bacterial infections. The superhydrophobic surface is an effective method to limit the formation of biofilm, which can inhibit the adhesion of bacteria to the material surface.

The bactericidal effect on Gram-negative bacteria (*Escherichia coli*, *E. coli*) and Gram-positive bacteria (*Staphylococcus aureus*, *S. aureus*) was evaluated to determine whether the superhydrophobic SiO_2 nanosphere coating had a pronounced antibacterial effect. As shown in Figure 6, after co-culture of PTFE-SiO_2 catheters on the solid medium of two bacteria, bacteriostatic circles appeared, and the areas of bacteriostatic processes were 4.05 and 8.75 mm^2, respectively. Compared the antibacterial effects of the three groups of samples, it can be found that the commercial group samples did not show evident antibacterial rings after co-culture on the two kinds of colony media, and the PTFE catheter only showed small antibacterial

10.3389/fbioe.2022.1067139

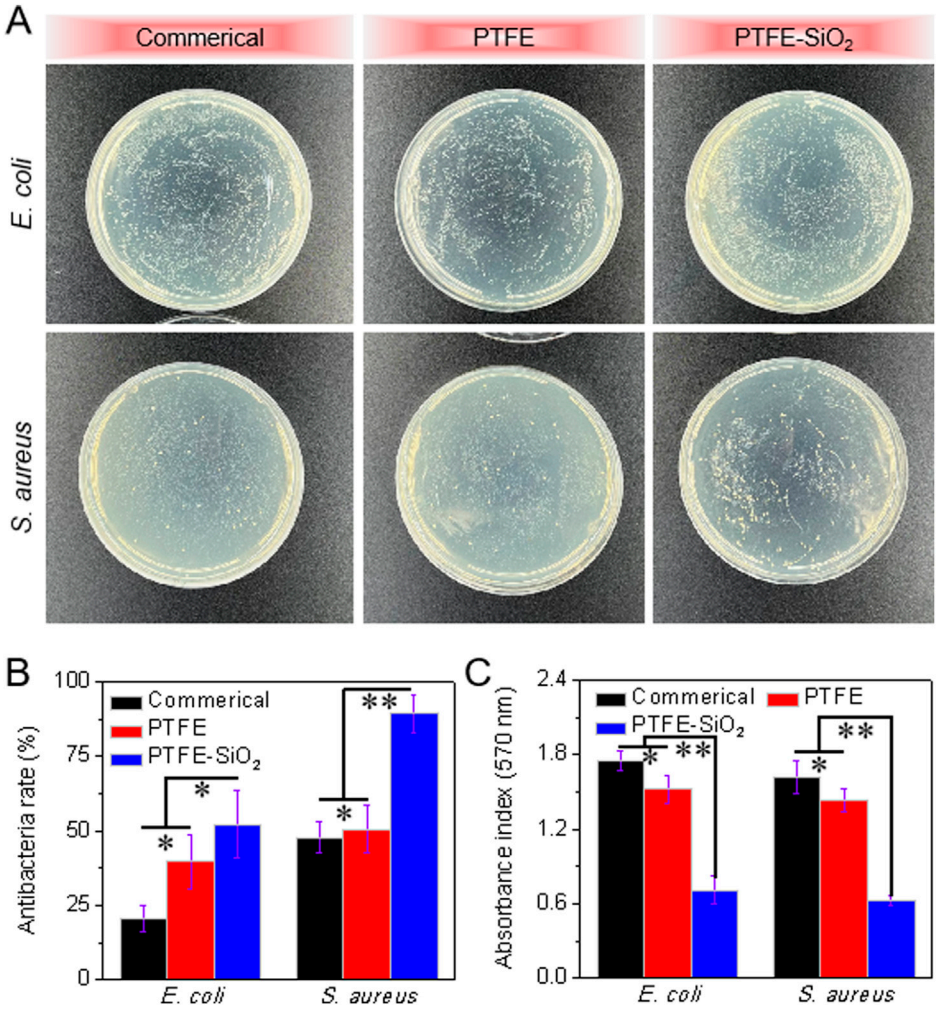

FIGURE 7
Quantitative analysis of the antibacterial properties of catheter: **(A)** Conoly-counting assay of catheter against *E. coli* and *S. aureus*; **(B)** Antibacterial rate of catheter after 6 h incubation with *E. coli* and *S. aureus* (quantitative analysis of colony statistics); **(C)** Quantitative analysis of photometric method after 6 h incubation with *E. coli* and *S. aureus*. (*n* = 5, *$p < 0.05$, **$p < 0.01$)

rings on the surface of the medium with *S. aureus*. These results indicate that the superhydrophobic conduit coated with SiO_2 nanospheres has specific antibacterial properties.

We also compared the bacteriostatic rate of the three groups of samples by colony statistical test. As shown in Figure 7A, *E. coli* and *S. aureus* were cultured for 6 h, respectively. Then, a certain amount of bacterial liquid was drawed and placed in a sterile centrifuge. After adding the three samples to the corresponding centrifuge tubes, the centrifuge tubes were placed in a constant temperature shaker for co-cultivation for a certain period of time, and the bacterial solution was diluted 10,000 times. Then take 10 μL of the diluted bacterial culture solution, spread it evenly on the surface of the petri dish containing the solid medium in one direction, place it in a constant temperature shaker for 6 h, and count the number of colonies. After superhydrophobic modification using SiO_2 nanospheres, the antibacterial rate of the catheter against *E. coli* was enhanced from 39.7% to 52.1%, and the antibacterial rate against *S. aureus* was increased from 50.5% to 89.3% (as shown in Figure 7B). It shows that the coating using SiO_2 nanospheres enhances the antibacterial activity of the PTFE catheter, which may due to the superhydrophobic coating of SiO_2 nanospheres not being conducive to the formation of the bacterial film.

To illustrate that the modified PTFE catheter has prominent antibacterial properties, the antibacterial properties were quantitatively analyzed by photometry. As shown in Figure 7C, after co-culturing the catheter with the bacterial solution for 6 h, the absorbance of the commerical group and the PTFE group was significantly higher than that of the PTFE-SiO_2 group, regardless of whether it was *E. coli* and *S. aureus*. It shows that the catheter of the commercial group does not have antibacterial properties, which is consistent with the inhibition zone and colony statistics results. In conclusion, the antibacterial ability of the PTFE catheter was significantly improved after the layer modification.

Surface functionalization is an effective strategy to improve the application potential of medical catheters. Proper surface wettability is the key to improve the antibacterial ability of the catheter (Chauhan et al., 2014). The mechanism of antibacterial activity of SiO_2 nanosphere coated tough catheter against *S. aureus* was examined by SEM images. As in Figure 8, SEM images showed large numbers of

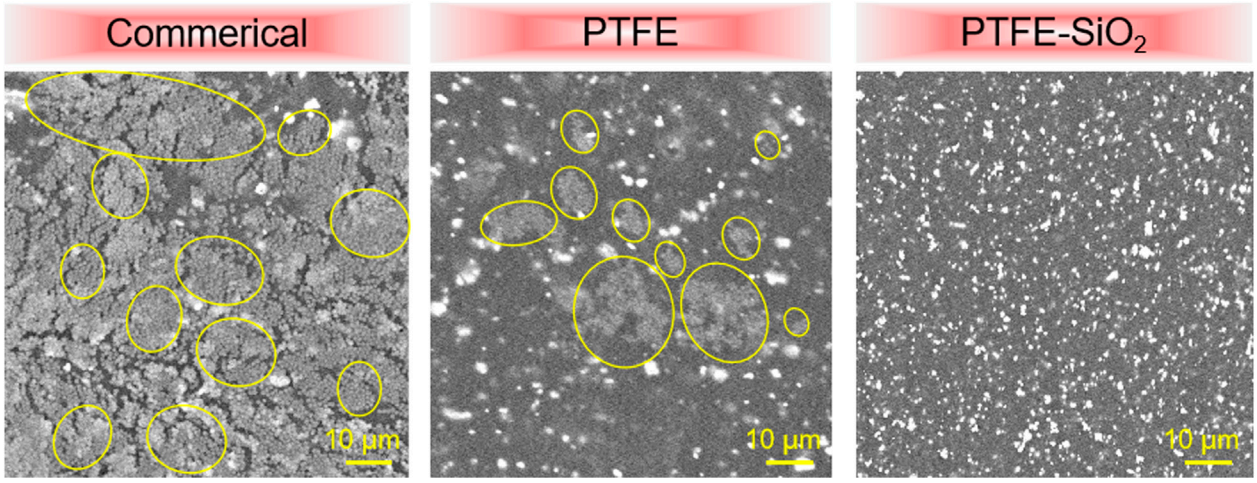

FIGURE 8
SEM images of *S. aureus* on the surfaces of commerical catheter, PTFE catheter, and PTFE-SiO_2 catheter, respectively. (Yellow solid represent bacteria in biofilm).

S. aureus on the suefaces of commerical catheter. On the surface of PTFE catheter, SEM images show the number of viable *S. aureus* to be greatly reduced, confirming the anti-*S. aureus* nature of the surface of electronegativity of PTFE. It is worth noting that although PTFE-SiO_2 catheter has a large contact angle, it also prevents the formation of *S. aureus* biofilm, possibly because of the large surface anionic charge of SiO_2, which were uniformly distributed on the PTFE surface.

4 Conclusion

In the present study, we developed a SiO_2 nanosphere-coated PTFE catheter (PTFE-SiO_2) based on hydroxyl-rich materials obtained by hydroboration oxidation. SEM, FTIR, water contact angle, mechanical tests, cell and blood compatibility test *in vitro* were used to analyze the chemical structure, microstructure, surface wettability, cytocompatibility, and hemocompatibility of PTFE-SiO_2 catheter. The results show that the SiO_2 nanospheres can be uniformly dispersed on the surface of the PTFE catheter, and the coating will not significantly change the bending resistance of the catheter. Moreover, the catheter demonstrated a safe hemolysis rate of less than 5% while also not causing coagulation. Finally, antibacterial experiments showed that PTFE-SiO_2 catheter was the group with the highest antibacterial rate among the three groups. In conclusion, the SiO_2 nanospheres-coated PTFE catheter with regular morphology and high bending resistance property has a potential application prospect in anticoagulant and anti-infective catheters.

Data availability statement

The original contributions presented in the study are included in the article/Supplementary Material, further inquiries can be directed to the corresponding author.

Author contributions

WZ was responsible for the design of the experimental scheme and the writing of the paper; JD was responsible for the processing of experimental data; TZ was responsible for the revision of the paper; RW was responsible for the data review and revision of the paper.

Acknowledgments

The authors sincerely appreciate projects sponsored by Technology Support Project of Science and Technology Commission of Shanghai Municipality (19441906700).

Conflict of interest

The authors declare that the research was conducted in the absence of any commercial or financial relationships that could be construed as a potential conflict of interest.

Publisher's note

All claims expressed in this article are solely those of the authors and do not necessarily represent those of their affiliated organizations, or those of the publisher, the editors and the reviewers. Any product that may be evaluated in this article, or claim that may be made by its manufacturer, is not guaranteed or endorsed by the publisher.

Supplementary material

The Supplementary Material for this article can be found online at: https://www.frontiersin.org/articles/10.3389/fbioe.2022.1067139/full#supplementary-material

References

Alvarenga, Dalila Junqueira, Matias, Laira Maria Faria, Oliveira, Lucas Martins, Leao, Luiz Paulo Melchior de Oliveira, Hawkes, Jamie Anthony, Raimundo, Breno Vilas Boas, et al. (2020). Exploring how structural changes to new Licarin A derivatives effects their bioactive properties against rapid growing mycobacteria and biofilm formation. *Microb. Pathog.* 144, 104203. doi:10.1016/j.micpath.2020.104203

Akhrass, Fadi Al, Ray, Hachem, Mohamed, Jamal A., Tarrand, Jeffrey, Kontoyiannis, Dimitrios P., Chandra, Jyotsna, et al. (2011). Central venous catheter–associated*Nocardia*Bacteremia in cancer patients. *Emerg. Infect. Dis.* 17 (9), 1651–1658. doi:10.3201/eid1709.101810

Balikci, Elif, Yilmaz, Bengi, Tahmasebifar, Aydin, Turker Baran, Erkan, and Kara, Ekrem (2021). Surface modification strategies for hemodialysis catheters to preventcatheter–relatedinfections: A review. *J. Biomed. Mater. Res. Part B-Applied Biomaterials* 109 (3), 314–327. doi:10.1002/jbm.b.34701

Boinovich, Ludmila B., Modin, Evgeny B., Aleshkin, Andrey V., Emelyanenko, Kirill A., Zulkarneev, Eldar R., Kiseleva, Irina A., et al. (2018). Effective antibacterial nanotextured surfaces based on extreme wettability and bacteriophage seeding. *ACS Appl. Nano Mater.* 1 (3), 1348–1359. doi:10.1021/acsanm.8b00090

Brescia, Fabrizio, Pittiruti, Mauro, Scoppettuolo, Giancarlo, Zanier, Chiara, Nadalini, Elisa, Bottos, Paola, et al. (2021). Taurolidine lock in the treatment of colonization and infection of totally implanted venous access devices in cancer patients [J]. *J. Vasc. Access* 00 (0), 1–5.

Chauhan, Ashwini, Bernardin, Aude, Mussard, Windy, Kriegel, Irene, Esteve, Marc, Ghigo, Jean-Marc, et al. (2014). Preventing biofilm formation and associated occlusion by biomimetic glycocalyxlike polymer in central venous catheters. *J. Infect. Dis.* 210 (9), 1347–1356. doi:10.1093/infdis/jiu249

Costello, C. A., and McCarthy, T. J. (1984). Surface modification of poly(tetrafluoroethylene) with benzoin dianion. *Macromolecules* 17 (12), 2940–2942. doi:10.1021/ma00142a094

Dan, Yoav, Buzhor, Marina, Raichman, Daniel, Menashe, Eti, Rachmani, Oren, and Amir, Elizabeth (2020). Covalent surface functionalization of nonwoven fabrics with controlled hydrophobicity, water absorption, and pH regulation properties. *J. Appl. Polym. Sci.* 138 (6), e49820. doi:10.1002/app.49820

Erathodiyil, Nandanan, Chan, Hsi-Min, Wu, Hong, and JackieYing, Y. (2020). Zwitterionic polymers and hydrogels for antibiofouling applications in implantable devices. *Mater. Today* 38, 84–98. doi:10.1016/j.mattod.2020.03.024

Faustino, Celia M. C., Lemos, Sara M. C., Monge, Nuno, and IsabelRibeiro, A. C. (2020). A scope at antifouling strategies to prevent catheter-associated infections. *Adv. Colloid Interface Sci.* 284, 102230. doi:10.1016/j.cis.2020.102230

Ferreira, Janita, Camargos Moreira, Paulo Augusto, Rosado, Viviane, HenriqueMourao, PauloOrlandi, and Maia de Castro Romanelli, Roberta (2020). Risk factors for central venous catheter-related bloodstream infection in neonates. *Am. J. Infect. Control* 48 (9), 1102–1103. doi:10.1016/j.ajic.2019.12.004

Gilbert, Ruth, Harron, Katie, Mok, Quen, and Gamble, Carrol (2013). Impregnated central venous catheters should be readily used to reduce risk of bloodstream infection. *Br. Med. J.* 347, f7169. doi:10.1136/bmj.f7169

Goncalves, Idalina, Matama, Teresa, Cavaco-Paulo, Artur, and Silva, Carla (2014). Laccase coating of catheters with poly(catechin) for biofilm reduction. *Biocatal. Biotransformation* 32 (1), 2–12. doi:10.3109/10242422.2013.828711

Gunaratnam, Gubesh, Spengler, Christian, Trautmann, Simone, Jung, Philipp, Mischo, Johannes, Wieland, Ben, et al. (2020). Human blood plasma factors affect the adhesion kinetics of *Staphylococcus aureus* to central venous catheters. *Sci. Rep.* 10 (1), 20992. doi:10.1038/s41598-020-77168-x

Hitz, Felicitas, Klingbiel, Dirk, Omlin, Aurelius, Riniker, Salome, Zerz, Andreas, and Cerny, Thomas (2012). Athrombogenic coating of long-term venous catheter for cancer patients: A prospective, randomised, double-blind trial. *Ann. Hematol.* 91 (4), 613–620. doi:10.1007/s00277-011-1343-8

Huang, Xu, Wang, Deren, Hu, Leyong, Song, Juanjuan, and Chen, Yiqing (2018). Preparation of a novel antibacterial coating precursor and its antibacterial mechanism. *Appl. Surf. Sci.* 465, 478–485. doi:10.1016/j.apsusc.2018.09.160

Jana, Basas, Palau, Marta, Ratia, Carlos, Josedel Pozo, L., Martin-Gomez, Maria Teresa, Gomis, Xavier, et al. (2018). High-dose daptomycin is effective as an antibiotic lock therapy in a rabbit model of staphylococcus epidermidis catheter-related infection [J]. *Antimicrob. Agents Chemother.* 62 (2), 017777. doi:10.1128/AAC.01777-17

Li, Linhua, Yang, Li, Liao, Yanbiao, Yu, Hongchi, Liang, Zhen, Zhang, Bo, et al. (2020). Superhydrophilic versus normal polydopamine coating: A superior and robust platform for synergistic antibacterial and antithrombotic properties. *Chem. Eng. J.* 402, 126196. doi:10.1016/j.cej.2020.126196

Li, Mingyu, Liu, Kunpeng, Liu, Wenqi, Chen, Nuoya, Wang, Yanan, Zhang, Fanjun, et al. (2022). A universal anti-thrombotic and antibacterial coating: A chemical approach directed by fenton reaction and silane coupling. *Appl. Surf. Sci.* 600, 154143. doi:10.1016/j.apsusc.2022.154143

Liu, Qiaohong, Singha, Priyadarshini, Handa, Hitesh, and Locklin, Jason (2017). Covalent grafting of antifouling phosphorylcholine-based copolymers with antimicrobial nitric oxide releasing polymers to enhance infection-resistant properties of medical device coatings. *Langmuir* 33 (45), 13105–13113. doi:10.1021/acs.langmuir.7b02970

Meng, Xiangtao, York, Emily A., Liu, Shu, and KevinEdgar, J. (2015). Hydroboration–oxidation: A chemoselective route to cellulose ω-hydroxyalkanoate esters. *Carbohydr. Polym.* 133, 262–269. doi:10.1016/j.carbpol.2015.06.080

Monzillo, Vincenzina, Corona, Silvia, Lanzarini, Paolo, Dalla Valle, Claudia, and Marone, Piero (2012). Chlorhexidine-silver sulfadiazine-impregnated central venous catheters: *In vitro* antibacterial activity and impact on bacterial adhesion. *New Microbiol.* 35 (2), 175–182.

Ozkan, Ekrem, Mondal, Arnab, Douglass, Megan, Hopkins, Sean P., Garren, Mark, Ryan, Devine, et al. (2021). Bioinspired ultra-low fouling coatings on medical devices to prevent device-associated infections and thrombosis. *J. Colloid Interface Sci.* 608, 1015–1024. doi:10.1016/j.jcis.2021.09.183

Pant, Bishnu D., Benin, Bogdan M., Abeydeera, Nalin, Kim, Min-Ho, and SongpingHuang, D. (2022). Bi_2O_3 nanoparticles exhibit potent broad-spectrum antimicrobial activity and the ability to overcome Ag-ciprofloxacin- and meropenem-resistance in *P. aeruginosa*: The next silver bullet of metal antimicrobials? [J]. *Biomaterials Sci.* 10 (6), 1523–1531. doi:10.1039/d1bm01844b

Radu Mihu, Mircea, Cabral, Vitor, Pattabhi, Rodney, Tar, Moses T., Davies, Kelvin P., Friedman, Adam J., et al. (2017). Sustained nitric oxide-releasing nanoparticles interfere with methicillin-resistant *Staphylococcus aureus* adhesion and biofilm formation in a rat central venous catheter model. *Antimicrob. Agents Chemother.* 61 (1), 020200. doi:10.1128/AAC.02020-16

Schalk, Enrico, Schmitt, Timo, Panse, Jens, Fiegle, Eva, Naendrup, Jan-Hendrik, Schmidt-Hieber, Martin, et al. (2022). Central venous catheter-related bloodstream infections in patients with haematological malignancies during the SARS-CoV-2 pandemic. *Br. J. Haematol.* 199 (4), e16–e20. doi:10.1111/bjh.18442

Schindler, Ralf, Heemann, Uwe, Haug, Ulrike, Stoelck, Benjamin, Karatas, Aysun, Pohle, Cosima, et al. (2010). Bismuth coating of non-tunneled haemodialysis catheters reduces bacterial colonization: A randomized controlled trial. *Nephrol. Dial. Transplant.* 25 (8), 2651–2656. doi:10.1093/ndt/gfq052

Shimizu, Yoshiyuki, Hatachi, Takeshi, Takeshita, Jun, Yu, Inata, Kyogoku, Miyako, Aoki, Yoshihiro, et al. (2020). Occurrence and risk factors for unplanned catheter removal in a PICU: Central venous catheters versus peripherally inserted central venous catheters. *Pediatr. Crit. Care Med.* 21 (9), E635–E642. doi:10.1097/pcc.0000000000002426

Yu, Kai, Amal, Alzahrani, Khoddami, Sara, Ferreira, Demian, Kymora Scotland Cheng Yazdani, B. John T. J. Hossein, Ahmadabadi, Yan, et al. (2021). Self-limiting mussel inspired thin antifouling coating with broad-spectrum resistance to biofilm formation to prevent catheter-associated infection in mouse and porcine models. *Adv. Healthc. Mater.* 10 (6), 2001573. doi:10.1002/adhm.202001573

Yu, Kai, JoeyLo, C. Y., Yan, Mei, Yang, Xiaoqiang, Brooks, Donald E., Hancock, Robert E. W., et al. (2017). Anti-adhesive antimicrobial peptide coating prevents catheter associated infection in a mouse urinary infection model. *Biomaterials* 116, 69–81. doi:10.1016/j.biomaterials.2016.11.047

Zhan, Yanlong, Yu, Sirong, Amirfazli, Alidad, Siddiqui, Abdul Rahim, and Wen, Li (2021). Recent advances in antibacterial superhydrophobic coatings. *Adv. Eng. Mater.* 24 (4), 2101053. doi:10.1002/adem.202101053

Zhang, Shuai, Wang, Liyun, Liang, Xinjin, Jan, Vorstius, Keatch, Robert, George, Corner, et al. (2019). Enhanced antibacterial and antiadhesive activities of silver-PTFE nanocomposite coating for urinary catheters. *ACS Biomaterials Sci. Eng.* 5 (6), 2804–2814. doi:10.1021/acsbiomaterials.9b00071

Zhou, Chao, Wu, Yang, Venkata Thappeta, Kishore Reddy, Subramanian, JoThy Lachumy, Pranantyo, Dicky, Kang, En-Tang, et al. (2017). *In vivo* anti-biofilm and anti-bacterial non-leachable coating thermally polymerized on cylindrical catheter. *ACS Appl. Mater. Interfaces* 9 (41), 36269–36280. doi:10.1021/acsami.7b07053

Zhu, Tonghe, Gu, Hongbing, Zhang, Hongmei, Wang, Hongsheng, Xia, Huitang, Mo, Xiumei, et al. (2021). Covalent grafting of PEG and heparin improves biological performance of electrospun vascular grafts for carotid artery replacement. *Acta Biomater.* 119, 211–224. doi:10.1016/j.actbio.2020.11.013

frontiers | Frontiers in Bioengineering and Biotechnology

TYPE Original Research
PUBLISHED 12 January 2023
DOI 10.3389/fbioe.2022.1091122

OPEN ACCESS

EDITED BY
Muhammad Wajid Ullah,
Jiangsu University, China

REVIEWED BY
Meifeng Zhu,
Nankai University, China
Arunkumar Palaniappan,
Vellore Institute of Technology (VIT), India

*CORRESPONDENCE
Pinhua Rao,
raopinhua@sues.edu.cn
Jiale Jin,
22018143@zju.edu.cn
Yi Chai,
chaiyi@renji.com

SPECIALTY SECTION
This article was submitted to Biomaterials, a section of the journal Frontiers in Bioengineering and Biotechnology

RECEIVED 06 November 2022
ACCEPTED 22 December 2022
PUBLISHED 12 January 2023

CITATION
Luo J, Sun F, Rao P, Zhu T, Liu Y, Du J, Chen S, Jin X, Jin J and Chai Y (2023), A poly (glycerol-sebacate-acrylate) nanosphere enhanced injectable hydrogel for wound treatment.
Front. Bioeng. Biotechnol. 10:1091122.
doi: 10.3389/fbioe.2022.1091122

A poly (glycerol-sebacate-acrylate) nanosphere enhanced injectable hydrogel for wound treatment

Jiajia Luo[1], Fenglei Sun[2], Pinhua Rao[1]*, Tonghe Zhu[1], Yonghang Liu[1], Juan Du[1], Sihao Chen[1], Xiangyun Jin[3], Jiale Jin[4]* and Yi Chai[5]*

[1]School of Chemistry and Chemical Engineering, Institute for Frontier Medical Technology, Shanghai Engineering Research Center of Pharmaceutical Intelligent Equipment, Shanghai Frontiers Science Research Center for Druggability of Cardiovascular Non-coding RNA, Shanghai University of Engineering Science, Shanghai, China, [2]Department of Neurosurgery, Weifang People's Hospital, Weifang, Shandong, China, [3]Department of Orthopaedics, Renji Hospital, School of Medicine, Shanghai Jiao Tong University, Shanghai, China, [4]Spine Lab, Department of Orthopaedic Surgery, The First Affiliated Hospital, Zhejiang University, Hangzhou, China, [5]Department of Neurosurgery, Renji Hospital, School of Medicine, Shanghai Jiao Tong University, Shanghai, China

Wound repair remains a huge clinical challenge, which can cause bleeding, infection, and patient death. In our current research, a bioactive, injectable, multifunctional composite hydrogel doped with nanospheres was prepared with antibacterial and angiogenesis-promoting functions for the treatment of wounds. Amino groups in ε-polylysine (ε-EPL) undergo dynamic Schiff base reaction cross-linking with oxidized hyaluronic acid (OHA), and F127 exhibits unique temperature sensitivity to form an injectable thermosensitive hydrogel (FHE10), which can form a hydrogel to cover the wound at body temperature. Nanospheres (PNs) prepared using poly (glyceryl-sebacate-acrylate) (PGSA) were loaded into hydrogels (FHE10) for promoting wound repair. The prepared FHE10 exhibited rapid gelation, good injectable abilities, and showed resistance to the flourish of *Escherichia coli* (*E. coli*) and *Staphylococcus aureus* (*S. aureus*). *In vitro* investigations showed that FHE10 had good hemocompatibility and cytocompatibility. FHE10@PNs exhibited good proliferation, migration, and tube formation of human umbilical vein endothelial cells (HUVECs) and human foreskin fibroblasts (HFF-1). Furthermore, FHE10@PNs significantly promoted reepithelialization and collagen deposition as well as micro-vascularization compared with the use of FHE10 or PNs alone, thereby accelerating the repair of wounds. In general, this study demonstrated that the multifunctional injectable composite hydrogel showed great potential in wound treatment.

KEYWORDS

poly (glycerol-sebacate-acrylate) nanosphere, injectable hydrogel, antibacterial, vascularization, wound treatment

1 Introduction

Poly (glycerol-sebacate) (PGS) elastomer (Wang Y D et al., 2002) is obtained by polycondensation of two natural metabolic intermediates, glycerol, and sebacic acid, and have good biocompatibility and biodegradability. PGS can be used as scaffolds for cardiovascular (Rai et al., 2015), nerve (Saudi et al., 2019), cartilage (Souza et al., 2017), and bone (Piszko et al., 2021) tissue engineering, and has good applications in drug delivery systems (Hsieh et al., 2018) and wound repair (Keirouz et al., 2020). However, the traditional thermal crosslinking curing method requires long-term high-temperature reaction conditions

(Wang Y D et al., 2002), and the cured product cannot be further processed, which leads to its limited application in biomedicine. PGS is modified in the presence of acrylate groups to form polyglyceryl sebacate acrylate (PGSA) (Nijst et al., 2007). PGSA has the ability of fast photocuring in the presence of photoinitiators, which not only solves the high-temperature problem of the reaction but also greatly reduces response time. PGSA also has good biocompatibility and biodegradability and can be used as a scaffold for tissue engineering such as heart and nerve, as well as the ability to enhance tissue vascular reconstruction and promote wound repair (Jiang et al., 2021).

Hyaluronic acid (HA) is a polysaccharide derived from the extracellular matrix in tissues, which is vital in angiogenesis (Kang et al., 2019) and wound healing (Wu et al., 2017). A variety of hydrogel scaffolds were prepared from hyaluronic acid for tissue regeneration and proved to be able to absorb body fluids rapidly, with good water retention, biodegradability, and biocompatibility (Rezaeeyazdi et al., 2018). Studies have shown that some peptides have obvious antibacterial properties (Sathoff et al., 2018). Shime and Sakai (Shima and Sakai, 1977) first discovered in the 1970s that *Streptomyces* Albicans can produce ε-polylysine, a natural polypeptide composed of L-lysine monomers, which has biodegradable properties, good water solubility, non-toxic, and other advantages. ε-EPL can be used in the food industry as an antibacterial agent (Ge et al., 2022), and in recent years, its application in biomedicine has gradually increased (Shukla et al., 2012), such as drug carrier (de la Torre et al., 2018), interferon inducer (Wakamoto et al., 2007), dental adhesive (Xie et al., 2019), wound dressings (Sun et al., 2020), *etc.* F127 has received more and more attention as a drug delivery system, biomaterial, and tissue engineering hydrogel thanks to its marvelous biocompatibility and temperature sensitivity (Park et al., 2006), but owing to its insufficient mechanical properties and rapid degradation, limiting its appliance in regenerative medicine. By modifying it or combining it with other substances, it can be widely used after improving the above shortcomings (Li et al., 2020). The Schiff base reaction is a chemical reaction that forms dynamic covalent imine bonds through the cross-linking of amine groups and aldehyde groups (McKay and Finn, 2014). The dynamic cross-linked network are important to form self-healing hydrogels in a mild way, which can make the self-healing hydrogels automatically restore their original structure and function after damage (Xu et al., 2019).

Whether it is disease or physical stimulation, it may cause skin damage, and even affect the life and health of patients in severe cases. Therefore, the development of effective wound dressings is crucial for clinical treatment. The wound dressing should have hemostatic function, keep the tissue isolated from the external environment, prevent bacterial infection, and promote the repair of wound. The wound is easy got infected by bacteria in the procedure of wound healing which leads to the long-term failure of the wound to heal, which may lead to an inflammatory response and affect the normal function of the infected tissue (Holubová et al., 2021). Therefore, the preparation of materials with antibacterial properties that can promote wound healing is crucial. The important courses of wound healing include migration, proliferation, deposition of cell, and formation of extracellular matrix (Telgenhoff and Shroot, 2005; Jie et al., 2007), all of which require the transport of oxygen, nutrients, and cytokines with the help of blood vessels, so the building of new blood vessels in wound is crucial (Michalczyk et al., 2019). Injectable hydrogels (Xuan et al., 2021) are promising candidate materials with structures like the extracellular matrix, which can be injected to cover irregular wounds, absorb body fluids at the wound surface, and isolate the external environment.

In this study, we used HA to form oxidized hyaluronic acid (OHA) by modifying it with sodium periodate. At room temperature or physiological conditions, OHA interacts with ε-EPL through Schiff base reaction to form hydrogels. F127 is temperature-sensitive and automatically form a gel at room temperature or under physiological conditions. After mixing the above three substances uniformly, an injectable multifunctional hydrogel with temperature-sensitive properties can be formed at room temperature or under physiological conditions. PGSA was synthesized by modifying PGS with acryloyl chloride. Under the action of the photoinitiator, PGSA undergoes free radical polymerization to form nanospheres. The nanospheres were doped into the hydrogel to prepare an injectable and multifunctional wound repair hydrogel dressing for promoting angiogenesis.

2 Materials and methods

2.1 Materials

Glycerol was provided by China National Pharmaceutical Group Co. (Shanghai, China). Sebacic acid (SA), acryloyl chloride, ethyl acetate (EA), ethanol, ethylene glycol, and triethylamine were purchased from Adamas Reagent, Ltd. (Shanghai, China). DMAP, I2959, is referred to Irgacure 2959 and Dichloromethane (DCM) were supplied by Aladdin Reagent Co. (Shanghai, China). Sodium hyaluronate was provided by Shanghai Yuanye Biotechnology Co. (Shanghai, China). Sodium periodate (NaIO4), F127, is referred to Pluronic F127 and ε-polylysine (EPL) were gained from Aladdin Reagent Co. (Shanghai, China). Deionized water was self-made by laboratory instruments. All materials and solvents were used as received without any further purification unless otherwise noted.

2.2 Methods

2.2.1 Synthesis of poly (glyceryl-sebacate-acrylate) (PGSA) and preparation of PGSA nanospheres

The synthesis of poly (glycerol-sebacate) (PGS) was according to Wang's research (Wang Y D et al., 2002), then synthesized poly (glyceryl-sebacate-acrylate) (PGSA) by modifying PGS with acryloyl chloride (Nijst et al., 2007). The structure of PGS and PGSA was verified by ^{1}H nuclear magnetic resonance (^{1}H-NMR) and Fourier Transform Infrared (FTIR) spectrometry. The acrylation degree of PGSA was computed from the ^{1}H-NMR according to previous study (Chen et al., 2018).

The preparation method of nanospheres was as follows: At first, 30 mg PGSA was mixed in a 3 mL of ethanol and distilled water solution (V_E: V_W = 1:2) to dissolve into a homogeneous solution. Photoinitiator solution was prepared by dissolving I2959 powder with deionized water, then 40 μL I2959 (2 mg/mL) was mixed with the above PGSA solution. Magnetic stirring was performed while irradiating the above solution with a UV lamp, and PGSA nanospheres (PNs) were obtained after 30 s.

2.2.2 Synthesis of oxidized hyaluronic acid (OHA) and preparation of injectable hydrogels

Hyaluronic acid (HA) was oxidized to oxidized hyaluronic acid (OHA) by sodium periodate ($NaIO_4$) (Hongyi et al., 2022). The structure of OHA was tested by ^{1}H-NMR and FTIR spectrometry. The oxidation degree of OHA was obtained through the hydroxylamine hydrochloride method (Hongyi et al., 2022). The proportion of aldehyde groups in the OHA molecular chain, is calculated as following:

$$\mathrm{HA-(CHO)_2+2NH_2-OH\cdot HCl \rightarrow HA-(CH=N-OH)_2+2HCl}$$
$$\mathrm{HCl+NaOH=NaCl+H_2O}$$
$$\mathrm{n=\Delta V\times C_{NaOH}/2}$$
$$\mathrm{W=n\times M_{HA-CHO}+m\times M_{HA}}$$
$$\mathrm{oxidation\ degree\,(100\%)=n/(n+m)}$$
$$\mathrm{=n/\left[(W-n\times M_{HA-CHO})/M_{HA}+n\right]}$$

ΔV (mL) is the volume of sodium hydroxide solution consumed when adjusting the pH of the reaction solution; n (mol) is the number of repeating units of aldehyde groups on the OHA molecular chain; W (g) is the mass of OHA; $M_{HA\text{-}CHO}$ = 375 g/mol is the molecular weight of the OHA repeating unit; M_{HA} = 379 g/mol is the molecular weight of the hyaluronic acid repeat unit.

The preparation of hydrogels was referred to Wang's research (Wang et al., 2019), briefly summarized as follows: OHA was freeze-dried and dissolved into an 80 mg/mL solution by using distilled water. ε-EPL was dissolved into a solution by using the same method with a concentration of 50 mg/mL and 100 mg/mL. Then F127 was dissolved into a 400 mg/mL solution under 4°C. According to the volume ratio of F127: ε-EPL: OHA as 3:0:0, 3:0:1, 3:1:1, the F127 solution and the ε-EPL solution were sequentially mixed at 4°C, and the OHA solution was added after mixing evenly, then the solution was put in a thermostatic shaker for gelation, hydrogels were named as F127, FH, FHE5, FHE10, respectively.

PNs combined with FHE10 hydrogel were prepared by the above procedure. After mixing the F127 solution and the ε-EPL solution at 4°C, PNs were dispersed in the mixing solution. Then the OHA solution was mixed with above solution at 37°C to obtain the hybrid hydrogel.

2.2.3 Characterizations and testing

The microstructure of PNs was observed by SEM and TEM, then the diameter of PNs was evaluated by ImageJ. The study of particle size and z-potential was using a DLS. The injectability of PNs was tested by needle injection to observe whether it can be extruded smoothly.

Using SEM to observe the microstructure of hydrogels, and the pore size was measured *via* ImageJ. Testing whether the FHE10 can be successfully extruded from a needle proves its injectability. Phosphate buffer solution (PBS) was dropped into the test tube with hydrogels several times until the volume no longer changes and then weighed the mass. The hydrogel was lyophilized and weighed, and its water absorption ratio was computed through formula (1):

$$\textbf{\textit{Water absorption ratio}}\,(\%)=\frac{W-W_0}{W_0}\times 100\% \tag{1}$$

When hydrogel was at swelling equilibrium, the weight was W, and when it was lyophilized, the weight was W_0.

The prepared hydrogel was weighed and placed in an environment of 37°C with a relative humidity of 70% and then the weight of it was recorded every 1 h. The water retention ratio was computed through formula (2):

$$\textbf{\textit{Water retention ratio}}\,(\%)=\frac{W_X-W}{W_0-W}\times 100\% \tag{2}$$

In the start, the weight of the hydrogel was W_0, W_X was the weight of the hydrogel at the X hour, and after lyophilized the weight was W.

The free radical scavenging rate of hydrogel was measured by DPPH assay to evaluate its antioxidant capacity. The fresh 0.1 mM 1,1-diphenyl-2-trinitrophenylhydrazine (DPPH)/ethanol solution was prepared in the darkness. 30 mg of hydrogel was mixed with 3 mL of DPPH solution and cultured for 3 h and 24 h in the dark. Then a UV-Vis spectrophotometer was applied to measure the absorbance of the solution at 517 nm. The scavenging rate was computed by formula (3):

$$\textbf{\textit{Scavenging rate}}\,(\%)=\frac{A-A_0}{A_0}\times 100\% \tag{3}$$

The absorbance of the control group was A_0, and A was the absorbance of the samples incubated with DPPH solution after 3 and 24 h.

2.2.4 Blood compatibility test *in vitro*

Blood compatibility test was carried out according to the method of GB/T 16886.4-2003 of China. The procedure is described below. 4 mL of carotid artery blood was collected from healthy SD rats, and anticoagulated whole blood was prepared using aqueous trisodium citrate solution, then freshly diluted anticoagulated whole blood was prepared using PBS buffered solution. The materials F127, FH, FHE5 and FHE10 were placed in centrifuge tubes, 3 mL of PBS solution was added to each of them, and the shaker's temperature was set at 37°C. Then put the centrifuge tubes in the shaker, and incubated for 30 min. After 60 μL of freshly diluted anticoagulated whole blood was added to each of them, the incubation was continued for 1 h. The tubes were centrifuged at 2000 rpm/min for 5 min to get the supernatant, and then test the supernatant at 545 nm to get the absorbance value L. The same volume of distilled water and diluted anticoagulated whole blood was added to the tube as positive control group and the absorbance was tested as M. The same volume of PBS buffer solution and diluted anticoagulated whole blood was added to the tube as negative control group and the absorbance was tested as N. Three parallel samples were tested in each group. The hemolysis ratio was calculated by formula (4):

$$\textbf{\textit{Hemolysis ratio}}\,(\%)=\frac{H_X-H_N}{H_P}\times 100\% \tag{4}$$

H_X was the absorbance of the experimental group, and H_N, H_P was the absorbance of the negative and positive group respectively.

2.2.5 Antibacterial performance test

Escherichia coli and *Staphylococcus aureus* were selected to evaluate the antibacterial performance of FHE series hydrogels. The procedure was as follows: 0.5 g of each of F127, FH, FHE5, and FHE10 hydrogels were accurately weighed in a tube and sterilized under UV for 30 min 10 μL of bacterial suspension was placed on top of the hydrogels, and after 12 h of contact, 10 mL of PBS solution was added to the tube, vortexed for 2 min, and then 10 μL of the above

vortexed solution was added to the culture medium, and the bacterial solution was evenly coated on the sheep blood agar (SBA) plates using the spread-plate method and placed in a constant temperature incubator for 24 h. After the culture was completed, the antibacterial effect of the hydrogel was evaluated by observing the growth of the photographed bacteria.

2.2.6 *In vitro* experiments

To assess the cytocompatibility of the materials, we selected human umbilical vein endothelial cells (HUVECs) and human foreskin fibroblasts (HFF-1). HUVECs and HFF-1 were purchased from Shanghai Cell Bank of Chinese Academy of Sciences (Shanghai, China). HUVECs were taken as an example to illustrate the culture of cells. HUVECs were grown in the culture flasks in endothelial cell medium (ECM) with 5% fetal bovine serum (FBS), 1% penicillin/streptomycin (P/S) and 1% endothelial cell growth supplement (ECGS). The flask was placed in a CO_2 cell incubator.

The proliferation of cells co-cultured with materials was evaluated by a Cell Counting Kit-8 (CCK-8) assay. The appropriate amount of lyophilized samples F127, FH, FHE5, and FHE10 were weighed, and a solution with a concentration of 10 mg/mL by soaking in serum-free medium for 24 h were prepared. HUVECs were seeded on a 24-well plate at 1×10^4 per well and placed in a CO_2 cell incubator for 24 h, then the ECM medium was replaced by the ECM medium containing materials to culture cells for 1, 3, and 5 days. At a set point in time, 450 μL of ECM medium and 50 μL of the pre-warmed CCK-8 solution was placed to each well, then placed in a cell incubator for 1 h. After that, the solution was added to a 96-well plate, and then a microplate reader was used to survey the absorbance value at 450 nm wavelength.

The cytoskeletal proteins and nuclei were labeled by FITC-labeled phalloidin and 4′,6-diamidino-2-phenylindole (DAPI) respectively. The same samples were used as the CCK-8 assay. The nucleus staining was visualized under the DAPI channel (excitation = 405 nm; emission = 437-552 nm), and cytoskeletal proteins were visualized under the GFP channel (excitation = 488 nm, emission = 505-545 nm). HUVECs were planted in a 24-well plate at a density of 2×10^4 per well, and placed in a CO_2 cell incubator for 3 days. The cells were first washed three times with ice PBS for 15 min, and then covered with 4% cold paraformaldehyde for 15 min. For permeabilization, cells were treated with 0.1% Triton X-100 for 15 min and blocked with 1% BSA for 1 h. Finally, cells were incubated with primary antibodies at 4°C overnight. The cells were washed three times with PBS for 15 min among each step. After primary antibody incubations, cells were washed for 3 × 5 min in PBS-T (0.1% Tween 20%). Subsequently, fluorescent-labeled secondary antibody was used to incubated with cells for 2 h in dark and then DAPI was used on the cells for 15 min. All steps were washed with PBS-T. The results were observed *via* a confocal microscope.

Cell migration was tested by the transwell assay to measure the influences of materials, taking HUVECs as an example. HUVECs were planted in the upper chamber of a 24-well transwell, and 5×10^4 cells were plated in each well. 600 μL of ECM medium containing materials were placed to the lower chamber and the ECM medium to the control group. The same samples were used as the CCK-8 assay. The culture plate was taken out after 8 h of culture and the migrated cells in upper chamber were washed with PBS for 3 times and fixed with 4% paraformaldehyde for 15 min, and stained with 0.1% crystal violet staining solution for 5 min and dried overnight. The cells were observed and taken pictures under a microscope. Counting the number of migrated cells using ImageJ.

TABLE 1 Primer sequences used for qRT-PCR.

Gene	Gene bank	Primer sequences (5′-3′)	Tm (°C)
VEGF	NCBI	F: AGGGCAGAATCATCACGAAGT	61.2
	geneID7422	R: AGGGTCTCGATTGGATGGCA	62.9
PDGF	NCBI	F: CTCGATCCGCTCCTTTGATGA	61.7
	geneID5155	R: CGTTGGTGCGGTCTATGAG	60.2
bFGF	NCBI	F: AGAAGAGCGACCCTCACATCA	62.7
	geneID2247	R: CGGTTAGCACACACTCCTTTG	61.2
GAPDH	NCBI	F: ACAACTTTGGTATCGTGGAAGG	62.1
	geneID2597	R: GCCATCACGCCACAGTTTC	61.1

The materials' ability to promote HUVECs angiogenesis was tested by using Matrigel *in vitro*. 100 μL of well-mixed Matrigel was placed in the 48-well plate, then the plate was put in a cell incubator for 30 min. Each well of the plate was seeded with 3×10^4 cells and ECM with materials was added to it, the control group was contained with ECM medium. Then the well plate was put in a cell incubator for 6 h. After this, the vascularized network structure on the surface of Matrigel was observed and photographed using a light microscope, and vessels were counted by ImageJ.

To explore the effects of materials on the gene expression of vascular endothelial growth factor (VEGF), platelet-derived growth factor (PDGF), and basic fibroblast growth factor (bFGF), HUVECs and HFF-1 were placed on 6-well plates at a density of 4 × 10 per well. After 3 days, RNA was collected from different cell samples with TRIzol reagent. qRT-PCR was then achieved with ChamQ SYBR qPCR Master Mix. The gene expression levels were normalized to GAPDH, and the expression of related genes was analyzed by the $2^{-\Delta\Delta t}$ method. The sequences of target genes and internal reference genes are shown in Table 1.

2.1.7 *In vivo* experiments

All animal experiments were authorized by the Animal Research Ethics Committee of the First Affiliated Hospital of Zhejiang University and were performed by the National Institutes of Health Guidelines for the Care and Use of Laboratory Animals. Forty healthy rats were randomly selected as experimental rats and divided into four groups, which were marked as the control group, PNs group, FHE10 group, and FHE10@PNs group. A rat skin defect model was established based on previous research methods (Wang et al., 2013). Each rat was weighed and 4%Pentobarbital (40 mg/kg) was used to anesthetize by intraperitoneal administration. After the injection, the vital signs of the rat were noted. Two symmetrical circular marks with a diameter of 2 cm were made on the depilation area on the back of the rat, and the full-thickness skin was cut off. The bleeding was compressed by the gauze until there was no obvious bleeding. In the next step, the wound was covered with materials and wrapped with gauze. After the operation, penicillin was injected to prevent infection, and the health of the rats was closely observed. Rats in each group were sacrificed 7 and 14 days after surgery, and the skin tissues at the edge of the wound were collected for immunohistochemical analysis.

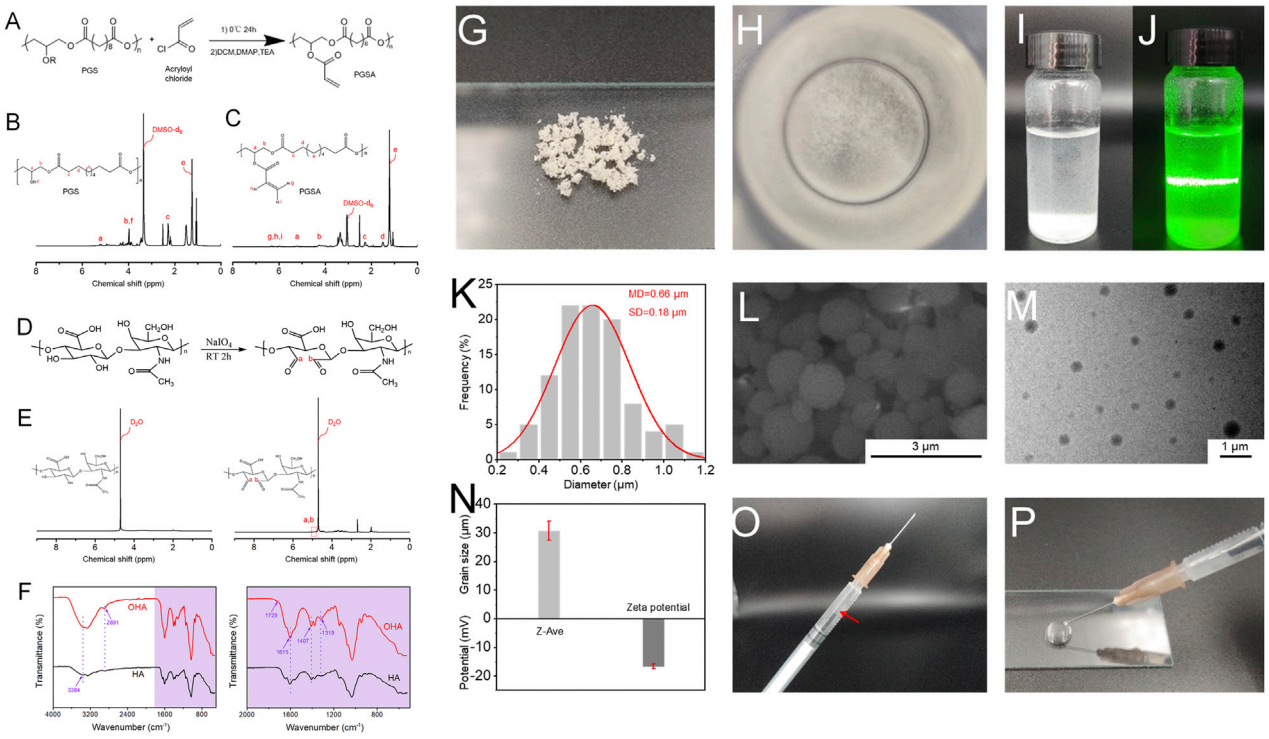

FIGURE 1
(A) The reaction mechanism route of PGSA; **(B)** ^{1}H-NMR spectrum of PGS; **(C)** ^{1}H-NMR spectrum of PGSA. **(D)** The reaction mechanism route of OHA; **(E)** ^{1}H-NMR spectrum of HA and OHA; **(F)** FTIR spectrum of HA and OHA. **(G)** Apparent morphology of PNs, as revealed by digital images; **(H)** Digital photographs of PNs dispersed in deionized water; **(I)** and **(J)** PNs were uniformly dispersed in deionized water under natural light, and Tyndall effect appeared after beam irradiation; **(K)** The diameter distribution histograms of PNs; **(L)** SEM image of PNs; **(M)** TEM image of PNs; **(N)** Particle size and potential of PNs; **(O)** and **(P)** Schematic illustration of the injectability of PNs. The red arrow means PNs were uniformly dispersed in the syringe.

The healing of skin wounds on days 0, 3, 7, and 14 after the operation was recorded by a camera, and the area of the wound was calculated by ImageJ. The wound healing ratio was computed by formula (5):

$$\textit{Wound healing ratio}\,(\%) = \frac{S_0 - S}{S_0} \times 100\% \tag{5}$$

Wound area on day 0 was represented by S_0, and the wound area on days 3, 7, and 14 was represented by S.

The skin tissues were completely immersed in 10% formalin solution overnight, then in graded alcohol (75%, 85%, 95%, 100%) for dehydrating. Paraffin was used to embedded the cleared tissues, and the tissue block was cooled overnight then cut into 5 μm of sections.

The regeneration of wound *epidermis* was assessed by staining the tissue sections with hematoxylin and eosin (H&E). H&E staining was carried out according to previous study (Yoon et al., 2016). For H&E staining, paraffin-embedded sections were first deparaffinized and hydrate to water. Then, nucleus was stained with Hematoxylin Solution (Solarbio, China) for 15 min followed by rinsing in running tap water. Next, the tissue section was differentiated by Differentiation Solution (Solarbio, China) for 3 min and re-dyed with Eosin Y Aqueous Solution (Solarbio, China) for 1 min. After the sections were dehydrated and sealed, photos were taken and analyzed. The wound reepithelialization ratio was calculated using formula (6):

$$\textit{Reepithelialization ratio}\,(\%) = \frac{L_0 - L}{L_0} \times 100\% \tag{6}$$

L_0 represents the original wound length, and L represents the incompletely healed wound *epidermis* length.

Masson's trichrome staining was accomplished on tissue sections to evaluate the collagen deposition. Masson's trichome staining were carried out according to previous study (Zhao et al., 2017). For Masson's trichome stain, a Masson trichrome staining kit (Sigma-Aldrich, America) was used to stain the tissue section according to the manufacturer's protocol. To observe and photograph the stained sections with an optical microscope. The area of the blue part was counted and quantitatively analyzed using ImageJ to evaluate the collagen deposition rate in the new tissue.

CD31 immunohistochemical staining and CD31/α-SMA immunofluorescence staining were performed on tissue sections to evaluate angiogenesis in wound tissue. CD31 immunohistochemical staining were carried out according to previous study (Kong et al., 2018). As for CD31immunohistochemical staining: A two-step immunohistochemistry kit (Zhongshan Golden Bridge Biotechnology, China) was used for this study according to the manufacturer's protocol. To observe and photograph the stained sections with a light microscope, and two pathologists were asked to count the number of blood vessels in the stained sections under double-blind conditions.

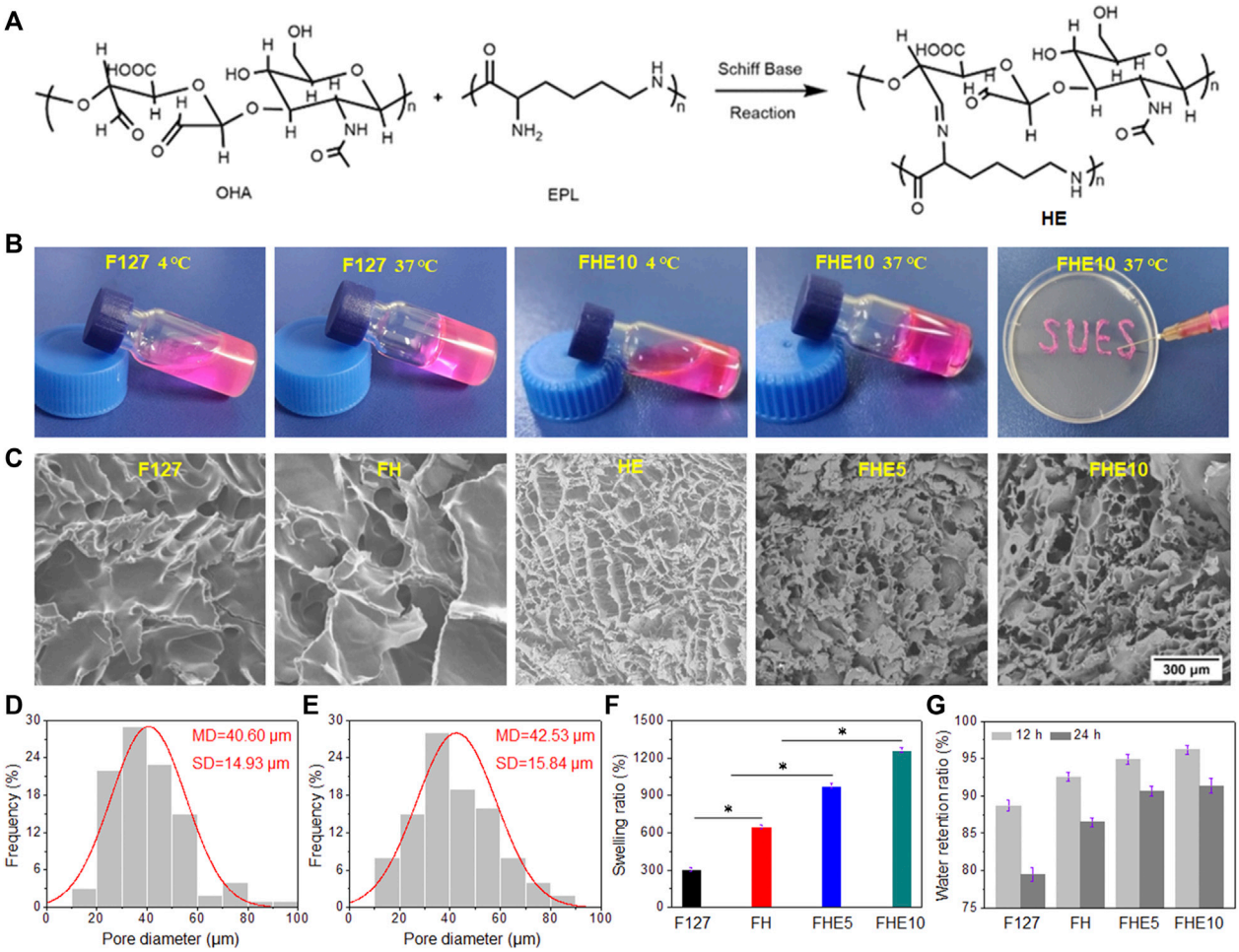

FIGURE 2
(A) Schiff base reaction mechanism route; **(B)** Photographs of F127 and FHE10 hydrogel before and after gelation, and FHE10 proved its injectability by extruding SUES; **(C)**The SEM images of F127, FH, HE, FHE5 and FHE10 hydrogel; **(D)** and **(E)** The pore diameter distribution of FHE5 and FHE10, respectively; **(F)** The swelling ratio of F127, FH, FHE5, and FHE10 hydrogel; **(G)** The water retention ratio of F127, FH, FHE5, and FHE10 hydrogel.

2.1.8 Statistical analysis

Three parallel samples were prepared for the experiments, and the mean ± standard deviation was employed as the analysis data. One-way ANOVA was applied to process statistical differences between groups. When $p < 0.05$ (*) $p < 0.01$ (**) the differences had statistical significance.

3 Results and discussions

3.1 Characterization of PNs and FHE hydrogel

PGS and PGSA were successfully synthesized (Figures 1A–C and Supplementay Figure S1). The ^{1}H-NMR analysis indicates that the degree of acylation was 32%. OHA was obtained by modification (Figures 1D–F). The oxidation degree of OHA was 12.5% by the method of hydroxylamine hydrochloride (Wang et al., 2019). In the presence of photoinitiator, the aqueous ethanol solution of PGSA was subjected to ultraviolet irradiation and magnetic stirring to form nanospheres PNs with uniform particle size.

Figures 1G, H showed the state of the PNs under dry conditions and the state of dispersion in water, respectively. The PNs nanospheres are easy to aggregate together in the dry state, which may be caused by their viscosity. When it was put in deionized water, it can be evenly dispersed. Using a beam to irradiate the PNs solution, the Tyndall effect can be observed from Figures 1I, J, indicating that the nanospheres were uniformly dispersed. It can be seen from the SEM image (Figure 1L) that PNs have a relatively smooth surface. Through ImageJ statistical calculation, it can be obtained that the particle size distribution of PNs (Figure 1K) is in the range of 0.2–1.2 μm, mainly in the range of 0.6–0.8 μm, which is relatively uniform. The dispersion of PNs can be seen from the transmission electron microscopy (TEM) image (Figure 1M). There is a certain difference between the particle size range measured by the dynamic light scattering (DLS) (Figure 1N) instrument and the results of scanning electron microscope (SEM). It is speculated that during the test process, the PNs aggregated due to the sedimentation of their weight, and the measured particle size reached several tens of microns. The surface charge of PNs is negative (Figure 1N). The extrusion experiment of a 1 mL syringe with a needle size of 0.45 × 16 mm proved that PNs could be extruded without sticking to the needle tube (Figures 1O, P). As can be seen the white PNs are evenly dispersed in the syringe and do not adhere to the wall. By

10.3389/fbioe.2022.1091122

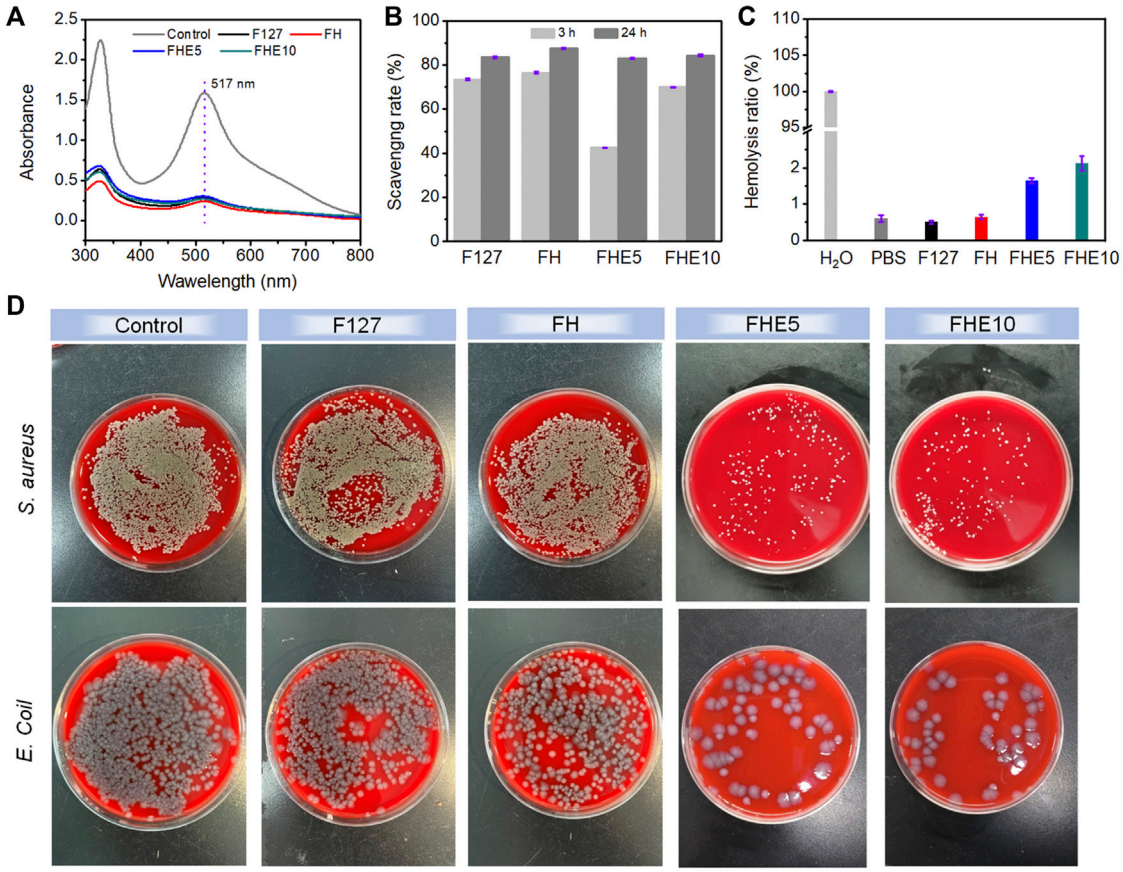

FIGURE 3
(A) UV absorption of DPPH solution after co-incubation with F127, FH, FHE5, and FHE10 hydrogel; **(B)** Scavenging rate of F127, FH, FHE5, and FHE10 hydrogel; **(C)** Hemolysis ratio of F127, FH, FHE5, and FHE10 hydrogel; **(D)** Photographs of survival bacteria clones on SBA plates after coculturing with F127, FH, FHE5, and FHE10 hydrogel.

extruding on the glass slide, PNs have good injectability and will not block the needle tube.

F127 is a temperature-sensitive material. At low temperature, it is in a solution state, and when the temperature is raised, it transforms into a gel state. After mixing F127 with OHA and EPL, the whole solution has temperature sensitive properties. When the temperature was at 4°C, the mixed solution became a sol state, and when the temperature was raised up to 37°C, it became a gel, so it belonged to a thermosensitive gel (Figure 2B). After the gel was loaded into the syringe, it was slowly extruded into letters such as "SUES" (Figure 2B), and the extrusion was smooth without clogging, which proved that the hydrogel system has good injectable performance. It can be seen from Figure 2C that F127 and FH hydrogel had no pores, while FHE hydrogel had pores. The measurement of pore diameter was by ImageJ, and Figures 2D, E were the pore size of FHE5 and FHE10, respectively. Figure 2F is the swelling ratio of hydrogels. The swelling ratio of FHE5 and FHE10 hydrogel increased significantly, which may be due to the reticular pore structure formed after the chemical reaction, thereby improving the water absorption, and swelling ability of the hydrogel. Due to the prolongation of time, and the inevitable loss of water, the FHE5 and FHE10 hydrogel has a stronger water-locking ability (Figure 2G).

A UV spectrophotometer was used to measure the absorbance of the mixed solution, the UV absorption of the solution after co-incubation with the material decreased (Figure 3A) and the color faded (Supplementary Figure S2) compared with the control group. The scavenging rate of F127, FH, FHE5, and FHE10 hydrogel reached more than 80% after 24 h (Figure 3B), indicating that the materials have good antioxidant properties. The ability to scavenge free radicals should come from many hydroxyl groups in the F127 molecule. In addition, the molecular chain of OHA also contains many hydroxyl groups, so the hydrogel has a strong ability to scavenge free radicals.

Supplementary Figure S2 showed that except for the control group, the centrifuge tubes containing the material were centrifuged after incubation, the red blood cells were deposited at the bottom without breaking, the supernatant was clarified, and the hemolysis ratio was less than 5% (Figure 3C), proving that the material did not cause hemolysis. The prepared hydrogels, only FHE5 and FHE10 have certain antibacterial properties (Figure 3D). Judging from the growth of bacteria in the control group and the F127 and FH groups, the bacterial colonies on the medium grew well, and it was speculated that the pure F127 hydrogel and FH hydrogel did not have antibacterial effects. Comparing the FHE5 and FHE10 groups, the growth of bacteria is inhibited, which is attributed to the fact that ε-EPL itself has a certain antibacterial activity, and the protonated amino group can damage the cell wall of bacteria and lead to bacterial death.

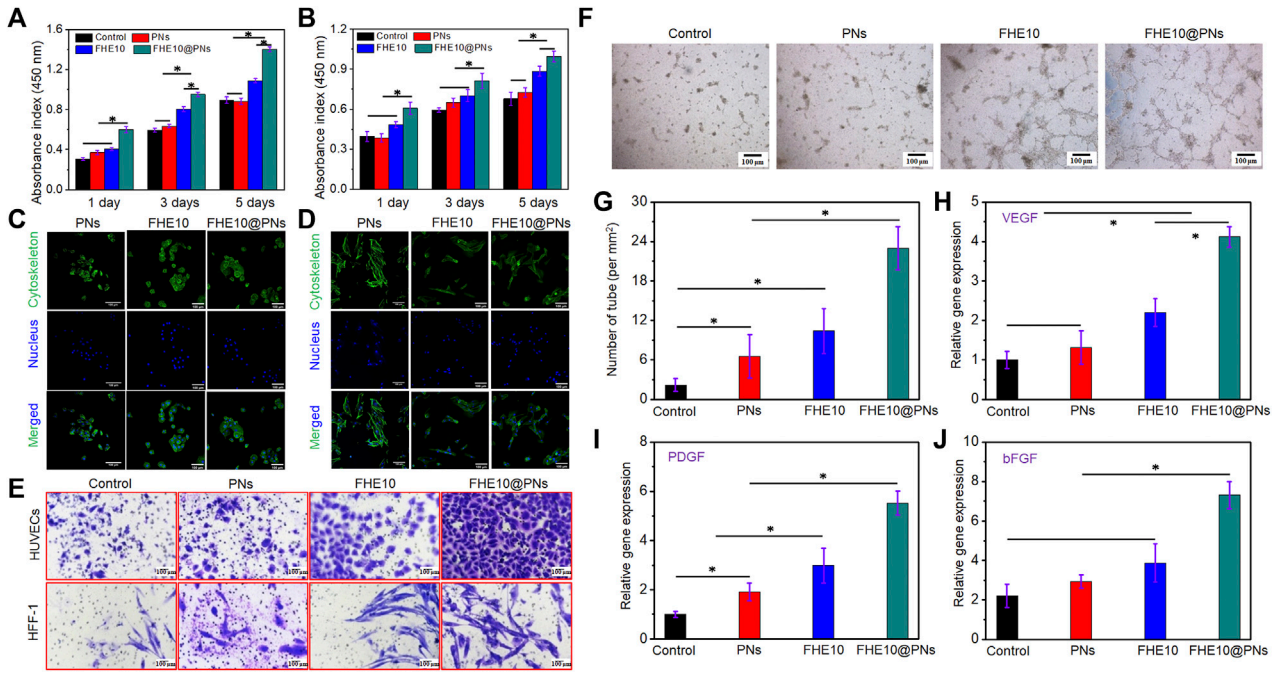

FIGURE 4
(A,B) CCK-8 assay indicated that proliferation of HUVECs and HFF-1 after culturing with PNs, FHE10, and FHE10@PNs, respectively; **(C,D)** DAPI (blue)/FITC-phalloidin (green) staining assay of HUVECs and HFF-1 with PNs, FHE10, and FHE10@PNs after culturing, respec-tively; **(E)** Transwell assay showed that migration of HUVECs and HFF-1 were stained by crystal violet; **(F)** Tube formation assay; **(G)** Quantitative analysis of tube formation; **(H–J)** qRT-PCR analysis of VEGF, PDGF, and bFGF.

In summary, FHE10 hydrogel and PNs were selected for follow-up studies.

3.2 Effects of PNs, FHE10, and FHE10@PNs on proliferation, morphology, migration, the tube formation, and angiogenesis-related gene expression *in vitro*

HUVECs and HFF-1 in good growth state were cultured by using the material extract. The FHE10@PNs promoted cell proliferation more than PNs or FHE10 alone, and with the increase of culture time, cell proliferation gradually increased, indicating that cells also adapted to the surrounding environment and achieved the best growth state (Figures 4A, B).

HUVECs and HFF-1 were cultured for 3 days, then their morphology was observed by a light microscope (Figures 4C, D). HUVECs cells in experiment group have no significant change in cell morphology when compared to the control group. The cell body of HFF-1 was fusiform or irregular triangular, with an oval nucleus in the center and a cytoplasmic protrusion, which was radial when growing. The characteristics were consistent with the normal proliferation of HUVECs and HFF-1.

The migration of HUVECs and HFF-1 co-cultured with the material was observed by a transwell migration assay (Figure 4E). The groups added with materials all could promote cell migration, and the FHE10@PNs had the strongest ability to promote cell migration, so the combined action of the two had a synergistic effect on cell migration. By a quantitative analysis of the number of migrating cells (Supplementary Figure S3), the results were consistent with the staining, which proved that the materials indeed had the chemotactic attraction to cells.

In vitro tube formation assay was performed by co-cultured PNs, FHE10, and FHE10@PNs with HUVECs to evaluate the tube formation ability (Figures 4F, G). HUVECs co-cultured with each group and formed a network of capillary-like structures on the Matrigel after 6 h, and each group had some differences. The tube's diameter is shown in the supporting information (Supplementary Figure S4). Compared with the control group, the PNs, FHE10, and FHE10@PNs groups all could promote angiogenesis, and the FHE10@PNs group had the best-promoting effects.

The effects of PNs, FHE10, and FHE10@PNs on the expression of angiogenesis-related genes after co-culture with HUVECs and HFF-1 for 7 days were evaluated (Figures 4H–J). The gene expression levels of VEGF, PDGF, bFGF in the PNs, FHE10, and FHE10@PNs groups were better than those in the control group, while the FHE10@PNs group had the best gene expression levels.

3.3 *In vivo* wound tissue-repair ability

Encouraged by the controllable injectability, favorable biocompatibility and antibacterial activity, outstanding pro-angiogenic properties of the prepared hydrogels revealed above, FHE10@PNs was chosen and further used as a potential wound dressing for skin repair to evaluate the *in vivo* wound healing performance. Figure 5A visually showed the wound healing progress treated by the saline, PNs, FHE10, and FHE10@PNs for 0, 3, 7, and 14 days, respectively. The wound healing rates of the control, PNs, FHE10, and FHE10@PNs groups were measured by

10.3389/fbioe.2022.1091122

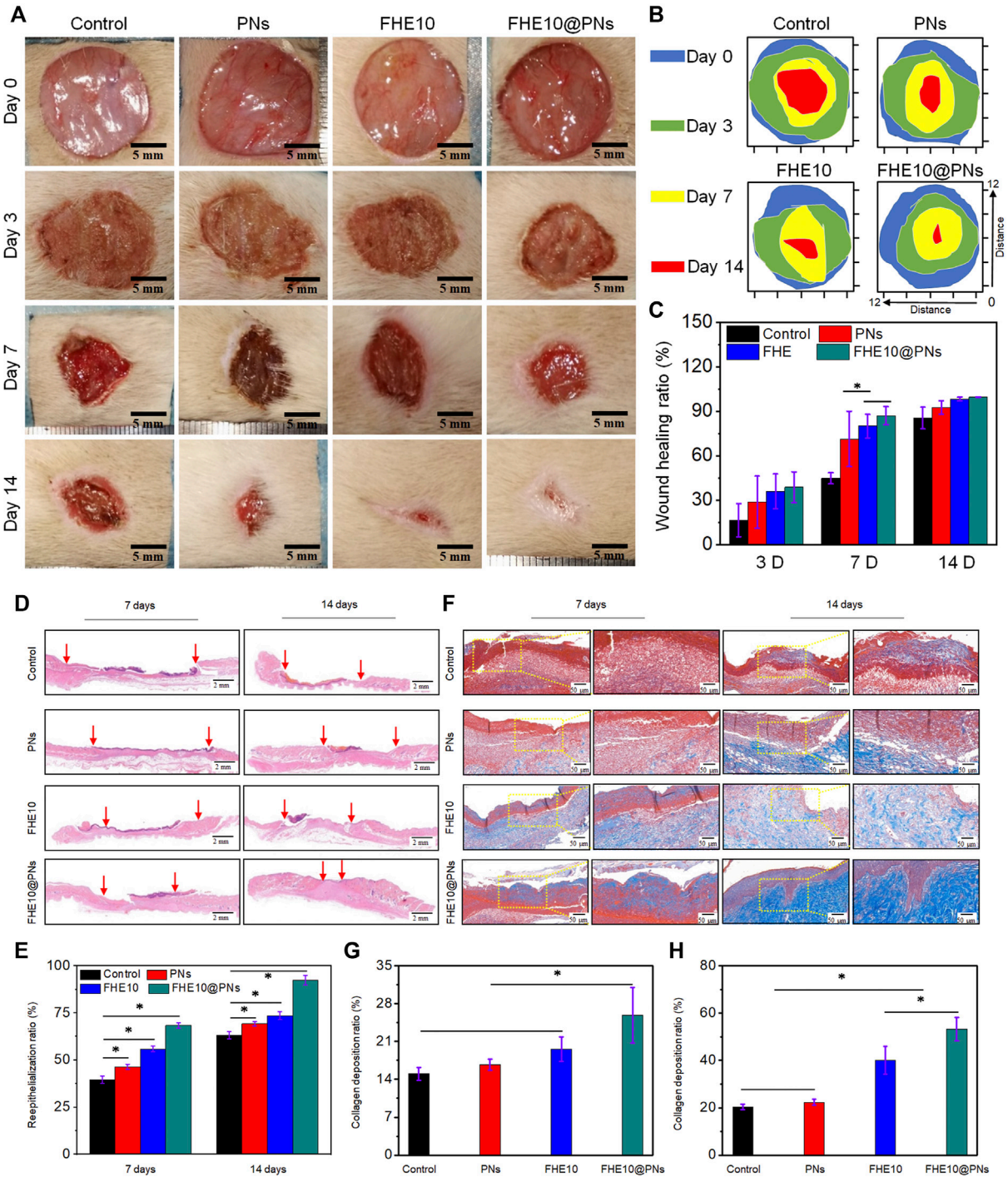

FIGURE 5
(A) Wound images of control, PNs, FHE10, FHE10@PNs at 0, 3, 7 and 14 days post-operation; **(B)**Traces of wound repair for each treatment group *in vivo*. Blue, green, yellow, and red areas correspond to the wound area at n (n = 0, 3, 7 and 14) days, respectively; **(C)** Wound healing ratio of the defects treated with saline (control), PNs, FHE10, FHE10@PNs at 0, 3, 7 and 14 days post-operation; **(D)** H&E stained images; **(E)** The reepithelialization rate of wound defect at 7 and 14 days after treatment with saline (control), PNs, FHE10, and FHE10@PNs; **(F)** Masson's trichrome stained images; **(G,H)**The collagen deposition in the wound sites was evaluated by ImageJ.

using ImageJ at each observation time point, and the FHE10@PNs group showed the best performance in wound healing rate, as compared with the other three groups with a significant difference at Day 7 ($p < 0.05$). The average wound healing rates of control, PNs, FHE10, and FHE10@PNs were 44.8%, 71.3%, 80.0%, and 87.1%, respectively. The continuous observation for up to 14 days after operation showed unhealed wounds in the control, PNs, and FHE10 groups, which almost completely healed in the FHE10@PNs group with a wound healing rate of 99.5% (Figures 5A–C).

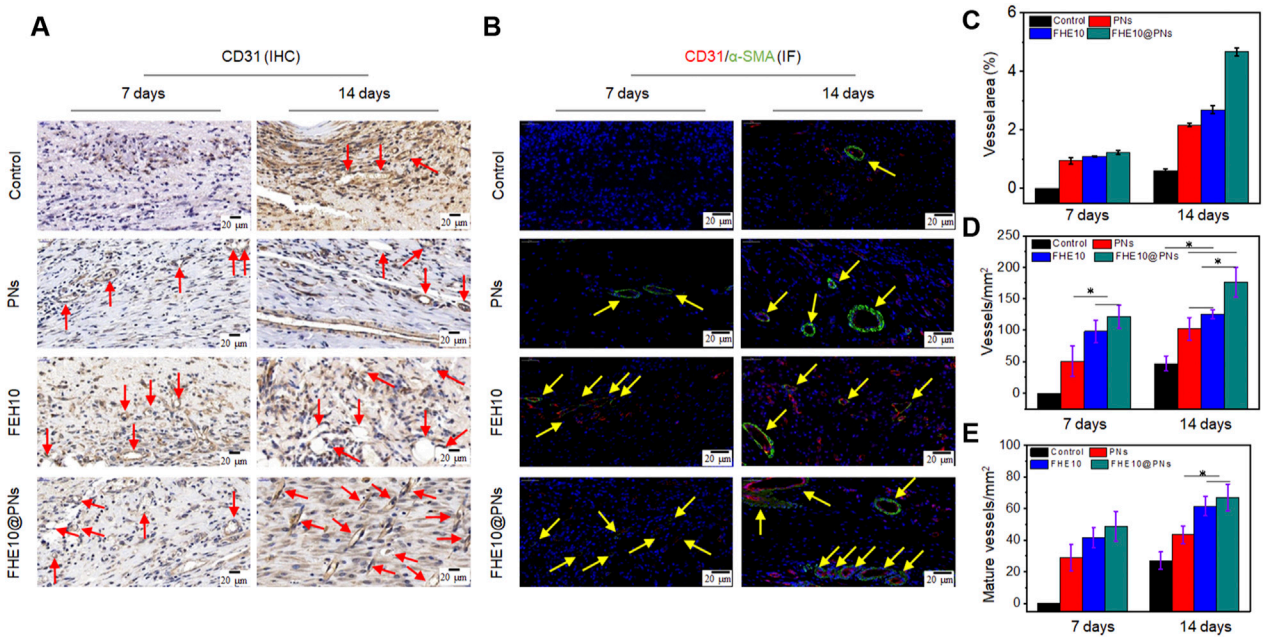

FIGURE 6
IHC and IF analysis of neovascularization in wound of control, PNs, FHE10, and FHE10@PNs groups, respectively. **(A)** IHC staining for CD31, red arrows mean newly formed blood vessels; **(B)** IF co-staining for α-SMA and CD31, yellow arrows mean mature vessels; **(C)** Area analysis of mature blood vessels at 7 and 14 days post-operation; **(D)** Quantitative analysis of newly formed blood vessels at 7 and 14 days post-operation; **(E)** Quantitative analysis of mature vessels at 7 and 14 days post-operation.

We further clarified the quality of regenerated wound tissue by using H&E staining and Masson trichrome staining at the observation time points of day 7 and day 14 (Figures 5D, F). FHE10@PNs exhibited better healing effects than the other three groups (Figures 5D, E). After 7 days of the skin defect, the epidermal regeneration rates of the control group, PNs group, FHE group, and FHE10@PNs group reached 39.5%, 46.3%, 55.8%, and 68.3%, respectively. After 14 days of treatment, the wounds treated with FHE10@PNs exhibited almost no open wounds with a healing rate of 92.3% and become smooth with new epidermal tissue. In contrast, most of the wounds in the other groups remained significantly more open and the scars were uneven.

Collagen fibers are a key component related to granulation tissue and the dermal extracellular matrix during the wound healing processes (Diller and Tabor, 2022). Thus, Masson staining was performed to evaluate the deposition and organization of collagen fibers in regenerative skin tissue at 7 and 14 days post-surgery (Figures 5F, G). As presented in Figure 5G, in terms of the area of collagen deposition, a significant difference was found across the groups at 7 days (15.05%, 16.71%, 19.61%, 25.89% for control, PNs, FHE10, FHE10@PNs, respectively). On day 14, mature collagen fibers are observed in the FHE10@PNs group and the collagen deposition is denser and more organized (Figure 5H). On the other hand, the collagen fibers presented in the other groups are still partially dysplastic.

3.4 FHE10@PNs hydrogel facilitates angiogenesis

The angiogenesis is essential for nutrient and oxygen supply in the process of skin wound repair. To better elucidate the properties of the FHE10@PNs hydrogel on angiogenesis, CD31 and α-SMA were selected for immunohistochemical staining analysis. As plotted in Figures 6A, D, the FHE10@PNs group exhibited significantly increased neovascularization based on a high level of CD31 expression on both day 7 and day 14. In contrast, either PNs or FHE10 alone displayed less CD31 expression, confirming that the FHE10@PNs hydrogels provided a favorable 3D microenvironment scaffold for blood vessel formation.

Moreover, the colocalization of α-SMA and CD31 was seen as a biomarker of a normalized vessel (Wu et al., 2020). Positively stained endothelial cells and smooth muscle cells lining the abundant vessel networks were observed in the skin regenerated tissue treated with FHE10@PNs, but significantly, less were observed in the control or other material-treated groups. The mature vessel areas on day 7 and day 14 was significantly bigger than the other groups (Figures 6B,C,E). On the basis of the above results, FHE10@PNs hydrogels not only showed the ability to facilitate neovascularization but also to promote subsequent vascular maturation in the process of skin wound repair.

4 Conclusion

In this study, a hybrid hydrogel was prepared by preparing PGS acrylate derivative photocurable nanospheres and mixing them with injectable oxidized hyaluronic acid hydrogel FHE10. The *in vitro* results showed that the FHE10@PNs group could up-regulate the proliferation, migration, and expression of genes related to angiogenesis of HUVECs and HFF-1. *In vivo* studies further demonstrated that the prepared FHE10@PNs group significantly promoted wound reepithelialization, collagen deposition, and neovascularization, and finally promoted wound healing. Therefore,

the preparation of injectable FHE10@PNs has better effects on promoting reepithelialization, collagen deposition, angiogenesis and wound healing than using PNs or FHE10 hydrogel alone. In conclusion, the FHE@PNs may be a potential material to promote reepithelialization, collagen deposition, and angiogenesis in wound healing.

Data availability statement

The original contributions presented in the study are included in the article/Supplementary Material, further inquiries can be directed to the corresponding authors.

Ethics statement

The animal study was reviewed and approved by Animal Research Ethics Committee of the First Affiliated Hospital of Zhejiang University.

Author contributions

JL: investigation, methodology, and writing original draft. FS, YL, JD, SC, XJ, and JJ: methodology, and conceptualization. PR, YC, TZ, FS, and JL: conceptualization, project administration, and writing-review and editing.

Funding

This research was funded by the Shanghai Rising-Star Program (20QC1401300), National Natural Science Foundation of China (81902186), Technology Support Project of Science and Technology Commission of Shanghai Municipality (22S31904700), Construction Project of Shanghai Engineering Technology Research Center (20DZ2255900), and the Shanghai Sailing Program (22YF1423500).

Acknowledgments

We thank the excellent technical support (microscopy platform: Xingguang Liang, Fangjie Lu, Yahong Wu, flow cytometry platform: Yi Guo) by the corefacility, Central Laboratory, the First Affiliated Hospital, Zhejiang University School of Medicine with the confocal laser microscopy, and flow cytometry.

Conflict of interest

The authors declare that the research was conducted in the absence of any commercial or financial relationships that could be construed as a potential conflict of interest.

Publisher's note

Supplementary material

The Supplementary Material for this article can be found online at: https://www.frontiersin.org/articles/10.3389/fbioe.2022.1091122/full#supplementary-material

References

Chen, J. Y., Hwang, J. V., Ao-Ieong, W. S., Lin, Y. C., Hsieh, Y. K., Cheng, Y. L., et al. (2018). Study of physical and degradation properties of 3D-printed biodegradable, photocurable copolymers, PGSA-co-PEGDA and PGSA-co-PCLDA. *Polymers* 10 (11), 1263. doi:10.3390/polym10111263

de la Torre, C., Dominguez-Berrocal, L., Murguia, J. R., Dolores Marcos, M., Martinez-Manez, R., Bravo, J., et al. (2018). ϵ-polylysine-capped mesoporous silica nanoparticles as carrier of the C9*h* peptide to induce apoptosis in cancer cells. *Chemistry-a Eur. J.* 24 (8), 1890–1897. doi:10.1002/chem.201704161

Diller, R. B., and Tabor, A. J. (2022). The role of the extracellular matrix (ECM) in wound healing: A review. *Biomimetics* 7 (3), 87. doi:10.3390/biomimetics7030087

Ge, L., Li, Z., Han, M., Wang, Y., Li, X., Mu, C., et al. (2022). Antibacterial dialdehyde sodium alginate/ε-polylysine microspheres for fruit preservation. *Food Chem.* 387, 132885. doi:10.1016/j.foodchem.2022.132885

Holubová, A., Chlupáčová, L., Cetlová, L., Cremers, N. A. J., and Pokorná, A. (2021). Medical-grade honey as an alternative treatment for antibiotics in non-healing wounds—a prospective case series. *Antibiotics* 10, 918. doi:10.3390/antibiotics10080918

Hongyi, W., Nitong, B., Jie, C., Yuanyuan, C., Runzhi, S., Chunhua, W., et al. (2022). Construction of konjac glucomannan/oxidized hyaluronic acid hydrogels for controlled drug release. *Polymers* 14, 927. doi:10.3390/polym14050927

Hsieh, Y.-K., Chang, C.-T., Jen, I. H., Pu, F.-C., Shen, S.-H., Wan, D., et al. (2018). Use of gold nanoparticles to investigate the drug embedding and releasing performance in biodegradable poly(glycerol sebacate). *Acs Appl. Nano Mater.* 1 (9), 4474–4482. doi:10.1021/acsanm.8b00723

Jiang, W.-C., Hsu, W.-Y., Ao-Ieong, W.-S., Wang, C.-Y., Wang, J., and Yet, S.-F. (2021). A novel engineered vascular construct of stem cell-laden 3D-printed PGSA scaffold enhances tissue revascularization. *Biofabrication* 13, 045004. doi:10.1088/1758-5090/ac1259

Jie, L., Chen, J., and Kirsner, R. (2007). Pathophysiology of acute wound healing. *Clin. Dermatology* 25 (1), 9–18. doi:10.1016/j.clindermatol.2006.09.007

Kang, L., Jia, W., Li, M., Wang, Q., Wang, C., Liu, Y., et al. (2019). Hyaluronic acid oligosaccharide-modified collagen nanofibers as vascular tissue-engineered scaffold for promoting endothelial cell proliferation. *Carbohydr. Polym.* 223, 115106. doi:10.1016/j.carbpol.2019.115106

Keirouz, A., Zakharova, M., Kwon, J., Robert, C., Koutsos, V., Callanan, A., et al. (2020). High-throughput production of silk fibroin-based electrospun fibers as biomaterial for skin tissue engineering applications. *Mater. Sci. Eng. C-Materials Biol. Appl.* 112, 110939. doi:10.1016/j.msec.2020.110939

Kong, L., Wu, Z., Zhao, H., Cui, H., Shen, J., Chang, J., et al. (2018). Bioactive injectable hydrogels containing desferrioxamine and bioglass for diabetic wound healing. *Acs Appl. Mater. Interfaces* 10 (36), 30103–30114. doi:10.1021/acsami.8b09191

Li, Z., Xiong, X., Peng, S., Chen, X., Liu, W., and Liu, C. (2020). Novel folated pluronic F127 modified liposomes for delivery of curcumin: Preparation, release, and cytotoxicity. *J. Microencapsul.* 37 (3), 220–229. doi:10.1080/02652048.2020.1720030

McKay, C. S., and Finn, M. G. (2014). Click chemistry in complex mixtures: Bioorthogonal bioconjugation. *Chem. Biol.* 21 (9), 1075–1101. doi:10.1016/j.chembiol.2014.09.002

Michalczyk, E. R., Chen, L., Maia, M. B., and DiPietro, L. A. (2019). A role for low-density lipoprotein receptor-related protein 6 in blood vessel regression in wound healing. *Adv. Wound Care* 9, 1–8. doi:10.1089/wound.2019.1019

Nijst, C., Bruggeman, J. P., Karp, J. M., Ferreira, L., Langer, R., Bettinger, C. J., et al. (2007). Synthesis and characterization of photocurable elastomers from poly(glycerol-co-sebacate). *Biomacromolecules* 8 (10), 3067–3073. doi:10.1021/bm070423u

Park, K., Jung, H. H., Son, J. S., Rhie, J.-W., Park, K. D., Ahn, K.-D., et al. (2006). "Thermosensitive and cell-adhesive pluronic hydrogels for human adipose-derived stem cells," in 7th Asian Symposium on Biomedical Materials (ASBM7)), Cheju Isl, South Korea, August 20–23, 2006, 342–343.

Piszko, P., Wlodarczyk, M., Zielinska, S., Gazinska, M., Plocinski, P., Rudnicka, K., et al. (2021). PGS/HAp microporous composite scaffold obtained in the TIPS-TCL-SL method: An innovation for bone tissue engineering. *Int. J. Mol. Sci.* 22 (16), 8587. doi:10.3390/ijms22168587

Rai, R., Tallawi, M., Frati, C., Falco, A., Gervasi, A., Quaini, F., et al. (2015). Bioactive electrospun fibers of poly (glycerol sebacate) and poly (ε-caprolactone) for cardiac patch application. *Adv. Healthc. Mater.* 4 (13), 2012–2025. doi:10.1002/adhm.201500154

Rezaeeyazdi, M., Colombani, T., Memic, A., and Bencherif, S. A. (2018). Injectable hyaluronic acid-co-gelatin cryogels for tissue-engineering applications. *Materials* 11 (8), 1374. doi:10.3390/ma11081374

Sathoff, A. E., Velivelli, S., Shah, D. M., and Samac, D. A. (2018). Plant defensin peptides have antifungal and antibacterial activity against human and plant pathogens. *Phytopathology* 109, 402–408. doi:10.1094/phyto-09-18-0331-r

Saudi, A., Rafienia, M., Kharazi, A. Z., Salehi, H., Zarrabi, A., and Karevan, M. (2019). Design and fabrication of poly (glycerol sebacate)-based fibers for neural tissue engineering: Synthesis, electrospinning, and characterization. *Polym. Adv. Technol.* 30 (6), 1427–1440. doi:10.1002/pat.4575

Shima, S., and Sakai, H. (1977). Polylysine produced by Streptomyces. *Agric. Biol. Chem.* 41 (9), 1807–1809. doi:10.1271/bbb1961.41.1807

Shukla, S. C., Singh, A., Pandey, A. K., and Mishra, A. (2012). Review on production and medical applications of ε-polylysine. *Biochem. Eng. J.* 65, 70–81. doi:10.1016/j.bej.2012.04.001

Souza, M. T., Tansaz, S., Zanotto, E. D., and Boccaccini, A. R. (2017). Bioactive glass fiber-reinforced PGS matrix composites for cartilage regeneration. *Materials* 10 (1), 83. doi:10.3390/ma10010083

Sun, A., He, X., Li, L., Li, T., Liu, Q., Zhou, X., et al. (2020). An injectable photopolymerized hydrogel with antimicrobial and biocompatible properties for infected skin regeneration. *Npg Asia Mater.* 12 (1), 25. doi:10.1038/s41427-020-0206-y

Telgenhoff, D., and Shroot, B. (2005). Cellular senescence mechanisms in chronic wound healing. *Cell Death Differ.* 12, 695–698. doi:10.1038/sj.cdd.4401632

Wakamoto, H., Matsuda, H., Kawamoto, K., and Makino, S.-I. (2007). Epsilon-polylysine microparticle adjuvant drives cytokine production to Th1 profile. *J. Veterinary Med. Sci.* 69 (7), 717–723. doi:10.1292/jvms.69.717

Wang, C., Wang, M., Xu, T., Zhang, X., Lin, C., Gao, W., et al. (2019). Engineering bioactive self-healing antibacterial exosomes hydrogel for promoting chronic diabetic wound healing and complete skin regeneration. *Theranostics* 9 (1), 65–76. doi:10.7150/thno.29766

Wang, X., Ge, J., Tredget, E. E., and Wu, Y. (2013). The mouse excisional wound splinting model, including applications for stem cell transplantation. *Nat. Protoc.* 8 (2), 302–309. doi:10.1038/nprot.2013.002

Wang, Y. D., Ameer, A. G, S. B. J., R, L., and Langer, R. (2002). A tough biodegradable elastomer. *Nat. Biotechnol.* 20, 602–606. doi:10.1038/nbt0602-602

Wu, J., Chen, J., Feng, Y., Zhang, S., Lin, L., Guo, Z., et al. (2020). An immune cocktail therapy to realize multiple boosting of the cancer-immunity cycle by combination of drug/gene delivery nanoparticles. *Sci. Adv.* 6 (40), eabc7828. doi:10.1126/sciadv.abc7828

Wu, S., Deng, L., Hsia, H., Xu, K., He, Y., Huang, Q., et al. (2017). Evaluation of gelatin-hyaluronic acid composite hydrogels for accelerating wound healing. *J. Biomaterials Appl.* 31 (10), 1380–1390. doi:10.1177/0885328217702526

Xie, S.-X., Boone, K., VanOosten, S. K., Yuca, E., Song, L., Ge, X., et al. (2019). Peptide mediated antimicrobial dental adhesive system. *Appl. Sciences-Basel* 9 (3), 557. doi:10.3390/app9030557

Xu, J., Liu, Y., and Hsu, S.-h. (2019). Hydrogels based on Schiff base linkages for biomedical applications. *Molecules* 24 (16), 3005. doi:10.3390/molecules24163005

Xuan, H., Wu, S., Fei, S., Li, B., Yang, Y., and Yuan, H. (2021). Injectable nanofiber-polysaccharide self-healing hydrogels for wound healing. *Mater. Sci. Eng. C* 128, 112264. doi:10.1016/j.msec.2021.112264

Yoon, D. S., Lee, Y., Ryu, H. A., Jang, Y., Lee, K.-M., Choi, Y., et al. (2016). Cell recruiting chemokine-loaded sprayable gelatin hydrogel dressings for diabetic wound healing. *Acta Biomater.* 38, 59–68. doi:10.1016/j.actbio.2016.04.030

Zhao, L., Niu, L., Liang, H., Tan, H., Liu, C., and Zhu, F. (2017). pH and glucose dual-responsive injectable hydrogels with insulin and fibroblasts as bioactive dressings for diabetic wound healing. *Acs Appl. Mater. Interfaces* 9 (43), 37563–37574. doi:10.1021/acsami.7b09395

frontiers | Frontiers in Bioengineering and Biotechnology

TYPE Original Research
PUBLISHED 09 February 2023
DOI 10.3389/fbioe.2023.1096390

OPEN ACCESS

EDITED BY
Tonghe Zhu,
Shanghai University of Engineering Sciences, China

REVIEWED BY
Jianhai Chen,
Peking University People's Hospital, China
Lichen Wang,
Stevens Institute of Technology, United States
Kaihu Li,
Xiangya Hospital, Central South University, China

*CORRESPONDENCE
Chengyu Zhuang,
zhuangchengyu@msn.com
Lei Wang,
ray_wangs@hotmail.com

†These authors have contributed equally to this work

SPECIALTY SECTION
This article was submitted to Biomaterials, a section of the journal Frontiers in Bioengineering and Biotechnology

RECEIVED 12 November 2022
ACCEPTED 30 January 2023
PUBLISHED 09 February 2023

CITATION
Li G, Zhang Y, Wu J, Yang R, Sun Q, Xu Y, Wang B, Cai M, Xu Y, Zhuang C and Wang L (2023), Adipose stem cells-derived exosomes modified gelatin sponge promotes bone regeneration. *Front. Bioeng. Biotechnol.* 11:1096390. doi: 10.3389/fbioe.2023.1096390

Adipose stem cells-derived exosomes modified gelatin sponge promotes bone regeneration

Gen Li[1†], Yin Zhang[1†], Jiezhou Wu[2†], Renhao Yang[1], Qi Sun[2], Yidong Xu[1], Bo Wang[2], Ming Cai[2], Yang Xu[1], Chengyu Zhuang[1*] and Lei Wang[1*]

[1]Department of Orthopaedics, Ruijin Hospital, Shanghai Jiaotong University School of Medicine, Shanghai, China, [2]Department of Orthopaedics, Shanghai Tenth People's Hospital, Tongji University School of Medicine, Shanghai, China

Background: Large bone defects resulting from trauma and diseases still a great challenge for the surgeons. Exosomes modified tissue engineering scaffolds are one of the promising cell-free approach for repairing the defects. Despite extensive knowledge of the variety kinds of exosomes promote tissue regeneration, little is known of the effect and mechanism for the adipose stem cells-derived exosomes (ADSCs-Exos) on bone defect repair. This study aimed to explore whether ADSCs-Exos and ADSCs-Exos modified tissue engineering scaffold promotes bone defects repair.

Material/Methods: ADSCs-Exos were isolated and identified by transmission electron microscopy nanoparticle tracking analysis, and western blot. Rat bone marrow mesenchymal stem cells (BMSCs) were exposed to ADSCs-Exos. The CCK-8 assay, scratch wound assay, alkaline phosphatase activity assay, and alizarin red staining were used to evaluate the proliferation, migration, and osteogenic differentiation of BMSCs. Subsequently, a bio-scaffold, ADSCs-Exos modified gelatin sponge/polydopamine scaffold (GS-PDA-Exos), were prepared. After characterized by scanning electron microscopy and exosomes release assay, the repair effect of the GS-PDA-Exos scaffold on BMSCs and bone defects was evaluated *in vitro* and *in vivo*.

Results: The diameter of ADSCs-exos is around 122.1 nm and high expressed exosome-specific markers CD9 and CD63. ADSCs-Exos promote the proliferation migration and osteogenic differentiation of BMSCs. ADSCs-Exos was combined with gelatin sponge by polydopamine (PDA)coating and released slowly. After exposed to the GS-PDA-Exos scaffold, BMSCs have more calcium nodules with osteoinductive medium and higher expression the mRNA of osteogenic related genes compared with other groups. The quantitative analysis of all micro-CT parameters showed that GS-PDA-Exos scaffold promote new bone formed in the femur defect model *in vivo* and confirmed by histological analysis.

Conclusion: This study demonstrates the repair efficacy of ADSCs-Exos in bone defects, ADSCs-Exos modified scaffold showing a huge potential in the treatment of large bone defects.

KEYWORDS

adipose stem cells, exosomes, tissue engineering, bone defect, Biomaterials

Introduction

Despite the great advance of bone tissue engineering in the last few years, bone defect caused by various reasons such as trauma and infection is still a challenge for clinicians in orthopedic surgery (NIGUEZ SEVILLA et al., 2019; TOROS and OZAKSAR, 2019).Traditional methods to repair the bone defect include autografts, allografts, and xenografts, which exhibit excellent osteoconductive and osteoinductive properties, they still have several limits include repetitive surgery, immune rejection, and risk of disease transmission. Bioactive implants may provide an effective solution for this problem. To improve the bioactivity of the implants, many researchers use different substances, including polymer materials (DONG et al., 2015), ions (FERRANDEZ-MONTERO et al., 2019), growth factors (LIU et al., 2017; CABALLERO AGUILAR et al., 2019), cells (LIU et al., 2017), to modified different implant materials.

Among these, mesenchymal stem cells (MSCs) show strong osteogenesis activity in bone defect repair and have emerged as an alternative modified method to improve the implants (ANNAMALAI et al., 2019). However, MSCs have relative limitations in the maintenance of biological activity, and the logistics delivery in clinical therapies (AL-MORAISSI et al., 2019).

Recently, MSC paracrine effects are considered to be principally responsible for the tissue repair potential, and increasing interest has focussed on the exosomes (AGHAJANI NARGESI et al., 2017; PHINNEY and PITTENGER, 2017). MSCs derived exosomes show lower immunogenicity, and will not directly form tumors compared with MSCs. Using MSCs derived exosomes may get around MSCs' side effects (QI et al., 2016). Compared with stem cells, MSCs derived exosomes show a safe, low-cost and efficient manner without immune or ethical restrictions (LIU et al., 2021)

Exosomes, secreted by most cell types with a diameter of 30–180 nm, are released into the extracellular environment with the cell membrane. Exosomes can carry many bioactive molecules such as lipids, proteins, mRNAs, tRNA, lncRNAs, and miRNAs (SOKOLOVA et al., 2011; GURUNATHAN et al., 2019). Researchers found the source of MSCs influence the biological effects of MSC-derived exosomes. MSCs obtained from bone marrow (BMSCs) are the most frequently used stem cells in cell therapy and tissue engineering. BMSCs derived exosomes also promote bone regeneration (FURUTA et al., 2016). Although most research on MSC-based cell therapy focused on BMSCs, there is an increasing importance of adipose tissue as an alternative MSCs source. Compared with an equivalent amount of bone marrow, adipose tissue can provide up to 500-fold more MSCs (HASS et al., 2011). Thus, adipose tissue can be the most efficient source of MSCs (DUSCHER et al., 2017). Several studies show that exosomes derived from adipose-derived stem cells (ADSCs-Exos) promote angiogenesis, cutaneous healing, and nerve regeneration (YANG et al., 2018; HONG et al., 2019). However, the repair effect of ADSCs-Exos on bone defect remains unclear. Here, we aim to evaluate the impact of ADSCs-Exos on BMSCs osteogenic differentiation *in vitro* and repair effect of ADSCs-Exos after combined with materials on bone defect *in vivo*, to estimate its potential therapeutic value on bone defect.

Materials and methods

Ethics statement and animals

All the animal procedures and operations complied with the Guidelines of Shanghai Laboratory Animal Center and the Policies on the Use of Humans and Animals in Research of the Shanghai Tenth People's Hospital (SYXK: 2014-0026) and demonstrated to the principles outlined in the Declaration of Helsinki. All the animals in this work were looked after humanely, and all efforts were made to remove their discomfort.6-weeks and 8-weeks age male Sprague–Dawley (SD) rats were purchased from Bikai Experimental Animal Company (Shanghai, China). All the rats were housed in the standard cage with thermostatic room (25°C) in a 12 h light and 12 h dark cycle. The standard diet and water were supplied. The rats were adapted to the experimental environment at least 2 weeks before starting this study.

Isolation and culture of ADSCs

ADSCs derived from the inguinal fat pad of 6-weeks SD rats. In brief, the capillaries were removed from the lipoaspirate, minced with phosphate-buffered solution (PBS, GenomSciences, Hangzhou, China) and digested with 1% collagenase A (Gibco, Carlsbad, United States) for 1 h at 37°C. After filtration, the mixture was centrifuged (1,000 rpm, 10 min) at room temperature (RT), and the supernatant was discarded. The collected cells were washed with PBS, centrifuged (1,000 rpm, 5 min) and then resuspended in DMEM/F12 medium (Gibco, Carlsbad, United States) with 10% fetal calf serum (FCS; Gibco, Carlsbad, United States) and 1% penicillin-streptomycin (PS) in a humidified 5% CO_2 at 37°C; When the cells passed 3 generations, they were identified and used for next experiments.

Flow cytometry

This study used stem cell surface markers to evaluate the phenotype of cells, including CD29-PE, CD90-FITC, CD105-PE-cy5, CD45-APC (all the antibodies from Abcam, Cambridge, United Kingdom) after 1 week expansion. In brief, cells were cultured with antibodies for 30 min at room temperature, and the analysis was performed by a FACSCalibur flow cytometer (BD Biosciences, San Jose, United States). The nonspecific IgG-labeled cells were used as controls. The data were analyzed by FlowJo software (Tree Star, Ashland, OR).

ADSCs differentiation

ADSCs ($2*10^5$ per well in 6-well plates) were treated with adipogenic media to induce adipogenesis. Adipogenic medium consisted of 0.5 mM 3-isobutyl-1-methyl-xanthine, 1 μM dexamethasone, 5 μg/mL insulin, and 50 μM indomethacin. The culture medium was replaced every 3 days. Seven days later, Oil Red O staining (Beyotime Institute of Biotechnology, Haimen, China) was used to measure lipid vesicles. For osteogenic differentiation, Osteogenic medium consisted of 100 nM dexamethasone, 10 mM βglycerophosphate, and 0.05 mM L-ascorbic acid-2-phosphate, the media was changed with osteogenic induction media supplied with the differentiation media every 3 days. After 21 days, osteonectin was detected. For chondrogenic differentiation, ADSCs were cultured in a chondrogenic differentiation medium (Cyagen, Santa Clara, CA, United States)

and refreshed every 3 days. 21 days later, cartilage matrix protein was detected. All the pictures were captured by an Olympus IX51 light microscope (Olympus, Tokyo, Japan).

Exosomes isolation and identification

The exosomes derived from ADSCs were purified from serum-free cell medium by series centrifugation and filtration steps. Briefly, collected supernatant centrifuged at 300 g for 10 min to remove dead cells, 5,000 g for 10 min to remove cellular debris. Then the supernatant was ultrafiltrated by 0.22 μm filter (Whatman, Maidstone, United Kingdom) and centrifuged at 120,000 g for 90 min. The final pellets were resuspended in 1 mL PBS and stored at −80°C.The collected pellets were distinguished by transmission electron microscopy (TEM, Zeiss, Axio, Germany) and nanoparticle tracking analysis (NTA, NanoSight LM10, Malvern Instruments, Westborough, MA).

PKH67-labeled exosomes

ADSCs derived exosomes were labeled with PKH67 (Sigma-Aldrich, St. Louis, MO). In brief, 2 μL PKH67 was incubated with exosomes in a total of 1 mL of diluent for 15 min. 1 mL of 1% of BSA was added into the mixture to stop the labeling and was centrifuged at 120,000g for 2 h in 4°C. Then, the supernatant was discarded, resuspended the pellets in 5 mL of PBS, and centrifuged at 120,000g for 1 h in 4°C. Finally, PKH67-labeled-exosomes were resuspended in 1 mL of PBS and stored at −80°C.

Western blot

ADSCs or exosomes were lysed in RIPA buffer (Beyotime, Shanghai, China). The samples were separated on a 10%–15% SDS polyacrylamide gel and transferred to polyvinylidene difluoride (PVDF, Millipore, Billerica, MA, US) membranes. Then the PVDF membranes were blotted with 5% BSA for 1 h and incubated with primary antibodies overnight at 4°C. The membranes were incubated with horseradish peroxidase-conjugated anti-rat IgG (1:5,000, Santa Cruz Biotechnology, US) and visualized with an enhanced chemiluminescence kit (Amersham, GE Healthcare, Waukesha, WI, US) and quantified by ImageJ software ver. 1.52. Primary polyclonal antibodies against CD9 and CD63 (1: 1,000, Cell Signaling Technology).

Fabrication and characterization of adipose stem cells-derived exosomes modified gelatin sponge/polydopamine scaffolds (GS-PDA-Exos)

Gelatin sponges were purchased from Guangzhou Kuaikang Medical Apparatus Co. (Guangzhou, China). According to the previous study (DINH et al., 2018), the gelatin sponges soaked in dopamine (DA) solution (2 mg/mL in 10 mM Tris-HCl, pH 8.5, Sigma-Aldrich, St. Louis, US) were incubated with shaking at 37°C for 24 h to form the polydopamine (PDA) coating. To remove the non-adherent PDA, the gelatin sponge/polydopamine (GS-PDA) scaffolds were gently shaken in an ultrasonic cleaner with distilled water for 5 times. The GS-PDA scaffolds were dried and sterilized by ethylene oxide before the next step. Then the GS-PDA scaffolds were immersed in PKH67-labeled or non-labeled ADSCs-Exos solution (10^{10}particles/scaffold) with shaking at 37°C for 12 h. To remove the non-adherent exosomes, and the GS-PDA-Exos scaffolds were gently shaken in an ultrasonic cleaner with distilled water for 5 times. The distribution of PKH67-labeled exosomes on the scaffolds was observed with the confocal imaging system (Nikon, Japan). To measure the ADSCs-Exos release effect of GS-PDA-Exos scaffolds. The amount of ADSCs-Exos released was measured using CD63 ELISA (Beyotime, Shanghai, China) assay. Scanning electron microscopy (SEM, Hitachi, Tokyo, Japan) was used to observe the surface morphology of the scaffolds.

Isolation and culture of BMSCs

BMSCs were isolated from the femurs and tibias of 6-week SD male rats. In brief, The bone marrow was separated from the femurs and tibias of rats by flushing with a serum-free culture medium (DMEM/F12; Gibco, USA). The red blood cells were lysed in the lysate and cultured in DMEM/F12 (containing 10% FBS) and 1% penicillin-streptomycin (PS) in a humidified 5% CO2 at 37°C. Change the medium after 24–48 h, then replace the medium once every 2–3 days later. When the cells passed 3 generations, they were identified and used for next experiments BMSCs used in this study were P3-P6 generation cells.

Cell proliferation and migration assay

The regulation of ADSCs-Exos and GS-PDA-Exos on the proliferation of rat BMSCs was assessed by the Cell Counting Kit-8 (CCK-8) assay (Dojindo, Kyushu Island, Japan) (ZHU et al., 2019). Briefly, BMSCs were seeded into 96 well plates at a density of 4,000 cells per well, respectively. The cells were cultured with 100 μL of growth medium containing different concentrations of exosomes (0, EXO-L 1×10^9 particles/mL, EXO-H 1×10^{10} particles/mL) or 100 μL of growth medium with scaffolds immersed. Each well was incubated with 10 μL CCK-8 solution and cell proliferation curves were constructed at a wavelength of 450 nm.

Scratch wound assays assessed the effect of ADSCs-Exos and GS-PDA-Exos on Cell migration. 1.5×10^5 BMSCs were seeded into 6-well plates and cultured in growth medium for 12 h. Next, one scratch was made in each well using a 200 μL pipette tip. After washing with PBS, the medium was then replaced with serum-free medium supplemented with ADSCs-Exos (0, 1×10^9, 1×10^{10} particles/mL), or serum-free medium with scaffolds immersed. Wound closure was measured by capturing images at different time points. The scratched areas were measured using Image-Pro Plus software.

Alkaline phosphatase activity assay and alizarin red staining

As described above, BMSCs were seeded into 6 well plates and cultured with growth medium containing different concentrations of

exosomes or with scaffolds immersed. After 24 h, the medium was replaced with the normal or osteoinductive (OIC) medium for 10 days, At different time points (1, 4, 7, and 10 days), the alkaline phosphatase (ALP) activity assay of the supernatant was performed with an ALP Assay Kit (Beyotime, Shanghai, China). To assess mineralization, cells were induced for 3 weeks, fixed with 4% paraformaldehyde solution and washed with PBS for 3 times, then gently washed with distilled water and stained with 2% Alizarin red (ARS, Sigma-Aldrich, St. Louis, US). To quantify the coloration of ARS. 10% of acetic acid was added to each cell. After incubation for 12 h, the suspension transferred to tubes and centrifuged at 20,000 g for 15 min. The supernatant was transferred to another tube and neutralized with 10% ammonium hydroxide. Then 100 μL of each sample was measured at a wavelength of 405 nm.

RNA extraction and real-time quantitative-PCR (RT-PCR)

RT-PCR assessed the regulation of ADSCs-Exos and GS-PDA-Exos on the osteogenic differentiation related genes. Rat BMSCs were grown in normal, and osteoinductive media in the presence of ADSCs-Exos or scaffolds. The total RNA of the samples was isolated based on the manufacturer's protocol using the RNAiso plus kit (TaKaRa, Tokyo, Japan). The RNA was treated with DNase in a 10 μL reaction and conducted at 42°C for 2 min. Then, the PrimeScript RT reagent Kit (TaKaRa, Tokyo, Japan) was used in a total volume of 20 μL for the mRNAs in a 15 min incubation period at 37°C and stopped after a 5 s enzyme denaturing step at 85°C.

Real-time amplification was performed by the SYBR Premix Ex Taq (TaKaRa, Tokyo, Japan) in an ABI 7900 thermocycler (ABI; Foster City, CA, United States). The PCR cycling was 95°C for 30 s, followed by 40 cycles of 95°C for 5 s and 60°C for 30 s. Then a dissociation curve was at 95°C for 15 s, 60°C for 15 s, and 95°C for 15 s. GAPDH was used as a relative control and analyzed using the 2 the number of^-ΔΔCT method. Primer sequences used in this work were described in Supplementary Table S1.

Animal experiment

The studies involving animals were reviewed and approved by RuiJin Hospital Ethics Committee. Eight-week-old male Sprague Dawley (SD) rats were obtained from the Bikai Experimental Animal Company (Shanghai, China). In total, 24 animals were randomly divided into four groups as follows: 1) empty defect (control) 2) GS scaffold 3) GS-PDA scaffold and 4) GS-PDA-Exos scaffold, each group has 6 animals. After adaptation for two weeks, 300~350 g SD rats were used for establishing the critical-sized rat femoral bone defect model. Briefly, All animals were anesthetized by intraperitoneal injecting 2.5% pentobarbital (40 mg/kg). The knee was shaved and sterilized, after cut open one by one to expose the distal femur, a diameter of 3.0 mm defect was made at the femoral condyle with a slow-speed electric drill. The ice saline solution was locally used to lower the temperature. Then the scaffolds were implanted into the defects, and the incision was stitched.

Radiologic and histological analysis

At 2 and 4 weeks after implantation, the femurs of the animals were harvested and evaluated the new bone formation within the bone defect using micro-computed tomography (micro-CT; Skyscan 1,076, Bruker, Belgium) with a spatial resolution of 12 μm. The center of the bone tunnel of a 3 mm diameter was selected as the region of interest (ROI). The Scanco software was used to measure bone mineral density (BMD), bone tissue volume/total tissue volume (BV/TV), trabecular thickness (Tb.Th) and trabecular separation/spacing (Tb.Sp). After the micro-CT scan, the femurs were used for histology analysis. The samples were fixed in 4% paraformaldehyde for 48 h and decalcified in 10% ethylenediaminetetraacetic acid for 4 weeks. After decalcification, the samples were dehydrated and embedded in paraffin. Hematoxylin and eosin (HE) staining was performed with the 5 μm thick sections.

Statistical analysis

The SPSS 17.0 software was used for statistical analyses. All data were presented as mean ± standard deviation (SD). Differences among groups were assessed with one-way ANOVA. The statistical significance was $p < 0.05$. All experiments were repeated at 3 replicates.

Results

Acquisition and identification of ADSCs in SD rats

We obtained the ADSCs by standard methods and then performed the identification of surface markers. Flow cytometry results showed that over 99% of cells (passage 1) were positive for the mesenchymal stem cell markers CD29, CD90, or CD105 and negative for the leukocyte marker CD45 (Figure 1A). The ADSCs underwent 21-day chondrogenic, and adipogenic induction and experienced 14-day osteogenic induction to evaluate their multilineage differentiation potential. The ADSCs were positive for Oil Red O staining after adipogenic induction (Figure 1B). Cell immunofluorescence showed the ADSCs cultured in osteogenic induction positive expression of osteonectin. After adipogenic induction, ADSCs showed the expression of cartilage matrix protein as detected by immunofluorescence. The results indicate that the cells we obtained are ADSCs (Figure 1B).

Characterization of ADSCs-derived exosomes

TEM analysis showed that the exosomes isolated from the supernatants of ADSCs is a round membranous vesicle, which diameter of approximately 100 nm (Figure 1C).NTA analysis indicated that the parameters of the exosomes ranged mainly from 80 to 180 nm (Figure 1D). Western blotting analysis (Figure 1E) showed that the exosome-specific markers CD63 and CD9 were detected in ADSCs-derived exosomes, and the expression of abundance is high.

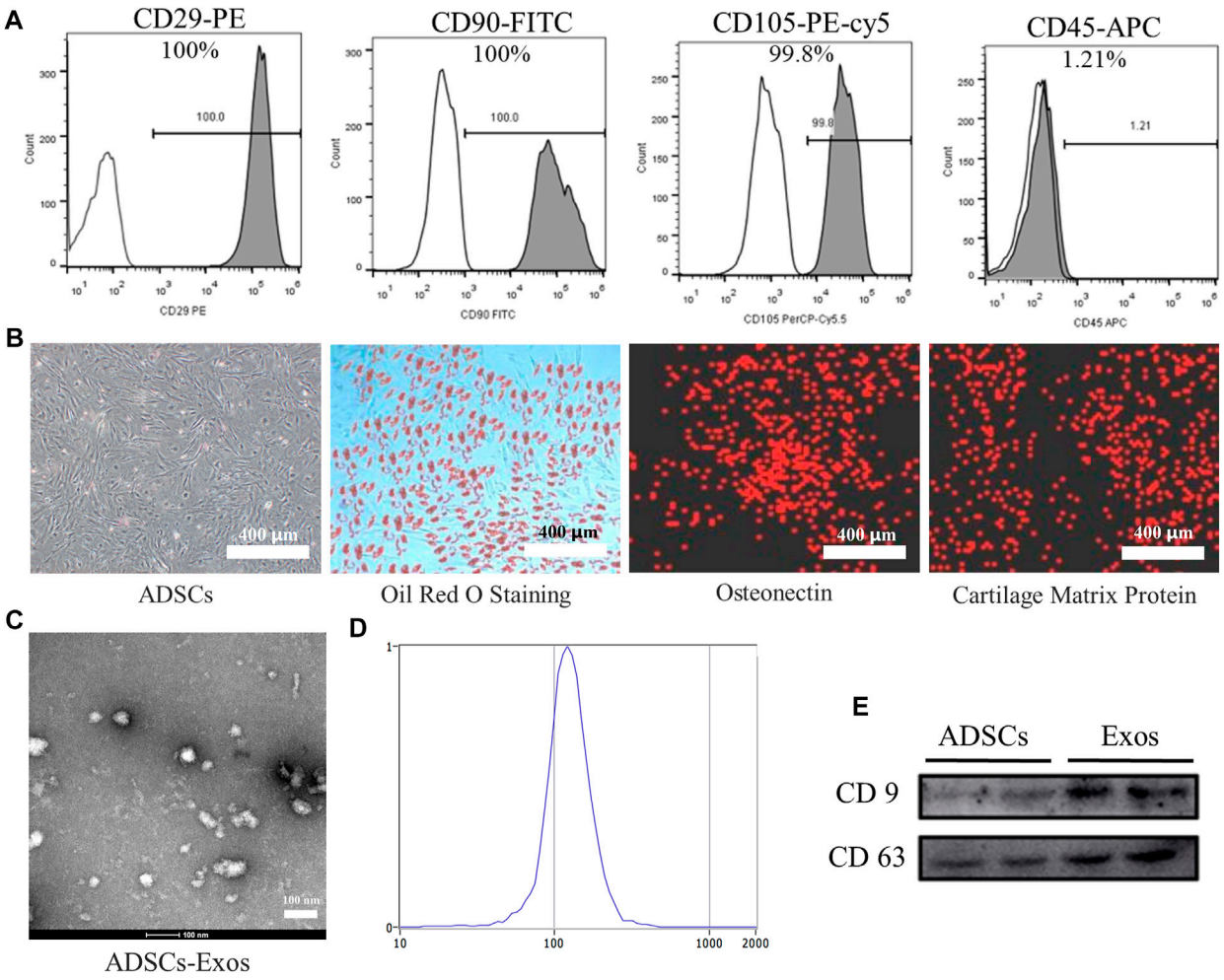

FIGURE 1
Identification of ADSCs and ADSCs-Exos. **(A)**. Characterization of ADSCs marker expression by flow cytometry analysis. ADSCs stained with CD29-PE, CD90-FITC, CD105-PE-cy5, and CD45-APC antibodies, respectively. **(B)**. Undifferentiated and differentiated ADSCs. Phenotypic characterization of ADSCs at high confluency; ADSCs were induced to differentiate into adipogenic cells under adipogenic differentiation conditions for 21 days and stained positive for Oil Red O; Under osteogenic differentiation conditions, ADSCs formed Calcium crystals and expressed osteonectin by immunofluorescence stained; Under chondrogenic differentiation conditions, ADSCs differentiate into chondrogenic cells and immunohistochemical stained positive for cartilage matrix protein. (200×) **(C)**. Morphology of exosomes derived from ADSCs (ADSCs-Exos) observed by transmission electron microscopy (TEM). **(D)**. Particle size distribution of ADSCs-Exos measured by nanoparticle tracking analysis: the diameter of exosomes mainly distributed at 80–180 nm; the peak value is 122.1 nm. **(E)**. Western blots of exosomal protein of ADSCs-Exos. Blots were probed using antibodies against CD9 and CD63.

ADSCs-derived exosomes promote BMSCS proliferation, migration, and osteogenic differentiation

Recent research has found that exosomes are the key substance of the paracrine function of stem cells for participating in the repair process of various tissues. Therefore, exosomes may be an ideal material to improve the osteogenic differentiation ability of stem cells.

The CCK-8 assay was used to determine whether ADSCs-derived exosomes affects the proliferation activity of BMSCs. Compared with the Exos-L and CON group, the OD value of Exos-H increased significantly at 4 and 7 days, and the results showed that ADSCs-derived exosomes could promote the proliferation of BMSCs (Figure 2A). After BMSCs were treated with Exos and stimulated for 12 h, the scratch test results showed that the migration distance of BMSCs cells in the Exos-H group was longer than that in the Exos-L group. The mobility of Exos-L was (28.33 ± 3.05) %. The migration rate of Exos-H was (45.67 ± 3.51) %, which was statistically significant compared with the migration rate of the CON group (15.00 ± 3.00) % (Figure 2B). The result suggests that ADSCs-derived exosomes can promote the migration of BMSCs cells. And the effect is related to the number of exosomes particles. ARS staining and quantitative analysis showed that compared with Exos-L and CON, the Exos-H group had the most significant number of mineralized nodules. And ADSCs-derived exosomes could promote the mineralization of BMSCs as the concentration increases (Figure 2C). The expression level of ALP in BMSCs treated by ADSCs-derived exosomes during osteogenesis induction was detected to evaluate whether the exosomes promoted osteogenic differentiation. The results showed that ADSCs-derived exosomes could promote BMSCs osteogenic differentiation, which is related to the exosomes concentration (Figure 2D). Further RT-PCR results showed that ADSCs-derived exosomes could increase mRNA

10.3389/fbioe.2023.1096390

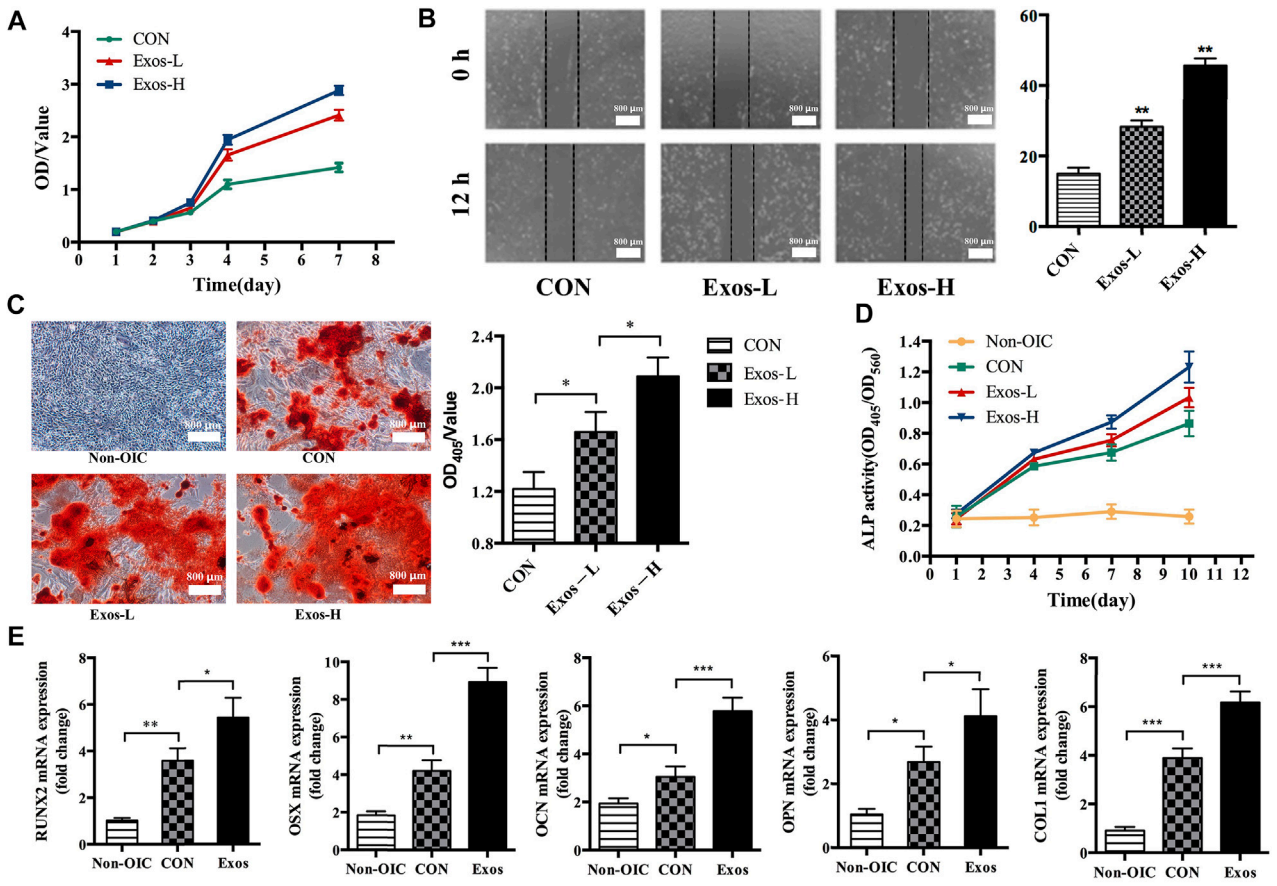

FIGURE 2
ADSCs-Exos promote the proliferation, migration, and osteogenic differentiation of BMSCs. **(A)**. CCK-8 assay showed that BMSCs treated by Exos-H (1×10^{10} particles/ml) cultured grows faster with culture days as compared to Exos-L (1×10^{9} particles/ml) or CON in conditioned-media. **(B)**. The scratch wound assay of BMSCs treated with Exos-H, Exos-L, and CON, respectively. By 12 h, the scratch test results showed that compared with the CON group, BMSCs had longer migration distances in both Exos-H and Exos-L groups. **(C)**. Microscopic images showing the formation of mineralized nodules. The number of BMSCs in the normal medium (NON-OIC) group increased gradually within 21 days, but no mineralized nodules observed. On day 21, mineralized nodules were found in CON, Exos-L, Exos-H groups by ARS staining. Among them, the number of mineralized nodules in Exos-L, Exos-H group is larger than that in CON, and the Exos-H group has the most mineralized nodules. **(D)**. The activity of alkaline phosphatase (ALP) in BMSCs was detected at 1, 4, 7, and 10 days. The ALP activity of Exos-L and Exos-H group was significantly higher than that of the CON group at the time points of 7 and 10 days, and there was a significant difference between the groups of Exos-L and Exos-H. **(E)**. The effect of ADSCs-Exos on osteogenic differentiation related genes, including RNUX2, OSX, OCN, OPN, and COL1a. BMSCs from ADSCs-Exos group cultured in OIC medium for 10 days high expressed mRNA of osteogenic differentiation related gene. (*, $p < 0.05$; **, $p < 0.01$; ***, $p < 0.001$).

expression of runt-related transcription factor 2 (Runx2), Osterix (OSX), osteocalcin (OCN), osteopontin (OPN), and Collagen type I (COL1) during osteogenesis induction in BMSCs (Figure 2E).

Fabrication and characterization of GS-PDA-Exos scaffolds

As shown in Figure 3A, the GS turned brown or black after soaked in DA solution and formed the PDA coating, but the GS-PDA and GS-PDA-Exos scaffolds maintained their shape as naked GS. The form of the PDA coating did not cause damage to the structure of the fibrous. Shown in SEM pictures, the surface of the GS scaffold was smooth, but that of GS-PDA and GS-PDA-Exos scaffolds exhibited increased surface roughness. Similarly, A considerable number of PKH-67-labeled exosomes (green dots) could be found on the surface of the scaffolds with the confocal scanning microscopic imaging. The cumulative release curve of the amount of ADSCs-Exos released from GS-PDA-Exos scaffolds is shown in Figure 3B; the ADSCs-Exos showed burst release within 3 days, followed by a relatively slow release until 7 days.

GS-PDA-Exos scaffold promotes osteogenesis differentiation of rat BMSCs in Vitro

The proliferation of rat BMSCs were compared at days 1, 2, 3, 4, and 7. The cell proliferation of BMSCs increased with time within the 7 days monitoring span. Compared with GS and GS-PDA scaffolds and control groups, the optical density value in the GS-PDA-Exos scaffold group was significantly higher from the fourth to seventh day (Figure 4A). The migration ability of BMSCs with GS-PDA or GS-PDA-Exos was enhanced (Figure 4B). Alizarin Red S staining showed

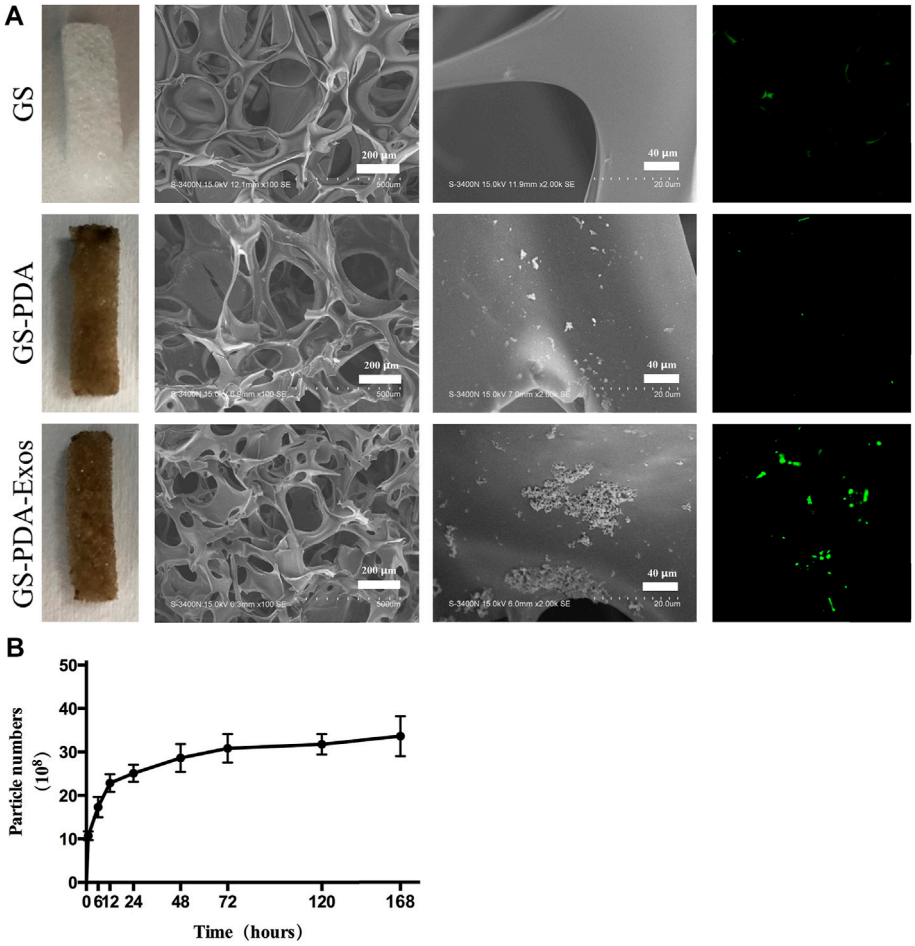

FIGURE 3
Characterization of GS-PDA-Exos scaffolds **(A)**. Three scaffolds including gelatin sponge (GS), GS with the polydopamine coating scaffold (GS-PDA), and ADSCs-Exos modified GS-PDA scaffold (GS-PDA-Exos) were prepared. Scanning electron micrographs showing the surface morphology of the scaffolds. The adhesion of PKH67 labeled ADSCs-exos on GS-PDA-Exos was observed by fluorescence microscopy. **(B)**. The release curve of ADSCs-Exos from GS-PDA-Exos scaffold.

GS-PDA-Exos significantly increased the calcified nodules and promoted BMSCs osteogenesis (Figure 4C). Compared with other groups, the ALP activity of the GS-PDA-Exos scaffold group was higher on day 7 and 10 days (Figure 4D). After cultured in OIC media for 10 days, all osteogenic differentiation-related genes of BMSCs, including RUNX2, OSX, OCN, OPN, and Col1 significantly upregulated in GS-PDA-Exos group than that in other groups (Figure 4D). These data demonstrated the GS-PDA-Exos scaffold could promote osteogenesis *in vitro*.

GS-PDA-Exos promotes bone repair in the femur defect model *in vivo*

The critical-sized femoral bone defect model of rats were made to analysis the effect of scaffolds on bone repair (Figure 5A). After 2 or 4 weeks of implantation, animals' femurs harvested for micro-CT and histological tests. In the representative HE stained sections, the defect areas were filled with newly formed tissues in GS, GS-PDA, and GS-PDA-Exos groups. On the contrary, newly formed bone tissue was observed only along the border of the defect in the control group (Figure 5B). The bone defect area of the rat femoral defect was analyzed by micro-CT. As shown in Figure 5C, GS-PDA-Exos group had obvious new bone formation as compared with other groups at 2 and 4 weeks. The quantitative analysis of all micro-CT parameters, including BMD, BV/TV, Tb.Th and Tb. Sp confirmed that GS-PDA-Exos promotes bone repair in the femur defect model *in vivo* (Figure 5D).

Discussion

The exosomes are released by most cell types and involved in a wide range of tissue regeneration, including the skin, heart, kidney, and skeletal musculature (DONG et al., 2019; GRANGE et al., 2019; MENDT et al., 2019). Taisuke Furuta et al. revealed that exosomes derived by bone marrow-derived MSCs promote fracture healing in a mouse model (FURUTA et al., 2016). In this study, we have successfully synthesized PDA coated GS for the controlled delivery of GS-PDA-Exos. We aimed here to elucidate whether ADSCs-derived exosomes could promote bone repair and whether GS-PDA-Exos could promote the new bone generation of a critical-sized defect in the

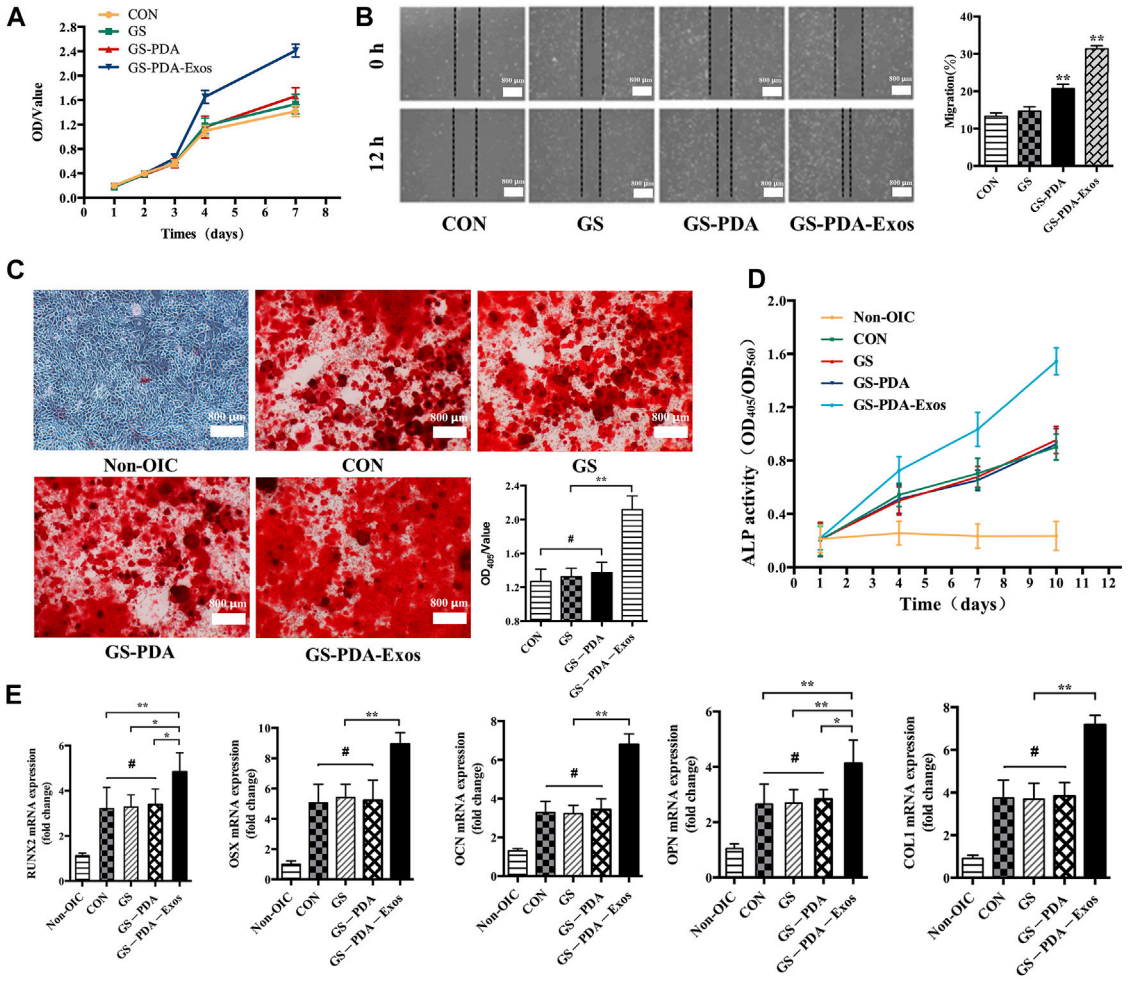

FIGURE 4
GS-PDA-Exos scaffold promotes the proliferation, migration, and osteogenic differentiation of BMSCs **(A)**. The CCK-8 assay detected the effects of GS, GS-PDA, and GS-PDA-Exos on BMSCs proliferation. **(B)**. The scratch wound assay detected the effects of GS, GS-PDA, and GS-PDA-Exos on the migration of BMSCs. Compared with the CON, GS, and GS-PDA, the mobility of BMSCs in the GS-PDA-Exos group increased significantly. **(C)**. The number of mineralized nodules of BMSCs was detected by ARS staining. The results showed a large number of mineralized nodules were observed in CON, GS, GS-PDA, and GS-PDA-Exos groups. The number of stained nodules in GS-PDA-Exos was significantly higher than that in other groups. **(D)**. The ALP activity of BMSCs was detected after exposure to the CON, GS-PDA, and GS-PDA-Exos scaffolds. The expression level of ALP in GS-PDA-Exos increased continuously within 10 days. At 4 days, it was higher than that of the CON, GS and GS-PDA groups, but there was no significant difference, while at 7 and 10 days, ALP expression was significantly higher than that of the other groups. **(E)**. Effects of materials on mRNA expression of BMSCs osteogenesis related genes (RUNX2, OSX, OCN, OPN, and Col1a) detected by RT-PCR. There was no significant difference between GS and GS-PDA and CON. Compared with other groups, GS-PDA-Exos significantly promoted the expression of RUNX2, OSX, OCN, OPN, and Col1a. ($^{\#}$, no significant difference *, $p < 0.05$; **, $p < 0.01$).

SD rat femur. Based on the *in vitro* and *in vivo* experiments, ADSCs-derived exosomes contribute to bone repair *via* inducing BMSCs osteogenic differentiation *in vitro*, and the implant of GS-PDA-Exos exerted an excellent bone healing capability in the critical-sized bone defect of the SD rat femur.

Different kinds of MSCs have been used for tissue engineering and regenerative medicine. Among these, BMSCs serve as ideal seed cells for tissue engineering in numerous studies, ADSCs share many of the characteristics of BMSCs. Meanwhile, ADSCs can be obtained more easily *in vitro* and abundant storage *in vivo*. With varies advantages, ADSCs are more applicable than other MSCs to use for tissue engineering. As shown in Figures 1A, B, the characterization of ADSCs was identified by flow cytometry and adipogenic, osteogenic, and chondrogenic differentiation, as in previous study (CHEN et al., 2019). Emerging evidence has shown the crucial roles of exosomes from MSCs promote tissue repair (CHEW et al., 2019). MSCs-derived exosomes, as a critical product of paracrine secretion, are a kind of sphere-shaped extracellular vesicle whose diameter is about 30–180 nm. Previous studies have demonstrated that exosomes secreted by human-induced pluripotent stem cells could promote bone regeneration in critical-sized calvarial defects (QI et al., 2016). Qin et al. reported that exosomes secreted by BMSCs could improve bone regeneration in a calvarial defects model (QIN et al., 2016). Thomas Thomou et al. reported that Adipose-derived exosomal miRNAs could regulate gene expression in other tissues and serve as a vital adipokine (THOMOU et al., 2017). Based on these findings, we hypothesized that ADSCs-derived exosomes could promote bone regeneration. Firstly, the exosomes were isolated from ADSCs serum-free cell medium and characterized by TEM, NTA, and western blot. (Figures 1C–E).Secondly, Our results displayed ADSCs-derived-exos

10.3389/fbioe.2023.1096390

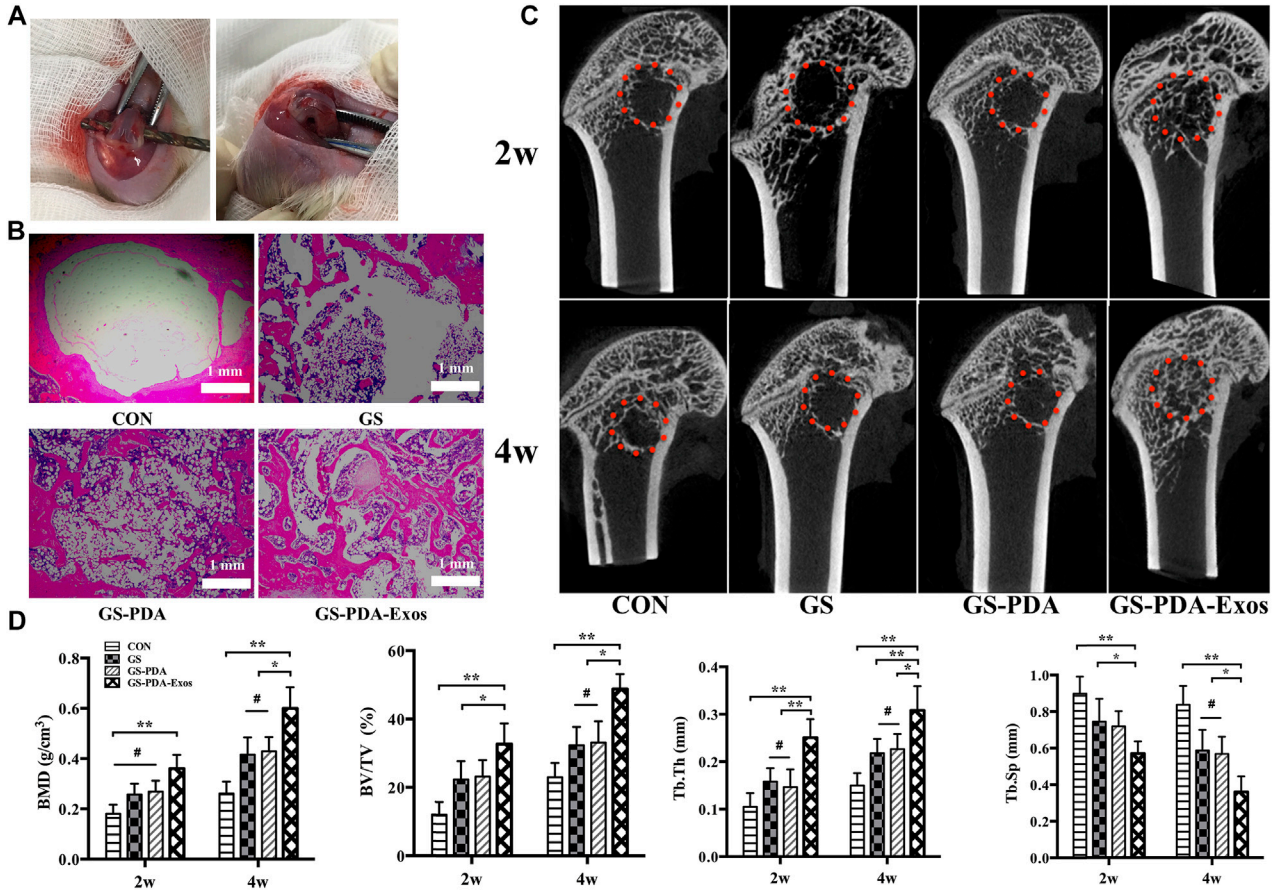

FIGURE 5
Micro-CT and histological analysis of the effect of GS-PDA-Exos on bone repair *in vivo*. **(A)**. Construction of the critical-sized femoral bone defect model of rats. **(B)**. Representative images of hematoxylin-eosin (HE) staining of the decalcification bones slice, showing the newly formed tissue, including the fibrous tissue, newly mineralized bone tissue. **(C)**. Representative two-dimensional micro-CT images showing the effect of different scaffolds (CON, GS, GS -PDA, and Gs-PDA-Exos) on the new bone tissue formation inside the defect site. The red dot line circled the region of interest (ROI). **(D)**. Summarized data showing the micro-architectural parameters of the newly formed bone tissue at 2 and 4 weeks by analyzing the micro-CT images using image analysis software. Bone mineral density (BMD), bone tissue volume/total tissue volume (BV/TV), trabecular thickness (Tb.Th), and trabecular separation/spacing (Tb.Sp) were shown in the panel. (#, no significant difference *, $p < 0.05$; **, $p < 0.01$).

effectively accelerate the migration and proliferation of BMSCs (Figures 2A, B). More importantly, ADSCs-derived-exos could significantly increase the mRNA expression of osteogenesis-related genes such as RUNX2, OSX, OCN, OPN, COL1 (Figure 2E).Similarly, ALP activity was dramatically higher in ADSCs-derived-exos groups (Figure 2D). Compared with the control group, the ADSCs-derived-exos significantly enhanced the mineralized matrix production of BMSCs when culturing for osteogenesis differentiation (Figure 2C). Our results suggested ADSCs-derived-exos effectively promote BMSCs' osteogenic differentiation.

To deal with bone defects, varies kinds of bone graft substitutes are being synthesized to promote bone repair (KOKUBO et al., 2004; CAO et al., 2014; KANDA et al., 2015). In this study, we use GS as a scaffold to combine ADSCs-derived-exos.GS is a partial hydrolysis product of collagen with excellent biocompatibility, biodegradability, and low immunogenicity. Besides this, high interconnected pores with macroporous morphology of the GS could enhance cell growth. These characteristics make GS an ideal biomaterial for tissue engineering. To better carry exosomes than usual physical adsorption methods, here we introduce the mussel-inspired PDA coating to adhere to and carry exosomes. The PDA coating has strong adhesion to various substrates and could second modification by other substrates through chemical reaction (LAVOIE et al., 2005). By this method, we synthesized a new biomaterial GS-PDA-Exos. As shown in Figure 3, exosomes could be immobilized by PDA coating and slowly released from the material.

Further, we investigated the effect of GS-PDA-Exos *in vitro* and *in vivo*. *In vitro*, Compared with other groups, GS-PDA-Exos could accelerate the migration and proliferation of BMSCs (Figures 4A, B), promote the activity of ALP (Figure 4D), increase mineralized nodules formation (Figure 4C), and significantly upregulated osteogenic differentiation-related genes, including, RUNX2, OSX, OCN, OPN, COL1 (Figure 4E). Based on these findings, we further investigated the *in vivo* osteogenesis functionality of the GS-PDA-Exos with a femur defect model of rats (Figure 5A). Consistent with the observation *in vitro*, micro-CT and histological analyses showed that the GS-PDA-Exos significantly promote bone repair in the femur defect model than the control groups (Figures 5B–D).

In summary, the present study suggests that ADSCs-derived exosomes enhance the migration, proliferation, and osteogenic differentiation of BMSCs *in vitro*, and a new tissue engineering GS-

PDA scaffold combined with ADSCs-derived exosomes significantly enhanced bone repair in the femur defect model *in vivo*.

Data availability statement

The original contributions presented in the study are included in the article/Supplementary Material, further inquiries can be directed to the corresponding authors.

Ethics statement

The animal study was reviewed and approved by Ruijin Hospital Ethics Committee.

Author contributions

GL, YZ, and JW contributed equally to this work. GL: Conceptualization, data curation, formal analysis, funding acquisition, project administration, software, supervision, validation, writing—original draft, writing—review and editing. JW: Conceptualization, data curation, formal analysis, funding acquisition, project administration, software, supervision, validation, writing—original draft, writing—review and editing. YZ: Data curation, formal analysis, funding acquisition, project administration, software. RY: Investigation, methodology, project administration, resources, software, supervision, validation, visualization. QS: Resources, software, supervision, validation, visualization. YiX: Data curation, formal analysis, investigation. BW: Data curation, formal analysis, investigation, methodology. MC: Conceptualization, data curation, formal analysis, funding acquisition, project administration, supervision. YaX: Data curation, investigation, methodology. CZ: Conceptualization, Data curation, formal analysis, funding acquisition, project administration, supervision, validation, visualization, writing—review and editing. LW: Conceptualization, data curation, formal analysis, funding acquisition, project administration, resources, supervision, validation, visualization, writing—review and editing.

Funding

This work was supported by the National Natural Science Foundation of China (82102618 and 32171317), Shanghai Municipal Health Commission Health Industry Clinical Research Project (20204Y0351), key project of "Star of Jiaotong University" Biomedical Engineering Foundation (YG2021ZD06) and Local projects guided by the central government (YDZX20213100003001).

Conflict of interest

The authors declare that the research was conducted in the absence of any commercial or financial relationships that could be construed as a potential conflict of interest.

Publisher's note

All claims expressed in this article are solely those of the authors and do not necessarily represent those of their affiliated organizations, or those of the publisher, the editors and the reviewers. Any product that may be evaluated in this article, or claim that may be made by its manufacturer, is not guaranteed or endorsed by the publisher.

References

Aghajani Nargesi, A., Lerman, L. O., and Eirin, A. (2017). Mesenchymal stem cell-derived extracellular vesicles for kidney repair: Current status and looming challenges. *Stem Cell Res. Ther.* 8 (1), 273. doi:10.1186/s13287-017-0727-7

Al-Moraissi, E. A., Oginni, F. O., Mahyoub Holkom, M. A., et al. (2019). Tissue-engineered bone using mesenchymal stem cells versus conventional bone grafts in the regeneration of maxillary alveolar bone: A systematic review and meta-analysis [J]. *Int. J. oral Maxillofac. implants*.

Annamalai, R. T., Hong, X., Schott, N. G., Tiruchinapally, G., Levi, B., and Stegemann, J. P. (2019). Injectable osteogenic microtissues containing mesenchymal stromal cells conformally fill and repair critical-size defects. *Biomaterials* 208, 32–44. doi:10.1016/j.biomaterials.2019.04.001

Caballero Aguilar, L. M., Silva, S. M., and Moulton, S. E. (2019). Growth factor delivery: Defining the next generation platforms for tissue engineering. *J. Control. release official J. Control. Release Soc.* 306, 40–58. doi:10.1016/j.jconrel.2019.05.028

Cao, L., Wang, J., Hou, J., Xing, W., and Liu, C. (2014). Vascularization and bone regeneration in a critical sized defect using 2-N,6-O-sulfated chitosan nanoparticles incorporating BMP-2. *Biomaterials* 35 (2), 684–698. doi:10.1016/j.biomaterials.2013.10.005

Chen, S., Zhu, J., Wang, M., Huang, Y., Qiu, Z., Li, J., et al. (2019). Comparison of the therapeutic effects of adipose-derived and bone marrow mesenchymal stem cells on erectile dysfunction in diabetic rats. *Int. J. Mol. Med.* 44 (3), 1006–1014. doi:10.3892/ijmm.2019.4254

Chew, J. R. J., Chuah, S. J., Teo, K. Y. W., Zhang, S., Lai, R. C., Fu, J. H., et al. (2019). Mesenchymal stem cell exosomes enhance periodontal ligament cell functions and promote periodontal regeneration. *Acta biomater.* 89, 252–264. doi:10.1016/j.actbio.2019.03.021

Dinh, T. N., Hou, S., Park, S., Shalek, B. A., and Jeong, K. J. (2018). Gelatin hydrogel coRmbined with polydopamine coating to enhance tissue integration of medical implants. *ACS biomaterials Sci. Eng.* 4 (10), 3471–3477. doi:10.1021/acsbiomaterials.8b00886

Dong, R., Liu, Y., Yang, Y., Wang, H., Xu, Y., and Zhang, Z. (2019). MSC-derived exosomes-based therapy for peripheral nerve injury: A novel therapeutic strategy. *BioMed Res. Int.* 2019, 6458237. doi:10.1155/2019/6458237

Dong, R., Zhou, Y., Huang, X., Zhu, X., Lu, Y., and Shen, J. (2015). Functional supramolecular polymers for biomedical applications. *Adv. Mater.* 27 (3), 498–526. doi:10.1002/adma.201402975

Duscher, D., Maan, Z. N., Luan, A., Aitzetmuller, M. M., Brett, E. A., Atashroo, D., et al. (2017). Ultrasound-assisted liposuction provides a source for functional adipose-derived stromal cells. *Cytotherapy* 19 (12), 1491–1500. doi:10.1016/j.jcyt.2017.07.013

Ferrandez-Montero, A., Lieblich, M., and Gonzalez-Carrasco, J. L. (2019). Development of biocompatible and fully bioabsorbable PLA/Mg films for tissue regeneration applications [J]. *Acta biomater*.

Furuta, T., Miyaki, S., Ishitobi, H., Ogura, T., Kato, Y., Kamei, N., et al. (2016). Mesenchymal stem cell-derived exosomes promote fracture healing in a mouse model. *Stem cells Transl. Med.* 5 (12), 1620–1630. doi:10.5966/sctm.2015-0285

Grange, C., Skovronova, R., Marabese, F., and Bussolati, B. (2019). Stem cell-derived extracellular vesicles and kidney regeneration. *J. Cells* 8 (10), 1240. doi:10.3390/cells8101240

Gurunathan, S., Kang, M. H., Jeyaraj, M., Qasim, M., and Kim, J. H. (2019). Review of the isolation, characterization, biological function, and multifarious therapeutic approaches of exosomes. *J. Cells* 8 (4), 307. doi:10.3390/cells8040307

Hass, R., Kasper, C., Bohm, S., and Jacobs, R. (2011). Different populations and sources of human mesenchymal stem cells (MSC): A comparison of adult and neonatal tissue-derived MSC. *Cell Commun. Signal. CCS* 9, 12. doi:10.1186/1478-811x-9-12

Hong, P., Yang, H., Wu, Y., Li, K., and Tang, Z. (2019). The functions and clinical application potential of exosomes derived from adipose mesenchymal stem cells: A comprehensive review. *Stem Cell Res. Ther.* 10 (1), 242. doi:10.1186/s13287-019-1358-y

Kanda, N., Anada, T., Handa, T., Kobayashi, K., Ezoe, Y., Takahashi, T., et al. (2015). Orthotopic osteogenecity enhanced by a porous gelatin sponge in a critical-

sized rat calvaria defect. *Macromol. Biosci.* 15 (12), 1647–1655. doi:10.1002/mabi.201500191

Kokubo, S., Mochizuki, M., Fukushima, S., Ito, T., Nozaki, K., Iwai, T., et al. (2004). Long-term stability of bone tissues induced by an osteoinductive biomaterial, recombinant human bone morphogenetic protein-2 and a biodegradable carrier. *Biomaterials* 25 (10), 1795–1803. doi:10.1016/j.biomaterials.2003.08.030

Lavoie, M. J., Ostaszewski, B. L., Weihofen, A., Schlossmacher, M. G., and Selkoe, D. J. (2005). Dopamine covalently modifies and functionally inactivates parkin. *Nat. Med.* 11 (11), 1214–1221. doi:10.1038/nm1314

Liu, A., Lin, D., Zhao, H., Chen, L., Cai, B., Lin, K., et al. (2021). Optimized BMSC-derived osteoinductive exosomes immobilized in hierarchical scaffold via lyophilization for bone repair through Bmpr2/Acvr2b competitive receptor-activated Smad pathway. *Biomaterials* 272, 120718. doi:10.1016/j.biomaterials.2021.120718

Liu, X., Wang, J., Dong, F., Song, P., Li, H., and Hou, Y. (2017). Study of composite vascular scaffold combining with differentiated VSMC- and VEC-like cells *in vitro* and *in vivo*. *J. biomaterials Appl.* 32 (2), 219–229. doi:10.1177/0885328217715363

Mendt, M., Rezvani, K., and Shpall, E. (2019). Mesenchymal stem cell-derived exosomes for clinical use. *Bone marrow Transplant.* 54 (2), 789–792. doi:10.1038/s41409-019-0616-z

Niguez Sevilla, B., Rabadan-Ros, R., Alcaraz-Banos, M., Martinez Diaz, F., Mate Sanchez de Val, J. E., Lopez-Gonzalez, I., et al. (2019). Nurse's A-phase–silicocarnotite ceramic–bone tissue interaction in a rabbit tibia defect model. *J. Clin. Med.* 8 (10), 1714. doi:10.3390/jcm8101714

Phinney, D. G., and Pittenger, M. F. (2017). Concise review: MSC-derived exosomes for cell-free therapy. *Stem cells* 35 (4), 851–858. doi:10.1002/stem.2575

Qi, X., Zhang, J., Yuan, H., Xu, Z., Li, Q., Niu, X., et al. (2016). Exosomes secreted by human-induced pluripotent stem cell-derived mesenchymal stem cells repair critical-sized bone defects through enhanced angiogenesis and osteogenesis in osteoporotic rats. *Int. J. Biol. Sci.* 12 (7), 836–849. doi:10.7150/ijbs.14809

Qin, Y., Wang, L., Gao, Z., Chen, G., and Zhang, C. (2016). Bone marrow stromal/stem cell-derived extracellular vesicles regulate osteoblast activity and differentiation *in vitro* and promote bone regeneration *in vivo*. *Sci. Rep.* 6, 21961. doi:10.1038/srep21961

Sokolova, V., Ludwig, A. K., Hornung, S., Rotan, O., Horn, P. A., Epple, M., et al. (2011). Characterisation of exosomes derived from human cells by nanoparticle tracking analysis and scanning electron microscopy. *Colloids surfaces B, Biointerfaces* 87 (1), 146–150. doi:10.1016/j.colsurfb.2011.05.013

Thomou, T., Mori, M. A., Dreyfuss, J. M., Konishi, M., Sakaguchi, M., Wolfrum, C., et al. (2017). Adipose-derived circulating miRNAs regulate gene expression in other tissues. *Nature* 542 (7642), 450–455. doi:10.1038/nature21365

Toros, T., and Ozaksar, K. (2019). Reconstruction of traumatic tubular bone defects using vascularized fibular graft. *Injury* 52, 2926–2934. doi:10.1016/j.injury.2019.08.013

Yang, Y., Cai, Y., Zhang, Y., Liu, J., and Xu, Z. (2018). Exosomes secreted by adipose-derived stem cells contribute to angiogenesis of brain microvascular endothelial cells following oxygen–glucose deprivation *in vitro* through MicroRNA-181b/TRPM7 Axis. *J. Mol. Neurosci. MN* 65 (1), 74–83. doi:10.1007/s12031-018-1071-9

Zhu, Y., Jia, Y., Wang, Y., Xu, J., and Chai, Y. (2019). Impaired bone regenerative effect of exosomes derived from bone marrow mesenchymal stem cells in type 1 diabetes. *Stem cells Transl. Med.* 8 (6), 593–605. doi:10.1002/sctm.18-0199

frontiers | Frontiers in Bioengineering and Biotechnology

TYPE Review
PUBLISHED 29 March 2023
DOI 10.3389/fbioe.2023.1133995

OPEN ACCESS

EDITED BY
Yawei Du,
Shanghai Jiao Tong University, China

REVIEWED BY
Lichen Wang,
Stevens Institute of Technology, United States
Giovanna Desando,
Rizzoli Orthopedic Institute (IRCCS), Italy

*CORRESPONDENCE
Wei Lin,
linwei@scu.edu.cn
Guanglin Wang,
wglfrank@wchscu.cn

†These authors have contributed equally to this work

SPECIALTY SECTION
This article was submitted to Biomaterials, a section of the journal Frontiers in Bioengineering and Biotechnology

RECEIVED 29 December 2022
ACCEPTED 14 March 2023
PUBLISHED 29 March 2023

CITATION
Dong C, Tan G, Zhang G, Lin W and Wang G (2023), The function of immunomodulation and biomaterials for scaffold in the process of bone defect repair: A review.
Front. Bioeng. Biotechnol. 11:1133995.
doi: 10.3389/fbioe.2023.1133995

The function of immunomodulation and biomaterials for scaffold in the process of bone defect repair: A review

Changchao Dong[1,2], Gang Tan[2], Guangyan Zhang[3†], Wei Lin[4*] and Guanglin Wang[1,5*]

[1]Trauma Medical Center, Department of Orthopedics Surgery, West China Hospital, Sichuan University, Chengdu, Sichuan, China, [2]Department of Orthopedics, West China School of Public Health and West China Fourth Hospital, Sichuan University, Chengdu, Sichuan, China, [3]Department of Respiratory Medicine, The 7th Hospital of Chengdu, Chengdu, Sichuan, China, [4]Department of Gynecology, West China Second Hospital, Sichuan University, Chengdu, Sichuan, China, [5]Department of Orthopedics, West China Hospital, Orthopedics Research Institute, Sichuan University, Chengdu, Sichuan, China

The process of bone regeneration involves the interaction of the skeletal, blood, and immune systems. Bone provides a solid barrier for the origin and development of immune cells in the bone marrow. At the same time, immune cells secrete related factors to feedback on the remodeling of the skeletal system. Pathological or traumatic injury of bone tissue involves changes in blood supply, cell behavior, and cytokine expression. Immune cells and their factors play an essential role in repairing foreign bodies in bone injury or implantation of biomaterials, the clearance of dead cells, and the regeneration of bone tissue. This article reviews the bone regeneration application of the bone tissue repair microenvironment in bone cells and immune cells in the bone marrow and the interaction of materials and immune cells.

KEYWORDS

bone regeneration, BMSCs, immune cells, biomaterials, interaction

1 Introduction

Bone is a dynamic, complex system composed of organic and inorganic matter. The inorganic mineral scaffold of bone is endowed with a high degree of plasticity and dynamism of the skeletal tissue through the mosaic of the living cells, the cellular matrix, blood, and the immune system.

The organic and inorganic components occupy approximately 30% and 70% of the bone in the biogenic hierarchical composite matrix (Behzadi et al., 2017). The inorganic component as a bone framework mainly comprises hydroxycarbonated apatite (HA) with a crystal structure (Zhang et al., 2007). Due to its high biocompatibility, engineered HA has been widely used in the biomedical research field of bone regeneration materials. Various cells [Bone marrow mesenchymal stem cells (BMSCs), osteoblasts, osteoclasts, immune cells] embedded in the lacunar steel pipe network of the inorganic framework secrete many functional proteins and extracellular matrix, such as type I collagen fibers, proteoglycan molecules, Osteopontin (OPN), Bone morphogenetic protein (BMP) (Behzadi et al., 2017), Phosphate regulating gene with homologies to endopeptidases on the X

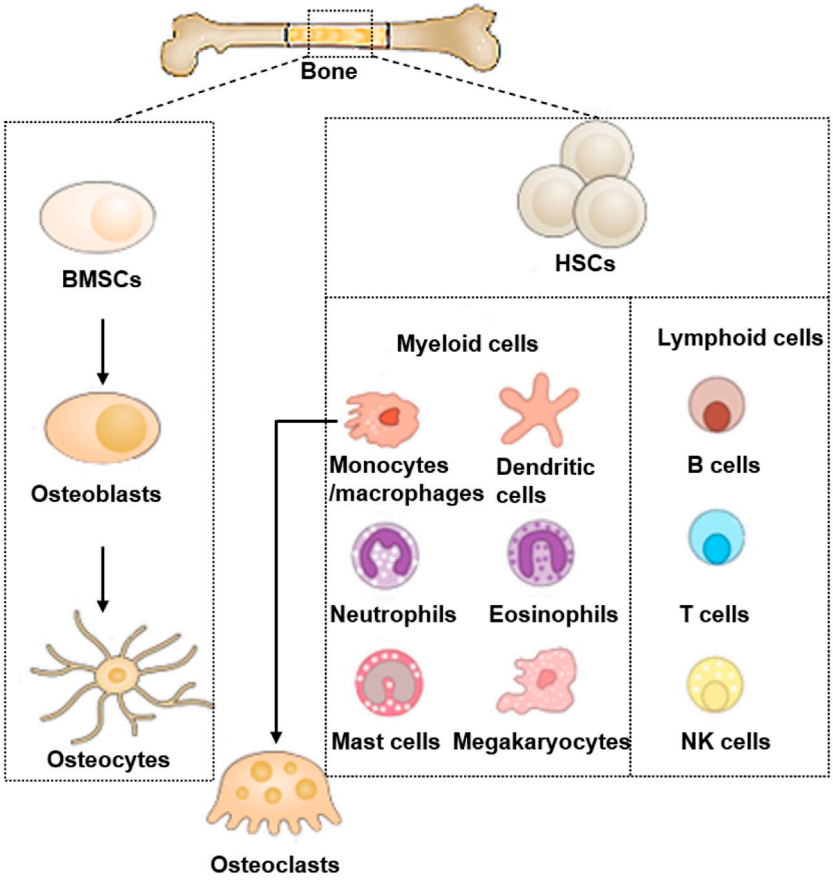

FIGURE 1
Bone cells and immune cells in bones.

chromosome (PHEX) enzyme. The extracellular matrix and signaling molecules constitute the organic components of the bone tissue framework. The delicate "sculpting" of the bone matrix and HA cavity framework by organic functional protein molecules is essential for bone growth and fracture repair.

Bone marrow is the principal place of organisms' hematopoiesis. The multi-polarized bone marrow cavity mainly contains hematopoietic stem cells (HSC), bone marrow and lymphoid progenitor cells, and mature immune cells. The immune cell population includes B, neutrophils, Macrophages, and T cells (Okamoto et al., 2017). Bone and immune cells and other cells in the bone marrow share the same variable microenvironment (Figure 1). In the complex and changeable microenvironment, they interact with each other to perform the "bone immune system" function. The prosperity of osteoimmunology as a self-governed research subject has significantly contributed to the observation of increased bone resorption in every kind of inflammatory skeleton diseases, such as Rheumatoid Arthritis (RA), Osteoporosis (OP), Osteoarthritis (OA), and periodontitis (Tsukasaki and Takayanagi, 2019).

The causes of bone resorption in RA, OP, and OA are not fully elucidated. The scientific community has summarized several reasons. Some views suggest that bone loss occurs due to dysregulation of the microenvironment surrounding these lesions, characterized by increased RANKL expression. Osteocytes, Immune cells (T cells and B cells), and Inflammatory synovial fibroblasts are thought to be important factors in the production of RANKL (Vis et al., 2013; Weber et al., 2019; Fischer and Haffner-Luntzer, 2022; Komatsu and Takayanagi, 2022). In addition, it has been reported that the increased expression of inflammatory factors (IL-6, TNF-α, etc.) is also an important cause of bone loss. On the one hand, these inflammatory factors assist RANKL in inducing osteoclast formation. On the other hand, it regulates Dickkopf-1 (Dkk-1) and sclerostin (SOST) to inhibit the Wnt signaling pathway for reducing osteoblast diffiration (Hickman and Pierson, 2016; Weber et al., 2019; Komatsu and Takayanagi, 2022). The researchers have designed a variety of excellent biomaterials to interfere with the inflammatory process in three diseases. Strontium-substituted bioactive glass (SR-BG) significantly inhibited bone loss by inhibiting p38 and NF-KB pathways downstream of RANKL (Huang et al., 2020). Chitosan, similar to the structure of biological tissue glycosaminoglycans, has made polymer and derivative forms that improve the oral utilization of the drugs of Risedronate sodium and Alendronate sodium to achieve good effects in inhibiting osteoclasts (Rahimi et al., 2022). Bioactive particles such as HAMA microspheres (Li et al., 2022), modified liposomes (Feng et al., 2020), and chitosan-modified nanoparticles (Shi et al., 2018) can be used as gene delivery vectors (IL-6-siRNA, TNF-α, etc.)

to treat arthritis and bone loss by decreasing the expression of inflammatory factors in RA and OA.

Unlike the self-repair of minor fractures, the ability to self-heal from bone damage with large defects may be limited. The migration and differentiation of osteoblast precursor cells is the key process of bone injury repair, but it is difficult for these cells to find the attachment site in the condition of large bone injury (Abbasi et al., 2020). Therefore, applying biomaterials provides a promising solution for this kind of damage. The application of Osteogenic glue and artificial periosteum has successfully repaired comminuted fracture and large bone defect models (Wu et al., 2020; Xin et al., 2020; Tang et al., 2021). These successful cases of preclinical bioactive materials will provide references for developing more clinical biomaterials applications.

The application of autologous bone, allogeneic bone, or bone substitute material has been a common strategy in the surgical treatment of bone defects. The generation of blood vessels and the invasion of osteoblast precursor cells are the keys to the successful treatment of bone defects. Insufficient vascularization and poorly cast bone matrix may lead to cell necrosis or detachment of bone substitutes (Gotz et al., 2012; Zheng et al., 2022). Thus, the coupling of angiogenesis and osteogenesis is the key to the successful repair of bone defects. Autocrine and paracrine factors determine the interaction between osteogenesis and angiogenesis. Factors such as Vascular endothelial growth factor (VEGF), Hypoxia-inducible factor (HIF), and Osteopontinntin can act bidirectionally on endothelium and osteoblasts (Gotz et al., 2012). It is beneficial for angiogenesis and new bone formation. Materials biologists have combined these factors to design a variety of advanced biomaterials that are different from conventional implantation therapy. Cross-linked engineered VEGF (TG-VEGF) modified fibrin matrix significantly promoted early vascular invasion and osteogenic differentiation of critical-size skull defects (Burger et al., 2022). In addition, exosomes from BMSCs carrying HIF-1α load onto traditional β-TCP scaffolds contribute to new bone regeneration and Neovascularization in critical-size bone defects (Ying et al., 2020). With the further study of bone immunology, the combination of immune factors has been introduced into new bioactive scaffolds for osteogenesis and angiogenesis. 3D-printed PCL scaffolds of Plla electrospun microfiber (3D-M-EF) and nanofiber (3D-N-EF) composites have the ability to modulate macrophage M2 polarization, and VEGF and BMP-2 are secreted by M2 to promote angiogenesis and osteogenesis of rat skull defect (Liu et al., 2021). Various metal particles have been studied for the interaction between immune cells and bone regeneration (Zhao et al., 2021a; Wan et al., 2022; Wu et al., 2022; Li et al., 2023). Therefore, the intervention of immune microenvironment materials will open a new chapter for the repair strategy of bone regeneration.

Innovation in biomedical technology will provide a better basis for bone defect repair, 3D printing technology has been successfully applied to materials science, optics, Robotics and chemistry, and other scientific fields. With the application of 3D printing in biomedicine, it has been successfully applied to print living cells or specific tissues, but there are some challenges in the application of 3D printing technology. The choice of printing ink determines its Biocompatibility and cellular distribution. In addition, changes in forced shear and photothermal induction during 3D printing may have a greater impact on cell viability. The biggest problem with 3D printing is that it cannot respond to the biological needs of the tissue. These reasons led to the development of 4D bio-printing technology. Materials scientists have studied 4D bio-printing techniques that are programmable, multi-material combinatorial, and bio-tissue responsive to adaptation. Although the 4D printing technology has great challenges in easy manufacturing, economy, and extensibility, its considerable biomedical application prospect is worth paying attention to (Osouli-Bostanabad et al., 2022).

Various immune cells (T, B, Dc) regulate bone homeostasis. Moreover, Various molecules (cytokines, chemokines, and signaling molecules) in the bone microenvironment are regulated and utilized by various cells in the bone marrow (Okamoto et al., 2017). In addition, A growing body of evidence suggests that bone and immune cells regulate each other to regulate hematopoietic function further. Regarding the evolutionary perspective, the simultaneous development of acquired immunity and the skeletal system maybe lead to shared mechanisms and close the effect of skeletal cells and immune cells. Further, various cells and molecules interact with each other to regulate their development.

The interaction between the immune system and the biological material relies on the relationship between the graft and the surrounding tissues, mediating processes such as cell-specific innate defense and adaptive immune response. It is increasingly evident that macrophages residing in tissues or macrophages recruited from other regions play different parts in the healing stage, and the same material implanted in different parts will cause different effects (Reid et al., 2015). However, a common feature of biomaterials is to induce unfavorable immune responses, leading to excessive inflammation, tissue destruction, healing disorders, fibrotic encapsulation, and even isolation and rejection of medical materials. Resolving these side effects requires further exploration of the interaction between the material and the surrounding tissue microenvironment, which is both a challenge and an innovation.

2 Effects of the immune system on bone marrow cells

2.1 Bone marrow cells

Continuous bone remodeling occurs in the bones throughout the organism's life cycle. Osteoblasts, osteoclasts, and osteocytes work together to complete the dynamic bone remodeling of bones (Figure 2) (Naik and Wala, 2013; Behzadi et al., 2017). Bone remodeling involves the Interplay of the time and space of osteoblast, which leads to bone formation, and osteoclast, which leads to bone resorption (Naik and Wala, 2013).

Osteoblasts are clusters of bone marrow mesenchymal stem cells covering the bone's surface. They are metabolically active and can synthesize and secret collagen and non-collagen bone matrix proteins deposited between bone cells and the surface. These uncalcified deposits are called osteoid, and the osteoid mineralization cycle is 10 days. BMSCs can differentiate into osteoblasts. The process involves the expression of Runx2 and Osterix transcription factors based on external stimuli such as Parathyroid hormone (PTH), Prostaglandin E 2 (PGE2), and Insulin-like Growth Factor (IGF) (Tsukasaki and Takayanagi,

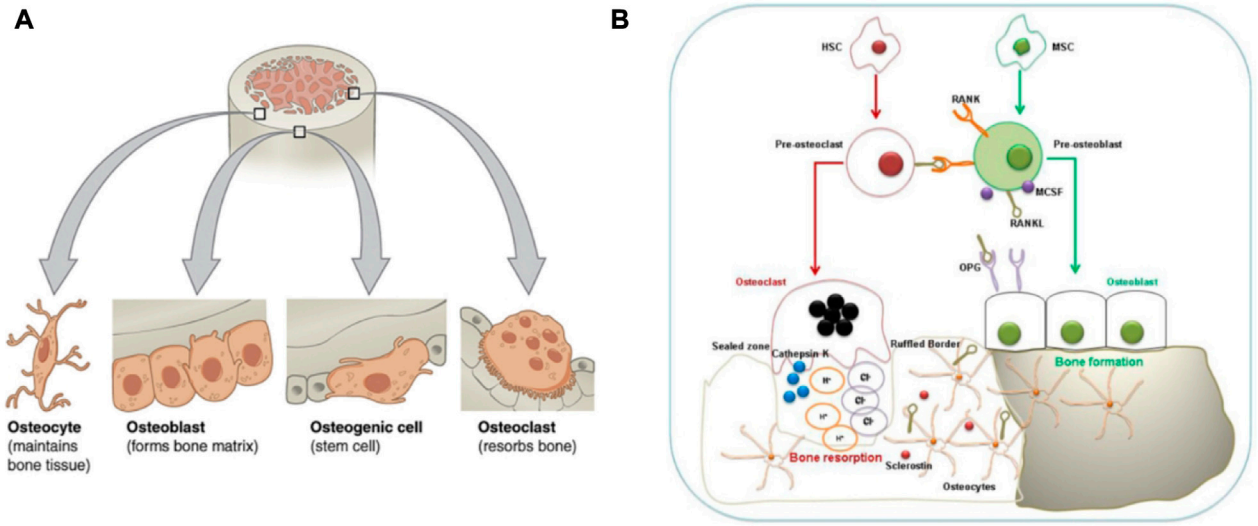

FIGURE 2
Bone remodeling and its involved cells. **(A)**:Four types of cells are found within bone tissue. **(B)**: Interaction between Osteoblasts-Osteoclasts-Osteocytes during bone remodeling. The graph was reprinted with permission from (Behzadi et al., 2017) and (Dar et al., 2018).

2019). Moreover, BMP-2 and Wnt signal pathways are responsible for osteoblast or BMSCs differentiation.

Osteocytes connect through a small tube connected to the bone surface and form a network, the dense signal communication path in the bones. Osteocytes are derived from bone osteoblasts, then wrapped in the bone matrix. However, Osteocytes begin to express some specific genes, but osteoblasts do not express these genes. Sclerostin is a product of osteocytes, which can bind to low-density lipoprotein receptor-related protein (LRP) and inhibit the Wnt signal pathway to reduce bone formation (Poole et al., 2005). Function Sclerostin (SOST) gene encoding sclerostin mutations results in an increased bone mass loss in humans, called sclerosis.

Osteoclasts originate from HSCs. HSCs first develop into monocytes. Then monocytes develop into mature osteoclasts under the stimulation of related factors. Osteoclast production requires macrophage colony-stimulating factor (M-CSF) and receptor activator of nuclear factor-κ B ligand (RANKL) as induction signals. Osteogenic precursor cells, stromal cells, and synovial endothelial cells express M-CSF and RANKL to induce osteoclastogenesis. Along with BMMs, they differentiate and form mature osteoclasts. At this time, osteoclasts also begin to express specific genes and fuse. Moreover, RANKL is expressed on preosteoblasts and activated T cells (Wada et al., 2006; McInnes and Schett, 2007). RANKL combines its receptor RANK with pro-osteoclast cells, which is grave for the differentiation of osteoclasts and their bone resorption capacity. The interaction between RANKL and RANK is regulated by the RANKL competitive receptor OPG, which inhibits osteoclast production *in vitro* and *in vivo*. In addition to the RANKL and RANK affecting each other, other key pro-osteoclast signaling pathways depend on trigger receptors (TREM) expressed on bone marrow cells. The OSCAR and the tyrosine kinase DAP12 interact with triggering receptors expressed on myeloid cells (TREM), which strongly promotes osteoclastogenesis (Barrow et al., 2011).

2.2 Immune system

The immune system is essential for organisms to defend against foreign objects. In addition, the invasion of pathogens can also stimulate the evolution of the immune system. The body's adaptability and innate immune response participate in this process. As mentioned above, both immune and bone cells are present in bone. Meanwhile, the two systems influence each other (Lee et al., 2019) (Figure 3A). Bone cells and their surrounding environment secrete chemokines [Macrophage chemoattractant protein-1 (MCP-1), Stromal cell-derived factor 1 (SDF-1), etc.] that attract the arrival of immune cells, which subsequently secrete cytokines (RANKL, IL-1, IL-6, IL-10, TNF-α, etc.) that affect the development of bone cells. Thus, basic and clinical researchers explore the interaction between immune cells and their factors with bone cells (Naik and Wala, 2013). Although immune cells are various, they originate from a common ancestor-HSCs. HSCs are finally differentiated into T cells, B cells, macrophages, NK cells, and neutrophils through pluripotent stem cells, myeloid stem cells, and lymphoid stem cells and enter different tissues or organs with the bloodstream to exert their physiological functions further.

2.2.1 Macrophages

Macrophages belong to the mononuclear phagocytic cell system. They also originate from HSCs. In the bone marrow, HSCs develop into monocytes through immature monocytes, enter connective tissues and other organs with the bloodstream, and then turn into macrophages. The body's homeostasis processes include inflammation, foreign body removal, and bone tissue repair (Figure 3B) based on macrophages' differentiation and function (Xie et al., 2020).

Macrophages are a class of highly plastic immune cells whose main function is to play the role of phagocytosis. It engulfs foreign

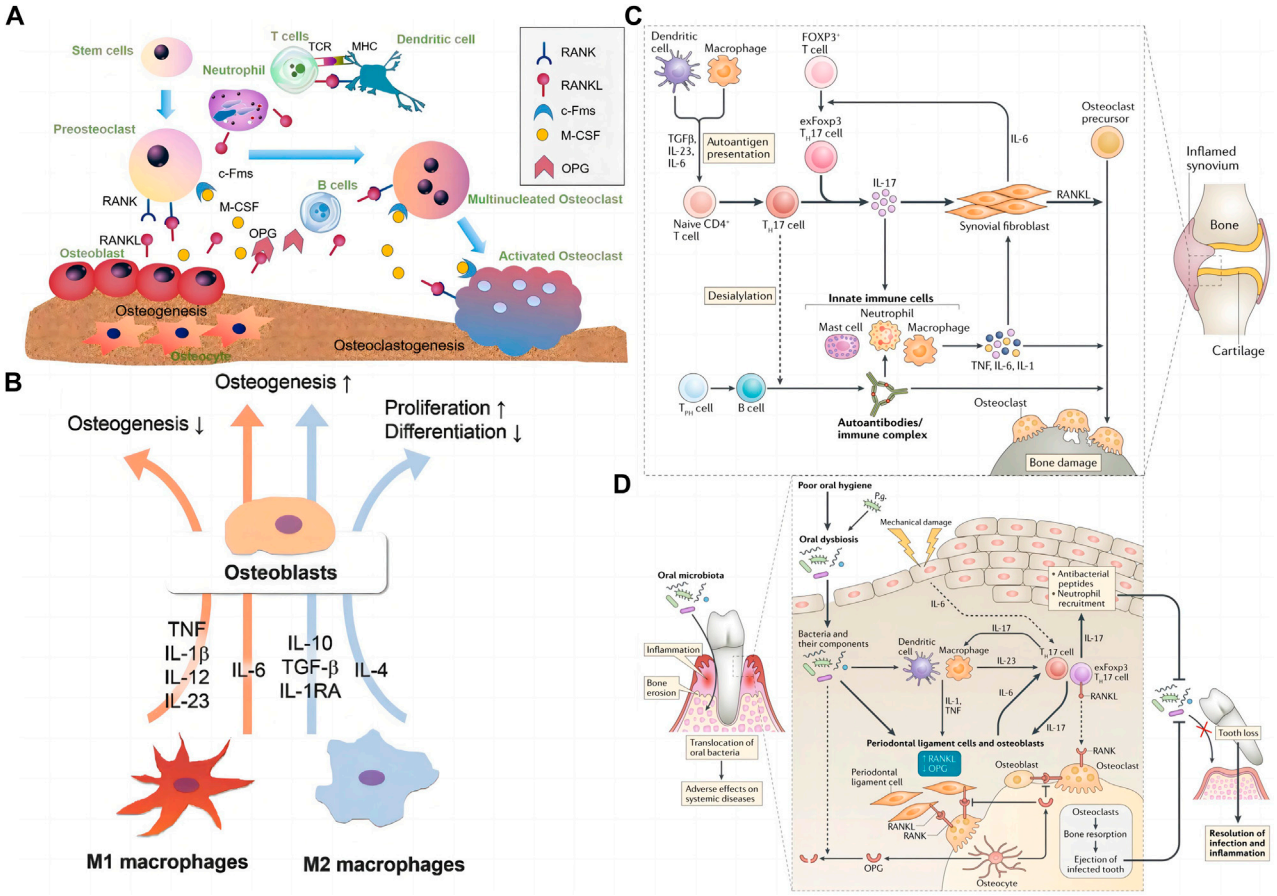

FIGURE 3
The interaction of the skeletal system and the immune system. **(A)** Interaction between skeletal and immune cells by secreting related factors, the graph was reprinted with permission from (Xie et al., 2020). **(B)** M1 and M2 interact with osteoblasts through cytokines such as IL-6, IL-23, IL-10, and TGF-β. The graph was reprinted with permission from (Lee et al., 2019). **(C)** T cells, macrophages, and neutrophils' role in rheumatoid arthritis-induced bone erosion, the graph was reprinted with permission from (Tsukasaki and Takayanagi, 2019). **(D)** The role of T cells, macrophages, and DCs, in bacterial periodontitis-induced bone erosion, the graph was reprinted with permission from (Tsukasaki and Takayanagi, 2019).

bodies (bacteria, viruses, nanoparticles, etc.) that invade the organism and engulfs the dead and apoptotic cells it produces. Phagocytosis of different substances by macrophages produces different body responses. Macrophages form the "classical activated" M1 phenotype after phagocytosis of pathogens and dead cells, which mainly plays a pro-inflammatory role, whereas, when macrophages engulf apoptotic cells, they mainly form "alternatively activated" M2 phenotype, which promotes tissue repair by secreting repair factors such as IL-10 and TGF-β (Xie et al., 2020; Schlundt et al., 2021). In bone defect repair, plasma proteins and foreign bodies attract macrophages to the defect. In the early phase of inflammation, macrophages transform into M1 macrophages, which in the early phase play a clearing role of foreign bodies and dead cells, and subsequently, the transformation of macrophages into M2 type initiates the process of bone tissue regeneration. Therefore, the ratio of M1/M2 macrophages is a key process in the transition from inflammation to regeneration (Zhao et al., 2021b).

Compared with monocytes, multi-nucleated cells formed by the fusion of macrophages have a phagocytic affinity for significant substances. The ability of macrophages puts them at the center of the evolutionary and functional roles of the bones and immune system because monocytes can form granulomas and other giant cells in inflammation regions, and they can also fuse in bones to form large multi-nucleated cells called osteoclasts. The decision to proceed with osteoclast forming is only controlled by the local cells factor environment of RANKL (Dar et al., 2018). Part of macrophages participate in the fight against harmful damage at the site of tissue inflammation; they can perform multiple functions. Inflammatory macrophages can clear apoptotic cells, proliferate and resident matrix, infiltrate white blood cells, and kill parenchymal cells (Naik and Wala, 2013). In addition, heterotopic bone formation in fibrodysplasia ossificans progressiva (FOP) patients is thought to be triggered by inflammation such as macrophages and mast cells l (Convente et al., 2018).

2.2.2 T cells

T cells are lymphoid stem cells derived from the bone marrow. They are a group of cells that develop and mature after migrating into the thymus. It mainly includes CD4 T cells and CD8 T cells. CD4 T cells mainly develop into Th cells. Naïve Th cells can transform into subgroups according to the antigens and cytokine

stimuli they receive during activation. And then, Th cells can be well divided into four subgroups, namely, Th1, Th2, Treg, and Th17 cells. Unactivated Th cells can inhibit the formation of osteoclasts *in vitro* (Toraldo et al., 2003) or *in vivo* (Li et al., 2007). Under steady-state conditions, Th cells cannot secrete RANKL (Dar et al., 2018). In contrast, the activation of T cells under inflammatory conditions can lead to increased production of RANKL and Tumor Necrosis Factor-α (TNF-α), which promote osteoclast production and bone loss under kinds of inflammatory and autoimmune conditions (Colucci et al., 2004), such as periodontitis (Brunetti et al., 2005), cancer (Colucci et al., 2004) and osteoporosis (Faienza et al., 2009). However, not all kinds of T cells can activate osteoclasts. It is reported that $CD8^+$ T cells have osteoprotective effects. $CD8^+$ T cells can inhibit osteoclastogenesis by secreting OPG (Dar et al., 2018).

Th1 cells can secret Interleukin-2 (IL-2), Interleukin-12 (IL-12), interferon-γ (IFN-γ), and TNF-α to participate in the clearance of pathogens. Moreover, Th2 cells can secret IL-4, IL-5, IL-6, IL-9, and IL-13 cytokines to participate in the clearance of parasitic infections, extracellular microorganisms, and allergic diseases. It is now known that Th1 and Th2 cells can inhibit the formation of osteoclasts in different populations by secreting their iconic cytokines IFN-γ and IL-4, respectively (Harrington et al., 2006). In the past decade, two new $CD4^+$ Th cell subgroups have been reported, which were Th17 cells (Harrington et al., 2006) and Treg cells. Rorγt transcription factor defines Th17 cells, and the Foxp3 transcription factor specifically defines Treg cells. They have been confirmed that these two kinds of Th cells are the primary T cells that regulate osteoclast production (Dar et al., 2018).

Transforming growth factor-β (TGF-β), IL-6, and inflammatory stimuli induce Naïve Th cells to transform into Th17 cells. Th17 cells produce IL-17, the hallmark factor of Th17 cells, as well as IL-22, IL-26, and IFN-γ (Harrington et al., 2006; Gao et al., 2007). Th17 cells induce osteoclastogenesis by producing IL-17, a common factor that promotes osteoclastogenesis by inducing RANKL (Adamopoulos et al., 2010). However, IL-17 can promote osteoclast production through direct and indirect action, mainly through two inflammatory factors, TNFα and IL-1 (Dar et al., 2018). These cytokines in cells enhance the expression of RANKL that support osteoclastogenesis, activating pro-osteoclast through the RANKL-rank signal pathway. In the occurrence of various bone diseases, Th17 cells are involved, such as RA (Figure 3C) (Tsukasaki and Takayanagi, 2019), periodontitis (Figure 3D) (Tsukasaki and Takayanagi, 2019), osteoporosis, and OA (Maddur et al., 2012).

It has been reported that a specific type of TH17 cells-exFoxp3TH17 cells, compared with TH17 cells, can activate osteoclasts. Treg cells express the specific molecule Forkhead Box Protein P3 (FOXP3). In arthritis animals, when CD25loFoxp3+T cells lose FOXP3 expression and start to transform into TH17 cells, inflammation stimulates IL-6 produced by synovial cells. Importantly, Foxp3+IL-17+T cells are particularly prominent in the synovial tissue of patients with active RA but not detected in the synovial fluid of inactive patients, which has been observed in membrane tissue. It indicates the pathogenic effect of exFoxp3TH17 cells in RA. Furthermore, the increase of IL-6 secreted by synovial fibroblasts contributes to the production of exFoxp3TH17 cells. In turn, the increase of IL-17 can stimulate the production of CCL20, IL-6, granulocyte-macrophage colony-stimulating factor (GM-CSF), and RANKL in synovial tissue, thereby exacerbating local inflammation and joint destruction (Hirota et al., 2018). Therefore, Bone-destructive T cells and synovial tissue's malignant circulation mechanism is an effective research field for treating bone diseases.

$CD4^+$ Treg cells and TH17 cells have opposite effects. $CD4^+$ Treg cells can suppress osteoclast differentiation and function by secreting a kind of cytokines which include TGF-β and IL-4 cytokines, in a cytokine-dependent manner. Recently, In the ovariectomized osteoporosis model, by producing IL-10 and TGF-β1, Treg cells can reduce osteoclast differentiation and bone resorption. Another reported mechanism is that Treg cells can produce Cytotoxic T Lymphocyte-Associated Antigen-4 (CTLA-4) to control immune function, bind to CD80/CD86 on pre-osteoclast cells, and inhibit inflammation (Dar et al., 2018). According to reports, oral probiotic *Lactobacillus* rhamnosus GG can stimulate osteogenesis through the Wnt process of Treg cells acting on CD8+T cells. In addition, in the process of bone healing, it is shown that Vγ6+γδ T cells produce IL-17 and promote bone formation (Ono et al., 2016). These findings demonstrate the critical role of immune cells in calcification formation.

NK T cells can clear viral infections, transformations, or abnormal cells. Activating natural NK T (iNK T) can cause active osteoclasts. In the synovial fluid of a confirmed RA patient, NK T cells account for 20% of all lymphocytes. Moreover, CD56bright NK T cell subgroups upregulate many adhesion molecules and chemokine receptors, which can help preferentially recruit NK T cells to RA In the patient's inflamed synovium. NK T cells also produce M-CSF and RANKL, which are beneficial for inducing osteoclastogenesis (Dar et al., 2018).

2.2.3 B cells

The role of B cells with other immune cells and bone cells is complex and diverse (Dar et al., 2018). B cells are differentiated from HSCs in the skeleton. The osteoblast cells, which are in the skeleton niche, can support HSC and B cell differentiation. B cells play a vital function in the pathogenesis of RA. High serum RA factor and Anti-Citrullinated Protein Ab (ACPA) are related to the course of aggressive bone injury. Immune complexes, including ACPA, have been seen to enhance osteoclast differentiation by activating Fcγ receptors on Osteoclast progenitor cells (OPCs) (Harre et al., 2015). It is a rare immune complex function separated from the host's defense environment. ACPA also accelerates osteoclast production through its Fab fragments. The citrulline epitopes on OPCs and osteoclasts bind to ACPA to stimulate TNF and IL-8 production, thereby enhancing osteoclast production in an autocrine manner (Krishnamurthy et al., 2016).

It has been reported that both B cell and B cell-derived plasma cells can express RANKL, decoy receptor 3 (DcR3), or IL-7 secretion (a potent bone resorption stimulator), which indirectly regulates osteoclastogenesis. Plasma cells derived from the tumor in patients with multiple myeloma can reduce bone formation by producing cellular molecules (like dickkopf-related protein 1 and sclerostin) (Dar et al., 2018). The lack of estrogen can cause the increase of B lymphocytes, and the corresponding treatment can inhibit the increase of B lymphocytes. Interestingly, the immature B cell population that expresses B220 can even be transdifferentiated into the osteoclast differentiation pathway under *in vitro*

conditions, which provides a source of osteoclast precursors for the bone loss caused by ovariectomy. It has been shown that the RANKL expression of B220+ cells is enhanced in ovariectomized mice. In addition, it has been reported that postmenopausal mammalian-derived B cells from the bone can secrete RANKL, and B cells have a positive role in OP, like OPG, whose lack can lead to increased osteoclast production. In addition, the effect of B and T cells can regulate the forming of many bone cell factors because B cells inhibit osteoclast production by Th1 cell activation but promote osteoclasts when it comes to Th2 cell s activation (Li et al., 2007). The two types of cells can also influence the OPG from B lineage cells through the CD40/CD40L interaction pathway, which limits basal bone resorption *in vivo* (Yamamoto et al., 2019).

2.2.4 Dendritic cells (DCs)

DCs are highly effective APCs and are key in treating pathogens and tumors mediated by cellular immunity. Under the action of immune cell CD4 T cells, mouse $CD11c^{+}$DCs can successfully transform into functional osteoclasts and induce osteoclast-mediated bone loss (Dar et al., 2018). These findings suggest the strong effect of $CD11c^{+}$DC subpopulations in osteoclast forming. The RANK-RANKL signaling pathway also plays a role in the osteoclast transformation process of DCs (Tucci et al., 2011). In addition, mature DC can promote Th17 cells to express IL-17, enhancing osteoclastogenesis (Dhodapkar et al., 2008).

2.2.5 Neutrophils

Neutrophils are derived from hematopoietic stem cells of bone marrow. After differentiation and development in bone marrow, neutrophils enter the blood or tissues. In the start stages of inflammation caused by bacterial infections, environmental exposures, and certain cancers, neutrophils are essential to innate immunity. In addition, high concentrations of RANKL are also derived from the neutrophils of the mammalian immune system, thereby activating bone loss (Dar et al., 2018). It has been further reported that neutrophils can regulate osteoblast function, leading to increased bone resorption (Brunetti et al., 2013).

2.3 Bone marrow cells regulation of HSCs and immune cells

The balance of HSCs in the bone is inseparable from the role of cytokines like Stem cell factor and chemokine C-X-C ligand12 (CXCL12). Since CXCL12 is produced in the body by abundant reticulocytes and leptin receptor-positive osteoblasts or osteoprogenitor cells instead of mature osteocytes, it is an essential source of these niche factors regulated by HSCs (Zhou et al., 2014). Immune cells originate from the bone. Osteoblasts modulate the differentiation of immune cells beyond doubt. For example, it has been reported that consuming osteoblasts' CXCL12 reduces the number of B lymphoid progenitor cells in the bone marrow. Moreover, osteoblasts express Notch ligand delta-like 4, which helps support the growth of T cell progenitor cells (Yu et al., 2015). Under certain conditions, osteoblasts may also have different roles in the process of hematopoiesis. For example, bone cell-derived Dickkopf-1 (DKK1) directly promotes hematopoietic reconstitution after bone marrow suppression by inhibiting HSCs senescence and indirectly promotes hematopoietic reconstitution by inducing the secretion of bone epidermal growth factor. It is reported that bone marrow endothelial cells (Himburg et al., 2017) and osteoblasts can regulate red blood cell production. Activated osteoblasts can weaken the development of leukemia (Krevvata et al., 2014). Activated $CD4^{+}$ T cells reduce the bone formation of osteoblasts and lead to imperfect B-cell lymphocyte production, which proves an interaction between bone and immune cells (Shono et al., 2010).

The osteoclast bone resorption produces the bone marrow cavity where the secretion of osteoblasts, bone cells, and other cells are attached. Due to the abnormal balance of osteoclastic and osteogenic differentiation in osteosclerotic animals, there is insufficient space in the bone marrow to support the differentiation of hematopoietic cells, ultimately leading to abnormal extramedullary hematopoiesis in the spleen and liver. This abnormal process is detrimental to the formation of immune cell differentiation and function (Okamoto et al., 2017). Patients with bone sclerosis may appear with anemia and infections due to abnormal hematopoietic function (Sreehari et al., 2011). Therefore, the cavity microenvironment formed by osteoclast resorption is necessary for normal functional hematopoiesis. Moreover, osteoclasts play a certain role in the mobilization of HSCs.

3 Interaction of materials and immune cells

3.1 Biomaterials

With the development of biomaterials, their status in medical care is getting higher and higher. At the same time, many new disciplines have been produced, and huge development and applications have been achieved, such as medical implants, drug delivery, tissue engineering, and immunotherapy (Vishwakarma et al., 2016; Roseti et al., 2017). Biomaterials include a series of compounds with very different functions and structural characteristics, from macromolecules taken from nature to completely synthetic nanoparticles. Biomaterials should be mechanically resilient, Biocompatibility, or capable of degradation in the time required for bone cell colonization and mineralization. Biocompatibility is the primary target of choice for bone implant materials. Moreover, bone is a load-bearing organ with certain mechanical strength, and biomaterials with the same Young's modulus as bone are highly sought after. For repairable bone injuries, biomaterials are generally selected to be biodegradable at a rate comparable to the bone healing cycle (Borchers and Pieler, 2010; Gorejová et al., 2018; Zhu et al., 2022).

There are many classification methods for biomaterials, which are classified into natural polymers and synthetic polymers according to polymers. The most commonly used tissue regeneration materials, especially orthopedics materials, like synthetic polymers, ceramics, and natural polymers (Mariani et al., 2019). Ceramic materials (glass, alumina, zirconia, calcium phosphate) are mainly used in orthopedics, dental implants, and bone filling. They have the characteristics of low elasticity, high-temperature resistance/hardness, and high brittleness. The chemical structure and physical properties similar to natural bone tissue show

TABLE 1 The effects of material properties on cell behavior.

Biomaterials	Features	Function	Ref
PCL/P3ANA-RGD nanofibers	Higher surface area and better mechanical properties	Favored cell attachment, proliferation, and osteogenic activity	Guler et al. (2017)
Laminin–PHB fibrous	Simulation of surface morphology and chemical composition of extracellular matrix (ECM)	The adhesion and proliferation of nerve cells are promoted	Sangsanoh et al. (2017)
PEDOT/Cs/Gel scaffolds	The incorporation of PEDOT on the scaffold increased the electrical conductivity, hydrophilicity, mechanical properties, and thermal stability	The adhesion and proliferation of neuron-like cells are promoted	Wang et al. (2017)
PLGA-GNP fibers	Poly (lactide-co-glycolide) (PLGA) can effectively control the loading of gold nanoparticles (GNP)	Osteogenic differentiation of human adipose-derived stem cells is increased	Lee et al. (2018)
β-Tricalcium phosphate (TCP) scaffolds decorated with polydopamine nanoparticles PDA-NPs	Affinity for a variety of proteins and peptides	Excellent osteoinductivity and bone-regeneration	Wang et al. (2016)
Cylindrical PVA hydrogel	Stiffness gradient	Investigate the effects of substrate stiffness on stem cell differentiation into specific cell types	Kim et al. (2015)
Randomly-oriented fibrous scaffolds	Different topographic materials utilized as bio-scaffolds *in vivo*	Cytoskeletal tension release abrogated the divergent differentiation pathways on different substrate topography	Yin et al. (2015)

Biomaterial polymers include natural and synthetic biomaterial polymers (Wei et al., 2020) (Table 2).

TABLE 2 Classification of biological materials.

Natural biomaterial polymers	Synthetic biomaterial polymers
Collagen	PCL, PGA
Chitosan	PLGA, PHB
Fibrin	Biodegradable Ceramics
Silk Fibroin	Bioactive glasses and biodegradable metals

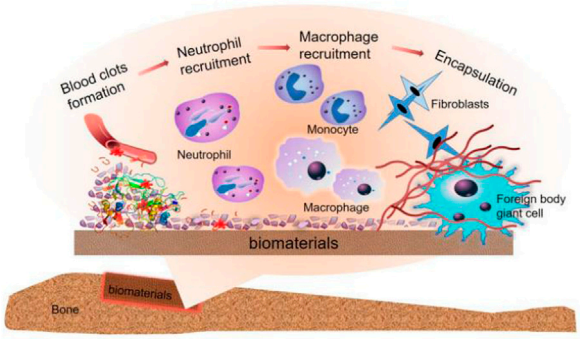

FIGURE 4
Immune cascade after bone implant material, the graph was reprinted with permission from (Xie et al., 2020).

good biocompatibility (Mariani et al., 2019). Synthetic polymers as promising biomaterials for bone tissue engineering research and use. Moreover, natural polymers similar to natural ECM make them great biocompatible. They combine synthetic and natural polymers' advantages, including immunological properties. The morphology and physical properties of the materials have different effects on cell behavior (Table 1). With the development of material technology, biodegradable biomaterials are particularly popular in bone tissue engineering.

The most common natural biomaterial polymers are collagen, chitosan, fibrin, and silk fibroin, which have good histocompatibility and low immunogenicity due to their close similarity to animal tissue components. Decomposition products are also the best raw materials for the body's biosynthesis, so they are prevalent in tissue engineering. However, these single materials have poor mechanical strength and rapid degradation, and their application in bone tissue is limited. Therefore, these materials are often combined with bioceramics and synthetic polymers.

Synthetic biomaterial polymers such as poly(ε-caprolactone) (PCL), polylactic acid, PGA, copolymer PLGA, poly(3-hydroxybutyrate) PHB, biodegradable ceramics, bioactive glasses, and biodegradable metal materials, which are biocompatible and have a controllable rate of degradation, and their degradation products have no toxic effects on tissues *in vivo*. Moreover, manual control of design and synthesis parameters can produce polymers with better mechanical properties.

3.2 Immune cell responses to biomaterial implants

Preparing the materials mentioned above into biodegradable composite materials is the focus of current research. These composites possess excellent biocompatibility, osteoconductivity, mechanical strength, and osteogenic properties. Meanwhile, these composite materials have become the most promising materials in bone defect repair with the help of new preparation technologies that have emerged in recent years. A systematic understanding of the specific processes of materials in bone regeneration in the emergency immune response is the practical basis for designing

composite materials for immune cell regulation (Xie et al., 2020) (Figure 4).

The implant is placed a second later, and blood from the damaged blood vessel surrounds the biomaterial and begins interacting with the graft. And then, Plasma contents of the body, including proteins (fibrinogen, albumin, vitronectin, fibronectin, gamma globulin), attach to the implant surface quickly and autonomously (Wilson et al., 2005). These are affected by the process, quantity, composition, and conformational changes of adsorbed molecules of biological materials.

The clot formed by blood exudate defines the temporary matrix surrounding the biological material (Ekdahl et al., 2011) and is cleaved into fibrin by thrombin. Moreover, the complement protein is activated when it comes into contact with biological materials to support platelet adhesion and activation. The recruitment and adhesion of sufficient immune cells are seduced by abundant pro-inflammatory cytokines, chemokines, and growth factors (Anderson et al., 2008), and with the formation of the temporary matrix, acute and chronic inflammation also follows.

The chemokine produced by the host cell or damaged tissue induces activated neutrophils to be recruited from the peripheral blood and adhere to the implantation site (*via* β2 integrin). It also attempts to produce engulfing proteolytic enzymes and ROS to destroy/degrade biological materials (Grandjean-Laquerriere et al., 2007).

After neutrophils are activated, they will synthesize a large number of immunomodulatory signals (Mariani et al., 2019): CXCL8 (the most significant chemokine, the main target of which is the neutrophil itself), CCL2 (C Chemokine ligands2), and CCL4. CCL2 and CCL4 are both effective chemotactic and activating factors for immune cells (Yamashiro et al., 2001). The gradual increase of these chemokines promotes the infiltration of monocytes and inhibits the infiltration of neutrophils. The lack of this signal cannot further activate neutrophils, enter the apoptotic pathway, and then be cleared from the site by phagocytes (Anderson et al., 2008). At the same time, circulating monocytes respond to chemotactic agents and bind to the fibrinogen in the temporary matrix of biological materials, thereby being activated (Shen et al., 2004) and differentiated into classical activation or "M1" macrophages (Mariani et al., 2019). The classification of these cells is based on the secretion of IL-1β, IL-6, TNF-α, chemokines (Jones et al., 2007; Mesure et al., 2010), and enzymes.

Macrophages induce invasion of inflammatory cells *via* CCL2, CCL4, and CXCL8 (Jones et al., 2007), and before experiencing the "frustrated" phagocytosis (because the biological material is too large), they try to decompose the biological materials by producing ROS and releasing degrading enzymes (Mariani et al., 2019). This pathway eventually leads to increased cytokine release (Underhill and Goodridge, 2012). Like the wound healing stage (Mariani et al., 2019), the adherent macrophages may eventually transfer to the "M2" phenotype (Mariani et al., 2019), which secrete IL-10 and so on (various anti-inflammatory cytokines). These cytokines can reduce their degradation ability, complete body activity reproduction, induce fibroblast movement and proliferation, and then achieve bone regeneration. Conversion between M1 and M2 and the mechanism of blocked phagocytosis leads to the fusion of macrophage membranes and the formation of foreign body giant cells (FBGCs), a sign of chronic inflammation on the coverage of biological materials. FBGCs formation is usually a landmark part of Foreign body reaction (FBR) induced by biological materials. It promotes the formation of FBR by activating mast cells, basophils, and Th cells. These cells can produce IL-4 and IL-13, enhancing the fusion of macrophages on biological materials (Brodbeck et al., 2005).

In the chronic inflammatory stage, some cytokines are secreted by Th cells. Their rich cytokines produce a wide range of regulation of pro-inflammatory or anti-inflammatory sequels (Mariani et al., 2019). The interactions between M1 and M2 macrophages and the changes of Th1 to Th2 cells express cell factors, indicating that T cells play a vital role in promoting the resolution and regeneration of inflammation.

The synergy of immune cells induces the production of pro-fibrotic factors, such as Platelet-derived growth factor (PDGF) (Shen et al., 2006), vascular endothelial growth factor (VEGF) (Chen et al., 2010), and TGF-β (Garg et al., 2009), which can recruit some fibroblasts. Experimental repair of damaged tissue, activated type I and type III collagen. Fibroblasts are responsible for accumulating new substrate, which is the process of fibrosis reaction.

Regarding the mechanism of promoting regeneration, M2 macrophages with anti-inflammatory/anti-fibrotic phenotypes promote regeneration through mutual interference with regulatory T cell subsets (Tregs) that play a vital part in the immune system. These cells regulate the tilt of the local immune response to inflammation, which further promotes the cascade of tissue regeneration and repair. Moreover, maintain anti-inflammatory and anti-fibrotic phenotypes by secreting IL-10. In addition, Tregs can enhance the ability to heal by inducing type 2 responses. After the reduction of T cells, the level of resident Tregs is still elevated, which may be because they lack epidermal growth factor receptor (EGFR) (Zaiss et al., 2013; Arpaia et al., 2015), whose expression can promote the cell factors secreting by mast cells to keep the Tregs in the damaged spot (Zaiss et al., 2013). Once Treg cells appear, they will proliferate and upregulate the secretion of bimodules, which is necessary for cell regeneration and may produce cell proliferation or induce cell differentiation. Treg cells may also enhance the regeneration ability of endogenous stem cells and progenitor cells through growth factors secret.

4 Immunomodulatory applications of biomaterials in skeletal disease

The exploration of immunomodulation in biomaterials in regenerative medicine has attracted much attention. An in-depth understanding of materials' immune cascade reaction principle (Xie et al., 2020) (Figure 5A) is critical in developing and innovating new materials.

4.1 The application of neutrophils in the design of biomaterials

Although neutrophils do not make up much in the bone marrow, they are the first cells to be mobilized in inflammatory

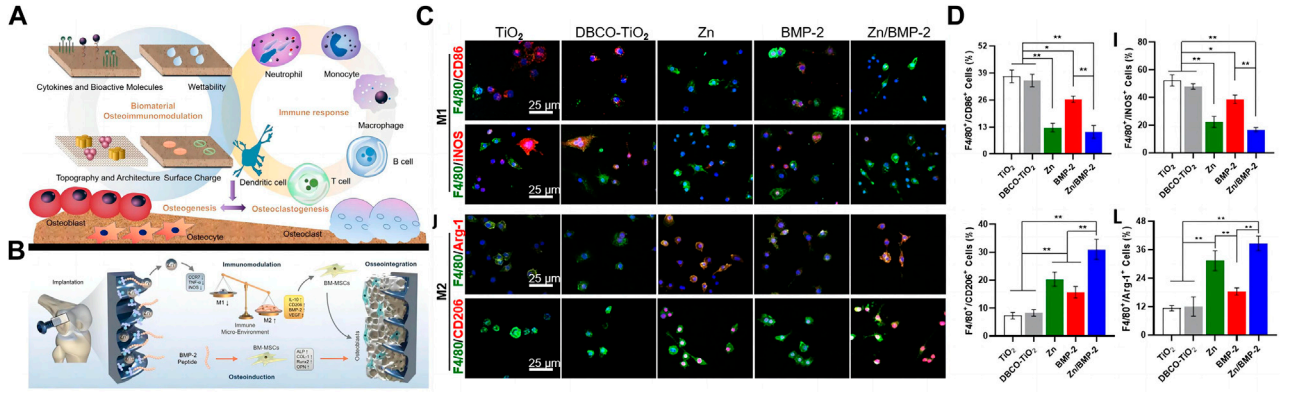

FIGURE 5
Immune cascade after bone implant material. **(A)** The interaction of biomaterials, skeletal cells, and immune cells, the graph was reprinted with permission from (Xie et al., 2020). **(B–D)** Zn^{2+} and BMP-2 peptide-modified titanium screws promote macrophage M2 polarization and synergize with BMP-2 to promote bone formation. The graph was reprinted with permission from (Wang et al., 2022).

and traumatic fractures. Neutrophils, pioneer cells of the inflammatory response, play a dual role in bone regeneration and repair. On the one hand, neutrophils eliminate cell debris, infectious substances, and phagocytic material scaffolds at the injury site by secreting proteases (e.g., matrix metalloproteinases, collagenases) and provide sites for subsequent bone regeneration. Cytokines such as IL-17 and TNF-α synthesized by neutrophils activate osteoclast through the RANKL-RANK signaling pathway (Chang et al., 2013). On the other hand, neutrophils stimulate angiogenesis (Christoffersson et al., 2012) and bone regeneration through direct or indirect action. Neutrophils in liver injury achieve angiogenesis and maturation by secreting MMP-9 to promote the expression of VEGF (Christoffersson et al., 2012). In the early stage of inflammation, neutrophils alleviate acute inflammation and reduce the secretion of inflammatory cytokines, thereby reducing the activation of osteoclast precursor cells and promoting bone repair (Bastian et al., 2018). The application of biologically active neutrophil membrane materials is enthusiastically sought after by scientific researchers. After implantation, the membrane material simulates the post-inflammatory process, and the apoptosis of neutrophils induces the entrapment of macrophages, which further promotes the polarization of macrophages to M2 to play an anti-inflammatory role and promotes bone regeneration. During this process, TGF-β and IL-10 secreted by macrophages promote anti-inflammatory and bone regeneration repair. IL-8-induced polarization of neutrophils contributes to endochondral ossification (Cai et al., 2021). These will provide strong support for designing materials to regulate neutrophil behavior.

4.2 The application of macrophages in the design of biomaterials

The application of macrophage polarization in the regeneration of bone defect sites is favored. The changes in macrophage behavior promote vascular and bone regeneration (Loi et al., 2016; ElHawary et al., 2021). Angiogenesis provides various nutrients and cells for bone repair. Therefore, coupling blood vessels and bone regeneration is another entry point for material design in fracture repair. The modified application of various bioactive molecules combined with biomaterials promotes vascular or bone regeneration by regulating macrophage polarization (Loi et al., 2016; Wang et al., 2022). Calcium silicate combined with β-tricalcium silicate stimulates the polarization of macrophages to M1/M2 by releasing IFN-γ and Si to secrete further vascular growth factors (VEGF, CXCL-12, PDGF-BB) to promote angiogenesis (Loi et al., 2016). Mesoporous silica (MNS)-loaded BMP bioactive molecules were incorporated into 3D printed scaffolds made of modified GelMA to release bioactive molecules and promote macrophage M2 polarization, BMP active molecules, and M2-secreted anti-inflammatory cells factors to promote the repair of diabetic bone defects. The release of BMP-2 and zinc particles regulates the increased proportion of M2 macrophages on the screw-coated surface to promote bone regeneration (Wang et al., 2022) (Figures 5B–D). Although macrophage polarization occurs in both angiogenesis and bone regeneration, there is a particular deviation in the macrophage's temporal and spatial control time. It is urgent to develop new biomaterials to simultaneously realize the classification of the fate of macrophages in angiogenesis and bone regeneration.

4.3 The application of T cells in the design of biomaterials

T cells play an indirect role in bone regeneration and repair, and factors secreted by various T cell subtypes indirectly regulate the process of bone regeneration. Like macrophages, T cells can be roughly divided into pro-inflammatory cell subtypes (Th1, Th17) and anti-inflammatory cell subtypes (Th2, Treg). Th1 cells can inhibit the expression of RUNX2 in BMSCs by secreting the IFN-γ

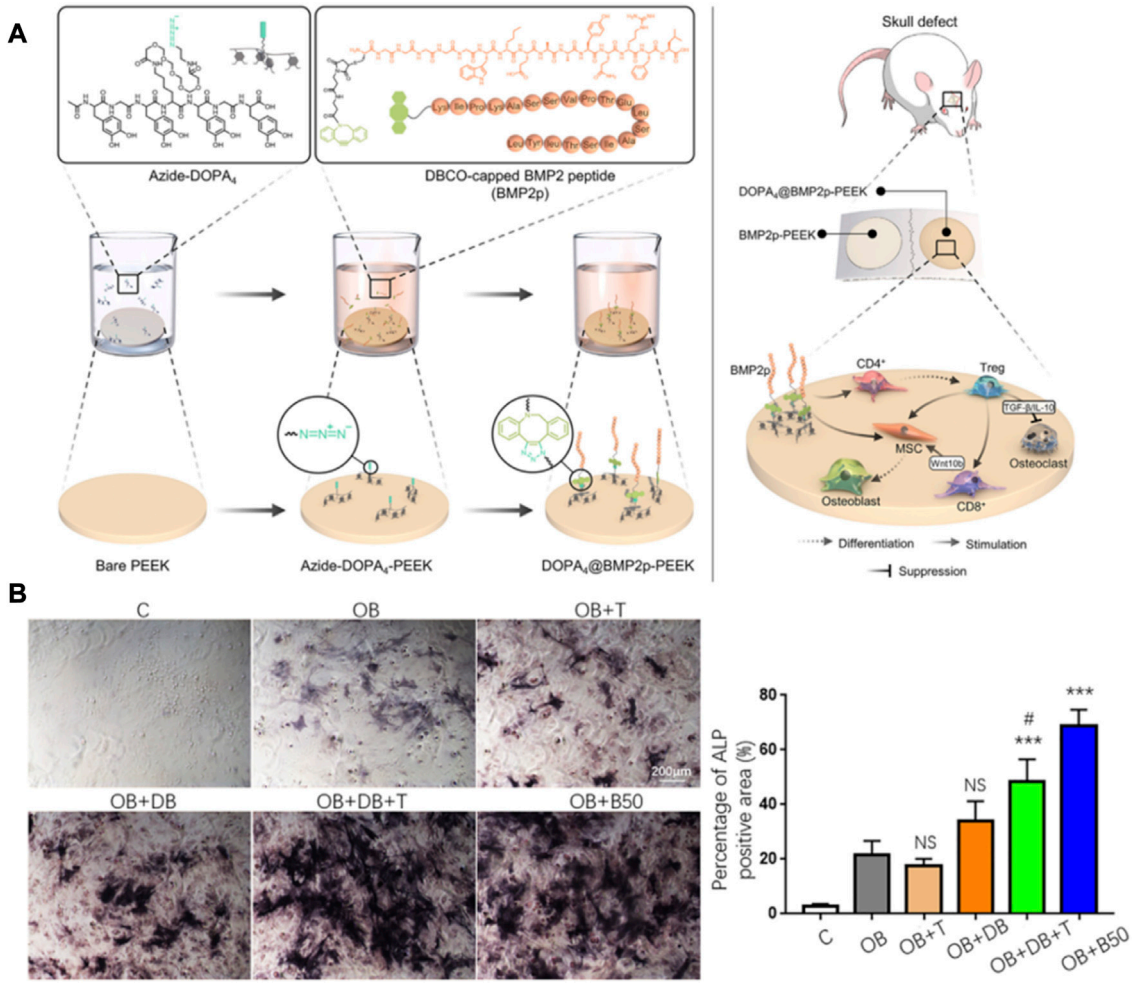

FIGURE 6
Immunomodulatory material for bone regeneration. **(A,B)** DOPA4@BMP2pPEEK material regulates the differentiation of CD4 T cells and synergizes with BMP-2 to promote bone regeneration. The graph was reprinted with permission from (Zhao et al., 2021c).

factor to reduce bone repair ability (Liu et al., 2011). In addition, IFN-γ secreted by Th1 cells is associated with the polarization of M1 macrophages, and sustained M1 polarization leads to sustained inflammatory activation that prevents bone repair from occurring (Spiller et al., 2015). Th17 acts as the ability to secrete pro-inflammatory cytokine IL-17, but its role can promote bone regeneration and repair. IL-17A combined with BMP-2 can significantly enhance the osteogenic ability of BMSCs (Moon et al., 2016). Th2 and Treg cells promote bone homeostasis towards osteogenesis and bone regeneration by inducing the formation of M2 macrophages (Chen et al., 2012) and inhibiting osteoclast differentiation (Lu et al., 2017). And the surface of PEEK implants promotes bone regeneration by regulating T cell differentiation *via* lickable mussel-inspired azide-DOPA4 and BMP2p coupling (Zhao et al., 2021c) (Figure 6). Although there are few studies on T cells in bone regeneration biomaterials, the regulation of macrophages and osteoclasts by T cells will be a practical starting point for biomaterials to regulate the immune microenvironment to achieve bone regeneration and bone disease treatment. This will provide new therapeutic strategies for clinical bone defect regeneration and disease treatment.

5 Conclusion and future perspectives

The research of biomaterials is reviewed in bone regeneration and repair. We summarize some defects and improvement schemes of biomaterials and analyze the promising prospect of bone immune materials. It can be used for reference in the design of immune materials for bone regeneration.

1) Tricalcium phosphate ceramics (β-TCP) have been used as bone-filling materials in clinical practice due to their high biocompatibility and bone conductivity, but their non-degradability limits their application in bone regeneration. Then, biodegradable biomaterials with the same mechanical strength as β-TCP will be gradually explored. And the high biocompatibility and plasticity of the extracellular matrix (ECM) components will provide a broad application prospect for the research of bone regeneration materials.
2) Electrospun fibers' tenacity, plasticity, and core-shell structure can carry hydrophilic and non-hydrophilic drugs, proteins, peptides, etc. They have been used as periosteal-like and filling delivery materials in bone defect models to promote

bone regeneration. Still, the application of cytotoxic solvents in their synthesis process has not been able to promote their clinical application. The development of biological fibers will provide a new direction for the wide application of nanofibers.

3) 3D bio-printing materials have been widely used in the study of bone regeneration because of their ability to simulate organisms' tissue structure accurately. Although it can print a material resembling bone, it can not respond to internal activity when implanted in organisms. The intelligent programming of 4D bio-printing materials and the function of responding to the activity of implants will provide broad application space for the research of bone regeneration.
4) M1 macrophages are important in clearing foreign bodies and dead cells at defect sites. They are indispensable in bone defect repair. Therefore, controlling the ratio of M1/M2 is the key to regeneration repair. In addition, how to transform macrophages from type M1 to type M2 after implantation is also the key to initiating the regenerative repair.
5) Numerous articles have focused on the effects of materials on macrophage behavior, with little focus on studies of other immune cells such as T cells, neutrophils, and DC cells. Different subtypes of T cells play multiple roles in the regeneration process, and neutrophils are also key cell populations that initiate the regenerative function of macrophages. The design of immunomodulatory materials targeting T cell subtypes and other immune cell behaviors may provide a new route for regenerative applications.

The success or failure of biomaterials in bone injury repair is determined by the interaction of the host immune system with biomaterials. Continued activation of the inflammatory response will lead to a delay in the repair process or tissue necrosis. Therefore, the rational regulation of the foreign body reaction effect is the key to bone injury regeneration and repair. From the selection of raw materials and the synthesis process, Biomaterials endowed with bioactive factors or their characteristics regulate immune cells, thus realizing the regulation of tissue regeneration. Competent biomaterials regulate the biological behavior of immune cells such as neutrophils, macrophages, or T cells. It promotes the differentiation of these immune cells to an anti-inflammatory phenotype, further promoting bone tissue regeneration. The research of new biomaterials to promote the real-time regulation of immune cell behavior to adapt to the high degree of compatibility between the immune system and bone regeneration, the tacit cooperation of these new biomaterials in innate and adaptive immunity needs to be further explored. Therefore, the design of biomaterials must consider the activation of immune cells and the mutual interference between different innate and adaptive cellular components to meet the research needs of clinical medicine.

Author contributions

Conceptualization, GW; investigation, CD and GT; resources, CD and G-YZ; writing original draft preparation, CD; writing-review and editing, WL; supervision, GW; project administration, GW. All authors have read and agreed to the published version of the manuscript.

Conflict of interest

The authors declare that the research was conducted in the absence of any commercial or financial relationships that could be construed as a potential conflict of interest.

Publisher's note

All claims expressed in this article are solely those of the authors and do not necessarily represent those of their affiliated organizations, or those of the publisher, the editors and the reviewers. Any product that may be evaluated in this article, or claim that may be made by its manufacturer, is not guaranteed or endorsed by the publisher.

References

Abbasi, N., Hamlet, S., Love, R. M., and Nguyen, N. T. (2020). Porous scaffolds for bone regeneration. *J. Sci. Adv. Mater. devices* 5 (1), 1–9.

Adamopoulos, I. E., Chao, C. C., Geissler, R., Laface, D., Blumenschein, W., Iwakura, Y., et al. (2010). Interleukin-17A upregulates receptor activator of NF-κB on osteoclast precursors. *Arthritis Res. Ther.* 12 (1), R29. doi:10.1186/ar2936

Anderson, J. M., Rodriguez, A., and Chang, D. T. (2008). Foreign body reaction to biomaterials. *Semin. Immunol.* 20 (2), 86–100. doi:10.1016/j.smim.2007.11.004

Arpaia, N., Green, J. A., Moltedo, B., Arvey, A., Hemmers, S., Yuan, S., et al. (2015). A distinct function of regulatory T cells in tissue protection. *Cell* 162 (5), 1078–1089. doi:10.1016/j.cell.2015.08.021

Barrow, A. D., Raynal, N., Andersen, T. L., Slatter, D. A., Bihan, D., Pugh, N., et al. (2011). OSCAR is a collagen receptor that costimulates osteoclastogenesis in DAP12-deficient humans and mice. *J. Clin. investigation* 121 (9), 3505–3516. doi:10.1172/jci45913

Bastian, O. W., Croes, M., Alblas, J., Koenderman, L., Leenen, L. P. H., and Blokhuis, T. J. (2018). Neutrophils inhibit synthesis of mineralized extracellular matrix by human bone marrow-derived stromal cells *in vitro*. *Front. Immunol.* 9, 945. doi:10.3389/fimmu.2018.00945

Behzadi, S., Luther, G. A., Harris, M. B., Farokhzad, O. C., and Mahmoudi, M. (2017). Nanomedicine for safe healing of bone trauma: Opportunities and challenges. *Biomaterials* 146, 168–182. doi:10.1016/j.biomaterials.2017.09.005

Borchers, A., and Pieler, T. (2010). Programming pluripotent precursor cells derived from Xenopus embryos to generate specific tissues and organs. *Genes (Basel)* 1 (3), 413–426. doi:10.3390/genes1030413

Brodbeck, W. G., Macewan, M., Colton, E., Meyerson, H., and Anderson, J. M. (2005). Lymphocytes and the foreign body response: Lymphocyte enhancement of macrophage adhesion and fusion. *J. Biomed. Mater Res. A* 74 (2), 222–229. doi:10.1002/jbm.a.30313

Brunetti, G., Colucci, S., Pignataro, P., Coricciati, M., Mori, G., Cirulli, N., et al. (2005). T cells support osteoclastogenesis in an *in vitro* model derived from human periodontitis patients. *J. Periodontol.* 76 (10), 1675–1680. doi:10.1902/jop.2005.76.10.1675

Brunetti, G., Faienza, M. F., Piacente, L., Ventura, A., Oranger, A., Carbone, C., et al. (2013). High dickkopf-1 levels in sera and leukocytes from children with 21-hydroxylase deficiency on chronic glucocorticoid treatment. *Am. J. Physiol. Endocrinol. Metab.* 304 (5), E546–E554. doi:10.1152/ajpendo.00535.2012

Burger, M. G., Grosso, A., Briquez, P. S., Born, G. M., Lunger, A., Schrenk, F., et al. (2022). Robust coupling of angiogenesis and osteogenesis by VEGF-decorated matrices for bone regeneration. *Acta Biomater.* 149, 111–125. doi:10.1016/j.actbio.2022.07.014

Cai, B., Lin, D., Li, Y., Wang, L., Xie, J., Dai, T., et al. (2021). N2-Polarized neutrophils guide bone mesenchymal stem cell recruitment and initiate bone regeneration: A missing piece of the bone regeneration puzzle. *Adv. Sci.* 8 (19), 2100584. doi:10.1002/advs.202100584

Chang, J., Liu, F., Lee, M., Wu, B., Ting, K., Zara, J. N., et al. (2013). NF-κB inhibits osteogenic differentiation of mesenchymal stem cells by promoting β-catenin degradation. *Proc. Natl. Acad. Sci.* 110 (23), 9469–9474. doi:10.1073/pnas.1300532110

Chen, F., Liu, Z., Wu, W., Rozo, C., Bowdridge, S., Millman, A., et al. (2012). An essential role for TH2-type responses in limiting acute tissue damage during experimental helminth infection. *Nat. Med.* 18 (2), 260–266. doi:10.1038/nm.2628

Chen, S., Jones, J. A., Xu, Y., Low, H. Y., Anderson, J. M., and Leong, K. W. (2010). Characterization of topographical effects on macrophage behavior in a foreign body response model. *Biomaterials* 31 (13), 3479–3491. doi:10.1016/j.biomaterials.2010.01.074

Christoffersson, G., Vågesjö, E., Vandooren, J., Liden, M., Massena, S., Reinert, R. B., et al. (2012). VEGF-A recruits a proangiogenic MMP-9–delivering neutrophil subset that induces angiogenesis in transplanted hypoxic tissue. *Blood, J. Am. Soc. Hematol.* 120 (23), 4653–4662. doi:10.1182/blood-2012-04-421040

Colucci, S., Brunetti, G., Rizzi, R., Zonno, A., Mori, G., Colaianni, G., et al. (2004). T cells support osteoclastogenesis in an *in vitro* model derived from human multiple myeloma bone disease: The role of the OPG/TRAIL interaction. *Blood* 104 (12), 3722–3730. doi:10.1182/blood-2004-02-0474

Convente, M. R., Chakkalakal, S. A., Yang, E., Caron, R. J., Zhang, D., Kambayashi, T., et al. (2018). Depletion of mast cells and macrophages impairs heterotopic ossification in an *Acvr1*^{R206H} mouse model of fibrodysplasia ossificans progressiva. *J. Bone Min. Res.* 33 (2), 269–282. doi:10.1002/jbmr.3304

Dar, H. Y., Azam, Z., Anupam, R., Mondal, R. K., Srivastava, R. K., et al. (2018). Osteoimmunology: The Nexus between bone and immune system. *Front. Bioscience-Landmark* 23 (3), 464–492. doi:10.2741/4600

Dhodapkar, K. M., Barbuto, S., Matthews, P., Kukreja, A., Mazumder, A., Vesole, D., et al. (2008). Dendritic cells mediate the induction of polyfunctional human IL17-producing cells (Th17-1 cells) enriched in the bone marrow of patients with myeloma. *Blood* 112 (7), 2878–2885. doi:10.1182/blood-2008-03-143222

Ekdahl, K. N., Lambris, J. D., Elwing, H., Ricklin, D., Nilsson, P. H., Teramura, Y., et al. (2011). Innate immunity activation on biomaterial surfaces: A mechanistic model and coping strategies. *Adv. Drug Deliv. Rev.* 63 (12), 1042–1050. doi:10.1016/j.addr.2011.06.012

ElHawary, H., Baradaran, A., Abi-Rafeh, J., Vorstenbosch, J., Xu, L., and Efanov, J. I. (2021). Bone healing and inflammation: Principles of fracture and repair. *Semin. Plast. Surg.* 35 (3), 198–203. doi:10.1055/s-0041-1732334

Faienza, M. F., Brunetti, G., Colucci, S., Piacente, L., Ciccarelli, M., Giordani, L., et al. (2009). Osteoclastogenesis in children with 21-hydroxylase deficiency on long-term glucocorticoid therapy: The role of receptor activator of nuclear factor-κb ligand/osteoprotegerin imbalance. *J. Clin. Endocrinol. Metab.* 94 (7), 2269–2276. doi:10.1210/jc.2008-2446

Feng, N., Guo, F., and Nanoparticle-siRNA (2020). A potential strategy for rheumatoid arthritis therapy? *J. Control. Release* 325, 380–393. doi:10.1016/j.jconrel.2020.07.006

Fischer, V., and Haffner-Luntzer, M. (2022). Interaction between bone and immune cells: Implications for postmenopausal osteoporosis. *Semin. Cell Dev. Biol.* 123, 14–21. doi:10.1016/j.semcdb.2021.05.014

Gao, Y., Grassi, F., Ryan, M. R., Terauchi, M., Page, K., Yang, X., et al. (2007). IFN-gamma stimulates osteoclast formation and bone loss *in vivo* via antigen-driven T cell activation. *J. Clin. Invest.* 117 (1), 122–132. doi:10.1172/jci30074

Garg, K., Sell, S. A., Madurantakam, P., and Bowlin, G. L. (2009). Angiogenic potential of human macrophages on electrospun bioresorbable vascular grafts. *Biomed. Mater* 4 (3), 031001. doi:10.1088/1748-6041/4/3/031001

Gorejová, R., Haverová, L., Oriňaková, R., Orinak, A., and Orinak, M. (2018). Recent advancements in Fe-based biodegradable materials for bone repair. *J. Mater. Sci.* 54 (3), 1913–1947. doi:10.1007/s10853-018-3011-z

Gotz, W., Reichert, C., Canullo, L., Jager, A., and Heinemann, F. (2012). Coupling of osteogenesis and angiogenesis in bone substitute healing - a brief overview. *Ann. Anat.* 194 (2), 171–173. doi:10.1016/j.aanat.2011.10.002

Grandjean-Laquerriere, A., Tabary, O., Jacquot, J., Richard, D., Frayssinet, P., Guenounou, M., et al. (2007). Involvement of toll-like receptor 4 in the inflammatory reaction induced by hydroxyapatite particles. *Biomaterials* 28 (3), 400–404. doi:10.1016/j.biomaterials.2006.09.015

Guler, Z., Silva, J. C., and Sezai Sarac, A. (2017). RGD functionalized poly (ε-caprolactone)/poly (m-anthranilic acid) electrospun nanofibers as high-performing scaffolds for bone tissue engineering RGD functionalized PCL/P3ANA nanofibers. *Int. J. Polym. Mater. Polym. Biomaterials* 66 (3), 139–148. doi:10.1080/00914037.2016.1190929

Harre, U., Lang, S. C., Pfeifle, R., Rombouts, Y., FruhbeiBer, S., Amara, K., et al. (2015). Glycosylation of immunoglobulin G determines osteoclast differentiation and bone loss. *Nat. Commun.* 6, 6651. doi:10.1038/ncomms7651

Harrington, L. E., Mangan, P. R., and Weaver, C. T. (2006). Expanding the effector CD4 T-cell repertoire: The Th17 lineage. *Curr. Opin. Immunol.* 18 (3), 349–356. doi:10.1016/j.coi.2006.03.017

Hickman, H. D., and Pierson, T. C. (2016). Zika in the brain: New models shed light on viral infection. *Trends Mol. Med.* 22 (8), 639–641. doi:10.1016/j.molmed.2016.06.004

Himburg, H. A., Doan, P. L., Quarmyne, M., Yan, X., Sasine, J., Zhao, L., et al. (2017). Dickkopf-1 promotes hematopoietic regeneration via direct and niche-mediated mechanisms. *Nat. Med.* 23 (1), 91–99. doi:10.1038/nm.4251

Hirota, K., Hashimoto, M., Ito, Y., Matsuura, M., Ito, H., Tanaka, M., et al. (2018). Autoimmune Th17 cells induced synovial stromal and innate lymphoid cell secretion of the cytokine GM-CSF to initiate and augment autoimmune arthritis. *Immunity* 48 (6), 1220–1232 e5. doi:10.1016/j.immuni.2018.04.009

Huang, D., Zhao, F., Gao, W., Chen, X., Guo, Z., and Zhang, W. (2020). Strontium-substituted sub-micron bioactive glasses inhibit ostoclastogenesis through suppression of RANKL-induced signaling pathway. *Regen. Biomater.* 7 (3), 303–311. doi:10.1093/rb/rbaa004

Jones, J. A., Chang, D. T., Meyerson, H., Colton, E., Kwon, I. K., Matsuda, T., et al. (2007). Proteomic analysis and quantification of cytokines and chemokines from biomaterial surface-adherent macrophages and foreign body giant cells. *J. Biomed. Mater Res. A* 83 (3), 585–596. doi:10.1002/jbm.a.31221

Kim, T. H., An, D. B., Oh, S. H., Kang, M. K., Song, H. H., and Lee, J. H. (2015). Creating stiffness gradient polyvinyl alcohol hydrogel using a simple gradual freezing–thawing method to investigate stem cell differentiation behaviors. *Biomaterials* 40, 51–60. doi:10.1016/j.biomaterials.2014.11.017

Komatsu, N., and Takayanagi, H. (2022). Mechanisms of joint destruction in rheumatoid arthritis—Immune cell–fibroblast–bone interactions. *Nat. Rev. Rheumatol.* 18 (7), 415–429. doi:10.1038/s41584-022-00793-5

Krevvata, M., Silva, B. C., Manavalan, J. S., Galan-Diez, M., Kode, A., Matthews, B. G., et al. (2014). Inhibition of leukemia cell engraftment and disease progression in mice by osteoblasts. *Blood* 124 (18), 2834–2846. doi:10.1182/blood-2013-07-517219

Krishnamurthy, A., Joshua, V., Haj Hensvold, A., Jin, T., Sun, M., Vivar, N., et al. (2016). Identification of a novel chemokine-dependent molecular mechanism underlying rheumatoid arthritis-associated autoantibody-mediated bone loss. *Ann. Rheum. Dis.* 75 (4), 721–729. doi:10.1136/annrheumdis-2015-208093

Lee, D., Heo, D. N., Lee, S. J., Heo, M., Kim, J., Choi, S., et al. (2018). Poly (lactide-co-glycolide) nanofibrous scaffolds chemically coated with gold-nanoparticles as osteoinductive agents for osteogenesis. *Appl. Surf. Sci.* 432, 300–307. doi:10.1016/j.apsusc.2017.05.237

Lee, J., Byun, H., Madhurakkat Perikamana, S. K., Lee, S., and Shin, H. (2019). Current advances in immunomodulatory biomaterials for bone regeneration. *Adv. Healthc. Mater* 8 (4), e1801106. doi:10.1002/adhm.201801106

Li, C., Du, Y., Lv, H., Zhang, J., Zhuang, P., Yang, W., et al. (2022). Injectable amphipathic artesunate prodrug-hydrogel microsphere as gene/drug nano-microplex for rheumatoid arthritis therapy. *Adv. Funct. Mater.* 32 (44), 2206261. doi:10.1002/adfm.202206261

Li, S., Zhang, L., Liu, C., Kim, J., Su, K., Chen, T., et al. (2023). Spontaneous immunomodulation and regulation of angiogenesis and osteogenesis by Sr/Cu-borosilicate glass (BSG) bone cement to repair critical bone defects. *Bioact. Mater.* 23, 101–117. doi:10.1016/j.bioactmat.2022.10.021

Li, Y., Toraldo, G., Li, A., Yang, X., Zhang, H., Qian, W. P., et al. (2007). B cells and T cells are critical for the preservation of bone homeostasis and attainment of peak bone mass *in vivo*. *Blood* 109 (9), 3839–3848. doi:10.1182/blood-2006-07-037994

Liu, P., Cheng, H., Santiago, S., Raeder, M., Zhang, F., Isabella, A., et al. (2011). Oncogenic PIK3CA-driven mammary tumors frequently recur via PI3K pathway–dependent and PI3K pathway–independent mechanisms. *Nat. Med.* 17 (9), 1116–1120. doi:10.1038/nm.2402

Liu, X., Chen, M., Luo, J., Zhao, H., Zhou, X., Gu, Q., et al. (2021). Immunopolarization-regulated 3D printed-electrospun fibrous scaffolds for bone regeneration. *Biomaterials* 276, 121037. doi:10.1016/j.biomaterials.2021.121037

Loi, F., Cordova, L. A., Pajarinen, J., Yao, Z., and Goodman, S. B. (2016). Inflammation, fracture and bone repair. *Bone* 86, 119–130. doi:10.1016/j.bone.2016.02.020

Lu, Z., Xie, J., Wu, G., Shen, J., Collins, R., Chen, W., et al. (2017). Fasting selectively blocks development of acute lymphoblastic leukemia via leptin-receptor upregulation. *Nat. Med.* 23 (1), 79–90. doi:10.1038/nm.4252

Maddur, M. S., Miossec, P., Kaveri, S. V., and Bayry, J. (2012). Th17 cells: Biology, pathogenesis of autoimmune and inflammatory diseases, and therapeutic strategies. *Am. J. Pathol.* 181 (1), 8–18. doi:10.1016/j.ajpath.2012.03.044

Mariani, E., Lisignoli, G., Borzi, R. M., and Pulsatelli, L. (2019). Biomaterials: Foreign bodies or tuners for the immune response? *Int. J. Mol. Sci.* 20 (3), 636. doi:10.3390/ijms20030636

McInnes, I. B., and Schett, G. (2007). Cytokines in the pathogenesis of rheumatoid arthritis. *Nat. Rev. Immunol.* 7 (6), 429–442. doi:10.1038/nri2094

Mesure, L., De Visscher, G., Vranken, I., Lebacq, A., and Flameng, W. (2010). Gene expression study of monocytes/macrophages during early foreign body reaction and identification of potential precursors of myofibroblasts. *Plos One* 5 (9), e12949. doi:10.1371/journal.pone.0012949

Moon, R. J., Harvey, N. C., Curtis, E. M., de Vries, F., van Staa, T., and Cooper, C. (2016). Ethnic and geographic variations in the epidemiology of childhood fractures in the United Kingdom. *Bone* 85, 9–14. doi:10.1016/j.bone.2016.01.015

Naik, S. R., and Wala, S. M. (2013). Inflammation, allergy and asthma, complex immune origin diseases: Mechanisms and therapeutic agents. *Recent Pat. Inflamm. Allergy Drug Discov.* 7 (1), 62–95. doi:10.2174/187221313804004682

Okamoto, K., Nakashima, T., Shinohara, M., Negishi-Koga, T., Komatsu, N., Terashima, A., et al. (2017). Osteoimmunology: The conceptual framework unifying the immune and skeletal systems. *Physiol. Rev.* 97 (4), 1295–1349. doi:10.1152/physrev.00036.2016

Ono, T., Okamoto, K., Nakashima, T., Nitta, T., Hori, S., Iwakura, Y., et al. (2016). IL-17-producing γδ T cells enhance bone regeneration. *Nat. Commun.* 7, 10928. doi:10.1038/ncomms10928

Osouli-Bostanabad, K., Masalehdan, T., Kapsa, R. M. I., Quigley, A., Lalatsa, A., Bruggeman, K. F., et al. (2022). Traction of 3D and 4D printing in the healthcare industry: From drug delivery and analysis to regenerative medicine. *ACS Biomater. Sci. Eng.* 8 (7), 2764–2797. doi:10.1021/acsbiomaterials.2c00094

Poole, K. E., Van Bezooijen, R. L., Loveridge, N., Hamersma, H., Papapoulos, S. E., Lowik, C. W., et al. (2005). Sclerostin is a delayed secreted product of osteocytes that inhibits bone formation. *FASEB J.* 19 (13), 1842–1844. doi:10.1096/fj.05-4221fje

Rahimi, M., Mir, S. M., Baghban, R., Charmi, G., Plummer, C. M., Shafiei-Irannejad, V., et al. (2022). Chitosan-based biomaterials for the treatment of bone disorders. *Int. J. Biol. Macromol.* 215, 346–367. doi:10.1016/j.ijbiomac.2022.06.079

Reid, B., Gibson, M., Singh, A., Taube, J., Furlong, C., Murcia, M., et al. (2015). PEG hydrogel degradation and the role of the surrounding tissue environment. *J. Tissue Eng. Regen. Med.* 9 (3), 315–318. doi:10.1002/term.1688

Roseti, L., Parisi, V., Petretta, M., Cavallo, C., Desando, G., Bartolotti, I., et al. (2017). Scaffolds for bone tissue engineering: State of the art and new perspectives. *Mater Sci. Eng. C Mater Biol. Appl.* 78, 1246–1262. doi:10.1016/j.msec.2017.05.017

Sangsanoh, P., Israsena, N., Suwantong, O., and Supaphol, P. (2017). Effect of the surface topography and chemistry of poly(3-hydroxybutyrate) substrates on cellular behavior of the murine neuroblastoma Neuro2a cell line. *Polym. Bull.* 74 (10), 4101–4118. doi:10.1007/s00289-017-1947-9

Schlundt, C., Fischer, H., Bucher, C. H., Rendenbach, C., Duda, G. N., and Schmidt-Bleek, K. (2021). The multifaceted roles of macrophages in bone regeneration: A story of polarization, activation and time. *Acta Biomater.* 133, 46–57. doi:10.1016/j.actbio.2021.04.052

Shen, E. C., Chou, T. C., Gau, C. H., Tu, H. P., Chen, Y. T., and Fu, E. (2006). Releasing growth factors from activated human platelets after chitosan stimulation: A possible bio-material for platelet-rich plasma preparation. *Clin. Oral Implants Res.* 17 (5), 572–578. doi:10.1111/j.1600-0501.2004.01241.x

Shen, M., Garcia, I., Maier, R. V., and Horbett, T. A. (2004). Effects of adsorbed proteins and surface chemistry on foreign body giant cell formation, tumor necrosis factor alpha release and procoagulant activity of monocytes. *J. Biomed. Mater Res. A* 70 (4), 533–541. doi:10.1002/jbm.a.30069

Shi, Q., Rondon-Cavanzo, E.-P., Dalla Picola, I. P., Tiera, M. J., Zhang, X., Dai, K., et al. (2018). *In vivo* therapeutic efficacy of TNFα silencing by folate-PEG-chitosan-DEAE/siRNA nanoparticles in arthritic mice. *Int. J. nanomedicine* 13, 387–402. doi:10.2147/ijn.s146942

Shono, Y., Ueha, S., Wang, Y., Abe, J., Kurachi, M., Matsuno, Y., et al. (2010). Bone marrow graft-versus-host disease: Early destruction of hematopoietic niche after MHC-mismatched hematopoietic stem cell transplantation. *Blood* 115 (26), 5401–5411. doi:10.1182/blood-2009-11-253559

Spiller, K. L., Freytes, D. O., and Vunjak-Novakovic, G. (2015). Macrophages modulate engineered human tissues for enhanced vascularization and healing. *Ann. Biomed. Eng.* 43 (3), 616–627. doi:10.1007/s10439-014-1156-8

Sreehari, S., Naik, D. R., and Eapen, M. (2011). Osteopetrosis: A rare cause of anemia. *Hematol. Rep.* 3 (1), e1. doi:10.4081/hr.2011.e1

Tang, J., Xi, K., Chen, H., Wang, L., Li, D., Xu, Y., et al. (2021). Flexible osteogenic glue as an All-In-One solution to assist fracture fixation and healing. *Adv. Funct. Mater.* 31 (38), 2102465. doi:10.1002/adfm.202102465

Toraldo, G., Roggia, C., Qian, W. P., Pacifici, R., and Weitzmann, M. N. (2003). IL-7 induces bone loss *in vivo* by induction of receptor activator of nuclear factor kappa B ligand and tumor necrosis factor alpha from T cells. *Proc. Natl. Acad. Sci. U. S. A.* 100 (1), 125–130. doi:10.1073/pnas.0136772100

Tsukasaki, M., and Takayanagi, H. (2019). Osteoimmunology: Evolving concepts in bone-immune interactions in health and disease. *Nat. Rev. Immunol.* 19 (10), 626–642. doi:10.1038/s41577-019-0178-8

Tucci, M., Stucci, S., Strippoli, S., Dammacco, F., and Silvestris, F. (2011). Dendritic cells and malignant plasma cells: An alliance in multiple myeloma tumor progression? *Oncologist* 16 (7), 1040–1048. doi:10.1634/theoncologist.2010-0327

Underhill, D. M., and Goodridge, H. S. (2012). Information processing during phagocytosis. *Nat. Rev. Immunol.* 12 (7), 492–502. doi:10.1038/nri3244

Vis, M., Guler-Yuksel, M., and Lems, W. F. (2013). Can bone loss in rheumatoid arthritis be prevented? *Osteoporos. Int.* 24 (10), 2541–2553. doi:10.1007/s00198-013-2334-5

Vishwakarma, A., Bhise, N. S., Evangelista, M. B., Rouwkema, J., Dokmeci, M. R., Ghaemmaghami, A. M., et al. (2016). Engineering immunomodulatory biomaterials to tune the inflammatory response. *Trends Biotechnol.* 34 (6), 470–482. doi:10.1016/j.tibtech.2016.03.009

Wada, T., Nakashima, T., Hiroshi, N., and Penninger, J. M. (2006). RANKL-RANK signaling in osteoclastogenesis and bone disease. *Trends Mol. Med.* 12 (1), 17–25. doi:10.1016/j.molmed.2005.11.007

Wan, Q.-Q., Jiao, K., Ma, Y.-X., Gao, B., Mu, Z., Wang, Y. R., et al. (2022). Smart, biomimetic periosteum created from the cerium (III, IV) oxide-mineralized eggshell membrane. *ACS Appl. Mater. Interfaces* 14 (12), 14103–14119. doi:10.1021/acsami.2c02079

Wang, S., Sun, C., Guan, S., Li, W., Xu, J., Ge, D., et al. (2017). Chitosan/gelatin porous scaffolds assembled with conductive poly (3, 4-ethylenedioxythiophene) nanoparticles for neural tissue engineering. *J. Mater. Chem. B* 5 (24), 4774–4788. doi:10.1039/c7tb00608j

Wang, T., Bai, J., Lu, M., Huang, C., Geng, D., Chen, G., et al. (2022). Engineering immunomodulatory and osteoinductive implant surfaces via mussel adhesion-mediated ion coordination and molecular clicking. *Nat. Commun.* 13 (1), 160. doi:10.1038/s41467-021-27816-1

Wang, Z., Wang, K., Zhang, Y., Jiang, Y., Lu, X., Fang, L., et al. (2016). Protein-affinitive polydopamine nanoparticles as an efficient surface modification strategy for versatile porous scaffolds enhancing tissue regeneration. *Part. Part. Syst. Charact.* 33 (2), 89–100. doi:10.1002/ppsc.201500187

Weber, A., Chan, P. M. B., and Wen, C. (2019). Do immune cells lead the way in subchondral bone disturbance in osteoarthritis? *Prog. Biophys. Mol. Biol.* 148, 21–31. doi:10.1016/j.pbiomolbio.2017.12.004

Wei, S., Ma, J. X., Xu, L., Gu, X. S., and Ma, X. L. (2020). Biodegradable materials for bone defect repair. *Mil. Med. Res.* 7 (1), 54. doi:10.1186/s40779-020-00280-6

Wilson, C. J., Clegg, R. E., Leavesley, D. I., and Pearcy, M. J. (2005). Mediation of biomaterial-cell interactions by adsorbed proteins: A review. *Tissue Eng.* 11 (1-2), 1–18. doi:10.1089/ten.2005.11.1

Wu, L., Gu, Y., Liu, L., Tang, J., Mao, J., Xi, K., et al. (2020). Hierarchical micro/nanofibrous membranes of sustained releasing VEGF for periosteal regeneration. *Biomaterials* 227, 119555. doi:10.1016/j.biomaterials.2019.119555

Wu, Z., Bai, J., Ge, G., Wang, T., Feng, S., Ma, Q., et al. (2022). Regulating macrophage polarization in high glucose microenvironment using lithium-modified bioglass-hydrogel for diabetic bone regeneration. *Adv. Healthc. Mater.* 11 (13), 2200298. doi:10.1002/adhm.202200298

Xie, Y., Hu, C., Feng, Y., Li, D., Ai, T., Huang, Y., et al. (2020). Osteoimmunomodulatory effects of biomaterial modification strategies on macrophage polarization and bone regeneration. *Regen. Biomater.* 7 (3), 233–245. doi:10.1093/rb/rbaa006

Xin, T., Mao, J., Liu, L., Tang, J., Wu, L., Yu, X., et al. (2020). Programmed sustained release of recombinant human bone morphogenetic protein-2 and inorganic ion composite hydrogel as artificial periosteum. *ACS Appl. Mater. interfaces* 12 (6), 6840–6851. doi:10.1021/acsami.9b18496

Yamamoto, K., Kitawaki, T., Sugimoto, N., Fujita, H., Kawase, Y., Takaori-Kondo, A., et al. (2019). Anti-inflammatory modulation of human myeloid-derived dendritic cell subsets by lenalidomide. *Immunol. Lett.* 211, 41–48. doi:10.1016/j.imlet.2019.05.012

Yamashiro, S., Kamohara, H., Wang, J. M., Yang, D., Gong, W. H., and Yoshimura, T. (2001). Phenotypic and functional change of cytokine-activated neutrophils: Inflammatory neutrophils are heterogeneous and enhance adaptive immune responses. *J. Leukoc. Biol.* 69 (5), 698–704. doi:10.1189/jlb.69.5.698

Yin, Z., Chen, X., Song, H.-x., Hu, J. j., Tang, Q. m., Zhu, T., et al. (2015). Electrospun scaffolds for multiple tissues regeneration *in vivo* through topography dependent induction of lineage specific differentiation. *Biomaterials* 44, 173–185. doi:10.1016/j.biomaterials.2014.12.027

Ying, C., Wang, R., Wang, Z., Tao, J., Yin, W., Zhang, J., et al. (2020). BMSC-exosomes carry mutant HIF-1α for improving angiogenesis and osteogenesis in critical-sized calvarial defects. *Front. Bioeng. Biotechnol.* 8, 565561. doi:10.3389/fbioe.2020.565561

Yu, V. W., Saez, B., Cook, C., Lotinun, S., Pardo-Saganta, A., Wang, Y. H., et al. (2015). Specific bone cells produce DLL4 to generate thymus-seeding progenitors from bone marrow. *J. Exp. Med.* 212 (5), 759–774. doi:10.1084/jem.20141843

Zaiss, D. M., van Loosdregt, J., Gorlani, A., Bekker, C., Grone, A., Sibilia, M., et al. (2013). Amphiregulin enhances regulatory T cell-suppressive function via the epidermal growth factor receptor. *Immunity* 38 (2), 275–284. doi:10.1016/j.immuni.2012.09.023

Zhang, S., Gangal, G., and Uludag, H. (2007). Magic bullets' for bone diseases: Progress in rational design of bone-seeking medicinal agents. *Chem. Soc. Rev.* 36 (3), 507–531. doi:10.1039/b512310k

Zhao, H., Wang, X., Zhang, W., Wang, L., Zhu, C., Huang, Y., et al. (2021). Bioclickable mussel-derived peptides with immunoregulation for osseointegration of PEEK. *Front. Bioeng. Biotechnol.* 9, 780609. doi:10.3389/fbioe.2021.780609

Zhao, Z., Li, G., Ruan, H., Chen, K., Cai, Z., Lu, G., et al. (2021). Capturing magnesium ions via microfluidic hydrogel microspheres for promoting cancellous bone regeneration. *ACS Nano* 15 (8), 13041–13054. doi:10.1021/acsnano.1c02147

Zhao, Z., Wang, Z., Li, G., Cai, Z., Wu, J., Wang, L., et al. (2021). Injectable microfluidic hydrogel microspheres for cell and drug delivery. *Adv. Funct. Mater.* 31 (31), 2103339. doi:10.1002/adfm.202103339

Zheng, J., Zhao, H., Ouyang, Z., Zhou, X., Kang, J., Yang, C., et al. (2022). Additively-manufactured PEEK/HA porous scaffolds with excellent osteogenesis for bone tissue repairing. *Compos. Part B Eng.* 232, 109508. doi:10.1016/j.compositesb.2021.109508

Zhou, B. O., Yue, R., Murphy, M. M., Peyer, J. G., and Morrison, S. (2014). Leptin-receptor-expressing mesenchymal stromal cells represent the main source of bone formed by adult bone marrow. *Cell Stem Cell* 15 (2), 154–168. doi:10.1016/j.stem.2014.06.008

Zhu, J., Li, Z., Zou, Y., Lu, G., Ronca, A., D'Amora, U., et al. (2022). Advanced application of collagen-based biomaterials in tissue repair and restoration. *J. Leather Sci. Eng.* 4 (1), 30. doi:10.1186/s42825-022-00102-6

frontiers | Frontiers in Bioengineering and Biotechnology

TYPE Original Research
PUBLISHED 03 May 2023
DOI 10.3389/fbioe.2023.1139649

OPEN ACCESS

EDITED BY
Yawei Du,
Shanghai Jiao Tong University, China

REVIEWED BY
Gang Li,
Soochow University, China
Tuo Yang,
University of California, San Diego, United States

*CORRESPONDENCE
Shanliang Han,
hanshanliang523@163.com
Chongwei Ke,
shchweiz@126.com

†These authors have contributed equally to this work and share first authorship

RECEIVED 07 January 2023
ACCEPTED 17 April 2023
PUBLISHED 03 May 2023

CITATION
Cao Z, Chen L, Niu G, Li Y, Hu Z, Hong R, Zhang X, Hong L, Han S and Ke C (2023), Preparation and characterization of a novel triple composite scaffold containing silk fibroin, chitosan, extracellular matrix and the mechanism of Akt/FoxO signaling pathway in colonic cancer cells cultured in 3D. *Front. Bioeng. Biotechnol.* 11:1139649. doi: 10.3389/fbioe.2023.1139649

Preparation and characterization of a novel triple composite scaffold containing silk fibroin, chitosan, extracellular matrix and the mechanism of Akt/FoxO signaling pathway in colonic cancer cells cultured in 3D

Zhipeng Cao†, Liang Chen†, Gengming Niu, Yan Li, Zhiqing Hu, Runqi Hong, Xiaotian Zhang, Liang Hong, Shanliang Han* and Chongwei Ke*

Department of General Surgery, Fifth People's Hospital of Shanghai, Fudan University, Shanghai, China

This work examined the physical and chemical properties and biocompatibility *in vivo* and *in vitro* of a unique triple composite scaffold incorporating silk fibroin, chitosan, and extracellular matrix. The materials were blended, cross-linked, and freeze-dried to create a composite scaffold of silk fibroin/chitosan/colon extracellular matrix (SF/CTS/CEM) with varying CEM contents. The SF/CTS/CEM (1:1:1) scaffold demonstrated the preferable shape, outstanding porosity, favorable connectivity, good moisture absorption, and acceptable and controlled swelling and degradation properties. Additionally, HCT-116 cells cultivated with SF/CTS/CEM (1:1:1) showed excellent proliferation capacity, cell malignancy, and delayed apoptosis, according to the *in vitro* cytocompatibility examination. We also examined the PI3K/PDK1/Akt/FoxO signaling pathway and discovered that cell culture using a SF/CTS/CEM (1:1:1) scaffold may prevent cell death by phosphorylating Akt and suppressing FoxO expression. Our findings demonstrate the potential of the SF/CTS/CEM (1:1:1) scaffold as an experimental model for colonic cancer cell culture and for replicating the three-dimensional *in vivo* cell growth environment.

KEYWORDS

extracellular matrix, silk fibroin, chitosan, scaffolds, Akt/FoxO signaling pathway

1 Introduction

With over 940,000 annual deaths, colonic carcinoma (CC) is the second most lethal malignant tumor around the world, followed by lung cancer (Sung et al., 2021). Due to their socioeconomic development, developed countries have the highest incidence of this disease (Dekker et al., 2019). The occurrence and development of tumors are multi-stage processes involving multiple biological pathways, and the mechanisms involved are relatively complex (Zhang et al., 2018). By combining the construction of the tumor environment with the study of the biological behavior of tumors and utilizing new research technologies and methods,

greater understanding and progress have been made in tumor research in recent years. Therefore, developing novel tumor models and advancing tumor research are quite important.

These studies suggest that tumor growth has its own internal microenvironment. Cells are encapsulated by the outer matrix, and there are dynamic interactions between cells and the matrix and between cells and signal molecules. With different methods of building a tumor microenvironment, the goal is to simulate a microenvironment closer to the growth of tumors *in vivo* and facilitate biological behavior that is closer to real tumors *in vivo*. At this stage, biological research on tumors is mainly carried out at the level of two-dimensional (2D) single-cell culture. However, 2D culture has some limitations in the study of biological behavior and drug sensitivity of colorectal cancer, such as the reduction of tumor malignancy and changes in cell-related properties, such as differentiation and interaction between polarity and extracellular matrix (ECM), which cannot represent the real tumor focus. It has been reported that monolayer cell culture differs from the *in vivo* cells in terms of tumor drug mechanism and resistance, whereas various physiological activities of colon cancer cells in a three-dimensional culture environment are closer to the real environment *in vivo* (Shin et al., 2018). Cells in a three-dimensional (3D) culture system may retain a healthy proliferative state for a longer amount of time compared to 2D culture conditions, and cell activity is greatly increased. Therefore, we established previously a 3D tumor model for tumor drug screening (Lovitt et al., 2018). Although 3D scaffold materials are widely used in tissue engineering, there are few reports in the field of tumors, especially in colon cancer (Liang et al., 2020). Tissue engineering materials are creatively used to seed specific tumor cells into certain biomaterials, form cell biomaterial composites after *in vitro* culture, and implant them into mice to investigate the similarities and differences between tumor characteristics and traditional culture methods (Xie et al., 2016). In a 3D model, cells continue to proliferate and secrete matrix. At the same time, 3D materials are gradually absorbed. The final tumor tissue demonstrates significant differences in morphology, function, and other aspects of the tumor tissue with simple subcutaneous tumorigenesis. Therefore, some scholars have proposed that a 3D structure constructed *in vitro* should be fully used to simulate the tumor microenvironment (Landberg et al., 2020).

In three-position scaffold materials, the use of high-molecular-weight substances such as silk fibroin (SF) and chitosan (CTS) has been widespread. SF has a wide range of sources and good biological properties (Algarrahi et al., 2018; Galvez Alegria et al., 2019); thus, its increasing use in tissue engineering and has good prospects. The fast rate of breakdown of SF, however, limits its use (Chomchalao et al., 2013). As a linear polysaccharide with naturally occurring positively charged bases, CTS has excellent biofunctionality, plasticity, biodegradability, and safety (Zhao et al., 2020). A CTS 3D scaffold can provide space for cells to grow, multiply, and finally approximate the characteristics of organs with certain functions, which can then be used to study tumor tissues (Patrulea et al., 2015). Other components, including elastin, collagen, glycoproteins, and proteoglycans, can be found in the ECM. According to previous studies, the ECM can have an impact on a cell's basic functions, including cell division, proliferation, adhesion, and phenotypic expression. In addition to help organizing tissues, it also provides crucial biochemical and biomechanical cues for regulating vascular and immune development, cell proliferation, migration, and differentiation. Furthermore, the ECM can control how dynamically cancers develop.

Researchers have been exploring composite systems with diverse polymers to overcome the drawbacks of scaffolds made of a single material. Combinations of various polymers are expected to confer their individual properties and form scaffolds that may promote cell adhesion, proliferation, and differentiation (Ghosh et al., 2019). Moreover, composite material scaffolds have been used and studied for cartilage repair (Bhardwaj et al., 2011), sciatic space repair (Gu et al., 2014), and bone defect reconstruction (Ríos et al., 2009).

This paper presents a new study on CC 3D culture using SF/CTS/colon extracellular matrix (CEM) composite scaffolds *in vitro*. For the first time, we investigated the creation of composite scaffolds based on the SF/CTS/CEM polymer system. We established a new 3D tumor cell culture system by seeding HCT-116 cells on SF/CTS/CEM scaffolds.

2 Materials and methods

2.1 Materials and animals

Genuine silkworm cocoons were obtained from farmers in Shiquan, Shanxi province. CTS powder (900,000 Da, 95% deacetylated), acetic acid, lithium bromide, dimethyl sulfoxide, absolute ethanol, cell counting kit (CCK)-8, dialysis bags, 4% paraformaldehyde, 1-Ethyl-3-(3-Dimethylaminopropyl) carbodiimide hydrochloride (EDC), and N-Hydroxysuccinimide (NHS) were purchased from Sangon Biotech (Shanghai) Co., Ltd., and sodium carbonate was acquired from the Sinopharm Chemical Reagent Co., Ltd. DMEM medium, 4,6-Diamidino-2-phenylindole dihydrochloride (DAPI), DY-554-Phalloidin staining, YF-488-Annexin V, and PI Apoptosis Kit were purchased from Share-bio Co., Ltd. Fetal bovine serum was purchased from Shrabio (Shanghai) Co., Ltd. Female naked mice aged 6 weeks were purchased from JSJ-lab (Shanghai) Co., Ltd. The mice were housed in a germ-free environment. The human CRC cell line HCT-116 was obtained from the Cell Bank of Shanghai Fifth People's Hospital and cultured in DMEM medium.

2.1.1 Extraction of silk fibroin and preparation of chitosan solution

The silkworm cocoon shell was cut into 1 cm^2 pieces, immersed in 0.5% sodium carbonate solution, and boiled three times for 1 h each. It was then fully dried in an oven at 65 C after being rinsed three times in distilled water. The processed silk fibers were placed in a 9 M lithium bromide solution to form another solution, which was then dialyzed against distilled water (renewed every 12 h) in a dialysis bag (3.5 KD) for 72 h to obtain a 3% SF solution. To create a 3% CTS solution, CTS was dissolved in a solution of 3% glacial acetic acid.

2.1.2 Preparation of colonic extracellular matrix

The colon tissue was soaked in 2% SDS+0.5% EDTA solution, which was changed every 3 h, shaken at room temperature for 12 h, and rinsed up with PBS buffer. The tissues were then immersed in

1% Triton X100 + 0.5% EDTA, which was changed every 3 h, shaken at room temperature for 12 h, and then rinsed up with PBS buffer to obtain the CEM. The CEM was ground into a powder by cold extraction with liquid nitrogen.

2.2 Scaffold synthesis and block design

As previously reported, chemical cross-linking techniques and freeze-drying technology were used to create the scaffolds used in the study (Li et al., 2017). SF scaffolds were made using only the 3% SF solution. SF and CTS were combined in a 1:1 (w/w) ratio to create SF/CTS (1:1) scaffolds. Three distinct mass ratios of the SF solution, CTS solution, and CEM powder were used to make the SF/CTS/CEM scaffolds with different ratios: 1:1:0.5, 1:1:1, and 1:1:2 (w/w). The mixture was then added to a solution containing 95% aqueous ethanol, 50 mmol/L EDC, and 18 mmol/L NHS, and the combination was agitated magnetically for 30 min to produce a homogenous solution. The solutions were then cast into well-sized 24-well and 96-well plates and crosslinked for 12 h at 4 C. The samples were then frozen at −20 C for 12 h and stored at −80 C for a further 12 h. To create the scaffolds, the samples were put into a freeze-dryer for 48 h. Before beginning cell culture, we used a low-temperature plasma sterilizer to decontaminate the scaffolds.

2.3 Characterization of the scaffolds

2.3.1 Macroscopic appearance

Front and lateral views photographs were used to compare the various scaffold groups after they had been removed from the 24-well plate.

2.3.2 Internal morphology

After removing the scaffolds from the 24-well place, a layer of scaffold film with the scaffold's cross-sectional structure was left at the bottom of the well, and the structure of the scaffold film was examined under an optical microscope and captured on camera. The microstructures of the scaffolds were observed using a scanning electron microscope (SEM). The scaffolds were cut into small fragments with a surgical blade. We placed the prepared samples on the sample table and plated them with platinum. Then, the samples were put into the SEM and observed after vacuuming. We observed the microstructure and the microchannel of the scaffolds under the SEM and took photographs.

2.3.3 Porosity evaluation

The liquid replacement method is used to assess scaffold's porosity. Briefly, the scaffold is placed in anhydrous ethanol with a volume of V_0. The volume of pure ethanol and the submerged scaffold after full immersion was V_1. V_2 was the volume remaining after the impregnated scaffold was removed. The following formula was used to determine porosity: $(V_0\text{-}V_2)/(V_1\text{-}V_2) \times 100\%$.

2.3.4 Water uptake ratio

The mass of the scaffold in the dry state was recorded as W_1. PBS buffer was used to rehydrate the dried scaffolds for 24 h at 37°C. With the aid of filter paper, any remaining liquid on the surface was removed, and the wet sample's weight was recorded as W_2. The following formula was used to compute water uptake ratio: $(W_2\text{-}W_1)/W_1 \times 100\%$.

2.3.5 Degradation property

The mass of the scaffold in a dry environment was W_0. The scaffolds were placed in 6-well cell plate medium in PBS solution at 37 C, and then dried for 12 h at 65 C before being weighed at 1 d (day), 3 d, 7 d and 14 d (W_n). The following formula was used to compute the degradation ratio: $(W_0 – W_n)/W_0 \times 100\%$.

2.4 Cell incorporation into scaffolds

Scaffolds were sterilized at low temperature in advance. We seeded 50,000 cells into each scaffold in 24-well plates, then slowly shook these plates, and finally added 1 mL of complete medium to each well. Every other day, the culture medium was changed.

2.4.1 Cell adhesion in scaffolds

In a nutshell, HCT-116 105 cell (A_0) cell suspensions were seeded on pre-wetted scaffolds, and adhesion rates were assessed 1, 3, and 6 h later. The scaffolds were taken out of the wells, and cells were counted (A_1). Cells clinging to the well walls were digested and counted when the media was removed (A_2). The following formula was used to calculate the cell adhesion rate: $(A_0\text{-}A_1\text{-}A_2)/A_0 \times 100\%$. Three experiments were performed for each condition, and the average adhesion rate was calculated.

2.4.2 Cell proliferation in scaffold

CCK-8 was used to track cell proliferation in 2D plates, SF/CTS (1:1), and SF/CTS/CEM (1:1:1) scaffolds. Then, 100 μL of a cell suspension containing 10^3 HCT-116 cells was seeded onto scaffolds in 96-well plates. Following the manufacturer's instructions, proliferation of cell was assessed on 1 d, 3 d, and 5 d. Briefly, 10 μL CCK-8 reagent and 90 μL DMEM mixture was added to each well and the plate was placed for 90 min in the dark. Subsequently, we shocked the plates for 15 min and then the scaffolds were removed. To test absorbance at 450 nm, the remaining liquid was transferred to a fresh 96-well plate.

2.4.3 Cell growth, micro-structure, and ultra-structure in scaffolds

2.4.3.1 DAPI and DY-455-Phalloidin staining

HCT-116 cells (5×10^5) were cultured in a pre-prepared scaffold. For cytoskeletal staining, 0.5% Triton X-100 in PBS was used to permeabilize the cells for 10 min at room temperature after cells being fixed with 4% paraformaldehyde for 15 min on ice. Using 10 g/mL, cytoskeletons were stained after incubation for 20 min at room temperature with a solution of DY-455-Phalloidin conjugates, then rinsed with PBS to get rid of any unbound DY-455-Phalloidin conjugates. Nuclear staining was performed with DAPI. A fluorescent microscope was used to record the images (Leica DM2500).

2.4.3.2 Scanning electron microscope

HCT-116 cells were cultured on different groups of scaffolds. On days 1 and 3, the scaffold was washed with PBS for 3 times after the culture medium was removed. Then we used 4% paraformaldehyde to fix the cells. The plates were then placed in a refrigerator set at

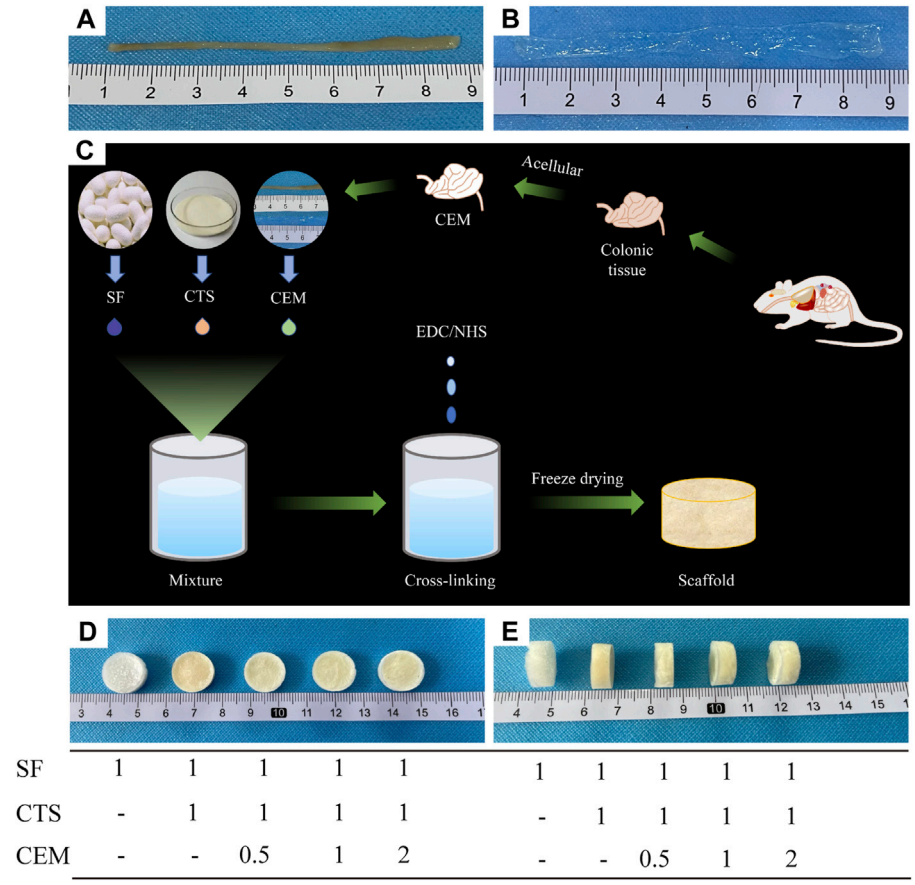

SF	1	1	1	1	1	1	1	1	1	1
CTS	-	1	1	1	1	-	1	1	1	1
CEM	-	-	0.5	1	2	-	-	0.5	1	2

FIGURE 1
Colon of fresh nude mice and its extracellular matrix after acellular treatment **(A, B)**; Flowchart of the preparation of composite scaffolds by freeze-drying technique **(C)**; Front and side views of SF, SF/Cs (1: 1), SF/Cs/CEM (1: 1: 0.5), SF/Cs/CEM (1: 1: 1), and SF/Cs/CEM (1: 1: 2) scaffolds **(D, E)**. SF, silk fibroin; CTS, chitosan; CEM, colon extracellular matrix.

80 °C for 12 h before being frozen at 20 C for another 12 h. The culture plates were then freeze-dried in a freeze-dryer for 48 h, and a SEM was used to examine the cell morphology on the scaffold.

2.4.3.3 Hematoxylin-eosin staining

Hematoxylin and eosin (HE) staining was performed to observe biocompatibility of scaffolds *in vivo* and *in vitro*. On days 1 and 3 of scaffold culture, the composites were fixed with 4% paraformaldehyde. Meanwhile, 1 month after subcutaneous implantation of the scaffold containing cells, the nude mice were treated and the tumor was removed. HCT-116 cells and scaffolds from the removed tumors were fixed with 4% paraformaldehyde. After embedding in paraffin, the tissues were sectioned into slices of 3 μm thickness. Slices where then stained for HE and photographed with a Leica DM2500 microscope and an oil-immersion lens.

2.5 DY-488-Annexin V staining and flow cytometry assay

HCT-116 cells were seeded into different scaffolds and cultured in a 1 g/L low-glucose medium for 24 h to induce apoptosis. Cells were digested with trypsin without EDTA (ShareBio, Shanghai, China) and collected in Eppendorf tubes. Cells were stained using the Annexin V FITC Apoptosis Kit (ShareBio, Shanghai). A flow observation analyzer was used to assess the staining.

2.6 Protein extraction and Western blotting

A RIPA solution containing 1% PMSF was used to lyse the cells, and the entire protein extraction process was carried out on ice. Following that, protein samples were centrifuged for 15 min at 10,000 rpm at 4°C. Using the BCA reagent, protein concentrations were measured. Proteins were separated by electrophoresis on SDS gels and then transferred to PVDF membranes. Prior to being incubated with primary antibodies for 14 h at 4 C, the PDVF membranes were blocked with 5% nonfat milk for 1–2 h at room temperature. The secondary antibody was incubated for 1–2 h at room temperature after three membrane washes. After washing the secondary antibody solution from the membrane three times, protein expression was detected using an enhanced chemiluminescence reagent.

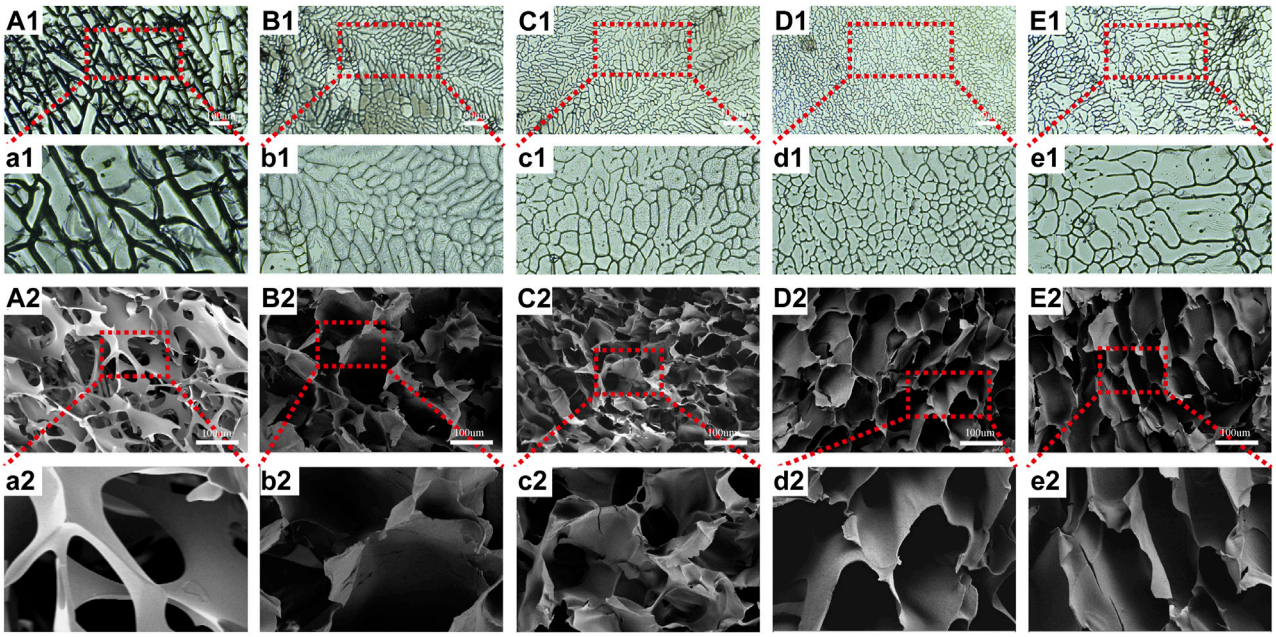

FIGURE 2
Images of optical microscope **(A1–E1, a1–e1)** and scanning electron microscope **(A2–E2, a2–e2)** of SF, SF/CTS (1: 1), SF/CTS/CEM (1: 1: 0.5), SF/CTS/CEM (1: 1: 1), and SF/CTS/CEM (1: 1: 2) scaffolds. SF, silk fibroin; CTS, chitosan; CEM, colon extracellular matrix.

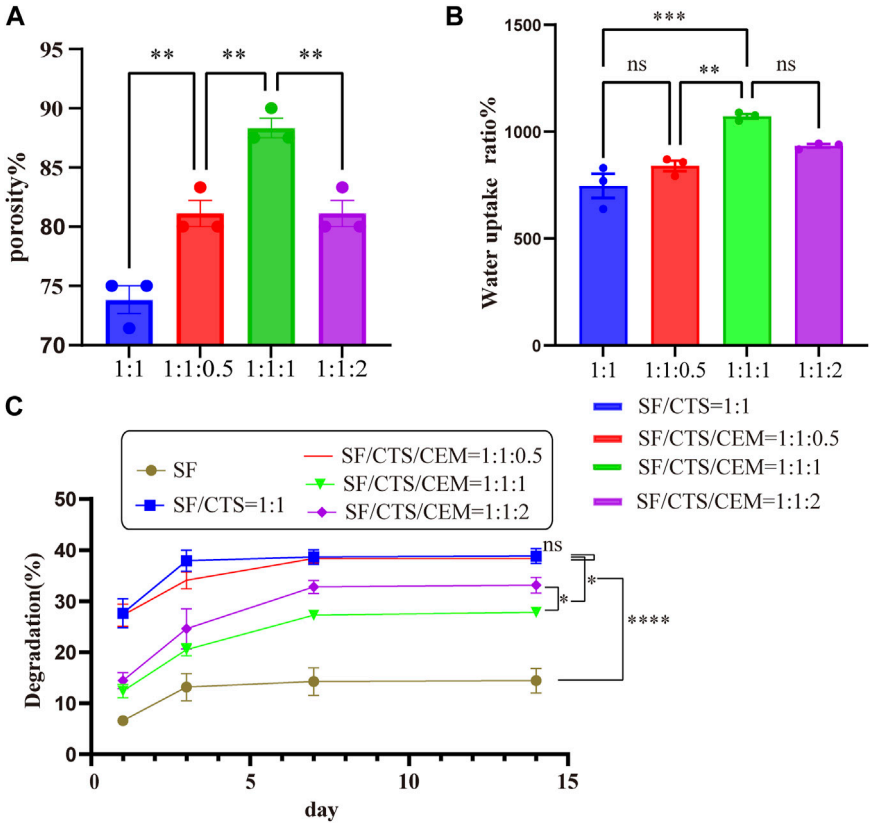

FIGURE 3
Results of porosity **(A)**, water uptake rate **(B)** and degradation rate **(C)** of different groups of scaffolds.*$p < 0.05$, **$p < 0.01$, ***$p < 0.001$.

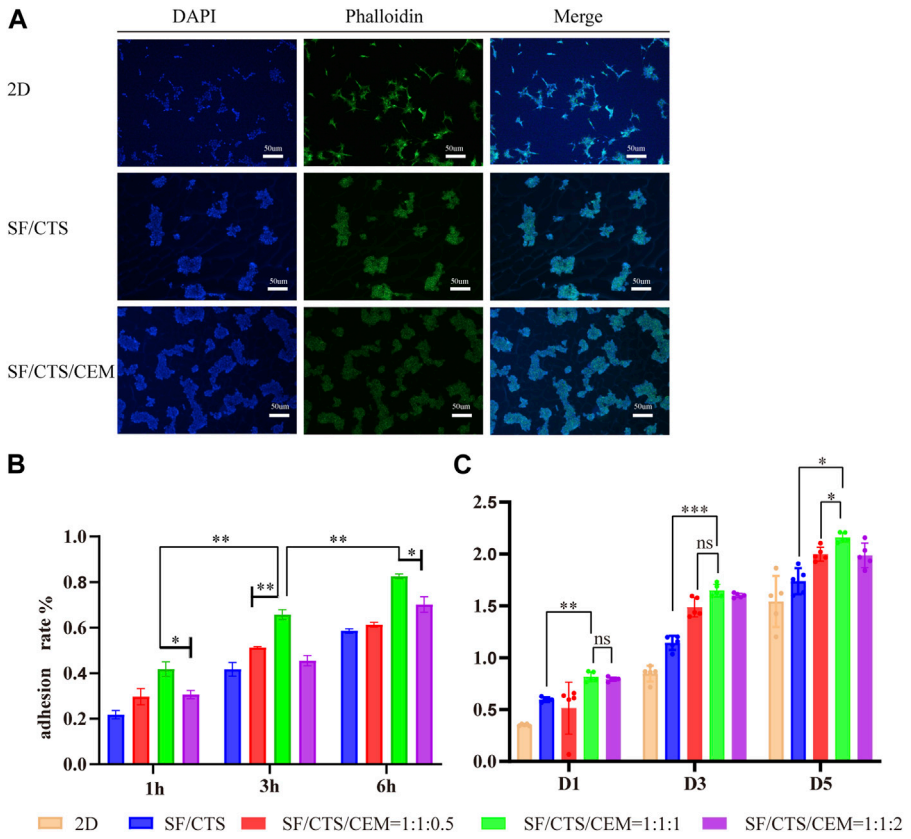

FIGURE 4
DAPI staining, Phalloidin staining and merging diagram of cultured HCT-116 cells in 2D, SF/CS (1:1) and SF/CS/CEM (1:1:1) **(A)**. Results of adhesion rate **(B)** and cell proliferation **(C)** of the different groups of scaffolds.*$p < 0.05$, **$p < 0.01$, ***$p < 0.001$. SF, silk fibroin; CTS, chitosan; CEM, colon extracellular matrix.

2.7 Immunohistochemical

Six-week-old mice were brought up in a pathogen-free environment. HCT-116 cells that had been conditioned in 2D, SF/CTS (1:1), and SF/CTS/CEM (1:1:1) were implanted subcutaneously into mice flanks. Using antibodies for Ki-67, PCNA, TUNEL, and Bcl-2 staining, tumor samples from mice were fixed in formalin and embedded in paraffin, sectioned into 5 μm slices, and subjected to immunohistochemical (IHC) staining. This was done 2 weeks and 1 month following cell implantation.

2.8 Statistical analysis

For all statistical calculations, the Graph Pad Prism 8 software was utilized. Each experiment was performed in triplicate. The mean and standard deviation (SD) were used to present quantitative data. The statistical significance was established using the Student's t-test and analysis of variance (ANOVA). When differences were *$p < 0.05$, **$p < 0.01$, or ***$p < 0.001$, they were deemed significant.

3 Results

3.1 Characterization of the composite scaffolds in 3D

3.1.1 Macroscopic appearance

Figure 1 depicts the macroscopic characteristics of the SF, SF/CTS (1:1), SF/CTS/CEM (1:1:0.5), SF/CTS/CEM (1:1:1), and SF/CTS/CEM (1:1:2) scaffolds. We noticed that the shapes of all the scaffolds were comparable. Most of the scaffolds were yellowish-white in color, whereas the SF scaffold was completely white.

3.1.2 Internal structure

To understand the internal structure of the scaffolds, we employed an optical microscope and SEM. As seen in Figure 2, every scaffold contained porous networks with architectures featuring various pore sizes, homogeneity, and strong pore connection. The addition of CTS and CEM changed the structure of pure SF scaffolds. The pore diameters and homogeneity of the SF/CTS/CEM (1:1:0.5), SF/CTS/CEM (1:1:1), and SF/CTS/CEM (1:1:2) scaffolds varied. As the proportion of CEM increased, the scaffold's pore size steadily grew.

10.3389/fbioe.2023.1139649

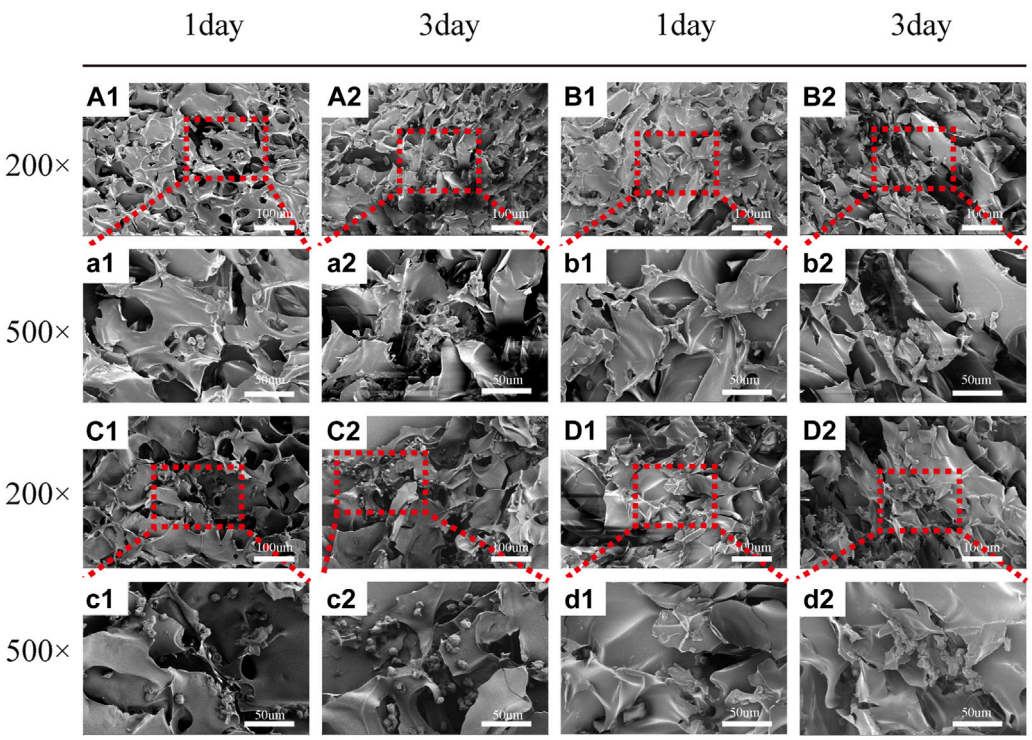

FIGURE 5
Scanning electron microscope images of HCT-116 cells on SF/CTS (1: 1), SF/CTS/CEM (1: 1: 0.5), SF/CTS/CEM (1: 1: 1), and SF/CTS/CEM (1: 1: 2) scaffolds. HCT-116 cells were cultured on different groups of scaffolds on day 1 **(A1–D1, a1–d1)** and day 3 **(A2–D2, a2–d2)**. SF, silk fibroin; CTS, chitosan; CEM, colon extracellular matrix.

3.1.3 Physical and chemical properties

3.1.3.1 Porosity

All scaffolds had porosities greater than 68.69% (Figure 3A). Of all the scaffolds, the SF/CTS/CEM (1:1:1) scaffold had the highest porosity (88.33% ± 3.58%), followed by the SF/CTS/CEM (1:1:2) scaffold (81.11% ± 4.78%). The porosities of the SF/CTS and SF/CTS/CEM (1:1:0.5) scaffold were 81.11% ± 4.78% and 73.81% ± 5.12%, respectively. Our findings demonstrated that there was a statistically significant difference in the porosity of the SF/CTS (1:1) and SF/CTS/CEM (1:1:1) scaffolds ($p < 0.05$).

3.1.3.2 Water uptake ratio

The water uptake ratios of the scaffolds are shown in Figure 3B. All of the scaffolds had water absorption rates in deionized water that were more than 501.9%. The maximum water uptake ratio was observed in the SF/CTS/CEM (1:1:1) scaffold (1,072% ± 48%), followed by the SF/CTS/CEM (1:1:2) scaffold (933.5% ± 36%). In contrast, the scaffold with the lowest water uptake ratio was the SF/CTS (1:1) scaffold (745.92% ± 44%). The results showed that there was significant difference in water absorption between SF/CTS (1:1) and SF/CTS/CEM (1:1:1) scaffolds.

3.1.3.3 Degradation rates

Figure 3C displays the scaffolds' degradation rates submerged in the PBS solution. The addition of CEM slowed the deterioration of the scaffolds. The SF/CTS/CEM (1:1:1) scaffold exhibited the lowest degradation rate, followed by the SF/CTS/CEM (1:1:2) scaffold. A significant difference observed between the two groups ($p < 0.05$). All five groups of scaffolds degraded to varying degrees within 14 days; however, the overall trends were similar. Day 3 was the turning point, as in the first 3 days degradation occurs rapidly, slowing down during the subsequent 4 days. From the 7th to 14th days, degradation stabilizes.

3.2 Cell incorporation into scaffolds

3.2.1 Cell adhesion in scaffolds

Counting cells on a cytometry plate at 1, 3, and 6 h after seeding the cells on the pre-wetted scaffolds allowed assessing cell adherence to the scaffolds. Figure 4B depicts the cell adhesion rate, showing that the SF/CTS/CEM (1:1:1) and SF/CTS/CEM (1:1:2) scaffolds had the highest rates. The SF/CTS/CEM (1:1:1) scaffold showed higher cell adhesion.

3.2.2 Cell proliferation in scaffold

To gauge cell proliferation on the various scaffold groups, the CCK-8 kit was used (Figure 4C). According to our findings, the scaffold with the highest proportion of proliferating cells at each time point was the SF/CTS/CEM (1:1:1) scaffold. Based on the statistical findings, the cell proliferation of the two scaffolds was not significantly different on day 1, whereas the cell proliferation of the triple scaffold was significantly higher on days 3 and 5.

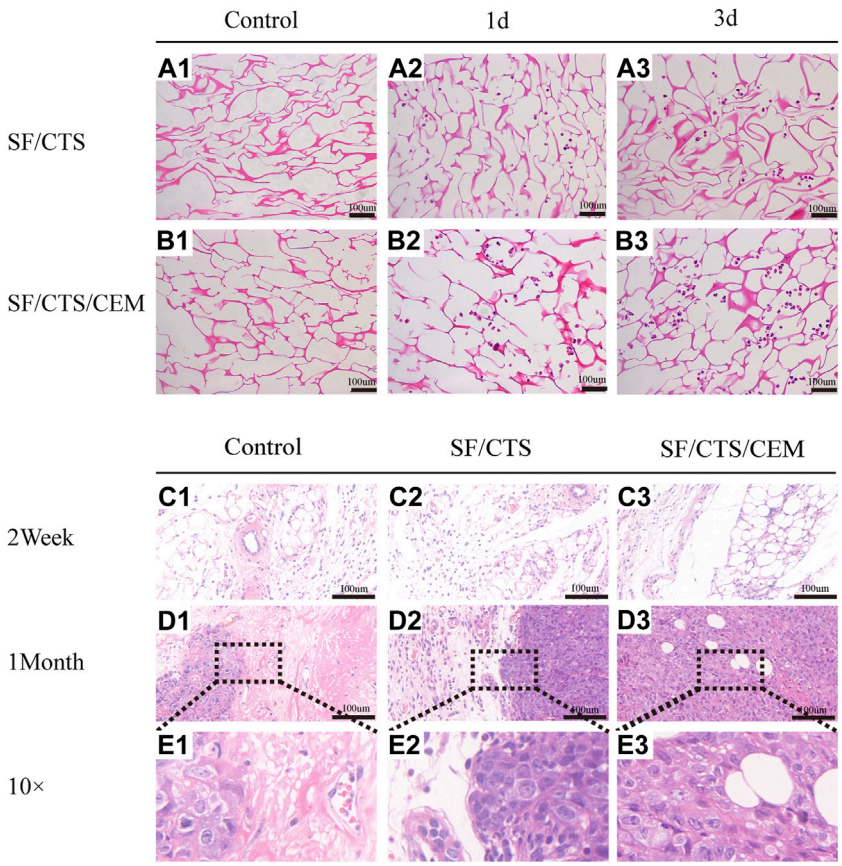

FIGURE 6
(A) Images of hematoxylin and eosin staining of scaffolds. Control groups were untreated SF/CTS (1:1) and SF/CTS/CEM (1:1:1) scaffolds, HCT-116 cells were cultured on SF/CTS (1:1) and SF/CTS/CEM (1:1:1) scaffolds on day 1 and day 3. **(B)** Images of hematoxylin and eosin staining of tumors formed after subcutaneous implantation of SF/CTS (1:1) and SF/CTS/CEM (1:1:1) scaffolds for 2 weeks and 1 month in nude mice. SF, silk fibroin; CTS, chitosan; CEM, colon extracellular matrix.

3.2.3 Cell growth, micro-structure and ultra-structure in scaffolds

3.2.3.1 DAPI and DY-488-Phalloidin staining

To visualize the cytoskeleton organization, we stained actin filaments with DY-488-Phalloidin-FITC and imaged the cells using a light microscope Leica DM2500 (Figure 4A). In 2D culture, the majority of the cells were long and fusiform, while the majority of the cells seeded in SF/CTS (1:1) and SF/CTS/CEM (1:1:1) scaffolds were spherical, which was more representative of the *in vivo* cell morphology. However, cell-cell attachments tended to be more pronounced in the SF/CTS/ECM (1:1:1) scaffold than in the SF/CTS (1:1) scaffold, with a spherical morphology. Additionally, we used DAPI to stain cell nuclei to confirm cell division, as shown in Figure 4A, which shows a statistically significant difference in the number of cells across the three scaffolds (2D, SF/CTS (1:1), and SF/CTS/CEM (1:1:1)) at all time points ($p < 0.001$). The proliferation ability of the SF/CTS/CEM (1:1:1) group was the highest.

3.2.3.2 SEM

Figure 5 depicts the SEM images of the cells on the scaffolds, displaying their morphology and health state. There was more room for cell division and proliferation in the SF/CTS/CEM (1:1:1) scaffold because the channel diameter was larger than that of the SF/CTS group (1:1). More cells proliferated on CEM-containing scaffolds. SF/CTS/CEM (1:1:1) scaffolds supported higher cell proliferation than SF/CTS (1:1) scaffolds under the same conditions. When compared to typical culture dishes, the cell morphologies in 3D scaffolds (SF/CTS/CEM (1:1:1) and SF/CTS (1:1)) were very different. In 3D scaffolds, the cells do not fully adhere to the scaffold and retain their body shape. The cells cultured in these scaffolds also had integrated spheres and, even though the number of cells grew over time, they did not spread across the inner surface of the scaffold. We also observed that the SF/CTS/CEM (1:1:1) scaffold supported a higher cell proliferation under the same conditions. The center portions of the scaffolds and the image are obtained (Figures 10 and 11). Figure 10 shows that internal situation of SF/CTS/CEM(1:1:1) scaffolds. Figure 11 shows the cell growth in the inner area of the scaffold with different material components. HCT-116 cells grow in the inner area of the different scaffolds. It was found that compared with the control group, the cells in SF/CTS/CEM (1:1:1) scaffolds group grew in lumps and had stronger proliferation ability.

3.2.3.3 HE staining

Images of HE-stained scaffolds are shown in Figure 6. Under the same conditions, the SF/CTS/ECM (1:1:1) scaffolds supported higher cell proliferation than the SF/CTS (1:1) counterparts. Compared with cells cultured in traditional 2D culture, cells on the scaffold tend to aggregate and grow. Notably, scaffolds implanted subcutaneously

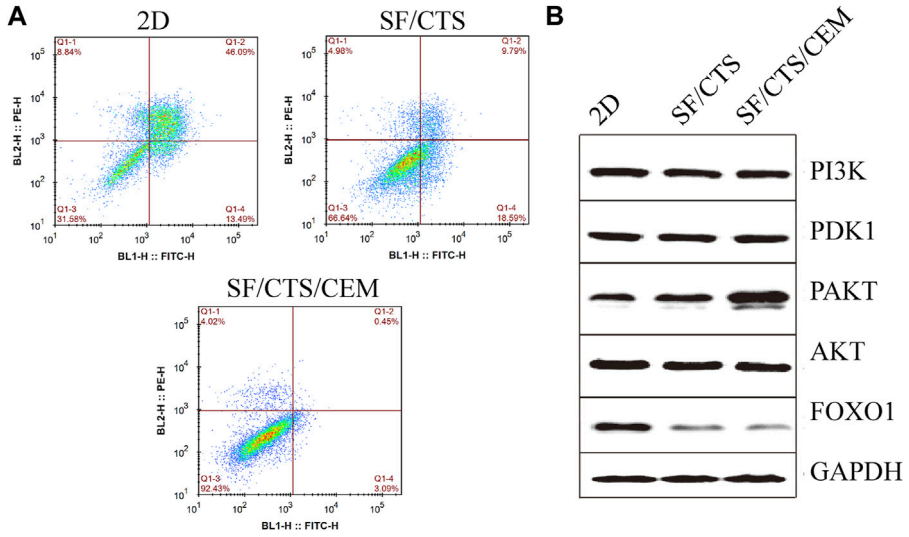

FIGURE 7
(A) Images of flow cytometry apoptosis of HCT-116 cells cultured in 2D, SF/CTS (1:1), and SF/CTS/CEM (1:1:1) scaffolds after apoptosis induction. **(B)** Analysis of protein expression of HCT-116 cells cultured on 2D, SF/CTS (1:1), and SF/CTS/CEM (1:1:1) scaffolds for 14 days. SF, silk fibroin; CTS, chitosan; CEM, colon extracellular matrix.

were gradually absorbed over time, and the tumor cells grew gradually. We also observed angiogenesis in the tumor.

3.3 Flow cytometry assay

Flow cytometry analysis of apoptosis is shown in Figure 7. Under the same induction conditions, the apoptosis of HCT-116 cells cultured with the SF/CTS/CEM scaffold was the lowest, followed by the SF/CTS scaffold, with the highest apoptosis being observed in the 2D group.

3.4 Protein extraction and Western blotting

To confirm the influence of SF/CTS/CEM scaffolds on apoptosis, the PI3K/PDK1/Akt/FoxO signaling pathway was investigated by gel electrophoresis using protein samples of cells cultured for 14 days in the different conditions. SF/CTS/CEM (1:1:1) scaffolds activated Akt phosphorylation and inhibited the expression of pro-apoptotic FoxO compared with SF/CTS (1:1) and 2D cultures, as shown by protein expression (Figure 7).

3.5 IHC staining

We subcutaneously injected HCT-116 cells grown on SF/CTS/CEM scaffolds or controls into the flanks of naked mice to determine whether tumor malignancy was reduced *in vivo* (n = 5 per scaffold). Figure 8 and Figure 9 illustrate how tumor cells cultured on SF/CTS/CEM scaffolds expressed Ki67 and PCNA at significantly higher levels than cells cultured in 2D. Bcl-2 and TUNEL expression were also downregulated.

4 Discussion

Conventional and classic 2D cell culture methods offer a practical platform for *in vitro* cancer. Cells cultivated on the surface of 2D flat Petri dishes, however, exhibit much less malignant phenotypes and do not accurately represent the same cell-ECM and cell-cell interactions as tumor formations *in vivo* (Smalley et al., 2006). To create scaffolds with the ideal culture properties, SF, CTS, and CEM have stimulated the development of 3D cell culture systems. Compared to SF scaffolds of pure silkworm, the blended scaffolds have different morphologies, porosities, elasticities, swelling behaviors, and biochemical compositions. Previously, the SF/CTS (1:1) mixture has been shown to be a potential biomaterial for the generation of scaffolds for cancer treatment (Gupta et al., 2009). In contrast to substrates made of pure biomaterials or synthetic polymers, according to a recent study 3D cell culture utilizing SF/CTS (1:1) scaffolds can promote cell proliferation in prostate cancer (Bäcker et al., 2017). Our preliminary experimental findings, however, indicated that SF/CTS (1:1) scaffolds had poor water absorption, a slow rate of breakdown, and a slow rate of cell adhesion, which restricts their use in 3D cell culture. Solid tumors are made up of genetically-mutated cancer cells surrounded by ECM and an additional group of genetically normal cells. The latter two elements are part of the tumor microenvironment and are important regulators of tumor biology, which has an impact on patients' prognoses. The tumor ECM has been the focus of research for the past 20 years, exposing the fundamental biochemical and biological concepts and mechanisms underlying its function in tumor cell survival and proliferation. The ECM, however, also has a significant impact on immune cells in the microenvironment, controlling their differentiation and infiltration into tumor cells, as well as their proliferation and survival (Kolesnikoff et al., 2022).

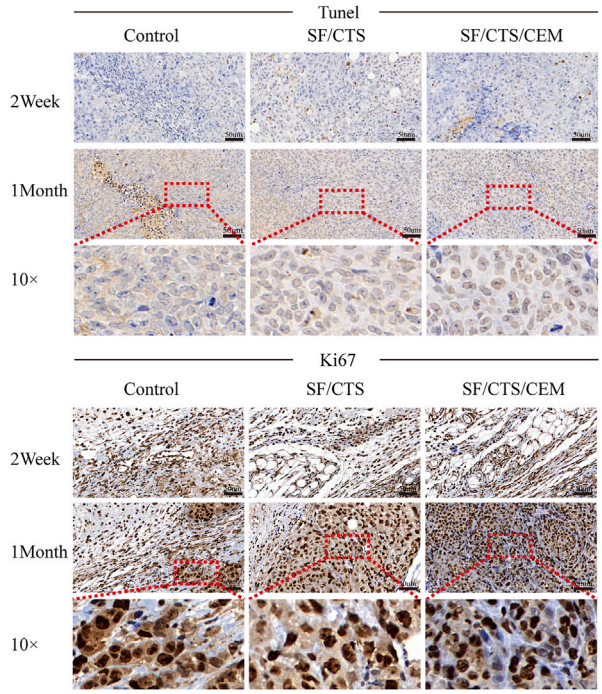

FIGURE 8
Immunohistochemical staining images of tumors formed by subcutaneous implantation of scaffolds. Two weeks and 1 month after implantation, tumor samples were subjected to immunohistochemical staining against TUNEL, and Ki67.

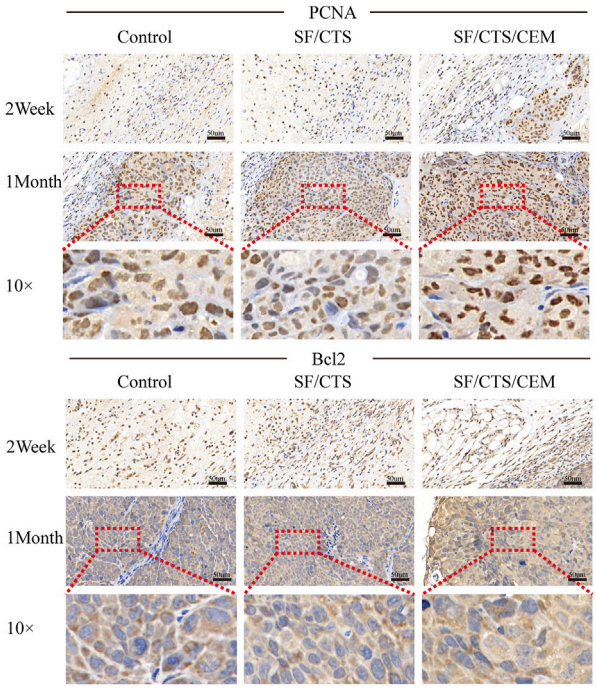

FIGURE 9
Immunohistochemical staining images of tumors formed by subcutaneous implantation of scaffolds. Two weeks and 1 month after implantation, tumor samples were subjected to immunohistochemical staining against PCNA and Bcl-2.

Currently, it is believed that the ECM chemical cues are the primary forces behind cancer formation and progression. Although the ECM mechanical forces have previously received little attention, they are now believed to be crucial to the development of illness and malignant cellular activity (Walker et al., 2018). The ECM surrounds the tumor cells, which interact dynamically with cytokines and signal transduction in its highly complicated milieu. The tumor microenvironment is a fertile ground for cell proliferation and malignant transformation, which can deter immune attacks, allow cancer cells to escape immune surveillance, cause surrounding infiltration and metastasis, and affect prognosis (Lu et al., 2020). We examined the changes in the biological features of cells following *in vivo* and *in vitro* culture using a 3D scaffolding method in order to evaluate the interaction between cells and the microenvironment (Liu et al., 2020). A 3D culture system was constructed, and preliminary exploration of the tumor microenvironment was performed (Wei et al., 2018). The study looked at how cells interact with the matrix using the biological framework of the TME that was built (Kievit et al., 2010; Mao et al., 2012). Based on the abovementioned advantages, to enhance the SF/CTS (1:1) composite scaffolds' qualities and make them better suited for cell culture, we added CEM to them. Furthermore, the interior structure of the SF/CTS (1:1) scaffold is simpler than the tumor cell microenvironment *in vivo*, notably in terms of chemical composition, while being more complex than that of a 2D cell culture system. The scaffold's chemical complexity can be increased, improving its ability to mimic the tumor milieu. This is accomplished by adding a CEM component. We predicted that the triple biomaterial composite scaffold would perform better than those consisting of just two biomaterials in terms of both features and performance. Our findings were intriguing in that HCT-116 cell spheres displayed tumor-like morphological characteristics seen *in vivo* in all four 3D scaffolds (SF/CTS (1:1), SF/CTS/CEM (1:1:0.5), SF/CTS/CEM (1:1:1), and SF/CTS/CEM (1:1:2)). The extremely aggressive activity typical of tumor cells *in vivo* was more likely to be displayed by cells growing in a 3D scaffold made of SF/CTS/CEM (1:1:1).

The Interaction between the OH- and COO- groups in SF, CTS, and CEM complexes is thought to produce interactions, enhancing the tensile strength of triple composite polymers. CEM might be added to the SF/CTS (1:1) composite scaffolds to increase their overall porosity and average pore diameter. Cells require physical room to function, which improves their ability to utilize nutrients and oxygen, as well as promoting effective removal of metabolic waste. These variables significantly affect the metabolic processes, cell attachment, proliferation, distribution, and differentiation (Nava et al., 2016). The optimal pore diameter depends on the specific cell type (Murphy et al., 2016). In our study, the SF/CTS/CEM (1:1:1) scaffold was the best for the culture and development of HCT-116 cells, due to its wide average pore width. High-porosity scaffolds improve mechanical interlocking and cell infiltration (Ionescu and Mauck, 2013). The SF/CTS/CEM (1:1:1) scaffold showed the best improvement of cell proliferation in our investigation and had the maximum porosity (88.33% ± 3.58%). For cell-infiltrating

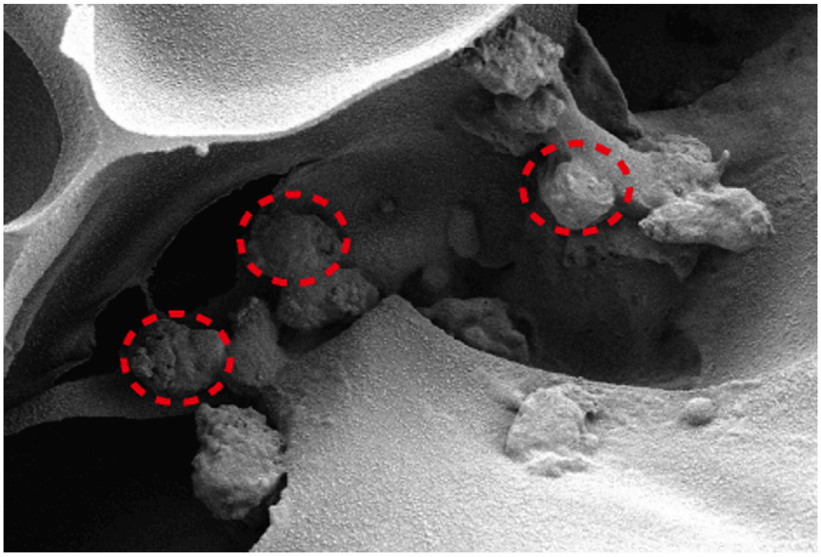

FIGURE 10
The interior environment of the SF/CTS/CEM(1:1:1) scaffolds can be seen in SEM images. The indicated region demonstrates how cells are expanding within the pores.

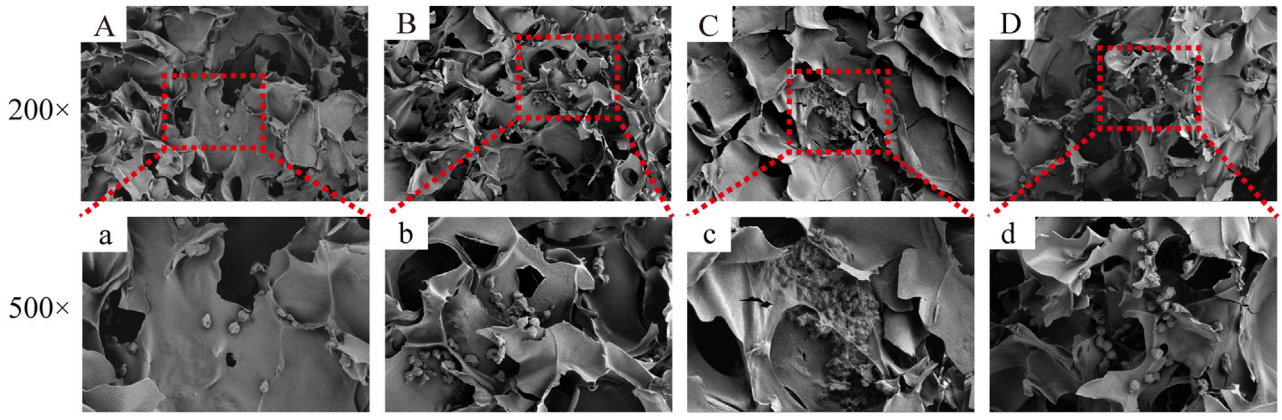

FIGURE 11
The figure shows the cell growth in the inner area of the scaffold with different material components. HCT-116 cells grow in the inner area of the SF/CS, SF/CTS/CEM(1:1:0.5), SF/CTS/CEM(1:1:1) and SF/CTS/CEM(1:1:2) scaffold **(A-D, a-d)**. Compared with **(A, a; B, b; D, d)**, the cells in SF/CTS/CEM (1:1:1) scaffolds group **(C, c)** grew in lumps and had stronger proliferation ability.

scaffolds, higher water absorption is preferred. A lower expansion rate helps maintain the structural stability of the scaffold. Here, a rise in the CEM percentage was associated with an increase in swelling and water absorption. According to our findings, the SF/CTS/CEM (1:1:1) scaffold exhibited a high water uptake ratio (1,072% ± 48%), was porous, and degraded at an optimum rate (Figure 3). Further characterization of the biological features of these scaffolds showed that the cells on the SF/CTS/CEM (1:1:1) scaffold exhibited the highest cell adhesion and proliferation rates (Figure 4), which supported the cell growth and morphological characteristics shown in the SEM images (Figure 5). The complete analysis of the biological features suggest that the optimal scaffold for the *in vitro* investigation of CC cells may be the SF/CTS/CEM (1:1:1) scaffold (Figure 10). Staining of the scaffold and cells revealed that the cells in the 3D scaffold kept their *in vivo* shape. Significant alterations in cell structure, protein expression, and mechanical properties occur during their migration through new tissues *in vivo* or in a new environment *in vitro*. It is well known that during movement, migration, adhesion, and proliferation, the cytoskeleton can undergo changes (Jin et al., 2012). In addition, cytoskeletal networks are essential for preserving cell shape (Ma et al., 2012). According to previous reports, a crucial condition for cell cycle progression is the cytoskeleton's proper configuration (Jiang et al., 2013). According to our findings, the 2D culture cells developed the slowest, followed by those on the SF/CTS/CEM (1:1:1) and the SF/CTS (1:1) scaffolds. The majority

of the cells in the 2D condition were long and fusiform, but the cells on the SF/CTS/CEM (1:1:1) and SF/CTS (1:1) scaffolds were round or nearly round (Figure 11). This indicated that the cells cultivated on scaffolds were more compatible with the growth status of cells *in vivo*. The HCT-116 cells transplanted on the 3D scaffold tended to assemble into multicellular spheres in contrast to the 2D monolayer model. These 3D multicellular aggregates serve as a useful alternative to traditional tumor models in cancer research (Hirschhaeuser et al., 2010). Our findings demonstrated that, compared to the SF/CTS (1:1) scaffold, the SF/CTS/CEM (1:1:1) scaffold supported sphere growth more significantly (Figure 5) and (Figure 11).

We also found that the cells cultured on SF/CTS/CEM (1:1:1) scaffolds showed significant proliferative ability, malignancy, and delayed tumor cell apoptosis compared with the those cultured in SF/CTS (1:1) scaffolds and 2D conditions. The PI3K/PDK/Akt/FoxO signaling pathway is a classical apoptosis regulator; therefore, we assessed the expression of this pathway. The findings demonstrated that p-Akt expression was upregulated and FoxO expression was downregulated in SF/CTS/CEM-cultured cells. These results suggest that the delay in apoptosis in scaffold culture is related to the PI3K/PDK/Akt/FoxO signal transduction pathway.

Despite the fact that our research sheds light on the development and possibility of fabricating composite scaffolds employing complimentary biopolymers, some issues still need to be addressed. As an example, the fundamental mechanisms observed in this study are still not well understood. In addition, in terms of porosity, water absorption, cell adhesion, proliferation, and sphere formation, our SF/CTS/CEM (1:1:1) scaffold performed well, although it came in second place in terms of disintegration rate. The association between the rate of degradation and cell proliferation cannot be inferred. Before these 3D models may be altered and widely used in medicine and basic science, further research is required to validate and clarify our findings and to better understand the potential mechanisms of cell growth and proliferation on these scaffolds.

5 Conclusion

The biological activity of CC cells differed depending on the type of material employed, as demonstrated by our analysis of the different HCT-116 cell culture conditions (2D, SF/CTS (1:1), and SF/CTS/CEM (1:1:1) scaffolds). According to our findings, the SF/CTS/CEM (1:1:1) scaffold has the potential to be a useful tumor model for CC cell culture studies and a realistic representation of cell growth in a 3D environment, as in living organisms.

Data availability statement

The original contributions presented in the study are included in the article/Supplementary Material, further inquiries can be directed to the corresponding authors.

Ethics statement

The animal study was reviewed and approved by Department of Laboratory Animal Science, Fudan University. Written informed consent was obtained from the owners for the participation of their animals in this study.

Author contributions

ZC, CK, and LC conceived the project and supervised all experiments. ZC designed the experiments and wrote the manuscript. LC analyzed the data. GN, YL, ZH, RH, XZ, and LH provided support with experimental techniques. The manuscript was revised by LC, SH, GN, YL, LH, and CK. All authors reviewed the manuscript. All authors read and approved the final manuscript.

Funding

This study was supported by the Medical System of Shanghai Minhang District (No.2020MWDXK02), the High-level professional physician training program of Minhang District (No.2020MZYS21), and the Health Profession Clinical Research Funds of Shanghai Municipal Health Commission (No.20204Y0390).

Acknowledgments

We appreciate Editage's (www.editage.cn) assistance with English language editing.

Conflict of interest

The authors declare that the research was conducted in the absence of any commercial or financial relationships that could be construed as a potential conflict of interest.

Publisher's note

Supplementary material

The Supplementary Material for this article can be found online at: https://www.frontiersin.org/articles/10.3389/fbioe.2023.1139649/full#supplementary-material

References

Algarrahi, K., Affas, S., Sack, B. S., Yang, X., Costa, K., Seager, C., et al. (2018). Repair of injured urethras with silk fibroin scaffolds in a rabbit model of onlay urethroplasty. *J. Surg. Res.* 229, 192–199. doi:10.1016/j.jss.2018.04.006

Bäcker, A., Erhardt, O., Wietbrock, L., Schel, N., Göppert, B., Dirschka, M., et al. (2017). Silk scaffolds connected with different naturally occurring biomaterials for prostate cancer cell cultivation in 3D. *Biopolymers* 107, 70–79. doi:10.1002/bip.22993

Bhardwaj, N., Nguyen, Q. T., Chen, A. C., Kaplan, D. L., Sah, R. L., and Kundu, S. C. (2011). Potential of 3-D tissue constructs engineered from bovine chondrocytes/silk fibroin-chitosan for *in vitro* cartilage tissue engineering. *Biomaterials* 32, 5773–5781. doi:10.1016/j.biomaterials.2011.04.061

Chomchalao, P., Pongcharoen, S., Sutheerawattananonda, M., and Tiyaboonchai, W. (2013). Fibroin and fibroin blended three-dimensional scaffolds for rat chondrocyte culture. *Biomed. Eng. OnLine.* 12, 28. doi:10.1186/1475-925X-12-28

Dekker, E., Tanis, P. J., Vleugels, J. L. A., Kasi, P. M., and Wallace, M. B. (2019). Colorectal cancer. *Lancet* 394, 1467–1480. doi:10.1016/S0140-6736(19)32319-0

Galvez Alegria, C., Gundogdu, G., Yang, X., Costa, K., and Mauney, J. R. (2019). Evaluation of acellular bilayer silk fibroin grafts for onlay tracheoplasty in a rat defect model. *Otolaryngol. Head. Neck Surg.* 160, 310–319. doi:10.1177/0194599818802267

Ghosh, M., Halperin-Sternfeld, M., and Adler-Abramovich, L. (2019). Bio mimicking of extracellular matrix. *Adv. Exp. Med. Biol.* 1174, 371–399. doi:10.1007/978-981-13-9791-2_12

Gu, Y., Zhu, J., Xue, C., Li, Z., Ding, F., Yang, Y., et al. (2014). Chitosan/silk fibroin-based, Schwann cell-derived extracellular matrix-modified scaffolds for bridging rat sciatic nerve gaps. *Biomaterials* 35, 2253–2263. doi:10.1016/j.biomaterials.2013.11.087

Gupta, V., Aseh, A., Ríos, C. N., Aggarwal, B. B., and Mathur, A. B. (2009). Fabrication and characterization of silk fibroin-derived curcumin nanoparticles for cancer therapy. *Int. J. Nanomedicine.* 4, 115–122. doi:10.2147/ijn.s5581

Hirschhaeuser, F., Menne, H., Dittfeld, C., West, J., Mueller-Klieser, W., and Kunz-Schughart, L. A. (2010). Multicellular tumor spheroids: An underestimated tool is catching up again. *J. Biotechnol.* 148, 3–15. doi:10.1016/j.jbiotec.2010.01.012

Ionescu, L. C., and Mauck, R. L. (2013). Porosity and cell preseeding influence electrospun scaffold maturation and meniscus integration *in vitro*. *Tissue Eng. Part a.* 19, 538–547. doi:10.1089/ten.TEA.2012.0052

Jiang, J., Jin, H., Liu, L., Pi, J., Yang, F., and Cai, J. (2013). Curcumin disturbed cell-cycle distribution of HepG2 cells via cytoskeletal arrangement. *Scanning* 35, 253–260. doi:10.1002/sca.21058

Jin, H., Pi, J., Huang, X., Huang, F., Shao, W., Li, S., et al. (2012). BMP2 promotes migration and invasion of breast cancer cells via cytoskeletal reorganization and adhesion decrease: An AFM investigation. *Appl. Microbiol. Biotechnol.* 93, 1715–1723. doi:10.1007/s00253-011-3865-3

Kievit, F. M., Florczyk, S. J., Leung, M. C., Veiseh, O., Park, J. O., Disis, M. L., et al. (2010). Chitosan-alginate 3D scaffolds as a mimic of the glioma tumor microenvironment. *Biomaterials* 31, 5903–5910. doi:10.1016/j.biomaterials.2010.03.062

Kolesnikoff, N., Chen, C. H., and Samuel, M. S. (2022). Interrelationships between the extracellular matrix and the immune microenvironment that govern epithelial tumour progression. *Clin. Sci. (Lond.).* 136, 361–377. doi:10.1042/CS20210679

Landberg, G., Fitzpatrick, P., Isakson, P., Jonasson, E., Karlsson, J., Larsson, E., et al. (2020). Patient-derived scaffolds uncover breast cancer promoting properties of the microenvironment. *Biomaterials* 235, 119705. doi:10.1016/j.biomaterials.2019.119705

Li, J., Wang, Q., Gu, Y., Zhu, Y., Chen, L., and Chen, Y. (2017). Production of composite scaffold containing silk fibroin, chitosan, and gelatin for 3D cell culture and bone tissue regeneration. *Med. Sci. Monit.* 23, 5311–5320. doi:10.12659/msm.905085

Liang, W., Gao, M., Lou, J., Bai, Y., Zhang, J., Lu, T., et al. (2020). Integrating silicon/zinc dual elements with PLGA microspheres in calcium phosphate cement scaffolds synergistically enhances bone regeneration. *J. Mat. Chem. B* 8, 3038–3049. doi:10.1039/c9tb02901j

Liu, Z., Tamaddon, M., Gu, Y., Yu, J., Xu, N., Gang, F., et al. (2020). Cell seeding process experiment and simulation on three-dimensional polyhedron and cross-link design scaffolds. *Front. Bioeng. Biotechnol.* 8, 104. doi:10.3389/fbioe.2020.00104

Lovitt, C. J., Shelper, T. B., and Avery, V. M. (2018). Doxorubicin resistance in breast cancer cells is mediated by extracellular matrix proteins. *BMC Cancer* 18, 41. doi:10.1186/s12885-017-3953-6

Lu, Z., Zou, J., Li, S., Topper, M. J., Tao, Y., Zhang, H., et al. (2020). Epigenetic therapy inhibits metastases by disrupting premetastatic niches. *Nature* 579, 284–290. doi:10.1038/s41586-020-2054-x

Ma, L., Song, B., Jin, H., Pi, J., Liu, L., Jiang, J., et al. (2012). Cinobufacini induced MDA-MB-231 cell apoptosis-associated cell cycle arrest and cytoskeleton function. *Bioorg. Med. Chem. Lett.* 22, 1459–1463. doi:10.1016/j.bmcl.2011.11.095

Mao, M., He, J., Liu, Y., Li, X., and Li, D. (2012). Ice-template-induced silk fibroin-chitosan scaffolds with predefined microfluidic channels and fully porous structures. *Acta Biomater.* 8, 2175–2184. doi:10.1016/j.actbio.2011.12.025

Murphy, C. M., Duffy, G. P., Schindeler, A., and O'Brien, F. J. (2016). Effect of collagen-glycosaminoglycan scaffold pore size on matrix mineralization and cellular behavior in different cell types. *J. Biomed. Mat. Res. A* 104, 291–304. doi:10.1002/jbm.a.35567

Nava, M. M., Draghi, L., Giordano, C., and Pietrabissa, R. (2016). The effect of scaffold pore size in cartilage tissue engineering. *J. Appl. Biomater. Funct. Mat.* 14, e223–e229. doi:10.5301/jabfm.5000302

Patrulea, V., Ostafe, V., Borchard, G., and Jordan, O. (2015). Chitosan as a starting material for wound healing applications. *Eur. J. Pharm. Biopharm.* 97, 417–426. doi:10.1016/j.ejpb.2015.08.004

Ríos, C. N., Skoracki, R. J., Miller, M. J., Satterfield, W. C., and Mathur, A. B. (2009). *In vivo* bone formation in silk fibroin and chitosan blend scaffolds via ectopically grafted periosteum as a cell source: A pilot study. *Tissue Eng. Part a.* 15, 2717–2725. doi:10.1089/ten.TEA.2008.0360

Shin, H. S., Hong, H. J., Koh, W. G., and Lim, J. Y. (2018). Organotypic 3D culture in nanoscaffold microwells supports salivary gland stem-cell-based organization. *ACS Biomater. Sci. Eng.* 4, 4311–4320. doi:10.1021/acsbiomaterials.8b00894

Smalley, K. S., Lioni, M., and Herlyn, M. (2006). Life isn't flat: Taking cancer biology to the next dimension. *in vitro* cell. *Dev. Biol. Anim.* 42, 242–247. doi:10.1290/0604027.1

Sung, H., Ferlay, J., Siegel, R. L., Laversanne, M., Soerjomataram, I., Jemal, A., et al. (2021). Global cancer statistics 2020: GLOBOCAN estimates of incidence and mortality worldwide for 36 cancers in 185 countries. *CA Cancer J. Clin.* 71, 209–249. doi:10.3322/caac.21660

Walker, C., Mojares, E., and Del Río Hernández, A. (2018). Role of extracellular matrix in development and cancer progression. *Int. J. Mol. Sci.* 19, 3028. doi:10.3390/ijms19103028

Wei, G., Wang, J., Lv, Q., Liu, M., Xu, H., Zhang, H., et al. (2018). Three-dimensional coculture of primary hepatocytes and stellate cells in silk scaffold improves hepatic morphology and functionality *in vitro*. *J. Biomed. Mat. Res. A* 106, 2171–2180. doi:10.1002/jbm.a.36421

Xie, M., Fan, D., Chen, Y., Zhao, Z., He, X., Li, G., et al. (2016). An implantable and controlled drug-release silk fibroin nanofibrous matrix to advance the treatment of solid tumour cancers. *Biomaterials* 103, 33–43. doi:10.1016/j.biomaterials.2016.06.049

Zhang, X., Hu, F., Li, G., Li, G., Yang, X., Liu, L., et al. (2018). Human colorectal cancer-derived mesenchymal stem cells promote colorectal cancer progression through IL-6/JAK2/STAT3 signaling. *Cell. Death Dis.* 9, 25. doi:10.1038/s41419-017-0176-3

Zhao, J., Li, J., Jiang, Z., Tong, R., Duan, X., Bai, L., et al. (2020). Chitosan, N,N,N-trimethyl chitosan (TMC) and 2-hydroxypropyltrimethyl ammonium chloride chitosan (HTCC): The potential immune adjuvants and nano carriers. *Int. J. Biol. Macromol.* 154, 339–348. doi:10.1016/j.ijbiomac.2020.03.065

frontiers | Frontiers in Bioengineering and Biotechnology

TYPE Mini Review
PUBLISHED 30 May 2023
DOI 10.3389/fbioe.2023.1217067

OPEN ACCESS

EDITED BY
Yawei Du,
Shanghai Jiao Tong University, China

REVIEWED BY
Junjie Li,
Soochow University, China
Weifeng Zeng,
University of Wisconsin-Madison, United States

*CORRESPONDENCE
Yuan-Yu Hsueh,
yyhsueh@mail.ncku.edu.tw

RECEIVED 04 May 2023
ACCEPTED 23 May 2023
PUBLISHED 30 May 2023

CITATION
Hsu M-W, Chen S-H, Tseng W-L, Hung K-S, Chung T-C, Lin S-C, Koo J and Hsueh Y-Y (2023), Physical processing for decellularized nerve xenograft in peripheral nerve regeneration. *Front. Bioeng. Biotechnol.* 11:1217067. doi: 10.3389/fbioe.2023.1217067

Physical processing for decellularized nerve xenograft in peripheral nerve regeneration

Ming-Wei Hsu[1], Szu-Han Chen[1,2,3], Wan-Ling Tseng[4], Kuo-Shu Hung[1], Tzu-Chun Chung[5], Sheng-Che Lin[6], Jahyun Koo[7] and Yuan-Yu Hsueh[1,2,3]*

[1]Division of Plastic and Reconstructive Surgery, Department of Surgery, National Cheng Kung University Hospital, College of Medicine, National Cheng Kung University, Tainan, Taiwan, [2]Center of Cell Therapy, National Cheng Kung University Hospital, College of Medicine, National Cheng Kung University, Tainan, Taiwan, [3]International Research Center for Wound Repair and Regeneration, National Cheng Kung University, Tainan, Taiwan, [4]Division of Plastic and Reconstructive Surgery, Department of Surgery, Tainan Hospital, Ministry of Health and Welfare, Tainan, Taiwan, [5]Department of Orthopedic Surgery, E-Da Hospital, Kaohsiung, Taiwan, [6]Division of Plastic Surgery, Department of Surgery, An-Nan Hospital, China Medical University, Tainan, Taiwan, [7]School of Biomedical Engineering, Korea University, Seoul, Republic of Korea

In severe or complex cases of peripheral nerve injuries, autologous nerve grafts are the gold standard yielding promising results, but limited availability and donor site morbidity are some of its disadvantages. Although biological or synthetic substitutes are commonly used, clinical outcomes are inconsistent. Biomimetic alternatives derived from allogenic or xenogenic sources offer an attractive off-the-shelf supply, and the key to successful peripheral nerve regeneration focuses on an effective decellularization process. In addition to chemical and enzymatic decellularization protocols, physical processes might offer identical efficiency. In this comprehensive minireview, we summarize recent advances in the physical methods for decellularized nerve xenograft, focusing on the effects of cellular debris clearance and stability of the native architecture of a xenograft. Furthermore, we compare and summarize the advantages and disadvantages, indicating the future challenges and opportunities in developing multidisciplinary processes for decellularized nerve xenograft.

KEYWORDS

decellularized nerve xenograft, peripheral nerve regeneration, physical processing, freeze-thaw, perfusion, immersion and agitation, sonication, supercritical fluids

1 Introduction

The current gold standard for peripheral nerve repair in segmental defects is autologous nerve grafting (Kalomiri et al., 1994). However, several limitations hamper the clinical practice, such as limited supply, donor site morbidity, and size discrepancy (Hu et al., 2009). Alternative autologous nerve substitutes, such as autologous veins, muscles, and tendons have been utilized with variable outcomes (Ray et al., 2011). Because of the abovementioned drawbacks, tissue engineered nerve grafts (TENG) were developed, aiming to provide a biomimetic scaffold for peripheral nerve regeneration (Houschyar et al., 2016). Although the Food and Drug Administration had approved several off-the-shelf synthetic nerve conduits on the market, but most of them are limited to nerve gaps <3 cm or <0.5 cm in small or large diameter nerves, respectively (de Ruiter et al., 2009). In addition, a recent review does not support the use of currently available TENG over standard nerve repair (Thomson et al.,

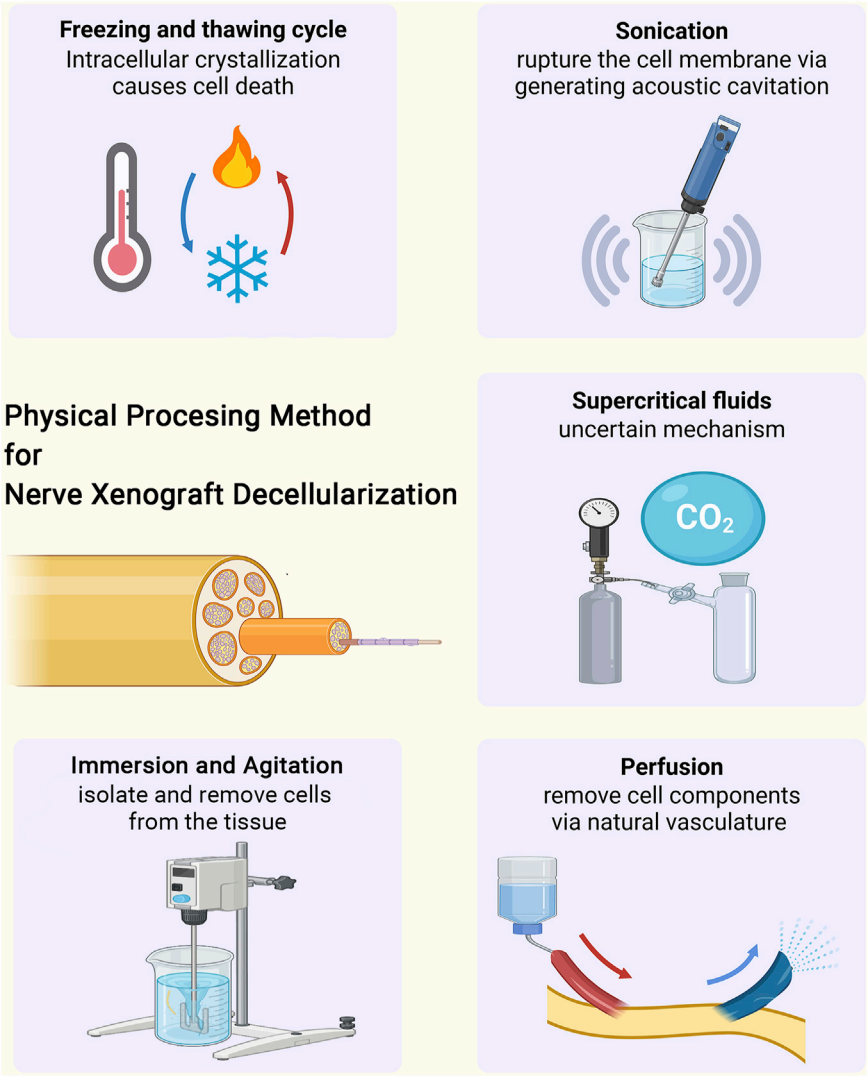

FIGURE 1
The physical processing methods for tissue decellularization of nerve xenograft, including freezing and thawing cycle, sonication, immersion and agitation, perfusion and supercritical fluids.

2022). To achieve a better outcome in longer nerve gaps, nerve allografts are harvested and processed under a commercial decellularization process. Avance®, a mature commercial product which is produced by processing human nerve tissue with a combination of detergent decellularization, chondroitinase CSPG degradation, and gamma-irradiation sterilization, has clinical evidence to overcome up to 70 mm nerve gap in sensory, mixed, and motor nerve repair (Gunn et al., 2010; Safa et al., 2020). However, limited donor sources, high costs, low temperature preservation, and potential immune rejection still remain as clinical concerns for its wide usage.

Xenotransplantation was developed due to the unlimited availability of sources. In general, fresh xenografts elicit an immune response that causes graft rejection. The presence of non-self-antigenic epitopes triggers the activation of T- and B-lymphocytes. This, in turn, leads to the activation of an immune response mediated by antibodies, ultimately resulting in the rejection of these cells. (Fox et al., 2001; Vadori and Cozzi, 2014; Lopresti et al., 2015). Despite using immunosuppressive drugs, decellularization is an effective approach to utilize the xenogeneic and allogeneic tissues. The cellular components of tissues are the main cause of an adverse host response. To mitigate immune rejection, several decellularization techniques were developed to remove cellular components to reduce immunogenic reactions while preserving native scaffold or extracellular matrix (ECM) microstructure (Rana et al., 2017). Several recent studies reported that acellular nerve xenografts have similar effects on regeneration and immunocompatibility compared with acellular nerve allografts (Zhang et al., 2010; Huang et al., 2015). The concept of Decellularized extracellular matrix (dECM) is established as using various methods (physical, enzymatic, or chemical) to lyse cells and remove the intracellular components from a tissue while preserving the native extracellular components and the cues for cell proliferation and differentiation (Dahl et al., 2003; Lopresti et al.,

TABLE 1 Summary of current physical processing methods for decellurized nerve xenograft.

Method	Mechanism	Xenograft source	Advantages	Disadvantages	References
Freeze-thaw cycles	Intracellular crystallization causes cell death	porcine, rabbit, dog	easy, low-cost	limited ability to eliminate cells	Ide (1983), Ide, Tohyama, Yokota, Nitatori, & Onodera (1983), Osawa et al. (1990), Evans et al. (1998), Hess et al. (2007), Jesuraj et al. (2014), Kaizawa et al. (2017), Philips et al. (2018)
Sonication	rupture the cell membrane via generating acoustic cavitation	rabbit	low-cost; can shorten processing time	can't remove DNA content	Hudson et al. (2004), Boriani et al. (2017), Bolognesi et al. (2022), Suss et al. (2022)
Perfusion	Pressure induced by perfusion via natural vasculature can remove cellular components	porcine	might overcome long nerve gap avoid ischemic damage and central necrosis	surgical complexity, donor site morbidity and limited nerve availability	Wüthrich et al. (2020)
Immersion and Agitation	isolate and remove cells from the tissue	rat	Easy, might overcome long nerve gap	Time consumable	Vasudevan et al. (2014)
Supercritical fluids	Uncertain	porcine	environmental friendly, nontoxicity, low cost, disinfection	low ability of defatting	Isenschmid et al. (1995), White et al. (2006), Casali et al. (2018), Topuz et al. (2020), Wei et al. (2022)

2015; Kim et al., 2019). Although regeneration can occur in short nerve gaps regardless of an immune response, nerve growth was suppressed in long nerve gaps (Choi and Raisman 2003).

Zhang and Chen summarized several decellularization protocols along with their mechanisms and disadvantages, including physical, chemical, and enzymatic treatments in organ or tissue (Zhang et al., 2022). For nerve growth, a biomimetic neural scaffold is crucial, and thus, limited decellularization methods are applicable. Chemical-based decellularization was widely used in nerve tissues, but the major concern was the possible interruption of nerve growth by the residual chemical agents (Han et al., 2019). Enzymatic treatments provide high specificity for the removal of cellular components; however, they cannot be removed completely that might induce severe distortion of the ECM structure.

This minireview aims to focus on the latest five physical-based decellularization methods for peripheral nerve xenotransplantation (Figure 1). Table 1 summarizes the mechanisms, advantages, and disadvantages of the current physical processing methods.

2 Different approaches of physical processing

This minireview aims to clarify the latest four physical-based decellularization methods for peripheral nerve xenotransplantation (Figure 1). Table 1 summarizes the mechanisms, advantages, and disadvantages of the current physical processing methods.

2.1 Freeze–thaw cycles

Freeze–thaw cycles refer to a repetitive freeze-drying process (Zhang et al., 2022). In nerve xenografts, the aim of cold preservation and freeze–thaw cycles is to destroy the nerve cell membranes by inducing the formation of intracellular ice crystals, thereby reducing the immunogenicity of nerve xenografts (Hare et al., 1993; Fox et al., 2005; Philips et al., 2018). Cold preservation and freeze–thaw cycles are easy to manipulate and an initial step in many decellularization protocols, as the protocols can be adjusted according to nerve length and diameter, depending on the laboratory preferences (Lasso and Deleyto, 2017).

However, studies have shown that the ultrastructure of nerves may be damaged by the freeze–thaw cycles, although the mechanical properties of the nerves are preserved (Osawa et al., 1990; Evans et al., 1998). A slower recovery in rats that received frozen grafts compared with those that received fresh autografts in a 2 cm median-nerve-gap rat model using Beagle dog acellular frozen xenografts indicate that freezing leads to a barren microenvironment for nerve regeneration (Accioli De Vaconcellos et al., 1999). Furthermore, the freeze–thaw process led to nerve xenograft rejection caused by the residual cells and debris (Lu et al., 2009). Despite the easy manipulation of freeze-thaw cycles, they might be responsible for damage to the nerve microstructure and a depleted environment for nerve regeneration.

2.2 Perfusion

Perfusion refers to the process of introducing circulating agents through the intrinsic vascular system of organs or tissues. This technique is typically used in larger, thicker tissues or whole organs (Goh et al., 2018). Only one study has reported the use of perfusion decellularization in peripheral nerve repair. Wüthrich and Lese applied perfusion decellularization to surgically procured vascularized porcine sciatic nerves (Wüthrich et al., 2020). A 3D microcomputed tomography imaging showed preserved vasculature and the ECM component. The dissected graft contained more external connective tissues, and the measurable growth factors were detectable at low levels. These results suggest that the biological activity of the graft may be retained and could

promote nerve regeneration. An *in vitro* study revealed the potential for re-endothelialization, but no *in vivo* study has been conducted yet. These nerve scaffolds can be created for specific lesions and are becoming increasingly available, with the potential to overcome large nerve gaps.

2.3 Immersion and agitation

Immersion and agitation refers to the process of submerging tissues into decellularization solutions with constant mechanical agitation (Crapo et al., 2011; Zhang et al., 2022). Compared with perfusion treatment, immersion and agitation is used in processing small, fragile and thin sections of tissues without innate vascular structures (Alshaikh et al., 2019). The efficiency of this method depends on different paraments including agitation intensity, decellularization agent and tissue dimension (Duisit et al., 2018). Immersion and agitation methods of tissue decellularization have been described for a wide variety of tissues, including peripheral nerves (Hudson et al., 2004; Karabekmez et al., 2009; Vasudevan et al., 2014). However, most of the decellularization solutions were chemical, detergent, or enzymatic solutions (Keane et al., 2015). To the best of our knowledge, only Vasudevan et al. reported an immersion and agitation method with detergent-free solution in peripheral nerve field (Vasudevan et al., 2014). In their design, the nerve grafts were immersed with detergent-free solution and were cultured at 37°C with 5% CO2 for 2 weeks under constant agitation, which was performed to initiate Wallerian degeneration *in vitro* to clear axonal and myelin debris inside the nerves. In the 3.5-cm sciatic nerve transection rat model, nerve regeneration was identical to that of detergent-processed grafts, while the functional nerve regeneration was only observed in detergent-free decellularized grafts at 12 weeks. This method did not significantly affect the ECM surface structure, collagen structure and integrity, mechanical strength, and GAG content, but may cause more damages to tissues due to the limited diffusion of chemical, detergent, or enzymatic decellularization solutions by agitation (Wilson et al., 2016; Simsa et al., 2019; Zhang et al., 2022).

2.4 Sonication

Sonication is a method of rupturing the cell membrane by generating acoustic cavitation bubbles and inducing shear stress effect. It can assist in the penetration of agents by vibration as well as remove cellular debris. It was demonstrated that coupling freeze–thawing with sonication contributes to a cell-free and aseptic xenograft in a shorter time than applying freeze–thawing alone in a rabbit peripheral nerve model (Boriani et al., 2017). Based on these results, they further developed a new method of soaking the nerve tissues in decellularizing solutions, with combination of sonication and freeze–thaw cycles (Bolognesi et al., 2022). This new method was validated through histology and immunohistochemistry, showing its application to decellularized xenografts with similar or better results compared with the Hudson technique (Hudson et al., 2004). However, it was observed that sonication during chemical decellularization did not remove deoxyribonucleic acid (DNA) content but only cellular debris and myelin sheaths (Suss et al., 2022). So far, no study has utilized sonication as a single process for xenograft decellularization.

2.5 Supercritical fluids

Supercritical fluids are fluids above their critical pressure and temperature that possess characteristics such as low viscosity and high diffusivity. Supercritical carbon dioxide ($ScCO_2$) is an environmentally friendly solvent that is widely used in the field of biomedicine and biomaterials due to its nontoxicity, low cost, and superior disinfection and sterilization abilities (Subramaniam et al., 1997; Casali et al., 2018). It has a critical pressure 7.38 MPa and a critical temperature 31°C. $ScCO_2$ has been shown to remove cells from the tissues while maintaining the ECM structure. However, the exact mechanism by which this occurs is unclear. The hypothesis that high pressure induces cell bursting, as claimed by Topuz et al., has been refuted (Isenschmid et al., 1995; White et al., 2006). It is hypothesized that ScCO2 might induce hypoxia, which has been validated by histological and morphological analyses after successful decellurization of bovine optic nerves using ScCO2 (Topuz et al., 2020). Wei et al. developed a porcine acellular nerve xenograft based on supercritical extraction technology and validated it in a 15-mm rat sciatic nerve model (Wei et al., 2022). A porous nerve basement membrane with a well-preserved 3D structure was observed. Low cytotoxicity was noted *in vitro*, leading to decreased immune response *in vivo*. The $ScCO_2$ treatment group was found to be similar to the autologous nerves in terms of regenerated nerve quality, target muscle wet weight regain, and motor function recovery. Moreover, the hybrid detergent plus $ScCO_2$ treatment demonstrated better outcomes in terms of decellularization and defatting compared to $ScCO_2$ alone (Casali et al., 2018).

3 Challenges and opportunities

In recent decades, tissue engineering has been applied in the field of regenerative medicine to peripheral nerve repair, relying on the three main pillars: scaffolds, cells, and growth factors (Carvalho et al., 2019). In scaffolds, preserving the biomimetic microenvironment is essential, whereas in xenografts, the removal of cells is critical to prevent subsequent immune rejection. Gilpin and Yang et al. measured four aspects of the decellularized ECM to assess the quality of decellularization: removal of cells, elimination of genetic material, preservation of the protein content, and retention of the mechanical properties (Gilpin and Yang, 2017). Carpo et al. proposed specific criteria for assessing the efficacy of cell removal: the decellularized ECM must have the following: 1) less than 50 ng double-stranded DNA per mg ECM dry weight, 2) less than 200 bp DNA fragment length, and 3) no visible nuclear material by 4′,6-diamidino-2-phenylindole staining (Crapo et al., 2011).

Chemical and enzymatic approaches are the most widely applied methods for peripheral nerve decellularization, but the possible toxicity of the chemicals and destruction of the ECM proteins

are major drawbacks of these methods. Physical treatments like modulating temperature or pressure have been effective, but it comes with limitations because of the natural architecture of nerves. Freeze–thawing is widely used and an important step in all decellularization protocols. However, debris retention and potential microstructure damage might restrict the *in vivo* therapeutic effects. Perfusion decellularization was developed to overcome long nerve gaps using vascularized porcine sciatic nerves, but the evidence of an *in vivo* study is lacking. Immersion and agitation decellularization is commonly used but generally with chemical, detergent, and/or enzymatic solutions. Sonication is integrated with other methods to assist in removing cellular debris. However, the clearance of DNA content is questionable. Supercritical fluids show promise with advantages of nontoxicity, low cost, superior disinfection and sterilization abilities, and can solely and effectively remove cells. Pure physical treatment has a limited but acceptable effect in decellularization compared with chemical and enzymatic approaches. Both immersion and agitation and supercritical fluids had shown that identical decellularization efficacy can be achieved as compared to chemical or enzymatic approaches. Further investigations are required to validate the *in vivo* therapeutic outcomes. With comprehensive understanding of the physical processing methods, multidisciplinary integration of different approaches are expected to elicit accumulative benefits, in terms of reducing immunogenicity and preserving the mechanical properties and microenvironment of native nerve tissue.

Author contributions

M-WH, S-HC, W-LT, K-SH, and T-CC wrote the manuscript, S-CL, JK, and Y-YH conceived the idea of the study, supervised, and revised the manuscript. All authors contributed to the article and approved the submitted version.

Funding

This study was supported in part by grants from the National Science and Technology Council (111-2311-B-006-001 and 111-2923-B-006-001-MY2 to Y-YH; 111-2314-B-006-095 to S-HC) and National Cheng Kung University Hospital (NCKUH-11109014 to Y-YH) in Taiwan.

Acknowledgments

The authors would like to express their sincere gratitude to Ko-Chung Yen and Dar-Jen Hsieh from ACRO biomedical company in Taiwan, for the explanation of terminology and concept to the decellularization process. The research was supported in part by Higher Education Sprout Project, Ministry of Education to the Headquarters of University Advancement at National Cheng Kung University (NCKU).

Conflict of interest

The authors declare that the research was conducted in the absence of any commercial or financial relationships that could be construed as a potential conflict of interest.

Publisher's note

All claims expressed in this article are solely those of the authors and do not necessarily represent those of their affiliated organizations, or those of the publisher, the editors and the reviewers. Any product that may be evaluated in this article, or claim that may be made by its manufacturer, is not guaranteed or endorsed by the publisher.

References

Accioli De Vaconcellos, Z. A., Duchossoy, Y., Kassar-Duchossoy, L., and Mira, J. C. (1999). Experimental median nerve repair by fresh or frozen nerve autografts and xenografts. *Ann. Chir. Main. Memb. Super.* 18 (1), 74–84.

Alshaikh, A. B., Padma, A. M., Dehlin, M., Akouri, R., Song, M. J., Brannstrom, M., et al. (2019). Decellularization of the mouse ovary: Comparison of different scaffold generation protocols for future ovarian bioengineering. *J. Ovarian Res.* 12 (1), 58.

Bolognesi, F., Fazio, N., Boriani, F., Fabbri, V. P., Gravina, D., Pedrini, F. A., et al. (2022). Validation of a cleanroom compliant sonication-based decellularization technique: A new concept in nerve allograft production. *Int. J. Mol. Sci.* 23 (3).

Boriani, F., Fazio, N., Fotia, C., Savarino, L., Nicoli Aldini, N., Martini, L., et al. (2017). A novel technique for decellularization of allogenic nerves and *in vivo* study of their use for peripheral nerve reconstruction. *J. Biomed. Mater Res. A* 105 (8), 2228–2240.

Carvalho, C. R., Oliveira, J. M., and Reis, R. L. (2019). Modern trends for peripheral nerve repair and regeneration: Beyond the hollow nerve guidance conduit. *Front. Bioeng. Biotechnol.* 7, 337.

Casali, D. M., Handleton, R. M., Shazly, T., and Matthews, M. A. (2018). A novel supercritical CO 2 -based decellularization method for maintaining scaffold hydration and mechanical properties. *J. Supercrit. Fluids* 131, 72–81.

Crapo, P. M., Gilbert, T. W., and Badylak, S. F. (2011). An overview of tissue and whole organ decellularization processes. *Biomaterials* 32 (12), 3233–3243.

Dahl, S. L. M., Koh, J., Prabhakar, V., and Niklason, L. E. (2003). Decellularized native and engineered arterial scaffolds for transplantation. *Cell Transpl.* 12 (6), 659–666.

de Ruiter, G. C., Malessy, M. J., Yaszemski, M. J., Windebank, A. J., and Spinner, R. J. (2009). Designing ideal conduits for peripheral nerve repair. *Neurosurg. Focus* 26 (2), E5.

Duisit, J., Amiel, H., Orlando, G., Dedriche, A., Behets, C., Gianello, P., et al. (2018). Face graft scaffold production in a rat model. *Plast. Reconstr. Surg.* 141 (1), 95–103.

Evans, P. J., Mackinnon, S. E., Levi, A. D., Wade, J. A., Hunter, D. A., Nakao, Y., et al. (1998). Cold preserved nerve allografts: Changes in basement membrane, viability, immunogenicity, and regeneration. *Muscle Nerve* 21 (11), 1507–1522.

Fox, A., Mountford, J., Braakhuis, A., and Harrison, L. C. (2001). Innate and adaptive immune responses to nonvascular xenografts: Evidence that macrophages are direct effectors of xenograft rejection. *J. Immunol.* 166 (3), 2133–2140.

Fox, I. K., Jaramillo, A., Hunter, D. A., Rickman, S. R., Mohanakumar, T., and Mackinnon, S. E. (2005). Prolonged cold-preservation of nerve allografts. *Muscle Nerve* 31 (1), 59–69.

Gilpin, A., and Yang, Y. (2017). Decellularization strategies for regenerative medicine: From processing techniques to applications. *Biomed. Res. Int.* 2017, 9831534.

Goh, S. K., Bertera, S., Vaidya, V., Dumpe, S., Barner, S., Mathew, S., et al. (2018). Development of perfusion bioreactor for whole organ engineering - a culture system that enhances cellular engraftment, survival and phenotype of repopulated pancreas. *Technology* 6 (3-4), 118–134.

Gunn, S., Cosetti, M., and Roland, J. T., Jr. (2010). Processed allograft: Novel use in facial nerve repair after resection of a rare racial nerve paraganglioma. *Laryngoscope* 120 (4), S206.

Han, G. H., Peng, J., Liu, P., Ding, X., Wei, S., Lu, S., et al. (2019). Therapeutic strategies for peripheral nerve injury: Decellularized nerve conduits and schwann cell transplantation. *Neural Regen. Res.* 14 (8), 1343–1351.

Hare, G. M., Evans, P. J., Mackinnon, S. E., Nakao, Y., Midha, R., Wade, J. A., et al. (1993). Effect of cold preservation on lymphocyte migration into peripheral nerve allografts in sheep. *Transplantation* 56 (1), 154–162.

Hess, J. R., Brenner, M. J., Fox, I. K., Nichols, C. M., Myckatyn, T. M., Hunter, D. A., et al. (2007). Use of cold-preserved allografts seeded with autologous Schwann cells in the treatment of a long-gap peripheral nerve injury. *Plast. Reconstr. Surg.* 119 (1), 246–259.

Houschyar, K. S., Momeni, A., Pyles, M. N., Cha, J. Y., Maan, Z. N., Duscher, D., et al. (2016). "The role of current techniques and concepts in peripheral nerve repair." *Plast. Surg. Int. 2016*, 4175293.

Hu, X., Huang, J., Ye, Z., Xia, L., Li, M., Lv, B., et al. (2009). A novel scaffold with longitudinally oriented microchannels promotes peripheral nerve regeneration. *Tissue Eng. Part A* 15 (11), 3297–3308.

Huang, H., Xiao, H., Liu, H., Niu, Y., Yan, R., and Hu, M. (2015). A comparative study of acellular nerve xenografts and allografts in repairing rat facial nerve defects. *Mol. Med. Rep.* 12 (4), 6330–6336.

Hudson, T. W., Liu, S. Y., and Schmidt, C. E. (2004). Engineering an improved acellular nerve graft via optimized chemical processing. *Tissue Eng.* 10 (9-10), 1346–1358.

Ide, C. (1983). Nerve regeneration and schwann cell basal lamina: Observations of the long-term regeneration. *Arch. Histol. Jpn.* 46 (2), 243–257.

Ide, C., Tohyama, K., Yokota, R., Nitatori, T., and Onodera, S. (1983). Schwann cell basal lamina and nerve regeneration. *Brain Res.* 288 (1-2), 61–75.

Isenschmid, A., Marison, I. W., and von Stockar, U. (1995). The influence of pressure and temperature of compressed CO2 on the survival of yeast cells. *J. Biotechnol.* 39 (3), 229–237.

Jesuraj, N. J., Santosa, K. B., Macewan, M. R., Moore, A. M., Kasukurthi, R., Ray, W. Z., et al. (2014). Schwann cells seeded in acellular nerve grafts improve functional recovery. *Muscle Nerve* 49 (2), 267–276.

Kaizawa, Y., Kakinoki, R., Ikeguchi, R., Ohta, S., Noguchi, T., Takeuchi, H., et al. (2017). A nerve conduit containing a vascular bundle and implanted with bone marrow stromal cells and decellularized allogenic nerve matrix. *Cell Transpl.* 26 (2), 215–228.

Kalomiri, D. E., Soucacos, P. N., and Beris, A. E. (1994). Nerve grafting in peripheral nerve microsurgery of the upper extremity. *Microsurgery* 15 (7), 506–511.

Karabekmez, F. E., Duymaz, A., and Moran, S. L. (2009). Early clinical outcomes with the use of decellularized nerve allograft for repair of sensory defects within the hand. *Hand (N Y)* 4 (3), 245–249.

Keane, T. J., Swinehart, I. T., and Badylak, S. F. (2015). Methods of tissue decellularization used for preparation of biologic scaffolds and *in vivo* relevance. *Methods* 84, 25–34.

Kim, Y. S., Majid, M., Melchiorri, A. J., and Mikos, A. G. (2019). Applications of decellularized extracellular matrix in bone and cartilage tissue engineering. *Bioeng. Transl. Med.* 4 (1), 83–95.

Lasso, J. M., and Deleyto, E. (2017). *Current status in peripheral nerve xenotransplantation*. Xenotransplantation - New Insights.

Lopresti, S. T., and Brown, B. N. (2015). "Chapter 4 - host response to naturally derived biomaterials," in *Host response to biomaterials* (Oxford: Academic Press), 53–79.

Lu, L. J., Sun, J. B., Liu, Z. G., Gong, X., Cui, J. L., and Sun, X. G. (2009). "Immune responses following mouse peripheral nerve xenotransplantation in rats." *J. Biomed. Biotechnol. 2009*, 412598.

Osawa, T., Tohyama, K., and Ide, C. (1990). Allogeneic nerve grafts in the rat, with special reference to the role of Schwann cell basal laminae in nerve regeneration. *J. Neurocytol.* 19 (6), 833–849.

Philips, C., Cornelissen, M., and Carriel, V. (2018). Evaluation methods as quality control in the generation of decellularized peripheral nerve allografts. *J. Neural Eng.* 15 (2), 021003.

Rana, D., Zreiqat, H., Benkirane-Jessel, N., Ramakrishna, S., and Ramalingam, M. (2017). Development of decellularized scaffolds for stem cell-driven tissue engineering. *J. Tissue Eng. Regen. Med.* 11 (4), 942–965.

Ray, W. Z., Kale, S. S., Kasukurthi, R., Papp, E. M., Johnson, P. J., Santosa, K. B., et al. (2011). Effect of cold nerve allograft preservation on antigen presentation and rejection. *J. Neurosurg.* 114 (1), 256–262.

Safa, B., Jain, S., Desai, M. J., Greenberg, J. A., Niacaris, T. R., Nydick, J. A., et al. (2020). Peripheral nerve repair throughout the body with processed nerve allografts: Results from a large multicenter study. *Microsurgery* 40 (5), 527–537.

Simsa, R., Vila, X. M., Salzer, E., Teuschl, A., Jenndahl, L., Bergh, N., et al. (2019). Effect of fluid dynamics on decellularization efficacy and mechanical properties of blood vessels. *PLoS One* 14 (8), 0220743.

Subramaniam, B., Rajewski, R. A., and Snavely, K. (1997). Pharmaceutical processing with supercritical carbon dioxide. *J. Pharm. Sci.* 86 (8), 885–890.

Suss, P. H., Ribeiro, V. S. T., Motooka, C. E., de Melo, L. C., and Tuon, F. F. (2022). Comparative study of decellularization techniques to obtain natural extracellular matrix scaffolds of human peripheral-nerve allografts. *Cell Tissue Bank.* 23 (3), 511–520.

Thomson, S. E., Ng, N. Y., Riehle, M. O., Kingham, P. J., Dahlin, L. B., Wiberg, M., et al. (2022). Bioengineered nerve conduits and wraps for peripheral nerve repair of the upper limb. *Cochrane Database Syst. Rev.* 12 (12), CD012574.

Topuz, B., Günal, G., Guler, S., and Aydin, H. M. (2020). Use of supercritical CO(2) in soft tissue decellularization. *Methods Cell Biol.* 157, 49–79.

Vadori, M., and Cozzi, E. (2014). Immunological challenges and therapies in xenotransplantation. *Cold Spring Harb. Perspect. Med.* 4 (4), a015578.

Vasudevan, S., Huang, J., Botterman, B., Matloub, H. S., Keefer, E., and Cheng, J. (2014). Detergent-free decellularized nerve grafts for long-gap peripheral nerve reconstruction. *Plast. Reconstr. Surg. Glob. Open* 2 (8), 201.

Wei, S., Hu, Q., Ma, J., Dai, X., Sun, Y., Han, G., et al. (2022). Acellular nerve xenografts based on supercritical extraction technology for repairing long-distance sciatic nerve defects in rats. *Bioact. Mater.* 18, 300–320.

White, A., Burns, D., and Christensen, T. W. (2006). Effective terminal sterilization using supercritical carbon dioxide. *J. Biotechnol.* 123 (4), 504–515.

Wilson, S. L., Sidney, L. E., Dunphy, S. E., Dua, H. S., and Hopkinson, A. (2016). Corneal decellularization: A method of recycling unsuitable donor tissue for clinical translation? *Curr. Eye Res.* 41 (6), 769–782.

Wüthrich, T., Lese, I., Haberthür, D., Zubler, C., Hlushchuk, R., Hewer, E., et al. (2020). Development of vascularized nerve scaffold using perfusion-decellularization and recellularization. *Mater. Sci. Eng. C* 117, 111311.

Zhang, X., Chen, X., Hong, H., Hu, R., Liu, J., and Liu, C. (2022). Decellularized extracellular matrix scaffolds: Recent trends and emerging strategies in tissue engineering. *Bioact. Mater* 10, 15–31.

Zhang, Y., Luo, H., Zhang, Z., Lu, Y., Huang, X., Yang, L., et al. (2010). A nerve graft constructed with xenogeneic acellular nerve matrix and autologous adipose-derived mesenchymal stem cells. *Biomaterials* 31 (20), 5312–5324.

frontiers | Frontiers in Bioengineering and Biotechnology

TYPE Original Research
PUBLISHED 06 June 2023
DOI 10.3389/fbioe.2023.1187500

OPEN ACCESS

EDITED BY
Yawei Du,
Shanghai Jiao Tong University, China

REVIEWED BY
Ludovica Cacopardo,
University of Pisa, Italy
Junjie Li,
Soochow University, China

*CORRESPONDENCE
Cian O'Leary,
cianoleary@rcsi.ie

RECEIVED 16 March 2023
ACCEPTED 04 May 2023
PUBLISHED 06 June 2023

CITATION
Khalid T, Soriano L, Lemoine M, Cryan S-A, O'Brien FJ and O'Leary C (2023), Development of tissue-engineered tracheal scaffold with refined mechanical properties and vascularisation for tracheal regeneration. *Front. Bioeng. Biotechnol.* 11:1187500. doi: 10.3389/fbioe.2023.1187500

Development of tissue-engineered tracheal scaffold with refined mechanical properties and vascularisation for tracheal regeneration

Tehreem Khalid[1,2,3], Luis Soriano[1,2,4], Mark Lemoine[2,3,5], Sally-Ann Cryan[1,2,3,4,5], Fergal J. O'Brien[2,3,4,5] and Cian O'Leary[1,2,3]*

[1]School of Pharmacy and Biomolecular Sciences, RCSI University of Medicine and Health Sciences, Dublin, Ireland, [2]Tissue Engineering Research Group, RCSI University of Medicine and Health Sciences, Dublin, Ireland, [3]Advanced Materials and Bioengineering Research (AMBER) Centre, RCSI and Trinity College Dublin, Dublin, Ireland, [4]Centre for Research in Biomedical Devices (CÚRAM), NUI Galway, Galway, Ireland, [5]Trinity Centre for Biomedical Engineering, Trinity College Dublin, Dublin, Ireland

Introduction: Attempted tracheal replacement efforts thus far have had very little success. Major limiting factors have been the inability to efficiently re-vascularise and mimic the mechanical properties of native tissue. The major objective of this study was to optimise a previously developed collagen-hyaluronic acid scaffold (CHyA-B), which has shown to facilitate the growth of respiratory cells in distinct regions, as a potential tracheal replacement device.

Methods: A biodegradable thermoplastic polymer was 3D-printed into different designs and underwent multi-modal mechanical assessment. The 3D-printed constructs were incorporated into the CHyA-B scaffolds and subjected to *in vitro* and *ex vivo* vascularisation.

Results: The polymeric backbone provided sufficient strength to the CHyA-B scaffold, with yield loads of 1.31–5.17 N/mm and flexural moduli of 0.13–0.26 MPa. Angiogenic growth factor release (VEGF and bFGF) and angiogenic gene upregulation (KDR, TEK-2 and ANG-1) was detected in composite scaffolds and remained sustainable up to 14 days. Confocal microscopy and histological sectioning confirmed the presence of infiltrating blood vessel throughout composite scaffolds both *in vitro* and *ex vivo*.

Discussion: By addressing both the mechanical and physiological requirements of tracheal scaffolds, this work has begun to pave the way for a new therapeutic option for large tracheal defects.

KEYWORDS

trachea, tissue engineering, 3D printing, respiratory, vascularisation

1 Introduction

Replacement of large tracheal defects is a complex issue, with little clinical success to date in spite of other advancements in modern medicine. Two key issues facing tracheal replacement are 1) the mechanical differences between the implant and surrounding native tissue and 2) of host acceptance of implants and integration into the host

vascular network. Many promising studies have investigated novel approaches to replacing tracheal defects using additive manufacturing techniques (Les et al., 2019; Kang et al., 2019; Ricardo et al., 2019; Xia et al., 2019; Lee et al., 2020). The most notable were the Marlex™ mesh porous prosthesis, these showed promise in animal studies with 16 months of graft survival and patency (Beall et al., 1962). However, they did not perform well in humans due to stenosis and erosion of surrounding blood vessels (Maziak et al., 1996). Tracheal allografts have also been investigated since 1979 (Rose et al., 1979). Recent developments by Delaere et al. (2012), Delaere et al. (2014), and Delaere et al. (2019) saw the development of a two-step technique in which the donor trachea is revascularised in the patient's forearm before implantation. A cadaveric trachea was decellularised, implanted in the forearm of the recipient and seeded with buccal mucosa to enhance vascularisation prior to implantation (Delaere et al., 2010). This approach was further explored with four additional patients, but tracheal necrosis and poor vascularisation hampered the outcome of this clinical trial (Omori et al., 2008). 3D-printing has also been utilised to treat tracheal defects in paediatric patients as 3D printed airway splints have been granted FDA approval (Pacetti, 2020). First reported in 2013 to treat a severe case of tracheobronchomalacia (TBM) (Zopf et al., 2013), the splints have been successfully implanted in a wider set of patients with low mortalities (Les et al., 2019; Morrison1 et al., 2017; Huang et al., 2016; Morrison et al., 2017). However, their use has been restricted to paediatric patients. Only one attempt has been reported in an adult, with maintained airway patency 3-month post implantation. Overall, there is currently no established gold standard for tracheal regeneration that fully addresses all major concerns.

The mechanical discrepancy between native tracheal tissue and that of the replacement graft is often one of the major causes for implant failure *in vivo* and within clinical efforts (Grimmer et al., 2004; Azorin et al., 2006; Luo et al., 2013; Wood et al., 2014; Elliott et al., 2017). The trachea is composed of distinct structural regions that each fulfill a distinct role in tracheal stability, as well as respond differently to mechanical stimuli, which collectively gives the trachea its unique anisotropic mechanical properties (Teng et al., 2012). The trachea's horse-shoe shaped hyaline cartilage rings, smooth muscle and annular ligament, collectively produce an anisotropic tissue that allows for longitudinal extensibility and lateral rigidity (Teng et al., 2008; Teng et al., 2012; Boazak and Auguste, 2018). Therefore, any tracheal substitute must be mechanically robust in order to withstand intra-thoracic pressure changes that occur during respiration (Rose et al., 1979; Maziak et al., 1996). Conversely, they must also be able to deform radially to allow for changes in the cross-sectional area during coughing and swallowing (Boazak and Auguste, 2018). These complicated native tissue characteristics, coupled with a lack of standardised protocols to accurately quantify tracheal biomechanics as guidance for implant design, constitute a significant hurdle for tracheal biomaterial scaffold fabrication.

Heterogenous methods to characterise native tracheal mechanics include different specimen types, shapes, testing methods, and parameters suffer from inconsistency [reviewed in Soriano et al. (2021)]. This lack of consistency is likely due to the geometry of the trachea, together with its unique structural regions, which make it difficult to define the most appropriate mechanical tests to perform to best capture the correct biomechanics (Lambert et al., 1991; Rains et al., 1992; Roberts et al., 1997; Hoffman et al., 2016; Siddiqi, 2017). The inability to collectively define the mechanical properties of the trachea has resulted in studies simply using uniaxial compression testing alone to characterise their scaffolds, which upon *in vivo* implantation, have subsequently failed due to the mismatch in mechanical properties provoking graft collapse or dislodgement (Grimmer et al., 2004; Wood et al., 2014). To this end, we propose to establish a benchmark of different mechanical test types that are able to evaluate the bulk radial compressive properties of our scaffold but also their flexibility and resistance to applied static load over time, ultimately to recapitulate the mechanical environment of the trachea.

3D-printing (3DP) provides the capacity to generate complex and custom designs that enable the fabrication of patient-specific constructs. Furthermore, due to its reproducibility and the ability to alter mechanical properties of printed constructs through the fine-tuning of complex design features, 3DP was selected in this study to fabricate a polymeric tubular framework for a composite tracheal scaffold. To generate a structure that can produce a tracheal scaffold with mechanical support similar to native cartilage rings, polycaprolactone (PCL) was selected as the printing material due its strong mechanical properties, non-cytotoxic degradation products and long-term stability (Sun et al., 2006; Woodruff and Hutmacher, 2010) These properties have meant that the use of 3DP PCL in tracheal replacement efforts has been widespread, with studies fabricating tracheal scaffolds that display excellent resistance to compressive stresses and facilitate cartilage tissue formation (Gao et al., 2017; Best et al., 2018; Les et al., 2019; Xia et al., 2019; She et al., 2021). However, 3DP PCL constructs *in vivo* have also suffered from poor results due to inflammatory responses that cause granulation tissue formation and stenosis (Lin et al., 2009; Gao et al., 2017; Rehmani et al., 2017; Kaye et al., 2019; Xia et al., 2019). Notably, in a recent study of a 3D-printed scaffold coated in a chondrocyte suspension and implanted within a rabbit model, all animals had died by 10 weeks, with 75% of deaths occurring linked to excess granulation tissue. Furthermore, no re-epithelisation was found to have occurred (Kaye et al., 2019). Thus, while PCL holds great potential as a base material for mechanically robust tracheal scaffolds, additional components are needed to augment the construct's integration to its surrounding mucosal and submucosal tissue.

The other key issue facing tracheal replacement is that of vascularisation of the implant. This is a critical consideration to avoid tissue necrosis in the implant site and to support new cartilage and epithelium formation (Walles et al., 2004; Li et al., 2019). Tracheal revascularisation—or, more precisely, the lack thereof—was deemed to be a key factor in a high prolife case of scientific misconduct in this field, which involved the implantation of solid polymer tubes seeded with stem cells as tracheal replacement (Delaere and Van Raemdonck, 2016; Delaere et al., 2019). These studies highlighted the importance of the trachea's blood supply, and the need for any substitute graft to effectively support revascularisation and ensure clinical success. Pre-vascularisation prior to implantation has shown higher survival rate of animals, lower rates of stenosis and increased re-epithelisation, suggesting the presence of an established vascular network enhances graft survivability (Luo et al., 2013; Maughan et al., 2017; Wu et al., 2017; Bae et al., 2018).

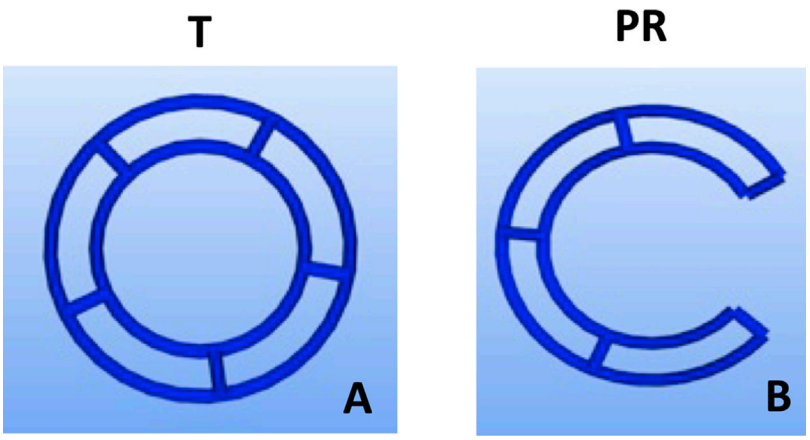

FIGURE 1
Design iterations of 3DP tracheal scaffolds. Two main design features were fabricated: Tubular T; **(A)** and Partial Ring PR; **(B)**.

TABLE 1 Dimensions and structural differences of tracheal scaffold designs.

Scaffold Design	Dimensions (Inner Ring Radius, mm)	Dimensions (Outer Ring Radius, mm)	Opening (degrees)	Number of Struts
Tubular (T)	4.8	6.8	—	5
Partial Ring (PR)	4.8	6.8	72	5

Indeed, our in-house approach to engineer a prevascularised within collagen scaffolds with co-culture of human umbilical vein endothelial cells (HUVECs) and human mesenchymal stem cells (hMSCs) provided *in vitro* and *in vivo* stable vessel formation (Hoffman et al., 2016).

Therefore, we propose that the integration of a 3DP PCL framework within a pre-vascularised collagen matrix can enhance implant integration into surrounding tracheal tissue, as a biocompatible substrate for successful cellular attachment and growth. In this study, building on our bilayered collagen-hyaluronic acid (CHyA-B) matrix (O'Leary et al., 2016), our objective was to incorporate a 3DP PCL framework to produce a reinforced composite CHyA-B scaffold, and demonstrate successful pre-vascularisation as a proof-of-concept prior to future preclinical animal studies.

2 Materials and methods

2.1 Design and manufacture of 3D-printed PCL framework

Fused deposition modelling 3D-printing was utilised to fabricate novel tubular frameworks with the aim to optimise printing parameters and to mechanically characterise scaffolds for tracheal replacement. The frameworks were designed using custom G-code developed from Python programs, which contain toolpaths for the print head, to generate a design with either a complete 360° tubular ring (T) or 288° partial ring (PR). Both designs featured two rings, 2 mm apart, connected by five struts (Figure 1; Table 1). The designs were 3D printed using an Allevi II Bioprinter (Allevi, United States) with 25 kDa PCL (Polysciences, Germany). PCL was heated to 90°C and extruded at a pressure of 60 psi at a printing speed of 260 mm/min. All designs were printed using a 25G metal needle (Micron-S, Fisnar, ECT Adhesives, Ireland).

2.2 Mechanical testing

2.2.1 Radial compression

To determine the mechanical strength of the different designs and the influence of molecular weights of PCL, radial compression was performed using a universal mechanical testing machine Z005 (Zwick/Roell, German, A702416) with a 50 N load cell. The 3DP frameworks were compressed radially at an applied strain of 50% at 0.6 mm/min. The yield point was calculated from the load-deformation curves using the 0.2% offset method. The partial ring designs (PR1-3) were tested in two different testing positions: lateral (L) and anterior-posterior (A-P) to assess the influence of the opening gap on mechanical strength.

2.2.2 Cyclical testing

To assess the durability of the different designs, the 3DP frameworks were subjected to cyclical testing. With the universal mechanical testing machine and 50 N load cell, the strain rate was adjusted to mimic a fast-breathing rate of adult humans at 20 breaths per minute for 250 cycles. The designs were placed vertically onto the machine and fine grit sandpaper was placed between the framework and the testing platens to prevent slippage. The peak load at cycles 1 and 250 was measured and the percentage cyclical strain recovery was calculated to elucidate the design's

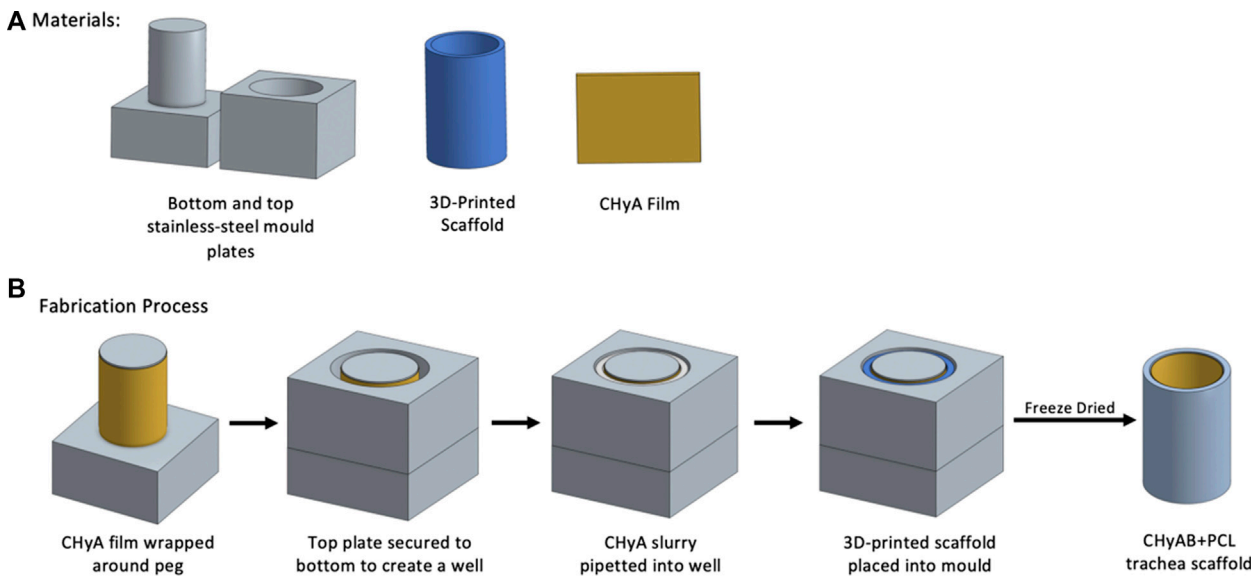

FIGURE 2
Schematic overview of fabrication of reinforced composite CHyA-B tracheal scaffolds. **(A)** Materials required for scaffold fabrication. **(B)** Fabrication process of reinforced composite CHyA-B tracheal scaffolds. In brief, CHyA films are wrapped around the pegs of the bottom mould plates and top plates is secured on forming a well in which CHyA slurry is pipetted into. Following this, the 3D-printed frameworks are placed into the mould and freeze dried to form a reinforced composite CHyA-B tubular scaffold.

ability to recovery to its original shape. The percentage of strain recovery after 250 cycles was determined using Eq. 1, where $\varepsilon_m$is the applied strain and $\varepsilon_p(N)$ is the strain after N cycles (Lendlein et al., 2001).

$$R_r = \frac{\left(\varepsilon_m - \varepsilon_p(N)\right)}{\varepsilon_m} \quad (1)$$

2.2.3 Three-point bend testing

To examine the flexibility of the designs, a 3-point bending rig was used to assess the bending stiffness of the frameworks. In order to provide comparable data, flexural moduli of the scaffolds were assessed as seen in literature for tracheal scaffolds (Park et al., 2018). Frameworks were compressed at 50% strain until failure with the universal mechanical testing machine and 50 N load cell. The partial ring designs were again assessed in two different orientations, firstly with the opening facing down towards the lower plate and secondly with the opening facing out sideways, to assess the influence of the gap on the flexibility of the design.

2.3 Manufacture and characterisation of reinforced composite CHyA-B scaffolds

2.3.1 Collagen-hyaluronate slurry and film preparation

Collagen-hyaluronic acid (CHyA) slurry and films were prepared using a previously described method (O'Leary et al., 2016). In short, 0.5% w/v collagen (type 1 collagen, bovine tendon) (Collagen Solution, United Kingdom) and 0.044% hyaluronic acid (Hyaluronic acid sodium salt from *Streptococcus* equi; Sigma-Aldrich, Arklow, Ireland) in 0.5 M acetic acid were homogenously mixed using an Ultra Turrax T18 Overhead Blender (IKA Works Inc., United States) at 15,000 rpm at 4°C for 3.5 h, and subsequently degassed to 4,000 mTorr under a vacuum to produce a CHyA slurry, which was stored at 4°C. To manufacture CHyA films, 50 mL of the CHyA slurry was cast into 12.5 cm^2 × 12.5 cm^2 stainless steel moulds clamped to a polytetrafluoroethylene (PTFE) plate and dehydrated overnight under a constant air flow to produce a thin and transparent CHyA film.

2.3.2 Reinforced composite CHyA-B scaffold manufacture

Prior to incorporating the 3D-printed frameworks to CHyA slurry for freeze-drying, the constructs were surface treated with 3 M sodium hydroxide (NaOH) for 48 h at room temperature, and then rinsed three times with diH20 to remove any residual NaOH. Following the surface treatment, a custom stainless-steel mould was used to fabricate the reinforced composite CHyA-B scaffolds (Figure 2). The mould consists of a bottom plate with 16 pegs, 26 mm in height and 7.8 mm in diameter and a top plate with 14 mm wide circular holes. First, CHyA films were cut into strips of 26 mm × 30 mm and rehydrated in 0.5 M acetic acid for 1 h at room temperature. Upon rehydration, the films were wrapped around the pegs of the bottom plate and left overnight under a constant air flow to dehydrate the films, enabling them to firmly attach to the metal pegs. The following day, the top plate of the mould was then secured on, creating a well in which 1,750 µL of CHyA slurry was pipetted into and then 3D-printed frameworks were then gently placed into the slurry. Subsequently, the films were allowed to rehydrate in the collagen slurry within the mould for 2 h and then freeze-dried using a customised anneal freeze drying cycle. The scaffolds were subjected to an initial freezing step to −20°C for 1 h in which ice crystals formed within the collagen slurry. Following this, the

temperature was raised to −10°C, an annealing step, which merged the ice crystals resulting in larger pores. Finally, to allow for sublimation and drying of the scaffolds, the pressure was decreased to 200 mTorr.

2.4 Scaffold ultrastructure

Reinforced composite CHyA-B scaffolds were examined using scanning electron microscopy (SEM) in order to evaluate the collagen integration and the ultrastructure between the PCL fibres. Samples were mounted to an aluminium stub and sputter-coated with gold/palladium (Cressington 108auto, Cressington Scientific Instruments, United Kingdom) at a current of 40 mA for 80 s. Imaging of the scaffolds was performed using a Zeiss Ultra Plus scanning electron microscope (Zeiss, Germany). Images were captured at 5 kV using the secondary electron mode. Three scaffolds from two batches of reinforced CHyA-B scaffolds were used for imaging.

2.5 Pore size analysis

Having established the 3DP design and mechanical properties of the scaffolds, the scaffold's ability to support cell infiltration and growth was assessed by measuring the mean pore size of the collagen sub-layer of composite scaffolds. Pore size of the reinforced composite and non-reinforced CHyA-B matrix were analysed to assess the effect of the incorporating tubular 3D-printed framework on the mean pore size of CHyA-B matrices. Samples of reinforced CHyA-B scaffolds were cut into 1 cm × 1 cm sections and analysed using a technique optimised for pore size analysis of collagen scaffolds (O'Brien et al., 2005). In short, the scaffolds were dehydrated using a series of increasing concentrations of ethanol and then embedded in JB-4® glycolmethacrylate (Polysciences Europe, Eppelheim, Germany). Sections of 10 µm thickness of embedded samples were sectioned using a carbon steel blade (C35, PFM, Laboratory Instruments and Supplies, Ireland) on a microtome (Leica RM 2255, Leica, Germany). Sections were stained using 0.5% toluidine blue for 4 min and imaged at ×10 magnification using a microscope (Eclipse 90i, Nikon, Japan), with attached camera (DS Ri1, Nikon, Japan). Captured images were analysed using a custom-made MATLAB (MathWorks Inc., MA, United States) script developed by our group in conjunction with the Sigmedia Research Group in the Electrical Engineering Department at Trinity College Dublin, Ireland. Images were converted to binary form (black and white) and using a best fit of elliptical lengths the average pore diameter was measured. For each sample, sections were taken every 100 µm spanning the entire length of the scaffold and three scaffolds of each group from two batches of freeze-drying were analysed.

2.6 HUVEC and hMSC co-culture on reinforced composite CHyA-B scaffolds

2.6.1 Scaffold fabrication for cell culture

In order to biologically characterise the reinforced composite CHyA-B scaffolds, 6 mm × 6 mm sections were 3D-printed as previously described (Section 2.3) and incorporated and freeze-dried with CHyA slurry and film (Section 2.3.2; Figure 3). Non-reinforced CHyA-B matrices were used as control and were sectioned from a tubular non-reinforced CHyA-B matrices.

2.6.2 Sterilisation and crosslinking

All scaffolds for cell study were placed under 254 nm UV light for 30 min on each side for sterilisation at a distance of 10 cm before being chemically cross-linked using 1-ethyl-3-(3-dimethylaminopropyl) carbodiimide hydrochloride (EDAC) (Haugh et al., 2011; Lemoine, 2020). Scaffolds were firstly pre-hydrated in Dulbecco's Phosphate Saline (DPBS) before being submerged into a solution of 6 mM EDAC per gram of collagen was mixed with N-hydroxysuccinimide (NHS) at a molar ratio of 2.5 M EDAC: 1 M NHS in 70% ethanol. The scaffolds were then washed three times with sterile DPBS to remove residual cytotoxic product. Scaffolds were stored at 4°C for up to a week after crosslinking or used immediately for *in vitro* experiments. All steps were performed under sterile conditions.

2.6.3 Cell sources and media

All cells present in this study were obtained from Lonza. hMSCs were originally isolated from bone marrow aspirates obtained from the iliac crest of healthy human donors by the commercial supplier with ethical approval (Lonza, Switzerland). HUVECs were commercially acquired (pooled, CC-2719; Lonza, Switzerland). Cells were cultured at 37°C and 5% CO2 under humidified atmosphere. hMSC growth medium corresponded to low glucose (1 g/L) Dulbecco's modified Eagle's medium supplemented (LG-DMEM, Sigma-Aldrich, Ireland) with 10% foetal bovine serum (FBS; Biosera, Ringmer, United Kingdom) and 1% penicillin/streptomycin. HUVEC growth medium corresponded to endothelial growth medium-2 (EGM-2, Lonza, Switzerland). Medium was replaced every 3 days, and upon reaching 80%–90% confluence, cells were passaged using trypsin-EDTA solution. For all experiments described below, the highest passage number used for both cell types were passage 5.

2.6.4 Scaffold seeding

To evaluate the influence of 3DP PCL framework on *in vitro* vascularisation of reinforced composite CHyA-B scaffolds, a previously optimised vascularisation cell culture model was utilised, compromising of a co-culture of HUVECs and hMSCs at a ratio of 4:1, respectively (McFadden et al., 2013). All chemically crosslinked and sterilised scaffolds were preconditioned overnight in EGM-2 prior to seeding. Scaffolds were then seeded in a delayed stepwise manner on their porous collagen sub-layer, using 25 µL of cell suspension containing 2 × 105 HUVECs in a dropwise manner. The samples were subsequently incubated for 1 h to allow for cell attachment, followed by the addition of EGM-2. Three days post-HUVEC seeding, scaffolds were seeded with 5 × 104 hMSCs in 25 µL, using the same approach.

2.7 Cell viability

To assess and compare cellular viability of the co-culture cells on scaffolds, a battery of tests was performed over a 14-day period using

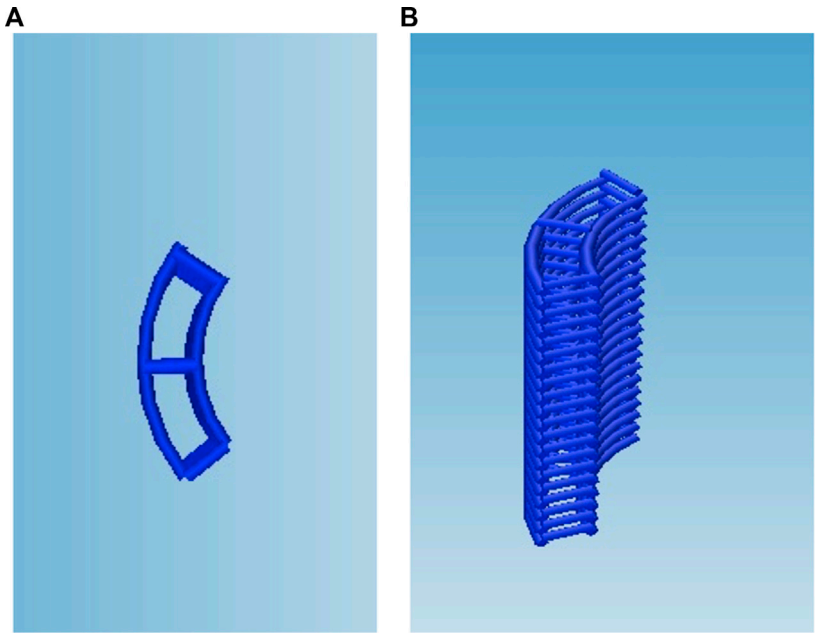

FIGURE 3
Scaffold design for cell culture study, the g-code script was altered to reduce the circumference and height of the scaffold to retain the **(A)** strut as **(B)** a stacked 6 × 6 mm scaffold.

assays. An alamarBlue™ metabolic assay (Invitrogen, BioSciences, Ireland) and PicoGreen dsDNA assay (Invitrogen) were performed at days 6, 10 and 14 of culture, in addition to fluorescent imagining of live and dead cells at day 14 using LIVE/DEAD® Viability/Cytotoxicity Kit (Thermofisher, Ireland) all according to the manufacture's protocol.

2.8 Vessel formation in reinforced composite CHyA-B scaffolds

2.8.1 Immunofluorescence

To image the formation of vessel-like structures within scaffolds, scaffolds were harvested at days 6, 10 and 14, for fluorescence labelling (do Amaral et al., 2019a). The scaffolds were washed with PBS and fixed in 10% neutral buffered formalin solution (Sigma-Aldrich, Ireland) for 1 h at room temperature. Following fixation, scaffolds were washed three times with PBS and cut in half transversely to expose the cross-section for imaging. 0.3% Triton X-100 in PBS followed by 3% bovine serum albumin (BSA; Sigma-Aldrich, Ireland) in PBS were applied for 20 min each to permeabilise cells and block unspecific antigen binding. Monoclonal mouse anti-human CD31 antibody (Dako, M0823) diluted to 1:50 in 1% BSA in PBS was used for HUVEC identification and a rabbit polyclonal antibody for α-smooth muscle actin (α-SMA; Abcam, ab5694) diluted at 1:100 in 1% BSA in PBS was applied to detect hMSCs. Primary antibodies were incubated overnight at 4°C. Rat anti-mouse IgH (H + L) secondary antibody, Fluorescein isothiocyanate (FITC; Biosciences, Ireland, 11401185), diluted at 1:100 in 1% BSA in PBS and goat anti-rabbit IgG (H + L) cross-adsorbed secondary antibody, Alexa Flour 633 (Invitrogen, A-21070), diluted at 1:400 in 1% BSA in PBS was applied for 1 h at room temperature. Thereafter, 1:600 diluted Phalloidin–Tetramethylrhodamine B isothiocyanate (TRITC; Sigma-Aldrich, Ireland) in 1% BSA in PBS was applied for 20 min to stain the cell cytoskeleton followed by 4′, 6-Diamidino-2-phenlindole dihydrochloride (DAPI; Sigma-Aldrich, Ireland) at 1: 1,000 dilution in PBS for 20 min for nuclei staining. Samples were stored in PBS at 4°C until imaging with a Carl Zeiss LSM 710 confocal microscope with a W N-Achroplan 10x (numerical aperture 0.3) lens. Z-stack images were taken at 30 µm depths below the surface to yield a total 150 µm total depth.

2.8.2 Chick chorioallantoic membrane (CAM) model

To assess the influence of the 3DP PCL framework within the CHyA-B matrix on vessel infiltration *ex vivo*, scaffolds were incubated within a chick chorioallantoic membrane (CAM) model as previously described (do Amaral et al., 2019a; Ryan et al., 2019; do Amaral et al., 2019b). Fertilised chicken eggs (Ovagen Group Ltd., Co. Mayo, Ireland) were purchased at day 0 of development and incubated at 37°C for 3 days. Following incubation, the eggs were cracked into 100 mm diameter petri dishes (Corning Inc., New York, United States), which in turn were then placed within larger 150 mm diameter petri dishes containing sterile PBS, to form a humidified chamber. The chicks were incubated for a further 4 days, completing 7 days of total development, viability of embryos was firstly ensured and checked at every day from this point forward; when cross-linked and sterilised CHyA-B matrices and reinforced composite CHyA-B scaffolds were placed within the chick membrane and incubated for a further 5 days, allowing for vessel ingrowth. At day 12 the samples were harvested and imaged. The vascularisation around the scaffolds was quantified using ImageJ software after treatment with the "Mexican Hat Filter" to outline

the blood vessels, and then converted to 8-bit and the blood vessel area was measured.

2.8.3 Histology

Harvested scaffolds from CAM were stained with haematoxylin and eosin (H&E) to observe vessel infiltration throughout the scaffold. Scaffolds were fixed overnight in 10% neutral buffered formalin solution at 4°C. Following fixation, scaffolds were dehydrated in increasing concentrations of ethanol until 100% ethanol was reached. Scaffolds were then placed within xylene solution under agitation, to dissolve out PCL filaments, after which they were processed using an automated tissue processor (ASP300, Leica, Germany) for paraffin infiltration. The samples were then embedded into paraffin blocks and were sectioned as described in Section 2.5 to obtain sections with a thickness of 7 μm in their cross-section to observe vessels infiltration. Sections were rehydrated in decreasing concentrations of ethanol, and then incubated with Harris haematoxylin (Sigma-Aldrich, Ireland) for 5 min before being washed in tap water for 5 min. Differentiation of the samples was then performed with acidified 70% ethanol, before being stained with 0.1% eosin Y (Sigma-Aldrich, Ireland) in 95% ethanol. Finally, slides were dehydrated and mounted with DPX. Images were captured as described in Section 2.5.

2.8.4 Pro-angiogenic protein expression

The expression of pro-angiogenic markers vascular endothelial growth factor (VEGF) and basic fibroblast growth factor (b-FGF) were quantified using ELISA kits (R&D, Biotechne, Ireland). Supernatants on days 6, 10 and 14 were collected and analysed following the manufacturer's protocol.

2.8.5 Pro-angiogenic gene expression

To assess gene expression within scaffolds seeded with the co-culture model, scaffolds were harvested and stored at −80°C in 1 mL of Qiazol lysis reagent (Qiagen, Crawley, United Kingdom). Total RNA was isolated using a RNeasy Mini Kit according to manufactures protocol (Qiagen). RNA quality and quantity was determined using Nanodrop 2000 Spectrophotometer (Thermofisher, Ireland). Reverse transcription of RNA lysates was performed on 400 ng of total RNA using the QuantiTect Reverse Transcription kit (Qiagen) according to manufacturer's protocol on a MiniAmp Thermal Cycler (A37834, Thermofisher). Quantitative real time polymerase chain reactions were performed in duplicate on a 7500 Real-Time PCR system (Applied Biosystems) using QuantiTect SYBR Green PCR kit (Qiagen). The mRNA relative expression was calculated by $2^{-\Delta\Delta CT}$ method, in which CHyA-B matrices were used as control relative to each respective timepoint. Target mRNAs analysed were KDR (QT00069818, Qiagen), ANG1 (QT00046865, Qiagen), ANG2 (QT00100947, Qiagen), TEK2 (QT01666322, Qiagen), FLT1 (QT00270823, Qiagen) and 18S (QT00199367, Qiagen) was used as a housekeeping gene.

2.9 Data analysis

Quantitative data were analysed using GraphPad Prism 8.0 software. Two-tailed student t-tests were used for statistical analysis between two groups, and 1-way or 2-way ANOVA was used for statistical analysis between multiple groups. Sidak's multiple comparison *post hoc* analysis was performed in all ANOVA assessment.

3 Results

3.1 Scaffold characterisation

3.1.1 Mechanical testing

To determine the mechanical strength of the two designs, uni-axial compressive testing was carried out (Figure 4). A significant increase in the yield load was calculated in the tubular design, 5.177 ± 0.219 N/mm, and the A-P and L partial-ring designs, 5.523 ± 0.744 N/mm and 1.313 ± 0.061 N/mm respectively, compared to CHyA-B matrices, 0.307 ± 0.453 N/mm. Notably, a difference in yield load was observed between the two orientations of the PR design, suggesting this design better recapitulated the anisotropic mechanical properties found in native tracheal tissue.

Moreover, to assess the durability of the different designs, and whether the 3D printed scaffolds could withstand the constant mechanical loading and unloading that the trachea experiences during respiration, all scaffold designs underwent cyclical testing. Irrespective of design feature, all scaffold designs withstood cyclical loading over 250 cycles and remained patent, with no visible cracks or failure sites observed when inspected visually. However, a significant 2N difference in average peak load was observed between tubular and partial ring design at cycle 1, which reduced to a 1N difference at cycle 250, highlighting the influence of the partial ring design when under radial mechanical stresses (Figure 4B). Nonetheless, the difference in structural design did not influence the percentage cyclical strain recovery (Figure 4C). Scaffolds recovered an average of 67% of the applied strain following 250 cycles to 15% applied strain in the tubular design and 71% in the partial ring design, significantly greater than the non-reinforced CHyA-B matrix.

To determine the flexibility of the scaffolds, both designs underwent three-point bend testing. The partial ring design was tested under two different orientations in relation to the position of the opening gap (Figure 4D). The tubular design exhibited a higher flexural modulus of 0.153 ± 0.010 MPa. Additionally, the partial ring design also exhibited a similar high flexural modulus in the lateral position (0.131 ± 0.005 MPa) but was significantly more flexible in the second testing position A-P (0.266 ± 0.022 MPa).

3.1.2 Scaffold ultrastructure

Having successfully mechanically characterised the 3DP designs, we next sought to evaluate the ultrastructure of the reinforced composite CHyA-B scaffolds after incorporating the 3DP frameworks into CHyA-B matrices using SEM. Scaffolds were imaged using SEM to assess the influence of the PCL fibres and scaffold design on collagen matrix infiltration. Subsequent SEM assessment captured successful integration of collagen within the PCL fibres (Figure 5). Therefore, a favourable structure was achieved through a reproducible process achieving successful integration of a porous collagen network around a 3D-printed backbone structure.

3.1.3 Pore size analysis

To assess the scaffold's ability to support cellular infiltration and growth, the mean pore size of the collagen matrix in the sub-layer of

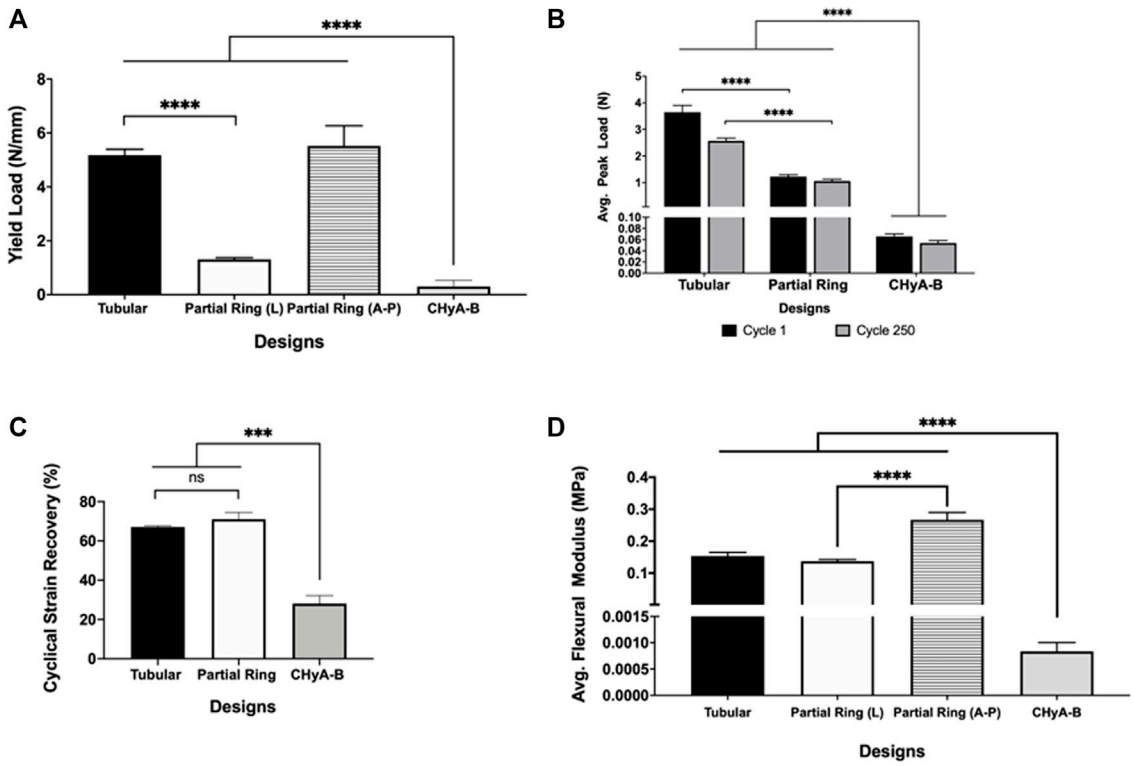

FIGURE 4
Mechanical properties of 3DP tracheal framework designs. Scaffolds were subjected to multimodal mechanical assessment to compare the influence of different scaffold designs. **(A)** Compression testing, **(B, C)** cyclical testing, **(D)** Three-point bending. Results displayed as mean ± SEM, $n = 4$. ns = $p > 0.05$, ***$p < 0.001$, ****$p < 0.0001$.

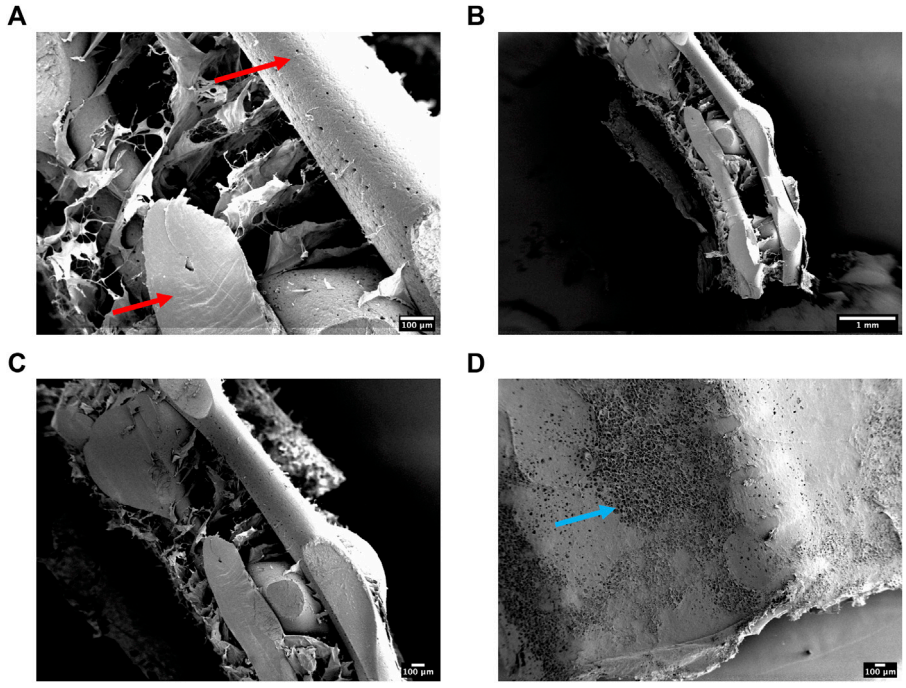

FIGURE 5
(A–C) Scanning electron micrographs showing the ultrastructure of cross-sectioned reinforced composite CHyA-B scaffolds. PCL indicated with red arrow. **(D)** A representative surface image of the non-film outer collagen surface layer showing the porosity (blue arrow) of the collagen sub-layer. $n = 2$, in triplicate.

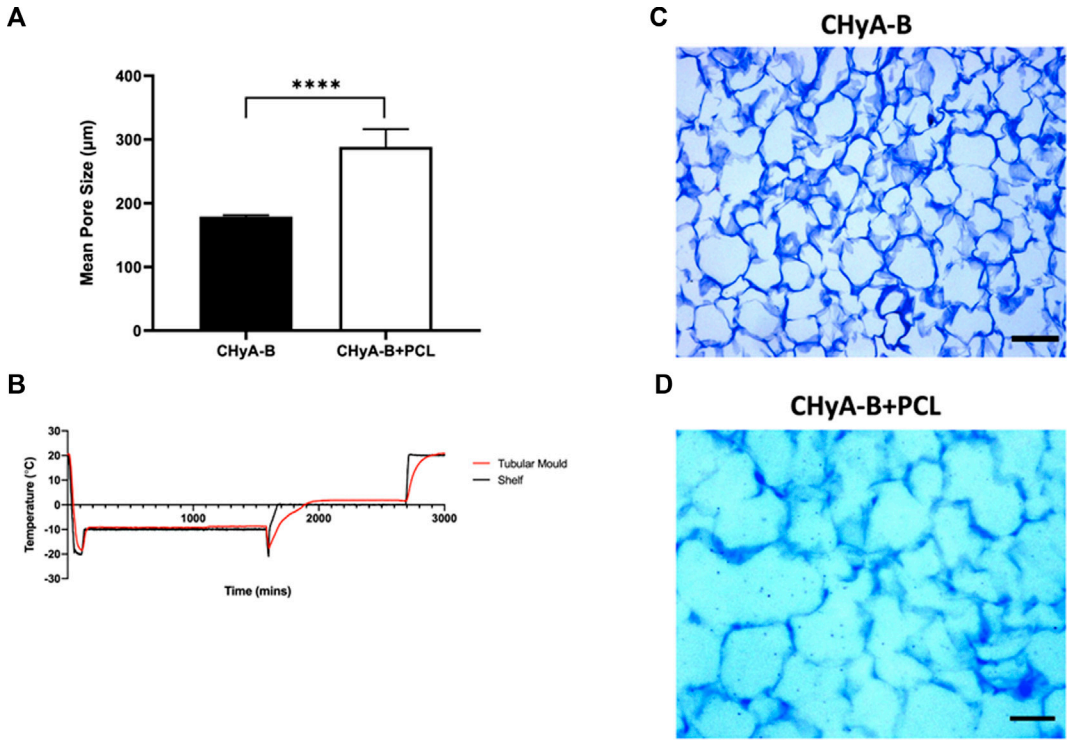

FIGURE 6
Pore size analysis of bilayered composite scaffold. **(A)** Mean pore diameter of non-reinforced (CHyA-B) matrices and reinforced composite (CHyA-B+PCL) scaffold. **(B)** Temperature profile of tubular moulds during −20 anneal cycle in comparison to shelf temperature, data captured by Dr. Derek Whelan, RCSI (n = 1). Toluidine blue sections of CHyA-B **(C)** and CHyA-B+PCL **(D)** scaffolds used for software analysis Scale bar = 100 µm. Results displayed as mean ± SEM, n = 3, in quadruple. ****p < 0.0001.

reinforced composite CHyA-B scaffolds was analysed. The inclusion of the 3D-printed PCL framework within CHyA-B tubular matrix resulted in an average pore size of 290 ± 27.66 µm compared to an average pore size of 180 ± 1.962 µm in non-reinforced tubular CHyA-B matrices (Figure 6A). Temperature probes placed within the tubular moulds and freeze-dryer shelf recorded differences in freeze drying profiles (Figure 6B), with the temperature within the tubular moulds requiring a longer time to be brought up back to temperature during the cycle, possibly influencing the pore size of the resultant scaffolds (Figures 6C, D).

3.2 Cell viability

In an aim to assess and compare cell viability of the vascularisation co-culture system on reinforced CHyA-B scaffold to that of CHyA-B matrix, scaffolds were subjected to multiple viability assays (Figure 7). Cell metabolic activity measured in reinforced composite CHyA-B scaffolds was comparable to measurements in control CHyA-B matrices over 14 days of culture period (Figure 7A). Notably, double stranded DNA (dsDNA) content was two-fold greater in reinforced composite CHyA-B scaffolds compared to CHyA-B matrices over 14 days of cell culture (Figure 7B). LIVE/DEAD® imaging also confirmed the presence of a high population of green viable cells on both scaffold types (Figure 7C). Overall, the mix of quantitative and qualitative data indicate that the inclusion of 3DP PCL framework within CHyA-B matrices sustains vascular cell viability, and potentially facilitates increased proliferation.

3.3 Vessel formation in reinforced composite CHyA-B scaffolds

3.3.1 Immunofluorescence

To image the formation of vessel-like structures within scaffolds, cells were fluorescently labelled and then imaged using confocal microscopy. The presence of vessel-like structures was visible in reinforced composite CHyA-B scaffolds and CHyA-B matrices across 14 days of culture (Figure 8; white arrows), with fewer vessel-like structures on the post-peak timepoint of day 14. Furthermore, fluorescence labelling of endothelial cell makers CD31 and pericyte cell marker α-SMA on day 10 of cultured samples (Figure 9) confirmed the presence of both cell types around vessel-like tubules. Thus, we confirmed that the incorporation of 3DP PCL framework within CHyA-B matrix did not impede of vessel formation *in vitro*.

3.3.2 Pro-angiogenic protein expression

The expression of pro-angiogenic markers VEGF and b-FGF was quantified using ELISA kits on days 6, 10 and 14 of *in vitro* culture. Although no significant difference was observed between reinforced composite CHyA-B scaffolds and CHyA-B matrices; over

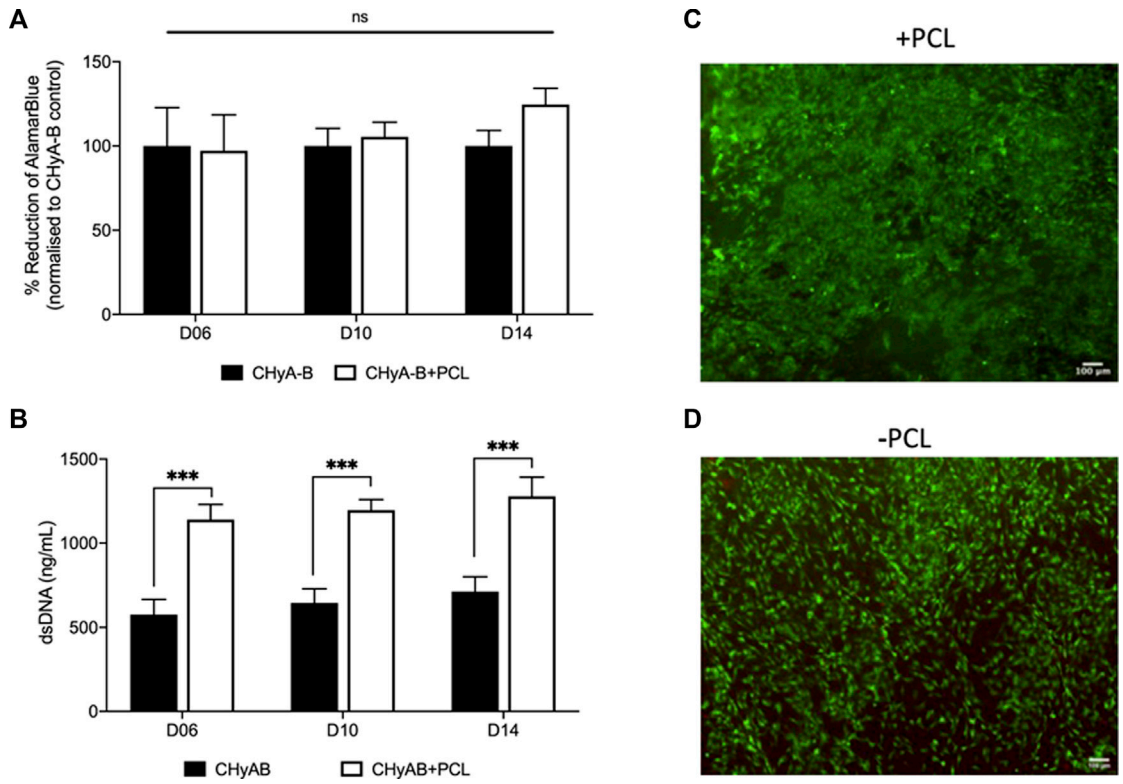

FIGURE 7
Assessment of cell viability of reinforced composite CHyA-B scaffolds. CHyA-B matrices and reinforced composite CHyA-B scaffolds were subjected to cell viability tests to assess their biocompatibility with HUVECs and hMSCs. **(A, B)** Cellular metabolic activity and double stranded DNA content measured in reinforced composite scaffolds (CHyA-B+PCL) and non-reinforced matrix (CHyA-B). Representative LIVE/DEAD® images taken of the surface of CHyA-B **(C)** and CHyA-B+PCL **(D)** scaffolds at day 14 at ×4 magnification. Scale bar = 100 μm. Results displayed as mean ± SEM, $n = 3$, in triplicate. ns = $p > 0.05$, ***$p \leq 0.001$.

the 14 days of culture period, comparable levels of VEGF and b-FGF was measured (Figure 10).

3.3.3 Pro-angiogenic gene expression

The influence of reinforced composite CHyA-B scaffolds on HUVEC and hMSC co-culture gene expression of KDR, TEK 2, ANG 1, ANG 2, and FLT 1 was analysed to assess the effect of the 3DP PCL framework on angiogenic gene expression. The inclusion of the 3DP PCL framework was found to not significantly alter the expression of angiogenic genes (Figure 11), with gene expression sustained over 14 days of *in vitro* culture. Taken together with the expression of pro-angiogenic proteins (Figure 10), this work demonstrates the mechanically-reinforced tracheal scaffold's ability to sustain angiogenic marker expression *in vitro*.

3.3.4 Chick chorioallantoic membrane (CAM) model

To assess the influence of the 3DP PCL framework on vessel infiltration *ex vivo*, scaffolds were analysed using a CAM model, in which they were placed within fertilised chick eggs and incubated to allow for living blood vessels to infiltrate. Image analysis of macro-images of harvested samples (Figure 12A) calculated an increase in vascularised area in the reinforced composite CHyA-B scaffolds over its non-reinforced counterpart, although not statistically significant (Figure 12B). Furthermore, sectioned samples of reinforced composite scaffolds also confirmed the presence of vessels penetrating the scaffolds confirming that the incorporation of PCL fibres did not disrupt vessel infiltration (Figures 12C–F). These are important findings as we have shown the successful fabrication of a novel mechanically reinforced tubular scaffold for tracheal tissue regeneration, with the ability to successfully vascularise *in vitro* and *in vivo*, which would enhance graft survivability post implantation.

4 Discussion

In this study, we sought to fabricate a composite biomaterial-based scaffold for the regeneration of damaged tissue in large tracheal defects. The major objective of the study was to investigate the potential of fabricating reinforced CHyA-B scaffolds tubular constructs with similar mechanical properties to native tracheal tissue by incorporating a 3D-printed PCL framework within the porous collagen sub-layer. In particular, we assessed the feasibility of 3D-printing tubular constructs, evaluated the mechanical properties of different design, and validated their *in vitro* biocompatibility and then the ability to successfully vascularise. Multi-modal mechanical assessment led to the

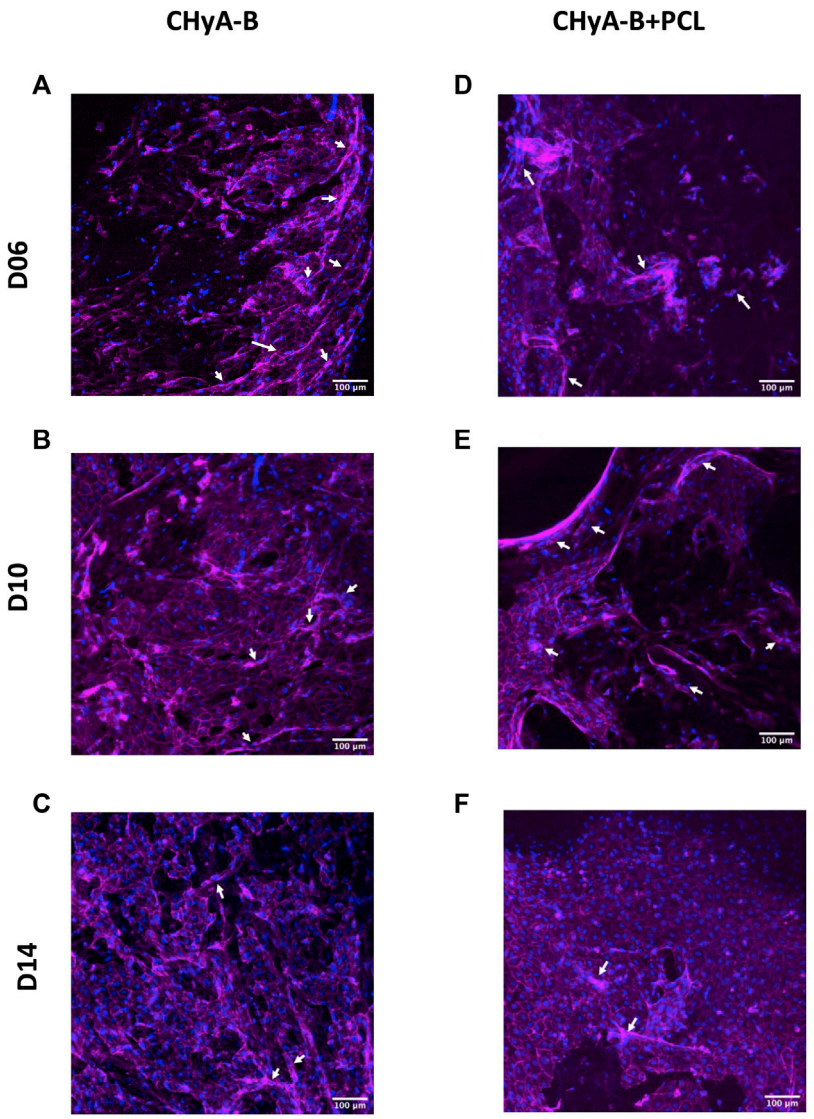

FIGURE 8
Actin cytoskeleton and nuclei staining on reinforced composite CHyA-B scaffolds and CHyA-B matrices *in vitro* vascularisation. HUVECs were cultured with hMSCs on either **(A–C)** non-reinforced matrices (CHyA-B) or **(D–E)** reinforced composite scaffolds (CHyA-B+PCL) scaffolds for 14 days. Maximum intensity projections reconstructed from z-stack images display cells arranged in tubule-like structures (white arrows). Magenta = f-actin, blue = nuclei. *n* = 3, in triplicate. Scale bar = 100 µm.

mechanical characterisation of the 3DP framework to achieve two lead designs (tubular and partial ring) with mechanical properties comparable to native tracheal tissue. Furthermore, the incorporation of the 3DP framework and tubular form-factor generated a scaffold with greater mean pore diameter, ideal for cellular infiltration. Biological characterisation of the reinforced composite CHyA-B scaffolds demonstrated their ability to support cellular growth. Additionally, vascularisation within the PCL-reinforced collagen matrix was maintained with no adverse outcome; vessel-like tubules were observed repeatability in scaffolds using a suite of methods. The expression of pro-angiogenic markers was also investigated, to examine the effect of 3DP PCL on protein and gene expression, with no significant difference observed to the standard vascularised scaffold controls. Finally, in the first step to *in vivo* validation of the scaffolds, the CAM model was utilised and confirmed sustained levels of vascularisation within the reinforced composite scaffolds compared to CHyA-B matrices. Collectively, the data presented within this chapter confirmed that the incorporation of 3DP PCL for mechanically reinforcing CHyA-B matrices maintained successful vascularisation within the collagen matrix and represented a step towards a functional, multi-cellular, and viable construct for tracheal regeneration. Taken together, the results demonstrate that a composite CHyA-B scaffold can be developed to recapitulate the mechanical properties of native tracheal tissue with no negative effects on cell proliferation and vascularisation.

Tracheal scaffold designs were conceptualised with the aim to match the aforementioned mechanical properties of native trachea. The use of 3DP technology has become more widespread within the field of bioengineering for customised tissue replacement or

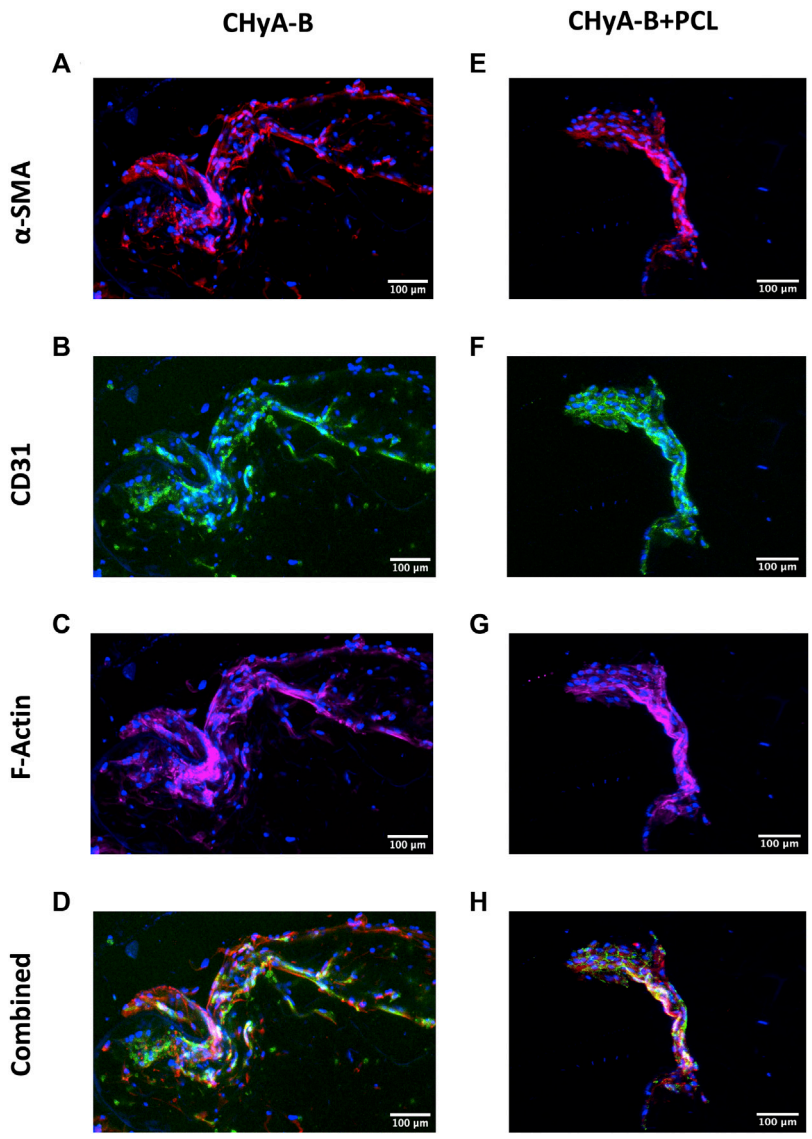

FIGURE 9
CD31 and α-SMA expression by HUVECs and hMSCs in co-culture on reinforced composite CHyA-B scaffolds and CHyA-B matrices at day 10 on *in vitro* culture. HUVECs were cultured with hMSCs on either **(A–D)** non-reinforced matrices (CHyA-B) or **(E–H)** reinforced composite scaffolds (CHyA-B+PCL). Maximum intensity projections reconstructed from z-stacks display tubule-like structures lined with HUVECs CD31 stained in green; **(B, F)** and hMSCs in proximity α-SMA stained in red; **(C, G)**. *n* = 3, in triplicate. Scale bar = 100 μm. Nuclei = blue, f-actin = magenta, α-SMA = red, CD31 = green.

regeneration strategies for an array of organ systems. PCL was selected as the printing material due to its excellent printing characteristics. The thermoplastic nature of PCL and its low melting point temperature (60°C–70°C), makes it available for use for a wide variety of 3D printing methods. Furthermore, the mechanical properties of PCL has seen its widespread use in cartilage replacement in tissue engineering, and investigative studies in tracheal tissue engineering (Pfeiffer et al., 2008; Kundu et al., 2013; Hollister et al., 2016; Morrison et al., 2017; Les et al., 2019). Forgoing the solid polymer tubular design commonly used in recent tracheal scaffold fabrication attempts (Pfeiffer et al., 2008; Zych et al., 2012; Gao et al., 2017; O'Sullivan et al., 2019), two rings of PCL were fabricated into either complete 360° tubular ring or a 288° partial ring. The use of struts was hypothesised to not only generate pores for the collagen matrix to infiltrate within the 3DP framework, but also to provide a polymeric backbone with a degree of flexibility by generating space between the two rings. Also, layer-by-layer stacking of struts and rings were hypothesised to generate mechanical integrity and robustness—thus, producing framework designs that could potentially generate the necessary mechanical strength but also be flexible (Kaye et al., 2019).

To assess whether the 3D-printed tracheal framework designs could match the trachea's anisotropic mechanical properties, all designs firstly underwent radial compressive testing (Figure 4A). Radially compressing samples is often performed on pipes for assessment of resistance to external compressive forces in cases where classical dog bone shaped samples are not feasible, as with curved tubular structures. Unconfined, uniaxial compression testing

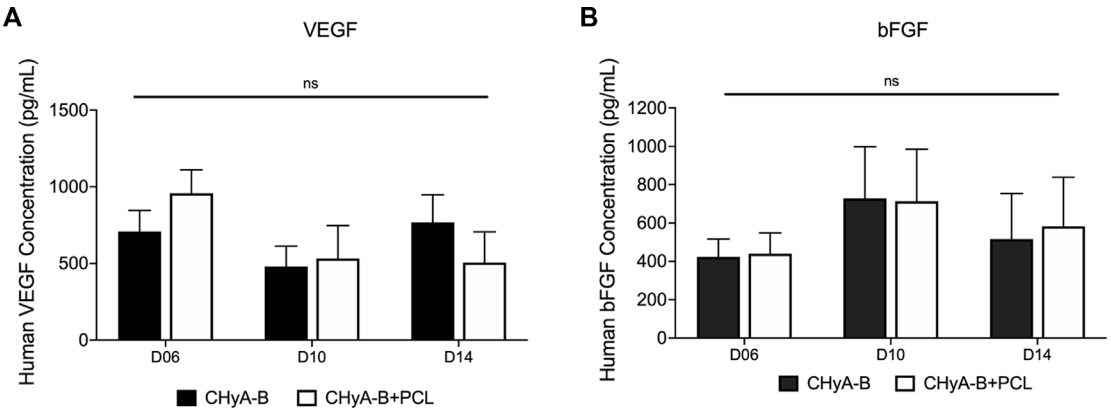

FIGURE 10
Expression of pro-angiogenic proteins **(A)** VEGF and **(B)** b-FGF were measured over 14-day culture period on scaffolds in co-culture of HUVECs and hMSCs on reinforced composite scaffolds (CHyA-B+PCL) and non-reinforced CHyA-B matrices. Results displayed as mean ± SEM. $n = 3$, in triplicate. ns = $p > 0.05$.

was utilised to assess the substrate stiffness of the 3D-printed frameworks radially between the different design features and the molecular weights of PCL. The resistance to compressive forces within the framework designs were greater than reported figures of human trachea which ranged from 1.06 to 1.08 N A-P and 0.55–2.32 N L (Huang et al., 2021), however, a study investigating the difference in mechanical properties within different large animal models and the influence on specimen length on mechanical properties reported figures within range of calculated values of our scaffolds, ranging from 2 to 5 N (Gao et al., 2017; Huang et al., 2021) in complete segments of tracheas tested at 4–8 rings in length at 50% deformation. For tracheal specimens radially compressed in both anterior-posterior and lateral testing positions, values of 2.38 N in canine and 2 N (A-P) and 2 N (L) both at 50% radial compression and 5 N at 40% in a goat trachea have been reported (Gao et al., 2017; Morrison et al., 2017). As already highlighted, the importance of matching the mechanical properties of the native tissue and implanted scaffold is vital, therefore while the mechanical strength of scaffold designs may be too high for human trachea, these designs could still be utilised for animal models. This also further supports the use of 3DP as it would allow for the adjustment of the designs to match mechanical properties of animal model with relative ease. Additionally, the resistance of mechanical forces of our scaffolds is much lower than other tissue-engineering attempts. 3DP PCL scaffolds fabricated for tracheal replacement reported values of approximately 23 N (She et al., 2021) and 30 N (Xia et al., 2019) of full length scaffolds, whereas electrospun tracheal scaffolds have generated values of 32.9 N (L) and 104 N (A-P) (Best et al., 2018) when displaced to 75% of luminal diameter, which are too mechanically stiff compared to native tissue. The 3DP frameworks generated in this study could therefore be beneficial for tissue integration as a function of their reduced mechanical resistance.

Although the trachea has excellent stability and radial strength in order to prevent collapse, it also needs to deform and quickly recover during breathing and coughing (Zhao et al., 2019). In an attempt to investigate similar durability of the PCL frameworks and also the influence of strut numbers on durability, cyclical loading and unloading was carried out for 250 cycles. Testing the designs in this manner would in theory increase the possibility of delamination occurring between the 3DP layers, leading to a loss of structural stiffness and ultimately failure of the scaffold design (Baumann and Hausmann, 2021). Positively, we found that all framework designs survived 250 cycles at 15% applied strain (Figures 4B, C). Cyclical testing of tracheal scaffolds has not been widely investigated, with researchers usually conducting simple lateral compressive or tensile tests only, however an ovine model tested under cyclical loading over 250 cycles under 15% strain reported a peak load of 0.06 N at cycle 1 and 0.04 N at cycle 250 (Mansfield et al., 2016). Through testing the different designs of our scaffolds, we were able to confirm that the 3DP PCL could withstand radial deformation over a large number of cycles without failure; furthermore, no visible failure sites or delamination were observed. A notable difference was observed between the two main design features, with the tubular design resistant to much higher radial compressive forces than the partial ring design. From the same testing regime of cyclical testing, the cyclical strain recovery was calculated to assess the percentage recovery of all the designs over 250 cycles of compressive loading. Notably, although a large difference in peak load was observed between tubular and partial ring designs, there was no significant difference in percentage recovery between the two main design features. This may be due to the high elastic modulus of PCL itself, which has been reported to correlate to the higher degree of crystallinity of 3DP PCL filaments and resultant higher elastic modulus and percentage recovery (Soufivand et al., 2020).

The final mechanical assessment assessed the flexibility of the 3DP designs by a three-point bending test. To reiterate, the trachea not only needs to radially deform to allow for narrowing and widening for passing of food through the oesophagus and coughing, but also needs to have a high degree of flexibility to allow for movement of the neck with ease (Rains et al., 1992; She et al., 2021). Furthermore, a highly flexible scaffold is less likely to dislodge when a patient suffers from a coughing fit, which has been an outcome *in vivo* and clinical trials of previous tracheal

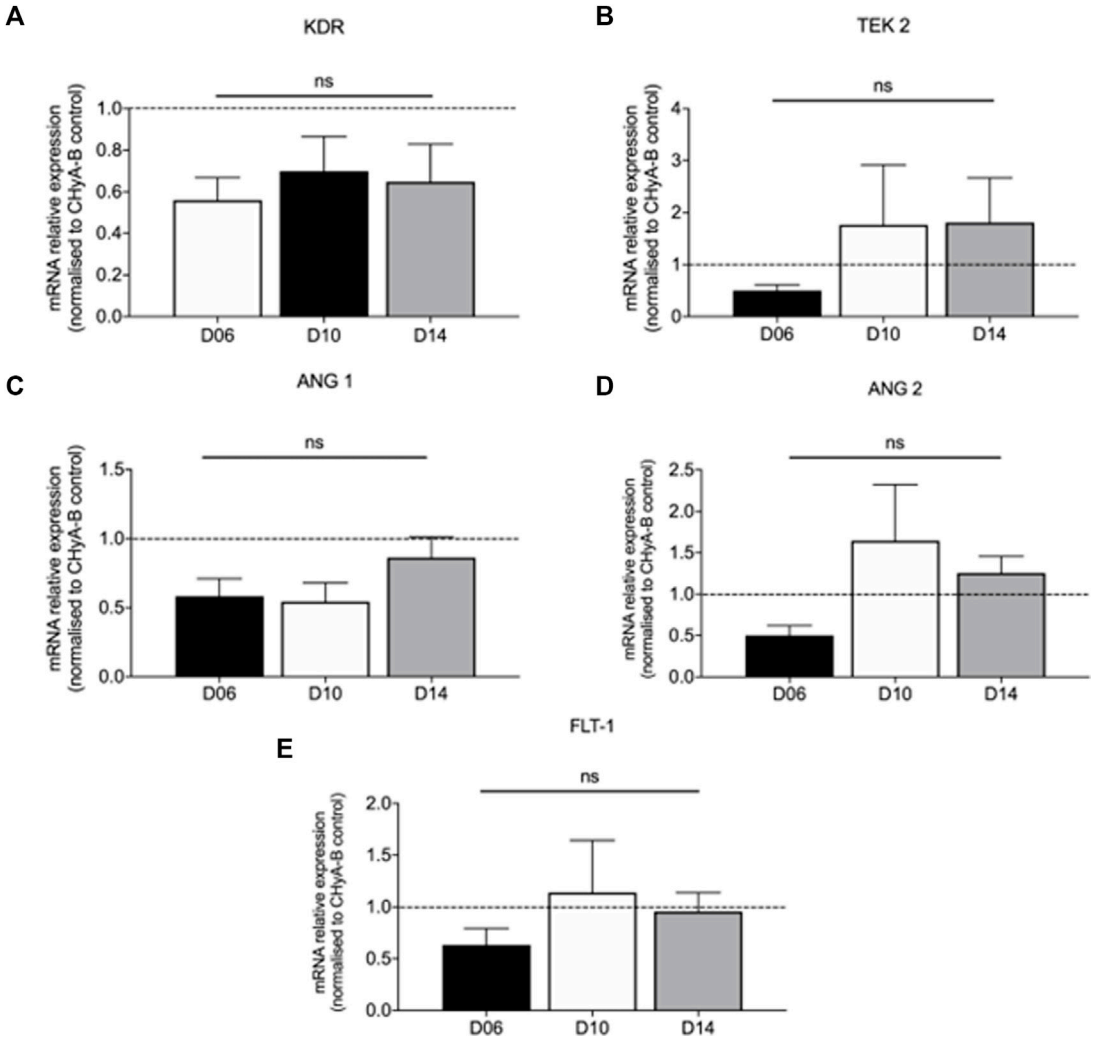

FIGURE 11
Expression of pro-angiogenic genes expressed in co-culture of HUVECs and hMSCs on reinforced composite CHyA-B+PCL scaffolds over 14-day culture period. Quantification of mRNA expression of **(A)** KDR expression **(B)** TEK 2 expression **(C)** ANG 1 expression **(D)** ANG 2 and FLT-1 expression **(E)** displayed as mean ± SEM with expression relative to mRNA expression in CHyA-B matrices at each relative time point. $n = 3$; in triplicate. ns = $p > 0.05$.

replacement efforts and a huge cause for failure (Grimmer et al., 2004; Azorin et al., 2006; Luo et al., 2013; Wood et al., 2014; Elliott et al., 2017). Designs T and PR generated flexural moduli of 0.13–0.26 MPa (Figure 4D), an order of magnitude lower than other tissue-engineering tracheal scaffold studies using 3DP PCL with a flexural modulus of 1.088 MPa (Park et al., 2018), thus making this study's scaffold design much more flexible and compliant. However, the flexural moduli of rabbit trachea has been reported to range between 0.214 and 0.25 MPa (Pfeiffer et al., 2008; Best et al., 2018). Although no reported literature exists that has analysed the flexural moduli of human trachea, which is likely to be greater than smaller rabbit trachea, a study into the changes in mechanical properties of cell-seeded implanted tracheal scaffolds did find a 60% increase in flexural moduli 8 weeks post implantation from 1.71 to 2.84 MPa (Lin et al., 2008). Compressive and cyclical testing confirmed both second generation framework designs are still able to withstand radial compressive forces and are durable, therefore, higher flexural moduli could potentially be achieved in either design through matrix remodelling of cell-seeded scaffolds. Next steps would seek further surgeon evaluation of our designs, especially blinded evaluation, which would provide vital feedback on the scaffolds handling for future reiterations of the scaffold.

After establishing final 3DP parameters, designs, and mechanical properties for the tracheal scaffolds, we sought to investigate the biological properties of the composite scaffolds. The 3DP tubular PCL framework was successfully incorporated with CHyA films and slurry to fabricate composite reinforced CHyA-B scaffolds with ease and reproducibility, generating scaffolds with uniform matrix incorporation and tubular form factor. The mean pore size of the porous collagen sub-layer was analysed to investigate whether the incorporation of 3DP PCL within CHyA-B matrix had an effect, if any, on the pore size. The results indicated that the change in form factor of tubular CHyA-B scaffolds from flat 2 mm CHyA-B matrix used as *in vitro* respiratory models increased from 80 μm (O'Leary et al., 2016) to

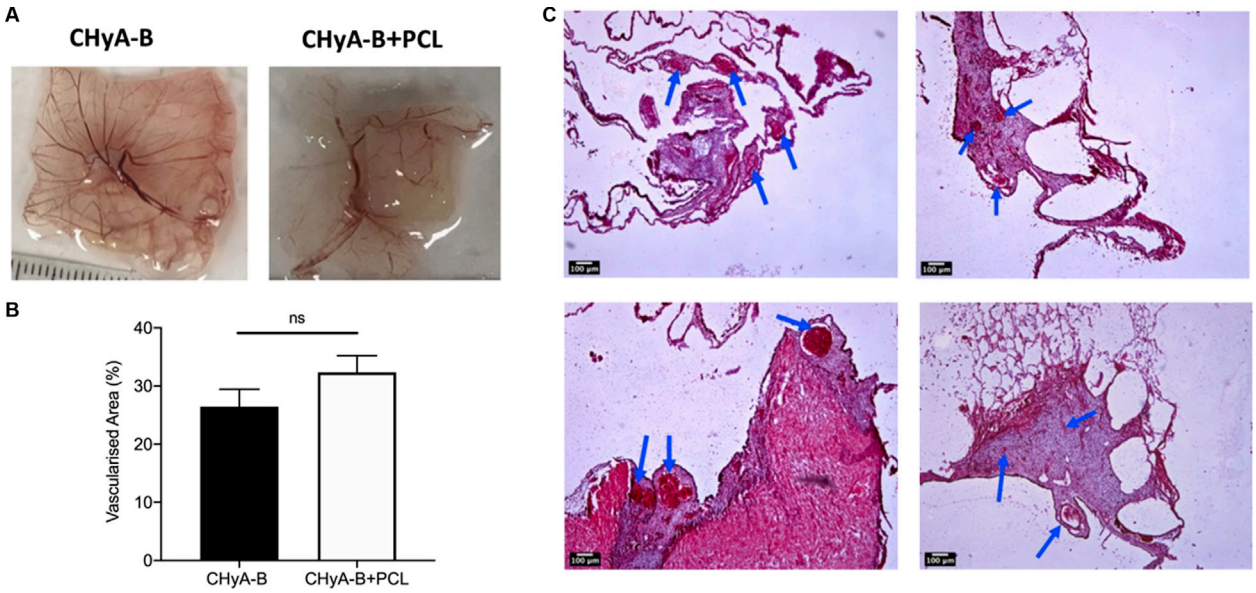

FIGURE 12
Reinforced composite CHyA-B scaffolds were vascularised *ex vivo* in a chick chorioallantoic membrane (CAM) model. **(A)** Macro-images taken of harvested scaffolds after incubation within CAM. **(B)** Image analysis of macro-images of harvested scaffolds calculated greater vascularised area within reinforced composite scaffolds (CHyA-B+PCL) than the non-reinforced CHyA-B matrices. **(C–F)** H&E stained sections of CHyA-B matrices **(C, D)** and reinforced composite CHyA-B+PCL scaffolds **(E, F)** imaged at ×4 magnification. Staining confirmed the presence of blood vessels infiltrating throughout the scaffolds as highlighted by blue arrows. Results displayed as mean ± SEM, $n = 5$. ns = $p > 0.05$. Scale bar = 100 μm.

180 μm. This increase in pore size may have been a result of the increase in mass of metal and overall different mould form factor of the tubular moulds in comparison to the smaller flat square moulds. This in turn influenced the freezing temperature within the mould, altering the freeze-drying profile of the −20 anneal cycle of the tubular scaffolds which impacted the pore size (Figure 6B). Moreover, the incorporation of the 3DP PCL framework into the CHyA-B matrix significantly increased the mean pore size from 180 μm to 290 μm (Figure 6A). Literature shows the ideal pore size for vascularisation is around 300–400 μm (Bai et al., 2010), therefore, the incorporation of 3DP PCL within the collagen matrix produced a composite scaffold with a sub-layer of collagen with a pore size ideal for cellular infiltration (Murphy et al., 2010) and vessel formation.

Having confirmed the feasibility of incorporating the 3DP PCL framework within the CHyA-B matrix and mechanically evaluated different designs for a tracheal replacement scaffold, we now sought to investigate the influence of incorporating the 3DP PCL framework on effective vascularisation *in vitro* and in the CAM model. Although collagen-glycosaminoglycan scaffolds are validated for *in vitro* and *in vivo* pre-vascularisation (McFadden et al., 2013), we wanted to ensure that the inclusion of the PCL reinforcement allowed for sustained vascularisation within the collagen matrix. The introduction of 3DP polymer fibres could impede cell-cell interactions, thereby decreasing vessel formation, and was a necessary risk to investigate. As such, the key objective of this study was to confirm the scaffolds' ability to support cell growth of the *in vitro* co-culture system of HUVECs and hMSCs.

As with most 3D cultures, it was important to initially confirm cell viability in the PCL-reinforced scaffolds prior to any extensive analysis of angiogenesis or vascularisation. The composite scaffold exhibited comparable levels of cellular metabolic activity over 14 days of culture with no significant difference observed (Figure 7A), whereas levels of dsDNA present within the reinforced composite scaffolds were observed to be 2-folds greater than their non-reinforced counterpart (Figure 7B). The incorporation of the 3DP framework to CHyA-B scaffolds increased the mean pore size of the collagen sub-layer from 180 μm to 290 μm (Figure 6), and plausibly facilitated more cellular growth through augmented cell infiltration, nutrient inflow, and waste outflow (Murphy et al., 2010). Differences between the two viability assays may have been due to the differences in application of each assay. With the measurement of dsDNA content, the scaffold is broken down and cells are lysed whereas with measuring the cellular metabolic activity there could be limitations in how far the solution penetrates the scaffolds and thus provides limited measurements of the cells on the periphery of the scaffold. Finally, the presence of a high coverage of green viable cells on the surface of reinforced composite CHyA-B scaffolds was observed when stained with LIVE/DEAD®. Taken together, this further confirmed the biocompatibility of the scaffolds, with sustained cell growth and proliferation maintained with the co-culture model on reinforced composite CHyA-B scaffolds.

It is important to note that the composition of the polymer framework can also have a significant impact on viability, in addition to its effects on composite scaffold porosity. As previously discussed, PCL does not release cytotoxic degradation products into the cell culture environment, and therefore its biodegradation process does not impact cell growth (Sun et al., 2006; Brittberg, 2008) In contrast, other 3DP materials investigated for tracheal tissue replacement such as PLA (polylactic acid) and PGLA (poly(lactic-co-glycolic acid)) have biodegradation products that have been found to trigger an inflammatory response leading to a low pH-environment (Liu and Cao, 2007), and therefore causing an accelerated loss of

structural integrity. For example, this was reported in a 3DP PLA tracheal scaffold which when implanted into the fascia of rabbits for pre-vascularisation, shrunk and deformed due to its instability whereas its PCL counterpart maintained its shape (Tsao et al., 2014). Thus, the addition of the 3DP PCL framework has shown to maintain cell viability while generating mechanical integrity.

The formation of vessel-like tubules was confirmed within reinforced composite CHyA-B scaffolds by several methods. The inclusion of the PCL framework to CHyA-B matrix has been shown to increase the pore size of the collagen matrix (Figure 6), thus it was imperative to assess if the change in pore size could impact vessel formation within the scaffolds. Firstly, confocal microscopy of fluorescently labelled cells within the scaffolds demonstrated the presence of vessel-like tubules for up to 14 days of culture (Figure 8). Notably, we also confirmed that the tubule-like structures were characterised by the lining of HUVECs (CD31) with hMSCs (α-SMA) in direct contact by staining with cell specific markers (Figure 9). As with the previously established model (McFadden et al., 2013), a similar trend was observed, with the strongest vessel formation occurring on day 10 of culture followed by noticeable vessel regression at day 14. As is the issue often associated with long term static *in vitro* culture of microvascular networks, disengagement of cells can take place, resulting in structural regression of the networks, thus limiting the extent to which vessel development within a scaffold can take place *in vitro*. However, once implanted in a dynamic environment *in vivo*, recruitment of host perivascular cells can promote further stabilisation of blood vessels (Montaño et al., 2010).

This possibility was bolstered by the analysis of angiogenic marker expression in cell-seeded scaffolds. No statistical difference seen between the CHyA-B matrix and the reinforced composite CHyA-B scaffolds with regards to expression of angiogenic genes (Figure 11) and proteins (Figure 10), indicating parity in vascularisation potential. The protein bFGF (also known as FGF-2) and its counterpart FGF-1, are potent pro-angiogenic markers which promote the proliferation and differentiation of endothelial cells (Lee et al., 2000; Oladipupo et al., 2014). The expression of both VEGF and bFGF is dynamic during vascularisation (Bautch, 2012; Brundo et al., 2013). The stabilising of KDR (also known as VEGF receptor 2) and FLT 1 (also known as VEGF receptor 1) expression at day 14 but the increase in expression of ANG 1 and its receptor TEK 2 could suggest the maturation of vessel-like structures occurring within the scaffolds from early vessel sprouts to more mature vessel tubules. KDR and FLT-1 are major signal transducer for angiogenesis, promoting vessel formation (Helfrich and Schadendorf, 2011) and when the pro-angiogenic VEGF binds and activates signalling via its receptor KDR on endothelial cells, extracellular matrix degradation, tip cell migration and endothelial proliferation are promoted to form new immature vessel sprouts. Whereas ANG 1 is a stimulator of vessel growth and along with its receptor TEK 2 promotes vessel stabilisation (Lambert et al., 1991; Roberts et al., 1997). However, the upregulation of ANG 2, a marker that causes disruption of vascularisation and destabilisation (Helfrich and Schadendorf, 2011) would suggest the co-culture model is not able to hold up angiogenesis at day 14 as confirmed previously (McFadden et al., 2013) and as shown in fluorescently labelled cultured scaffolds on day 14 imaged samples (Figure 8).

In the first step of *in vivo* validation of the reinforced scaffolds, their vascularisation potential was further validated using a CAM model, with an increased area of vascularisation measured within the reinforced composite CHyA-B scaffolds (Figure 12; $p = 0.1929$). As with the cellular proliferation, the increased pore size of the reinforced composite CHyA-B scaffolds may have allowed for greater blood vessel infiltration, as a mean pore diameter of 300–400 μm has been found to be ideal for vascularisation (Bai et al., 2010). Taken together, not only did the presence of 3DP PCL framework not have any detrimental impact on vessel formation, but it possibly may even enhance vascularisation within collagen-based scaffolds.

Indeed, several approaches to vascularise tracheal scaffolds have been investigated elsewhere in an attempt to accelerate neovascularisation of tracheal grafts, such as the application of angiogenic factors such as VEGF and human recombinant erythropoietin (hrEPO; 294,295). Although preliminary results showed promise in vascularising grafts, the maintenance of working concentrations of growth factors post-implantation has not yet been investigated (Tan et al., 2006). Furthermore, this approach relies of efficient host response and vascularisation may not occur in time to allow for graft survival. Another more widely-investigated approach has been pre-vascularising tracheal grafts through the means of implanting the graft into the patients forearm or omentum prior to implantation into the defect site (Lendlein et al., 2001; Delaere et al., 2019). The use of an initial heterotopic vascularisation period elsewhere in the body, prior to tracheal transfer, has been shown to generate a clinically significant blood supply (Kalathur et al., 2010; Kim et al., 2011; Udelsman et al., 2018; Li et al., 2019). However, such a strategy can take several weeks––or even months––to fully establish a vascular network and is therefore not adequate in emergency situations (Maughan et al., 2017). On the other hand, the means of pre-vascularising the reinforced composite CHyA-B scaffolds via the co-culture system, which we have shown can successfully vascularise *in vitro*, can establish a network of vasculature within the scaffolds to ensure success of graft acceptance into defect site within shorter time frames, as shown by previous success within our lab (McFadden et al., 2013). These mechanically reinforced pre-vascularised scaffolds can now be evaluated for their impact on enhancing epithelisation.

While this study has successfully achieved its objectives and developed a novel tubular scaffold for tracheal replacement, the lack of degradation data of our 3DP framework design, is a principal limitation. Although there are *in vivo* degradations studies on PCL that can provide an estimate 2–3 years degradation rate (Sun et al., 2006); the speed at which PCL breaks down is largely dependent on its surface area, geometry and molecular weight, all of which differ in studies. Completing a comprehensive degradation study would require a long-term animal study necessitating a large quantity of animals, which is unfortunately out the scope for the length of this research project. Reducing the number of animals required could be achieved by developing a non-invasive procedure to measure degradation within animals without requiring euthanasia, such as using micro-CT. Moreover, 3D-printed framework designs were mechanically assessed in a dry state due to the limitations of the testing machine, however, more appropriate assessment would be done under a hydrated state to mimic physiological conditions. Under hydration, PCL rate degradation would differ as the solution would enhance the hydrolytic breakdown of its ester bonds and thus allow for a more accurate measurement of each design's response to mechanical load. In particular, fatigue testing

performed in a hydrated state over a longer rate of cycles such as for spinal implants (ISO 12189:2008) would provide vital information of the scaffolds durability. Moreover, tracheal tissue is viscoelastic, as this study has successfully established the foundation for a mechanically compliant and flexible scaffold, future refinement of the scaffolds can look to characterise its viscoelastic features.

5 Conclusion

Overall, we were successfully able to fabricate a composite tissue engineered tracheal substitute that mimics the reported mechanical properties of native tracheal tissue and confirmed the incorporation of 3DP PCL framework within the CHyA-B matrix did not impede on vessel formation using an *in vitro* culture model. A battery of tests was developed to characterise the 3DP designs by measuring mechanical strength, robustness, and flexibility, all of which are integral tracheal properties. This has enabled us to establish two main designs which provide a range of mechanical properties close to animal models, allowing us to streamline a design in the future when more data becomes available on the exact mechanical properties of the trachea. The use of PCL in tissue engineering, in particular tracheal reconstruction, is becoming more widespread. Although PCL exhibits biocompatibility it is less biocompatible than natural polymers, and as previously discussed, tracheal scaffold attempts with PCL alone have induced foreign body and inflammatory reactions. However, the ease of printability and excellent mechanical properties of PCL are substantial advantages, therefore we combined the 3DP PCL with freeze-dried CHyA-B matrices to create a composite reinforced scaffold, which was confirmed to support the growth of cells *in vitro*. The successful pre-vascularisation of our reinforced composite CHyA-B scaffold lends itself resolving a major hurdle in the advancement of tracheal scaffolds. By addressing both the mechanical and physiological requirements of a tracheal scaffold, this work has begun to pave the way for a new therapeutic option to resolve the shortcomings of current treatment options, potentially improving patient outcomes.

Data availability statement

The raw data supporting the conclusion of this article will be made available by the authors, without undue reservation.

Author contributions

TK—Experimental, Lead scientist in lab, manuscript draft ML—Mechanical Testing and 3D printing contribution LS—Mechanical Testing and 3D printing contribution S-AC—Co-advisor on direction of work and overall study performance FO'B—Co-advisor on direction of work and overall study performance CO'L—Lead PI, idea generation, core study concept, project direction, final manuscript editing and submission. All authors listed have made a substantial, direct, and intellectual contribution to the work and approved it for publication.

Funding

This study was funded by the Science Foundation Ireland Advanced Materials and Bioengineering Research (SFI-AMBER) Centre (Grant 17/RC-PhD/3477).

Acknowledgments

We would like to acknowledge Dr Brenton Cavanagh and Dr Ronaldo Jose Farias Correa Do Amaral, RCSI, for the respective microscope training and CAM training provided to the first author.

Conflict of interest

The authors declare that the research was conducted in the absence of any commercial or financial relationships that could be construed as a potential conflict of interest.

Publisher's note

References

Azorin, J. F., Bertin, F., Martinod, E., and Laskar, M. (2006). Tracheal replacement with an aortic autograft. *Eur. J. Cardio-thoracic Surg.* 29 (2), 261–263. doi:10.1016/j.ejcts.2005.11.026

Bae, S. W., Lee, K. W., Park, J. H., Lee, J. H., Jung, C. R., Yu, J. J., et al. (2018). 3D bioprinted artificial trachea with epithelial cells and chondrogenic-differentiated bone marrow-derived mesenchymal stem cells. *Int. J. Mol. Sci.* 19 (6), 1624. doi:10.3390/ijms19061624

Bai, F., Wang, Z., Lu, J., Liu, J., Chen, G., Lv, R., et al. (2010). The correlation between the internal structure and vascularization of controllable porous bioceramic materials *in vivo*: A quantitative study. *Tissue Eng. - Part A* 16 (12), 3791–3803. doi:10.1089/ten.tea.2010.0148

Baumann, A., and Hausmann, J. (2021). Compression fatigue testing setups for composites—a review. *Adv. Eng. Mater* 23 (2), 2000646. doi:10.1002/adem.202000646

Bautch, V. L. (2012). VEGF-directed blood vessel patterning: From cells to organism. *Cold Spring Harb. Perspect. Med.* 2 (9), a006452. doi:10.1101/cshperspect.a006452

Beall, A. C. J., Harrington, B. O., Greenberg, D. S., Morris, G. C., and Usher, F. C. (1962). Tracheal replacement with heavy Marlex mesh. *Arch. Surg.* 84 (4), 390. doi:10.1001/archsurg.1962.01300220014002

Best, C. A., Pepper, V. K., Ohst, D., Bodnyk, K., Heuer, E., Onwuka, E. A., et al. (2018). Designing a tissue-engineered tracheal scaffold for preclinical evaluation. *Int. J. Pediatr. Otorhinolaryngol.* 104, 155–160. doi:10.1016/j.ijporl.2017.10.036

Boazak, E. M., and Auguste, D. T. (2018). Trachea mechanics for tissue engineering design. *ACS Biomater. Sci. Eng.* 4, 1272–1284. doi:10.1021/acsbiomaterials.7b00738

Brittberg, M. (2008). Autologous chondrocyte implantation-Technique and long-term follow-up. *Injury* 39 (1 Suppl. L), 40–49. doi:10.1016/j.injury.2008.01.040

Brundo, Y., Ennett-Shepard, A. B., Chen, R. R., Aizenberg, M., and Mooney, D. J. (2013). Enhancing microvascular formation and vessel maturation through temporal control over multiple pro-angiogenic and pro-maturation factors. *Biomaterials* 34 (36), 1–17.

Delaere, P., Decaluwé, H., Paul, D. L., Margot, D. H., Dooms, C., Meulemans, J., et al. (2019). *Tracheal transplantation: Current possibilities*. 1st ed Leuven: Leuven University Press, 107.

Delaere, P., and Van Raemdonck, D. (2016). Tracheal replacement. *J. Thorac. Dis.* 8 (2), S186–S196. doi:10.3978/j.issn.2072-1439.2016.01.85

Delaere, P., Vrancks, J., Verleden, G., De Leyn, P., and van Raemdonck, D. (2010). Tracheal allotransplantation after withdrawal of immunosuppressive therapy. *Bull. Acad. Natl. Med.* 194 (7), 1335–1337. doi:10.1016/s0001-4079(19)32213-7

Delaere, P. R., Vranckx, J. J., and Hondt, M. D. (2014). Tracheal allograft after withdrawal of immunosuppressive therapy. *N. Engl. J. Med.* 370 (16), 1568–1570. doi:10.1056/nejmc1315273

Delaere, P. R., Vranckx, J. J., Meulemans, J., Vander Poorten, V., Segers, K., Van Raemdonck, D., et al. (2012). Learning curve in tracheal allotransplantation. *Am. J. Transpl.* 12 (9), 2538–2545. doi:10.1111/j.1600-6143.2012.04125.x

do Amaral, R. J. F. C., Cavanagh, B., O'Brien, F. J., and Kearney, C. J. (2019). Platelet-derived growth factor stabilises vascularisation in collagen–glycosaminoglycan scaffolds *in vitro*. *J. Tissue Eng. Regen. Med.* 13 (2), 261–273. doi:10.1002/term.2789

do Amaral, R. J. F. C., Zayed, N. M. A., Pascu, E. I., Cavanagh, B., Hobbs, C., Santarella, F., et al. (2019). Functionalising collagen-based scaffolds with platelet-rich plasma for enhanced skin wound healing potential. *Front. Bioeng. Biotechnol.* 7, 371–422. doi:10.3389/fbioe.2019.00371

Elliott, M. J., Butler, C. R., Varanou-Jenkins, A., Partington, L., Carvalho, C., Samuel, E., et al. (2017). Tracheal replacement therapy with a stem cell-seeded graft: Lessons from compassionate use application of a GMP-compliant tissue-engineered medicine. *Stem Cells Transl. Med.* 6 (6), 1458–1464. doi:10.1002/sctm.16-0443

Gao, M., Zhang, H., Dong, W., Bai, J., Gao, B., Xia, D., et al. (2017). Tissue-engineered trachea from a 3D-printed scaffold enhances whole-segment tracheal repair. *Sci. Rep.* 7 (1), 5246–5312. doi:10.1038/s41598-017-05518-3

Grimmer, J. F., Gunnlaugsson, C. B., Alsberg, E., Murphy, H. S., Kong, H. J., Mooney, D. J., et al. (2004). Tracheal reconstruction using tissue-engineered cartilage. *Arch. Otolaryngol. - Head. Neck Surg.* 130 (10), 1191–1196. doi:10.1001/archotol.130.10.1191

Haugh, M. G., Murphy, C. M., McKiernan, R. C., Altenbuchner, C., and O'Brien, F. J. (2011). Crosslinking and mechanical properties significantly influence cell attachment, proliferation, and migration within collagen glycosaminoglycan scaffolds. *Tissue Eng. - Part a.* 17 (9–10), 1201–1208. doi:10.1089/ten.tea.2010.0590

Helfrich, I., and Schadendorf, D. (2011). Blood vessel maturation, vascular phenotype and angiogenic potential in malignant melanoma: One step forward for overcoming anti-angiogenic drug resistance? *Mol. Oncol.* 5 (2), 137–149. doi:10.1016/j.molonc.2011.01.003

Hoffman, B., Martin, M., Brown, B. N., Bonassar, L. J., and Cheetham, J. (2016). Biomechanical and biochemical characterization of porcine tracheal cartilage. *Laryngoscope* 126 (10), E325–E331. doi:10.1002/lary.25861

Hollister, S. J., Green, G. E., Morrison, R. J., Hollister, S. J., Niedner, M. F., Mahani, M. G., et al. Mitigation of tracheobronchomalacia with 3D-printed personalized medical devices in pediatric patients. 2016;7:1–12.

Huang, L., Wang, L., He, J., Zhao, J., Zhong, D., Yang, G., et al. (2016). Tracheal suspension by using 3-dimensional printed personalized scaffold in a patient with tracheomalacia. *J. Thorac. Dis.* 8 (11), 3323–3328. doi:10.21037/jtd.2016.10.53

Huang, Z., Wang, L., Zhang, C. X., Cai, Z. H., Liu, W. H., Li, W. M., et al. (2021). Biomechanical strength dependence on mammalian airway length. *J. Thorac. Dis.* 13 (2), 918–926. doi:10.21037/jtd-20-2970

Kalathur, M., Baiguera, S., and Macchiarini, P. (2010). Translating tissue-engineered tracheal replacement from bench to bedside. *Cell Mol. Life Sci.* 67 (24), 4185–4196. doi:10.1007/s00018-010-0499-z

Kang, Y., Wang, C., Qiao, Y., Gu, J., Zhang, H., Peijs, T., et al. (2019). Tissue-engineered trachea consisting of electrospun patterned sc-PLA/GO- g-IL fibrous membranes with antibacterial property and 3D-printed skeletons with elasticity. *Biomacromolecules* 20 (4), 1765–1776. doi:10.1021/acs.biomac.9b00160

Kaye, R., Goldstein, T., Grande, D. A., Zeltsman, D., and Smith, L. P. (2019). A 3-dimensional bioprinted tracheal segment implant pilot study: Rabbit tracheal resection with graft implantation. *Int. J. Pediatr. Otorhinolaryngol.* 117 (2018), 175–178. doi:10.1016/j.ijporl.2018.11.010

Kim, J. H., Kong, W. H., Kim, J. G., Kim, H. J., and Seo, S. W. (2011). Possibility of skin epithelial cell transdifferentiation in tracheal reconstruction. *Artif. Organs* 35 (2), 122–130. doi:10.1111/j.1525-1594.2010.01047.x

Kundu, J., Shim, J.-H., Jang, J., Kim, S.-W., and Cho, D.-W. (2013). An additive manufacturing-based PCL-alginate-chondrocyte bioprinted scaffold for cartilage tissue engineering: PCL-alginate-chondrocyte bioprinted scaffold for cartilage tissue engineering. *J. Tissue Eng. Regen. Med.* 9 (11), 1286–1297. doi:10.1002/term.1682

Lambert, R. K., Baile, E. M., Moreno, R., Bert, J., and Pare, P. D. (1991). A method for estimating the Young's modulus of complete tracheal cartilage rings. *J. Appl. Physiol.* 70 (3), 1152–1159. doi:10.1152/jappl.1991.70.3.1152

Lee, S. H., Schloss, D. J., and Swain, J. L. (2000). Maintenance of vascular integrity in the embryo requires signaling through the fibroblast growth factor receptor. *J. Biol. Chem.* 275 (43), 33679–33687. doi:10.1074/jbc.m004994200

Lee, S. J., Choi, J. S., Eom, M. R., Jo, H. H., Kwon, I. K., Kwon, S. K., et al. (2020). Dexamethasone loaded bilayered 3D tubular scaffold reduces restenosis at the anastomotic site of tracheal replacement: *In vitro* and *in vivo* assessments. *Nanoscale* 12 (8), 4846–4858. doi:10.1039/c9nr10341d

Lemoine, M. F. M. (2020). *Reinforced collagen based scaffolds for musculoskeletal tissue engineering*. Royal College of Surgeons in Ireland.

Lendlein, A., Schmidt, A. M., and Langer, R. (2001). AB-polymer networks based on oligo(ε-caprolactone) segments showing shape-memory properties. *Proc. Natl. Acad. Sci. U. S. A.* 98 (3), 842–847. doi:10.1073/pnas.98.3.842

Les, A. S., Ohye, R. G., Filbrun, A. G., Ghadimi, M., Flanagan, C. L., Daniels, R. C., et al. (2019). 3D-printed, externally-implanted, bioresorbable airway splints for severe tracheobronchomalacia. *Laryngoscope* 129 (8), 1763–1771. doi:10.1002/lary.27863

Li, D., Yin, Z., Liu, Y., Feng, S., Liu, Y., Lu, F., et al. (2019). Regeneration of trachea graft with cartilage support, vascularization, and epithelization. *Acta Biomater.* 89, 206–216. doi:10.1016/j.actbio.2019.03.003

Lin, C. H., Hsuhui, S., Huang, C. E., Cheng, W. T., and Su, J. M. (2009). A scaffold-bioreactor system for a tissue-engineered trachea. *Biomaterials* 30 (25), 4117–4126. doi:10.1016/j.biomaterials.2009.04.028

Lin, C. H., Su, J. M., and Hsu, S. H. (2008). Evaluation of type II collagen scaffolds reinforced by poly(ε-caprolactone) as tissue-engineered trachea. *Tissue Eng. - Part C Methods* 14 (1), 69–77. doi:10.1089/tec.2007.0336

Liu, W., and Cao, Y. (2007). Application of scaffold materials in tissue reconstruction in immunocompetent mammals: Our experience and future requirements. *Biomaterials* 28 (34), 5078–5086. doi:10.1016/j.biomaterials.2007.07.028

Luo, X., Liu, Y., Zhang, Z., Tao, R., Liu, Y., He, A., et al. (2013). Long-term functional reconstruction of segmental tracheal defect by pedicled tissue-engineered trachea in rabbits. *Biomaterials* 34 (13), 3336–3344. doi:10.1016/j.biomaterials.2013.01.060

Mansfield, E. G., Auguste, D. T., Greene, V. K., and Auguste, D. T. (2016). Patterned, tubular scaffolds mimic longitudinal and radial mechanics of the neonatal trachea. *Acta Biomater.* 33, 176–182. doi:10.1016/j.actbio.2016.01.034

Maughan, E. F., Hynds, R. E., Proctor, T. J., Janes, S. M., Elliott, M., Birchall, M. A., et al. (2017). Autologous cell seeding in tracheal tissue engineering. *Curr. Stem Cell Rep.* 3 (4), 279–289. doi:10.1007/s40778-017-0108-2

Maziak, D. E., Todd, T. R. J., Keshavjee, S. H., Winton, T. L., Van Nostrand, P., Pearson, F. G., et al. (1996). Adenoid cystic carcinoma of the airway: Thirty-two-year experience. *J. Thorac. Cardiovasc Surg.* 112 (6), 1522–1532. doi:10.1016/s0022-5223(96)70011-9

McFadden, T. M., Duffy, G. P., Allen, A. B., Stevens, H. Y., Schwarzmaier, S. M., Plesnila, N., et al. (2013). The delayed addition of human mesenchymal stem cells to pre-formed endothelial cell networks results in functional vascularization of a collagen-glycosaminoglycan scaffold *in vivo*. *Acta Biomater.* 9 (12), 9303–9316. doi:10.1016/j.actbio.2013.08.014

Montaño, I., Schiestl, C., Schneider, J., Pontiggia, L., Luginbühl, J., Biedermann, T., et al. (2010). Formation of human capillaries *in vitro*: The engineering of prevascularized matrices. *Tissue Eng. - Part A* 16 (1), 269–282. doi:10.1089/ten.tea.2008.0550

Morrison, R. J., Sengupta, S., Flanangan, C. L., Ohye, R. G., Hollister, S. J., and Green, G. E. (2017). Treatment of severe acquired tracheomalacia with a patient-specific, 3D-printed, permanent tracheal splint. *JAMA Otolaryngol. Neck Surg.* 143 (5), 523. doi:10.1001/jamaoto.2016.3932

Murphy, C. M., Haugh, M. G., and O'Brien, F. J. (2010). The effect of mean pore size on cell attachment, proliferation and migration in collagen-glycosaminoglycan scaffolds for bone tissue engineering. *Biomaterials* 31 (3), 461–466. doi:10.1016/j.biomaterials.2009.09.063

O'Brien, F. J., Harley, B. A., Yannas, I. V., and Gibson, L. J. (2005). The effect of pore size on cell adhesion in collagen-GAG scaffolds. *Biomaterials* 26 (4), 433–441. doi:10.1016/j.biomaterials.2004.02.052

Oladipupo, S. S., Smith, C., Santeford, A., Park, C., Sene, A., Wiley, L. A., et al. (2014). Endothelial cell FGF signaling is required for injury response but not for vascular homeostasis. *Proc. Natl. Acad. Sci. U. S. A.* 111 (37), 13379–13384. doi:10.1073/pnas.1324235111

O'Leary, C., Cavanagh, B., Unger, R. E., Kirkpatrick, C. J., O'Dea, S., O'Brien, F. J., et al. (2016). The development of a tissue-engineered tracheobronchial epithelial model using a bilayered collagen-hyaluronate scaffold. *Biomaterials* 85, 111–127. doi:10.1016/j.biomaterials.2016.01.065

Omori, K., Tada, Y., Suzuki, T., Nomoto, Y., Matsuzuka, T., Kobayashi, K., et al. (2008). Clinical application of *in situ* tissue engineering using a scaffolding technique for reconstruction of the larynx and trachea. *Ann. Otol. Rhinol. Laryngol.* 117 (9), 673–678. doi:10.1177/000348940811700908

O'Sullivan, K. E., Kreaden, U. S., Hebert, A. E., Eaton, D., and Redmond, K. C. (2019). A systematic review and meta-analysis of robotic versus open and video-assisted thoracoscopic surgery approaches for lobectomy. *Interact. Cardiovasc Thorac. Surg.* 28 (4), 526–534. doi:10.1093/icvts/ivy315

Pacetti, A. FDA Approves 3D-printed Airway Stents Developed by Cleveland Clinic Doctor [press release]. Cleveland Clinic [Internet]. 2020; Available at: https://newsroom.clevelandclinic.org/2020/01/08/fda-approves-3d-printed-airway-stents-developed-by-cleveland-clinic-doctor/

Park, H. S., Lee, J. S., Jung, H., Kim, D. Y., Kim, S. W., Sultan, M. T., et al. (2018). An omentum-cultured 3D-printed artificial trachea: *In vivo* bioreactor. *Nanomedicine Biotechnol.* 46 (3), S1131–S1140. doi:10.1080/21691401.2018.1533844

Pfeiffer, E., Vickers, S. M., Frank, E., Grodzinsky, A. J., and Spector, M. (2008). The effects of glycosaminoglycan content on the compressive modulus of cartilage engineered in type II collagen scaffolds. *Osteoarthr. Cartil.* 16 (10), 1237–1244. doi:10.1016/j.joca.2008.02.014

Rains, J. K., Bert, J. L., Roberts, C. R., and Pare, P. D. (1992). Mechanical properties of human tracheal cartilage. *J. Appl. Physiol.* 72 (1), 219–225. doi:10.1152/jappl.1992.72.1.219

Rehmani, S. S., Al-Ayoubi, A. M., Ayub, A., Barsky, M., Lewis, E., Flores, R., et al. (2017). Three-Dimensional-printed bioengineered tracheal grafts: Preclinical results and potential for human use. *Ann. Thorac. Surg.* 104 (3), 998–1004. doi:10.1016/j.athoracsur.2017.03.051

Ricardo, M., José Luiz, J., Fabio Biscegli Jatene, H. M., Guibert, N., Saka, H., Dutau, H., et al. Preliminary experiences in trachea scaffold tissue engineering with segmental organ decellularization. *Biomaterials*. 2019;126(4):9201–9209.

Morrison1, R. J., Hollister2, S. J., Niedner3, M. F., Ghadimi Mahani4, M., Park5, A. H., Mehta6, D. K., et al. Mitigation of tracheobronchomalacia with 3D-printed personalized medical devices in pediatric patients. 2017;155(1):3–12.

Roberts, C. R., Rains, J. K., Paré, P. D., Walker, D. C., Wiggs, B., and Bert, J. L. (1997). Ultrastructure and tensile properties of human tracheal cartilage. *J. Biomech.* 31 (1), 81–86. doi:10.1016/s0021-9290(97)00112-7

Rose, K. G., Sesterhenn, K., and Wustrow, F. (1979). Tracheal allotransplantation in man. *Lancet* 313 (8113), 433. doi:10.1016/s0140-6736(79)90902-4

Ryan, E. J., Ryan, A. J., González-Vázquez, A., Philippart, A., Ciraldo, F. E., Hobbs, C., et al. (2019). Collagen scaffolds functionalised with copper-eluting bioactive glass reduce infection and enhance osteogenesis and angiogenesis both *in vitro* and *in vivo*. *Biomaterials* 197, 405–416. doi:10.1016/j.biomaterials.2019.01.031

She, Y., Fan, Z., Wang, L., Li, Y., Sun, W., Tang, H., et al. (2021). 3D printed biomimetic PCL scaffold as framework interspersed with collagen for long segment tracheal replacement. *Front. Cell Dev. Biol.* 9, 629796–629814. doi:10.3389/fcell.2021.629796

Siddiqi, S. (2017). Tissue engineering of the trachea: What is the hold-up? *MOJ Cell Sci. Rep.* 4 (1), 1–5. doi:10.15406/mojcsr.2017.04.00076

Soriano, L., Khalid, T., Whelan, D., O'huallachain, N., Redmond, K. C., O'brien, F. J., et al. (2021). Development and clinical translation of tubular constructs for tracheal tissue engineering: A review. *Eur. Respir. Rev.* 30 (162), 210154. doi:10.1183/16000617.0154-2021

Soufivand, A. A., Abolfathi, N., Hashemi, A., and Lee, S. J. (2020). The effect of 3D printing on the morphological and mechanical properties of polycaprolactone filament and scaffold. *Polym. Adv. Technol.* 31 (5), 1038–1046. doi:10.1002/pat.4838

Sun, H., Mei, L., Song, C., Cui, X., and Wang, P. (2006). The *in vivo* degradation, absorption and excretion of PCL-based implant. *Biomaterials* 27 (9), 1735–1740. doi:10.1016/j.biomaterials.2005.09.019

Tan, Q., Steiner, R., Hoerstrup, S. P., and Weder, W. (2006). Tissue-engineered trachea: History, problems and the future. *Eur. J. Cardio-thoracic Surg.* 30 (5), 782–786. doi:10.1016/j.ejcts.2006.08.023

Tan, Q., Steiner, R., Yang, L., Welti, M., Neuenschwander, P., Hillinger, S., et al. (2007). Accelerated angiogenesis by continuous medium flow with vascular endothelial growth factor inside tissue-engineered trachea. *Eur. J. Cardio-thoracic Surg.* 31 (5), 806–811. doi:10.1016/j.ejcts.2007.01.045

Teng, Z., Ochoa, I., Li, Z., Lin, Y., Rodriguez, J. F., Bea, J. A., et al. (2008). Nonlinear mechanical property of tracheal cartilage: A theoretical and experimental study. *J. Biomech.* 41 (9), 1995–2002. doi:10.1016/j.jbiomech.2008.03.032

Teng, Z., Trabelsi, O., Ochoa, I., He, J., Gillard, J. H., and Doblare, M. (2012). Anisotropic material behaviours of soft tissues in human trachea: An experimental study. *J. Biomech.* 45 (9), 1717–1723. doi:10.1016/j.jbiomech.2012.04.002

Tsao, C. K., Ko, C. Y., Yang, S. R., Yang, C. Y., Brey, E. M., Huang, S., et al. (2014). An ectopic approach for engineering a vascularized tracheal substitute. *Biomaterials* 35 (4), 1163–1175. doi:10.1016/j.biomaterials.2013.10.055

Udelsman, B., Mathisen, D. J., and Ott, H. C. (2018). A reassessment of tracheal substitutes—A systematic review. *Ann. Cardiothorac. Surg.* 7 (2), 175–182. doi:10.21037/acs.2018.01.17

Walles, T., Giere, B., Hofmann, M., Schanz, J., Hofmann, F., Mertsching, H., et al. (2004). Experimental generation of a tissue-engineered functional and vascularized trachea. *J. Thorac. Cardiovasc Surg.* 128 (6), 900–906. doi:10.1016/s0022-5223(04)01142-0

Wood, M. W., Murphy, S. V., Feng, X., and Wright, S. C. (2014). Tracheal reconstruction in a canine model. *Otolaryngol. - Head. Neck Surg. (United States)* 150 (3), 428–433. doi:10.1177/0194599813516751

Woodruff, M. A., and Hutmacher, D. W. (2010). The return of a forgotten polymer - polycaprolactone in the 21st century. *Prog. Polym. Sci.* 35 (10), 1217–1256. doi:10.1016/j.progpolymsci.2010.04.002

Wu, T., Zheng, H., Chen, J., Wang, Y., Sun, B., Morsi, Y., et al. (2017). Application of a bilayer tubular scaffold based on electrospun poly(l-lactide-co-caprolactone)/collagen fibers and yarns for tracheal tissue engineering. *J. Mater Chem. B* 5 (1), 139–150. doi:10.1039/c6tb02484j

Xia, D., Jin, D., Wang, Q., Gao, M., Zhang, J., Zhang, H., et al. (2019). Tissue-engineered trachea from a 3D-printed scaffold enhances whole-segment tracheal repair in a goat model. *J. Tissue Eng. Regen. Med.* 13 (4), 694–703. doi:10.1002/term.2828

Zhao, W., Zhang, F., Leng, J., and Liu, Y. (2019). Personalized 4D printing of bioinspired tracheal scaffold concept based on magnetic stimulated shape memory composites. *Compos Sci. Technol.* 184, 107866. doi:10.1016/j.compscitech.2019.107866

Zopf, D. A., Hollister, S. J., Nelson, M. E., Ohye, R. G., and Green, G. E. (2013). Bioresorbable airway splint created with a three-dimensional printer. *N. Engl. J. Med.* 368 (21), 2043–2045. doi:10.1056/nejmc1206319

Zych, B., Popov, A. F., Stavri, G., Bashford, A., Bahrami, T., Amrani, M., et al. (2012). Early outcomes of bilateral sequential single lung transplantation after *ex-vivo* lung evaluation and reconditioning. *J. Hear Lung Transpl.* 31 (3), 274–281. doi:10.1016/j.healun.2011.10.008

frontiers | Frontiers in Bioengineering and Biotechnology

TYPE Original Research
PUBLISHED 22 June 2023
DOI 10.3389/fbioe.2023.1187914

OPEN ACCESS

EDITED BY
Vasil M. Garamus,
Helmholtz Centre for Materials and Coastal Research (HZG), Germany

REVIEWED BY
Kai Wang,
Nankai University, China
Yang Zhu,
Zhejiang University, China

*CORRESPONDENCE
Juan Du,
bairuochen12@163.com
Dian Chen,
cdism221@163.com
Feiying Liu,
liufeiying861218@163.com
Yang Dong,
dongyang6405@163.com

†These authors have contributed equally to this work

RECEIVED 16 March 2023
ACCEPTED 13 June 2023
PUBLISHED 22 June 2023

CITATION
Zhang H, Zhang Q, Du J, Zhu T, Chen D, Liu F and Dong Y (2023), Nanofibers with homogeneous heparin distribution and protracted release profile for vascular tissue engineering.
Front. Bioeng. Biotechnol. 11:1187914.
doi: 10.3389/fbioe.2023.1187914

Nanofibers with homogeneous heparin distribution and protracted release profile for vascular tissue engineering

Hongmei Zhang[1,2†], Qilu Zhang[3†], Juan Du[2*], Tonghe Zhu[1,2], Dian Chen[4*], Feiying Liu[5*] and Yang Dong[1*]

[1]Department of Orthopedics Surgery, Shanghai Sixth People's Hospital Affffliated to Shanghai Jiao Tong University School of Medicine, Shanghai, China, [2]School of Chemistry and Chemical Engineering, Shanghai University of Engineering Science, Shanghai, China, [3]School of Textiles and Fashion, Shanghai University of Engineering Science, Shanghai, China, [4]Department of Cardiothoracic Surgery, Shanghai Children's Medical Center, Shanghai Jiao Tong University School of Medicine, Shanghai, China, [5]School of Biotechnology, East China University of Science and Technology, Shanghai, China

In clinic, controlling acute coagulation after small-diameter vessel grafts transplantation is considered a primary problem. The combination of heparin with high anticoagulant efficiency and polyurethane fiber with good compliance is a good choice for vascular materials. However, blending water-soluble heparin with fat-soluble poly (ester-ether-urethane) urea elastomer (PEEUU) uniformly and preparing nanofibers tubular grafts with uniform morphology is a huge challenge. In this research, we have compounded PEEUU with optimized constant concentration of heparin by homogeneous emulsion blending, then spun into the hybrid PEEUU/heparin nanofibers tubular graft (H-PHNF) for replacing rats' abdominal aorta *in situ* for comprehensive performance evaluation. The *in vitro* results demonstrated that H-PHNF was of uniform microstructure, moderate wettability, matched mechanical properties, reliable cytocompatibility, and strongest ability to promote endothelial growth. Replacement of resected abdominal artery with the H-PHNF in rat showed that the graft was capable of homogeneous hybrid heparin and significantly promoted the stabilization of vascular smooth muscle cells (VSMCs) as well as stabilizing the blood microenvironment. This research demonstrates the H-PHNF with substantial patency, indicating their potential for vascular tissue engineering.

KEYWORDS

heparin, electrospun vascular grafts, mechanical compliance, thrombosis, patency rate

1 Introduction

In recent years, the incidence of arteriovenous fistula and peripheral vascular diseases are increasing year by year, and vascular bypass transplantation is the most important treatment method (Martinez-Gonzalez et al., 2017; Caliskan et al., 2020). Therefore, there is an urgent need for tissue engineered vascular grafts, especially small-diameter vascular grafts. The main challenge to the limited application of small-diameter artificial blood vessels is that early thrombosis, lumen stenosis, intimal hyperplasia and low long-term patency rate (Tatterton et al., 2012; Seifu et al., 2013; Zhu et al., 2021a; Zhuang et al., 2021; Li et al., 2023). In addition, the mechanical compatibility of small-diameter vascular grafts should be the focus of attention (Zhu et al., 2020; Zhu et al., 2021a; Zhi et al., 2022). Therefore, to

achieve a long-term patency rate, the ideal small-diameter vascular grafts should have proper mechanical properties, outstanding blood compatibility and biocompatibility (Stahl et al., 2023).

Biomedical polymeric nanofibers present unique advantages and wide applications in the field of vascular tissue engineering due to three-dimensional biomimetic extracellular matrix (ECM) structure, adjustable physical and mechanical properties, stable biocompatibility as well as easy processing (Fathi Karkan et al., 2019; Nemati et al., 2019; Purushothaman et al., 2020). Poly (ester-ether-urethane) urea (PEEUU) is a biocompatible polyurethane derivative, which present excellent physical and mechanical properties and special microphase separation structure (Asadpour et al., 2018; Zhu et al., 2022). The soft and hard segments form the key surface structure of hydrophilic and hydrophobic alternating blocks in PEEUU, which not only conforms to Okano's hypothesis of the relationship between anticoagulant blood and material surface structure, but also has a similar structure as in human blood vessels (He et al., 2010). But pure PEEUU still cannot achieve the ideal blood compatibility and histocompatibility. Therefore, through continuous exploration, previous researchers have developed a series of methods or technologies to improve the anticoagulation of polyurethane, which included the improvement of the hydrophilicity of polyurethane, the constructing of ionic polyurethane surface, surface grafting or blend using bioactive macromolecules.

Among many anticoagulant units, poly (ethylene glycol) (PEG) is often selected as the coating component grafting on the surfaces of vascular lumen to reduce the adsorption rate of plasma protein and platelet adhesion (Tseng and Park, 1992; Altankov et al., 2000). Kim et al. reported a method for grafting end-sulfonated PEG on the surfaces of polyurethane membranes. The results of blood compatibility showed that the PEG-grafted membrane significantly reduced the adhesion of platelets and prolonged the APTT time (YoungKim et al., 2003). Zhu et al. reported a functionalized nanofibers vascular grafts with PEG and heparin via the sequential covalent grafting method. The grafted PEG and heparin synergistically decreased the water contact angle of nanofibers as well as increased the capability for preventing platelet deposition (Zhu et al., 2021b). Lee et al. reported a modification method of PEO-PPO-PEO triblock copolymer mixed with polyurethane and then formed a film by solvent volatilization. The results revealed that the antiplatelet adhesion of the modified polyurethane was improved and increased with the increase of the proportion of PEO chain segments in the block copolymer (Lee et al., 1998). The surface modification using zwitterion is also an alternative method to improve the anticoagulation of materials (Ukita et al., 2019; Wang et al., 2020; Zhu Tianyu et al., 2021). The modified surface can reduce the adhesion of platelets on the surface of the material through electrostatic repulsion between negative charges. Yuan et al. also reported a surface grafting technique based on plasma treatment. Firstly, polyurethane membrane was treated with O_3 plasma. Then, acrylic acid was grafted on the membrane. Finally, 1, 3-propyl sulfonolactone was grafted on the membrane by two methods. The blood compatibility test showed that the anticoagulation of polyurethane grafted with sulfonic acid anion group was significantly improved (Mokhtari and Kharazi, 2021). Among many bioactive macromolecules, heparin has excellent anticoagulant properties and is the most commonly used anticoagulant. After more than 40 years of continuous development, the immobilization technology of heparin is showing more and more improvement in medical field. Although heparin presented obvious anti-coagulation and anti-hyperplasia effects, the existing immobilization methods, such as physical blending, ionic bonding, and covalent bonding by solution blending or solution grafting, cannot solve the problems of fast release, easy inactivation, and structural changes of heparin, which may be due to its very short half-life and easy dissolution in water rather than in organic solvents (Serrone et al., 2013; Kevin, 2015; Yang et al., 2022).

In this work, we propose a novel small diameter vascular graft to solve the above mentioned problems that the uneven dispersion of heparin in vascular material. Based on our previous research on nanofibers for sustained drug release and vascular tissue regeneration, the optimized concentration of heparin, was combined with synthetic PEEUU elastomer, following hybrid PEEUU/heparin nanofibers prepared by homogeneous emulsion blending and electrospinning for exploring blood vessel repair effect and mechanism. We evaluated the physicochemical properties, microscopic morphology, and cytocompatibility of hybrid PEEUU/heparin nanofibers, and then detected the activity of promoting tissue regeneration and inhibiting thrombosis and intimal hyperplasia. Finally, the abdominal aortic defect model of rats was used to evaluate the effect of hybrid PEEUU/heparin nanofibers tube.

2 Materials and methods

2.1 Materials

Poly (ester-ether-urethane)urea elastomer (PEEUU, Mw = 9.2×10^4) were synthesized via a two-step solution polymerization in synthesis laboratory of functional polymer of Shanghai University of Engineering Science. Heparin sodium powder (150 U/mg) (Hep) were purchased from Sigma-Aldrich Trading Co., Ltd. (Shanghai, China). Human umbilical vein endothelial cells (HUVECs) for *in vitro* experiments were obtained from Shanghai Cell Bank of Chinese Academy of Sciences (Shanghai, China). Cell counting kit (CCK-8) was obtained from Sigma-Aldrich Trading Co., Ltd. (Shanghai, China). Dulbecco's modified eagle medium (DMEM), Fetal bovine serum (FBS), and antibiotic-antibacterial medicine (penicillin/streptomycin) were purchased from Hyclone Trading Co., Ltd. (Shanghai, China). Hexafluoroisopropanol (HFIP, purity ≥99.2%) was obtained from Shanghai Darui Fine Chemicals Co., Ltd. (Shanghai, China). Unless otherwise specified, all the above reagents were used directly. All the materials were used as received, except where mentioned otherwise.

2.2 Preparation of nanofibers tubes

To prepare hybrid PEEUU/heparin nanofibers tubular graft (H-PHNF), PEEUU was dissolved in 10 mL of HFIP to form a mixture with 8.0 w/v% concentration with stirring until clarified.

TABLE 1 Settings of PEEUU, heparin sodium dosage, and HFIP bulk in control and experimental groups, respectively.

Samples	PEEUU (g)	Heparin sodium (mg)	HFIP (mL)
PNF	0.8	0	10
B-PHNF	0.8	10	10
H-PHNF	0.8	10	10

0.01 g of heparin sodium (150 U/mg) was dissolved in three drops (about 0.2 mL) of distilled water until clarified, following addition of above-clarified PEEUU/HFIP mixture forming electrospinning solution with a relative mass fraction W_{Hep}/W_{PEEUU} of 1.25% under vigorous stirring at room temperature for 72 h, respectively. Then, the 10 mL of the above prepared mixture solution were electrospun to generate nanofibers with a constant speed of 1.0 mL/h and a voltage of 12 kV.

Electrospinning solution for preparing PEEUU nanofibers (PNF) was prepared according to the following protocol: Synthetic 0.8 g PEEUU was dissolved in 10 mL HFIP formed a mixture with 8% concentration with stirring until clarified. To preparing the electrospinning solution for fabricating the blend PEEUU/heparin nanofibers (B-PHNF): Synthetic 0.8 g PEEUU was dissolved in 10 mL HFIP formed a mixture with 8% concentration. After stirring until clarified, quantitive heparin sodium powder (Hep) was added in the above-clarified mixture forming electrospinning solution with a relative mass fraction (W_{Hep}/W_{PEEUU}) of 1.25%.

The parameters to generate nanofbers showed in Table 1, respectively. The as-electrospun nanofibers were collected onto a stainless steel bar (2.0 mm diameter, 100.0 mm length, rorated at 200 rpm) or a flat aluminum foil board located 14 cm from the capillary to form nanofibers tubes or nanofibers mats, namely, PNF, B-PHNF, and H-PHNF, respectively. Then nanofibers tubes and nanofibers mats were vacuumed in a desiccator for 48 h to remove redisual HFIP.

2.3 Characterization and testing

The morphology and surface structure of nanofibers and nanofibers tubes were carried out using a scanning electron microscope (SEM, Phenom XL, Netherlands) operating with sputter gold plating for 35 s at 5 mA at an accelerating voltage of 10 kV. A contact angle measuring device (JC 2000D 2A, Shanghai Zhongchen Digital Technology Equipment Co., Ltd., China) was used to test the wettability of nanofibers tubes. To test this, 0.02 mL deionized water was added to the sample and three different positions of the sample were taken to measure the water contact angle and calculate the average value. Image-J (United States) was used to determine the diameter of nanofibers, inner diameter and wall thickness, and the pore diameter of nanofibers tubes.

The ethanol displacement method was applied to confirm the porosity of nanofibers tubes. The dried tubes were dipped in absolute ethanol, and the bubbles were removed. The porosity was determined by Eq. 1:

$$\text{Porosity } (\%) = \frac{V1 - V3}{V2 - V3} \times 100\% \quad (1)$$

where V_1 expresses the volume of known ethanol; V_2 stands for the bulk volume of the ethanol impregnated nanofibers tubes and ethanol; V_3 is the volume after removed the nanofibers tubes.

High-precision tensile testing machine (HY-025CS, Shanghai Hengyu Instrument Co., Ltd., China) with a transducer with a load range of 0–200 N was employed to testing the mechanical properties of nanofibers tubes in wet conditions at room temperature strictly according to ISO 7198: 1998. Each sample was cut into a cylindrical ring with length × inner diameter × wall thickness = 10.0 mm × 2.0 mm × 0.4 mm, then soaked in 0.01 M phosphate buffer (PBS, pH = 6.8) for 24 h. Finally, tensile tests were investigated at room temperature with a stretching speed of 1.0 mm/min. The specimens were extended until breaking under tensile force and the tensile stress-strain curves were recorded. Each test was repeated five times during mechanical analysis. The tensile strength, elongation at tensile strength, the representative modulus, and first order equation fitting of stress and strain within the magnification of calculating range were calculated according to the results of stress-strain.

2.4 Heparin density and sustained release tests *in vitro*

The presence of heparin in fibers were verified via toluidine blue staining. Briefly, a 0.005% toluidine blue solution was prepared in hydrochloric acid (0.01 M) containing 0.2% NaCl. The samples were incubated in the prepared toluidine blue solution for 12 h and dried at room temperature for further observation. The heparin density in fibers were verified via prepared toluidine blue staining assay. Electrospun tubes (2.0 mm inner diameter, 15.0 mm length) were immersed in 50 mL aqueous solution of toluidine blue [500 μmol/L toluidine blue solution dissolved in Milli Q water with a pH value of 10 (adjusted with NaOH)] and incubated in a vapor-bathing constant temperature vibrator at 37°C with a vibrating speed of 100 rpm for 12 h. Samples were then washed with dilute NaOH (pH = 10) five times followed by immersing in 50 mL aqueous solution of acetic acid with a concentration of 50% at 37°C with a constant vibrating speed of 100 rpm for 30 min. The OD value of toluidine blue released from fibers was read at 633 nm using a microplate reader (MK3, Thermo, United States).

The nanofiber samples for sustained release were placed in a constant temperature vibrator at 37°C (100 rpm). At the set time points, 3 mL of release solution was removed, while 3 mL of fresh PBS medium was added. Three test samples were set for each group. The cumulative release amount of heparin was calculated according to the standard heparin absorbance concentration at 260 nm. The percentage of accumulated release can be calculated by Eq. 2:

$$ARP\ (\%) = \frac{C \times 30 + \sum W}{\mathrm{m} \times \mathrm{R} \times 1000} \times 100\% \quad (2)$$

C-the concentration of heparin, μg/mL; ∑W-the mass of heparin accumulated release, μg; m-the mass of nanofibers tubes, mg; R-the percentage of drug within nanofiber.

2.5 Cell culture and blood compatibility tests *in vitro*

Human umbilical vein endothelial cells (HUVECs) were used to evaluate the activity of host cells, which were co-culture with PNF, B-PHNF, and H-PHNF nanofibers mats, respectively. HUVECs were obtained from Shanghai Cell Bank of Chinese Academy of Sciences (Shanghai, China) and cultured with growth medium consists of dulbecco's modified eagle medium (DMEM), 10% fetal bovine serum and 1% penicillin/streptomycin. The cell viability of HUVECs were tested by using the Cell Counting Kit-8 (CCK-8). The cells were cultured in PNF, B-PHNF, and H-PHNF nanofibers mats for 1 day, 3 days, and 5 days, respectively. Detailed procedures are available in the Supplementary Material.

Fresh blood, which was drawn from the marginal vein, and 3.2% sodium citrate solution in a volume ratio of 9:1 (v/v) were collected using a plastic vacuum blood collection tube (2.7 mL, Becton Dickinson, United States), containing 3.2% sodium citrate solution. All animal experimental protocols are in accordance with the policy of the Institutional Review Board for Human Investigations at Shanghai Sixth People's Hospital Afffliated to Shanghai Jiao Tong University School of Medicine. Detailed procedures are also available in the Supplementary Material (Mokhtari and Kharazi, 2021).

2.6 *In vivo* transplants to replace the abdominal aorta of rats

All rats were obtained from Shanghai Slaccas Experimental Animal Co., Ltd. (Shanghai, China) and all experimental schemes are in agreement with the requirements of the Institutional Animal Care and Use Committee (IACUC) of Shanghai Sixth People's Hospital Afffliated to Shanghai Jiao Tong University School of Medicine and accepted by IACUC. Ethical principles were followed throughout the experiment. All experimental plans were proceeded in conformity of the Animal Management Regulations of China (1988 and revised in 2001, Ministry of Science and Technology).

Sixty-three male Sprague-Dawley rats (age about 10 weeks; weighing approximately 300 g; 18 rats for standby application) were used as the abdominal aortic replacement models in the research. A 7.0 mm long defect of the abdominal aorta was created and replaced by nanofibers tubes (2.0 mm inner diameter, 7.0 mm length), and then the nanofibers tubes was end-to-end sutured to the abdominal aorta. Performance of the nanofibers tubes graft was evaluated on first, second, and fourth week after surgery in total of five animals per group for each time point.

At predetermined time points, rats were anesthetized by intraperitoneal injection of pentobarbital (3.5 mg/100 g; Nembutal). A color Doppler ultrasonography platform (GE LOGIQ 9, GE Medical Systems, United States) was used to acquire images to evaluate the patency rate of vessels. Then rats were sacrificed after injecting an overdose of isoprene barbiturate from the ear margin vein. Implanted nanofibers tubes were retrieved and analyzed by H&E staining, Masson's trichrome staining, Van Gieson, Saffron O, Von Kossa, and immunofluorescent staining. Detailed procedures are available in the Supplementary Material.

2.7 Statistical analysis

Data were presented as mean ± standard deviation. All data were analyzed by one-way ANOVA with Tukey's *post hoc* tests. *p*-values <0.05 (*) were deemed to be statistically significant. * indicates $p < 0.05$, ** indicates $p < 0.01$, *** indicates $p < 0.001$.

3 Results and discussion

Synthetic vascular grafts perform satisfactorily as large-diameter (e.g., aortoiliac) arterial substitutes but commonly fail when employed in small-diameter applications (Wang et al., 2019). To date, clinically available expanded poly (tetrafluoro-ethylene) (ePTFE) or poly (ethylene terephthalate) (PET) vascular grafts are suboptimal for reconstructing small-diameter (inner diameter ≤6 mm) arteries, owing to thrombosis in early and restenosis in late stage (Lim et al., 2021; Roina et al., 2022). Moreover, ePTFE or PET vascular prostheses connected to human artery cannot swell when subject to the blood pressure owing to their poor elasticity, and thus also result in the decline of blood flow rate and the formation of thrombosis. Some previous research reported that polyurethanes were being applied in medical devices because they have the capability to tolerate contractile forces that originate during the cardiac cycle without undergoing plastic deformation or failure, and the capability to imitate the behaviors of different tissues (Rahimi and Mashak, 2013; Uscategui et al., 2018; Kelly Navas-GomezValero and Valero, 2020). More importantly, the mechanical compliance and other properties of polyurethane can be further improved by structural design and functional modification (Zhang Zhenyan et al., 2022). Therefore, polyurethane may be an optimal candidate.

Heparin is the most widely used and reliable anticoagulant that can enhance the patency and inhibit the thrombus. A lack of heparin leads to blood clotting, while an excess of heparin causes bleeding. (Kevin, 2015). Furthermore, the half-life of heparin is less than 1 h in circulation (Yang et al., 2022). Thus, maintaining localized concentration and homodisperse of heparin at the target site for long time is essential for implant revascularization. In this study, a hybrid electrospun BEPU/heparin nanofibers tubular graft compound with optimized constant concentration of heparin by homogeneous emulsion blending, were prepared for replacing rats' abdominal aorta *in situ* for comparing with nanofibers tubular graft, which were prepared via resolution after blending of solute.

3.1 Microstructure and mechanical properties

We have compounded PEEUU/HFIP solution with heparin/distilled water solution, and then processed it into clarified PEEUU/HFIP/heparin/distilled water mixture according to the solvent compatibility of HFIP and water. PEEUU/heparin could be feasibly dissolved in HFIP/distilled water mixture to form a

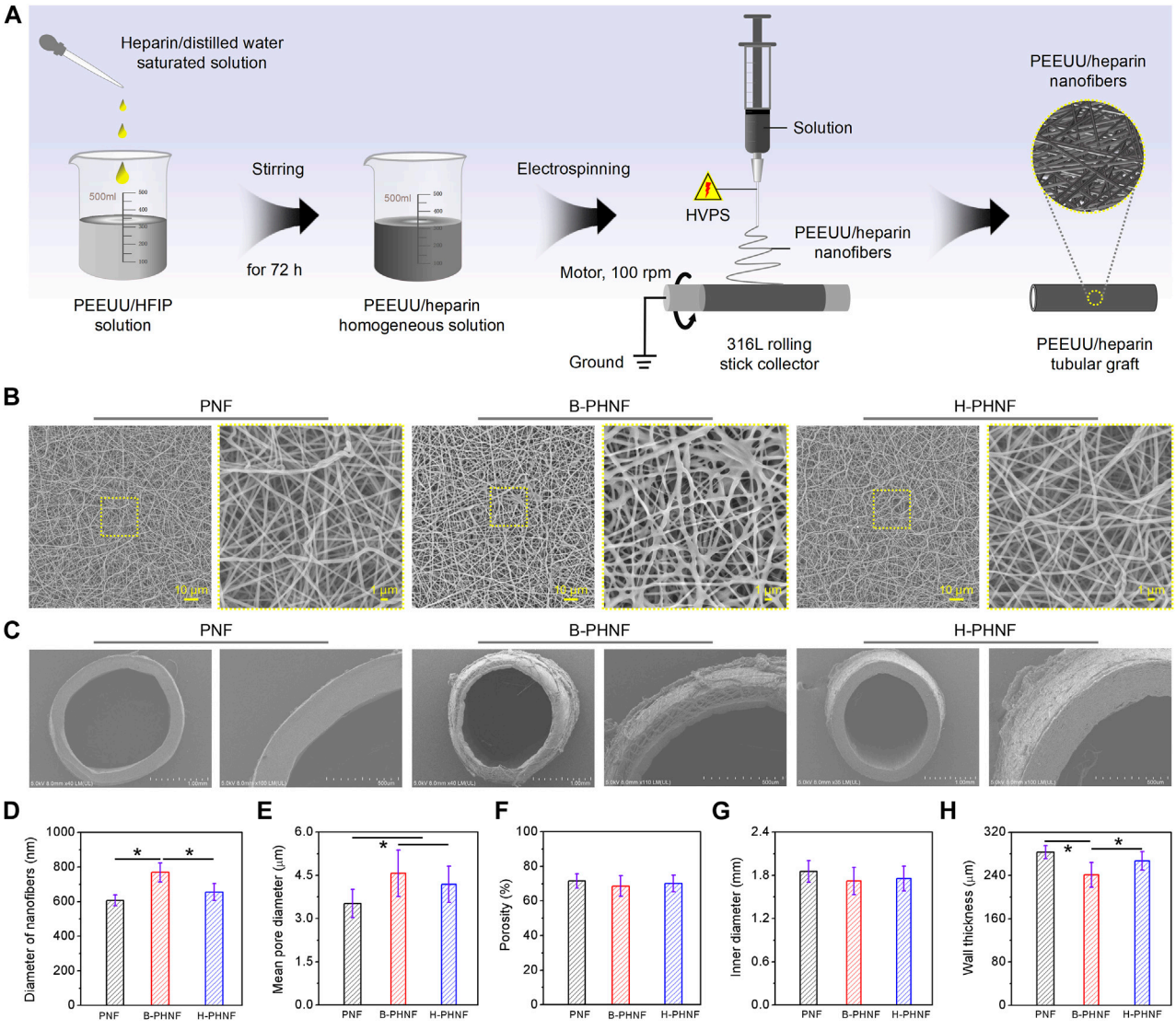

FIGURE 1
(A) The preparation diagram of PEEUU nanofibers tubular graft with heparin homogeneous distributions (H-PHNF); **(B, C)** SEM images of the lumen surface and the cross sections of PNF, B-PHNF, and H-PHNF, respectively; **(E–G)** Fibers diameters of the lumen surface, mean pore diameters, porosity, inner diameters, and wall thickness of PNF, B-PHNF, and H-PHNF, respectively. (Data are representatives of independent experiments and all data are given as mean ± SD, $n = 5$; $*p < 0.05$).

homogeneous hybrid solution for random electrospinning and collected by a 316 L rolling stick collector to obtain tubular grafts (Figure 1A). Similarly, control samples were also prepared in this way, except for the different electrospinning solution.

The morphology of prepared tubular grafts are shown in Figures 1B,C. The SEM images of the lumen surface of PNF, B-PHNF, and H-PHNF, in Figure 1B, showing its nonwoven structure formed by random stacking of nanofibers with the average diameter of 607 ± 31 nm, 769 ± 55 nm, 655 ± 49 nm, respectively, (Figure 1D). The diameter of both PNF and H-PHNF group were finespun but evenly distributed, while agglomeration appeared in B-PHNF group. Correspondingly, the pore sizes of both PNF and H-PHNF group are smaller than those of B-PHNF groups, and the porosity is larger than that of B-PHNF group (Figures 1D–F).

Moreover, as shown in Figure 1C, the electrospun grafts could maintain its tubular shape after being peeled from the 316 L rolling stick collector. The statistical data of inner diameter showed that the average diameter of PNF, B-PHNF, and H-PHNF groups were 1.854 ± 0.152, 1.719 ± 0.189, and 1.756 ± 0.172 mm as well as the average wall thickness of PNF, B-PHNF, and H-PHNF were 283 ± 12, 241 ± 23, and 267 ± 17 μm, respectively (Figures 1G,H). Compared with B-PHNF group, the inner diameter sizes and wall thickness of both PNF and H-PHNF groups are larger than those of B-PHNF groups. We attributed these appearance to the fibers size and structure of grafts, and the distribution of heparin in fibers.

In the design of small-diameter artificial blood vessel, the first consideration should be the mechanical properties (Zhu et al., 2020). Due to its small diameter and thin wall, small-diameter artificial blood vessels are not strong enough to resist external forces.

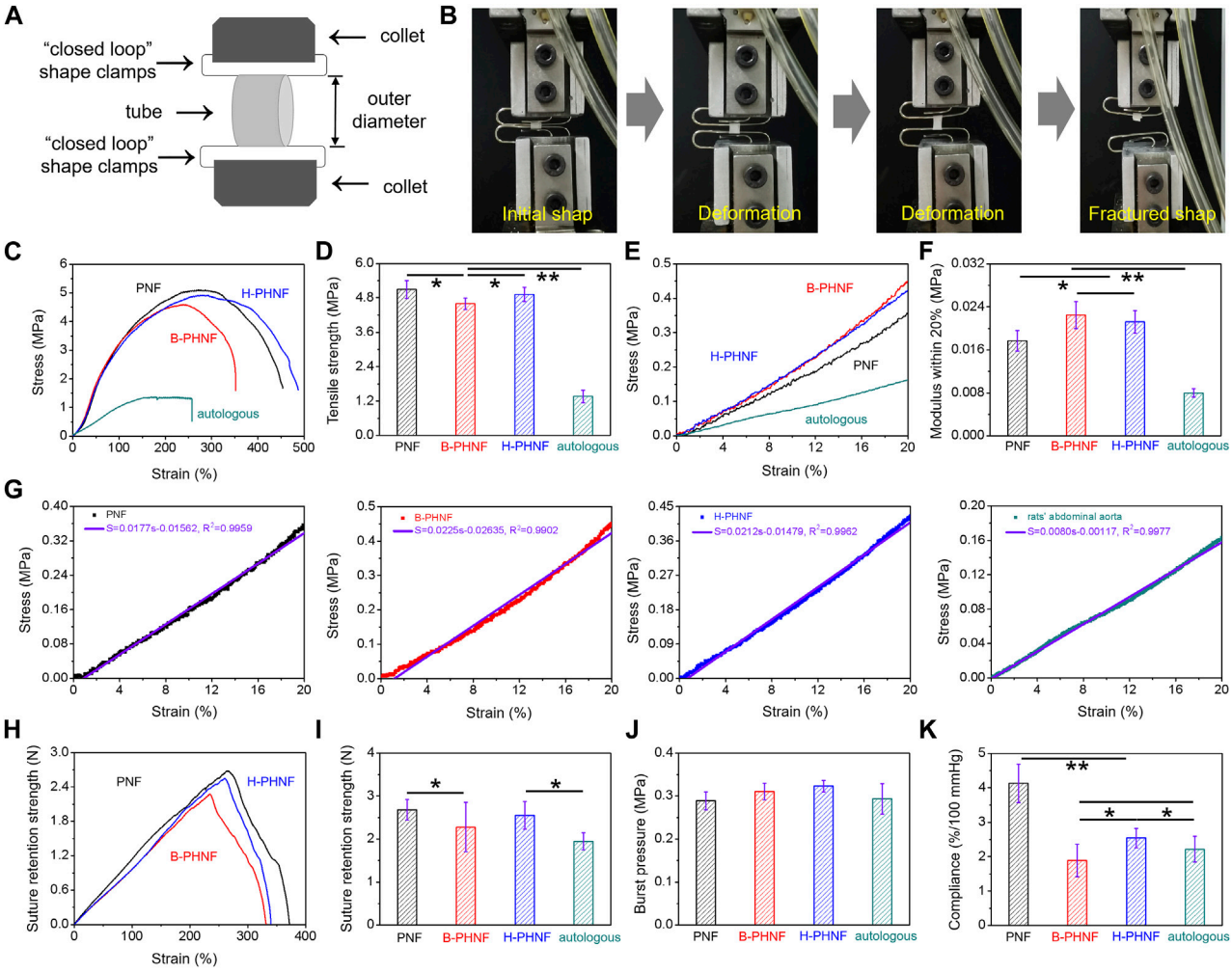

FIGURE 2
Mechanical properties of prepared nanofibers tubular grafts: presentative radial tensile results of PNF, B-PHNF, and H-PHNF under wet conditions. **(A)** Illustration of the measurement method for radial tensile properties of tubular grafts; **(B)** Digital photographs of initial shape and fractured shape of tubular grafts; **(C)** representative radial stress-strain curves; **(D)** Tensile strength; **(E)** The magnification of calculating range of 0–20% modulus; **(F)** Representative 0–20% modulus; **(G)** First order equation fitting of stress and strain within the magnification of calculating range of 0–20% modulus; **(H)** Suture retention strength-strain curves; **(I)** Maximum suture retention strength; **(J)** Burst pressure; **(K)** Complicance. (Data are representatives of independent experiments and all data are given as mean ± SD, $n = 5$; $*p < 0.05$, $**p < 0.01$).

Therefore, the designed small-diameter artificial blood vessels should be able to resist certain pressure in the body without deformation. Moreover, the artificial blood vessels must have a burst pressure similar to or higher than that of human blood vessels, which have a burst pressure of more than 1700 mmHg.

We have measured the mechanical properties of nanofibers tubular grafts in wet conditions at room temperature strictly according to ISO 7198: 1998 using the uniaxial radial high-precision tensile testing machine as the schematic illustration in Figures 2A,B. As shown in Figure 2B, the zone of breaks of tubular graft is located in the middle of the sample, which means this fracture test is effective. Representative radial stress-strain curves and maximum tensile strength of PNF, B-PHNF, and H-PHNF are presented in Figures 2C,D, respectively. The results showed that the maximum tensile strength of PNF, B-PHNF, and H-PHNF are 5.096 ± 0.310 MPa, 4.596 ± 0.201 MPa, and 4.916 ± 0.251 MPa, respectively, which are significantly larger than 1.365 ± 0.211 MPa of rats' abdominal aorta.

Natural blood vessels are viscoelastic bodies with viscoelastic characteristics such as creep and stress relaxation, which can be treated as elastic materials and have anisotropic nonlinear stress-strain relationship after sufficient preconditioning. As in Figures 2E–G, the representative radial stress-strain curves, representative 0–20% modulus, first order equation fitting of stress and strain within the magnification of calculating range of 0–20% modulus were calculated and fitted according to the dates in Figure 3E, respectively. It is clear that the modulus within the magnification of calculating range of 0–20% strain of H-PHNF significant increased compare to rats' abdominal aorta (Figure 2F). The increase of modulus also proves that H-PHNF have good anti-deformation performance after implantation *in vivo*. In short, three electrospun tubular grafs showed reliable resiliency, while H-PHNF

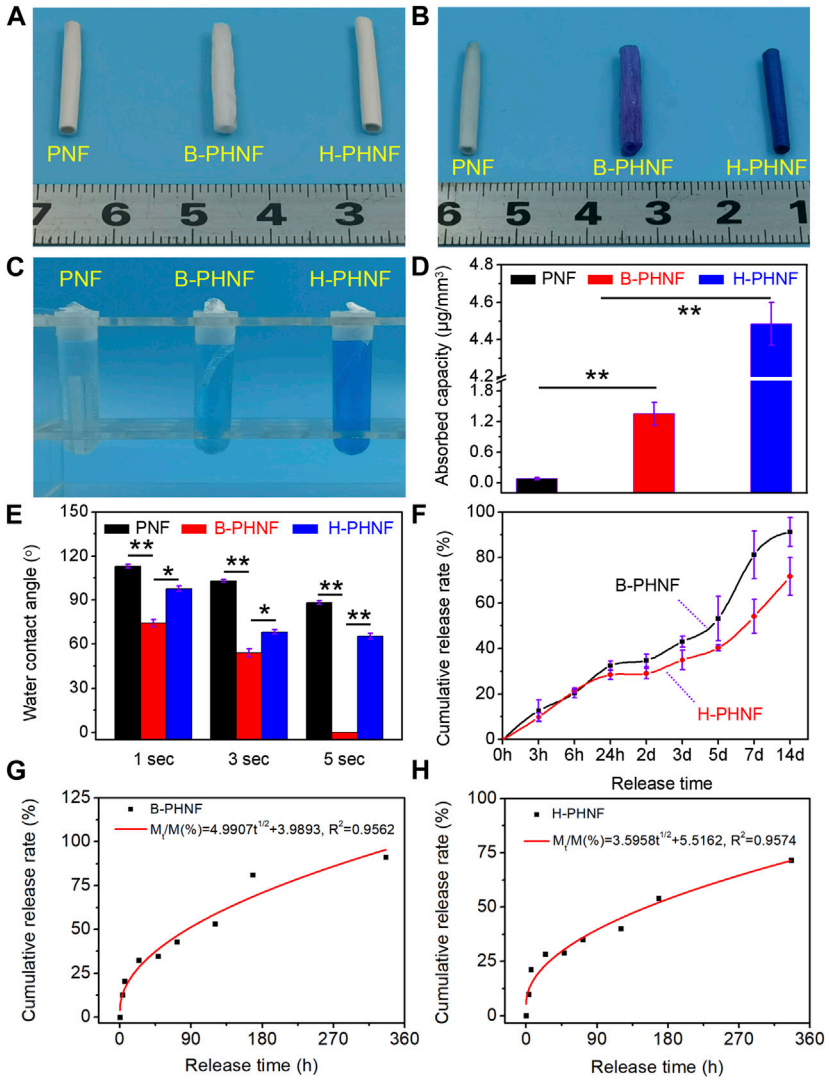

FIGURE 3
(A) The digital photos of PNF, B-PHNF, and H-PHNF, respectively; **(B)** Toluidine blue staining digital photos of PNF, B-PHNF, and H-PHNF in wet states, respectively; **(C)** Toluidine blue extract used acetic acid as treating agent; **(D)** Quantitative data of adsorption assays indicate in the amounts of toluidine blue in nanofibers tubular grafts; **(E)** Water contact angle at the 1, 3, and 5 s time point; **(F)** *In vitro* releases of heparin from B-PHNF and H-PHNF in pH = 6.8 PBS, respectively; **(G, H)** Higuchi equation fitting of cumulative release rate and release time of B-PHNF and H-PHNF, respectively. (Data are representatives of independent experiments and all data are given as mean ± SD, $n = 5$; $*p < 0.05$, $**p < 0.01$).

exhibited better initial elasticity, which was more suitable for application as a prosthetic blood vessel.

As shown in Figures 2H–J, the obtained burst pressure substantially reached those of both artery and saphenous vein which is the gold standard for bypass operation, whereas the suture retention strength was a little smaller than PNF but still quite larger than the rats' abdominal aorta (around 0.293 MPa) for surgical operation.

Compliance is defined as the volume change in response to changes in blood pressure, and constitutes an important parameter that influences the short- and long-term patency of artificial blood vessels (Stahl et al., 2023). Especially in the early stage of transplantation, the mismatch of mechanical compliance between vascular grafts and autologous blood vessels is more likely to cause acute thrombosis at the anastomosis site. The compliance of PNF, B-PHNF, H-PHNF, and rats' abdominal aorta were evaluated, respectively, as shown in Figure 2K. The compliance of both PNF and H-PHNF were larger than that of the other two groups. The compliance of H-PHNF is better than B-PHNF as well as rats' abdominal aorta. PEEUU/heparin tubular graft through a combination of homogeneous emulsion blending technology and electrospinning technology exhibit prominent stable mechanical compliance due to the homogeneous dispersion of heparin in the electrospun fibers.

3.2 Surface wettability and heparin sustained release properties

We obtained tubular grafts with a length of 2.0 cm and an inner diameter of 2.0 mm (Figure 3A). The presence of as hybrid heparin

was examined by toluidine blue staining and analyses exhibited color change from white to dark blue. Images of toluidine blue staining demonstrated that H-PHNF received more dye after staining (Figure 3B). This was in line with the quantitative study that the heparin-end groups had much higher absorbance than the other groups (Figures 3C,D). The results of water contact angle measurements are exhibited in Figure 3E. PNF showed its hydrophobic nature as the water drop well stood on its surface after it was dropped down and its contact angle was measured about 113° at the 1 s time point. When heparin molecule blended in the electrospun PEEUU fibers, the obtained B-PHNF exhibits higher hydrophilicity (the water contact angle is 74° at the 1 s time point), while the water contact angle of H-PHNF is 102° at the 1 s time point. We believe that the above phenomenon is not only closely related to the microstructure of the fiber, but also to the dispersion of the heparin molecules. Specifically, due to poor dispersion, more heparin molecules gathered on the surface of PEEUU fibers in B-PHNF, and these highly hydrophilic heparin molecules increased the roughness of the surface of PEEUU fibers. In general, the hydrophilicity of B-PHNF was stronger than that of H-PHNF.

In the process of drug release, the properties of drug release depend on complex physical and chemical phenomena (Zhu et al., 2021b). The factors controlling the drug release rate are not only the three-dimensional structure of the grafts, the interaction between molecules, the degradation rate of the material, the solubility of the drug, but also closely related to the dispersion of the drug in the polymer matrix. Figure 3F shows the cumulative drug release curve of heparin in B-PHNF and H-PHNF, where the *X*-axis is the release time, and the ordinate is the percentage of cumulative release in the total drug load. The release curves of heparin in B-PHNF and H-PHNF with similar drug concentration were compared. The release of heparin from both B-PHNF and H-PHNF mainly includes three stages: the initial drug release stage (0–24 h), controlled release stage (24 h–5 days), and late accelerated release stage (5 days~). At the initial release phase, the released heparin mainly comes from the surface of the PEEUU fiber. Most of this heparin, which exposed to the surface of the fiber, is very vulnerable to the surrounding tissue fluid wash and rapid release. It is obvious that heparin in both B-PHNF and H-PHNF exhibited obvious initial release, and the cumulative release rate at 3 h reaches 12.69% and 9.84%, respectively. On the 14th day, the final cumulative release of heparin in both B-PHNF and H-PHNF reached 91.26% and 71.67%, respectively, which shows a clear difference. In short, heparin in H-PHNF was released at the slower rate than B-PHNF after 24 h, which presumably achieve long-term inhibiting thrombus and intimal hyperplasia effect. Moreover, according to the time square root equation proposed by Higuchi, the least square regression analysis was carried out for the release time $t^{1/2}$ and the cumulative release amount M_t/M (%). The fitting equations were $M_t/M(\%) = 4.9907t^{1/2} + 3.9893$ and $M_t/M(\%) = 3.5958t^{1/2} + 5.5162$, and the fitting correlation coefficients were 0.9562 and 0.9574, respectively. Figures 3G,H show that the release of heparin at the initial stage of B-PHNF and H-PHNF conforms to the Higuchi equation, and diffusion is the main mechanism of heparin release.

3.3 Hemocompatibility *in vitro*

When the material comes into contact with blood, it causes platelet adhesion and activation of the clotting system. Since platelet and coagulation system work together to produce coagulation, the interaction between the two should be carefully considered in the design of blood compatible materials (Zhu et al., 2021b). After the contact between the isolated venous blood and the material, coagulation factors and the endogenous coagulation system are activated, and finally fibrin is generated and blood coagulation occurs. The time experienced in this stage is called coagulation time. Coagulation time can generally reflect the total coagulation ability of blood after contact with materials. After the whole blood incubation, the absorbance of the supernatant was measured at 540 nm, indicating the number of remaining erythrocytes, as shown in Figure 4A. Compared with the other two groups, the H-PHNF had the maximum absorbance at any time point. Under the same experimental conditions, the clotting time of both PNF and B-PHNF were significantly shorter, indicating that H-PHNF has anticoagulant properties, which may be due to its outstanding hydrophobic performance according to the contact angle results (Figure 3A).

All the clotting factors involved in endogenous clotting are supplied by plasma. When plasma comes into contact with the material, the surface charge activates the clotting factors in the plasma. In the presence of Ca^{2+}, these clotting factors bind to Ca^{2+} to form prothrombin complexes, which activate and convert to active thrombin in the presence of thrombin and Ca^{2+}. Subsequently, soluble fibrinogen in plasma is converted to insoluble fibrin by thrombin and Ca^{2+}, which eventually leads to clotting. Plasma recalcium curve is a method used to characterize the endogenous coagulation system. Recalcium time refers to the time required for plasma coagulation after the removal of calcium source and the addition of Ca^{2+}. The detailed anticoagulant mechanism is that Heparin forms a complex by binding with antithrombin III, which accelerates the inactivation of coagulation factors and thus inhibits the formation of prothrombin kinase. In addition, heparin calcium also acts on already formed prothrombin kinases, thus providing a stronger anticoagulant effect. Figure 4B shows the plasma recalcium kinetic curves of PNF, B-PHNF, H-PHNF, positive control group, and negative control group. The positive control has the fastest clot formation time at 15 min, while the clot formation time of PNF was 20 min. Notably, B-PHNF, H-PHNF consistently kept a low absorbance and closed to the negative control without emerging the inflection point. These results indicate that the grafts complexed with heparin can significantly inhibit endogenous coagulation activation and improve the anticoagulation performance of the grafts.

When the material comes into contact with red blood cells, the degree of damage to red blood cells can be characterized by the hemolysis rate. The smaller the hemolysis rate of the material, the better the blood compatibility of materials. The hemolysis rate test results of PNF, B-PHNF, and H-PHNF samples are shown in Figure 4C. Figure 4C showed that the hemolysis rates of the three grafts were all less than 5% as specified in the ISO10993-4 standard, indicating that the three grafts were non-hemolysis materials with good blood compatibility, non-toxicity, and no obvious damage to erythrocytes. Moreover, both the unheparined

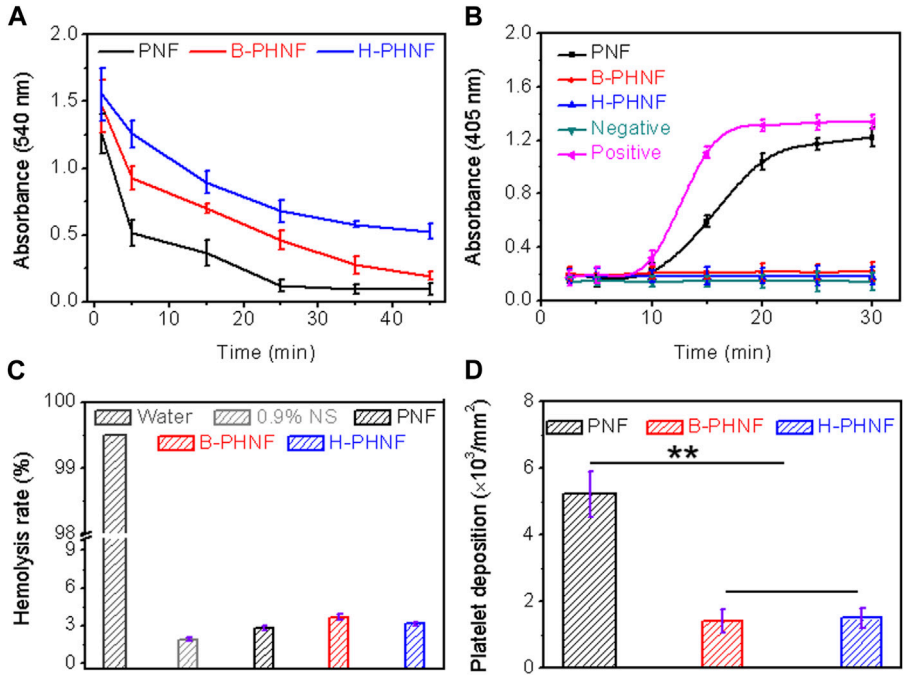

FIGURE 4
(A) Whole blood clotting time; **(B)** Plasma recalcification time; **(C)** Quantification of relative hemolysis rate; **(D)** Platelet deposition determined by lactate dehydrogenase assay. (For plasma recalcification time test, TCPs exposed to PPP with and without $CaCl_2$ were used as positive control and negative control, respectively; For hemolysis test, water and 0.9% normal saline (NS) serve as positive and negative groups, respectively; Data are representatives of independent experiments and all data are given as mean ± SD, $n = 5$; $*p < 0.05$, $**p < 0.01$).

and heparin-modified grafts had hemolysis rates of approximately 3%, indicating that heparinization did not affect the hemolytic properties of grafts.

The adhesion and activation of platelets can activate clotting factors and promote the formation of fibrin, which eventually leads to the formation of thrombus (Jordan et al., 2016). Therefore, the resistance against adhesion of platelets on the surface of materials is one of the important markers of the antithrombotic properties of materials. To compare the influence of compound heparin on the number of adherent platelets, the results of quantitative detection of the number of adherent platelets using the lactate dehydrogenase (LDH) kit are shown in Figure 4D. The number of platelet adhesion per unit area on the surface of the material is shown in Figure 4D. The platelets with obvious adhesion are on the surface of PNF, while the number of platelet adhesion is significantly reduced on both B-PHNF and H-PHNF surfaces due to the anticoagulation of heparin. In addition, there was no significant difference between the B-PHNF and H-PHNF groups, indicating that no matter which technique was used to combine heparin and PEEUU, the spatial conformation of heparin would not change significantly, let alone affect the anticoagulant effect of heparin in the short term.

3.4 Cytocompatibility *in vitro*

The inner layer of natural arterioles is rich in endothelial cells, which can resist thrombosis and regulate the transmission of signals and substances inside and outside the blood vessels. As an anticoagulant, heparin can avoid the clotting reaction induced by biomaterials *in vivo* as well as inhibits bacteria and cellulose adhesion. Introducing the biological function of heparin into polymer materials to achieve complete endothelization of the intima of tissue engineered vascular stent as soon as possible is an important content of the research on tissue engineered artificial blood vessels.

The proliferation of HUVECs grown onto PNF, B-PHNF, and H-PHNF after 3-day culture were evaluated, respectively (Figures 5A–C). It can be found from the fluorescence microscopy images in Figure 5A, the number of HUVECs in both B-PHNF group and H-PHNF groups were more than PNF group. As shown in Figures 5A,B, although the absorbance of the B-PHNF group was significantly higher than that of the H-PHNF group, the morphology of HUVECs in the H-PHNF group was significantly better than that in the B-PHNF group, and a large number of pseudopods were appeared. Figure 5C shows the growth morphology of HUVECs after culturing on the grafts for 3 days. It can be clearly observed that the number of endothelial cells adhered to B-PHNF is significantly higher than that of other groups, while HUVESs adhered to H-PHNF possessed abundant lamellipodia and filopodia, which indicates that the grafts loaded with heparin have almost no cytotoxicity and can support the adhesion and proliferation of endothelial cells. Furthermore, we selected two marker genes, eNOS and VEGF, to determine the functionality of HUVECs using reverse transcription polymerase chain reaction (RT-PCR) after 3 days of culture. H-PHNF markedly promoted HUVECs-related gene expression *in vitro* (Figures 5D,E).

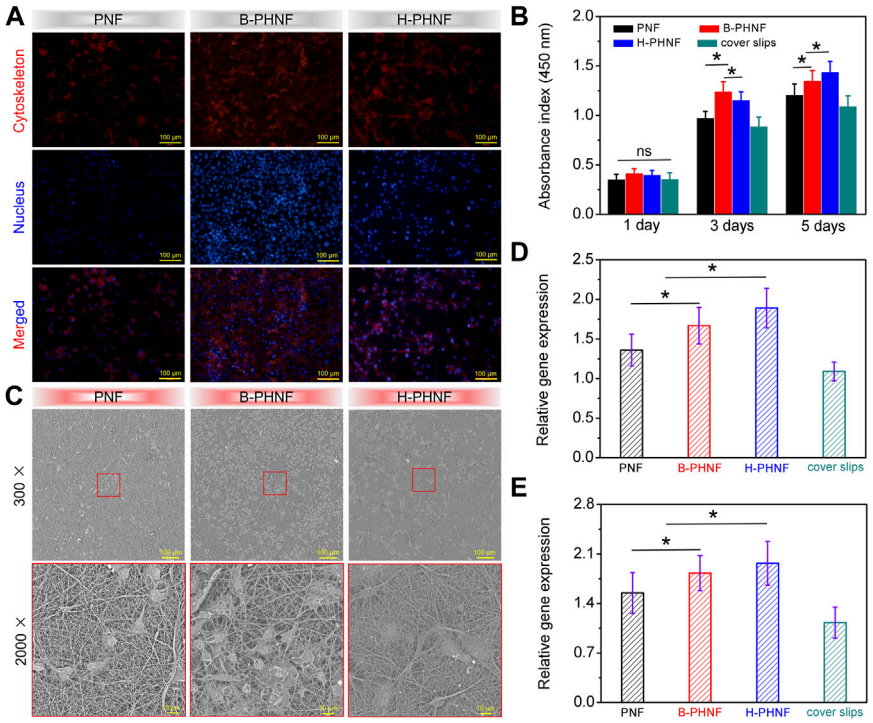

FIGURE 5
(A) Fluorescence microscopy images of HUVECs grown onto PNF, B-PHNF, and H-PHNF with labeling of cytoskeleton (red) and nucleus (blue) after 3-day culture, respectively; **(B)** CCK-8 assay of the proliferation viability of HUVECs cultured on PNF, B-PHNF, and H-PHNF for 1, 3, and 5 days culture, respectively; **(C)** SEM images of HUVECs grown onto PNF, B-PHNF, and H-PHNF after 3-day culture, respectively; **(D, E)** HUVECs-related gene expression of eNOS and VEGF after 7 days of culture, respectively. (Data are representatives of independent experiments and all data are given as mean ± SD, $n = 5$; $*p < 0.05$).

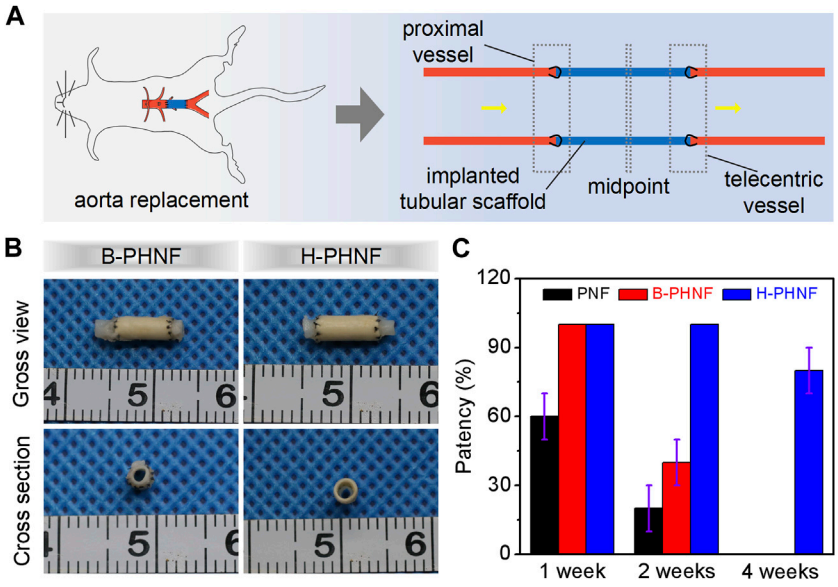

FIGURE 6
(A) Schematic diagram of nanofibers tubular grafts implanted into rats' abdominal aorta via end-to-end anastomosis; **(B)** Microscopical images of the surfaces and cross-sections of the retrieved B-PHNF, H-PHNF, and its neighboring native blood vessel after implantation for 4 weeks; **(C)** Patency rate statistics for each of electrospun tubular grafts at each time point ($n = 6$).

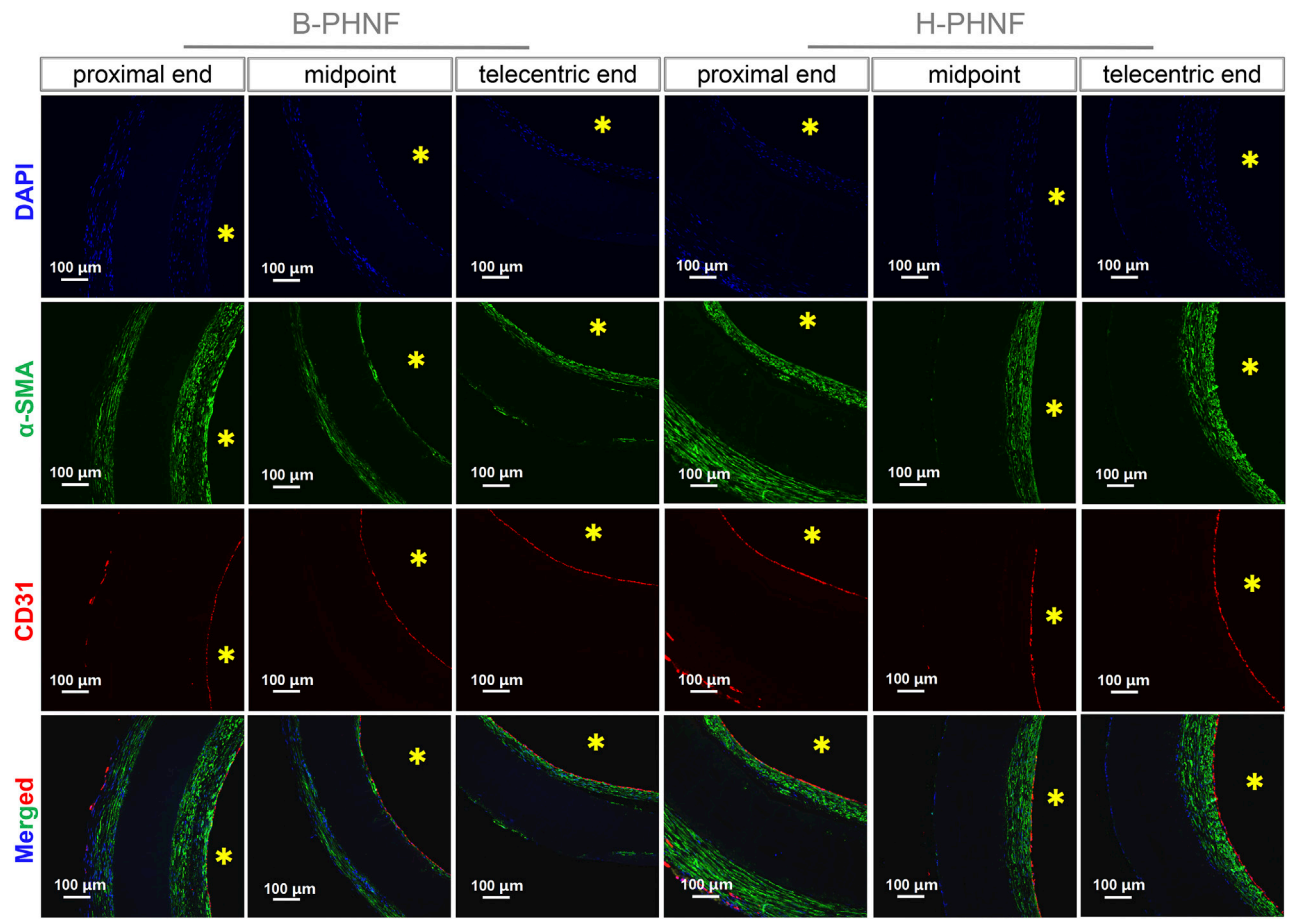

FIGURE 7
Immunofluorescent staining of cells nucleus (blue), α-SMA positive cells (green), and CD31 positive cells (red) in cross-sections of B-PHNF and H-PHNF in proximal end, midportion, and telecentric end after 4 weeks of implantation, respectively. Cell nuclei were stained with DAPI in blue, yellow * stands for lumen site.

The H-PHNF showed a synergistic promotive effect of heparin and matching microstructure on rapid endothelization and upregulated the expression of vascular endothelial cell-related genes.

3.5 Patency after abdominal aorta implantation of rats

We prepared grafts via homogeneous emulsion blending and electrospinning, followed by replacing isometric left abdominal aorta of SD rats with B-PHNF and H-PHNF by end-to-end anastomosis, respectively (Figure 6A). Nanofibers tubular grafts were retrieved for overall assessment 4 weeks after surgery. Macroscopically, the retrieved tubular graft maintained its white color and opaque texture, which can be easily distinguished from the native blood vessel that had semi-transparent appearance. More importantly, the surface of the endovascular lumen of unobstructed tubular grafts were smooth and there were no thrombus (Figure 6B). Tubular graft and native blood vessel had comparable diameters and fused well to form integrated tissue at the suture site (Figure 6B). The patency rate were detected after 1 week, 2 weeks, and 4 weeks transplantation, respectively, and the results are shown in Figure 6C. After 1 week transplantation, all the samples in both B-PHNF and H-PHNF groups remained unobstructed, while only 60% patency rate of PNF group was noted. With the increase of transplantation time, three tube of B-PHNF were blocked in the second week. In the fourth week, one tube was blocked in the H-PHNF group, and five tubes of both PNF and B-PHNF were blocked, respectively. Compared with the other groups, the H-PHNF had a longer-lasting release of heparin, which had leed to the obvious effect of inhibiting thrombus formation. This is mainly due to the technology that promotes more uniform mixing of PEEUU and heparin. Ultimately, H-PHNF exhibited stronger ability to blocks the rapid release of heparin molecules than B-PHNF.

3.6 Histological assessments after implantation *in situ*

As shown in Figure 7, the cross-sections of B-PHNF and H-PHNF in proximal end, midportion, and telecentric end after

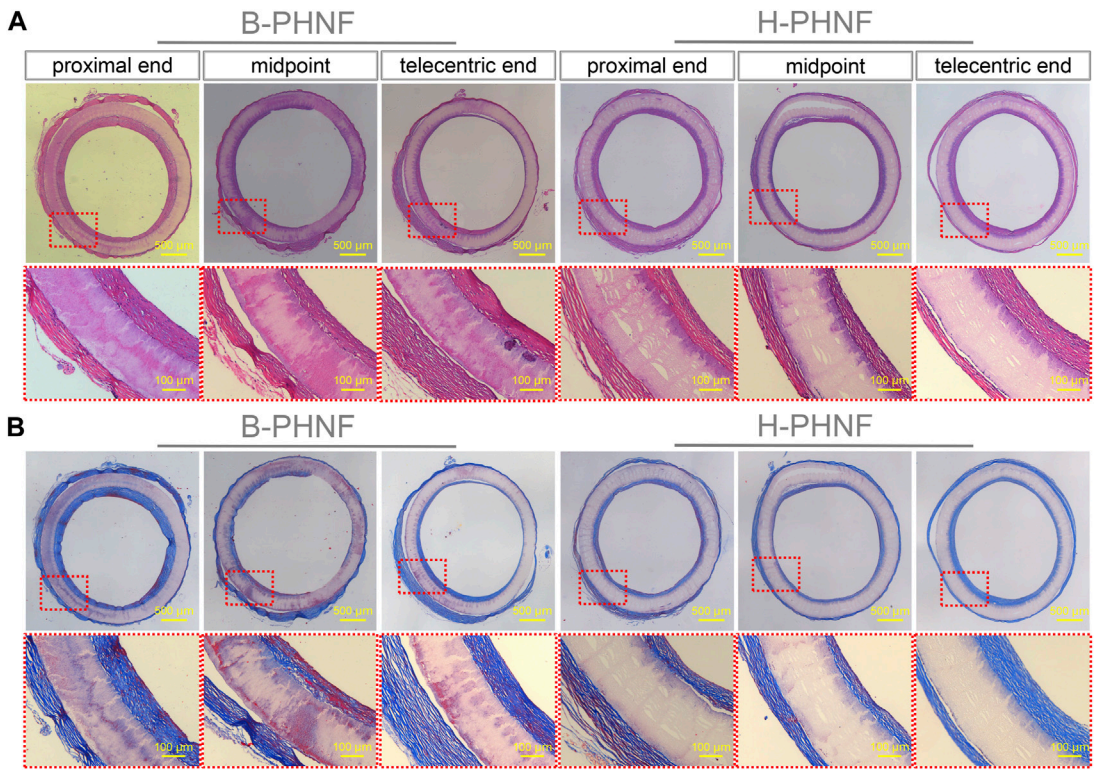

FIGURE 8
(A) H&E staining at three different locations, namely, proximal end, midpoint, and telecentric end of transverse section of B-PHNF and H-PHNF for 4 weeks implantation, respectively; **(B)** Masson's trichrome staining at three different locations, namely, proximal end, midpoint, and telecentric end of transverse section of B-PHNF and H-PHNF for 4 weeks implantation, respectively.

4 weeks of implantation were stained against CD31 and α-SMA antibodies and immunofluorescent imaged to demonstrate the presence of endothelial cells and smooth muscle cells, respectively. Both B-PHNF and H-PHNF had the apparent expressions of α-SMA after implantation for 4 weeks. Compared with B-PHNF, the regenerative SMCs layer in the lumen of H-PHNF was more analogous in SMCs layer thickness, no matter in proximal end, midportion, and telecentric end, which is mainly due to the uniform distribution of heparin in H-PHNF.

The intimal layer had positive expression of endothelial cells and smooth muscle cells. The internal wall of both B-PHNF and H-PHNF lumen were completely covered by an endothelial layer composed of monolayered and uniformly distributed endothelial cells (Figure 7). No thrombosis occurred within the lumen of grafts after 4 weeks. Taken together, these data indicated that hybrided heparin contributed to enhanced anticoagulant capacity, conferred rapid endothelization, and limited intimal hyperplasia.

The results of H&E and Masson's trichrome staining at proximal end, midpoint, and telecentric end of transverse section of B-PHNF and H-PHNF for 4 weeks implantation are shown in Figure 8. H&E and Masson's trichrome staining were used to observe the lumen area, neo-tissue formation and wall thickness of the patent grafts (Zhang Yan et al., 2022). The values of lumen diameter of proximal end, midpoint, and telecentric end in H-PHNF group were 1.98 ± 0.07 mm, 1.98 ± 0.10 mm, and 1.98 ± 0.09 mm. There was no big difference among these groups, while they were smaller than that of the B-PHNF group (1.92 ± 0.11 mm, 1.96 ± 0.08 mm, and 1.93 ± 0.13 mm for proximal end, midpoint, and telecentric end, respectively) (Figure 8A). The quantitative data is shown in Table 2. In addition, neo-tissue was observed on the luminal surface no matter in B-PHNF group or H-PHNF group. Moreover, there was discontinuous neo-tissue coverage detectable at the midpoint in B-PHNF group, while continuous neo-tissue coverage detectable at in H-PHNF group. Both H&E and Masson's trichrome staining showed that the structure of the implanted tubular grafts were composed of a large amount of radially circumaxial oriented collagen in both inner layer and outer layer, which may be secreted by the smooth muscle layer. Therefore, we speculate that the main source of SMCs encapsulating tubular grafts is these smooth muscle tissues are mainly from the autovascular tissue migrated from the anastomosis (Figure 8B). All in all, the migration of SMCs also indicates that tubular grafts may have vascular functions such as relaxation and contraction in the later stage.

Van Gieson staining showed that large amounts of elastic fibers were secreted in both the inner wall and outer wall of the artificial blood vessel, and elastic fibers was arranged along the circumference of the tubular grafts (Figure 9A). Elastin is an important guarantee of vascular elasticity and compliance, while elastic fibers mainly provides mechanical support. When the tubular grafts were implanted in the body to guide the orientation regeneration of smooth muscle cells, elastic fibers-oriented deposition was also

TABLE 2 The lumen diameter at proximal end, midpoint, and telecentric end of B-PHNF and H-PHNF for 4 weeks implantation, respectively.

Samples	Proximal end (mm)	Midpoint (mm)	Telecentric end (mm)
B-PHNF	1.92 ± 0.11	1.96 ± 0.08	1.93 ± 0.13
H-PHNF	1.98 ± 0.07	1.98 ± 0.10	1.98 ± 0.09

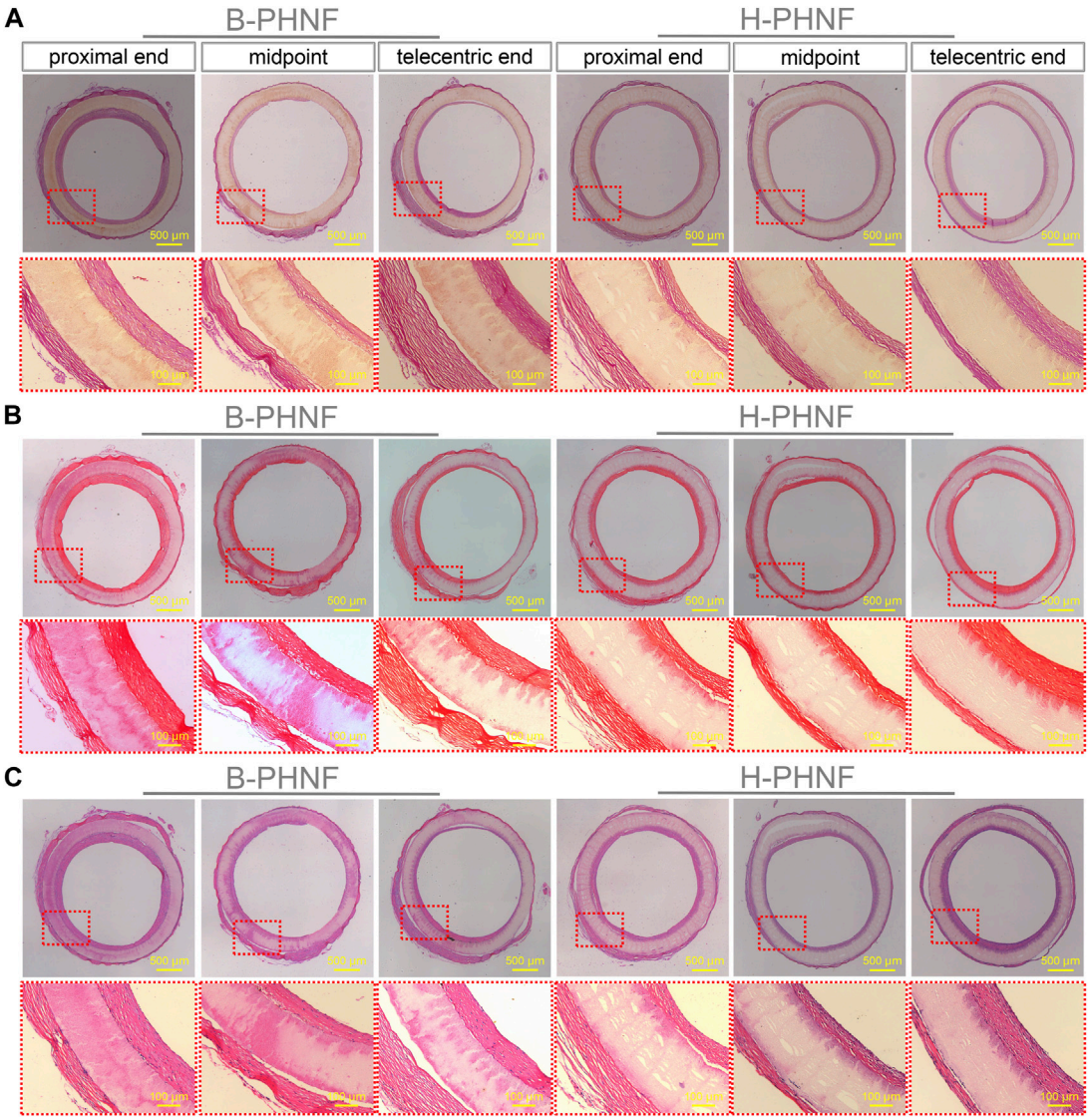

FIGURE 9
(A) Van Gieson, **(B)** Saffron O, and **(C)** Von Kossa staining at three different locations, namely, proximal end, midpoint, and telecentric end of transverse section of B-PHNF and H-PHNF for 4 weeks implantation, respectively.

achieved, which enhanced the radial mechanics of the tubular grafts and prevented the occurrence of aneurysms.

Another important substance in the natural extracellular matrix is mucopolysaccharide (GAG), a negatively charged straight-chain carbohydrate composed alternately of hexose carboxylic acids and hexose amine groups. GAG can not only form bond and regulate growth factors and cytokines, but also inhibit the decomposition of protease, and plays a positive role in the adhesion, migration, proliferation and differentiation of endothelial cells. Safranin O staining showed proteoglycan distribution on both outer and inner surfaces of tubular grafts (Figure 9B). Similarly, GAG was evenly distributed in the lumen of H-PHNF with a approximate thickness of GAG deposition, no matter proximal end, midpoint, or telecentric end, which is mainly due to the uniform distribution of heparin in H-PHNF, and that heparin is one of the main factors that stimulate the secretion of GAG in host cells.

Calcific degeneration remains a major obstacle facing the translation of tissue-engineered vascular grafts for arterial repair. The reasons that cause calcification are complex, including the elasticity of the material, the acid degradation products, and the hardness of the material. To check whether calcification had occurred after 4 weeks implantation, Von Kossa staining of transverse section of the explanted tubular graft was performed (Figure 9C). The results showed that no calcification was detected in the explanted tubular graft. Some previous studies have shown that heparin can inhibit the differentiation of vascular smooth muscle into osteoblasts in the environment as well as inhibit intracellular mineral deposition. In addition, the nanofibers with heparin homogeneous distributions promote sustained ECM secretion by host cells, which inhibits calcification due to the degradation of collagen.

4 Conclusion

In summary, anti-acute thrombosis cues of anticoagulant molecule heparin were incorporated into a nanofibers tubular graft (H-PHNF) of great compliance match with the native blood vessel by homogeneous emulsion blending and electrospinning. Structure and component modification confer to moderate wettability, matched mechanical and sustained drug release profile, and reliable blood compatibility of the obtained H-PHNF. H-PHNF showed prominent ability to promote endothelial cells growth and maintained patency without acute thrombosis formation in abdominal aorta implantation of rats *in situ*. This strategy may bring cell-free small-diameter synthetic vascular grafts toward clinical application.

Data availability statement

The original contributions presented in the study are included in the article/Supplementary Material, further inquiries can be directed to the corresponding authors.

Ethics statement

The animal study was reviewed and approved by the all rats were obtained from Shanghai Slaccas Experimental Animal Co., Ltd. (Shanghai, China) and all experimental schemes are in agreement with the requirements of the Institutional Animal Care and Use Committee (IACUC) of Shanghai Sixth People's Hospital Affliated to Shanghai Jiao Tong University School of Medicine and accepted by IACUC.

Author contributions

HZ: experiment, data analysis, manuscript writing; QZ: methodology, manuscript writing; JD: supervision, data analysis, manuscript writing and editing; TZ: Supervision; DC: supervision, methodology; FL: supervision, manuscript review and editing; YD: supervision, manuscript review and editing.

Acknowledgments

The authors sincerely appreciate projects sponsored by the National Natural Science Foundation of China (81902186), Shanghai Rising-Star Program (20QC1401300), Technology Support Project of Science and Technology Commission of Shanghai Municipality (22S31904700).

Conflict of interest

The authors declare that the research was conducted in the absence of any commercial or financial relationships that could be construed as a potential conflict of interest.

Publisher's note

Supplementary material

The Supplementary Material for this article can be found online at: https://www.frontiersin.org/articles/10.3389/fbioe.2023.1187914/full#supplementary-material

References

Altankov, G., Thom, V., Groth, T., Jankova, K., Jonsson, G., and Ulbricht, M. (2000). Modulating the biocompatibility of polymer surfaces with poly(ethylene glycol): Effect of fibronectin. *J. Biomed. Material Res.* 52 (1), 219–230. doi:10.1002/1097-4636(200010)52:1<219:aid-jbm28>3.0.co;2-f

Asadpour, S., Hamid, Y., Ai, J., and Ghanbari, H. (2018). A novel polyurethane modified with biomacromolecules for small-diameter vascular graft applications. *J. Mater. Sci.* 53 (14), 9913–9927. doi:10.1007/s10853-018-2321-5

Caliskan, E., Ramos de Souza, D., Boning, A., Liakopoulos, O. J., Choi, Y-H., Pepper, J., et al. (2020). Saphenous vein grafts in contemporary coronary artery bypass graft surgery. *Nat. Rev. Cardiol.* 17 (3), 155–169. doi:10.1038/s41569-019-0249-3

Fathi Karkan, S., Davaran, S., Rahbarghazi, R., Salehi, R., and Akbarzadeh, A. (2019). Electrospun nanofibers for the fabrication of engineered vascular grafts. *J. Biol. Eng.* 13 (1), 83. doi:10.1186/s13036-019-0199-7

He, C., Liu, G., Nie, H., and Ni, J. (2010). Synthesis and characterization of polyurethane. *J. Wuhan Univ. Technology-Materials Sci. Ed.* 25 (6), 984–986. doi:10.1007/s11595-010-0134-8

Jordan, C., Abbaspour, R., Wu, C., Bakir, M., and WilburLam, A. (2016). A microengineered matrix to decouple the biophysical and biochemical mechanisms of blood cell interactions with thrombi and vascular wall matrices. *Blood* 128 (22), 555. doi:10.1182/blood.v128.22.555.555

Kelly Navas-GomezValero, M. F., and Valero, M. F. (2020). Why polyurethanes have been used in the manufacture and design of cardiovascular devices: A systematic review [J]. *Materials* 13 (15), 3250. doi:10.3390/ma13153250

Kevin, I. (2015). Transdermal delivery of heparin: Physical enhancement techniques. *Int. J. Pharm.* 496 (2), 240–249. doi:10.1016/j.ijpharm.2015.11.023

Lee, J. H., Ju, Y. M., Lee, W. K., Park, K. D., and Kim, Y. H. (1998). Platelet adhesion onto segmented polyurethane surfaces modified by PEO- and sulfonated PEO-containing block copolymer additives. *J. Biomed. Mater. Res.* 40 (2), 314–323. doi:10.1002/(sici)1097-4636(199805)40:2<314:aid-jbm17>3.0.co;2-l

Li, Y., Zhou, Y., Qiao, W., Shi, J., Qiu, X., and Dong, N. (2023). Application of decellularized vascular matrix in small-diameter vascular grafts. *Front. Bioeng. Biotechnol.* 10, 1081233. doi:10.3389/fbioe.2022.1081233

Lim, J. K., Won, J., AhnBum, C., Kim, J., Kim, H. J., and Jung, J. S. (2021). Comparison of hemodynamic energy between expanded polytetrafluoroethylene and dacron artificial vessels. *J. Chest Surg.* 54 (2), 81–87. doi:10.5090/jcs.20.134

Martinez-Gonzalez, B., Reyes-Hernandez, C. G., Quiroga-Garza, A., Rodriguez-Rodriguez, V. E., Esparza-Hernandez, C. N., RodrigoElizondo-Omana, E., et al. (2017). Conduits used in coronary artery bypass grafting: A review of morphological studies. *Ann. Thorac. Cardiovasc. Surg.* 23 (2), 55–65. doi:10.5761/atcs.ra.16-00178

Mokhtari, N., and Kharazi, A. Z. (2021). Blood compatibility and cell response improvement of poly glycerol sebacate/poly lactic acid scaffold for vascular graft applications. *J. Biomed. Mater. Res. Part A* 109, 2673–2684. doi:10.1002/jbm.a.37259

Nemati, S., Kim, S., YoungShin, M., and Shin, H. (2019). Current progress in application of polymeric nanofibers to tissue engineering. *Nano Converg.* 6 (1), 36. doi:10.1186/s40580-019-0209-y

Purushothaman, A. E., Thakur, K., and Kandasubramanian, B. (2020). Development of highly porous, Electrostatic force assisted nanofiber fabrication for biological applications. *Int. J. Polym. Mater. Polym. Biomaterials* 69 (8), 477–504. doi:10.1080/00914037.2019.1581197

Rahimi, A., and Mashak, A. (2013). Review on rubbers in medicine: Natural, silicone and polyurethane rubbers. *Plastics Rubber Compos.* 42 (6), 223–230. doi:10.1179/1743289811y.0000000063

Roina, Y., Auber, F., Hocquet, D., and Herlem, G. (2022). ePTFE-based biomedical devices: An overview of surgical efficiency. *J. Biomed. Mater. Res. Part B-Applied Biomaterials* 110 (2), 302–320. doi:10.1002/jbm.b.34928

Seifu, D. G., Purnama, A., Mequanint, K., and Mantovani, D. (2013). Small-diameter vascular tissue engineering. *Nat. Rev. Cardiol.* 10 (7), 410–421. doi:10.1038/nrcardio.2013.77

Serrone, J. C., Andaluz, N., Brink, V., and Zuccarello, M. (2013). Systemic infusion and local irrigation with argatroban effective in preventing clot formation during carotid endarterectomy in a patient with heparin-induced thrombocytopenia[J]. *World Neurosurg.* 80 (1-2), 222. doi:10.1016/j.wneu.2013.01.037

Stahl, A., Dake, H., Barrera, J., Henn, D., Lin, S., Moeinzadeh, S., et al. (2023). A bioactive compliant vascular graft modulates macrophage polarization and maintains patency with robust vascular remodeling. *Bioact. Mater.* 19, 167–178. doi:10.1016/j.bioactmat.2022.04.004

Tatterton, M., Wilshaw, S-P., Ingham, E., and Homer-Vanniasinkam, S. (2012). The use of antithrombotic therapies in reducing synthetic small-diameter vascular graft thrombosis. *Vasc. Endovascular Surg.* 46 (3), 212–222. doi:10.1177/1538574411433299

Tseng, Y.-C., and Park, K. (1992). Synthesis of photoreactive poly(ethylene glycol) and its application to the prevention of surface-induced platelet activation. *J. Biomed. Material Res.* 26 (3), 373–391. doi:10.1002/jbm.820260308

Ukita, R., Wu, K., Lin, X., Carleton, N. M., Naito, N., Lai, A., et al. (2019). Zwitterionic poly-carboxybetaine coating reduces artificial lung thrombosis in sheep and rabbits. *Acta Biomater.* 92, 71–81. doi:10.1016/j.actbio.2019.05.019

Uscategui, Y. L., Diaz, L. E., and Valero, M. F. (2018). Biomedical applications of polyurethanes[J]. *Quimica Nova* 41 (4), 434–445. doi:10.21577/0100-4042.20170191

Wang, J., Qiu, M., and He, C. (2020). A zwitterionic polymer/PES membrane for enhanced antifouling performance and promoting hemocompatibility. *J. Membr. Sci.* 606, 118119. doi:10.1016/j.memsci.2020.118119

Wang, Z., Liu, C., Xiao, Y., Gu, X., Xu, Y., Dong, N., et al. (2019). Remodeling of a cell-free vascular graft with nanolamellar intima into a neovessel. *ACS Nano* 13 (9), 10576–10586. doi:10.1021/acsnano.9b04704

Yang, X., Wang, Q., Zhang, A., Shao, X., Liu, T., Tang, B., et al. (2022). Strategies for sustained release of heparin: A review. *Carbohydr. Polym.* 294, 119793. doi:10.1016/j.carbpol.2022.119793

YoungKim, H., DongHan, K., Dong Park, K., and Kim, S. H. (2003). Enhanced blood compatibility of polymers grafted by sulfonated PEO via a negative cilia concept. *Biomaterials* 24, 2213–2223. doi:10.1016/s0142-9612(03)00023-1

Zhang, Y., Xu, K., Zhi, D., Qian, M., Liu, K., Shuai, Q., et al. (2022b). Improving vascular regeneration performance of electrospun poly(ε-Caprolactone) vascular grafts via synergistic functionalization with VE-Cadherin/VEGF. *Adv. Fiber Mater.* 4, 1685–1702. doi:10.1007/s42765-022-00213-z

Zhang, Z., Liu, L., Xu, D., Zhang, R., Shi, H., Luan, S., et al. (2022a). Research progress in preparation and biomedical application of functional medical polyurethane elastomers※. *Acta Chim. Sin.* 80 (10), 1436–1447. doi:10.6023/a21120593

Zhi, D., Cheng, Q., Midgley, A. C., Zhang, Q., Wei, T., Li, Y., et al. (2022). Mechanically reinforced biotubes for arterial replacement and arteriovenous grafting inspired by architectural engineering. *Sci. Adv.* 8 (11), eabl3888. doi:10.1126/sciadv.abl3888

Zhu, J., Chen, D., Du, J., Chen, X., Wang, J., Zhang, H., et al. (2020). Mechanical matching nanofibrous vascular scaffold with effective anticoagulation for vascular tissue engineering. *Compos. Part B-Engineering* 186, 107788. doi:10.1016/j.compositesb.2020.107788

Zhu, T., Gao, W., Fang, D., Liu, Z., Wu, G., Zhou, M., et al. (2021c). Bifunctional polymer brush-grafted coronary stent for anticoagulation and endothelialization. *Mater. Sci. Eng. C-Materials Biol. Appl.* 120, 111725. doi:10.1016/j.msec.2020.111725

Zhu, T., Gu, H., Ma, W., Zhang, Q., Du, J., Chen, S., et al. (2021a). A fabric reinforced small diameter tubular graft for rabbits' carotid artery defect. *Compos. Part B-Engineering* 225, 109274. doi:10.1016/j.compositesb.2021.109274

Zhu, T., Gu, H., Zhang, H., Wang, H., Xia, H., Mo, X., et al. (2021b). Covalent grafting of PEG and heparin improves biological performance of electrospun vascular grafts for carotid artery replacement. *Acta Biomater.* 119, 211–224. doi:10.1016/j.actbio.2020.11.013

Zhu, T., Zhu, J., Lu, S., and Mo, X. (2022). Evaluation of electrospun PCL diol-based elastomer fibers as a beneficial matrix for vascular tissue engineering. *Colloids Surfaces B-Biointerfaces* 220, 112963. doi:10.1016/j.colsurfb.2022.112963

Zhuang, Y., Zhang, C., Cheng, M., Huang, J., Liu, Q., Yuan, G., et al. (2021). Challenges and strategies for *in situ* endothelialization and long-term lumen patency of vascular grafts. *Bioact. Mater.* 6 (6), 1791–1809. doi:10.1016/j.bioactmat.2020.11.028

frontiers | Frontiers in Bioengineering and Biotechnology

TYPE Review
PUBLISHED 04 July 2023
DOI 10.3389/fbioe.2023.1205792

OPEN ACCESS

EDITED BY
Juan Wang,
Shanghai Jiao Tong University, China

REVIEWED BY
Yanran Huang,
Chongqing Medical University, China
Chaoyong Liu,
Beijing University of Chemical Technology, China
Wei Nie,
Wake Forest Baptist Medical Center, United States

*CORRESPONDENCE
Fengxuan Han,
fxhan@suda.edu.cn

†These authors have contributed equally to this work

RECEIVED 14 April 2023
ACCEPTED 26 June 2023
PUBLISHED 04 July 2023

CITATION
Han F, Meng Q, Xie E, Li K, Hu J, Chen Q, Li J and Han F (2023), Engineered biomimetic micro/nano-materials for tissue regeneration.
Front. Bioeng. Biotechnol. 11:1205792.
doi: 10.3389/fbioe.2023.1205792

Engineered biomimetic micro/nano-materials for tissue regeneration

Feng Han[1†], Qingchen Meng[1†], En Xie[1], Kexin Li[1], Jie Hu[1], Qianglong Chen[1], Jiaying Li[1] and Fengxuan Han[1,2*]

[1]Department of Orthopaedic Surgery, The First Affiliated Hospital, Suzhou Medical College, Orthopedic Institute, Soochow University, Suzhou, Jiangsu, China, [2]China Orthopaedic Regenerative Medicine Group (CORMed), Hangzhou, Zhejiang, China

The incidence of tissue and organ damage caused by various diseases is increasing worldwide. Tissue engineering is a promising strategy of tackling this problem because of its potential to regenerate or replace damaged tissues and organs. The biochemical and biophysical cues of biomaterials can stimulate and induce biological activities such as cell adhesion, proliferation and differentiation, and ultimately achieve tissue repair and regeneration. Micro/nano materials are a special type of biomaterial that can mimic the microstructure of tissues on a microscopic scale due to its precise construction, further providing scaffolds with specific three-dimensional structures to guide the activities of cells. The study and application of biomimetic micro/nano-materials have greatly promoted the development of tissue engineering. This review aims to provide an overview of the different types of micro/nanomaterials, their preparation methods and their application in tissue regeneration.

KEYWORDS

micro/nano-materials, tissue engineering, repair, regeneration, biomimetic microstructure

1 Introduction

Due to lifestyle changes and population aging, the incidence of various diseases, such as degenerative diseases, cancer and trauma, has been increasing. Therefore, there is an increasing demand for tissue and organ transplantation in clinical practice (Bakhshandeh et al., 2017; Nii and Katayama, 2021). However, the repair or replacement of organs and tissues remains a complex and unsolved problem. Current graft materials cannot be widely used due to limitations such as material mismatch and immune rejection (Chung et al., 2017). Tissue engineering which integrates different disciplines, such as life sciences and materials sciences, has a potential for the development of alternative therapeutic strategies to repair damaged tissues and organs.

The basic concepts of tissue engineering include seeding cells on scaffolds of a certain shape, expanding the cells continuously to form a composite system of cells and biomaterials, and finally implanting them into the patient. After *in vivo* implantation, the polymer system will gradually degrade, allowing regeneration of new tissues. In this functional and biomimetic system, the three major elements are the selection of seed cells, the construction of scaffolds, and the regulation of cell-biomaterial interactions (Li et al., 2020). Biomaterials used for tissue engineering must have the following properties: (1) It has good biocompatibility, non-toxic side effects on cells and tissues; (2) The surface of the materials is conducive to cell adhesion and proliferation, and can induce cell growth

according to the predetermined morphology; (3) The degradation rate should match the new tissue formation rate; (4) Three-dimensional (3D) structure. Studies have shown that the surface microstructure of biomaterials has a great influence on cell morphology, adhesion, directional growth and bioactivity (Yu et al., 2020; Han et al., 2022).

Biomaterials are natural or artificial materials used to replace or repair tissue. For instance, the annulus fibrosus (AF) has a collagen-rich fibrous lamellar with highly aligned collagen fibers tilted 30° from the horizontal axis. The microstructure allows the spine to resist complex loading. Tendon has a hierarchical organization, and the subunits of the tendon are the fascicles, which consist of highly aligned collagen fibers. With the continuous improvement of tissue engineering and regeneration, plenty of biomaterials have been developed. With the in-depth understanding of the microstructure of different tissues and organs, researchers have noted that it is important to simulate the microstructure of tissues and organs by biomaterials at a more microscopic scale to achieve better tissue repair (Craciunescu et al., 2021). Tissue engineering generally controls the growth and development of cells in three scales. The millimeter scale determines the overall shape of the engineering tissue. The micron scale determines the pore size of the material and regulates cell migration and growth. The nanometer scale determines the physical and chemical properties of material surface, which regulates cell adhesion and gene expression. The properties of extracellular matrix (ECM), such as matrix stiffness, surface topography, and chemical composition, can affect cell behavior spatially and temporally, which is attributed to its fusion with mechanical transduction and molecular recognition (Wang et al., 2018). Those will affect cell phenotype, gene expression, and ultimately cell fate. Moreover, the geometry of ECM also has a great influence on their mechanical properties. It can be seen that the micro/nano structure of ECM has a great impact on regulating cell behavior, which in turn affects tissue organization. Therefore, the preparation of biomaterials with certain micro and nano structures is of great significance for tissue repair and regeneration.

As one of the three elements of tissue engineering, the scaffold is the foundation of constructing engineered tissues. Suitable 3D scaffolds can simulate the microstructure of tissues and provide a suitable microenvironment for cell and tissue growth. Micro/nano-materials have good properties of general biomaterials. The special pores of micro/nano-materials can support nutrient transport, absorption, and tissue growth (Carotenuto et al., 2022). For specific tissues, such as bone and cartilage, higher requirements are also put forward for the mechanical properties of micro/nano-materials. Therefore, more and more attention has also been paid to the mechanical properties. In recent years, a variety of multi-functional micro/nanomaterials have been applied in tissue engineering, exhibiting a broad application prospect. However, the application of micro/nano-materials in tissue engineering is still in the early stages, and there are still many problems regarding the clinical application that need to be solved. The problems include developing suitable micro/nanomaterials to simulate the microstructure of tissue, constructing an ideal cell-material interface to induce directional differentiation of cells, making allogeneic biological tissues and cells cultured on micro/nano scaffolds from immune system recognition and rejection, maintaining the viability and function of cultured cells for a long time, and further improving the biocompatibility of micro/nano-materials.

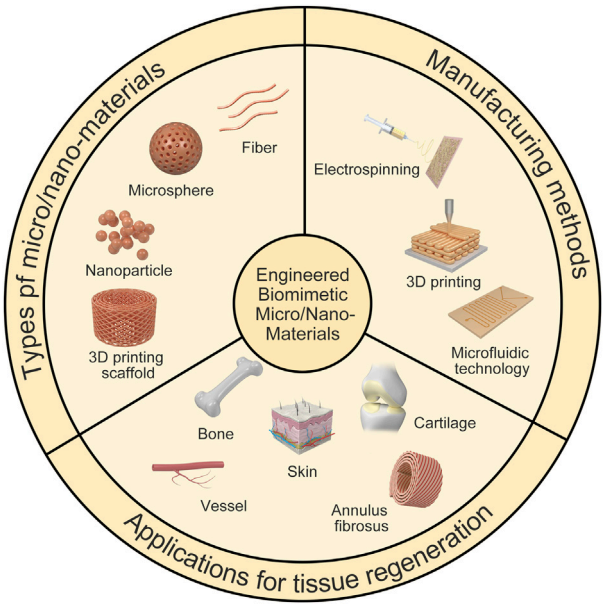

FIGURE 1
Illustration of engineered biomimetic micro/nano-materials for tissue regeneration. The micro/nano structures including micro/nano fiber, nanoparticle, microsphere and 3D printing scaffold, and the biomedical applications referring to bone repair, AF repair and vascular grafts are shown as examples. Manufacturing methods for different micro/nano-materials are also shown.

Herein, we provide a comprehensive overview of the current research progress on micro/nanomaterials and introduce the types of micro/nanomaterials and their applications (Figure 1). First, the importance of scaffold micro/nanomaterials on cell behavior and biomimetic microstructure is highlighted. Next, several preparation methods of scaffolds are introduced. Then, examples of the application of micro/nanomaterials in bone, cartilage, blood vessels and other tissues are introduced. Finally, some limitations and challenges are briefly discussed.

2 Manufacturing methods for micro/nano-materials

2.1 Electrospinning

Electrospinning technology can continuously produce micro/nano-sized ultrafine fibers (Zamani et al., 2018). The scaffold prepared using the electrospinning technology has a unique micro/nano structure and proper mechanical properties (Figure 2). It can simulate the micro/nano-network structure of natural ECM and has unique advantages in the preparation of tissue engineered scaffolds (Recum et al., 1996; Flemming et al., 1999; Mitragotri et al., 2015). Generally, the electrospinning device consists of a high-voltage source, a solution reservoir, and spraying and receiving devices. The electrospinning process can

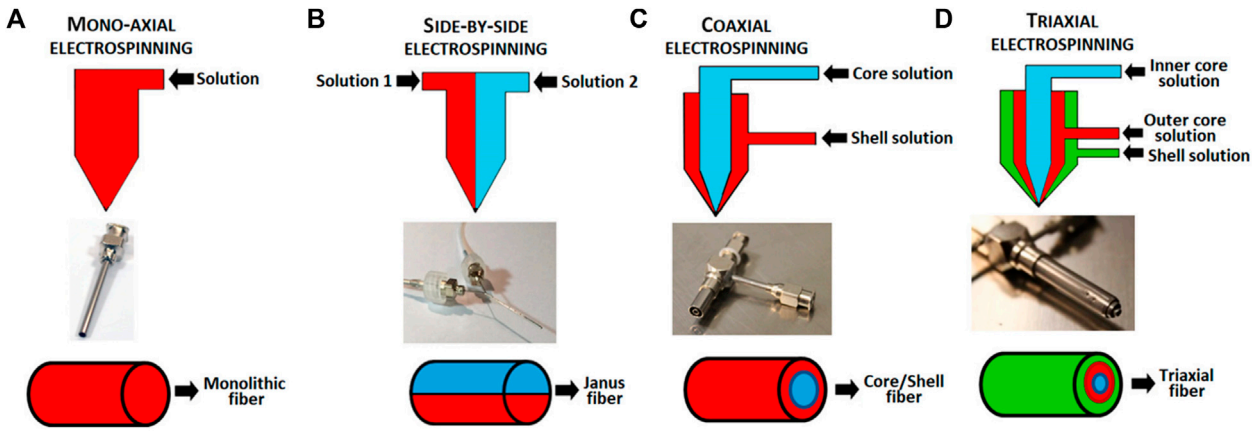

FIGURE 2
Schematic of electrospinning setup and the fibers output. **(A)** mono-axial electrospinning; **(B)** side-by-side electrospinning; **(C)** coaxial electrospinning and **(D)** triaxial electrospinning (Luraghi et al., 2021).

be divided into five processes, including fluid charging, Taylor cone formation, jet stretching and whipping, jet solidification, and fiber reception (Liu et al., 2012; Zamani et al., 2018). The most important process is the formation of the Taylor cone. The electrospinning process can be influenced by many factors such as the solvent properties (e.g., polymer type, concentration, viscosity, conductivity), the processing factors (e.g., electric field strength, flow rate, spray distance), and the ambient parameters (e.g., temperature, humidity) (Bhardwaj and Kundu, 2010; Pelipenko et al., 2015; Ye et al., 2019).

Core-shell nanofiber scaffold is a special type of nanofibers. Core-shell nanofiber can combine the excellent properties of two or more polymers. It uses the core-shell structure to encapsulate specific substances, such as drugs and growth factors, into nanofibers (Kim et al., 2004; Bölgen et al., 2007; Nie and Wang, 2007). In the fiber material system, nanofibers have the characteristics of high porosity, high specific surface area, and high surface activity. This structure is suitable for processes in which the fiber needs to fully contact and react with the surrounding environment, such as drug release. Mixing the drug directly into the nanofibers often results in burst release of the drug, while the core-shell nanofiber can encapsulate drugs in the core layer and prolong their release (Mohiti-Asli et al., 2017; da Silva et al., 2019). Some drugs or active substances should not be exposed to organic solvents. The core structural material can enclose the drugs or active substances inside to prevent them from being exposed to organic solvents. Because the drug or active substance is dissolved in the core solution, the surface modification of the fiber will not affect the activity of the internal drug. The main manufacturing methods of core-shell nanofibers reported in the literature are coaxial electrospinning and emulsion electrospinning.

2.1.1 Coaxial electrospinning

The difference between coaxial electrospinning and ordinary electrospinning lies in the design of the spinneret. Ordinary electrospinning uses a single-layer capillary while coaxial electrospinning uses a coaxial nozzle (Zupančič et al., 2016). A coaxial nozzle is formed by nesting two or more coaxial capillaries with each other, and a certain gap is left between the inner and outer capillaries to ensure the smooth flow of the shell liquid. In coaxial electrospinning, the solution of the core and shell material is divided into two different syringes, and the spinning system is composed of two coaxial but different inner diameter capillary tubes. Under the action of a high-voltage electric field, the outer shell liquid flows out (Huang et al., 2006). Coaxial electrospinning relies on complex electrospinning equipment such as coaxial nozzles.

2.1.2 Emulsion electrospinning

Emulsion electrospinning is a technical method capable of preparing nanofibers with core-shell structure in one step (Bazilevsky et al., 2007; Moydeen et al., 2018). In general, emulsion electrospinning solution mainly uses a water-in-oil or oil-in-water two-phase dispersion system to form an external phase by continuous polymer organic solution and an internal phase with drug aqueous solution in the emulsion. Amphiphilic emulsifiers are used to stabilize the interaction between the external phase and the internal phase to form an emulsion (Qi et al., 2006). The drug-loaded nanofibers prepared by this method can effectively solve the problem of burst drug release and can slow and control the release of the loaded substance (Liu et al., 2018). Compared with coaxial electrospinning, the advantage of emulsion electrospinning is that the device is simple without the requirement of coaxial nozzles. However, it has higher requirements for spinning solution, and the instability of the emulsion limits its wide application.

2.2 3D printing

3D printing technology, a type of rapid prototyping technology, is a digital model file based on the use of adhesive materials through layer-by-layer printing to construct an object. As a new technology, 3D printing is developing rapidly, as there are many established manufacturing techniques and a large number of experimental techniques (Li et al., 2020). The most popular 3D bioprinting

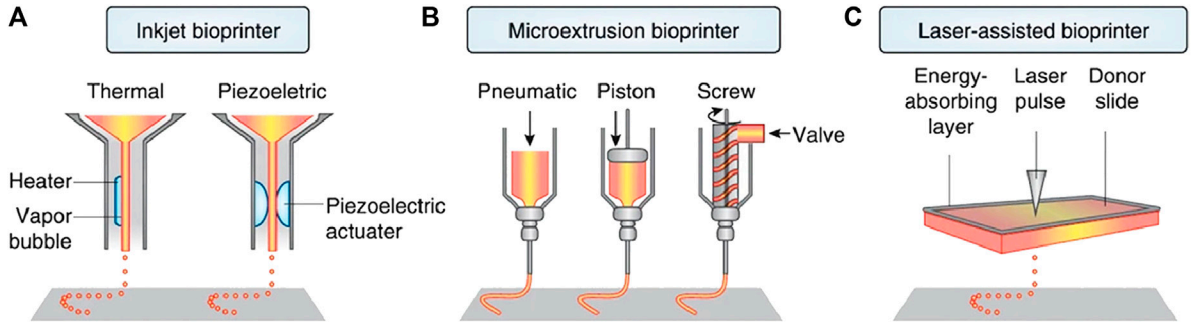

FIGURE 3
Three main 3D bioprinting technologies. **(A)** Inkjet printing; **(B)** Extrusion or robotic dispensing bioprinters; **(C)** Laser-assisted bioprinting (Bartolo et al., 2022).

technologies include laser-assisted bioprinting, inkjet printing, and extrusion and robotic dispensing bioprinters (Figure 3). In recent years, 3D printing technology has been applied to tissue engineering with the aim of constructing biomaterials that simulate the microstructure of tissues and organs. The 3D bio-printing process comprises three steps. (1) Data collection and software modeling. This mainly includes 3D image collection and digital 3D design; (2) choice of printing ink (materials and cells); and (3) improvement of the biomimetic structure, mechanical properties, and biological activity of the scaffolds (Zhu et al., 2016).

At present, many materials such as synthetic polymer materials (polyethylene glycol (PEG), polylactic acid (PLA), polycaprolactone (PCL), polyetheretherketone (PEEK)) and natural polymer materials (collagen, gelatin, hyaluronic acid) have been used in 3D printing. However, the accuracy of 3D printing is limited. Generally, it is used to print micron-sized materials; therefore, it is often necessary to combine it with other technologies to obtain tissue engineering scaffolds with higher accuracy.

2.3 Microfluidic technology

In recent years, the technological advances in materials science have contributed to the production of various micro/nano-materials such as microspheres for biomedical applications (Tien and Dance, 2021). Interestingly, the characteristics of microfluidic technology are helpful for preparing these micro-nano materials with precise control of reaction parameters in a short time and minimal reagent consumption. Generally, the synthesis of micro-nano materials in microfluidic platform can be achieved by mixing single or multiple miscible solvents (single-phase microfluidic) or mixing multiple immiscible solvents (multiphase microfluidic). The microfluidic reaction system has become a high-throughput and controlled tool, which can be used for materials with diverse biological and chemical applications. Due to the typical laminar flow environment of microfluidic channels, the reaction can be carried out in a highly controlled and reproducible manner (Domachuk et al., 2010). In addition, the size and composition of the product can be flexibly designed by adjusting the flow rate, characteristic geometry and the properties of the input reagent. Different from conventional methods, microfluidic technology allows the continuous production of new materials in a single workflow. Most importantly, many reactions in the microfluidic platform can be carried out under mild conditions, which is very beneficial to many bioactive reaction systems. Therefore, researchers use microfluidics to prepare a large number of materials for biological applications, including microspheres for biomedical applications (Figure 4), microcapsules for medical diagnosis applications, and micron (or nano) fibers for tissue engineering.

3 Types of micro/nano-materials

3.1 Fibers

Electrospinning is a feasible technology to produce nanofibers, which can be prepared from various types of biomaterials (Xue et al., 2019). The most commonly used materials are synthetic polymers, but natural polymers such as alginate are also used. In addition, synthetic materials offer many advantages over natural polymers, such as reliable sources, low immunogenicity and cost-effectiveness. Biodegradability and structural modifiability are additional advantages of synthetic polymers. The most commonly used polymers include PLA, polyglycolic acid (PGA), PCL, polyurethane (PU), poly (vinyl alcohol) (PVA) and poly- (ethylene oxide) (PEO). The microstructure of nanofibers is also very important for tissue repair and regeneration. Compared with random PCL nanofibers, aligned nanofibers have stronger AF repair effect (Gluais et al., 2019). Besides the arrangement of nanofibers, the stiffness and fiber size of nanofibers will also affect AF stem cell differentiation. According to different needs, specific stiffness and fiber size can be designed to guide cells to differentiate in a specific direction, regulate cell morphology and promote the expression of related ECM (Chu et al., 2019). To further improve the mechanical properties of nanofibers and enhance the interaction with cells, synthetic polymers are also often functionalized through the combination of two or more materials. Nanofibers can also be modified with bioactive cues such as ECM proteins, growth factors, peptides, and nucleic acids to control the cell attachment, migration, spreading, proliferation, and differentiation (Figure 5) (Taskin et al., 2021).

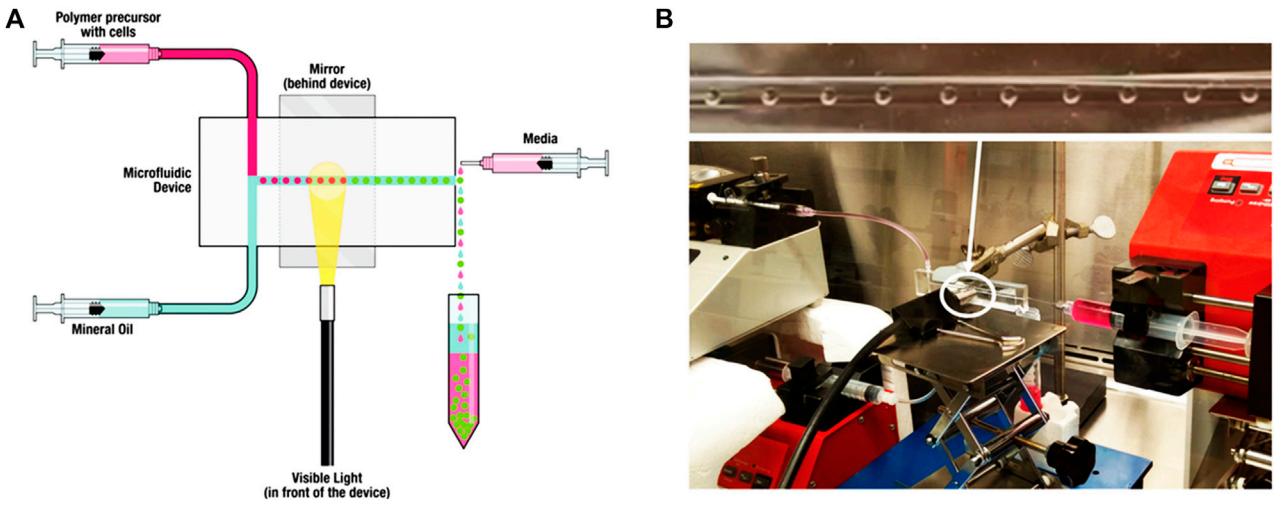

FIGURE 4
Microfluidic encapsulation platform using a novel custom design and device molding technique enables production of uniform hydrogel microspheres with a wide range of diameters. **(A)** Schematic of the microfluidic encapsulation platform. **(B)** Setup of the microfluidic encapsulation platform in a biosafety cabinet (Seeto et al., 2019).

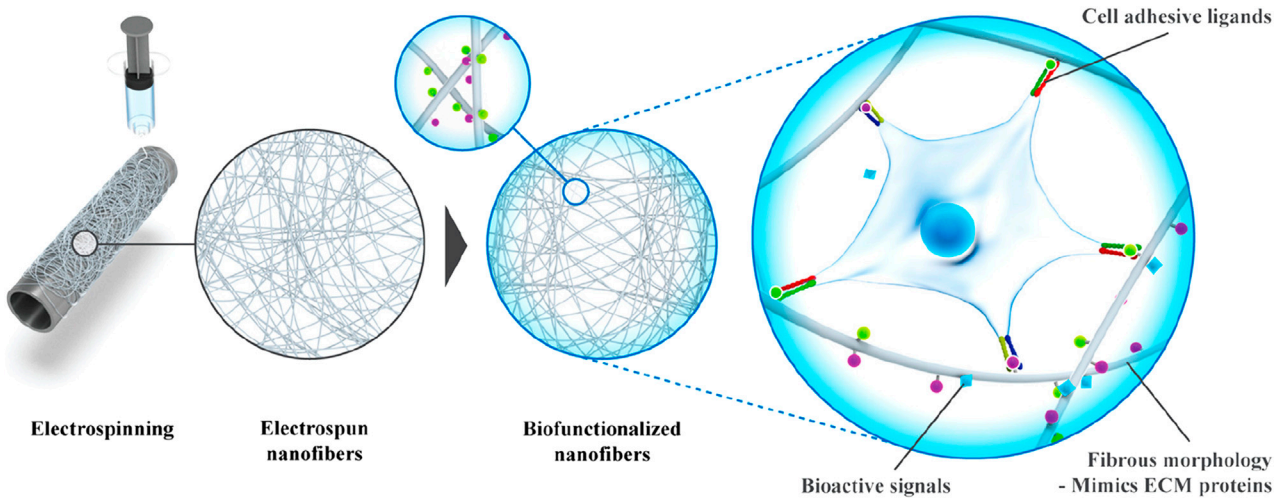

FIGURE 5
Fabrication of bioactive electrospun fibers mimicking the native ECM (Taskin et al., 2021).

When hydrophobic materials such as PCL are delivered to the body, immunological rejection may occur, resulting in unspecific protein adsorption and an inflammatory response (Ratner and Bryant, 2004). The incorporation of hydrophilic bioinert materials such as PEG, can effectively shield hydrophobic fibers, thus making the biomaterial resistant in the biological environment (Dash and Konkimalla, 2012). In addition, the surface of poly (L-lactic acid) (PLLA) scaffolds treated with plasma is more hydrophilic (Jin Seo et al., 2013). It was shown that PCL-α-CD fibers obtained from PCL co-electrospinning with cyclodextrins (CDs) promoted osteogenic differentiation of human adipose-derived stem cells compared with pristine PCL fibers (Zhan et al., 2012). The plasma-treated polyester fiber further improves the adhesion and proliferation of human mesenchymal stem cells (hMSCs), fibroblasts, osteoblasts and Schwann cells (Jia et al., 2008; Martins et al., 2009; Nandakumar et al., 2013). Moreover, studies have confirmed that polydopamine-coated nanofibers (e.g., PCL, PLLA and PLGA) support the deposition of serum proteins, accelerate cell attachment and are widely used for bone, cardiac, skin, nerve and vascular tissue engineering (Chen et al., 2007; Taskin et al., 2016). Furthermore, a variety of active proteins can be modified to nanofibers to enhance the biological activity of fibers, such as vascular endothelial growth factor (VEGF) and epidermal growth factor (EGF) (Choi et al., 2008; Li et al., 2008; Guex et al.,

2014; Heo et al., 2015). For instance, VEGF was immobilized on a nanofibrous scaffold and effectively stimulated endothelial cell proliferation (Guex et al., 2014). Shin et al. demonstrated that gelatin and EGF immobilized together on acrylic acid-grafted poly (lactide-co-ε-caprolactone) (PLCL) significantly enhanced the ability of hMSCs to differentiate into keratinocytes (Shin et al., 2015). Stable and self-assembled coatings on the surface of nanofibers play an important role in the delivery system, enabling precisely temporal release of encapsulated molecules (Yoo et al., 2009; Shah et al., 2011). For instance, polylaminate coating on PCL nanofibers can be used for the quick release of connective tissue growth factor (CTGF) and to regulate the release of bone morphogenetic protein-2 (BMP-2), with the aim of mimicking the natural bone healing process (Cheng et al., 2019). Functionalization of nanofibers can also be achieved through click chemistry (Callahan et al., 2013). The introduction of RGD peptide and osteogenic growth protein (OGP) on PCL nanofibers promoted the differentiation of preosteoblast cells into osteoblasts (Kim et al., 2015).

In addition to electrospinning, microfibers can be prepared by microfluidics (Costantini et al., 2016; Zuo et al., 2016; Wang et al., 2019). Zuo et al. designed a dual coaxial capillary microfluidic device that mimics the unique structure of the osteon (Zuo et al., 2016). The middle and outer layers of the fabricated bilayer hollow microfibers are composed of human umbilical vein epithelial cells (HUVECs) and human osteoblast-like cells (MG63), respectively, imitating the vascular layer and bone tissue. Furthermore, the microfibers consist of an alginate-GelMA composite hydrogel in the middle and outer layers, and hyaluronic acid in the inner layer. The incorporation of GelMA reduces the concentration of alginate and improves the biocompatibility of the composite hydrogel, without altering the mechanical properties of the composite hydrogel. Topological hydrogel microfibers have been successfully used to mimic muscle-like bundles (Costantini et al., 2017; Miri et al., 2018; Bansai et al., 2019). Bansai et al. demonstrated that C2C12 muscle precursor cells reorganized their cytoskeleton and formed longitudinal myofibrillar-like structure when wrapped in the collagen-rich core of hydrogel core-shell microfibers (Bansai et al., 2019). Moreover, the alginate shell enhances the mechanical stability of the microfibers and promotes C2C12 cell elongation and myogenesis.

The structure, physical and chemical properties and biological effects of nanofiber scaffolds are of great significance to the development of tissue engineering scaffolds. Although some achievements have been made in the preparation and research of nanofiber materials, how to improve the preparation process, shorten the preparation period of materials, reduce the processing cost of materials, increase the porosity of scaffold materials and control the size and distribution of pore size needs further study. In addition, ECM contains both micron pores and nano-space. There is a synergistic effect between them, which provides the necessary space for cell planting, growth and ECM formation, and provides channels for oxygen and nutrition transmission, information transmission, gene expression and metabolite excretion. Therefore, the ideal scaffold not only needs to be composed of continuous nanofibers with sufficient mechanical properties, but also needs to contain both micro and nano spaces. But up to now, we still lack sufficient understanding of the optimal fiber diameter and its corresponding pore size and distribution, the ideal ratio of nano-space to micro-space, and the interaction between nano-space and body tissue. It is believed that in the future, with the development of nanotechnology and its continuous penetration in the field of tissue engineering, there will be a breakthrough in the design, preparation and performance regulation of nanofiber scaffolds.

3.2 Microspheres

Microspheres have become advanced functional materials used in a wide range of biomedical applications, such as researchers prepared microcapsules and microcarriers as a vehicle for drug delivery, summarized the recent progress of engineering particles and their emerging applications in biomedical delivery and diagnosis, and reviewed a comprehensive and in-depth insight into droplet microfluidics, covering fundamental research from microfluidic chip fabrication and droplet generation to the applications of droplets in bio (chemical) analysis and materials generation (Hernandez et al., 2010; Choi et al., 2017; Shang et al., 2017). It is suggested that the distribution of microsphere-sized particles is thought to be an important factor affecting the choice of drug delivery route and the rate of drug release. The properties of microspheres are closely related to their size, structure, and composition; therefore, it is essential to manufacture microparticles in a controlled manner to improve the reliability of their application (Tran et al., 2011; Duncanson et al., 2012; Thiele, 2017). Currently, most of the custom microspheres are manufactured by microfluidics and electrohydrodynamic co-jetting (Yeh et al., 2006; Dendukuri and Doyle, 2009; Seo et al., 2015). Moreover, microspheres can be prepared from a host of materials, including nature polymer (collagen, gelatin, hyaluronic acid) and synthetic polymer (PEG, PLGA, polyglycerol, poly (acrylic acid) and poly (acrylamide)) (Velasco et al., 2012; Rossow et al., 2017).

Microspheres produced by droplet microfluidics can be used as excellent drug delivery microcarriers. To ensure the effectiveness of drug encapsulation, it is necessary to select the material with great compatibility with the drug. For instance, chitosan-based microspheres enable ampicillin or bovine serum albumin (BSA) encapsulation (Yang et al., 2007; Xu et al., 2012). Microspheres with core-shell structure allows the drug to be encapsulated in the core, while the shell acts as a diffusion barrier and controls the release curve (Lee et al., 2017). In addition, microspheres with pH-responsive properties show great potential for targeted drug delivery. Core-shell alginate microspheres tolerate acidic environments and degrade in alkaline environments while releasing encapsulated substance for intestine-targeted drug delivery (Huang et al., 2014). Hydrogel microspheres are exciting platforms for cell culture, because they act as 3D matrices that mimic ECM (Shum et al., 2008; Velasco et al., 2012; Zheng et al., 2023). In addition, hydrogel microspheres with porous structures and the high surface-to-volume ratios are conducive to the exchange of oxygen and nutrients between cells and the external environment, while maintaining cell activity. These advantages allow for the potential use of cell-loaded hydrogel microspheres in the field of cell life research (Huang et al., 2017; Rossow et al., 2017), drug delivery (Shembekar et al., 2016; Agarwal et al., 2017; Zhao et al., 2021), and tissue

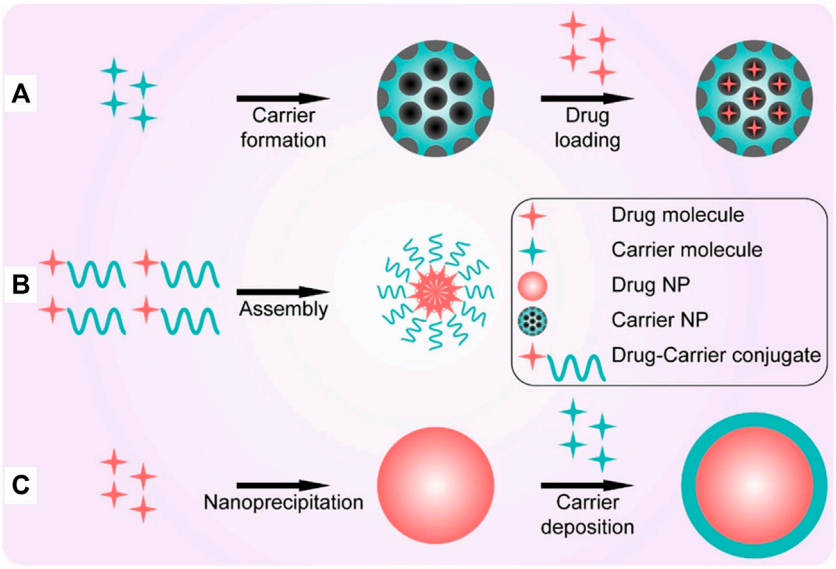

FIGURE 6
Three representative strategies for making high drug-loading nanoparticles. **(A)** Post-loading; **(B)** co-loading; **(C)** pre-loading (Liu et al., 2020).

engineering (Chung et al., 2012; Jiang et al., 2016). For instance, a 3D liver model made of heterotypic cells and core-shell microspheres was assembled (Chen et al., 2016). The layered assembly of hepatocytes in the core and fibroblasts in the outer shell leads to the formation of a spheroid of allotypic cells. The alginate shell allows the spheroid to be cultured for long periods, and the hepatocytes and fibroblasts to be spatially separated and co-cultured, which facilitates the expression of liver-specific functions. Furthermore, microspheres containing sensing components prepared by microfluidics have been used in sensing applications (Le Goff et al., 2015). Fluorescent polyacrylamide hydrogel microspheres are sensors with high sensitivity, biostability, durability, and injectability for continuous monitoring of *in vivo* blood glucose levels (Shibata et al., 2010).

However, there are still many problems in the preparation of microspheres, such as (1) the size of microspheres is difficult to be unified and the size distribution is uneven; (2) microspheres are easy to aggregate; (3) the preparation cost of microspheres is high. Therefore, it can be predicted that the future research trends of microspheres may be: (1) exploring how to unify the size of microspheres to improve the preparation efficiency; (2) choosing suitable methods to disperse the microspheres to prevent them from aggregation; (3) reducing the preparation cost of microspheres; (4) Further broadening the clinical application of microspheres.

3.3 Nanoparticles

Nanoparticles with high specific surface area and excellent encapsulation capabilities have a wide range of applications, including drug delivery, sensors, bioimaging, and catalytic and diagnostic systems (Chen et al., 2016; Li et al., 2017). Nanoparticle-based drug delivery systems offer significant advantages over traditional drugs, such as increasing drug solubility and stability, achieving controlled drug release, and overcoming biological barriers (Cui et al., 2016). The major classes of materials used to construct nanoparticles include lipid, polymers and inorganic materials (Ju et al., 2022).

Lipid nanoparticles (LNanoparticles), with a liposome-like structure, are widely used for the delivery of drugs (Mitchell et al., 2021; Eygeris et al., 2022). Nanoparticles can achieve drug loading in different ways including post-loading, co-loading, and pre-loading (Figure 6) (Liu et al., 2020). The efficacy of LNanoparticles for drug delivery, together with their simple synthesis, small size and serum stability, allow LNanoparticles to play an important role in personalized gene therapy, and in the penetration of the blood-brain barrier (Berraondo et al., 2019; Cheng et al., 2020; Hou et al., 2021).

Polymeric nanoparticles can be formed from natural or synthetic materials and monomeric or pre-polymeric polymers to effectively deliver a wide range of drugs, including hydrophobic and hydrophilic compounds, and carriers of varying molecular weights, allowing the precise control of the loading efficiency and release kinetics of these therapeutic agents by modulating properties such as composition, stability, reactivity, and surface charge (Caldorera-Moore et al., 2019; Knight et al., 2019; Zhang et al., 2020). PLGA has been approved by the FDA for its excellent biosafety, biodegradability and versatility, and is considered to be one of the most successful polymers in the biomedical field (Ulery et al., 2011; Martins et al., 2018; Niza et al., 2021). PLGA-based micro/nanoparticles have been used as carriers for small molecule and macromolecular drugs, with therapeutic benefits in diverse conditions such as diabetes or CNS related diseases (Bala et al., 2004; Rezvantalab et al., 2018; Essa et al., 2020; Ghitman et al., 2020). Furthermore, recent studies have proposed that PLGA itself can act as an active molecule. For instance, impaired lysosomal acidification occurs in neurodegenerative diseases, leading to lysosomal dysfunction (Udayar et al., 2022). This negative effect can be offset by the products of PLGA cleavage, such as lactic acid and

glycolic acid (Bourdenx et al., 2016; Zeng et al., 2019). Bourdenx et al. demonstrated that restoration of lysosomal function significantly reduced substantia nigra dopaminergic neurodegeneration (Bourdenx et al., 2016). Moreover, Paul et al. verified that PLGA nanoparticles could inhibit Aβ aggregation and improved the cell survival rate of cortical neurons in Aβ1-42 treated mice (Paul et al., 2022).

With the increase in research on silk sericin, it was found that silk sericin has remarkable biological functions and can be used as a potential biomaterial (Liu et al., 2022). Numerous studies have indicated that silk sericin has low immunogenicity and does not cause significant immunoreaction (Chouhan and Mandal, 2020; Siavashani et al., 2020; Ode Boni et al., 2022). In addition, silk sericin with antioxidant properties has been shown to regulate glycolipid metabolism and promote the proliferation of various cell types while maintaining their functions (Kato et al., 1998; Ersel et al., 2016; Jena et al., 2018). Due to their good bioactivity and biocompatibility, sericin-based nanomaterials are currently being widely used in tissue engineering. Sericin-based nanoparticles act as nanocarriers for insoluble molecules, providing curative effects and reducing side effects (Kanoujia et al., 2016; Suktham et al., 2018). In addition to being a drug carrier, silk sericin serves as a biomineralization matrix (Wang et al., 2017; He et al., 2017; Chaisabai et al., 2018; Tian et al., 2020). For instance, nucleation of hydroxyapatite (HA) crystals can be mediated by using sericin as a template (Yang et al., 2014).

Inorganic materials can be designed in a wide range of sizes, structures, and geometries, and for various drug delivery and imaging applications (Mitchell et al., 2021). $CaCO_3$ nanoparticles have the characteristics of biocompatibility and biodegradability, and controlled synthesis and easy functionalization (Trofimov et al., 2018). In addition, as a porous microcarrier, $CaCO_3$ nanoparticles can be used for drug delivery. Animal and clinical studies have shown that nasal delivery of porous $CaCO_3$ microcarrier can rapidly and effectively control blood glucose levels in diabetic patients (Haruta et al., 2003). No drug loss was observed when nifedipine, ibuprofen and other drugs with poor water solubility loaded onto $CaCO_3$ nanoparticles (Preisig et al., 2014). In addition, Ca^{2+} produced by the decomposition of $CaCO_3$ may serve as exogenous calcium sources to promote tissue repair, such as bone formation (Combes et al., 2006; Zhong et al., 2016).

Iron oxide is a commonly studied inorganic material and nanomedicines made from iron oxide nanoparticles are approved by the FDA (Bobo et al., 2016). Magnetic iron oxide nanoparticles consisting of magnetite (Fe_3O_4) or maghemite (Fe_2O_3) have superparamagnetic properties at specific sizes and have shown excellent promise as drug delivery carriers, contrast agents and thermotherapy agents (Arias et al., 2018). As common inorganic nanoparticles, silicon quantum dots are mainly used as unique nanoparticles for imaging applications *in vitro*, but they show prospect for *in vivo* diagnostics (Xu et al., 2019; Huang et al., 2020). Due to the different oxidation states of cerium (Ce^{3+}/Ce^{4+}), cerium oxide (CeO_2) nanoparticles have excellent resistance to oxidation, which has been reported in the treatment of diseases, such as spinal cord injury, inflammation, sepsis and Alzheimer disease (AD) (Selvaraj et al., 2015; Kwon et al., 2016; Kim et al., 2017). For instance, in a mouse model of AD, small and positively charged CeO_2 nanoparticles conjugated with triphenylphosphonium attenuated neuronal death, alleviated mitochondrial damage, and reduced reactive gliosis by scavenging reactive oxygen species (ROS) (Kwon et al., 2016).

3.4 3D printing scaffold

Modulation of macro, micro and nano structures can be achieved by bioprinting strategies (Tarassoli et al., 2018; Chakraborty et al., 2022). 3D bioprinting enables the rapid and precise spatial patterning of cells, growth factors and biomaterials to create complex 3D tissue structures (Matai et al., 2020; Kim et al., 2021). The printed structures should have excellent biocompatibility, great mechanical and biomimetic properties. To achieve this, a variety of bioinks are used for bioprinting, such as fibrinogen, agarose, alginate, collagen, gelatin, hyaluronic acid, pluronic or poly (ethylene glycol) (Shao and Vollrath, 2002; Muller et al., 2015; Wang et al., 2015; Axpe and Oyen, 2016; Mandrycky et al., 2016).

3D porous polymer scaffolds have been used to generate substitutes for skin tissue. A 3D bioprinted skin tissue model was developed using silk fibroin-gelatin (SF-G) bioink and human dermal fibroblasts, keratinocytes and melanocytes (Admane et al., 2019). The 3D bioprinted structure mimics the morphology of the dermal-epidermal junction and replicates the mechanical properties and biochemical characteristics of human skin, ultimately facilitating full-thickness wound healing (Xiong et al., 2017; Admane et al., 2019). In addition, 3D bioprinted skin tissue equivalents serve as *in vitro* models to test the biosafety of pharmaceuticals and cosmetics, contributing to the study of cell signaling and physiological response mechanisms (Chakraborty et al., 2022).

Multiple causes, such as trauma, can lead to bone defects. However, no consistent results have been achieved in terms of bone replacement in current bone tissue engineering strategies. Although it is challenging to simulate the complex anatomical structure and functional dynamics of native bone, 3D bioprinting can be a potential method for bone tissue replacement (Kacarevic et al., 2018). For instance, 3D printed scaffolds through combining SF, gelatin, hyaluronic acid and tricalcium phosphate (TCP) can support osteogenic differentiation of human adipose-derived mesenchymal stem cells (Du et al., 2019). It has also been shown that bioprinted BMSC-loaded GelMA/SFMA scaffolds can promote bone repair through vascularized osteogenesis (Yang et al., 2022). The microstructure of intervertebral disc is complex, which can be simulated by 3D printing technology. 3D printing of flexible polylactic acid (FPLA) can be used to fabricate a viscoelastic scaffold with tunable biomimetic mechanics for whole spine motion segment applications (Marshall et al., 2021).

Although 3D printing technology has many advantages that other materials cannot achieve, the types of printing materials are still limited, which is the main bottleneck that hinders the development of 3D printing technology. At present, the main way of 3D printing is to print materials in the form of “ink” and quickly solidify them. Therefore, while “ink” has good biocompatibility and biodegradability of general biomaterials, it should also be considered that after printing, it still needs to maintain its original biological activity and mechanical strength,

which greatly limits the application scope of 3D printing. The existing 3D printing equipment also has low printing precision and cannot meet the bionic requirements of tissues and organs.

3.5 Others

3.5.1 Micro-/nano-structured smart hydrogels

Smart hydrogels, a cross-linked polymer, can respond to small changes in environmental stimuli by significantly altering their volumes and other physico-chemical properties. The uniqueness of these hydrogels lies in their non-linear feedback. They respond to external stimuli primarily through reversible, intensity-scalable, repeatable and predictable phase volume shifts and are able to return to their original state after the stimulus has been removed. These transformations include changes in physical state and hydrophilicity, etc (Bordbar-Khiabani and Gasik, 2022). In addition, the flexibility of different response behaviors in response to different stimuli is important for broadening the application of smart hydrogels in various conditions. It is worth noting that micro-/nano-structured smart hydrogels show higher elasticity and respond faster and stronger to external stimuli than smart hydrogels without micro-/nano-structures (Wang et al., 2021).

Poly (N-isopropyl acrylamide) (PNIPAM) hydrogels are commonly used thermal responsive hydrogels with reversible swelling/contraction changes when the temperature is varied within the volume phase transition temperature (VPTT) range. In general, PNIPAM hydrogels formed by chemical crosslinking of N, N′-methylenebisacrylamide (BIS) and monomer N-isopropylacrylamide (NIPAM) have a slow response and poor elasticity. However, when PNIPAM nanogels with unsaturated C=C bonds are used to cross-link PNIPAM chains, micro/nanostructured PNIPAM hydrogels with remarkable elastic and responsive properties can be obtained (Xia et al., 2013). The transition from the fully swollen to the fully collapsed state of the nanogel cross-linked hydrogel takes only 6 min, much faster than the normal PNIPAM hydrogels. Moreover, the swelling ratio of nanogel cross-linked hydrogel is 10 times that of the normal PNIPAM hydrogel. In addition to responsive volume changes, smart hydrogels can achieve various stimuli responses (Isapour and Lattuada, 2018; Wen et al., 2019; Jia et al., 2021). For instance, it is often possible to obtain smart hydrogels with responsive color changes by designing colloidal nanocrystal structures in their polymer networks (Jia et al., 2021). BIS and graphene oxide nanosheets with photothermal properties can be used as double crosslinking agents to produce PNIPAM hydrogels with micron-scale network. This double cross-linked hydrogel allows ultra-high stretchability and rapid volume phase transition in response to NIR light (Wang et al., 2022).

3.5.2 Micro-/nano-scale liquid metal

As a new biological material, liquid metal (LM) has shown promising prospects in the biomedical field, such as tissue therapeutics, repair, bioimaging, and biosensors (Yan et al., 2018; Zeng and Fu, 2018; Miyako, 2021). LM with preeminent deformability can be molded into various shapes with different properties to cope with diverse application scenarios (Wang et al., 2018; Sun et al., 2019). In addition, the morphology of LM changes significantly in response to external stimuli such as pH, light, temperature, and magnetic fields. Additionally, the morphological changes induced by stimuli can help to expand the application of LM in drug delivery, thermotherapy and antimicrobial therapy (Wang et al., 2022) (Figure 7). For instance, LM nanoparticles generally have an oxide layer on their surface, which is due to self-limiting oxidation. The oxide layer can react with protons and dissolve in an acidic environment. Therefore, drug release from LM can be facilitated in an acidic microenvironment due to the removal of the oxide layer (Lu et al., 2015). Furthermore, under NIR irradiation, the shape of polydopamine (PDA)-coated LM nanoparticle changes from spheres to ellipsoids (Gan et al., 2019). Based on this transformation, the prepared LM nanorobots exhibit excellent photothermal properties and can be used for photothermal antibacterial therapy (Xu et al., 2021). LM with good biocompatibility has emerged as a potential material for tissue repair, including bone defect repair and nerve connectors (Yi et al., 2014; Liu et al., 2016; He et al., 2021). LM used in biomedicine generally include gallium (Ga) and its alloys, which can achieve solid-liquid transition at relatively low temperatures to satisfy the needs of different application environments via the component modulation. Kinds of Ga-based biomaterials such as Ga droplets and Ga-based hybrids show low toxicity in aqueous environments and mice bodies. At the same time, Ga-based LM possess good degradability in acidic biological environments, thus helping to reduce their potential systemic toxicity. In particular, Ga ions also exhibit antibacterial abilities and can be used to treat bacterial infections. In addition, an actuator using LM based on Ga can circumvent the problems of conventional actuators such as high drive potential, low strain and their time responsiveness. Thus, Ga and its alloys have great potential for tissue engineering applications (Wang et al., 2022).

4 Applications of micro/nano-structured materials for tissue regeneration

Micro/nanomaterials can simulate the microstructure of tissues and can also be used as carriers of drugs and growth factors. Research on micro/nanomaterials in tissue repair and regeneration is gaining increasing attention. Micro/nanomaterials play a very important role in the treatment of bone defects, cartilage injuries, cardiovascular diseases, skin injuries, intervertebral disc degeneration, and other diseases.

4.1 Bone

Bone tissue defect is caused by trauma, tumor and other diseases, and has become a common clinical disease. Currently, the use of orthopedic implants is an available option for treating these diseases. The use of bone grafts is on the rise, with more than 2.2 million cases of bone grafting worldwide each year (Wang and Yeung, 2017). In recent years, the development of nanotechnology, biomaterial science and tissue engineering has provided a broad prospect for the preparation of bone graft materials (Liu et al., 2022). Natural bone tissue has a unique structure, mainly composed of collagen, nanofibrils and nano-hydroxyapatite (Laubach et al., 2022). The use of micro-nanomaterials can play a key role in accelerating cell

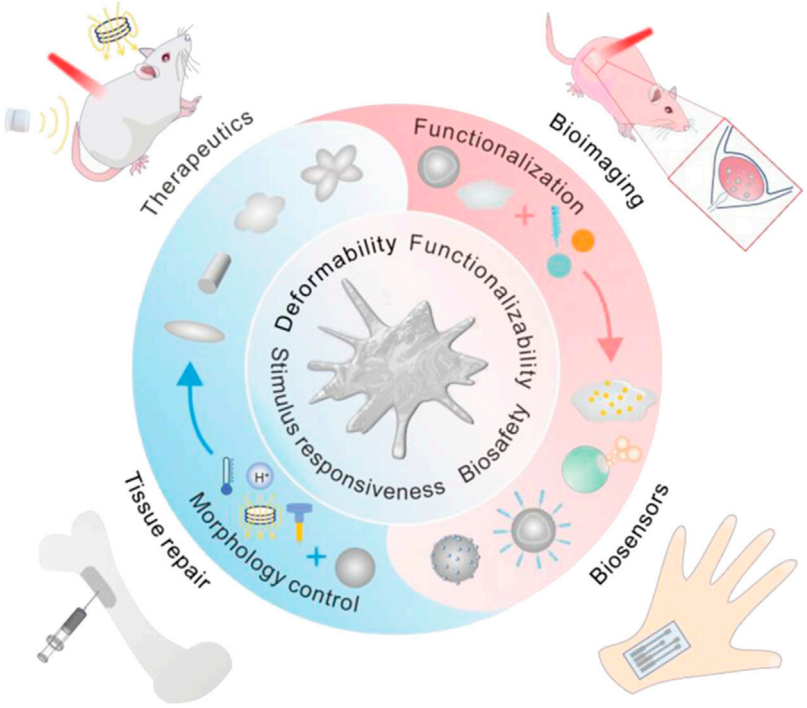

FIGURE 7
Schematic illustration of advantages and design of LM and their applications in biomedicine (Wang et al., 2022).

responses and guiding tissue regeneration. Therefore, it is necessary to construct bone tissue engineering scaffolds with consideration of aspects such as surface morphology, mechanical strength, and regulation of bioactive molecules. As a 3D scaffold for cells, bone tissue engineering scaffolds provide cells with the unique microstructure and microenvironment of bone tissue to maintain the survival and differentiation of cells (Park et al., 2016).

Nanofiber scaffold is a commonly used scaffold for bone tissue engineering (Shalumon et al., 2015). Biomimetic composite scaffold of HA/gelatin-chitosan core-shell nanofibers has been used for bone regeneration, as it can mimic both the specific structure and the chemical composition of natural bone. MG-63 was seeded on the nanofibers and it was proved that the nanofibers could enhance osteoblast cell proliferation (Chen et al., 2019). Incorporation of dual factors, HA, and laminin within the shell and core of nanofibers respectively via emulsion electrospinning is another method of fabricating core-shell nanofibers. Nanofibers play important roles in osteoblast proliferation and maturation (Tian et al., 2013). Electrospun core-shell nanofibers loaded with metronidazole (MNA) and nano-hydroxyapatites (nHA) have both anti-infection and osteogenesis capabilities (Wang et al., 2019). Another type of core-shell nanofiber can incorporate an osteogenic inductive peptide H1, derived from the cysteine knot (CT) domain of CTGF, in the core of SF and co-deliver HA from the shell of poly (L-lactic acid-co-ε-caprolactone) (PLCL). It can promote proliferation and osteoblastic differentiation of human induced pluripotent stem cell-derived mesenchymal stem cells (hiPS-MSCs). *In vivo* experiments further verified that SF-H1/PLCL-HA core-shell nanofibers can promote the repair of bone defects (Xu et al., 2019). Platelet-rich plasma (PRP) can be incorporated into SF/PCL/PVA nanofibers by coaxial electrospinning to avoid the rapid degeneration of the growth factors, and this core-shell nanofiber can release multiple growth factors to promote bone regeneration (Cheng et al., 2018). BMP-2 is a growth factor commonly used in bone tissue engineering to promote bone regeneration. The core-shell nanofiber scaffolds can work as a sustained delivery vehicle for BMP-2 protein. The controlled release of BMP-2 can effectively promote the regeneration of bone tissue (da Silva et al., 2019). BMP-2 and other drugs or growth factors are often co-encapsulated in the core-shell nanofiber scaffold to promote bone regeneration. BMP-2 and dexamethasone (DEX) were successfully incorporated into PLLACL/collagen nanofibers by means of coaxial electrospinning. The controlled release of the two growth factors from PLLACL/collagen nanofibrous mats can induce hMSC to differentiate into osteoblasts for bone tissue engineering (Su et al., 2012). Zein/PLLA nanofibers can also be fabricated to load BMP-2 and DEX. It can achieve the burst release of DEX and sustained release of BMP-2. It can enhance the osteogenic differentiation of MSCs and has great potential in bone tissue engineering applications (Li et al., 2018). Core-shell SF/PCL/PVA nanofibrous mats using coaxial electrospinning and layer-by-layer (LBL) techniques, where BMP-2 was incorporated into the core of the nanofibers and CTGF was attached onto the surface were also fabricated. According to the physiological needs of bone regeneration, this core-shell nanofiber scaffold induced sustained release of BMP-2 and sudden release of CTGF. *In vivo* experiments found that this scaffold has the largest bone repair area, and the new

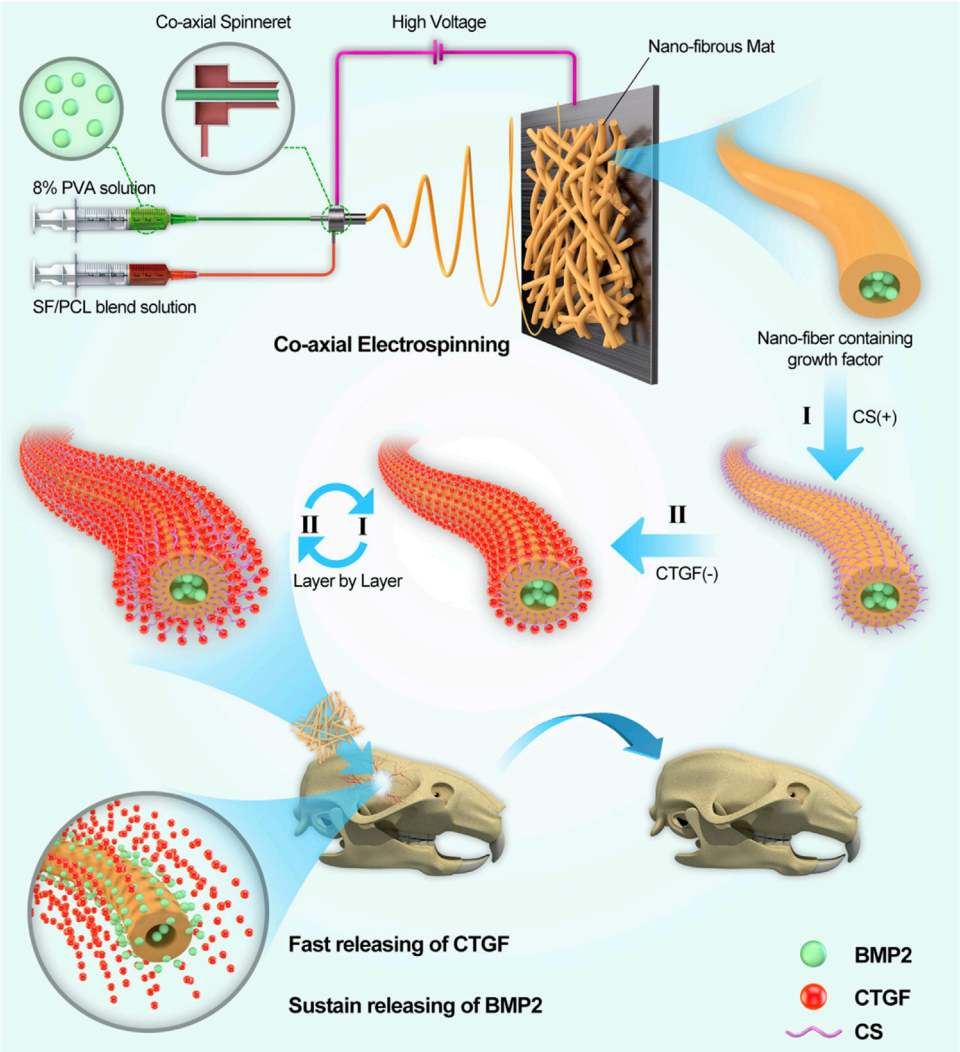

FIGURE 8
Schematic illustration of the $(SF/PCL)_{1:5}$/PVA-LBL20 coaxial fibers loaded with BMP2 and CTGF for bone tissue engineering (Cheng et al., 2019).

bone formed has the same tissue structure as normal bone. Therefore, it can provide a promising strategy to facilitate bone healing (Figure 8) (Cheng et al., 2019). The mechanical properties of bone repair materials are required. Studies have shown that nHA and Fe_3O_4 nanoparticles can improve the mechanical properties of materials and further promote the repair and regeneration of bone tissue (Zhao et al., 2019).

3D printing technology is considered to be an advantageous technology, which can also be used to construct simulated bone tissue microstructure. In addition, scaffolds produced through 3D printing can provide excellent delivery vehicles for topical, continuous delivery of drugs and/or biomolecules. PLA/PCL/HA composite bone scaffold prepared by 3D printing can effectively simulate the microstructure of bone and has good biocompatibility (Hassanajili et al., 2019). Hierarchical porous and recombinant human bone morphogenetic protein-2 (rhBMP-2)-loaded calcium phosphate (Ca-P) nanoparticle/poly (L-lactic acid) nanocomposite scaffolds can also be fabricated by 3D printing, in which sustained releases of Ca^{2+} ions and rhBMP-2 can be achieved (Wang et al., 2017).

Microspheres and nanoparticles are also widely used in bone tissue engineering because of their good injectability and drug-controlled release ability and etc. nHA microspheres prepared via a hydrothermal transformation method significantly improved the ability of the microspheres to adsorb the bioactive protein (BMP-2) and realize bone regeneration (Zhou et al., 2018). rhBMP-2 can be grafted on the surface of mesoporous bioglass nanoparticles (MBGNs) with an amide bond. It can realize the rhBMP-2 release in a controllable program during the early bone regeneration period and then sustained release of calcium and silicon ions to keep promoting osteogenesis in a long term (Xin et al., 2020).

LM have good biocompatibility, deformability, good electrical and thermal conductivity and have become a potential material in the field of tissue repair. Severe bone defects caused by some diseases, such as bone tumors and external trauma, often require

bone repair materials to replace the missing bone. Bismuth (Bi) alloys can be introduced as a bone defect repair material (bone cement) to fill the defect locations. Bi alloys have a low melting point and can be solidified at low temperatures to avoid damage to normal tissue. At the same time, the Bi alloys with its strong magneto-thermal effect can be utilized to alleviate mechanical and thermal pain sensitivity, so pain is relieved. This bone cement has a high affinity to bone and does not move significantly after implantation. Furthermore, the Bi alloys exhibited excellent imaging ability (Wang et al., 2022). In summary, LM have potential application in the field of tissue repair due to their unique advantages.

4.2 Cartilage

Cartilage lesions and defects caused by trauma, tumors, and inflammation are more common in the clinic. Cartilage is a tissue without blood vessels and nerves (Mow et al., 1992; Ahmed and Hincke, 2010; Gu et al., 2023), and it is extremely difficult to repair itself after injury, which seriously affects the health of patients. At present, cartilage defects can be repaired and reconstructed by cartilage tissue transplantation, chondrocyte or mesenchymal stem cell transplantation, and biomaterial filling. However, these methods have certain limitations, such as limited sources of autologous cartilage and allogeneic cartilage rejection (Haq-Siddiqi et al., 2023). Therefore, repair of cartilage defects and functional reconstruction are still difficult problems in surgical treatment. In recent years, the rapid development of tissue engineering technology has provided new directions for solving the above problems (Ma et al., 2005). Nanofibers loaded with growth factors can combine with seed cells to repair and regenerate cartilage tissue. Kartogenin (KGN) is a newly discovered small molecule compound that has a strong ability to promote cartilage differentiation and can effectively promote the differentiation of mesenchymal stem cells into chondrocytes (Xu et al., 2015). Coaxial electrospun fibers using poly (L-lactic acid-co-caprolactone) and collagen solution as shell fluid and KGN solution as core fluid was fabricated via coaxial electrospinning. KGN encapsulated in the core-shell nanofibers can be sustainedly released for about 2 months. The chondrogenic differentiation of bone marrow mesenchymal stem cells cultured on core-shell nanofibrous scaffold was promoted obviously (Yin et al., 2017). KGN can also be loaded into microspheres via microfluidics to realize the sustained release and eventually repair the cartilage (Wu et al., 2020). An injectable double positively charged functional hydrogel microsphere with “targeting cartilage extracellular matrix”, “cartilage penetration”, and “cellular phagocytosis” can also be designed for matching the structural characteristics of joints and addressing the difficulties of drug delivery in cartilage (Lin et al., 2022). Cartilage repair requires a large supply of cells, therefore microspheres can also be used as injectable cell carriers for cartilage tissue engineering (Li et al., 2023) (Figure 9).

4.3 Vessel

In recent years, cardiovascular diseases have become one of the most serious diseases that threaten human health (Tan et al., 2013). When vascular disease reaches the end stage, it is often necessary to use biologically active blood vessels for transplantation or bypass (Ezhilarasu et al., 2019). Due to the limited sources of autologous blood vessel transplantation and the limitations of their own vascular conditions, many of artificial blood vessel replacements are clinically required (Weinberg and Bell, 1986; Jia et al., 2013). In the past, various methods of allogeneic vascular transplantation have been tried, but their long-term effects were poor, including increased thrombosis, vascular degeneration and hyperplasia, and vascular stenosis. The introduction of tissue engineering in recent years have provided new options for this clinical problem. Based on cell biology, material science, and engineering as the basic theory, it can culture and expand seed cells *in vitro* and plant them in biocompatible organisms. A cell–biomaterial complex is formed and implanted in the body to replace tissue defects caused by diseases and trauma, in order to promote the repair and functional reconstruction of the host tissue structure (Wu et al., 2010; Fu et al., 2014). Micro/nano-materials can mimic the microstructure of blood vessels, regulate the microenvironment, and provide biological signals for blood vessel regeneration.

Nanofiber scaffolds are commonly used in vascular tissue engineering. Many studies have shown that it plays an important role in the repair and regeneration of blood vessels (Merkle et al., 2015a). Nanofiber scaffold can simulate the structure of blood vessels. PCL/collagen scaffold prepared via coaxial electrospinning was a suitable scaffold for vascular regeneration. PCL as the core can provide the mechanical property and integrity while collagen as the shell can improve the attachment and proliferation of vascular cells due to its excellent biocompatibility. The collagen shell was crosslinked by genipin and further bound with heparin. The scaffold can support the attached vascular cells to grow and proliferate on its surface, and also allows the infiltration of SMCs into its interior. The heparinized PCL/collagen scaffold with core/shell fiber structure has a promising application in vascular tissue engineering (Duan et al., 2016). Coaxial electrospun PCL/Gelatin-MA fibers which are composed of a PCL core and a functionalized gelatin (GelMA) shell were also proved to be suitable for vascular regeneration (Coimbra et al., 2017). Core-shell PVA/Gelatin electrospun nanofibers promote vascular tissue regeneration due to the potential of altering the proliferation and migration of HUVECs and rat smooth muscle cells (rSMC) (Merkle et al., 2015b). Highly aligned hyaluronan/PLLA nanofibers in core-shell structure were also reported to be an optional vascular graft (Yuan et al., 2016). The hollow microfibers created by microfluidic technology may simulate the structural characteristics of blood vessels. The scaffold is also biocompatible, allowing cells to proliferate and spread within the tube (Jia et al., 2019) (Figure 10).

4.4 Skin

Skin trauma, especially large-area full-cortex trauma is still one of the main diseases. The methods of accelerating the healing of the wound surface and reducing the occurrence of scars remain a clinical problem (Chaudhari et al., 2016; Yao et al., 2017). Skin transplantation is the primary method of treating such skin trauma, but patients with large-scale skin defects or skin burns who receive their own skin transplantation will have new wounds on the skin from other areas. The shortage of autologous skin supply is

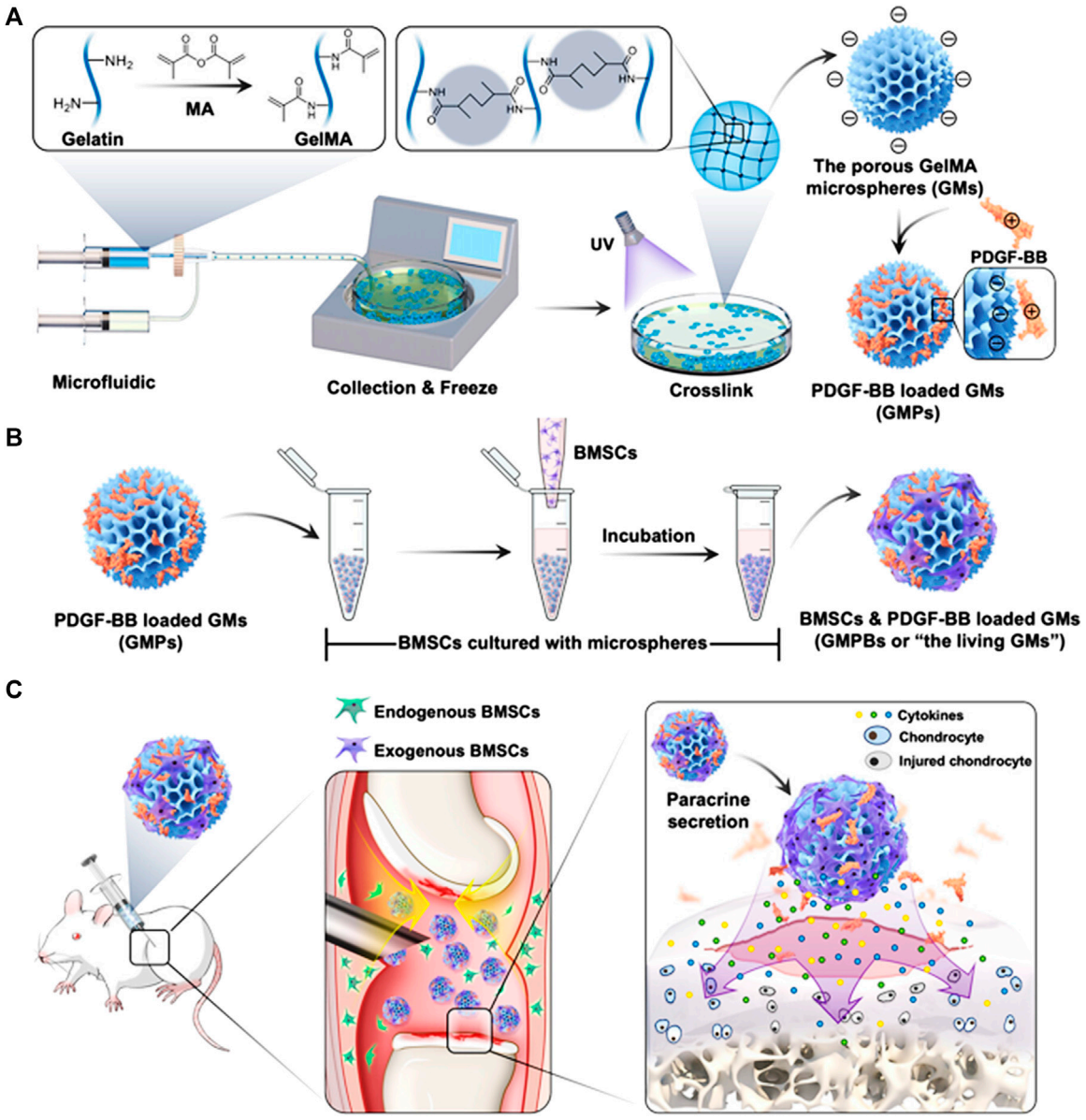

FIGURE 9
Schematic illustrations of the living GMs for cartilage regeneration. **(A)** The fabrication of GMs using microfluidic technology, and incorporation of PDGF-BB via the electrostatic force to engineer GMPs. **(B)** The BMSCs and PDGF-BB loaded GMs, or "the living GMs" were further developed through incubation with exogenous BMSCs. **(C)** The living GMs were injected into the joint cavity of the DMM rat. The enhanced paracrine activity was achieved by integrating the endogenous and exogenous regeneration mechanisms (Li et al., 2023).

another major factor that limits its application (Wu et al., 2021). Tissue-engineered skin organically combines engineering and life science principles to build skin replacements that improve, maintain, and restore function of the skin, and is expected to solve problems such as insufficient donor skin in repairing skin defects (Dai et al., 2004; Groeber et al., 2011; Li et al., 2023).

The nanofiber scaffold as an important part of skin tissue engineering provides a feasible method for promoting wound healing (Movahedi et al., 2020). Compared with traditional wound dressings, nanofibers have remarkable properties as dermal substitutes, because their structures are very similar to the skin's primary ECM, and cells can adhere, proliferate, and permeate scaffolds, inducing the regeneration of skin. Lawsone (2-hydroxy-1,4-naphthoquinone) was electrospun in polycaprolactone-gelatin (PCL/Gel) polymers in core-shell architecture to detect the effect of new core-shell nanofibers on wound regeneration. The core-shell nanofibers-encapsulated lawsone prolonged the release of lawsone over a period of 20 days. Moreover, it can promote cell adhesion and proliferation and promote the expression of healing-related genes. *In vivo* experiments further demonstrated that it has a strong promotion effect on wound healing (Adeli-Sardou et al., 2019). Hyaluronic acid-silk fibroin/zinc oxide (ZO) nanofibers can be used

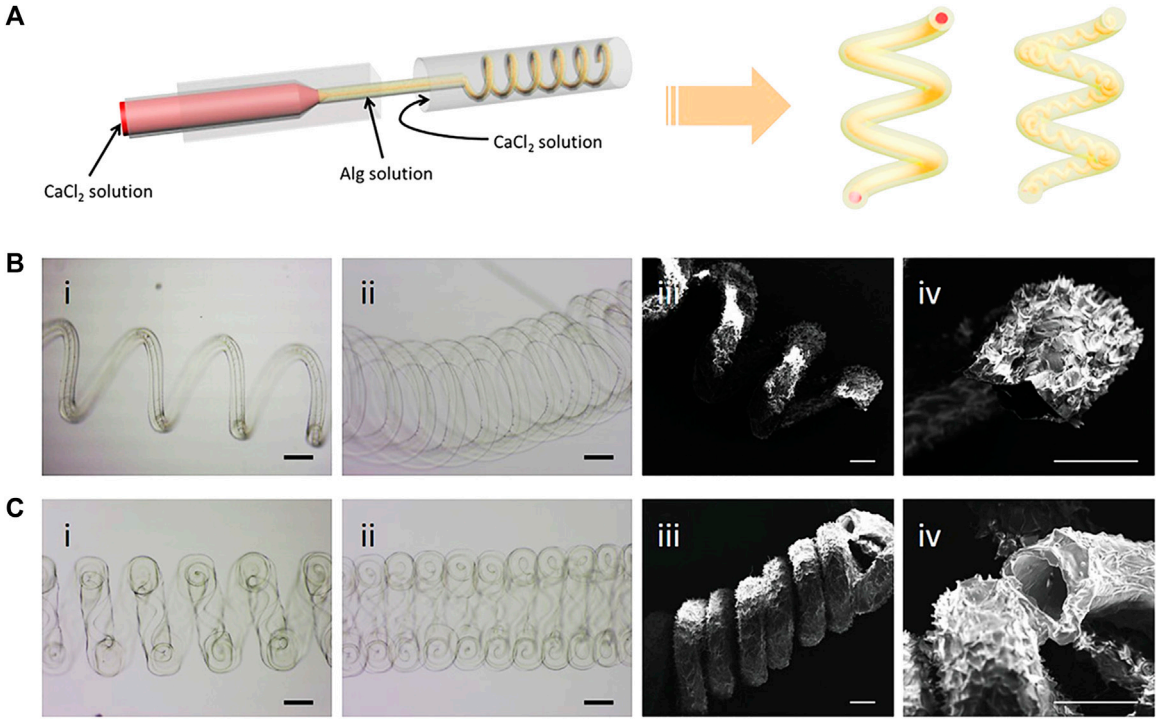

FIGURE 10
Generation of helical hollow alginate hydrogel microfibers with different channels. **(A)** Schematic illustration of the fabrication of the helical hollow microfibers. **(B, C-i, ii)** Optical microscopy and iii, iv) SEM images of helical hollow microfibers with **(B)** straight and **(C)** helical channels. Scale bars, 200 μm (Jia et al., 2019).

in the treatment of burn injuries. ZO as an antibacterial agent can be released sustainedly from the nanofibers. Nanofibers with appropriate ZO loading can effectively inhibit the inflammatory response at the injury site and promote wound healing (Hadisi et al., 2020). Single or multiple growth factors or drugs can be loaded into the core-shell nanofibers in order to achieve the slow release of growth factors and promote wound healing. CTGF is a signaling molecule that has multiple roles in tissue repair and regeneration. CTGF encapsulated electrospun dual porous PLA-PVA core-shell fiber based membranes can be used as excellent wound dressing mats for the treatment of diabetic wounds and other chronic ulcers due to the promotion of cell proliferation, migration and angiogenic potential (Augustine et al., 2019). Biodegradable and biocompatible scaffolds incorporated with multiple epidermal induction factors might serve as the most promising medical devices for skin tissue regeneration. Other studies have shown that aligned nanofiber scaffolds can mimic skin microstructure and induce macrophage M2 polarization (Xie et al., 2022).

The rise of 3D printing technology also provides a new method for the construction of skin tissue engineering scaffolds. Different 3D printing technologies can be used to construct stents with different diameters. 3D printing scaffolds have good biocompatibility and are suitable for cell proliferation and differentiation (Gao et al., 2021). According to the shape and depth of the wound, the 3D printing technology can print out biomaterial suitable for the wound. Scaffolds can also flexibly and accurately load different drugs and growth factors to promote tissue regeneration. Skin tissue can even be printed *in situ* on the wound surface using the layer-by-layer deposition principle (Weng et al., 2021). The integration of electronic skin (e-skin) and tissue has the potential to improve the quality of life for people in the areas of healthcare monitoring and chronic disease treatment. Ga-based alloys can be used to design gluten protein for fabricating e-skin with stretchability, self-healing ability, and biocompatibility. In addition, based on the incorporation of Ga-based alloys, the e-skin obtained has a stronger self-healing ability, and in animal experiments there are no adverse reactions when the e-skin is attached to the skin of rabbits. And in a variety of situations, from large-scale human movement to small strain changes, the e-skin shows a keen ability to sense strain. Therefore, LM-prepared electronic skin has great potential for sensing human movement (Chen et al., 2022).

4.5 Annulus fibrosus

Disc herniation is a common disease and one of the main causes of neck and low back pain, which seriously affects the quality of life of patients (Xia et al., 2023). At present, there is no effective means to directly repair damaged AF in clinical practice, and the simple removal of herniated intervertebral disc tissue cannot repair the AF defect at the same time, which has a certain postoperative recurrence rate. Although interbody fusion can treat disc herniation with intervertebral instability and prevent recurrence of disc

herniation, loss of intervertebral motion and adjacent segment retreat have become new problems. Therefore, there is an urgent need for AF tissue engineering in clinical practice. The microstructure of AF is a typical angle-ply laminated structure, and this special microstructure also guarantees its good mechanical properties. Aligned nanofibers can simulate the microstructure of AF, which brings great hope for the construction of AF tissue engineering. A novel aligned core-shell nanofibrous scaffold with angle-ply microstructure and co-delivery capacity can achieve burst release of ibuprofen to regulate the microenvironment, and sustained release of TGFβ3 to promote ECM secretion. In addition, it can repair the damaged AF and also realize regeneration of IVD (Han et al., 2022). Micro-nano scaffolds constructed by 3D printing technology can also reproduce the special angle-ply laminated structure of the AF, which is conducive to the growth and proliferation of cells, and can also provide good mechanical support (Bhunia et al., 2021).

5 Conclusion and future perspectives

This article reviewed the research progress of biomimetic micro/nano-materials prepared by different methods for the repair and regeneration of different tissues and organs. Common strategies for preparing nanofibers, microspheres and 3D-printing scaffolds were reviewed in order to elucidate the importance of material selection and 3D structure design for tissue repair and regeneration. To date, a large number of studies have shown that using micro/nanomaterials to mimic the microstructure of tissues can promote the repair and regeneration of tissues. Researchers have also modified the surface of scaffolds in multiple ways to adjust the hydrophilicity, adhesion, and mechanical properties of scaffolds. Additionally, studies have shown that these micro- and nano-structured scaffolds can also load drugs, ensuring both the biological activity of drugs and controlled drug release. However, it is not easy to prepare 3D scaffolds with suitable mechanical properties, porosity, surface morphology, degradation rate, and microstructure simulation. The accuracy of existing micro/nanomaterials is limited, and the microstructure of tissues and organs is complex. Therefore, it is still difficult to precisely mimic the microstructure. In addition, the existing micro/nanomaterials focus on the simulation of the microstructure and ignore the simulation of their components, which is another major problem of tissue engineering. The application of micro/nanomaterials is still in its infancy, and there are still many problems to be solved in clinical application such as the way of constructing an ideal cell-nanomaterial interface; preventing immune system, maintaining the survival rate and function of cultured cells for a long time, improving the biocompatibility of nano-materials. It is important to solve the above problems to prepare micro/nano "smart" materials with specific functions to better regulate the biological behaviors such as specific adhesion, proliferation and directional differentiation of seed cells, so as to obtain good biological activity and good biocompatibility and finally apply them to clinic.

Author contributions

FxH conceived and designed the review. FH and QM wrote the manuscript. EX, KL, JH, QC, and JL all participated the data search and analysis. FxH assisted with the revision of this article. All authors contributed to the article and approved the submitted version.

Funding

This work was supported by the National Natural Science Foundation of China (32130059 and 32171350), Medical and Health Science and Technology Innovation Project of Suzhou (SKY2022105), and the Priority Academic Program Development of Jiangsu Higher Education Institutions.

Conflict of interest

The authors declare that the research was conducted in the absence of any commercial or financial relationships that could be construed as a potential conflict of interest.

Publisher's note

References

Adeli-Sardou, M., Yaghoobi, M. M., Torkzadeh-Mahani, M., and Dodel, M. (2019). Controlled release of lawsone from polycaprolactone/gelatin electrospun nano fibers for skin tissue regeneration. *Int. J. Biol. Macromol.* 124, 478–491. doi:10.1016/j.ijbiomac.2018.11.237

Admane, P., Gupta, A. C., Jois, P., Roy, S., Chandrasekharan Lakshmanan, C., Kalsi, G., et al. (2019). Direct 3D bioprinted full-thickness skin constructs recapitulate regulatory signaling pathways and physiology of human skin. *Bioprinting* 15, 00051. doi:10.1016/j.bprint.2019.e00051

Agarwal, P., Wang, H., Sun, M., Xu, J., Zhao, S., Liu, Z., et al. (2017). Microfluidics enabled bottom-up engineering of 3D vascularized tumor for drug discovery. *ACS Nano* 11 (7), 6691–6702. doi:10.1021/acsnano.7b00824

Ahmed, T. A., and Hincke, M. T. (2010). Strategies for articular cartilage lesion repair and functional restoration. *Tissue Eng. Part B Rev.* 16 (3), 305–329. doi:10.1089/ten.TEB.2009.0590

Arias, L. S., Pessan, J. P., Vieira, A. P. M., Lima, T. M. T., Delbem, A. C. B., and Monteiro, D. R. (2018). Iron oxide nanoparticles for biomedical applications: A perspective on synthesis, drugs, antimicrobial activity, and toxicity. *Antibiotics* 7 (2), 46. doi:10.3390/antibiotics7020046

Augustine, R., Zahid, A. A., Hasan, A., Wang, M., and Webster, T. J. (2019). <p> CTGF loaded electrospun dual porous core-shell membrane for diabetic wound healing</p>. *Int. J. Nanomedicine* 14, 8573–8588. doi:10.2147/ijn.S224047

Axpe, E., and Oyen, M. L. (2016). Applications of alginate-based bioinks in 3D bioprinting. *Int. J. Mol. Sci.* 17 (12), 1976. doi:10.3390/ijms17121976

Bakhshandeh, B., Zarrintaj, P., Oftadeh, M. O., Keramati, F., Fouladiha, H., Sohrabi-jahromi, S., et al. (2017). Tissue engineering; strategies, tissues, and biomaterials. *Biotechnol. Genet. Eng. Rev.* 33 (2), 144–172. doi:10.1080/02648725.2018.1430464

Bala, I., Hariharan, S., and Kumar, M. N. (2004). PLGA nanoparticles in drug delivery: The state of the art. *Crit. Rev. Ther. Drug Carr. Syst.* 21 (5), 387–422. doi:10.1615/critrevtherdrugcarriersyst.v21.i5.20

Bansai, S., Morikura, T., Onoe, H., and Miyata, S. (2019). Effect of cyclic stretch on tissue maturation in myoblast-laden hydrogel fibers. *Micromachines* 10 (6), 399. doi:10.3390/mi10060399

Bartolo, P., Malshe, A., Ferraris, E., and Koc, B. (2022). 3D bioprinting: Materials, processes, and applications. *CIRP Ann.* 71 (2), 577–597. doi:10.1016/j.cirp.2022.06.001

Bazilevsky, A. V., Yarin, A. L., and Megaridis, C. M. (2007). Co-electrospinning of core-shell fibers using a single-nozzle technique. *Langmuir* 23 (5), 2311–2314. doi:10.1021/la063194q

Berraondo, P., Martini, P. G. V., Avila, M. A., and Fontanellas, A. (2019). Messenger RNA therapy for rare genetic metabolic diseases. *Gut* 68 (7), 1323–1330. doi:10.1136/gutjnl-2019-318269

Bhardwaj, N., and Kundu, S. C. (2010). Electrospinning: A fascinating fiber fabrication technique. *Biotechnol. Adv.* 28 (3), 325–347. doi:10.1016/j.biotechadv.2010.01.004

Bhunia, B. K., Dey, S., Bandyopadhyay, A., and Mandal, B. B. (2021). 3D printing of annulus fibrosus anatomical equivalents recapitulating angle-ply architecture for intervertebral disc replacement. *Appl. Mat. Today* 23, 101031. doi:10.1016/j.apmt.2021.101031

Bobo, D., Robinson, K. J., Islam, J., Thurecht, K. J., and Corrie, S. R. (2016). Nanoparticle-based medicines: A review of FDA-approved materials and clinical trials to date. *Pharm. Res.* 33 (10), 2373–2387. doi:10.1007/s11095-016-1958-5

Bölgen, N., Vargel, I., Korkusuz, P., Menceloğlu, Y. Z., and Pişkin, E. (2007). *In vivo* performance of antibiotic embedded electrospun PCL membranes for prevention of abdominal adhesions. *J. Biomed. Mat. Res. B Appl. Biomater.* 81 (2), 530–543. doi:10.1002/jbm.b.30694

Bordbar-Khiabani, A., and Gasik, M. (2022). Smart hydrogels for advanced drug delivery systems. *Int. J. Mol. Sci.* 23 (7), 3665. doi:10.3390/ijms23073665

Bourdenx, M., Daniel, J., Genin, E., Soria, F. N., Blanchard-Desce, M., Bezard, E., et al. (2016). Nanoparticles restore lysosomal acidification defects: Implications for Parkinson and other lysosomal-related diseases. *Autophagy* 12 (3), 472–483. doi:10.1080/15548627.2015.1136769

Caldorera-Moore, M., Vela Ramirez, J. E., and Peppas, N. A. (2019). Transport and delivery of interferon-alpha through epithelial tight junctions via pH-responsive poly(methacrylic acid-grafted-ethylene glycol) nanoparticles. *J. Drug Target.* 27 (5-6), 582–589. doi:10.1080/1061186X.2018.1547732

Callahan, L. A., Xie, S., Barker, I. A., Zheng, J., Reneker, D. H., Dove, A. P., et al. (2013). Directed differentiation and neurite extension of mouse embryonic stem cell on aligned poly(lactide) nanofibers functionalized with YIGSR peptide. *Biomaterials* 34 (36), 9089–9095. doi:10.1016/j.biomaterials.2013.08.028

Carotenuto, F., Politi, S., Ul Haq, A., De Matteis, F., Tamburri, E., Terranova, M. L., et al. (2022). From soft to hard biomimetic materials: Tuning micro/nano-architecture of scaffolds for tissue regeneration. *Micromachines* 13 (5), 780. doi:10.3390/mi13050780

Chaisabai, W., Khamhaengpol, A., and Siri, S. (2018). Sericins of mulberry and non-mulberry silkworms for eco-friendly synthesis of silver nanoparticles. *Artif. Cells Nanomed. Biotechnol.* 46 (3), 536–543. doi:10.1080/21691401.2017.1328686

Chakraborty, J., Mu, X., Pramanick, A., Kaplan, D. L., and Ghosh, S. (2022). Recent advances in bioprinting using silk protein-based bioinks. *Biomaterials* 287, 121672. doi:10.1016/j.biomaterials.2022.121672

Chaudhari, A. A., Vig, K., Baganizi, D. R., Sahu, R., Dixit, S., Dennis, V., et al. (2016). Future prospects for scaffolding methods and biomaterials in skin tissue engineering: A review. *Int. J. Mol. Sci.* 17 (12), 1974. doi:10.3390/ijms17121974

Chen, B., Cao, Y., Li, Q., Yan, Z., Liu, R., Zhao, Y., et al. (2022). Liquid metal-tailored gluten network for protein-based e-skin. *Nat. Commun.* 13 (1), 1206. doi:10.1038/s41467-022-28901-9

Chen, F., Lee, C. N., and Teoh, S. H. (2007). Nanofibrous modification on ultra-thin poly(e-caprolactone) membrane via electrospinning. *Mat. Sci. Eng. C* 27 (2), 325–332. doi:10.1016/j.msec.2006.05.004

Chen, G., Roy, I., Yang, C., and Prasad, P. N. (2016a). Nanochemistry and nanomedicine for nanoparticle-based diagnostics and therapy. *Chem. Rev.* 116 (5), 2826–2885. doi:10.1021/acs.chemrev.5b00148

Chen, P., Liu, L., Pan, J., Mei, J., Li, C., and Zheng, Y. (2019). Biomimetic composite scaffold of hydroxyapatite/gelatin-chitosan core-shell nanofibers for bone tissue engineering. *Mat. Sci. Eng. C Mat. Biol. Appl.* 97, 325–335. doi:10.1016/j.msec.2018.12.027

Chen, Q., Utech, S., Chen, D., Prodanovic, R., Lin, J. M., and Weitz, D. A. (2016b). Controlled assembly of heterotypic cells in a core-shell scaffold: Organ in a droplet. *Lab. Chip* 16 (8), 1346–1349. doi:10.1039/c6lc00231e

Cheng, G., Ma, X., Li, J., Cheng, Y., Cao, Y., Wang, Z., et al. (2018). Incorporating platelet-rich plasma into coaxial electrospun nanofibers for bone tissue engineering. *Int. J. Pharm.* 547 (1-2), 656–666. doi:10.1016/j.ijpharm.2018.06.020

Cheng, G., Yin, C., Tu, H., Jiang, S., Wang, Q., Zhou, X., et al. (2019). Controlled co-delivery of growth factors through layer-by-layer assembly of core-shell nanofibers for improving bone regeneration. *ACS Nano* 13 (6), 6372–6382. doi:10.1021/acsnano.8b06032

Cheng, Q., Wei, T., Farbiak, L., Johnson, L. T., Dilliard, S. A., and Siegwart, D. J. (2020). Selective organ targeting (SORT) nanoparticles for tissue-specific mRNA delivery and CRISPR-Cas gene editing. *Nat. Nanotechnol.* 15 (4), 313–320. doi:10.1038/s41565-020-0669-6

Choi, A., Seo, K. D., Kim, D. W., Kim, B. C., and Kim, D. S. (2017). Recent advances in engineering microparticles and their nascent utilization in biomedical delivery and diagnostic applications. *Lab. Chip* 17 (4), 591–613. doi:10.1039/c6lc01023g

Choi, J. S., Leong, K. W., and Yoo, H. S. (2008). *In vivo* wound healing of diabetic ulcers using electrospun nanofibers immobilized with human epidermal growth factor (EGF). *Biomaterials* 29 (5), 587–596. doi:10.1016/j.biomaterials.2007.10.012

Chouhan, D., and Mandal, B. B. (2020). Silk biomaterials in wound healing and skin regeneration therapeutics: From bench to bedside. *Acta Biomater.* 103, 24–51. doi:10.1016/j.actbio.2019.11.050

Chu, G., Yuan, Z., Zhu, C., Zhou, P., Wang, H., Zhang, W., et al. (2019). Substrate stiffness- and topography-dependent differentiation of annulus fibrosus-derived stem cells is regulated by Yes-associated protein. *Acta Biomater.* 92, 254–264. doi:10.1016/j.actbio.2019.05.013

Chung, B. G., Lee, K. H., Khademhosseini, A., and Lee, S. H. (2012). Microfluidic fabrication of microengineered hydrogels and their application in tissue engineering. *Lab. Chip* 12 (1), 45–59. doi:10.1039/c1lc20859d

Chung, L., Maestas, D. R., Housseau, F., and Elisseeff, J. H. (2017). Key players in the immune response to biomaterial scaffolds for regenerative medicine. *Adv. Drug Deliv. Rev.* 114, 184–192. doi:10.1016/j.addr.2017.07.006

Coimbra, P., Santos, P., Alves, P., Miguel, S. P., Carvalho, M. P., de Sá, K. D., et al. (2017). Coaxial electrospun PCL/Gelatin-MA fibers as scaffolds for vascular tissue engineering. *Colloids Surf. B Biointerfaces* 159, 7–15. doi:10.1016/j.colsurfb.2017.07.065

Combes, C., Miao, B., Bareille, R., and Rey, C. (2006). Preparation, physical-chemical characterisation and cytocompatibility of calcium carbonate cements. *Biomaterials* 27 (9), 1945–1954. doi:10.1016/j.biomaterials.2005.09.026

Costantini, M., Idaszek, J., Szoke, K., Jaroszewicz, J., Dentini, M., Barbetta, A., et al. (2016). 3D bioprinting of BM-MSCs-loaded ECM biomimetic hydrogels for *in vitro* neocartilage formation. *Biofabrication* 8 (3), 035002. doi:10.1088/1758-5090/8/3/035002

Costantini, M., Testa, S., Mozetic, P., Barbetta, A., Fuoco, C., Fornetti, E., et al. (2017). Microfluidic-enhanced 3D bioprinting of aligned myoblast-laden hydrogels leads to functionally organized myofibers *in vitro* and *in vivo*. *Biomaterials* 131, 98–110. doi:10.1016/j.biomaterials.2017.03.026

Craciunescu, O., Seciu, A. M., and Zarnescu, O. (2021). *In vitro* and *in vivo* evaluation of a biomimetic scaffold embedding silver nanoparticles for improved treatment of oral lesions. *Mat. Sci. Eng. C Mat. Biol. Appl.* 123, 112015. doi:10.1016/j.msec.2021.112015

Cui, J., Richardson, J. J., Bjornmalm, M., Faria, M., and Caruso, F. (2016). Nanoengineered templated polymer particles: Navigating the biological realm. *Acc. Chem. Res.* 49 (6), 1139–1148. doi:10.1021/acs.accounts.6b00088

da Silva, T. N., Gonçalves, R. P., Rocha, C. L., Archanjo, B. S., Barboza, C. A. G., Pierre, M. B. R., et al. (2019). Controlling burst effect with PLA/PVA coaxial electrospun scaffolds loaded with BMP-2 for bone guided regeneration. *Mat. Sci. Eng. C* 97, 602–612. doi:10.1016/j.msec.2018.12.020

Dai, N. T., Williamson, M. R., Khammo, N., Adams, E. F., and Coombes, A. G. (2004). Composite cell support membranes based on collagen and polycaprolactone for tissue engineering of skin. *Biomaterials* 25 (18), 4263–4271. doi:10.1016/j.biomaterials.2003.11.022

Dash, T. K., and Konkimalla, V. B. (2012). Poly-ϵ-caprolactone based formulations for drug delivery and tissue engineering: A review. *J. Control. Release* 158 (1), 15–33. doi:10.1016/j.jconrel.2011.09.064

Dendukuri, D., and Doyle, P. S. (2009). The synthesis and assembly of polymeric microparticles using microfluidics. *Adv. Mat.* 21 (41), 4071–4086. doi:10.1002/adma.200803386

Domachuk, P., Tsioris, K., Omenetto, F. G., and Kaplan, D. L. (2010). Bio-microfluidics: Biomaterials and biomimetic designs. *Adv. Mat.* 22 (2), 249–260. doi:10.1002/adma.200900821

Du, X., Wei, D., Huang, L., Zhu, M., Zhang, Y., and Zhu, Y. (2019). 3D printing of mesoporous bioactive glass/silk fibroin composite scaffolds for bone tissue engineering. *Mat. Sci. Eng. C Mat. Biol. Appl.* 103, 109731. doi:10.1016/j.msec.2019.05.016

Duan, N., Geng, X., Ye, L., Zhang, A., Feng, Z., Guo, L., et al. (2016). A vascular tissue engineering scaffold with core-shell structured nano-fibers formed by coaxial electrospinning and its biocompatibility evaluation. *Biomed. Mat.* 11 (3), 035007. doi:10.1088/1748-6041/11/3/035007

Duncanson, W. J., Lin, T., Abate, A. R., Seiffert, S., Shah, R. K., and Weitz, D. A. (2012). Microfluidic synthesis of advanced microparticles for encapsulation and controlled release. *Lab. Chip* 12 (12), 2135–2145. doi:10.1039/c2lc21164e

Ersel, M., Uyanikgil, Y., Karbek Akarca, F., Ozcete, E., Altunci, Y. A., Karabey, F., et al. (2016). Effects of silk sericin on incision wound healing in a dorsal skin flap wound healing rat model. *Med. Sci. Monit.* 22, 1064–1078. doi:10.12659/msm.897981

Essa, D., Kondiah, P. P. D., Choonara, Y. E., and Pillay, V. (2020). The design of poly(lactide-co-glycolide) nanocarriers for medical applications. *Front. Bioeng. Biotechnol.* 8, 48. doi:10.3389/fbioe.2020.00048

Eygeris, Y., Gupta, M., Kim, J., and Sahay, G. (2022). Chemistry of lipid nanoparticles for RNA delivery. *Acc. Chem. Res.* 55 (1), 2–12. doi:10.1021/acs.accounts.1c00544

Ezhilarasu, H., Sadiq, A., Ratheesh, G., Sridhar, S., Ramakrishna, S., Ab Rahim, M. H., et al. (2019). Functionalized core/shell nanofibers for the differentiation of mesenchymal stem cells for vascular tissue engineering. *Nanomedicine* 14 (2), 201–214. doi:10.2217/nnm-2018-0271

Flemming, R. G., Murphy, C. J., Abrams, G. A., Goodman, S. L., and Nealey, P. F. (1999). Effects of synthetic micro- and nano-structured surfaces on cell behavior. *Biomaterials* 20 (6), 573–588. doi:10.1016/s0142-9612(98)00209-9

Fu, W., Liu, Z., Feng, B., Hu, R., He, X., Wang, H., et al. (2014). Electrospun gelatin/PCL and collagen/PLCL scaffolds for vascular tissue engineering. *Int. J. Nanomedicine* 9, 2335–2344. doi:10.2147/ijn.S61375

Gan, T., Shang, W., Handschuh-Wang, S., and Zhou, X. (2019). Light-induced shape morphing of liquid metal nanodroplets enabled by polydopamine coating. *Small* 15 (9), 1804838. doi:10.1002/smll.201804838

Gao, C., Lu, C., Jian, Z., Zhang, T., Chen, Z., Zhu, Q., et al. (2021). 3D bioprinting for fabricating artificial skin tissue. *Colloids Surf. B Biointerfaces* 208, 112041. doi:10.1016/j.colsurfb.2021.112041

Ghitman, J., Biru, E. I., Stan, R., and Iovu, H. (2020). Review of hybrid PLGA nanoparticles: Future of smart drug delivery and theranostics medicine. *Mat. Des.* 193, 108805. doi:10.1016/j.matdes.2020.108805

Gluais, M., Clouet, J., Fusellier, M., Decante, C., Moraru, C., Dutilleul, M., et al. (2019). *In vitro* and *in vivo* evaluation of an electrospun-aligned microfibrous implant for Annulus fibrosus repair. *Biomaterials* 205, 81–93. doi:10.1016/j.biomaterials.2019.03.010

Groeber, F., Holeiter, M., Hampel, M., Hinderer, S., and Schenke-Layland, K. (2011). Skin tissue engineering-*in vivo* and *in vitro* applications. *Adv. Drug Deliv. Rev.* 63 (4-5), 352–366. doi:10.1016/j.addr.2011.01.005

Gu, Z., Wang, J., Fu, Y., Pan, H., He, H., Gan, Q., et al. (2023). Smart biomaterials for articular cartilage repair and regeneration. *Adv. Funct. Mat.* 33 (10), 2212561. doi:10.1002/adfm.202212561

Guex, A. G., Hegemann, D., Giraud, M. N., Tevaearai, H. T., Popa, A. M., Rossi, R. M., et al. (2014). Covalent immobilisation of VEGF on plasma-coated electrospun scaffolds for tissue engineering applications. *Colloids Surf. B Biointerfaces* 123, 724–733. doi:10.1016/j.colsurfb.2014.10.016

Hadisi, Z., Farokhi, M., Bakhsheshi-Rad, H. R., Jahanshahi, M., Hasanpour, S., Pagan, E., et al. (2020). Hyaluronic acid (HA)-based silk fibroin/zinc oxide core-shell electrospun dressing for burn wound management. *Macromol. Biosci.* 20 (4), 1900328. doi:10.1002/mabi.201900328

Han, F., Yu, Q., Chu, G., Li, J., Zhu, Z., Tu, Z., et al. (2022). Multifunctional nanofibrous scaffolds with angle-ply microstructure and co-delivery capacity promote partial repair and total replacement of intervertebral disc. *Adv. Healthc. Mat.* 11 (19), 2200895. doi:10.1002/adhm.202200895

Haq-Siddiqi, N. A., Britton, D., and Kim Montclare, J. (2023). Protein-engineered biomaterials for cartilage therapeutics and repair. *Adv. Drug Deliv. Rev.* 192, 114647. doi:10.1016/j.addr.2022.114647

Haruta, S., Hanafusa, T., Fukase, H., Miyajima, H., and Oki, T. (2003). An effective absorption behavior of insulin for diabetic treatment following intranasal delivery using porous spherical calcium carbonate in monkeys and healthy human volunteers. *Diabetes Technol. Ther.* 5 (1), 1–9. doi:10.1089/152091503763816409

Hassanajili, S., Karami-Pour, A., Oryan, A., and Talaei-Khozani, T. (2019). Preparation and characterization of PLA/PCL/HA composite scaffolds using indirect 3D printing for bone tissue engineering. *Mat. Sci. Eng. C Mat. Biol. Appl.* 104, 109960. doi:10.1016/j.msec.2019.109960

He, H., Tao, G., Wang, Y., Cai, R., Guo, P., Chen, L., et al. (2017). *In situ* green synthesis and characterization of sericin-silver nanoparticle composite with effective antibacterial activity and good biocompatibility. *Mat. Sci. Eng. C Mat. Biol. Appl.* 80, 509–516. doi:10.1016/j.msec.2017.06.015

He, Y., Zhao, Y., Fan, L., Wang, X., Duan, M., Wang, H., et al. (2021). Injectable affinity and remote magnetothermal effects of bi-based alloy for long-term bone defect repair and analgesia. *Adv. Sci.* 8 (14), 2100719. doi:10.1002/advs.202100719

Heo, Y., Shin, Y. M., Lee, Y. B., Lim, Y. M., and Shin, H. (2015). Effect of immobilized collagen type IV on biological properties of endothelial cells for the enhanced endothelialization of synthetic vascular graft materials. *Colloids Surf. B Biointerfaces* 134, 196–203. doi:10.1016/j.colsurfb.2015.07.003

Hernandez, R. M., Orive, G., Murua, A., and Pedraz, J. L. (2010). Microcapsules and microcarriers for *in situ* cell delivery. *Adv. Drug Deliv. Rev.* 62 (7-8), 711–730. doi:10.1016/j.addr.2010.02.004

Hou, X., Zaks, T., Langer, R., and Dong, Y. (2021). Lipid nanoparticles for mRNA delivery. *Nat. Rev. Mat.* 6 (12), 1078–1094. doi:10.1038/s41578-021-00358-0

Huang, H., Yu, Y., Hu, Y., He, X., Berk Usta, O., and Yarmush, M. L. (2017). Generation and manipulation of hydrogel microcapsules by droplet-based microfluidics for mammalian cell culture. *Lab. Chip* 17 (11), 1913–1932. doi:10.1039/c7lc00262a

Huang, K. S., Yang, C. H., Kung, C. P., Grumezescu, A. M., Ker, M. D., Lin, Y. S., et al. (2014). Synthesis of uniform core-shell gelatin-alginate microparticles as intestine-released oral delivery drug carrier. *Electrophoresis* 35 (2-3), 330–336. doi:10.1002/elps.201300194

Huang, K. W., Hsu, F. F., Qiu, J. T., Chern, G. J., Lee, Y. A., Chang, C. C., et al. (2020). Highly efficient and tumor-selective nanoparticles for dual-targeted immunogene therapy against cancer. *Sci. Adv.* 6 (3), 5032. doi:10.1126/sciadv.aax5032

Huang, Z. M., He, C. L., Yang, A., Zhang, Y., Han, X. J., Yin, J., et al. (2006). Encapsulating drugs in biodegradable ultrafine fibers through co-axial electrospinning. *J. Biomed. Mat. Res. A* 77 (1), 169–179. doi:10.1002/jbm.a.30564

Isapour, G., and Lattuada, M. (2018). Bioinspired stimuli-responsive color-changing systems. *Adv. Mat.* 30 (19), 1707069. doi:10.1002/adma.201707069

Jena, K., Pandey, J. P., Kumari, R., Sinha, A. K., Gupta, V. P., and Singh, G. P. (2018). Free radical scavenging potential of sericin obtained from various ecoraces of tasar cocoons and its cosmeceuticals implication. *Int. J. Biol. Macromol.* 120, 255–262. doi:10.1016/j.ijbiomac.2018.08.090

Jia, J., Duan, Y. Y., Yu, J., and Lu, J. W. (2008). Preparation and immobilization of soluble eggshell membrane protein on the electrospun nanofibers to enhance cell adhesion and growth. *J. Biomed. Mat. Res. A* 86 (2), 364–373. doi:10.1002/jbm.a.31606

Jia, L., Han, F., Yang, H., Turnbull, G., Wang, J., Clarke, J., et al. (2019). Microfluidic fabrication of biomimetic helical hydrogel microfibers for blood-vessel-on-a-chip applications. *Adv. Healthc. Mat.* 8 (13), 1900435. doi:10.1002/adhm.201900435

Jia, L., Prabhakaran, M. P., Qin, X., and Ramakrishna, S. (2013). Stem cell differentiation on electrospun nanofibrous substrates for vascular tissue engineering. *Mat. Sci. Eng. C Mat. Biol. Appl.* 33 (8), 4640–4650. doi:10.1016/j.msec.2013.07.021

Jia, Z. H., Xie, R., Qiu, Y., Lv, X. B., Ju, X. J., Wang, W., et al. (2021). Magnetically assembled photonic crystal gels with wide thermochromic range and high sensitivity. *Macromol. Rapid Commun.* 42 (15), 2100200. doi:10.1002/marc.202100200

Jiang, W., Li, M., Chen, Z., and Leong, K. W. (2016). Cell-laden microfluidic microgels for tissue regeneration. *Lab. Chip* 16 (23), 4482–4506. doi:10.1039/c6lc01193d

Jin Seo, H., Hee Lee, M., Kwon, B. J., Kim, H. L., Jin Lee, S., Kim, B. J., et al. (2013). Plasma treatment induces internal surface modifications of electrospun poly(L-lactic) acid scaffold to enhance protein coating. *J. Appl. Phys.* 114 (7), 073304. doi:10.1063/1.4818914

Ju, Y., Liao, H., Richardson, J. J., Guo, J., and Caruso, F. (2022). Nanostructured particles assembled from natural building blocks for advanced therapies. *Chem. Soc. Rev.* 51 (11), 4287–4336. doi:10.1039/d1cs00343g

Kacarevic, Z. P., Rider, P. M., Alkildani, S., Retnasingh, S., Smeets, R., Jung, O., et al. (2018). An introduction to 3D bioprinting: Possibilities, challenges and future aspects. *Materials* 11 (11), 2199. doi:10.3390/ma11112199

Kanoujia, J., Singh, M., Singh, P., and Saraf, S. A. (2016). Novel genipin crosslinked atorvastatin loaded sericin nanoparticles for their enhanced antihyperlipidemic activity. *Mat. Sci. Eng. C Mat. Biol. Appl.* 69, 967–976. doi:10.1016/j.msec.2016.08.011

Kato, N., Sato, S., Yamanaka, A., Yamada, H., Fuwa, N., and Nomura, M. (1998). Silk protein, sericin, inhibits lipid peroxidation and tyrosinase activity. *Biosci. Biotechnol. Biochem.* 62 (1), 145–147. doi:10.1271/bbb.62.145

Kim, J. W., Mahapatra, C., Hong, J. Y., Kim, M. S., Leong, K. W., Kim, H. W., et al. (2017). Functional recovery of contused spinal cord in rat with the injection of optimal-dosed cerium oxide nanoparticles. *Adv. Sci.* 4 (10), 1700034. doi:10.1002/advs.201700034

Kim, K., Luu, Y. K., Chang, C., Fang, D., Hsiao, B. S., Chu, B., et al. (2004). Incorporation and controlled release of a hydrophilic antibiotic using poly(lactide-co-glycolide)-based electrospun nanofibrous scaffolds. *J. Control. Release* 98 (1), 47–56. doi:10.1016/j.jconrel.2004.04.009

Kim, S. E., Wallat, J. D., Harker, E. C., Advincula, A. A., and Pokorski, J. K. (2015). Multifunctional and spatially controlled bioconjugation to melt coextruded nanofibers. *Polym. Chem.* 6 (31), 5683–5692. doi:10.1039/C5PY00282F

Kim, S. H., Hong, H., Ajiteru, O., Sultan, M. T., Lee, Y. J., Lee, J. S., et al. (2021). 3D bioprinted silk fibroin hydrogels for tissue engineering. *Nat. Protoc.* 16 (12), 5484–5532. doi:10.1038/s41596-021-00622-1

Knight, F. C., Gilchuk, P., Kumar, A., Becker, K. W., Sevimli, S., Jacobson, M. E., et al. (2019). Mucosal immunization with a pH-responsive nanoparticle vaccine induces protective CD8(+) lung-resident memory T cells. *ACS Nano* 13 (10), 10939–10960. doi:10.1021/acsnano.9b00326

Kwon, H. J., Cha, M. Y., Kim, D., Kim, D. K., Soh, M., Shin, K., et al. (2016). Mitochondria-targeting ceria nanoparticles as antioxidants for Alzheimer's disease. *ACS Nano* 10 (2), 2860–2870. doi:10.1021/acsnano.5b08045

Laubach, M., Suresh, S., Herath, B., Wille, M. L., Delbrück, H., Alabdulrahman, H., et al. (2022). Clinical translation of a patient-specific scaffold-guided bone regeneration concept in four cases with large long bone defects. *J. Orthop. Transl.* 34, 73–84. doi:10.1016/j.jot.2022.04.004

Le Goff, G. C., Srinivas, R. L., Hill, W. A., and Doyle, P. S. (2015). Hydrogel microparticles for biosensing. *Eur. Polym. J.* 72, 386–412. doi:10.1016/j.eurpolymj.2015.02.022

Lee, T. Y., Ku, M., Kim, B., Lee, S., Yang, J., and Kim, S. H. (2017). Microfluidic production of biodegradable microcapsules for sustained release of hydrophilic actives. *Small* 13 (29), 1700646. doi:10.1002/smll.201700646

Li, F., Lu, J., Kong, X., Hyeon, T., and Ling, D. (2017). Dynamic nanoparticle assemblies for biomedical applications. *Adv. Mat.* 29 (14), 1605897. doi:10.1002/adma.201605897

Li, G., Lai, Z., and Shan, A. (2023a). Advances of antimicrobial peptide-based biomaterials for the treatment of bacterial infections. *Adv. Sci.* 2023, 2206602. doi:10.1002/advs.202206602

Li, R., Ma, Y., Zhang, Y., Zhang, M., and Sun, D. (2018). Potential of rhBMP-2 and dexamethasone-loaded Zein/PLLA scaffolds for enhanced *in vitro* osteogenesis of mesenchymal stem cells. *Colloids Surf. B Biointerfaces* 169, 384–394. doi:10.1016/j.colsurfb.2018.05.039

Li, T., Chang, J., Zhu, Y., and Wu, C. (2020). 3D printing of bioinspired biomaterials for tissue regeneration. *Adv. Healthc. Mat.* 9 (23), 2000208. doi:10.1002/adhm.202000208

Li, W., Guo, Y., Wang, H., Shi, D., Liang, C., Ye, Z., et al. (2008). Electrospun nanofibers immobilized with collagen for neural stem cells culture. *J. Mat. Sci. Mat. Med.* 19 (2), 847–854. doi:10.1007/s10856-007-3087-5

Li, X., Li, X., Yang, J., Lin, J., Zhu, Y., Xu, X., et al. (2023b). Living and injectable porous hydrogel microsphere with paracrine activity for cartilage regeneration. *Small* 2023, 2207211. doi:10.1002/smll.202207211

Lin, J., Chen, L., Yang, J., Li, X., Wang, J., Zhu, Y., et al. (2022). Injectable double positively charged hydrogel microspheres for targeting-penetration-phagocytosis. *Small* 18 (40), 2202156. doi:10.1002/smll.202202156

Liu, C., Wang, C., Zhao, Q., Li, X., Xu, F., Yao, X., et al. (2018). Incorporation and release of dual growth factors for nerve tissue engineering using nanofibrous bicomponent scaffolds. *Biomed. Mat.* 13 (4), 044107. doi:10.1088/1748-605X/aab693

Liu, F., Yu, Y., Yi, L., and Liu, J. (2016). Liquid metal as reconnection agent for peripheral nerve injury. *Sci. Bull.* 61 (12), 939–947. doi:10.1007/s11434-016-1090-2

Liu, J., Shi, L., Deng, Y., Zou, M., Cai, B., Song, Y., et al. (2022a). Silk sericin-based materials for biomedical applications. *Biomaterials* 287, 121638. doi:10.1016/j.biomaterials.2022.121638

Liu, W., Thomopoulos, S., and Xia, Y. (2012). Electrospun nanofibers for regenerative medicine. *Adv. Healthc. Mat.* 1 (1), 10–25. doi:10.1002/adhm.201100021

Liu, X., Zhao, N., Liang, H., Tan, B., Huang, F., Hu, H., et al. (2022b). Bone tissue engineering scaffolds with HUVECs/hBMSCs cocultured on 3D-printed composite bioactive ceramic scaffolds promoted osteogenesis/angiogenesis. *J. Orthop. Transl.* 37, 152–162. doi:10.1016/j.jot.2022.10.008

Liu, Y., Yang, G., Jin, S., Xu, L., and Zhao, C. X. (2020). Development of high-drug-loading nanoparticles. *Chempluschem* 85 (9), 2143–2157. doi:10.1002/cplu.202000496

Lu, Y., Hu, Q., Lin, Y., Pacardo, D. B., Wang, C., Sun, W., et al. (2015). Transformable liquid-metal nanomedicine. *Nat. Commun.* 6, 10066. doi:10.1038/ncomms10066

Luraghi, A., Peri, F., and Moroni, L. (2021). Electrospinning for drug delivery applications: A review. *J. Control. Release* 334, 463–484. doi:10.1016/j.jconrel.2021.03.033

Ma, Z., Gao, C., Gong, Y., and Shen, J. (2005). Cartilage tissue engineering PLLA scaffold with surface immobilized collagen and basic fibroblast growth factor. *Biomaterials* 26 (11), 1253–1259. doi:10.1016/j.biomaterials.2004.04.031

Mandrycky, C., Wang, Z., Kim, K., and Kim, D. H. (2016). 3D bioprinting for engineering complex tissues. *Biotechnol. Adv.* 34 (4), 422–434. doi:10.1016/j.biotechadv.2015.12.011

Marshall, S. L., Jacobsen, T. D., Emsbo, E., Murali, A., Anton, K., Liu, J. Z., et al. (2021). Three-Dimensional-Printed flexible scaffolds have tunable biomimetic mechanical properties for intervertebral disc tissue engineering. *ACS Biomater. Sci. Eng.* 7 (12), 5836–5849. doi:10.1021/acsbiomaterials.1c01326

Martins, A., Pinho, E. D., Faria, S., Pashkuleva, I., Marques, A. P., Reis, R. L., et al. (2009). Surface modification of electrospun polycaprolactone nanofiber meshes by plasma treatment to enhance biological performance. *Small* 5 (10), 1195–1206. doi:10.1002/smll.200801648

Martins, C., Sousa, F., Araujo, F., and Sarmento, B. (2018). Functionalizing PLGA and PLGA derivatives for drug delivery and tissue regeneration applications. *Adv. Healthc. Mat.* 7 (1), 1701035. doi:10.1002/adhm.201701035

Matai, I., Kaur, G., Seyedsalehi, A., McClinton, A., and Laurencin, C. T. (2020). Progress in 3D bioprinting technology for tissue/organ regenerative engineering. *Biomaterials* 226, 119536. doi:10.1016/j.biomaterials.2019.119536

Merkle, V. M., Martin, D., Hutchinson, M., Tran, P. L., Behrens, A., Hossainy, S., et al. (2015a). Hemocompatibility of poly(vinyl alcohol)-gelatin core-shell electrospun nanofibers: A scaffold for modulating platelet deposition and activation. *ACS Appl. Mat. Interfaces* 7 (15), 8302–8312. doi:10.1021/acsami.5b01671

Merkle, V. M., Tran, P. L., Hutchinson, M., Ammann, K. R., DeCook, K., Wu, X., et al. (2015b). Core-shell PVA/gelatin electrospun nanofibers promote human umbilical vein endothelial cell and smooth muscle cell proliferation and migration. *Acta Biomater.* 27, 77–87. doi:10.1016/j.actbio.2015.08.044

Miri, A. K., Nieto, D., Iglesias, L., Goodarzi Hosseinabadi, H., Maharjan, S., Ruiz-Esparza, G. U., et al. (2018). Microfluidics-enabled multimaterial maskless stereolithographic bioprinting. *Adv. Mat.* 30 (27), 1800242. doi:10.1002/adma.201800242

Mitchell, M. J., Billingsley, M. M., Haley, R. M., Wechsler, M. E., Peppas, N. A., and Langer, R. (2021). Engineering precision nanoparticles for drug delivery. *Nat. Rev. Drug Discov.* 20 (2), 101–124. doi:10.1038/s41573-020-0090-8

Mitragotri, S., Anderson, D. G., Chen, X., Chow, E. K., Ho, D., Kabanov, A. V., et al. (2015). Accelerating the translation of nanomaterials in biomedicine. *ACS Nano* 9 (7), 6644–6654. doi:10.1021/acsnano.5b03569

Miyako, E. (2021). Convergence of liquid metal biotechnologies for our health. *Acc. Mat. Res.* 2 (10), 858–862. doi:10.1021/accountsmr.1c00126

Mohiti-Asli, M., Saha, S., Murphy, S., Gracz, H., Pourdeyhimi, B., Atala, A., et al. (2017). Ibuprofen loaded PLA nanofibrous scaffolds increase proliferation of human skin cells *in vitro* and promote healing of full thickness incision wounds *in vivo*. *J. Biomed. Mat. Res. B Appl. Biomater.* 105 (2), 327–339. doi:10.1002/jbm.b.33520

Movahedi, M., Asefnejad, A., Rafienia, M., and Khorasani, M. T. (2020). Potential of novel electrospun core-shell structured polyurethane/starch (hyaluronic acid) nanofibers for skin tissue engineering: *In vitro* and *in vivo* evaluation. *Int. J. Biol. Macromol.* 146, 627–637. doi:10.1016/j.ijbiomac.2019.11.233

Mow, V. C., Ratcliffe, A., and Poole, A. R. (1992). Cartilage and diarthrodial joints as paradigms for hierarchical materials and structures. *Biomaterials* 13 (2), 67–97. doi:10.1016/0142-9612(92)90001-5

Moydeen, A. M., Ali Padusha, M. S., Aboelfetoh, E. F., Al-Deyab, S. S., and El-Newehy, M. H. (2018). Fabrication of electrospun poly(vinyl alcohol)/dextran nanofibers via emulsion process as drug delivery system: Kinetics and *in vitro* release study. *Int. J. Biol. Macromol.* 116, 1250–1259. doi:10.1016/j.ijbiomac.2018.05.130

Muller, M., Becher, J., Schnabelrauch, M., and Zenobi-Wong, M. (2015). Nanostructured Pluronic hydrogels as bioinks for 3D bioprinting. *Biofabrication* 7 (3), 035006. doi:10.1088/1758-5090/7/3/035006

Nandakumar, A., Tahmasebi Birgani, Z., Santos, D., Mentink, A., Auffermann, N., van der Werf, K., et al. (2013). Surface modification of electrospun fibre meshes by oxygen plasma for bone regeneration. *Biofabrication* 5 (1), 015006. doi:10.1088/1758-5082/5/1/015006

Nie, H., and Wang, C. H. (2007). Fabrication and characterization of PLGA/HAp composite scaffolds for delivery of BMP-2 plasmid DNA. *J. Control. Release* 120 (1-2), 111–121. doi:10.1016/j.jconrel.2007.03.018

Nii, T., and Katayama, Y. (2021). Biomaterial-assisted regenerative medicine. *Int. J. Mol. Sci.* 22 (16), 8657. doi:10.3390/ijms22168657

Niza, E., Ocana, A., Castro-Osma, J. A., Bravo, I., and Alonso-Moreno, C. (2021). Polyester polymeric nanoparticles as platforms in the development of novel nanomedicines for cancer treatment. *Cancers (Basel)* 13 (14), 3387. doi:10.3390/cancers13143387

Ode Boni, B. O., Bakadia, B. M., Osi, A. R., Shi, Z., Chen, H., Gauthier, M., et al. (2022). Immune response to silk sericin-fibroin composites: Potential immunogenic elements and alternatives for immunomodulation. *Macromol. Biosci.* 22 (1), 2100292. doi:10.1002/mabi.202100292

Park, H., Lim, D. J., Lee, S. H., and Park, H. (2016). Nanofibrous mineralized electrospun scaffold as a substrate for bone tissue regeneration. *J. Biomed. Nanotechnol.* 12 (11), 2076–2082. doi:10.1166/jbn.2016.2306

Paul, P. S., Cho, J. Y., Wu, Q., Karthivashan, G., Grabovac, E., Wille, H., et al. (2022). Unconjugated PLGA nanoparticles attenuate temperature-dependent beta-amyloid aggregation and protect neurons against toxicity: Implications for alzheimer's disease pathology. *J. Nanobiotechnology* 20 (1), 67. doi:10.1186/s12951-022-01269-0

Pelipenko, J., Kocbek, P., and Kristl, J. (2015). Critical attributes of nanofibers: Preparation, drug loading, and tissue regeneration. *Int. J. Pharm.* 484 (1-2), 57–74. doi:10.1016/j.ijpharm.2015.02.043

Preisig, D., Haid, D., Varum, F. J., Bravo, R., Alles, R., Huwyler, J., et al. (2014). Drug loading into porous calcium carbonate microparticles by solvent evaporation. *Eur. J. Pharm. Biopharm.* 87 (3), 548–558. doi:10.1016/j.ejpb.2014.02.009

Qi, H., Hu, P., Xu, J., and Wang, A. (2006). Encapsulation of drug reservoirs in fibers by emulsion electrospinning: Morphology characterization and preliminary release assessment. *Biomacromolecules* 7 (8), 2327–2330. doi:10.1021/bm060264z

Ratner, B. D., and Bryant, S. J. (2004). Biomaterials: Where we have been and where we are going. *Annu. Rev. Biomed. Eng.* 6, 41–75. doi:10.1146/annurev.bioeng.6.040803.140027

Recum, A. F., Shannon, C. E., Cannon, C. E., Long, K. J., Kooten, T. G., and Meyle, J. (1996). Surface roughness, porosity, and texture as modifiers of cellular adhesion. *Tissue Eng.* 2 (4), 241–253. doi:10.1089/ten.1996.2.241

Rezvantalab, S., Drude, N. I., Moraveji, M. K., Guvener, N., Koons, E. K., Shi, Y., et al. (2018). PLGA-based nanoparticles in cancer treatment. *Front. Pharmacol.* 9, 1260. doi:10.3389/fphar.2018.01260

Rossow, T., Lienemann, P. S., and Mooney, D. J. (2017). Cell microencapsulation by droplet microfluidic templating. *Macromol. Chem. Phys.* 218 (2), 1600380. doi:10.1002/macp.201600380

Seeto, W. J., Tian, Y., Pradhan, S., Kerscher, P., and Lipke, E. A. (2019). Rapid production of cell-laden microspheres using a flexible microfluidic encapsulation platform. *Small* 15 (47), 1902058. doi:10.1002/smll.201902058

Selvaraj, V., Nepal, N., Rogers, S., Manne, N. D., Arvapalli, R., Rice, K. M., et al. (2015). Inhibition of MAP kinase/NF-kB mediated signaling and attenuation of lipopolysaccharide induced severe sepsis by cerium oxide nanoparticles. *Biomaterials* 59, 160–171. doi:10.1016/j.biomaterials.2015.04.025

Seo, K. D., Kim, D. S., and Sanchez, S. (2015). Fabrication and applications of complex-shaped microparticles via microfluidics. *Lab. Chip* 15 (18), 3622–3626. doi:10.1039/c5lc90091c

Shah, N. J., Macdonald, M. L., Beben, Y. M., Padera, R. F., Samuel, R. E., and Hammond, P. T. (2011). Tunable dual growth factor delivery from polyelectrolyte multilayer films. *Biomaterials* 32 (26), 6183–6193. doi:10.1016/j.biomaterials.2011.04.036

Shalumon, K. T., Lai, G. J., Chen, C. H., and Chen, J. P. (2015). Modulation of bone-specific tissue regeneration by incorporating bone morphogenetic protein and controlling the shell thickness of silk fibroin/chitosan/nanohydroxyapatite core-shell nanofibrous membranes. *ACS Appl. Mat. Interfaces* 7 (38), 21170–21181. doi:10.1021/acsami.5b04962

Shang, L., Cheng, Y., and Zhao, Y. (2017). Emerging droplet microfluidics. *Chem. Rev.* 117 (12), 7964–8040. doi:10.1021/acs.chemrev.6b00848

Shao, Z., and Vollrath, F. (2002). Surprising strength of silkworm silk. *Nature* 418 (6899), 741. doi:10.1038/418741a

Shembekar, N., Chaipan, C., Utharala, R., and Merten, C. A. (2016). Droplet-based microfluidics in drug discovery, transcriptomics and high-throughput molecular genetics. *Lab. Chip* 16 (8), 1314–1331. doi:10.1039/c6lc00249h

Shibata, H., Heo, Y. J., Okitsu, T., Matsunaga, Y., Kawanishi, T., and Takeuchi, S. (2010). Injectable hydrogel microbeads for fluorescence-based *in vivo* continuous glucose monitoring. *Proc. Natl. Acad. Sci. U. S. A.* 107 (42), 17894–17898. doi:10.1073/pnas.1006911107

Shin, Y. M., Lim, J. Y., Park, J. S., Gwon, H. J., Jeong, S. I., Ahn, S. J., et al. (2015). Modulation of human mesenchymal stem cell survival on electrospun mesh with co-immobilized epithelial growth factor and gelatin. *RSC Adv.* 5 (69), 55948–55956. doi:10.1039/c5ra01626f

Shum, H. C., Kim, J. W., and Weitz, D. A. (2008). Microfluidic fabrication of monodisperse biocompatible and biodegradable polymersomes with controlled permeability. *J. Am. Chem. Soc.* 130 (29), 9543–9549. doi:10.1021/ja802157y

Siavashani, A. Z., Mohammadi, J., Rottmar, M., Senturk, B., Nourmohammadi, J., Sadeghi, B., et al. (2020). Silk fibroin/sericin 3D sponges: The effect of sericin on structural and biological properties of fibroin. *Int. J. Biol. Macromol.* 153, 317–326. doi:10.1016/j.ijbiomac.2020.02.316

Su, Y., Su, Q., Liu, W., Lim, M., Venugopal, J. R., Mo, X., et al. (2012). Controlled release of bone morphogenetic protein 2 and dexamethasone loaded in core-shell PLLACL-collagen fibers for use in bone tissue engineering. *Acta Biomater.* 8 (2), 763–771. doi:10.1016/j.actbio.2011.11.002

Suktham, K., Koobkokkruad, T., Wutikhun, T., and Surassmo, S. (2018). Efficiency of resveratrol-loaded sericin nanoparticles: Promising bionanocarriers for drug delivery. *Int. J. Pharm.* 537 (1-2), 48–56. doi:10.1016/j.ijpharm.2017.12.015

Sun, X., Sun, M., Liu, M., Yuan, B., Gao, W., Rao, W., et al. (2019). Shape tunable gallium nanorods mediated tumor enhanced ablation through near-infrared photothermal therapy. *Nanoscale* 11 (6), 2655–2667. doi:10.1039/c8nr08296k

Tan, A., Farhatnia, Y., de Mel, A., Rajadas, J., Alavijeh, M. S., and Seifalian, A. M. (2013). Inception to actualization: Next generation coronary stent coatings incorporating nanotechnology. *J. Biotechnol.* 164 (1), 151–170. doi:10.1016/j.jbiotec.2013.01.020

Tarassoli, S. P., Jessop, Z. M., Al-Sabah, A., Gao, N., Whitaker, S., Doak, S., et al. (2018). Skin tissue engineering using 3D bioprinting: An evolving research field. *J. Plast. Reconstr. Aesthet. Surg.* 71 (5), 615–623. doi:10.1016/j.bjps.2017.12.006

Taskin, M. B., Ahmad, T., Wistlich, L., Meinel, L., Schmitz, M., Rossi, A., et al. (2021). Bioactive electrospun fibers: Fabrication strategies and a critical review of surface-sensitive characterization and quantification. *Chem. Rev.* 121 (18), 11194–11237. doi:10.1021/acs.chemrev.0c00816

Taskin, M. B., Xu, R., Gregersen, H., Nygaard, J. V., Besenbacher, F., and Chen, M. (2016). Three-dimensional polydopamine functionalized coiled microfibrous scaffolds enhance human mesenchymal stem cells colonization and mild myofibroblastic differentiation. *ACS Appl. Mat. Interfaces* 8 (25), 15864–15873. doi:10.1021/acsami.6b02994

Thiele, J. (2017). Polymer material design by microfluidics inspired by cell biology and cell-free biotechnology. *Macromol. Chem. Phys.* 218 (2), 1600429. doi:10.1002/macp.201600429

Tian, D., Xu, H., Xiao, B., Zhou, X., Liu, X., Zhou, Z., et al. (2020). Single-step formulation of levodopa-based nanotheranostics - strategy for ultra-sensitive high longitudinal relaxivity MRI guided switchable therapeutics. *Biomater. Sci.* 8 (6), 1615–1621. doi:10.1039/c9bm01799b

Tian, L., Prabhakaran, M. P., Ding, X., and Ramakrishna, S. (2013). Biocompatibility evaluation of emulsion electrospun nanofibers using osteoblasts for bone tissue engineering. *J. Biomater. Sci. Polym. Ed.* 24 (17), 1952–1968. doi:10.1080/09205063.2013.814096

Tien, J., and Dance, Y. W. (2021). Microfluidic biomaterials. *Adv. Healthc. Mat.* 10 (4), 2001028. doi:10.1002/adhm.202001028

Tran, V. T., Benoit, J. P., and Venier-Julienne, M. C. (2011). Why and how to prepare biodegradable, monodispersed, polymeric microparticles in the field of pharmacy? *Int. J. Pharm.* 407 (1-2), 1–11. doi:10.1016/j.ijpharm.2011.01.027

Trofimov, A. D., Ivanova, A. A., Zyuzin, M. V., and Timin, A. S. (2018). Porous inorganic carriers based on silica, calcium carbonate and calcium phosphate for controlled/modulated drug delivery: Fresh outlook and future perspectives. *Pharmaceutics* 10 (4), 167. doi:10.3390/pharmaceutics10040167

Udayar, V., Chen, Y., Sidransky, E., and Jagasia, R. (2022). Lysosomal dysfunction in neurodegeneration: Emerging concepts and methods. *Trends Neurosci.* 45 (3), 184–199. doi:10.1016/j.tins.2021.12.004

Ulery, B. D., Nair, L. S., and Laurencin, C. T. (2011). Biomedical applications of biodegradable polymers. *J. Polym. Sci. B Polym. Phys.* 49 (12), 832–864. doi:10.1002/polb.22259

Velasco, D., Tumarkin, E., and Kumacheva, E. (2012). Microfluidic encapsulation of cells in polymer microgels. *Small* 8 (11), 1633–1642. doi:10.1002/smll.201102464

Wang, C., Zhao, Q., and Wang, M. (2017a). Cryogenic 3D printing for producing hierarchical porous and rhBMP-2-loaded Ca-P/PLLA nanocomposite scaffolds for bone tissue engineering. *Biofabrication* 9 (2), 025031. doi:10.1088/1758-5090/aa71c9

Wang, D., Gao, C., Wang, W., Sun, M., Guo, B., Xie, H., et al. (2018a). Shape-transformable, fusible rodlike swimming liquid metal nanomachine. *ACS Nano* 12 (10), 10212–10220. doi:10.1021/acsnano.8b05203

Wang, G., Jia, L., Han, F., Wang, J., Yu, L., Yu, Y., et al. (2019a). Microfluidics-based fabrication of cell-laden hydrogel microfibers for potential applications in tissue engineering. *Molecules* 24 (8), 1633. doi:10.3390/molecules24081633

Wang, J., Yang, S., Li, C., Miao, Y., Zhu, L., Mao, C., et al. (2017b). Nucleation and assembly of silica into protein-based nanocomposites as effective anticancer drug carriers using self-assembled silk protein nanostructures as biotemplates. *ACS Appl. Mat. Interfaces* 9 (27), 22259–22267. doi:10.1021/acsami.7b05664

Wang, L., Lai, R., Zhang, L., Zeng, M., and Fu, L. (2022). Emerging liquid metal biomaterials: From design to application. *Adv. Mat.* 34 (37), 2201956. doi:10.1002/adma.202201956

Wang, S., Li, J., Zhou, Z., Zhou, S., and Hu, Z. (2018b). Micro-/nano-scales direct cell behavior on biomaterial surfaces. *Molecules* 24 (1), 75. doi:10.3390/molecules24010075

Wang, W., Li, P. F., Xie, R., Ju, X. J., Liu, Z., and Chu, L. Y. (2021). Designable micro-/nano-structured smart polymeric materials. *Adv. Mat.* 2021, 2107877. doi:10.1002/adma.202107877

Wang, W., and Yeung, K. W. K. (2017). Bone grafts and biomaterials substitutes for bone defect repair: A review. *Bioact. Mat.* 2 (4), 224–247. doi:10.1016/j.bioactmat.2017.05.007

Wang, Y., Jiang, Y., Zhang, Y., Wen, S., Wang, Y., and Zhang, H. (2019b). Dual functional electrospun core-shell nanofibers for anti-infective guided bone regeneration membranes. *Mat. Sci. Eng. C Mat. Biol. Appl.* 98, 134–139. doi:10.1016/j.msec.2018.12.115

Wang, Z., Abdulla, R., Parker, B., Samanipour, R., Ghosh, S., and Kim, K. (2015). A simple and high-resolution stereolithography-based 3D bioprinting system using visible light crosslinkable bioinks. *Biofabrication* 7 (4), 045009. doi:10.1088/1758-5090/7/4/045009

Weinberg, C. B., and Bell, E. (1986). A blood vessel model constructed from collagen and cultured vascular cells. *Science* 231 (4736), 397–400. doi:10.1126/science.2934816

Wen, X. Y., Liu, Z., Wang, J., Tang, X. Y., Wang, W., Ju, X. J., et al. (2019). Nanocomposite hydrogels with optic-sonic transparency and hydroacoustic-sensitive conductivity for potential antiscouting sonar. *ACS Appl. Mat. Interfaces.* 11 (22), 20386–20393. doi:10.1021/acsami.9b04463

Weng, T., Zhang, W., Xia, Y., Wu, P., Yang, M., Jin, R., et al. (2021). 3D bioprinting for skin tissue engineering: Current status and perspectives. *J. Tissue Eng.* 12, 204173142110285. doi:10.1177/20417314211028574

Wu, H., Shen, L., Zhu, Z., Luo, X., Zhai, Y., Hua, X., et al. (2020). A cell-free therapy for articular cartilage repair based on synergistic delivery of SDF-1 and KGN with HA injectable scaffold. *Chem. Eng. J.* 393, 124649. doi:10.1016/j.cej.2020.124649

Wu, L., Li, H., Li, S., Li, X., Yuan, X., Li, X., et al. (2010). Composite fibrous membranes of PLGA and chitosan prepared by coelectrospinning and coaxial electrospinning. *J. Biomed. Mat. Res. A* 92 (2), 563–574. doi:10.1002/jbm.a.32393

Wu, P., Liang, Y., and Sun, G. (2021). Engineering immune-responsive biomaterials for skin regeneration. *Biomater. Transl.* 2 (1), 61–71. doi:10.3877/cma.j.issn.2096-112X.2021.01.008

Xia, L. W., Xie, R., Ju, X. J., Wang, W., Chen, Q., and Chu, L. Y. (2013). Nano-structured smart hydrogels with rapid response and high elasticity. *Nat. Commun.* 4, 2226. doi:10.1038/ncomms3226

Xia, Y., Wang, H., Yang, R., Hou, Y., Li, Y., Zhu, J., et al. (2023). Biomaterials delivery strategies to repair degenerated intervertebral discs by regulating the inflammatory microenvironment. *Front. Immunol.* 14, 1051606. doi:10.3389/fimmu.2023.1051606

Xie, J., Wu, X., Zheng, S., Lin, K., and Su, J. (2022). Aligned electrospun poly(L-lactide) nanofibers facilitate wound healing by inhibiting macrophage M1 polarization via the JAK-STAT and NF-κB pathways. *J. Nanobiotechnology* 20 (1), 342. doi:10.1186/s12951-022-01549-9

Xin, T., Mao, J., Liu, L., Tang, J., Wu, L., Yu, X., et al. (2020). Programmed sustained release of recombinant human bone morphogenetic protein-2 and inorganic ion composite hydrogel as artificial periosteum. *ACS Appl. Mat. Interfaces* 12 (6), 6840–6851. doi:10.1021/acsami.9b18496

Xiong, S., Zhang, X., Lu, P., Wu, Y., Wang, Q., Sun, H., et al. (2017). A gelatin-sulfonated silk composite scaffold based on 3D printing technology enhances skin regeneration by stimulating epidermal growth and dermal neovascularization. *Sci. Rep.* 7 (1), 4288. doi:10.1038/s41598-017-04149-y

Xu, C., Nam, J., Hong, H., Xu, Y., and Moon, J. J. (2019a). Positron emission tomography-guided photodynamic therapy with biodegradable mesoporous silica nanoparticles for personalized cancer immunotherapy. *ACS Nano* 13 (10), 12148–12161. doi:10.1021/acsnano.9b06691

Xu, D., Hu, J., Pan, X., Sanchez, S., Yan, X., and Ma, X. (2021). Enzyme-powered liquid metal nanobots endowed with multiple biomedical functions. *ACS Nano* 15 (7), 11543–11554. doi:10.1021/acsnano.1c01573

Xu, J. H., Zhao, H., Lan, W. J., and Luo, G. S. (2012). A novel microfluidic approach for monodispersed chitosan microspheres with controllable structures. *Adv. Healthc. Mat.* 1 (1), 106–111. doi:10.1002/adhm.201100014

Xu, R., Zhang, Z., Toftdal, M. S., Møller, A. C., Dagnaes-Hansen, F., Dong, M., et al. (2019b). Synchronous delivery of hydroxyapatite and connective tissue growth factor derived osteoinductive peptide enhanced osteogenesis. *J. Control. Release* 301, 129–139. doi:10.1016/j.jconrel.2019.02.037

Xu, X., Shi, D., Shen, Y., Xu, Z., Dai, J., Chen, D., et al. (2015). Full-thickness cartilage defects are repaired via a microfracture technique and intraarticular injection of the small-molecule compound kartogenin. *Arthritis Res. Ther.* 17 (1), 20. doi:10.1186/s13075-015-0537-1

Xue, J., Wu, T., Dai, Y., and Xia, Y. (2019). Electrospinning and electrospun nanofibers: Methods, materials, and applications. *Chem. Rev.* 119 (8), 5298–5415. doi:10.1021/acs.chemrev.8b00593

Yan, J., Lu, Y., Chen, G., Yang, M., and Gu, Z. (2018). Advances in liquid metals for biomedical applications. *Chem. Soc. Rev.* 47 (8), 2518–2533. doi:10.1039/C7CS00309A

Yang, C. H., Huang, K. S., and Chang, J. Y. (2007). Manufacturing monodisperse chitosan microparticles containing ampicillin using a microchannel chip. *Biomed. Microdevices* 9 (2), 253–259. doi:10.1007/s10544-006-9029-z

Yang, J., Deng, C., Shafiq, M., Li, Z., Zhang, Q., Du, H., et al. (2022). Localized delivery of FTY-720 from 3D printed cell-laden gelatin/silk fibroin composite scaffolds for enhanced vascularized bone regeneration. *Smart Mat. Med.* 3, 217–229. doi:10.1016/j.smaim.2022.01.007

Yang, M., Shuai, Y., Zhang, C., Chen, Y., Zhu, L., Mao, C., et al. (2014). Biomimetic nucleation of hydroxyapatite crystals mediated by *Antheraea pernyi* silk sericin promotes osteogenic differentiation of human bone marrow derived mesenchymal stem cells. *Biomacromolecules* 15 (4), 1185–1193. doi:10.1021/bm401740x

Yao, C. H., Yeh, J. Y., Chen, Y. S., Li, M. H., and Huang, C. H. (2017). Wound-healing effect of electrospun gelatin nanofibres containing *Centella asiatica* extract in a rat model. *J. Tissue Eng. Regen. Med.* 11 (3), 905–915. doi:10.1002/term.1992

Ye, K., Kuang, H., You, Z., Morsi, Y., and Mo, X. (2019). Electrospun nanofibers for tissue engineering with drug loading and release. *Pharmaceutics* 11 (4), 182. doi:10.3390/pharmaceutics11040182

Yeh, J., Ling, Y., Karp, J. M., Gantz, J., Chandawarkar, A., Eng, G., et al. (2006). Micromolding of shape-controlled, harvestable cell-laden hydrogels. *Biomaterials* 27 (31), 5391–5398. doi:10.1016/j.biomaterials.2006.06.005

Yi, L., Jin, C., Wang, L., and Liu, J. (2014). Liquid-solid phase transition alloy as reversible and rapid molding bone cement. *Biomaterials* 35 (37), 9789–9801. doi:10.1016/j.biomaterials.2014.08.048

Yin, H., Wang, J., Gu, Z., Feng, W., Gao, M., Wu, Y., et al. (2017). Evaluation of the potential of kartogenin encapsulated poly(L-lactic acid-co-caprolactone)/collagen nanofibers for tracheal cartilage regeneration. *J. Biomater. Appl.* 32 (3), 331–341. doi:10.1177/0885328217717077

Yoo, H. S., Kim, T. G., and Park, T. G. (2009). Surface-functionalized electrospun nanofibers for tissue engineering and drug delivery. *Adv. Drug Deliv. Rev.* 61 (12), 1033–1042. doi:10.1016/j.addr.2009.07.007

Yu, L., Cai, Y., Wang, H., Pan, L., Li, J., Chen, S., et al. (2020). Biomimetic bone regeneration using angle-ply collagen membrane-supported cell sheets subjected to mechanical conditioning. *Acta Biomater.* 112, 75–86. doi:10.1016/j.actbio.2020.05.041

Yuan, H., Qin, J., Xie, J., Li, B., Yu, Z., Peng, Z., et al. (2016). Highly aligned core-shell structured nanofibers for promoting phenotypic expression of vSMCs for vascular regeneration. *Nanoscale* 8 (36), 16307–16322. doi:10.1039/c6nr05075a

Zamani, R., Aval, S. F., Pilehvar-Soltanahmadi, Y., Nejati-Koshki, K., and Zarghami, N. (2018). Recent advances in cell electrospining of natural and synthetic nanofibers for regenerative medicine. *Drug Res.* 68 (8), 425–435. doi:10.1055/s-0043-125314

Zeng, J., Martin, A., Han, X., Shirihai, O. S., and Grinstaff, M. W. (2019). Biodegradable PLGA nanoparticles restore lysosomal acidity and protect neural PC-12 cells against mitochondrial toxicity. *Ind. Eng. Chem. Res.* 58 (31), 13910–13917. doi:10.1021/acs.iecr.9b02003

Zeng, M., and Fu, L. (2018). Controllable fabrication of graphene and related two-dimensional materials on liquid metals via chemical vapor deposition. *Acc. Chem. Res.* 51 (11), 2839–2847. doi:10.1021/acs.accounts.8b00293

Zhan, J., Singh, A., Zhang, Z., Huang, L., and Elisseeff, J. H. (2012). Multifunctional aliphatic polyester nanofibers for tissue engineering. *Biomatter* 2 (4), 202–212. doi:10.4161/biom.22723

Zhang, L., Beatty, A., Lu, L., Abdalrahman, A., Makris, T. M., Wang, G., et al. (2020). Microfluidic-assisted polymer-protein assembly to fabricate homogeneous functionalnanoparticles. *Mat. Sci. Eng. C Mat. Biol. Appl.* 111, 110768. doi:10.1016/j.msec.2020.110768

Zhao, Y., Fan, T., Chen, J., Su, J., Zhi, X., Pan, P., et al. (2019). Magnetic bioinspired micro/nanostructured composite scaffold for bone regeneration. *Colloids Surf. B Biointerfaces* 174, 70–79. doi:10.1016/j.colsurfb.2018.11.003

Zhao, Z., Li, G., Ruan, H., Chen, K., Cai, Z., Lu, G., et al. (2021). Capturing magnesium ions via microfluidic hydrogel microspheres for promoting cancellous bone regeneration. *ACS Nano* 15 (8), 13041–13054. doi:10.1021/acsnano.1c02147

Zheng, L., Liu, Y., Jiang, L., Wang, X., Chen, Y., Li, L., et al. (2023). Injectable decellularized dental pulp matrix-functionalized hydrogel microspheres for endodontic regeneration. *Acta Biomater.* 156, 37–48. doi:10.1016/j.actbio.2022.11.047

Zhong, Q., Li, W., Su, X., Li, G., Zhou, Y., Kundu, S. C., et al. (2016). Degradation pattern of porous CaCO3 and hydroxyapatite microspheres *in vitro* and *in vivo* for potential application in bone tissue engineering. *Colloids Surf. B Biointerfaces* 143, 56–63. doi:10.1016/j.colsurfb.2016.03.020

Zhou, P., Wu, J., Xia, Y., Yuan, Y., Zhang, H., Xu, S., et al. (2018). Loading BMP-2 on nanostructured hydroxyapatite microspheres for rapid bone regeneration. *Int. J. Nanomedicine* 13, 4083–4092. doi:10.2147/ijn.S158280

Zhu, W., Ma, X., Gou, M., Mei, D., Zhang, K., and Chen, S. (2016). 3D printing of functional biomaterials for tissue engineering. *Curr. Opin. Biotechnol.* 40, 103–112. doi:10.1016/j.copbio.2016.03.014

Zuo, Y., He, X., Yang, Y., Wei, D., Sun, J., Zhong, M., et al. (2016). Microfluidic-based generation of functional microfibers for biomimetic complex tissue construction. *Acta Biomater.* 38, 153–162. doi:10.1016/j.actbio.2016.04.036

Zupančič, Š., Sinha-Ray, S., Sinha-Ray, S., Kristl, J., and Yarin, A. L. (2016). Controlled release of ciprofloxacin from core-shell nanofibers with monolithic or blended core. *Mol. Pharm.* 13 (4), 1393–1404. doi:10.1021/acs.molpharmaceut.6b00039

Frontiers in
Bioengineering and Biotechnology

Accelerates the development of therapies, devices, and technologies to improve our lives

A multidisciplinary journal that accelerates the development of biological therapies, devices, processes and technologies to improve our lives by bridging the gap between discoveries and their application.

Discover the latest Research Topics

See more →

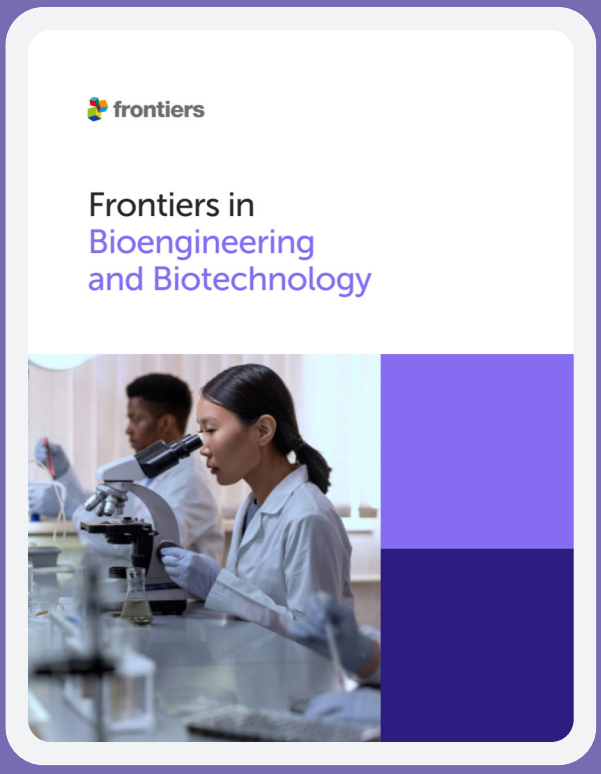

Frontiers

Avenue du Tribunal-Fédéral 34
1005 Lausanne, Switzerland
frontiersin.org

Contact us

+41 (0)21 510 17 00
frontiersin.org/about/contact